Interrogating fungal adjuvant and glycan nanoparticles for modulating interleukin-23 expression via the dendritic cell receptor DC-SIGN

Maisie Emma Holbrow-Wilshaw

Submitted in accordance with the requirements for the degree of Doctor of Philosophy

The University of Leeds

Faculty of Medicine and Health

Leeds Institute of Rheumatic and Musculoskeletal Medicine (LIRMM)

September 2025

The candidate confirms that the work submitted is their own, and that appropriate credit has been given where reference has been made to the work of others.

Acknowledgements

There are many people to whom I would like to extend my thanks to for helping me over the course of my PhD. Firstly, I would like to thank my primary supervisor, Professor Dennis McGonagle, for his guidance, ongoing support, and (extremely) enthusiastic belief in my skills as a chemist and immunologist. I would also like to thank my co-supervisors in the Schools of Chemistry, and Food Science and Nutrition; Professor's Dejian Zhou, Yuan Guo and Bruce Turnbull. Their guidance, teaching, and advice has helped me greatly throughout my time at the University of Leeds and on this project. A special thanks must also go to my supervisor Dr Thomas Macleod for educating me in many new techniques and being my go-to guru of all things immunology.

In addition I would like to thank those who have provided help and support with my project; Iain Manfield for his hard work in running my ITC samples, Ranjani Ganji and Chhaya Patole for their efforts with my proteomics samples and analysis and Stephen Reid for performing the ICP-MS analysis. I must also thank Inga Nehlmeier, Amy Madeleine Kempf, and Professor Dr Stefan Pöhlmann (German Primate Center, Göttingen, and Faculty of Biology and Psychology, Georg-August-University Göttingen) who prepared and performed the viral inhibition assays. Xinyu Ning and Qian Peng have been both wonderful colleagues and patient teachers, providing help with gold nanoparticle synthesis and DC-SIGN preparation. My gratitude goes to Darshita for synthesising well over three years' worth of dimannose.

Furthermore I would like to thank my friends who also happen to be colleagues. Nicole, Heather, Rekha, Ala, Mark, Tom and Chi; thank you for the well-timed coffee breaks at Thackeray and for always indulging me in conversation. Erin and Abi have been there for most things - coffees, deep discussions, co-op biscuit runs, two pints before dinner, and listening to me whine about self-inflicted triathlon training. You truly have been the best and most supportive colleagues and friends I could have shared an office with.

To my friends and family who I spend my life outside of academia with - I simply could not have done this without you. Without starting this PhD I wouldn't have met Anna, but without Anna I wouldn't have finished this PhD. Thank you for all the exercise, advice and giggles, there truly is no one else I'd rather run laps of West Park, or laugh late into the evening with. Thank you to Lucy for the weekly runs, and Meg and Anna B for the Bottle Chop bike rides. These have kept me sane throughout lab work and especially through write up. My parents and George, along with my oldest friend (literary genius Nina Booth), have been my biggest supporters since day one and have provided endless love and support in all my pursuits, no matter how outlandish they seemed at first. You are wonderful and I am so fortunate to have you.

Abstract

The seronegative spondyloarthropathies (SpA) are a group of inflammatory diseases affecting the joints. They are intricately linked to interleukin (IL) -23 biology and respond to anti-IL-23 directed therapy. Although established as a pivotal cytokine in the pathogenesis of SpA, the *in vivo* factors that regulate IL-23 production, both overproduction and downregulation, remain poorly defined. The IL-23/IL-17 pathway is also inextricably linked to fungal immunity and emerging evidence suggests that intestinal microbiota and fungal cell wall glycans may critically influence IL-23 production. Mannose and fucose containing carbohydrates represent a large proportion of the molecules present on bacterial and fungal surfaces and are key binders to the tetrameric C-type lectin DC-SIGN, making this lectin a potential candidate for triggering high IL-23 production by dendritic cells (DCs) *in vivo.*

This thesis is split into two parts and investigates how DC-SIGN is involved in the regulation and modulation of the IL-23/IL-17 axis in DCs. Part A explored the importance of multivalent lectin-glycan interactions (MLGIs). A detailed understanding of how multivalent ligands interact with tetrameric lectin DC-SIGN, including the underlying structural and biophysical mechanisms, is vital to design glycoconjugates that can potently and selectively target MLGIs for therapeutic intervention. Such insights can also clarify how variations in glycan type and flexibility induce distinct signalling outcomes. To this effect, glycan conjugated gold nanoparticles (GNP-glycans) were developed to probe MLGIs with DC-SIGN. Binding studies combining dynamic light scattering, isothermal titration calorimetry, and a fluorescence quenching assay were used to provide structural information on DC-SIGN, e.g. binding site orientation, binding mode, and inter-binding site spacing, which is critical to design specific multivalent binders. These studies further revealed how key aspects of glycoconjugate design can affect the binding affinity. Importantly, multivalency enhanced binding affinity into the low nanomolar range but was impacted by linker length, density and glycan type, which was intricately linked to both thermodynamic contributions and binding mode. Increasing the linker length weakened binding affinity due to the increased entropic penalty upon constraining longer, more flexible linkers, and lowering the glycan density reduced enthalpy changes of binding due to increased strain and a reduced ability of GNP-glycans to bridge multiple carbohydrate recognition domains (CRDs) on one lectin simultaneously. These GNP-glycans potently inhibited DC-SIGN-mediated augmentation of Ebola virus glycoprotein-driven cell entry, with a positive correlation observed between binding affinity and IC_{50}, demonstrating the therapeutic potential of multivalent glycoconjugates.

Part B explored how signalling through DC-SIGN can modulate IL-23 production in DCs. Cooperation between different innate signalling pathways in DCs is crucial for initiating

adaptive immunity to pathogens, and carbohydrate-specific signalling through DC-SIGN provides DCs with the plasticity to tailor immunity to the nature of invading microbes. Here, DCs were co-stimulated with Toll-like receptor ligands in the presence of the DC-SIGN ligands, and their cytokine responses were compared to controls in the absence of DC-SIGN ligands. While free fucose and dimannose ligands differentially regulated IL-23 production, GNP-glycans did not significantly modulate IL-23 production, despite exhibiting nanomolar binding affinity to DC-SIGN, highlighting the importance of ligand concentration and glycoconjugate shape/size, as well as binding strength, in initiating signalling cascades. Furthermore, fucose and dimannose ligands skewed T cell responses toward Th17 and Th2 profiles, respectively. Blocking DC-SIGN did not totally abrogate immune modulation, indicating the input of other mannose and fucose binding lectins in co-signalling. Therefore, a GNP based affinity pull down assay was developed as a way to isolate and identify other GNP-glycan binding proteins on the cell surface. Interaction between the dimannose based affinity tags and DC-SIGN was glycan specific, and selective over non-targets. Proteomic approaches were used to identify the isolated DC-SIGN from its peptide sequence.

Overall, these findings advance understanding of DC-SIGN–mediated regulation of the IL-23/IL-17 axis, reveal structural principles underpinning multivalent glycan recognition, and point toward strategies for therapeutic modulation of inflammatory and infectious disease pathways.

Table of Contents

List of Tables

List of Figures

List of Abbreviations

A	Acceptor fluorophore
APC	Antigen presenting cell
AS	Ankylosing spondylitis
BSA	Bovine serum albumin
CARD	Caspase recruitment domain-containing protein
cDC	Conventional dendritic cell
CLR	C-type lectin receptor
ConA	Concanavalin A
CRD	Carbohydrate recognition domain
CTLA	Cytotoxic T-lymphocyte associated protein
CuAAC	Copper catalysed azide alkyne cycloaddition
D	Donor fluorophore
DAMP	Damage associated molecular pattern
DCC	N,N'-Dicyclohexylcarbodiimide
DCM	Dichloromethane
DC	Dendritic cell
DC-SIGN	Dendritic cell-specific intercellular adhesion molecule-3 grabbing non-integrin
DC-SIGNR	DC-SIGN related
DHLA	Dihydrolipoic acid
D_h	Mean hydrodynamic diameter
Dimannose	Mannose-(1,2)-α-mannose
DLS	Dynamic light scattering
DMAP	4-Dimethylaminopyridine
DMF	Dimethylformamide
DMSO	Dimethyl sulfoxide
DTT	Dithiothreitol
EAE	Experimental autoimmune encephalomyelitis
EBOV	Ebolavirus
ECA	*Erythrina cristagalli* agglutinin
ECD	Extracellular domain
EDTA	Ethylenediaminetetraacetic acid
EG	Ethyleneglycol

ELISA	Enzyme-linked immunosorbent assay
ER	Endoplasmic reticulum
FBS	Foetal bovine serum
FCC	Flash column chromatography
FCS	Foetal calf serum
FITC	Fluorescein isothiocyanate
FMO	Fluorescence minus one
FRET	Fluorescent (Förster) resonance energy transfer
FWHM	Full width at half maximum
G5	5 nm Gold nanoparticle
G13	13 nm Gold nanoparticle
G27	27 nm Gold nanoparticle
Gal	D-galactose
GF	Germ free
GLR	Gold to ligand ratio
GM-CSF	Granulocyte-macrophage colony-stimulating factor
GNP	Gold nanoparticle
GP	Glycoprotein
HIV	Human immunodeficiency virus
HKST	Heat killed *salmonella typhimurium*
HLA	Human leukocyte antigen
HRMS	High resolution mass spectrometry
IAA	Iodoacetamide
IC_{50}	Concentration at 50% inhibition
ICAM	Intracellular adhesion molecule
ICP-MS	Inductively coupled plasma mass spectrometry
IFN	Interferon
IL	Interleukin
IPTG	Isopropyl β-D-1-thiogalactopyranoside
ITC	Isothermal titration calorimetry
HEPES	4-(2-hydroxyethyl)-1-piperazineethanesulfonic acid
HKST	Heat killed Salmonella typhimurium
K_a	Equilibrium binding association constant
K_d	Equilibrium binding dissociation constant
LA	Lipoic acid
LB	Lysogeny broth

LC-MS	Liquid chromatography mass spectrometry
LDL-R	Low-density lipoprotein receptor
LE	Labelling efficiency
LGI	Lectin glycan interaction
LPS	Lipopolysaccharide
Man	D-Mannose
MHC	Major histocompatibility complex
MLGI	Multivalent lectin glycan interaction
MMR	Macrophage mannose receptor
MoDC	Monocyte derived dendritic cell
MW	Molecular weight
m/z	Mass to charge ratio
n	Hill coefficient
NA	Normalised activity
NF-κB	Nuclear factor kappa-light-chain-enhancer of activated B cells
NLR	NOD-like receptor
NMR	Nuclear magnetic resonance
NND	Nearest neighbour distance
NOD	Nucleotide oligomerisation domain
NSET	Nano surface energy transfer
OD	Optical density
PAMP	Pathogen associated molecular pattern
PBMC	Peripheral blood mononuclear cell
PBS	Phosphate-buffered saline
PDB	Protein databank
pDC	Plasmacytoid dendritic cell
PCI	Protein carbohydrate interaction
P	Hill slope
PCI	Protein carbohydrate interaction
PGR	Protein to gold ratio
PMA	Phorbol myristate acetate
PNA	Peanut agglutinin
Pre cDC	Common DC progenitors
PRR	Pattern recognition receptor
PsA	Psoriatic arthritis
QD	Quantum dot

QE	Quenching efficiency
R_0	Forster radius
R^2	Coefficient of determination
RA	Rheumatoid arthritis
RPMI	Rosewell Park Memorial Institute
RCA	*Ricinus communis* agglutinin
r.t	Room temperature
SD	Standard deviation
SF	Sulfonyl fluoride
SNP	Single nucleotide polymorphism
SpA	Seronegative spondyloarthropathies
SPF	Specific pathogen free
SPR	Surface plasmon resonance
TBAI	Tetra-n-butylammonium iodide
TBTA	Tris[(1-benzyl-1H-1,2,3-triazol-4-yl)methyl]amine
TCEP	Tris (2-carboxyethyl) phosphine
TCR	T cell receptor
TEM	Transmission electron microscopy
TGF	Transforming growth factor
THF	Tetrahydrofuran
TLC	Thin layer chromatography
TLR	Toll-like receptor
TNF	Tumour necrosis factor
TNFR	Tumour necrosis factor receptor
Tris base	2-amino-2-(hydroxymethyl)propane-1,3-diol
UPR	Unfolded protein response
UV-Vis	Ultraviolet to visible light
VSV	Vesicular stomatitis virus
VSV-G	Vesicular stomatitis virus G protein
WB	Western blot
$\Delta G°$	Standard Gibbs free energy change of association
$\Delta H°$	Standard enthalpy change of association
$\Delta S°$	Standard entropy change of association
λ_{abs}	Absorption wavelength
λ_{em}	Emission wavelength
λ_{ex}	Excitation wavelength

Part A

Development of glyconanoparticles to investigate biophysical and structural mechanisms of DC-SIGN multivalent lectin-glycan binding

Chapter 1 – Introduction

1.1 Protein carbohydrate interactions

Protein-carbohydrate interactions (PCIs) are central to a wide array of biological processes, mediating functions such as cell adhesion, cell-cell communication and signal transduction. PCIs are crucial for pathogen recognition via pathogen associated molecular patters (PAMPs) thereby triggering host immune defences against infections. Protein trafficking, protein stability, cell growth, cytokine modulation and homeostatic regulation also all require specific PCIs to occur. These interactions are facilitated by carbohydrate binding proteins (e.g. lectins), glycosidases and antibodies, which recognise and bind specific glycan structures on glycoproteins, glycolipids or free oligosaccharides.(1) Due to the structural diversity of carbohydrates, PCIs are typically characterised by high specificity but are relatively low affinity for monovalent binding, often relying on multivalency and optimal spatial arrangements for biological effectiveness.(2)

In nature, PCIs are not limited to animal systems, but are also widespread and functionally significant in other organisms, including plants, fungi and bacteria. In plants, lectins play vital roles in defence mechanisms and nutrition storage, and fungi can secrete carbohydrate active enzymes to degrade plant cell walls to aid in nutrition acquisition. Additionally, in microbial systems, bacterial adhesins exploit host glycan structures to initiate colonisation, and viruses frequently depend on glycan receptors to enter host cells. These examples underscore the widespread importance of PCIs across different biological kingdoms.(3)

1.1.1 PCIs in immunology

In the extracellular matrix (e.g. in solution), PCIs are mostly involved in development, respiration, coagulation, angiogenesis and inflammation.(4) However in animal and host-microbe systems, membrane bound PCIs are indispensable players in innate and adaptive immune recognition, regulation and response. Immune cells utilise PCIs to sense their microenvironment and coordinate appropriate responses. On immune cell surfaces, glycan-binding proteins such as C-type lectins (CLRs), sialic acid binding immunoglobulin-like lectins (siglecs) and selectins act as molecular sensors of glycan patterns associated with pathogens or self-danger signals to facilitate immune surveillance and modulation.(5) Glycans act as molecular signals, with the type and structure of the glycans allowing cells to distinguish between self and non-self, healthy and diseased states. The ability to recognise and interpret these glycan patterns

underpins essential processes such as immune cell trafficking, pathogen elimination, inflammation and immunological tolerance (Figure 1.1).(6-8)

Pattern recognition receptors (PRRs) like CLRs bind pathogen-associated glycan motifs, initiating phagocytosis, endocytosis, antigen presentation and cytokine production. In parallel, cell adhesion molecules such as selectins guide the migration of leukocytes to sites of infection or injury by recognising glycosylated ligands on the endothelium, and siglecs help maintain tolerance to self-glycans.(9, 10) These interactions ensure that immune responses are precisely located and regulated. Furthermore, PCIs are not only vital for innate immunity, but also orchestrate interactions between antigen presenting cells (APCs) and lymphocytes, facilitating the activation of adaptive immunity.(11)

However, these systems can also be exploited to contribute to disease. Many viruses, including HIV, influenza and SARS-CoV-2 exploit lectin receptors to facilitate cell entry into cells and/or escape immune surveillance.(12) Once inside cells, some viruses can exploit CLR mechanisms to circumvent antigen processing and alter signalling, ultimately skewing T cell responses and escaping immunity.(13-15) Similarly, bacterial adhesins often recognise host glycan patterns to colonise tissues and initiate infection, exemplified by uropathogenic *Escherichia coli* which utilises its FimH adhesin to recognise and bind endothelial cell mannose in the urinary tract.(16) These pathogenic strategies demonstrate how PCIs can be manipulated to bypass immune surveillance and initiate infection.

In the context of cancer, altered glycosylation patterns is an indicator of malignant transformation. Tumour cells frequently express abnormal glycan structures such as *O*-glycans, or those with increased sialylation or fucosylation.(17) Such changes modulate the interaction of cancer cells with the immune system, either suppressing the immune response by masking receptor binding sites on the cancer cell surface, or engaging inhibitory receptors such as siglecs on NK cells and macrophages, thereby promoting immune suppression and tolerance of the tumour.(18) Additionally, PCIs between tumour cells and selectins on platelets or endothelial cells can promote tissue invasion.(19) Thus PCIs contribute not only to immune evasion but also to the physical spread of cancer.

PCIs are also deeply implicated in autoimmune and inflammatory diseases. In these diseases, immune cells may misinterpret self-glycans as foreign, leading to chronic immune activation and tissue damage. This breakdown in self-tolerance has been linked to conditions such as rheumatoid arthritis(20), type 1 diabetes(21), lupus and multiple sclerosis.(4) In some cases, pathogens may trigger autoimmunity through molecular mimicry, where foreign glycans resemble self-structures, misleading the immune system into attacking self-components.(22) Furthermore the dysregulation of glycan-mediated

signalling pathways can result in persistent inflammation and immune dysfunction, exacerbating disease progression (Figure 1.1).(23)

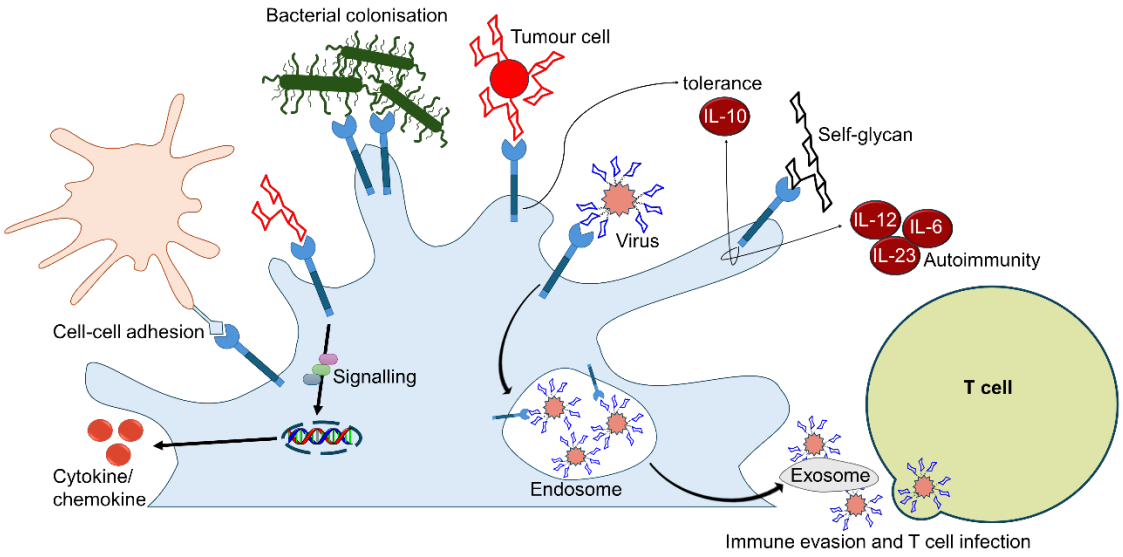

Figure 1.1 Schematic depicting the involvement of PCIs in many different immunological processes from cell adhesion, immune signalling and modulation, to bacterial colonisation of host cells, tumour cell mediated immune suppression, self-tolerance, autoimmune disease, and viral immune escape and T cell infection.

Given their ubiquitous nature in regular immune function and their role in cancer, infection and autoimmune diseases, PCIs have become attractive targets for studying to further understand their functions, and for the design of new immune-related therapeutics to combat these issues. For instance, the carbohydrate polymer hyaluronic acid (HA) has been employed on microparticles for targeted drug delivery of doxorubicin to $CD44^+$ tumour cells, while glycan modified peptides are being developed to dual inhibit HIV entry into both dendritic cells (DC) and T cells.(24, 25) Furthermore, carbohydrate immune modulation though PCI induced signalling offers new possibilities for immunotherapy and prolonged allograft survival.(26)

Understanding the molecular principles that govern these PCIs is critical for elucidating mechanisms of cellular communication and for advancing therapeutic and diagnostic strategies in fields such as oncology, infectious disease and immunology. This chapter provides an introduction to the relevance of PCIs in the immune system, specifically those mediated through the C-type lectin, DC-SIGN, and gives an overview of the use of glyconanotechnology to explore such interactions.

1.2 C-type lectin receptors

Many of the fundamental PCIs involved in immunity, and those which are studied in this thesis, are mediated through CLRs. CLRs are an extensively characterised class of

receptor, primarily expressed on cells of myeloid lineage (DCs, macrophages, monocytes), which bind to carbohydrate structures present on cell wall components of pathogens, in a calcium (Ca^{2+}) dependent manner.(27-30) Once bound to a carbohydrate motif, the main function of a CLR is to capture pathogens for intracellular degradation. CLRs can also transduce signals upon ligand recognition and induce cytokine production, however, most CLR signalling acts through modulating cellular signalling pathways initiated though ligand interactions with alternative receptors such as Toll-like receptors (TLRs) and nucleotide oligomerisation domain (NOD)-like receptors (NLRs).(31) While recognition of pathogenic carbohydrates by CLRs is vital in pathogen detection, pathogen internalisation and antigen presentation on APCs, CLRs are also able to differentiate between these structures and similar motifs on self (endogenous)-glycoproteins (such as blood group antigens).(30, 32) This allows tolerance to self-antigens and avoids the onset of autoimmune diseases.(33)

The CLR superfamily comprises over 1,000 proteins, which is further divided into 17 subgroups depending on their phylogeny and domain organisation.(34-36) Among these, two main structural types of CLR are expressed on DCs; type I and type II. These are distinguished primarily by their molecular orientation and domain architecture. Type I CLRs have their amino (N) termini pointing extracellularly whereas type II CLRs have their N termini pointing into the cytoplasm of the cell. They also differ in the number of carbohydrate recognition domains (CRDs) available for binding.(29) Type I CLRs possess multiple CRDs or CRD-like domains in their extracellular region enabling multivalent binding. In contrast, type II surface lectins contain just one CRD at their carboxyl-terminal extracellular domain. Both types are anchored in the cell membrane by a short transmembrane region, with a cytoplasmic tail extending into the cytoplasm which often contains signalling or internalisation motifs, important for signal transduction, immune activation and endocytosis (Figure 1.2).(37)

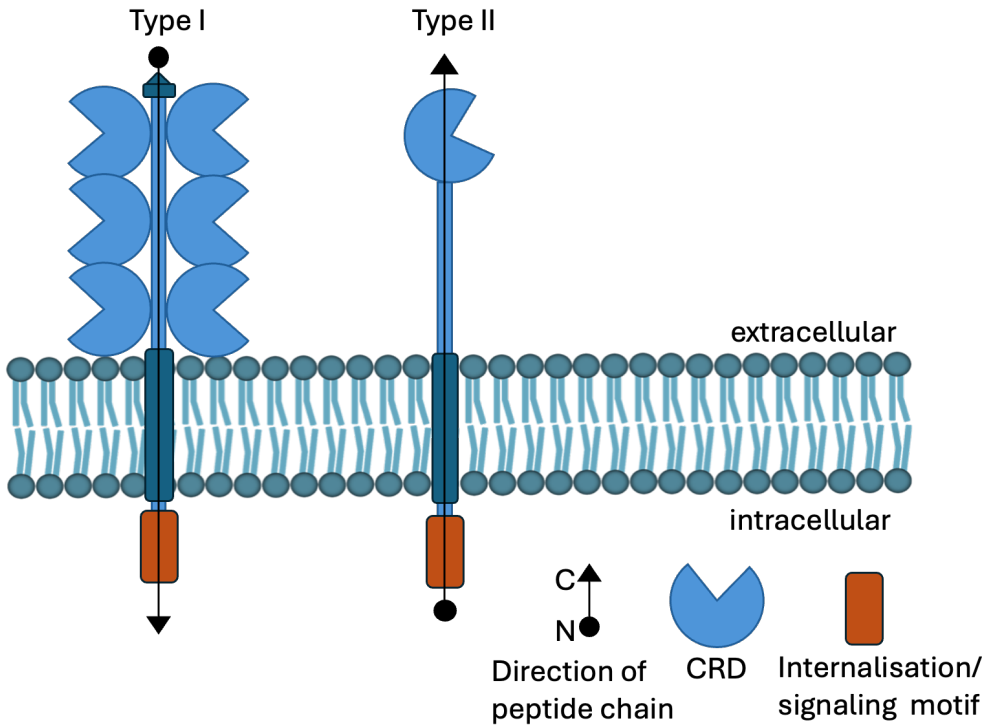

Figure 1.2 Representation of a typical type I and II C-type lectin.

Many different CLRs expressed on DCs have been described to date, most of which conform to the type II features. These include, but are not limited to; macrophage inducible C-type lectin receptor (Mincle), Dectin-1(38), Dectin-2, DC immunocore receptor (DCIR)(39), Langerhans cell-specific C-type lectin (langerin)(40), dendritic cell lectin (DLEC), dendritic cell-specific ICAM-3 grabbing non-integrin (DC-SIGN)(14), and C-type lectin 1 (CLEC)(41), which all contain just one CRD at each C-terminal end. Among frequently expressed type I transmembrane receptors are the macrophage mannose receptor (MMR) and DEC205 which have 8 and 10 CRDs, respectively.(42-45) Not all receptors are expressed by each subcategory of DCs. In fact, langerin is expressed exclusively by Langerhans cells, a skin resident DC subset.(46) Monocyte derived DCs express the widest range and diversity of CLRs.

Appropriate immune responses to invading pathogens are associated with the recognition of PAMPs by CLRs. Once a particular pattern has been recognised, an internalisation, degradation and antigen presentation sequence is triggered; a process that is highly dependent on specific internalisation motifs present in the cytoplasmic domains of the triggered receptor. These short-sequence motifs are recognised by adaptor proteins involved in the endocytic and sorting pathway which ensure dynamic movement and designated distribution of transmembrane receptors and ligands into intracellular compartments. Such sequences include the di-leucine motif (Leu-Leu), tyrosine based sequences or the tri acidic cluster (Glu-Glu-Glu).(47-49) Once delivered into a lysosome, the receptor-ligand complex is degraded, then the antigenic products of

this degradation are presented by MHC (major histocompatibility complex) class II molecules to $CD4^+$ T cells to initiate T cell priming. Under alternative conditions, the bound ligand may be released in the endosome for further processing but the receptor is recycled back to the cell surface to bind new ligands for further internalisation, resulting in enhanced antigen uptake and presentation by DCs (Figure 1.3).(50)

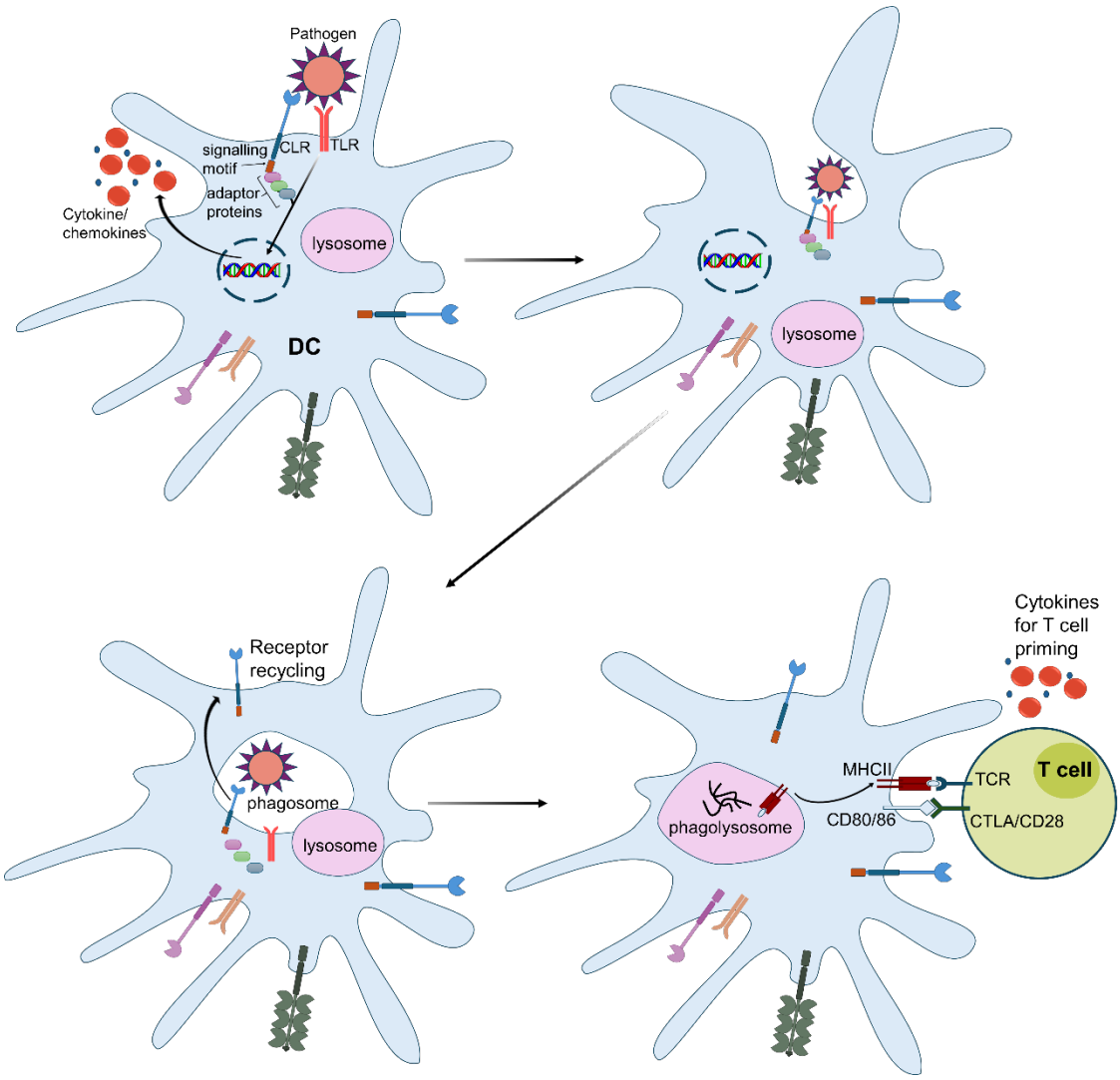

Figure 1.3 Schematic of the recognition of pathogens by CLRs and TLRs. Immature DCs express TLRs and CLRs that bind specific pathogen components and carbohydrate structures, respectively. Pathogen recognition by TLRs induces a signalling cascade, resulting in the production of cytokines and DC maturation (upregulation of CD80/86). The recognition of pathogens by C-type lectins leads to internalisation of pathogens and intracellular processing for presentation by MHC class I and II molecules to T cells through the T cell receptor (TCR).

Although many CLRs, such as DEC-205, MMR and langerin, exert endocytic activity, there is limited evidence to suggest that they alone can induce the gene transcription required for innate immunity to infection, instead requiring signalling cross-talk with TLRs to induce the desired immune response.(51) However, evidence suggests that, upon engagement, some CLRs can directly induce signalling pathways to elicit the production of tailor-made cytokine profiles, essentially orchestrating T cell differentiation and regulating innate and adaptive immune responses self-sufficiently.(49) Upon engagement of Dectin-1 by β-(1-3)-glucan (produced by fungi) intracellular signalling pathways activate transcription which ultimately results in efficient pro-inflammatory immune responses, which are crucial for antifungal immunity.(34, 38, 52) While some CLRs, such as Dectin-1, elicit pro-inflammatory responses, others will dampen myeloid cell activation and inhibit cytokine expression.(53)

It is undisputed that CLRs have a clearly defined role in immunity, however their function does not end with exertion against microbes. Myeloid CLRs are also essential in the detection of abnormal and dead cells as well as having functions related to cancer by supporting the interaction of cancer cells with platelets, leukocytes and endothelial cells, thereby facilitating immune suppression.(19) Dead cells are recognised by their exposed mannose and fucose structures and this process is crucial for maintaining tissue and organ homeostasis.(4, 34) The wide variety of functions displayed by CLRs makes them attractive targets for drug and vaccine candidates. This is, however, not without its difficulties, as broad overlaps in the specificities for naturally occurring carbohydrate ligands still makes targeting singular CLRs difficult, especially under *in vivo* conditions.(36)

1.3 Lectin glycan interactions

Lectin glycan interactions (LGIs) typically occur through a lectins' carbohydrate recognition domain (CRD), and binding within this site is dependent on complexation of carbohydrate hydroxyl groups to a Ca^{2+} cofactor, through the formation of Ca^{2+}-OH coordination bonds at the 3- and 4- hydroxyl sites (Figure 1.4).(32, 36, 54) Conserved amino acid residues within the CRD will determine its preference for a particular carbohydrate molecule, for example Glu-Pro-Asn and Gln-Pro-Asp confer specificity for mannose-type and galactose-type motifs, respectively.(35, 37, 55) This is due to the formation of four further H bonds between amino acid carbonyl residues with the 3- and 4- hydroxyl groups, which are spatially oriented in different positions in the cases of galactose and mannose, enabling the differing preference.(35) Mutation of calcium sites results in loss of ligand binding, showing Ca^{2+} complexation is fundamental to CLR-carbohydrate binding.(56) The specificity of a lectin is also shaped by its distinctive structural features. Strong LGIs can only occur when the carbohydrate residues on a

glycoprotein or complex glycan align to fit the spatial constraint imposed by the lectins' CRD binding pocket, so as to form strong intermolecular interactions while avoiding steric clashes.

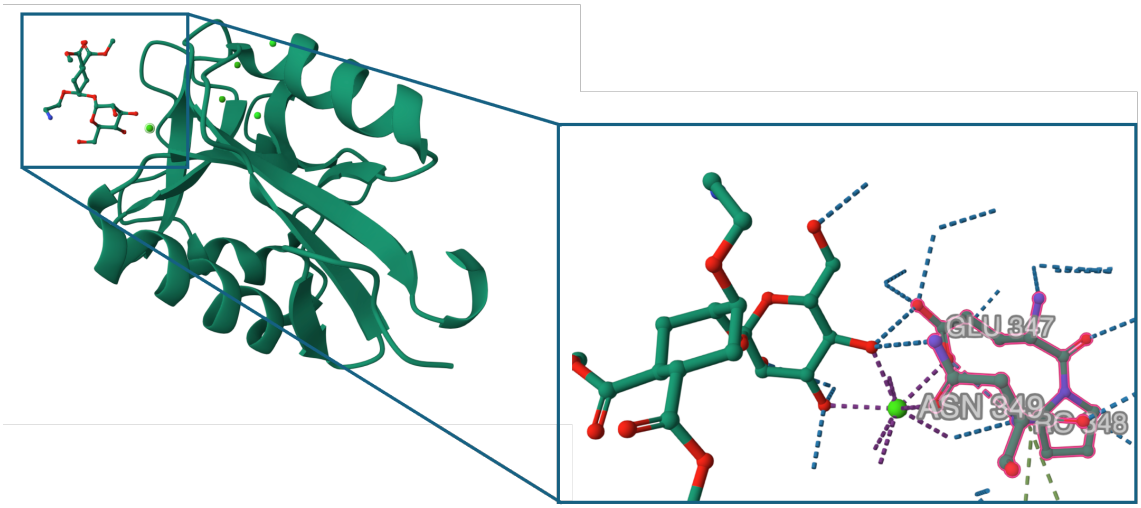

Figure 1.4 Diagram depicting calcium dependent binding within a CRD. Shown is a pseudo-mannosylated ligand bound in the major binding mode to DC-SIGN (PDB: 2XR5). The close-up highlights coordination of the mannose residue to the calcium ion (purple dash line, light green dot) through its 3-and 4-hydroxyl groups, illustrating the central role of calcium in carbohydrate recognition within a lectin CRD. Also highlighted are the directions of four further hydrogen bonds (blue dash lines) between 3- and 4- hydroxyl groups towards other DC-SIGN residues (Glu347, Asn349) which help determine the carbohydrate preference of a lectin.

The primary carbohydrate binding site on a CLR is located in the 'long loop' - a region of protein which is characterised by high flexibility, but this site is often shallow and exposed to surrounding solvent.(57) The resulting effect is that polar carbohydrates are constantly in binding competition with surrounding water molecules which engage in similar hydroxyl interactions within the CRD.(58) So despite having high specificity, as a consequence of competing coordination with water hydroxyl groups, monosaccharide binding is typically weak and is associated with high dissociation constants (K_d), often in the millimolar concentration range. Such level of binding is often too weak to be considered biofunctional.(36)

Binding strength can be increased when additional parts of an oligosaccharide interact with regions of the protein beyond the canonical Ca^{2+} site.(36) This multivalent engagement forms the basis for glycomimetic design, where synthetic molecules mimic not just the primary glycan structure, but also make contacts with surrounding regions of the protein to enhance affinity and specificity. As well as having low binding affinities, carbohydrates suffer from high polarity, quick metabolic turnover and other poor pharmacokinetic properties.(59) Development of glycomimetics looks to overcome these

disadvantages by designing molecules to be less polar and allowing secondary interactions. Common modifications might include the addition of an aryl moiety; able to participate in hydrophobic CH-pi stacking interactions.(60) Enhancing the binding affinity of sugars in this manner allows C-type lectins to become more plausible as ‘druggable’ targets.(58)

Although new glycomimetics are emerging and exhibit stronger binding compared to unmodified monosaccharides, the strongest binding is observed between C-type lectins and highly multivalent ligands with multiple branched, repeating structures that may engage multiple low-affinity binding sites simultaneously.(2, 61, 62). This high-affinity binding is a key influence in pathogen uptake, internalisation and degradation. Bacteria, parasites and fungi all have complex and unique glycosylation patterns, often coined their ‘carbohydrate fingerprint’, which are extended and branched and therefore able to engage multiple binding sites at once.(49, 63) This intricate pattern of carbohydrates increases specificity, and subtle differences in composition and quantity of particular carbohydrates in these ‘fingerprints’ assists DCs in being able to differentiate between similar structures on foreign and host cells. For example, structures with high mannose content and terminal mannose or *N*-acetylglucosamine are more prevalent in viral glycoprotein envelopes and are rarely found on mammalian cell surfaces, making host and foreign cells distinctly identifiable from one another.(64, 65)

Because of the need for multivalent interactions to propagate functional signalling cascades, and since many biologically relevant ligands are branched and multivalent, lectins will commonly form oligomers in which multiple CRDs are clustered together. This alters the specificity and affinity of carbohydrate recognition in a way such that a spatially matched multivalent ligand can bind multiple CRDs simultaneously and boost binding affinity into the nanomolar range. Such examples of clustering is observed in the mannose binding protein and DC-SIGN, which form trimers and tetramers, respectively.(66)

Biological systems use multivalent interactions for a number of functional advantages beyond increased specificity, including but not limited to; tight binding from ligands with low surface area, signalling induction by large conformational changes, changing molecular distribution, creating conformational contact between large biological surfaces and grading biological signalling.(2)

1.4 DC-SIGN

Since its discovery in 1992, arguably the most widely studied member of the CLR family is the dendritic cell-specific ICAM-3 grabbing non-integrin (DC-SIGN).(67) DC-SIGN is

most abundantly expressed by immature myeloid DCs and is also found on dermal, interstitial and a subset of blood DCs.(48, 68)

1.4.1 DC-SIGN structure

In the extracellular region, like other type II transmembrane proteins, DC-SIGN has just one carbohydrate recognition domain, atop of an alpha-helical neck region consisting of a 23 amino acid sequence, repeated 7.5 times.(69) A transmembrane region is then followed by the cytoplasmic tail, which contains the di-leucine, tri-acidic and tyrosine motifs, essential for ligand internalisation and receptor recycling.(15)

A central trait to DC-SIGN is its inclination to exist in a tetrameric format. The tetramerization of DC-SIGN is mediated by the alpha helices of the neck-repeat domain (Figure 1.5).(66, 70) The helical nature of the extracellular neck is archetypal of the hydrophobic amino acids residues present in recurring intervals of 3-5, which are driven to stack spontaneously in their quest to avoid the hydrophilic nature of the extracellular region. Lateral interactions between the 23 amino acid sequences in individual helices forms a coiled coil and stabilises oligomerisation.(71) By creating a series of truncated forms of DC-SIGN, Feinberg *et al.* even demonstrated that oligomerisation into a tetramer is reliant on at least 6 helical repeat units in the neck region. 3-5.5 Repeats will provoke an equilibrium between tetrameric and dimeric forms, while fewer than three repeats will put the equilibrium between dimer and monomer.(71)

The organisation of DC-SIGN into tetramers is extremely influential in the lectin's affinity in binding ligands bearing carbohydrate moieties.(72) The stabilising interactions between neck regions of DC-SIGN direct all four of the carbohydrate recognition domains to point upwardly from the cell surface.(73) This creates the perfect binding platform for a spatially matched ligand to interact in a multivalent manner. Simultaneous binding of spatially matched multivalent binding partners creates a single entity and, as such, gives the highest affinity enhancement and selectivity due to the most favourable enthalpy terms.(74) Oligomerisation of CRDs also enables amplification of ligand specificity and dictates the distinct sets of pathogens recognised by DC-SIGN; while both the mannose binding protein and DC-SIGN recognise mannose, the mannose binding protein is known to form trimers whereas DC-SIGN readily forms tetramers, giving rational to their distinct carbohydrate binding specificities.(66, 75)

A)

```
1   MSDSKEPRLQQLGLLEEEQLRGLGFRQTRGYKSLAGCLGHGPLVLQLLSFTLLA
55  GLLVQVSKVPSSISQEQSRQDAIYQNLTQLKAAVGELSEKSKLQEIYQELTQLK
109 AAVGELPEKSKLQEIYQELTRLKAAVGELPEKSKLQEIYQELTWLKAAVGELPE
163 KSKMQEIYQELTRLKAAVGELPEKSKQQEIYQELTRLKAAVGELPEKSKQQEIY
227 QELTRLKAAVGELPEKSKQQEIYQELTQLKAAVERLCHPCPWEWTFFQGNCYFM
271 SNSQRNWHDSITACKEVGAQLVVIKSAEEQNFLQLQSSRSNRFTWMGLSDLNQE
325 GTWQWVDGSPLLPSFKQYWNRGEPNNVGEEDCAEFSGNGWNDDKCNLAKFWICK
379 KSAASCSRDEEQFLSPAPATPNPPPA
```

B)

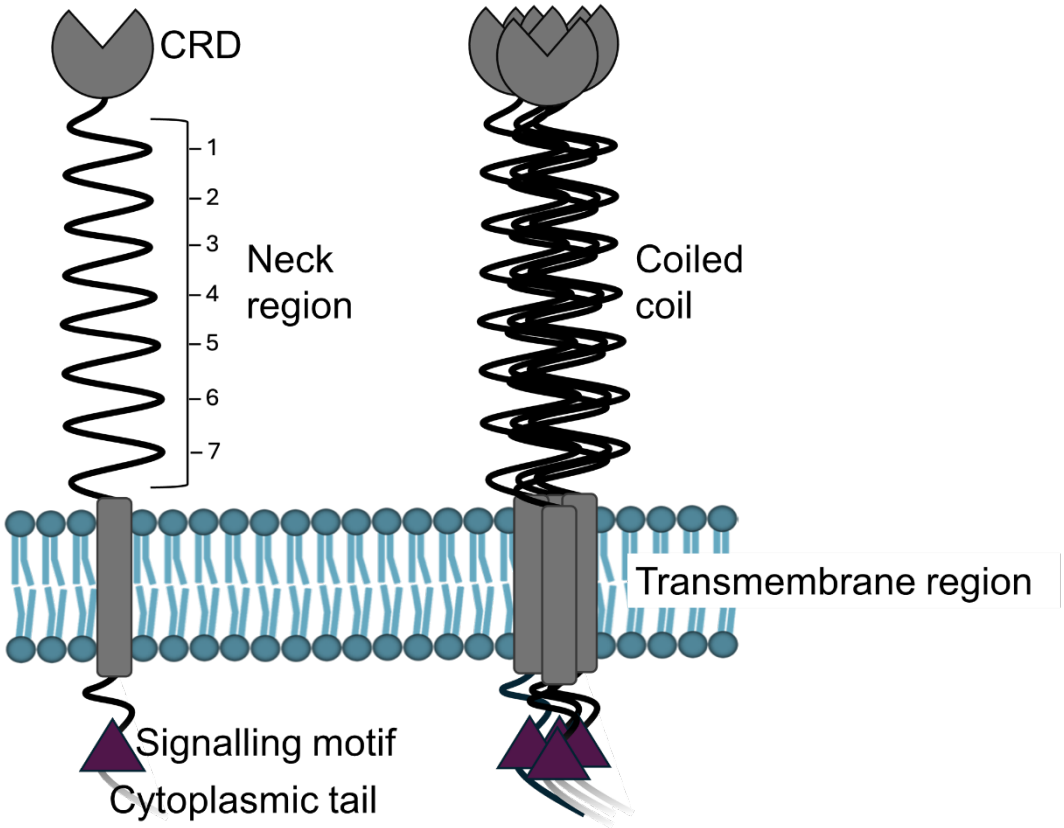

Figure 1.5 A) The amino acid sequence of DC-SIGN, where the bold blue shows the transmembrane region, grey highlights show the 7.5 neck repeat units and the bold red indicates the mannose binding motif. B) Labelled schematic of a DC-SIGN monomer (left) and a DC-SIGN tetramer (right). During tetramerization, four neck regions come together to form a coiled coil, thereby stabilising the tetramer.

1.4.2 DC-SIGN ligand binding

DC-SIGN is fairly unique due to its remarkably broad glycan binding specificity.(76, 77) The initial discovery of DC-SIGN was based on the observation that DCs could bind to the endogenous ligand ICAM-3 with high affinity.(68) ICAM-3 is a heavily glycosylated type I transmembrane protein, containing high mannose-type oligosaccharides.(78) Since this discovery, DC-SIGN has also been shown to bind to ICAM-2 but not ICAM-

1.(79) Studies into the enzymatic removal of N-linked carbohydrates from ICAM-3 and ICAM-2 show a complete elimination the ability of the proteins to bind to DC-SIGN, confirming the importance of these carbohydrates in this binding profile.(56)

From its strong interaction with ICAM-3 and ICAM-2 it is evident that DC-SIGN interacts with high mannose oligosaccharides. DC-SIGN binds less so with single terminal mannose, instead preferring upwards of 3 mannose residues located internally in the overall oligosaccharide.(75) Mannose recognition also appears to be dependent on its spacing on glycoproteins.(66) While DC-SIGN has been shown to bind high mannose containing structures, it exhibits dual specificity and also binds unsialated fucose-containing carbohydrates such as $Lewis^X$, $Lewis^y$, $Lewis^a$ and $Lewis^b$, which contain fucose through different anomeric linkages.(80) The interaction of DC-SIGN with mannose and fucose containing glycans underpins dendritic cell binding to envelope viruses like HIV(14) and Ebola(81), and to bacteria such as *Mycobacterium tuberculosis(52)*, *Candida albicans(82)* and *Helicobacter pylori*(83).

Further molecular insights into the binding profile of DC-SIGN have also shown interaction between DC-SIGN and blood group A/B antigens and their fragments, including α-galactose.(32) The interaction of galactose to DC-SIGN is weak but specific, and NMR studies show a possible dependency on the valine residue (V351) located at the primary Ca^{2+} binding site, having shown close proximity of GalH2 to this residue. V351 is also involved in binding of other ligands too, with its side chain packing perfectly against the hydrophobic cleft formed by certain glycans, but not all, showing that ligands have different, but overlapping binding sites.(80) In fact, binding sites for some ligands may even differ depending on the orientation of the molecule.(74) For small mannose ligands, coordination to DC-SIGN can be achieved in two distinct orientations. The major binding mode indicates that the reducing end of mannose is oriented away from the binding site whereas the minor binding mode has the reducing end towards the binding site. Fucose has its own distinct binding site to mannose.

Interestingly, fluorination of mannose in the 3-OH position and of galactose and fucose in the 4-OH position completely abrogates DC-SIGN binding, unambiguously indicating that no matter the binding site, binding of mannose, galactose and fucose is dependent on complexation of calcium to the 3-OH and 4-OH positions. These data are in agreement with molecular dynamics simulations on fucose which suggest a stable hydrogen bonding network is present between 3-OH, 4-OH and residues E347, N350, E376 and N365.(32)

1.4.3 DC-SIGN function

Like other CLRs, DC-SIGN is involved in antigen uptake, internalisation and degradation. The main function of DC-SIGN is pathogen capture and once a ligand has bound, rapid internalisation into lysosomal compartments is induced, facilitated by the di-leucine motif in the cytoplasmic tail.(29) As previously mentioned, the tri-acidic cluster in this cytoplasmic region also plays an important role in protein degradation and accurate trafficking into correct lysosomal compartments facilitating antigen presentation.(84) Importantly, DC-SIGN also behaves as a signalling receptor.(85) Although triggering of DC-SIGN by pathogens alone does not initiate cytokine secretion, it enables the shaping of immune responses by the modulation of TLR signalling at the transcriptional level.(52, 86)

Binding of DC-SIGN to self-glycoproteins such as ICAM-2 and ICAM-3 also allows DC-SIGN to function as a cell-adhesion receptor, facilitating interactions between dendritic cells with T cells, endothelial cells and neutrophils by the formation of an immunological synapse.(87, 88) The importance of DC-SIGN in mediating this DC-T cell contact has been validated by the observation that DC-T cell clustering was inhibited in the presence of anti-DC-SIGN antibodies.(14) T cell proliferation was also inhibited in the presence of these anti-DC-SIGN antibodies, an observation that highlights the importance of DC-SIGN in primary immune responses. Although transient, the interaction of DC-SIGN with ICAM-3 is strong enough to stabilise the DC-T cells interaction and enable screening of enough resting T cells to achieve efficient engagement of a productive TCR. While the above functions are largely based on the DC-SIGN-ICAM-3 interaction, the DC-SIGN-ICAM-2 interaction facilitates DC migration from blood to tissues. During this migration, DC maturation results in changes to the cell surface profile and allows DCs to attract resting T cells and present their antigenic load.

Due to its broad binding specificity, DC-SIGN interacts with numerous pathogens, with some resulting in unique immunological outcomes.(29, 52) Binding of DC-SIGN by distinct pathogens can lead to the modulation of TLR4 signalling, skewing type 1 and type 2 T cell responses.(89-91) The finding that DC-SIGN signalling could be ligand dependent has been well exemplified by Gringhuis *et al*. who showed that that carbohydrate specific ligation of DC-SIGN leads to a switch in the proximal DC-SIGN signalosome, which provides the basis for the plasticity that DC-SIGN shows in tailoring immunity in response to distinct pathogens.(92, 93)

Mycobacterium tuberculosis, a species of pathogenic bacteria in the family Mycobacteriaceae, interacts with DC-SIGN via the ligand ManLAM.(94) ManLAM is a mannose containing glycan abundantly expressed in mycobacterial cell walls.(95) Stimulation of DC-SIGN by ManLAM is not in itself enough to generate an immune

response, however, simultaneous activation of TLR4 with lipopolysaccharide (LPS) generates an intracellular TLR4 signalling cascade which leads to cytokine production (Figure 1.6A). Through studying the accumulation of various kinases potentially involved in DC-SIGN signalling, it was discovered that recruitment of the serine-threonine kinase Raf-1 is central to the modulation of TLR specific immune responses by DC-SIGN in response to mannose containing ligands. The recruitment of Raf-1 to the DC-SIGN signalosome, containing proteins; LSP1, KSR1 and CNK, by upstream effectors LARG and RhoA modulates TLR4 signalling and enhances expression of proinflammatory cytokines such as interleukin(IL)-12 and IL-6, as well as regulatory IL-10. For successful activation of Raf-1, conformational changes are essential and are carried out by translocation of Raf-1 to the membrane though interaction with the GTPase Ras. Once relocated, phosphorylation of Raf-1 on Ser338 and Tyr340/341 by PAKs and Src kinases respectively is necessary for phosphorylation and acetylation of the p65 subunit of the transcriptional factor NF-κB. Acetylation of p65 enhances and prolongs the transcriptional activity of NF-κB and thus induces cytokine gene expression.(52)

In contrast, *Helicobacter pylori* which interacts with DC-SIGN via fucose containing motifs, leads to an active dissociation of the KSR1-CNK-Raf-1 triad from the DC-SIGN signalosome, resulting in the failure to induce Raf-1 phosphorylation (Figure 1.6B). While this leads to the upregulation of IL-10, three inflammatory cytokines IL-12, IL-6 and IL-23 are downregulated in this instance. Cytokine production upon fucose-DC-SIGN binding was found to be LSP-1 dependent (in a similar manner to mannose) but Raf-1 independent.(52, 92) Follow up studies revealed that suppression of proinflammatory cytokines by fucose-DC-SIGN signalling was a result of the disturbance of the formation of the p65-p50 NF-kB dimer with the p65 subunit found to be almost completely absent after LPS/fucose co-stimulation. Simultaneous triggering of TLR4 with LPS and DC-SIGN with fucose leads to phosphorylation of ser252 on LSP1 though activation of the kinase MK2. This allows for the recruitment of kinases IKKε and CYLD to the LSP1 signalosome and leads to the accumulation of NF-κB family member BCL3. Binding of BCL3 to the p50 subunit results in a p50-p50 homodimer forming preferentially over the p65-p50 heterodimer. BCL3 is an atypical member of the NF-kB family and has previously been shown to restrict inflammation by suppressing IL-23 and inducing IL-10.(92)

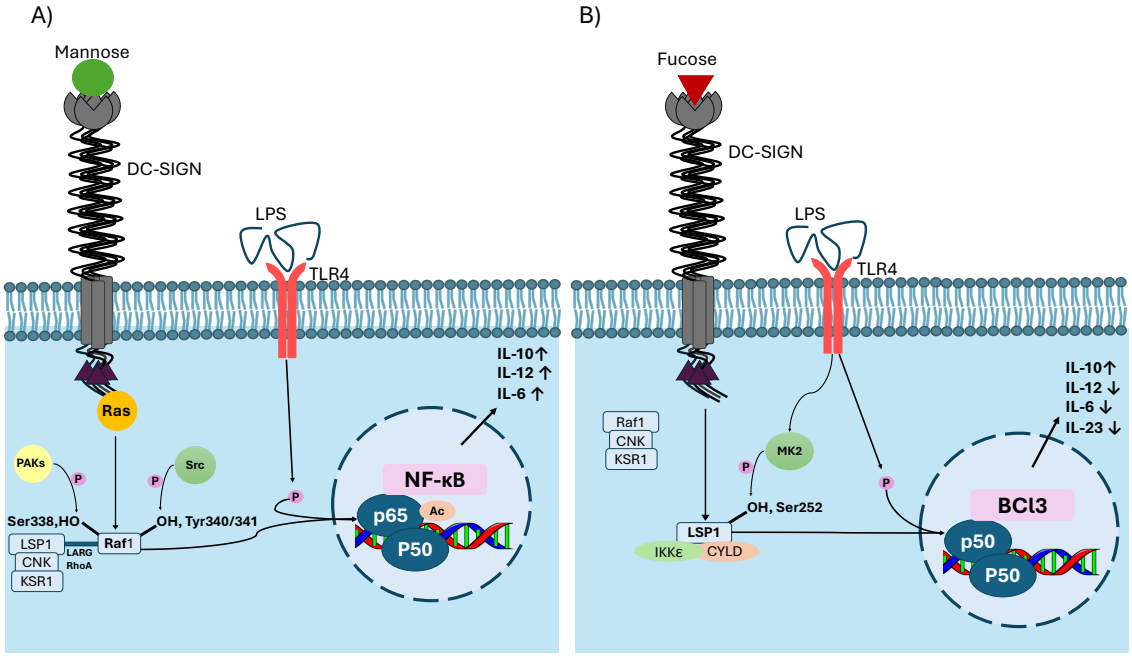

Figure 1.6 A) Mannose specific DC-SIGN signalling modulates TLR4 signalling through Raf1-dependent acetylation of p65 resulting in increased IL-10, IL-12 and IL-6 transcription B) Fucose specific DC-SIGN signalling modulates TLR4 signalling in a Raf1 independent manner leading to the association of BCL3 to the NF-kB p50 subunit, resulting in increased IL10 transcription but reduced IL-6, IL-12 and IL-23 transcription.

1.5 Multivalency

From the examples discussed above, it is clear that the functional capacity of DC-SIGN as a PRR is intimately linked to its ability to engage multivalently with a wide range of glycan structures presented on pathogens. These multivalent contacts, involving simultaneous engagement of tetrameric DC-SIGN CRDs with multivalent glycans are essential to achieve high affinity interactions which are subsequently necessary for effective pathogen recognition, internalisation, and downstream signalling.

Multivalency also provides an additional layer of specificity to LGIs. In this context, the term specificity is not only defined by the binding affinity, which refers to the strength of a single interaction between a lectins' CRD and a particular glycan, but is also influenced by the avidity, which is the cumulative binding strength of multiple simultaneous interactions. Together affinity and avidity can shape how selectively a receptor like DC-SIGN can discriminate between PAMPs and host glycans.

The binding affinity of a multivalent lectin glycan interaction (MLGI) (given by Equation 1.1 where L is the lectin, C is the glycan and LC is the lectin-glycan complex) can be quantified by the equilibrium dissociation constant K_d. K_d describes the strength of the lectin-glycan interaction by comparing the concentration of unbound glycans and lectins to the bound concentration present at equilibrium (Equation 1.2). More straightforwardly,

K_d indicates the concentration at which 50% of the lectins are bound at equilibrium. K_d is related to the Gibbs free energy change (ΔG) which is the overall energy required for the interaction to occur (Equation 1.3, where R is the ideal gas constant and T represents the temperature in Kelvin).

$$L + C \rightleftharpoons LC \qquad \textbf{Equation 1.1}$$

$$K_d = \frac{[L][C]}{[LC]} \qquad \textbf{Equation 1.2}$$

$$\Delta G = RTlnK_d \qquad \textbf{Equation 1.3}$$

Multivalency increases the individual binding strength of LGIs compared to their constituent monovalent affinities and the differences in binding strength can be compared based on two factors: the degree of cooperativity (α) or the enhancement factor (β). The degree of cooperativity α describes how multivalency augments ΔG in comparison to the same number of monovalent interactions (N) given by Equation 1.4. If α = 1 then there is no cooperative effect between one interaction and the next however, if α > 1 then the formation of the first interaction will enhance the interaction of the next. The interaction of haemoglobin with O_2 is a prime example of positive cooperativity whereby binding of one O_2 molecule encourages the binding of the three subsequent O_2, i.e. the free energy of binding for the second molecule of O_2 is more favourable than the first. Equally, negative cooperativity also exists with α<1, whereby the formation of one interaction will inhibit the formation of the next.

$$\Delta G_{poly,N} = \alpha N \Delta G_{mono} \qquad \textbf{Equation 1.4}$$

α measures how binding of one ligand affects the binding of another, but it does not quantify how much the overall affinity changes compared to the monovalent interaction, therefore β is generally a more useful descriptor of the affinity enhancement observed upon multivalent binding and is given by Equation 1.5. β is a quantitative comparison of K_d mono and K_d poly, and can be used when the number (N) of interactions is unknown.(2)

$$\beta = \frac{K_{d\ mono}}{K_{d\ poly,N}}$$ **Equation 1.5**

To further understand how multivalent interactions are energetically stabilised and biologically regulated, an insight into the enthalpic and entropic contributions is critical. The thermodynamics of MLGIs are complex, with both enthalpic and entropic components influencing binding strength and, as a result, biological function. The total enthalpy of a polyvalent interaction ($\Delta H_{poly,N}$) is primarily considered to be the sum of the enthalpies of the individual LGIs ($N\Delta H_{mono}$) which reflects the amount of energy involved in forming physical bonds between the lectin and the glycan. Thus, the greater the multivalency the more favourable the enthalpy change. However, this value can be modulated by other interactions around the binding site. Enthalpically enhanced binding occurs when the binding of one glycan to its lectin binding site makes the binding of subsequent glycans more favourable (i.e. $\Delta H_{poly} > N\Delta H_{mono}$). An example is the binding of pentameric cholera toxin to five GM1 moieties on a cell surface, where differences in free energy can be attributed to enthalpic enhancement.(96) Enthalpically diminished binding, conversely, occurs if the initial lectin-glycan binding interferes with subsequent binding events. In this case, the overall enthalpy of the polyvalent interaction becomes less favourable than expected from individual monovalent interactions (i.e. $\Delta H_{poly} < N\Delta H_{mono}$). This often happens when the formation of multiple LGIs involves energetically unfavourable molecular conformations. Rigid polyvalent glycans may be particularly susceptible to this, especially if there is a spatial mismatch between the glycans and lectin's binding sites. For instance, if a bivalent ligand's geometry does not perfectly match a bivalent receptor's spacing, both the ligand and receptor may need to distort for the second interaction to occur, introducing enthalpic strain.

Equally important to understanding MLGIs is the entropic component, which governs the thermodynamic feasibility of the interaction. The total entropy change ($\Delta S_{poly,N}$) for MLGIs can be considered to consist of the sum of the translational, rotational and conformation entropy changes, as well as a contribution from hydration entropy (Equation 1.6).

$$\Delta S_{\mathrm{poly}} = \Delta S_{\mathrm{trans}} + \Delta S_{\mathrm{rot}} + \Delta S_{\mathrm{conf}} + \Delta S_{\mathrm{H2O}}$$ **Equation 1.6**

Translational entropy changes (ΔS_{trans}) reflect the loss of freedom of the molecules to move in space upon binding, and rotational entropy changes (ΔS_{rot}) account for the loss of rotational freedom around the ligands' axes when they associate. Upon binding, six degrees of freedom are typically lost per molecule (three translational and three

rotational), contributing to the entropic cost. These factors are logarithmically related to the size and mass and inversely related to the concentration. Since the size and mass changes are usually within a factor of 10 and almost always within a factor of 100, then S_{trans} and S_{rot} are not strongly affected upon 1:1 binding. However, since each molecule adds its own contribution to the total degrees of freedom, binding of multiple lectins to the same glycan (and vice versa) can have a greater impact on the total entropy cost and therefore affinity.(2)

Since the rotational and translational entropic costs depend on the number of translational and rotational degrees of freedom, binding events occurring in three dimensions (in solution) incur the greatest entropic penalty, while two dimensional (cell surface bound lectin and cell surface bound glycan pair) or one dimensional systems (along filaments) reduce this cost.

Hydration entropy change (ΔS_{H2O}) typically is a positive contribution to total entropy change, as ligand binding, especially in the case of LGIs, often releases ordered water molecules from hydrophobic surfaces. This effect is usually consistent per binding unit and is additive across mono- and multivalent systems, so higher multivalency will lead to increased liberation of water molecules from binding sites and a higher ΔS_{H2O}.

Finally, conformational entropy change (ΔS_{conf}) depends on the flexibility of the linking group between binding sites. In an ideal system, the linkers would be perfectly rigid and exactly match the receptor binding space. This is not the case for most biological systems where both binding partners are likely to display some degree of flexibility prior to binding and hence a negative conformational entropy change occurs due to the restriction of molecular freedom upon binding. While ΔS_{conf} is therefore often large enough to outweigh ΔS_{H2O} to induce a negative ΔS_{poly} it can be compensated for by the enthalpy to induce overall favourable binding. High flexibility ligands can oftentimes alleviate steric strain of the system by minimising spatial mismatch and allowing the ligand to bridge multiple binding sites simultaneously, facilitating conditions where $\Delta H_{poly} > \Delta S_{poly}$ resulting in a negative Gibbs free energy change and therefore spontaneous, favourable binding.

Overall, a lectin's avidity is largely determined by the spatial compatibility between the glycans' structure and the lectin's multiple binding sites. This highlights the critical role of multivalency in governing high avidity interactions. Glycans that can simultaneously engage all of a lectin's binding sites with minimal steric hindrance will form the highest avidity complexes. In contrast, glycans which induce unfavourable conformational adjustments, or fail to bridge multiple binding sites will result in significantly weaker interactions. These suboptimal interactions may dissociate before eliciting any biological response.

1.6 Glyconanotechnology

Understanding the binding in MLGIs is essential for developing therapeutics, diagnostics, imaging or other functional applications.(97) The complexity of the enthalpic and entropic contributions involved in MLGIs makes it challenging to dissect individual variables by studying natural systems alone. As such, there is a need for a well-defined, tuneable platform to study multivalency in a controlled and quantifiable way. Glyconanotechnology offers a powerful solution to this challenge.

Nanotechnology refers to the science of studying, developing and operating materials at the nanoscale (approximately in the range 1-100 nm).(98) The development of nanotechnology was initially conceptualised by Richard Feynman in the 1950s in his vision to make machines that manipulated material on the atomic level. His ideas laid the conceptual groundwork of this field, and nanotechnology advanced from this point onwards.(99, 100) While much of the initial research in nanotechnology focused on applications relating to the fields of physics and chemistry, by the 1980s with the discovery of atomic microscopes and nano-carbon structures, nanoscale research and its principles had also begun to be adopted by the fields of biology and medicine with Nadrian Seeman in 1982 first conceptualising the idea of self-assembling DNA nanostructures.(101) Based off this idea, in the early 2000s, Paul Rothemund developed the first scaffold DNA origami.(102) Now in this decade, bio-nanotechnology is widely regarded by experts as one of the most intriguing fields within nanoscience. Nanotechnology has such wide scale use in biological research due to the complimentary sizes of nanomaterials and cellular structures. Nanomaterials are the perfect size to explore the interaction or applications of proteins and cell components/interfaces, and applying nanotechnology to these biology-related areas has led to significant advances in diagnostic techniques, drug delivery, drug potency, and molecular imaging, yielding outstanding results.(103)

Under the branch of bionanotechnology, glyconanotechnology emerged, which can be viewed as the integration of nanotechnology to explore biological and carbohydrate related medical questions.(104) When biomolecules such as glycans are coupled to nanomaterials which have unique catalytic, photonic, electronic, or magnetic properties not observed in their bulk forms, they form hybrid materials with functional properties that are highly capable of various applications.(105) Furthermore glyconanoparticles are of similar dimensions to many biological molecules and structures, making them suitable for therapeutic and diagnostic applications.

Glyconanoparticles, which are typically characterised by a nano-sized core made of proteins, polymers, dendrimers or inorganic materials, and are coated with glycan ligands, offer an excellent platform for a multivalent display of ligands which can boost

avidity and allow closer study of these interactions. This is vital for a fundamental understanding of the mechanisms underpinning all biological processes. Applying the unique properties of materials at the nanoscale scale and their complimentary size to biological structures, with their ability to mimic complex biological surfaces and mediate specific interactions with glycan-binding proteins such as lectins, yields for a powerful investigative tool.

Glyconanotechnology has indeed been used for a range of diverse and impactful applications, including vaccines(106, 107), drug delivery(108), pathogen inhibition(109, 110), cancer therapies(111, 112) and imaging tools(113, 114) amongst many others. Specifically, and related to the research in this thesis, glyconanomaterials serve as a multifunctional platform for fundamental interaction studies such as investigating multivalent lectin-glycan interactions (MLGIs) at the molecular level, which has previously been inaccessible by other, larger scale techniques. Using glyconanomaterials in this manner has provided valuable insights into the affinities and binding modes lectin-glycan interactions, while also highlighting their significant potential as therapeutic agents against a range of diseases and viral infections.(60, 115)

The highly tuneable nature of glyconanomaterials puts them at an advantage over conventional drugs when targeting MLGIs for therapeutic applications. Their biological activity can be intricately governed by a combination of physicochemical parameters, including scaffold type, multivalency, surface ligand chemistry (glycan type), size, shape, ligand density and flexibility (Figure 1.7). These features collectively determine the spatial presentation of glycans and therefore the strength of their interactions with biological targets. This is especially useful when targeting lectins which have overlapping monovalent glycan specificities, as varying their spatial arrangement can reintroduce specificity for a certain lectin and therefore increase drug potency while limiting side effects from binding to non-target lectins in the body. Despite significant progress, however, the rational design of glyconanoaparticles remains a challenge, particularly in optimising these interrelated parameters to achieve desired functional outcomes for lectins with unknown structures.

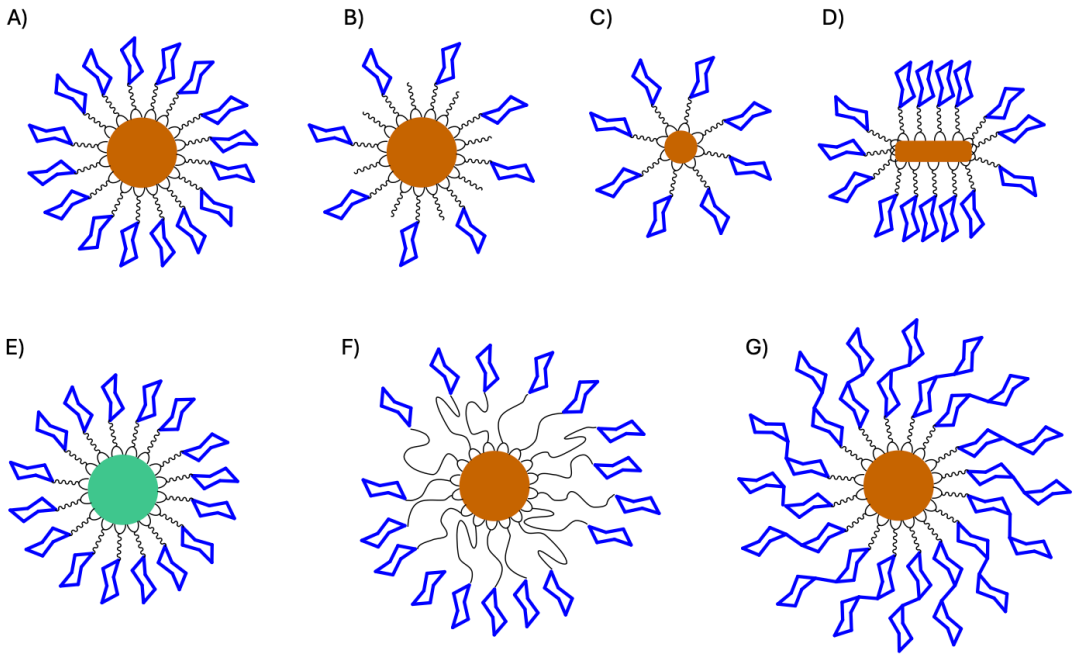

Figure 1.7 Schematic depicting the physiochemical parameters of glyconanoparticles which can be modified from nanoparticle (A) to optimise binding with biological targets, including; B) glycan density, C) core size, D) core shape, E) core material, F) ligand flexibility and G) glycan type.

.

1.7 Methods to provide quantitative and qualitative data on MLGIs

A fundamental starting point in using glyconanoparticles to study MLGIs is to measure their binding affinity. Alongside this, binding parameters such as enthalpy and entropy can be measured to help gain and understanding of what aspects of glycoconjugate design a) are essential for a high binding affinity and b) can be modified to fine tune their spatial/ orientational matches to give a greater affinity enhancement and produce MLGI pairs with optimal properties for the desired application.

1.7.1 Fluorescence resonance and nano surface energy transfer

Numerous techniques have been developed to provide quantitative data on multivalent glycoconjugates in the presence of their target lectin including surface plasmon resonance (SPR) and isothermal titration calorimetry (ITC).(62, 116-118) Some techniques also harness the unique physical properties of nanoparticles to do so. For example, Zhou, Guo and co-workers have previously employed glycan-conjugated quantum dots (glycan-QD) and glycan-conjugated gold nanoparticles (glycan-GNP) to study the MLGIs of DC-SIGN.(115, 119, 120) Both of these methods exploit the optical

characteristics of these materials to employ fluorescence spectroscopy techniques such as Förster resonance energy transfer (FRET) and fluorescence quenching via the nano surface energy transfer (NSET) to obtain accurate information on the binding affinity and binding parameters of these MLGI pairs.

Quantum dots are semiconducting nanocrystals which exhibit bright and stable fluorescence. As a result, they have been used to analyse binding interactions between glycans and a fluorescently labelled protein via FRET. FRET is a powerful and widely used technique to study the interaction and dynamics of binding pairs. It is the phenomenon whereby the energy absorbed after exciting a fluorescent donor molecule is transferred in a non-radiative process to an acceptor molecule. Two conditions must be met for FRET to occur; the emission spectrum of the donor must overlap with the absorption spectrum of the acceptor (Figure 1.8B) and the donor-acceptor pair must be in close proximity (typically 1-20 nm). The efficiency of this energy transfer is highly dependent on the distance between the donor and acceptor molecules making it an excellent spectroscopic ruler to measure molecular distances. Using Equation 1.7 the FRET efficiency, which describes the proportion of energy absorbed by the donor that is transferred to the acceptor, can be quantified, where R is the distance between the donor and the acceptor surface, and R_0 is the Förster separation distance, at which $E_{(NSET)}$ = 50%. N is number of acceptors in FRET interaction with the same donor at identical distance, and so in 1:1 binding it is assumed to be 1. This efficiency is known to vary with the 6th power of the distance between the donor-acceptor pair.(121)

$$E_{FRET} = \frac{1}{1 + \frac{1}{N}\left(\frac{R}{R_0}\right)^6} \qquad \textbf{Equation 1.7}$$

Quantum dots coated in glycans have been used to measure the binding affinity to fluorescently labelled DC-SIGN via a QD sensitised dye FRET readout. Since unbound species are likely to be too far away to participate in FRET, they produce no background signal, circumventing the need for separation of bound and unbound species before measurement (Figure 1.8A). QDs also have a board absorption and narrow emission profile, allowing for a wide choice of absorption wavelengths to minimise direct excitation of the acceptor dye to reduce background. A typical spectrum will show the donor (QD) emission (D_E) decreasing and the acceptor (protein) emission (A_E) increasing with concentration (Figure 1.8C). Given a constant donor-acceptor separation distance, the ratio A_E/D_E (defined as the FRET ratio) is proportional to the number of bound proteins, allowing for the direct measurement of the proportion of bound protein under constant

QD: protein ratio. By comparing the proportion of bound protein to the concentration, a Hill plot can be constructed to measure the K_d (Figure 1.8D). (122)

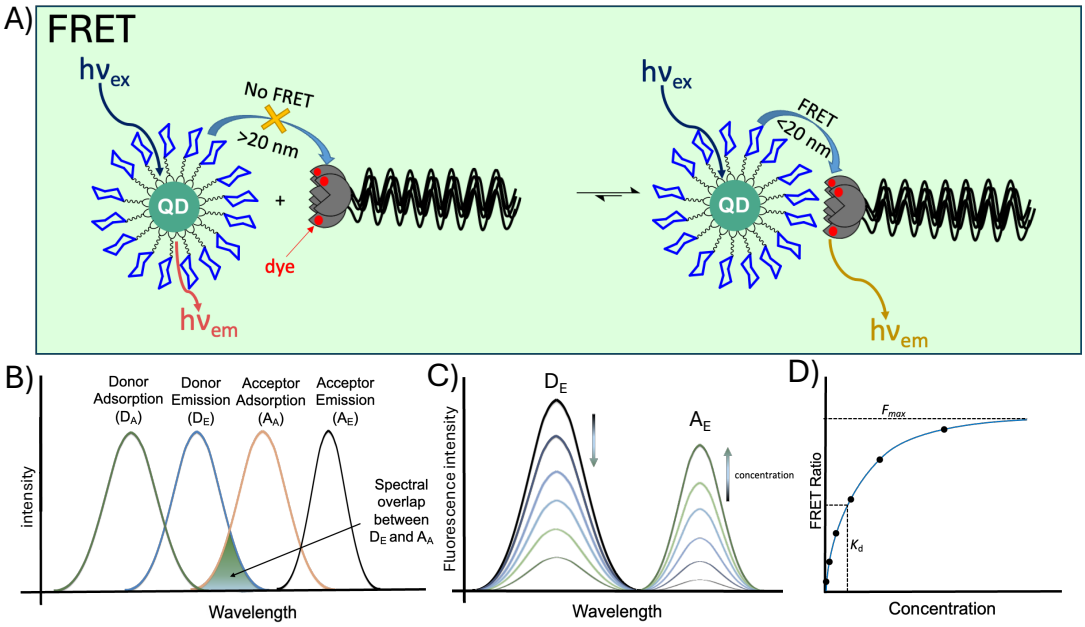

Figure 1.8 Diagram depicting examples for A) the FRET process between an excited QD-glycan and dye labelled DC-SIGN. B) The overlap between the emmision spectrum for a donor fluorophore (QD, D_E) and the absorption spectrum for the acceptor fluorophore (dye-labelled protein, A_A). The donor adsorption (D_A) and acceptor emmission (A_E) are also shown. Overlap between D_E and A_A is required for efficient energy trasnfer, overlap between D_A and A_A should be kept to a minimum to avoid direct excitation of the acceptor. C) The fluorescence spectrum of a FRET pair which inceases in trasnfer as concentration increases (D_E descreses and A_E increases). D) The change in FRET ratio (A_E/D_E) with concentration, showing the maximum FRET ratio (Fmax) and the dissociation constant (K_d).

Gold nanoparticles can also be involved in a non-radiative energy transfer process. However, since GNPs > 2 nm do not display fluorescence, they cannot be used in exactly the same way as quantum dots to measure binding. Instead, GNPs > 2 nm can absorb the energy from a donor fluorophore through NSET. NSET is a fluorescence-based technique which involves the transfer of energy from a fluorescent donor molecule to a metal nano surface via the resonance of its surface conduction electrons, resulting in quenching of the donor's fluorescence emission (Figure 1.9A). NSET quenching is also highly distance dependent, but relies on the 4th power of the donor-acceptor distance, leading to a greater effective distance range of up to 50 nm which makes it more sensitive than FRET in certain applications and enabling the study of larger complexes (Equation 1.8).(123) GNPs also convey an advantage to using QDs in that they are biocompatible and can be used in cellular and *in vivo* studies without introducing the toxicity of QDs.(124) They are also much simpler to produce.(125)

$$E_{NSET} = \frac{1}{1 + \left(\frac{R}{R_0}\right)^4}$$ **Equation 1.8**

While spectral overlap can enhance quenching via NSET, it is not strictly necessary and instead the distance between the donor and the acceptor plays the most critical role.(126-128) Upon exciting the fluorescently labelled protein and mixing it with GNP-glycans, any bound GNP-glycans (e.g. those within 50 nm) will non-radiatively quench the dye's fluorescence through electromagnetic coupling to the gold surface plasmons, resulting in a reduction in the intensity of the donors fluorescence emission (Figure 1.9B). GNPs can quench a wide range of fluorophores when in close proximity, and quenching decays with distance, making this a valuable method for measuring binding partner distances.(129) Assuming that any bound proteins are quenched, and control measurements of the lectin only are carried out under identical conditions as that of the glycan-GNP + lectin samples, then the quenching efficiency (QE) (calculated by Equation 1.9, where IF_0 is the integrated fluorescence of the protein control and IF is the integrated fluorescence of the protein+GNP sample) provides a readout strategy for measuring binding. This is carried out by plotting the QE over a concentration range and fitting the data using the Hill binding model to extract the binding affinity (Figure 1.9C).

$$QE(\%) = \frac{IF_0 - IF}{IF_0}\ x\ 100$$ **Equation 1.9**

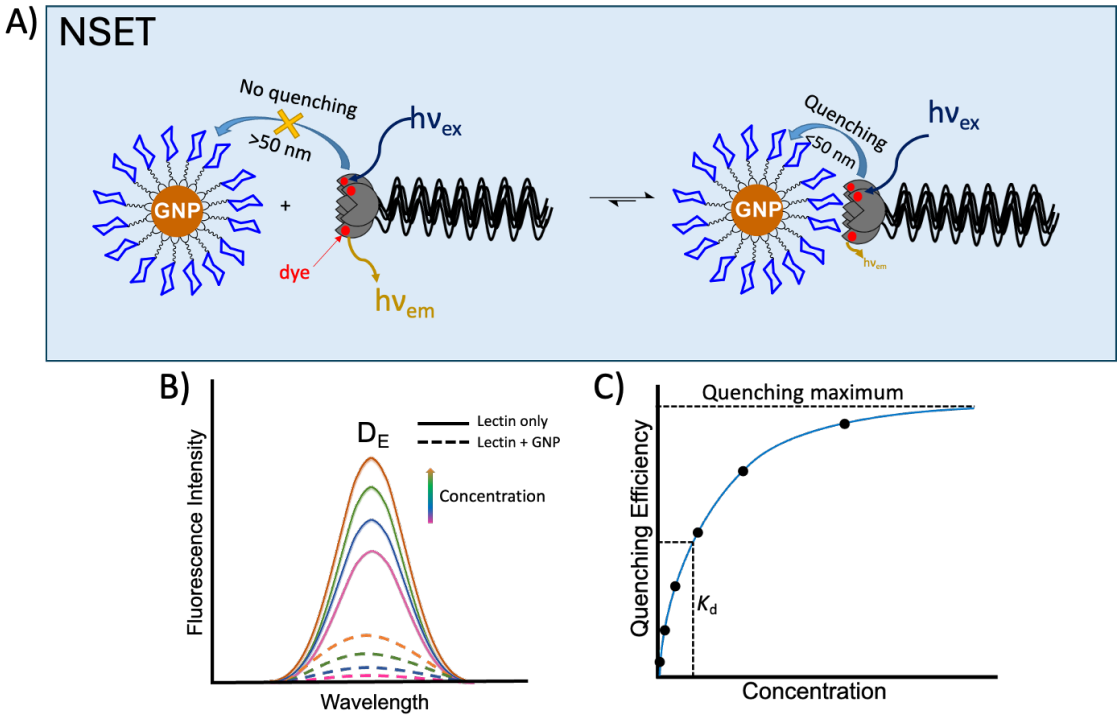

Figure 1.9 Diagram depicting examples for A) the NSET process between an excited dye labelled DC-SIGN and a GNP-glycan. B) The fluorescence emmission of the lectin donor (D_E) is quenched when bound to a GNP C) Example quenching efficiency vs concentration, showing the maximum quenching efficiency (QEmax) and the dissociation constant (K_d).

Glycosylated quantum dots, coated with mannose-(1,2)-α-mannose (dimannose) linked through a lipoic acid anchor containing either a 3 or 11 ethylene glycol units (QD-EG_n-dimannose), were used to quantitatively asses MLGIs with fluorescently labelled DC-SIGN using a QD-FRET readout.(119) In this experiment, the extracellular domain of DC-SIGN was site-specifically labelled through a cysteine site mutation, introduced near to but not in the glycan binding pocket of the CRD. This mutation was strategically placed close enough to enable efficient energy transfer to the bound-glycan coated nanoparticle while being a site nonessential for ligand binding. Since all other cysteine residues are tied up in disulfide bonds, this cysteine mutation allowed for selective labelling with a maleidimide-atto594 dye, which has good spectral overlap with these QDs, allowing for efficient FRET. QD-EG_3-dimannose demonstrated strong binding to DC-SIGN-atto594, with a K_d of 0.61 nM. This binding between DC-SIGN and QD-EG_3-dimannose displayed a great affinity enhancement factor, β, of approximately 1.5 x 10^6 compared to the monovalent interaction between dimannose with a single DC-SIGN CRD (K_d = 0.9 mM).(77) This remarkable increase in affinity demonstrates the power of multivalency in biology, where the simultaneous engagement of multiple weak interactions can produce particularly strong overall binding. Increasing the flexible linker from 3 to 11 EG units maintained strong multivalent enhancement, although this was >3-fold lower than that of

the EG_3 unit. This diminished binding is presumably due to the longer linker, which introduces additional conformational degrees of freedom. Upon binding, these must be restricted which results in a higher entropic penalty relative to the less flexible EG_3.

As well as measuring the apparent K_d, these FRET and NSET assays have been utilised to look at thermodynamic parameters such as changes in enthalpy, entropy and Gibbs free energy, to explain the discrepancies in the K_ds, although so far this has only been employed to look at binding differences observed between different size gold nanoparticles bearing the same linker/glycan, and not the effects of linker length.(130, 131) By conducting binding experiments at varying temperatures, then employing the van 't Hoff equation which relates the equilibrium binding constant to temperature, values for binding enthalpy and entropy changes can be measured. A van 't Hoff plot, which plots $\ln(K_d)$ vs. 1/T, is used to extract ΔH and ΔS from the slope and intercept, respectively. This approach enables the discrimination between binding differences driven by enthalpic factors such as spatial matches and those arising from entropic contributions including reduced conformational freedom.

Through this analysis, a deeper insight into how glyconanoparticle size affects the thermodynamic driving forces behind variations in binding affinity of MLGIs can be achieved. In this specific experiment employing GNPs of different core size, all GNP sizes displayed negative ΔS, however, the absolute negative values of ΔS were reduced as GNP scaffold size increased, implying that the unfavourable entropy changes upon GNP-glycan-DC-SIGN binding were reduced with the increasing GNP size (Table 1.1). This has been attributed to larger scaffolds having a higher proportion of unbound surface ligands which may have largely retained their conformational and rotational degrees of freedom upon binding. The lesser entropic penalty together with similar favourable binding ΔH can explain the stronger binding (lower apparent K_d) for larger GNP sizes bearing the same glycan.

Table 1.1 Summary of parameters for the binding of DC-SIGN with different size Gx-dimannose.(130)

Gx-dimannose	**Apparent K_d (nM)**	**ΔH^0 (kJ mol^{-1})**	**ΔS^0 (J mol^{-1} K^{-1})**	**ΔG^0 (kJ mol^{-1})**
G5-	5.8 ± 0.3	-132 ± 32	-288 ± 105	-47 ± 44
G13-	1.00 ± 0.03	-111 ± 10	-207 ± 33	-50 ± 14
G27-	0.22 ± 0.03	-100 ± 14	-138 ± 46	-59 ± 19

Apart from studying the effects of varying linker length and scaffold size, this GNP-NSET approach has also been employed to investigate how NP surface coverage and inter-glycan distance influence DC-SIGN binding. In one experiment, the GNP-NSET readout was used to compare the effects of using of glycan monomers (GNP-EG_2-dimannose) vs timers (GNP-(EG_2-dimmanose)$_3$) on apparent binding affinity, which found that trimers induced negligible multivalent enhancement in MLGIs with DC-SIGN compared to the monomers (K_d = 3.6 *vs* 3.9 nM).(115) A second explored the apparent binding affinities of gold nanoparticles with different glycan surface coverages, by introducing an inert spacer ligand to dilute the concentration of the glycan on the surface. Using a pseudo dimannose glycomimetic and glycan surface coverages of 100%, 75%, 50%, and 25% for a 5 nm GNP it was observed that apparent binding affinity became weaker with decreasing surface glycan concentration (0.22, 0.68, 1.38 and 2.74 nM, respectively). Lower surface coverages of 12.5% and 6.3% showed no MLGI enhancement, with their quenching efficiencies falling below a measurable threshold.(131)

These data indicate that under conditions of high glycan density and short inter-glycan distances, even monomer-coated surfaces are already high enough density to engage all four CRDs in the tetrameric structure of DC-SIGN, leaving little room for additional enhancement by multimeric binding through the addition of timers. On the other hand, reducing glycan concentration below monomer saturation reduces apparent binding affinity. This is likely due to the increased inter-glycan distances failing to align with the geometry of DC-SIGNs four CRDs and therefore incurring enthalpic loss through binding less than four CRDs. This highlights that the strongest MLGIs are only formed when all four CRDs in DC-SIGN are engaged in binding. This has not been confirmed experimentally but may be a worthwhile topic for future study

Taken together, these studies highlight how glycan density, linker length and NP scaffold size collectively influence binding strength through both enthalpic and entropic contributions. The combined QD-FRET and GNP-NSET assays have been indispensable in probing apparent binding affinities and are increasingly being used to dissect the underlying thermodynamic factors that govern MLGIs.

1.7.2 Isothermal titration calorimetry

Isothermal titration calorimetry (ITC) is another valuable method for measuring the thermodynamic parameters (ΔH, ΔS, ΔG, K_a, and stoichiometry) of binding partners in solution. It has long and widely been used as the gold standard for characterising molecular interactions between ligands and macromolecules.(132, 133) The ITC machine encompasses three fundamental pieces, 1: a reference cell containing buffer or solvent to normalise the enthalpy change during the experiment 2: a sample cell and 3: and injection syringe. During the experiment, a series of small aliquots (usually the

ligand) is titrated from the injection syringe into the sample cell containing the protein, enzyme or other binding partner. Upon binding, a change in temperature occurs; either an increase or decrease depending on whether the reaction is endothermic or exothermic, respectively. To maintain a constant temperature difference between the reference and sample cell, the isothermal titration calorimeter applies or reduces power and this change in power to maintain temperature is the instrument signal. The first injections causes large temperature changes and as binding saturation is reached, ΔT is reduced with each injection (Figure 1.10A). An ITC curve is generated by plotting the integral of the peaks generated by the required power against the mole ratio at each injection, which directly provides enthalpy ΔH, the binding stoichiometry N, and the association constant K_a (Figure 1.10B). Another important parameter in ITC is the Wiseman value 'c'. It is calculated via Equation 1.10, where n=number of binding sites and [M] is the concentration of the molecule in the ITC cell.(134)

$$c = n.K_a.[M] \qquad \textbf{Equation 1.10}$$

C is used to evaluate the suitability of an experiment for accurately determining binding thermodynamics. A value of 10<c<500 gives rise to the classic sigmoidal curve where all thermodynamic parameters can be reliably extracted. Ideally, if an expected K_a is known, then adjusting the protein concentration so that c falls within optimal range (estimated using Equation 1.10) ensures maximum data quality from an ITC experiment.

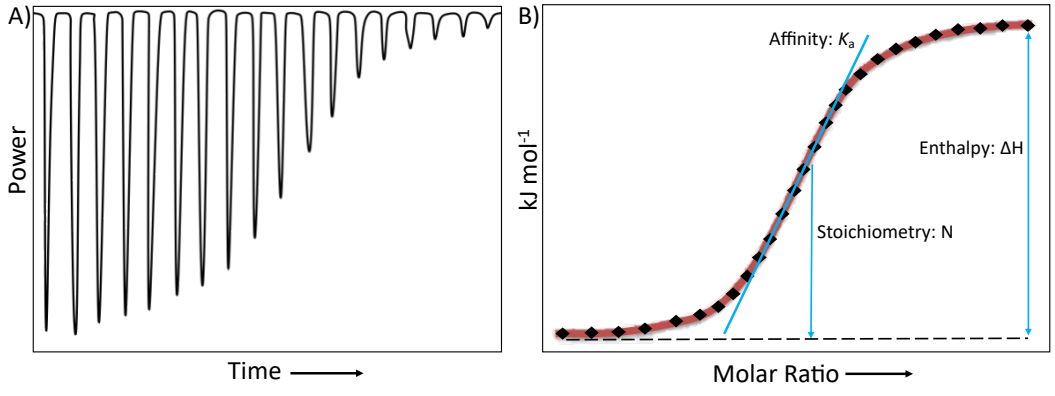

Figure 1.10 Example of A) an ITC thermogram where each peak represents the heat released or absorbed with each injection and B) an ITC titration curve. ΔH, K_a and N are obtained directly from the ITC titration curve.

ITC has traditionally been regarded as most suitable for studying high-affinity interactions, where the Wiseman parameter falls within the optimal range of approximately 10-500. It is widely assumed that when c values fall below 10, ITC

becomes ineffective for reliable thermodynamic analysis due to the appearance of a 'featureless flat line' in the binding isotherm, making fitting difficult.(135-138) As a result ITC has historically been considered unsuitable for investigating low-affinity systems.

However evidence now challenges this assumption and demonstrates that ITC can indeed be effectively applied to biologically relevant low-affinity interactions, such as those commonly observed in PCI systems.(139) For ITC to yield accurate thermodynamic data under low c conditions, specific requirements must be met, including a sufficiently broad binding isotherm and a known binding stoichiometry, to avoid over-parameterisation during curve fitting. Precise concentrations of both ligand and receptor must be used and a low signal to noise ratio is also necessary. Under these conditions, reliable estimates of the binding constant and the corresponding Gibbs free energy can be obtained.(139) However, ΔH is still susceptible to error under these conditions and moreover, ITC can suffer from the formation of aggregates during the titration and has limitations in accurately observing and interpreting more complex interactions such as cross-linking, which is not uncommonly observed in MLGIs.(140) Aggregation and cross-linking result in misleading data which hinders the extraction of correct thermodynamic parameters.(141)

Nevertheless, ITC has been used regularly to evaluate the binding affinity and thermodynamics of lectin-glycan-NP interactions.(142-147) ITC has also been used to confirm the thermodynamic contributions measured by the GNP-NSET readout discussed in Section 1.7.1. The enthalpy changes associated with binding of DC-SIGN with glycan coated 5 nm GNPs (G5) and 13 nm GNPs (G13) measured by NSET with van 't Hoff analysis, were compared to those measured by ITC, showing good consistency (-96.4 ± 2.6 vs -92.8 ± 1.6 kJ mol^{-1} for G5 and -93.0 ± 3.2 vs -99.9 ± 1.7 kJ mol^{-1} for G13).(131) This confirms the use of NSET as a valuable and accurate technique for measuring the thermodynamic contributions to binding affinities.

1.7.3 Dynamic light scattering and electron microscopy.

Dynamic light scattering (DLS) and electron microscopy (EM) offer alternative but complimentary ways to probe key behaviours of MLGIs. They have been used to detect proteins and confirm agglomeration, as well as provide information such as binding mode, protein organisation and binding affinity.(115, 148-152) These techniques can provide valuable insights into structural and organisational characteristics of the target lectin.

DLS measures the hydrodynamic diameter of a species in solution by analysing fluctuations in the intensity of light scattered at a fixed angle. These fluctuations arise due to Brownian motion, which states that smaller particles move faster, while larger

ones move more slowly in a liquid. As a result the frequency shifts in the scattered light are related to the size of the particle.(153) EM, on the other hand, provides high resolution visualisation of NPs, due to the strong absorption of electrons, allowing for direct observation of clustering. DLS in particular has advantages in terms of it being a non-destructive, label-free technique requiring only a small amount of sample with little preparation and is usually relatively quick to perform. Nanoparticle EM is also label free and requires small quantities of sample, but can involve a more complex set-up for imaging, requiring a slightly longer timeframe.

Both of these techniques have been used to monitor lectin binding to a range of glycosylated inorganic nanoparticles, for purposes of looking at both binding mode and binding affinity. Example systems which involve using DLS and transmission(T)EM to measure binding affinity include mannose coated silica particles (Man-SNP) binding to concanavalin A (ConA), and galactose (Gal)-SNPs binding to Ricinus Communis Agglutinin (RCA). In these experiments, Man-SNPs or Gal-SNPs were treated with various concentrations of ConA and RCA respectively and their size was measured by DLS and TEM. The results were consistent between the two techniques, showing an increase in size with increasing lectin concentration. By fitting the concentration dependant increase in size with a Hill binding model, K_d was obtained to be between 63 nM and 9200 nM for Man-SNP with ConA depending on particle size and ligand density.(152, 154) Equally, binding affinity between Gal-SNP and RCA was found to be 220 nM.(154)

DLS and EM have also been used to look at qualitative data such as binding mode (e.g. monolayer formation or cross-linking). Monolayer species have uniform hydrodynamic diameters additive of the NP and protein sizes, and can be well fitted by a single Gaussian distribution, with randomly distributed but relatively large nearest neighbour distances (NNDs). On TEM, they show up as single isolated particles. On the other hand, cross-linked species have much larger hydrodynamic sizes than monolayer species as measured by DLS, and by TEM they show as large scale, closely packed NPs with small and narrowly distributed NNDs.(119, 151)

Binding mode can provide information on CRD orientations which in turn can sometimes offer explanations into discrepancies observed in binding affinities. For example, DLS and TEM have been used to indicate that the strong binding affinity (K_d = ~3.6 nM) observed between GNP-EG_2-dimannose and DC-SIGN is due to the multivalent engagement of all four CRDs to form a monolayer protein coating around a single GNP. In this experiment the measured hydrodynamic diameter of the resulting complex was ~40 nm, corresponding to the formation of a single monolayer of DC-SIGN uniformly coating the GNP-glycan surface.(115) This observation supports the notion that all four

CRDs of DC-SIGN are oriented upwards towards the GNP surface, enabling full multivalent engagement of the four CRDs by just one GNP, facilitating a large multivalent enhancement.

If fewer CRDs were engaged in binding to one glycan-GNP, then it is likely that cross-linking would occur, as a second GNP-glycan would bind the remaining, unoccupied CRDs (Figure 1.11). This was observed to be the case for DC-SIGNR, a closely related protein to DC-SIGN. When repeating this experiment with DC-SIGNR, which shows 77 % amino acid homology to DC-SIGN, a larger species was present, up to ~2000 nm in hydrodynamic diameter.(115) This size greatly exceeds what would be expected from a protein monolayer coated single glycan-GNP particles and is strongly indicative of the occurrence of a cross-linking network. Because cross-linking can only occur if fewer than 4 CRDs are engaged in binding to any single glycan-GNP, this DLS result has been used to suggest that DC-SIGNR exhibits a different CRD orientation, with its CRDs projecting outwards rather than upwards, making binding of one GNP-glycan (especially with shorter, more rigid EG_2 linkers) to all four CRDs difficult .This has been used to validate that that the weaker binding affinity exhibited by DC-SIGNR with GNP-EG_2-dimannose (K_d = 152 nM) is due to a lesser multivalent enhancement observed when one GNP-glycan fails to engage all four CRDs, instead favouring cross-linking. These results were confirmed by TEM, where GNP-EG_2-dimannose and DC-SIGN showed single isolated particles with randomly distributed NNDs, whereas binding of DC-SIGNR to GNP-EG_2-dimannose produced large scale, closely packed GNP assemblies, hundreds of nm across with much smaller NNDs.

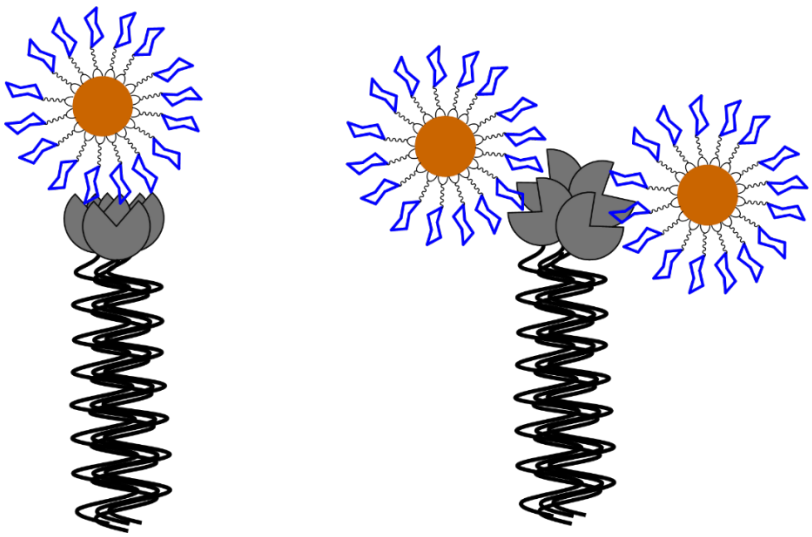

Figure 1.11 DC-SIGN binding to one GNP through all four of its CRDs vs a cross-linking binding mode for DC-SIGNR, where multiple GNPs bind to one DC-SIGNR tetramer.

1.8 Summary and research aims

In summary, C-type lectins, in particular DC-SIGN, play a key role in pathogen recognition through specific interactions with glycan containing PAMPs. Understanding these interactions at the molecular level is crucial for advancing both insight into fundamental immunology and the development of targeted therapeutic strategies. Advances in nanotechnology has enabled the presentation of glycans on well-defined nanoscale scaffold, such as QDs and GNPs, allowing for control over parameters such as core size, glycan density and linker flexibility/length. Several biophysical methods and techniques such as FRET, NSET, ITC as well as DLS and EM have been used to provide insights into multivalent lectin-glycan binding mechanisms, affinities, spatial orientations and spatial constraints.

Despite these advances, gaps in the knowledge of the structural characteristics and binding mechanisms of many multimeric membrane bound lectins remain incompletely understood, requiring further methods for elucidation. As discussed, GNP-glycans have proven to be a valuable tool to measure binding affinity and thermodynamic contributions to binding, and have further been used to evaluate and explain discrepancies in the binding modes and affinities of two closely related proteins (DC-SIGN and DC-SIGNR). The first half of this thesis built upon this knowledge and evaluated the following;

1. The synthesis and characterisation of glycosylated GNPs with varied size, surface glycan type, surface glycan density, and linker flexibility and the impact these parameters had on the DC-SIGN binding modes, measured by DLS (Chapter 3). These studies provided information on DC-SIGN CRD orientation and spatial arrangement during binding. It also provided insight into the number of CRDs bound, e.g. a cross-linking binding mode indicated <4 CRDs per DC-SIGN tetramer bound to one single glycan-GNP, but not the exact number.
2. Chapter 4 explored the thermodynamic contributions of GNP-glycans with these varying structural parameters on DC-SIGN binding, measured through temperature dependent affinity studies via NSET readout. Employing the temperature dependent K_ds into a van 't Hoff analysis revealed the number of CRDs involved in binding and which features of GNPs contributed to enhanced binding affinities. It also provided a rational to the binding modes observed in Chapter 3, by linking the size of the GNP-DC-SIGN complex to the number of CRDs bound. This was complimented by ITC studies to confirm that NSET is an accurate and valuable tool for the elucidation of the thermodynamic contributions of these GNP-glycans.

3. Finally, Chapter 4 also assed the use of GNP-glycans in a viral inhibition study and how the structural features and binding modes observed in solution can be applied to solid phase experiments.

Together these approaches provided a more comprehensive understanding of how nanoparticle design influences DC-SIGN recognition with potential implications for the design of antiviral therapeutics.

Part B of this thesis shifts focus to DC-SIGN binding and signalling in context of immune modulation, specifically related to a group of diseases termed the seronegative spondyloarthropathies. These chapters explored how GNP-glycans can be employed as bacterial and fungal adjuvants to modulate cytokine production through DC-SIGN. A discussion of the current literature can be found in Chapter 5, with an exploration of DC-SIGN mediated immune modulation in Chapter 7. Finally, the development of an affinity pull-down assay to reveal which GNP-glycan binding lectins on the DC surface, besides DC-SIGN, might also be involved to influence immune modulation was assessed in Chapter 8.

Chapter 2 – Materials and methods

2.1 Materials

D-mannose was purchased from Carbosynth, L-fucose, triphenyl phosphine, sodium azide, tetra-n-butylammonium iodide(TBAI), N,N'-Dicyclohexylcarbodiimide(DCC), Tris[(1-benzyl-1H-1,2,3-triazol-4-yl)methyl]amine (TBTA), Gold(III) chloride trihydrate and phenol were purchased from Alfar Aesar. Carbon tetrabromide, acetic anhydride, pyridine, sodium methoxide, sodium ascorbate, guanidine HCl, triton-X 100, Silica 60A, copper sulfate, dimethylformamide, chloroform d4, and tri sodium citrate were purchased from Sigma Aldrich. DL-Lipioc acid, and triethylamine were purchased from Acros Organics. 4-Dimethylaminopyridine (DMAP) and 2-[2-(2-Chloroethoxy)ethoxy]ethanol were purchased from Fluorochem. Sodium citrate, sodium hydroxide, HEPES, calcium chloride, sodium chloride, EDTA, HCl, H_2SO4, BSA, methanol, DCM, THF, petroleum ether, hexane, acetonitrile, ethanol, amberlight® IR-120 (H^+), Tween20, Tris base and HNO_3 were purchased from Fisher Scientific. β-mercaptoethanol was purchased from Bio-Rad. BSA was purchased form BioServ UK. Maleimide-Atto-643 was purchased from ATTO-TEC. PEG linkers (H_2N-EG_{12}-CCH, H_2N-EG_8-CCH, H_2N-EG_6-CCH, H_2N-EG_2-CCH) were purchased from PurePEG. Dry solvents were obtained using an Innovative Technology Inc. PureSolv® solvent purification system. Ultrapure water (resistance >18.2 MΩ cm) was purified by an ELGA Purelab classic UVF system and was used for all experiments and making buffers.

N_3-EG_2-dimannose and LA-EG_2-CCH were synthesised in-house by Dr Darshita Budhadev using previously established protocols. MS: calculated m/z for $C_{18}H_{37}N_4O_{13}$ (N_3-EG_2-dimannose) $[M+NH_4]^+$ 517.24, found 517.24; calculated m/z for $C_{15}H_{25}NO_3S_2Na$ (LA-EG_2-CCH) [M+Na]+ 354.12, found 354.12. (115, 119)

Common buffers included: Loading buffer (25 mM Tris, 1.25 M NaCl, 25 mM CaCl2, pH 7.8); HEPES binding buffer (20 mM HEPES, 100 mM, NaCl, 10 mM CaCl2, pH 7.8); elution buffer (20 mM HEPES, 100 mM NaCl, 2.5 mM EDTA, pH 7.8); binding buffer for dye labelling (20 mM HEPES, 100 mM NaCl, 10 mM CaCl2, pH 7.2); and elution buffer for dye labelling (20 mM HEPES, 100 mM NaCl, 2.5 mM EDTA, pH 7.2); tris buffer (10 mM tris base, pH 7.8); dialysis buffer (1.25 M NaCl, 25 mM tris pH 7.8, 25 mM $CaCl_2$). ITC buffer (100 mM NaCl, 20 mM tris pH 7.8, 2 mM $CaCl_2$).

2.2 General instrumentation and computation

All moisture-sensitive reactions were performed under nitrogen atmosphere using oven-dried glassware. Evaporations were performed under reduced pressure on a Buchi Rotavapor R-300. Concentration or washing was performed in Amicon ultra-S2 centrifugal filter tubes or Sartorius Stedim Lab vivaspin 500 with a molecular weight cut

off (MWCO) of 10,000 or 30,000 Da. Dialysis was performed using Thermofischer Scientific 14,000 MWCO BioDesign Dialysis Tubing. Flash column chromatography (FCC) was carried out by pre-absorption of the crude material onto silica gel 60A (Merk) or dissolving in the minimum volume of an appropriate eluent and loading on top. Solvents for FCC and TLC are listed in volume:volume percentages. Centrifugation was performed using either a Hettich Universal 320/320R, a Thermo Scientific Heraeus Fresco 17 or a Beckman Coulter Avanti JXN-30 centrifuge, depending on the speed and volume, at room temperature (r.t) unless otherwise stated. Lyophilisation was performed using a Virtis Benchtop K freeze dryer.

^{1}H NMR spectra were measured at 25^o C on a 500 or 400 MHz Bruker spectrometers using D_2O, Methanol-d4 or Chloroform-d with the residual solvent as the internal standard at room temperature. Chemical shifts are given in parts per million relative to TMS and the coupling constants (*J*) are given in Hertz. High resolution mass spectra (HR-MS) were obtained on a Bruker Impact QqTOF II mass spectrometer and m/z values are reported in Daltons to four decimal places. Liquid chromatography mass spectrometry (LC-MS) was used to analyse all other samples and was performed using a Bruker AmaZon speed mass spectrometer and are quoted to two decimal places. UV-Vis absorption spectra were recorded on a Varian Cary 50 bio UV-Visible Spectrophotometer over 200-800 nm using 1 mL quartz cuvette with an optical path length of 1 cm or on a Nanodrop 2000 spectrophotometer (Thermo scientific) over the range of 200-800nm using 1 drop of the solution with an optical path length of 1 mm. The hydrodynamic diameters were recorded on a Malvern ZETASizer-Nano using disposable polystyrene cuvettes. All fluorescence spectra were recorded on a Cary Eclipse Fluorescence Spectrophotometer using a 0.70 mL quartz cuvette. All numerical data were analysed and plotted using Origin 2019b or Graphpad Prism10 software.

2.3 Production and characterisation of proteins

Plasmids encoding for the wild type amino acid identity of DC-SIGN were made in-house (provided by Yuan Guo). For labelled protein, cysteine was introduced into the cDNA encoding the extracellular segment of DC-SIGN to replace residue Q274 for site specific dye labelling. The mutagenesis was carried out by using synthetic DNA restriction fragments to replace the corresponding wild-type sequences.(155) Standard recombinant DNA techniques were used throughout these experiments.

2.3.1 Wild type DC-SIGN (DC020)

100 mL of sterilised LB medium (25 g/L of dH_2O) containing ampicillin (50 mg/L) was inoculated with a flake of pre-prepared ampicillin resistant *E. coli* (BL21/DE3) glycerol stock containing the plasmid coding for the desired protein and incubated for 16 hours at 37 ^{o}C with shaking (200rpm). The resulting start culture (30-40 mL) was added to 1 L

of sterilised LB medium (25 g/L dH_2O) containing ampicillin (50 mg/L) and incubation at 37 °C, 200 rpm continued until an optical density at 550nm (OD_{550}) of 0.7 was reached (2-3 hrs). IPTG (1 mL, 100 mg/mL dH_2O) was added was added and incubation (37 °C, 200 rpm) continued for a further 150 minutes. Cells were then harvested by centrifugation at 5000 rpm, 4 °C for 10 minutes. The supernatant was discarded and the pellet resuspended in 400 mL Tris (10 mM Tris, pH 7.8), then centrifuged at 8000 rpm, 4 °C for 10 minutes. The supernatant was discarded and the pellet collected and stored at -80 °C until further use.

For 4 L of growth culture: The pellet was defrosted in 25 mL Tris buffer (10 mM Tris, pH 7.8) and sonicated 6 times with 2 minute burst (50% cycle and 60% power, keeping on ice for 1 min between rounds). The volume was increased to 100 mL with cold Tris buffer (10 mM Tris, pH 7.8) and the cells subjected to 4 further rounds of sonication (2 minute bursts, 50% cycle and 60% power, keeping on ice for 1 min between rounds). The dispersed cells were then disrupted via two cycles through a cell disruptor at 23 kPsi. The cells were then centrifuged at 10000 rpm at 4 °C for 15 minutes. The pellet was suspended in 100 mL buffer (100 mM Tris pH 7.0) containing guanidine (6M) and sonicated 2 times with 2 minute burst (50% cycle and 60% power) keeping on ice for 1 min between rounds. 40 µL of β-mercaptoethanol was added and further sonication carried out (50 % cycle, 60 % power, 2 cycles of 2 min sonication and 1 min on ice followed by 2 min sonication and 30 min on ice). The resulting solution was centrifuged at 20000 rpm, 4 °C for 30 minutes then poured into 300 mL Tris loading/dialysis buffer (1.25M NaCl, 25mM Tris pH7.8, 25mM $CaCl_2$) with gentle stirring and dialysed against 3L of the same buffer for around 45 hours where the buffer was changed 3 times. The dialysed material was recovered and centrifuged at 20000 rpm, 4 °C for 30 minutes.

A 4 mL mannose-sepharose affinity column was prepared, equilibrated with 30 mL Tris loading buffer (1.25 M NaCl, 25 mM Tris pH 7.8, 25 mM $CaCl_2$) and the protein supernatant was loaded onto the column. For wild type DC020, the column was washed with 20 mL HEPES washing buffer (20 mM HEPES, 100 mM NaCl, 10 mM $CaCl_2$, pH 7.8) before elution with 20 mL HEPES elution buffer (20 mM HEPES, 100 mM NaCl, 2.5 mM EDTA, pH 7.8). 15 x 1.5 mL fractions were collected and $CaCl_2$ (pH 7.4) was then added to the eluted fractions to a final concentration of 10 mM. The protein concentration of each fraction was obtained by UV-Vis spectroscopy applying the Beer Lambert law (Equation 2.1, where $A\lambda$ is the absorbance a specific wavelength λ, c is the concentration, ε is the extinction coefficient of protein at λ, and l is the sample path length), for absorbance at 280 nm (A_{280}) where εDC-SIGN = 70400 $M^{-1} \cdot cm^{-1}$. Fractions containing protein were combined and concentrated to a desired concentration by centrifugation at 4000 rpm, 4 °C using Amicon ultra-S2centrifugal filter tubes with a MWCO of 10 kDa. Protein was flash frozen and stored at -80 °C.

$$A\lambda = \varepsilon cl \qquad \textbf{Equation 2.1}$$

The protein molecular weight was confirmed from deconvolved HRMS where the value obtained represents one of the monomeric units corresponding to the tetrameric protein. The hydrodynamic size (D_h) of the tetramer was confirmed by DLS analysis.

DC-SIGN: HRMS calculated: 39197.22, found: 39201.53. DLS D_h: 14.0 ± 2.0 nm

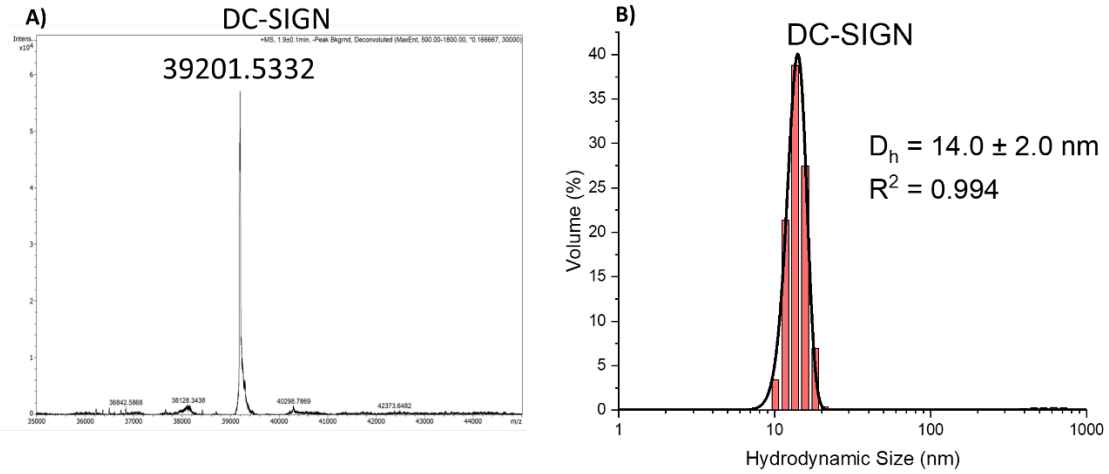

Figure 2.1 A) Deconvolved HRMS spectrum of the monomeric extracellular domain of DC-SIGN (wild type; WT, DC020), B) Volume population hydrodynamic size distribution histogram fitted with lognormal Gaussian distribution for the extracellular domain of DC-SIGN (WT, DC020).

2.3.2 Labelled DC-SIGN (DC020Q274C)

Labelled DC-SIGN (DC020Q274C) was produced from pre-prepared ampicillin-resistant *E. coli* glycerol stocks containing the plasmid coding for the desired protein, as described in Section 2.3.1. During mannose-sepharose purification the column was washed with 20 mL HEPES washing labelling buffer (20 mM HEPES, 100 mM NaCl, 10 mM $CaCl_2$, pH 7.2) before elution with 20 mL HEPES elution labelling buffer (20 mM HEPES, 100 mM NaCl, 2.5 mM EDTA, pH 7.2). 15 x 1.5 mL fractions were collected and $CaCl_2$ (pH 7.4) was then added to the eluted fractions to a final concentration of 25 mM. Fractions containing protein (determined by A_{280} using UV-Vis spectrometry) were combined and concentrated using Amicon ultra-S2 centrifugal filter tubes with a MWCO of 10,000 Da to a final A_{280} of > 0.6. Maleimide atto-643 was then added at a protein: dye ratio of 1: 1.5 and mixed immediately by vortex, followed by 2 hours on a rotary mixer at r.t in the dark, then kept at 4 ^{o}C overnight in the fridge.

A 4 mL mannose-sepharose affinity column was prepared, pre-equilibrated with HEPES washing buffer (20 mM HEPES pH7 .8, 100 mM NaCl, 10mM $CaCl_2$) and the labelled protein loaded on top. The column was washed with HEPES washing buffer (20 mM

HEPES, 100 mM NaCl, 10 mM $CaCl_2$, pH 7.8) until the excess dye was removed. The protein was eluted with HEPES eluting buffer (20 mM HEPES, 100 mM NaCl, 2.5 mM EDTA, pH 7.2) and $CaCl_2$ (pH 7.4) was then added to the collected fractions to a final concentration of 10 mM. The concentration was determined by UV-Vis spectrometry applying a modified Beer Lambert law (Equation 2.2 where $A\lambda$ is the absorbance a specific wavelength λ, $[\mathrm{P}]$ is the protein concentration, ε is the extinction coefficient of protein at λ, and l is the sample path length) to account for the atto-643 absorption.

$$[P] = \frac{A_{280} - (A_{643} \times 0.04)}{\varepsilon \times l} \qquad \textbf{Equation 2.2}$$

$$[D] = \frac{A_{643}}{1.5 \times 10^5} \qquad \textbf{Equation 2.3}$$

Protein molecular weights (MW) were confirmed from HRMS data, where calculated protein MW values were obtained from the amino acid sequences of one monomeric unit of the corresponding protein and LE was obtained from the ratio of the labelled protein to unlabelled protein peak areas. Alternatively, LE was obtained by the [P]/[D] ratio, were [D] is calculated using Equation 2.3.

DC020Q274C HRMS calculated: 39172.22, found: 39254.47.

D020Q274C-atto634: HRMS calculated: 40100.22, found: 40136.36. D_h: 14.4 ± 2.6 nm, LE: 82.3%.

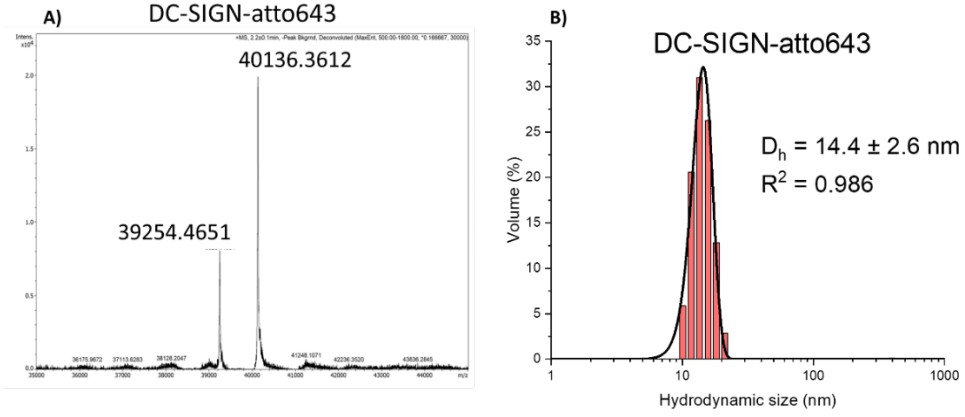

Figure 2.2 A) Deconvolved HRMS spectrum of the monomeric extracellular domain of DC-SIGN-atto643 (DC020Q274C-atto643), B) Volume population hydrodynamic size distribution histogram fitted with lognormal Gaussian distribution for the extracellular domain of DC-SIGN-atto643 (DC020Q274C-atto643).

2.4 Ligand and gold nanoparticle preparation

2.4.1 Ligand synthesis

8-Azido-3,6-dioxaoctyl-2,3,4-tri-*O*-acetyl-α-L-fucopyranoside (3)

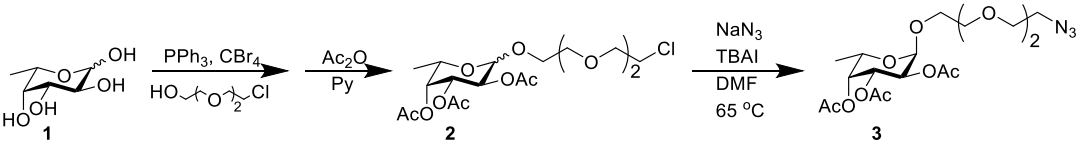

L-Fucose (1.0 g, 6.08 mmol) 2-[2-(2-chloroethoxy)ethoxy]ethanol (4.4 mL, 30.4 mmol), PPh_3 (158 mg, 0.6 mmol) and CBr_4 (200 mg, 0.6 mmol) were placed in a 10-mL round-bottom flask. The mixture was heated at 65°C for 4h. The reaction was then cooled to r.t and loaded on a short silica gel column to remove the excess of acceptor (EtOAc, then EtOAc:MeOH = 10:1). The crude fucoside was subjected to acetylation with Ac_2O (10 mL) and pyridine (10 mL). The reaction was stirred at RT overnight then concentrated *in vacuo* and rediluted with EtOAc (80 mL). The organic layer was washed with H_2O (40 mL), 1M HCl (40 mL), saturated $NaHCO_3$ (40 mL) and brine (40 mL). The organic layer was dried over Na_2SO_4, filtered and concentrated *in vacuo*. The crude mixture (1.5 g, 3.41 mmol) was then subjected to azidation by adding NaN_3 (1.11 g, 17.0 mmol), *n*Bu_4NI (125 mg, 0.34 mmol) and DMF (12 mL) and stirring at 65 °C overnight. The reaction mixture was concentrated *in vacuo* to remove the DMF then diluted with EtOAc (80 mL) and washed with saturated $NaHCO_3$ (40 mL) and the aqueous layer was extracted with EtOAc (3 × 20 mL). The combined organic extracts were dried over Na_2SO_4, filtered and concentrated *in vacuo.* The crude mixture was then purified by flash column chromatography (silica, Petroleum ether:$CHCl_3$:CH_3COCH_3 = 7:2:1.2) to afford the desired α-fucoside (1.17 g, α/β = 69:31, 2.61 mmol, 43% overall yield after three synthetic steps). Three separate fractions were collected from the column chromatography.

- fraction a: mass = 750 mg, α, 1.60 mmol, 26%.

- fraction b: mass = 178 mg, α/β = 50:50 mixture as determined from ^{1}H NMR data.

- fraction c: mass = 238 mg, α/β = 28:72 mixture as determined from ^{1}H NMR data.

^{1}H NMR (501 MHz, $CDCl_3$) (α anomer) δ 5.41 – 5.33 (m, 1H, H-2), 5.29 (dd, *J* = 3.4, 1.3 Hz, 1H, H-4), 5.14 – 5.07 (m, 2H, H-3, H-1), 4.22 (qd, *J* = 6.5, 1.3 Hz, 1H, H-5), 3.85 – 3.72 (m, 1H, -OCH_2-), 3.70 – 3.60 (m, 9H, -OCH_2-), 3.39 (t, *J* = 5.4 Hz, 2H, CH_2N_3), 2.15 (s, 3H, $COCH_3$), 2.06 (s, 3H, $COCH_3$), 1.97 (s, 3H, $COCH_3$), 1.13 (d, *J* = 6.6 Hz, 3H, CH_3). **^{13}C NMR** (126 MHz, $CDCl_3$) δ 170.78(C=O), 170.58 (C=O), 170.20 (C=O), 96.38(C-1), 71.34(C-4), 70.89 (OCH_2), 70.86(OCH_2), 70.38(OCH_2), 70.24(OCH_2) 68.30(C-3), 68.15(C-2), 67.61(OCH_2), 64.45(C-5) 50.80(CH_2N_3) 29.98(CO<u>C</u>H_3), 20.85(CO<u>C</u>H_3), 20.80(CO<u>C</u>H_3), 15.97(C-6). **MS**: calcd m/z for $C_{18}H_{28}N_3O_{10}Na$ $(M-H+Na)^+$ 469.18; found 469.93

8-Azido-3,6-dioxaoctyl-*O*-α-L-fucopyranoside (azido-fucose/fucoseN3) (4)

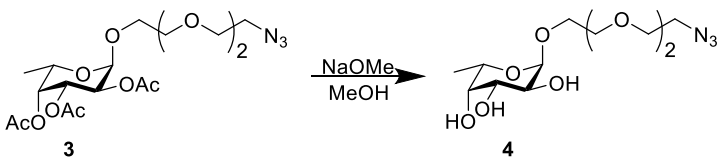

To a solution of α-azido fucoside **3** (370 mg, 0.83 mmol) in MeOH was added NaOMe and the reaction stirred at RT for 1h. The reaction was then neutralised with amberlist H^+ resin, filtered and concentrated *in vacuo*. Purification by flash column chromatography (silica, CH_2Cl_2:MeOH = 20:1 then 10:1) afforded the desired α-azido fucose (240 mg, 0.75 mmol 90 %) as a clear oil.

^{1}H NMR (400 MHz, $CDCl_3$) δ 4.90 (d, *J* = 3.3 Hz, 1H, H-1), 4.00 (q, *J* = 6.6 Hz, 1H, H-5), 3.90 – 3.75 (m, 4H, H-2, H-3, H-4, -OCH_2-), 3.71 – 3.62 (m, 9H, -OCH_2-), 3.40 (t, *J* = 5.2 Hz, 2H, CH_2N_3), 1.28 (d, *J* = 6.6 Hz, 3H, CH_3).**^{13}C NMR** (101 MHz, $CDCl_3$) δ 99.15(C-1), 71.87, 71.53, 70.80(OCH_2), 70.63(OCH_2), 70.33(OCH_2), 70.18(OCH_2), 69.58, 67.64(OCH_2), 66.26(C-5), 50.80(CH_2N_3), 16.37(C-6). **HRMS:** calculated m/z for $C_{12}H_{23}N_3O_7Na$ $(M+Na)^+$ 344.1428; found 344.1420

General protocol for preparing LA-EG$_n$-CCH linkers by amide coupling: A solution of H_2N-$(EG)_n$-CCH (1 eq), lipoic acid (1 eq) and DMAP (0.2 eq) in dry CH_2Cl_2 (0.2 M) was cooled to 0˚C under an N_2 atmosphere and stirred for 10 minutes. DCC (1.3 eq) in CH_2Cl_2 was added dropwise and the reaction was stirred at 0˚C for a further hour and then left to gradually return to r.t and stirred for 24 hours. The reaction mixture was filtered through celite and the solid washed with $CHCl_3$. The combined filtrate and washings were concentrated *in vacuo* and purification by flash column chromatography (silica, CH_2Cl_2:MeOH = 20:1) afforded the desired products as a yellow oils.

Lipoamide-hexa(ethylene glycol)-propargyl (LA-EG$_6$-CCH) (8b)

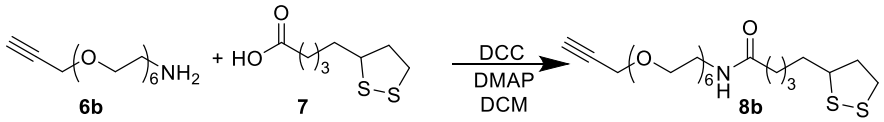

Yield: 1.57g, 3.09 mmol, 99%

^{1}H NMR (400 MHz, $CDCl_3$) δ 6.28 (s, 1H, N*H*), 4.20 (d, *J* = 2.4 Hz, 2H, C*H*$_2$CCH), 3.72 – 3.58 (m, 18H), 3.58 – 3.52 (m, 3H), 3.44 (td, *J* = 5.6, 4.4 Hz, 2H), 3.22 – 3.06 (m, 2H), 2.50 – 2.41 (m, 2H), 2.22 – 2.16 (m, 2H), 1.96 – 1.84 (m, 4H), 1.77 – 1.61 (m, 4H), 1.52 – 1.39 (m, 2H). **^{13}C NMR** (101 MHz, $CDCl_3$) δ 172.94(C=O), 106.6(*C*CH), 74.69(C*C*H), 70.72, 70.56, 70.36, 70.11, 69.25, 58.55 (*C*H$_2$CCH), 56.58(CH), 40.38, 39.31, 38.61, 36.47, 34.82, 29.08, 25.53. **MS**: calcd m/z for $C_{23}H_{42}NO_7S_2$ $(M+H)^+$ 508.24; found 508.21.

Lipoamide-dodeca(ethylene glycol)-propargyl (LA-EG$_{12}$-CCH) (8c)

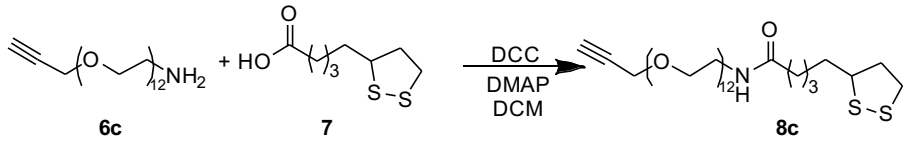

6c 7 8c

Yield: 262 mg, 0.34 mmol, 40%

^{1}H NMR (400 MHz, $CDCl_3$) δ 6.37 (s, 1H, N*H*), 4.19 (d, *J* = 2.4 Hz, 2H), 3.71 – 3.57 (m, 44H), 3.54 (dd, *J* = 5.6, 4.4 Hz, 3H), 3.43 (q, *J* = 4.4 Hz, 2H), 3.21 – 3.05 (m, 2H), 2.49 – 2.40 (m, 2H), 2.22 – 2.16 (m, 2H), 1.90 (dq, *J* = 12.7, 7.0 Hz, 1H), 1.76 – 1.58 (m, 4H), 1.53 – 1.38 (m, 2H). **^{13}C NMR** (101 MHz, $CDCl_3$) δ 172.94(C=O), 79.67, 74.56(C*C*H), 70.57, 70.52, 70.41, 70.21, 69.92, 69.11, 58.40 (*C*H_2CCH), 56.44(*C*H), 40.24, 39.22, 38.47, 36.25, 34.67, 28.93, 25.41. **MS**: calcd m/z for $C_{35}H_{66}NO_{13}S_2$ $(M+H)^+$ 772.39; found 772.62.

General protocol for preparing LA-glycan ligands via click chemistry: To a 1:1 (v:v) THF: H_2O solution (2.0-5.0 mL) containing the glycan (1.1 eq) and LA-conjugated linker (1 eq), was added $CuSO_4.5H_2O$ (0.036 eq), TBTA (0.063 eq) followed by sodium ascorbate (0.135 eq) and the resulting solution was stirred at r.t. After 3h, TLC confirmed the consumption of all starting materials. The solvent was evaporated and the crude product was purified by size exclusion chromatography using Biogel P2 column and 20 mM ammonium formate solution as the eluent to afford the pure products.

(LA-EG$_2$) α-L-fucopyranoside (LA-EG$_2$-fucose) (10a)

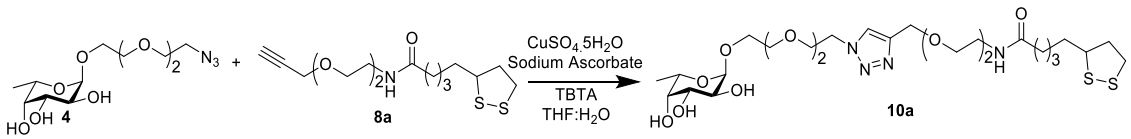

4 8a 10a

Yield: 9.2 mg, 0.014 mmol, 15%

^{1}H NMR (400 MHz, D_2O) δ 8.41 (s, 1H, N*H*), 8.02 (s, 1H, triazole-H), 4.80 (d, *J* = 3.9 Hz, 1H, Fuc-H1), 4.62 (s, 2H), 4.57 (t, *J* = 5.1 Hz, 2H), 4.01 – 3.94 (m, 1H), 3.90 (t, *J* = 5.1 Hz, 2H), 3.81 – 3.48 (m, 19H), 3.30 (t, *J* = 5.4 Hz, 2H), 3.11 (qt, *J* =11.4, 6.4 Hz, 2H), 2.39 (dq, *J* = 12.3, 6.1 Hz, 1H), 2.16 (t, *J* = 7.2 Hz, 2H), 1.88 (dd, *J* = 13.2, 6.7 Hz, 1H), 1.64 (dq, *J* = 13.8, 7.3 Hz, 1H), 1.52 (hept, *J* = 7.5, 6.8 Hz, 2H), 1.31 (p, *J* = 7.7 Hz, 2H), 1.12 (d, *J* = 6.8 Hz, 3H). **^{13}C NMR** (101 MHz, D_2O) δ 176.68 (C=O), 125.44(C*C*H), 98.61(Fuc-C1), 71.80, 69.73, 69.66, 69.58, 69.52, 69.46, 69.02, 68.91, 68.79, 68.08, 66.82, 66.59, 63.15, 56.57, 50.05, 40.27, 38.92, 38.15, 35.48, 33.76, 27.88, 25.07, 15.36. **HRMS**: calcd m/z for $C_{27}H_{49}N_4O_{10}S_2$ $(M+Na)^+$ 675.2710; found 675.2707.

(LA-EG$_6$) α-L-fucopyranoside (LA-EG$_6$-fucose) (10b)

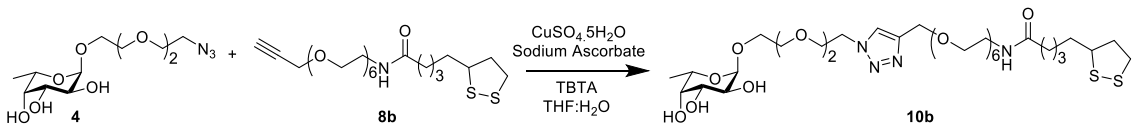

Yield: 28.3 mg, 0.034 mmol, 58%

^{1}H NMR (400 MHz, D_2O) δ 8.12 (s, 1H, triazole-H), 4.89 (d, *J* = 3.9 Hz, 1H, Fuc-H1), 4.72 (s, 2H), 4.66 (t, *J* = 5.0 Hz, 2H), 4.07 (q, *J* = 6.7 Hz, 1H), 4.00 (t, *J* = 5.0 Hz, 2H), 3.89 – 3.60 (m, 33H), 3.40 (t, *J* = 5.3 Hz, 2H), 3.22 (qt, *J* = 11.2, 6.4 Hz, 2H), 2.49 (dq, *J* = 12.0, 5.9 Hz, 1H), 2.27 (t, *J* = 7.2 Hz, 2H), 1.99 (dq, *J* = 13.5, 6.8 Hz, 1H), 1.76 (dq, *J* = 13.5, 7.2 Hz, 1H), 1.70 – 1.56 (m, 3H), 1.42 (p, *J* = 7.6 Hz, 2H), 1.21 (d, *J* = 6.5 Hz, 3H). **^{13}C NMR** (101 MHz, D_2O) δ 176.80(C=O), 125.48(C*C*H), 98.60(Fuc-C1), 71.80, 69.71, 69.66, 69.60, 69.56, 69.49, 69.44, 68.94, 68.89, 68.77, 68.07, 66.81, 66.59, 63.10, 56.54, 50.04, 40.27, 38.91, 38.10, 35.48, 33.74, 27.87, 25.04, 15.32. **HRMS**: calcd m/z for $C_{35}H_{64}N_4O_{14}S_2$ $(M+Na)^+$ 851.3758; found 851.3782.

(LA-EG$_{12}$) α-L-fucopyranoside (LA-EG$_{12}$-fucose) (10c)

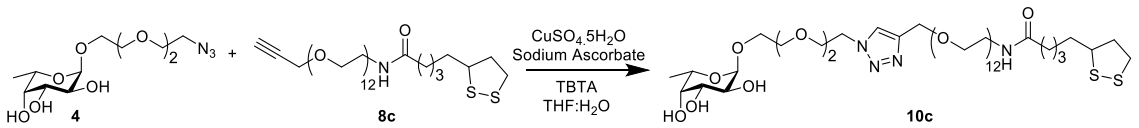

Yield: 29.5 mg, 0.027 mmol, 69%

^{1}H NMR (400 MHz, D_2O) δ 8.12 (s, 1H), 4.89 (d, *J* = 3.8 Hz, 1H, Fuc-H1), 4.71 (s, 2H), 4.66 (t, *J* = 5.0 Hz, 2H), 4.07 (q, *J* = 6.6, 5.9 Hz, 1H), 4.00 (t, *J* = 5.0 Hz, 2H), 3.87 (dd, *J* = 10.4, 3.2 Hz, 2H), 3.79 (s, 3H), 3.77 – 3.58 (m, 54H), 3.40 (t, *J* = 5.3 Hz, 2H), 3.30 – 3.15 (m, 1H), 2.57 – 2.45 (m, 1H), 2.28 (t, *J* = 7.1 Hz, 2H), 2.07 – 1.94 (m, 1H), 1.82 – 1.72 (m, 1H), 1.71 – 1.57 (m, 3H), 1.49 – 1.38 (m, 2H), 1.21 (d, *J* = 6.5 Hz, 3H). **^{13}C NMR** (101 MHz, D_2O) δ 98.60(Fuc-C1), 71.80, 69.59, 68.91, 68.77, 68.07, 66.81, 66.59, 63.08, 56.54, 50.02, 40.27, 38.91, 38.10, 35.48, 33.75, 27.87, 25.04, 15.31. **HRMS**: calcd m/z for $C_{47}H_{89}N_4O_{20}S_2$ $(M+H)^+$ 1094.56014; found 1094.5605.

(LA-EG$_2$) α-D-mannopyranosyl-(1→2)-α-D-mannopyranoside (LA-EG$_2$-dimannose) (11a)

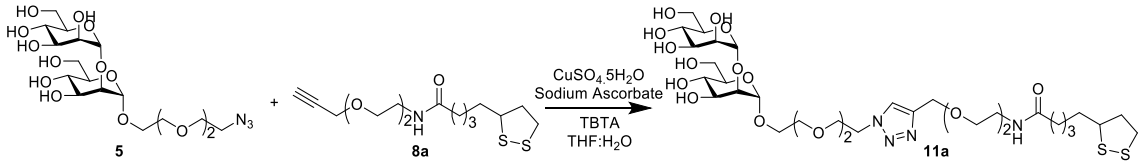

Yield: 64.8 mg, 0.078 mmol, 52%

^{1}H NMR (400 MHz, D_2O) δ 8.03 (s, 1H, triazole-H), 5.03 (d, *J* = 1.8 Hz, 1H, dimannose-H1), 4.95 (d, *J* = 1.8 Hz, 1H, dimannose-H1'), 4.63 (s, 2H), 4.58 (t, *J* = 5.0 Hz, 2H), 3.99 (s, 1H), 3.94 – 3.46 (m, 28H), 3.30 (t, *J* = 5.3 Hz, 2H), 3.12 (qt, *J* = 11.3, 6.4 Hz, 2H), 2.39 (dq, *J* = 12.3, 6.1 Hz, 1H), 2.16 (t, *J* = 7.2 Hz, 2H), 1.88 (dq, *J* = 13.5, 6.9 Hz, 1H), 1.64 (dq, *J* = 13.8, 7.3 Hz, 1H), 1.52 (hept, *J* = 7.7, 6.9 Hz, 3H), 1.31 (p, *J* = 7.6 Hz, 2H). **^{13}C NMR** (101 MHz, D_2O) δ 176.77(C=O), 170.93(*C*CH), 125.47(C*C*H), 102.30 (dimannose-C1'), 98.36 (dimannose-C1), 78.64, 73.25, 72.76, 70.30, 70.17, 69.94, 69.69, 69.54, 69.45, 69.01, 68.89, 68.81, 66.91, 66.87, 66.51, 63.13, 61.13, 60.89, 56.55, 50.07, 40.27, 38.92, 38.12, 35.47, 33.72, 27.84, 25.05. **HRMS**: calcd m/z for $C_{33}H_{59}N_4O_{16}S_2$ $(M+H)^+$ 831.3367; found 831.3367.

(LA-EG$_6$) α-D-mannopyranosyl-(1→2)-α-D-mannopyranose (LA-EG$_6$-dimannose) (11b)

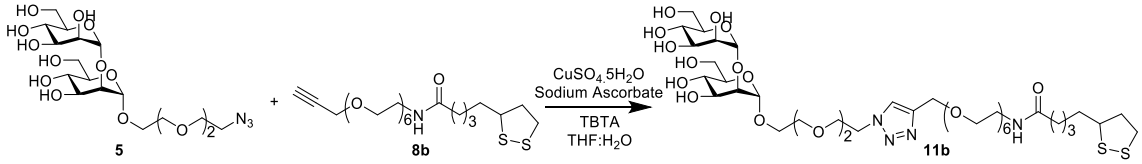

Yield: 35.0 mg, 0.035 mmol, 59%

^{1}H NMR (400 MHz, D_2O) δ 8.12 (s, 1H, triazole-H), 5.12 (d, *J* = 1.8 Hz, 1H, dimannose-H1), 5.03 (d, *J* = 1.8 Hz, 1H, dimannose-H1'), 4.72 (s, 2H), 4.67 (t, *J* = 5.0 Hz, 2H), 4.08 (dd, *J* = 3.4, 1.8 Hz, 1H), 4.04 – 3.96 (m, 3H), 3.96 – 3.60 (m, 41H), 3.40 (t, *J* = 5.3 Hz, 2H), 3.21 (ddt, *J* = 17.8, 11.0, 6.0 Hz, 2H), 2.50 (dq, *J* = 12.3, 6.0 Hz, 1H), 2.28 (t, *J* = 7.2 Hz, 2H), 1.99 (dq, *J* = 13.5, 6.9 Hz, 1H), 1.82 – 1.71 (m, 1H), 1.68 – 1.56 (m, 3H), 1.42 (p, *J* = 7.4 Hz, 2H). **^{13}C NMR** (101 MHz, D_2O) δ 176.82(C=O), 125.47(C*C*H), 102.29 (dimannose-C1'), 98.35 (dimannose-C1), 78.63, 73.25, 72.75, 70.29, 70.16, 69.93, 69.67, 69.60, 69.55, 69.53, 69.44, 68.93, 68.89, 68.80, 66.90, 66.87, 66.50, 63.09, 61.13, 60.89, 56.52, 50.05, 40.27, 38.91, 38.09, 35.48, 33.74, 27.86, 25.04. **HRMS**: calcd m/z for $C_{41}H_{76}N_4O_{20}S_2$ $(M+Na)^+$ 1029.4236; found 1029.4234.

(LA-EG$_{12}$) α-D-mannopyranosyl-(1→2)-α-D-mannopyranose (LA-EG$_{12}$-dimannose) (11c)

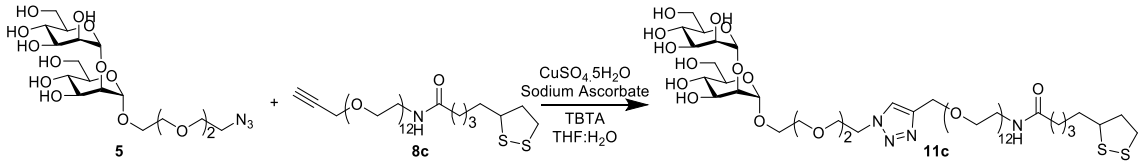

Yield: 27.5 mg, 0.022 mmol, 56%

^{1}H NMR (400 MHz, D_2O) δ 8.11 (s, 1H, triazole-H), 5.12 (d, *J* = 1.8 Hz, 1H, dimannose-H1), 5.03 (d, *J* = 1.8 Hz, 1H, dimannose-H1'), 4.71 (s, 2H), 4.66 (t, *J* = 5.0 Hz, 2H), 4.08 (s, 1H), 4.04 – 3.96 (m, 3H), 3.95 – 3.82 (m, 5H), 3.82 – 3.59 (m, 61H), 3.40 (t, *J* = 5.3 Hz, 2H), 3.31 – 3.13 (m, 2H), 2.50 (dq, *J* = 11.1, 5.5, 4.9 Hz, 1H), 2.32 – 2.23 (m, 3H), 2.00 (dq, *J* = 14.0, 7.0 Hz, 1H), 1.84 – 1.70 (m, 1H), 1.69 – 1.56 (m, 3H), 1.43 (p, *J* = 7.7 Hz, 2H). **^{13}C NMR** (101 MHz, D_2O) δ 176.82(C=O), 125.46(C<u>C</u>H), 102.29 (dimannose-C1'), 98.35 (dimannose-C1), 78.63, 73.25, 72.75, 70.29, 70.15, 69.93, 69.67, 69.58, 69.43, 68.91, 68.79, 66.88, 66.49, 63.06, 61.13, 60.89, 56.53, 50.03, 40.27, 38.91, 38.09, 35.48, 33.75, 27.87, 25.04. **HRMS**: calcd m/z for $C_{53}H_{102}N_4O_{26}S_2$ $(M+NH_4)^+$ 1288.2654; found 1288.6264

LA-EG$_6$-OH (12b)

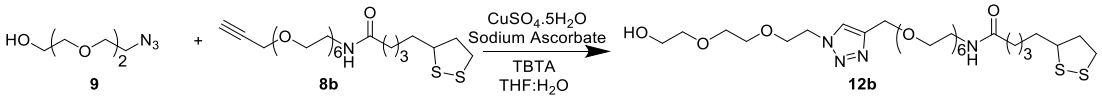

Yield: 37.0 mg, 0.054 mmol, 55%

^{1}H NMR (501 MHz, D_2O) δ 8.13 (s, 1H, triazole-H), 4.71 (s, 2H), 4.66 (t, *J* = 5.1 Hz, 2H), 3.99 (t, *J* = 5.1 Hz, 2H), 3.80 – 3.51 (m, 51H), 3.39 (t, *J* = 5.3 Hz, 2H), 3.30 – 3.14 (m, 2H), 2.49 (dq, *J* = 12.3, 6.1 Hz, 1H), 2.27 (t, *J* = 7.2 Hz, 2H), 1.99 (dq, *J* = 13.5, 6.8 Hz, 1H), 1.76 (dtd, *J* = 13.4, 7.9, 5.4 Hz, 1H), 1.70 – 1.55 (m, 3H), 1.42 (p, *J* = 7.6 Hz, 2H).**^{13}C NMR** (126 MHz, D_2O) δ 176.76(C=O), 71.67, 69.70, 69.66, 69.61, 69.56, 69.44, 69.37, 68.93, 68.90, 68.73, 63.10, 60.35, 56.53, 50.01, 40.27, 38.91, 38.10, 35.48, 33.76, 27.89, 25.05. **HRMS:** calcd m/z for $C_{29}H_{55}N_4O_{10}S_2$ $(M+H)^+$ 683.3360; found: 863.3354.

LA-EG$_{12}$-OH (12c)

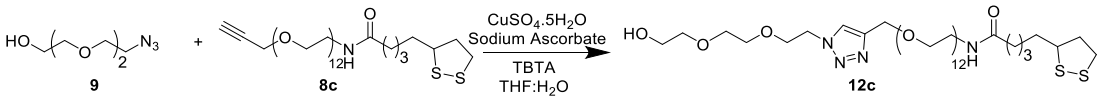

Yield: 28.7 mg, 0.03 mmol, 78%

^{1}H NMR (400 MHz, D2O) δ 8.14 13 (s, 1H, triazole-H), 4.71 (s, 2H), 4.66 (t, *J* = 5.0 Hz, 2H), 4.00 (t, J = 5.0 Hz, 2H), 3.81 – 3.61 (m, 55H), 3.56 (t, *J* = 4.7 Hz, 2H), 3.40 (t, *J* = 5.3 Hz, 2H), 3.23 (tq, *J* = 17.9, 8.1 Hz, 2H), 2.50 (dd, *J* = 12.5, 6.0 Hz, 1H), 2.28 (t, *J* = 7.2 Hz, 2H), 2.00 (dd, *J* = 13.2, 6.7 Hz, 1H), 1.83 – 1.71 (m, 1H), 1.70 – 1.58 (m, 3H), 1.50 – 1.37 (m, 2H).**^{13}C NMR** (101 MHz, D2O) δ 176.81(C=O), 71.66, 69.59, 69.44, 69.36, 68.90, 68.72, 63.10, 60.35, 56.54, 50.02, 40.27, 38.90, 38.09, 35.47, 33.75, 27.87, 25.04. **HRMS:** calcd m/z for $C_{41}H_{80}N_4O_{16}S_2$ $(M+2H)^{2+}$ 474.2506; found: 474.2183.

2.4.2 Gold nanoparticle synthesis

2.4.2.1 G5-citrate

Trisodium Citrate (97 mg, 0.33mmol) was dissolved in 150 mL ultrapure water. The solution was then transferred to a freshly cleaned 250 mL three-necked flask and stirred vigorously. Aqueous solutions of tannic acid (0.1 mL, 2.5 mM) and K_2CO_3 (1 mL, 150 mM) were added and the reaction heated to 75 ^oC for 30 minutes. $HAuCl_4$. $3H_2O$ (1 mL, 25 mM) was added and the reaction stirred for a further 30 minutes. The heating bath was then removed, and the solution was allowed to cool to r.t naturally. The prepared GNP solution was transferred to a clean glass container and stored at r.t.

2.4.2.2 G13-citrate

$HAuCl_4.3H_2O$ (79 mg, 0.2 mmol) was dissolved in 200 mL of ultrapure water. The solution was then transferred to a freshly cleaned 250 mL three-necked flask and heated to reflux in an oil bath under magnetic stirring. When the solution began to reflux, an aqueous solution of trisodium citrate (228 mg, 10 mL, 77.6 mM) was quickly added and the resulting solution was continuously refluxed. The colour of the solution changed from yellow to deep red in ~1 min. After refluxing for another 50 min, a stable deep red solution was obtained. The heating bath was then removed, and the solution was allowed to cool to r.t naturally. The prepared GNP solution was transferred to a clean glass container and stored at r.t.

2.4.2.3 G27-citrate

$HAuCl_4.3H_2O$ (20 mg, 0.05 mmol) was dissolved in 200 mL of ultrapure water. The solution was then transferred to a freshly cleaned 250 mL three-necked flask and stirred

vigorously for 10 minutes. An aqueous solution of NaOH (1 mL, 25 mM) was added and the reaction heated to reflux. An aqueous solution of trisodium citrate (3 mL, 165 mM) was added quickly and the reaction continued to stir for 1h. The heating bath was then removed, and the solution was allowed to cool to r.t naturally. The prepared GNP solution was transferred to a clean glass container and stored at r.t.

2.4.2.4 G5 Cap exchange

100 mL of G5-citrate stock was concentrated to ~ 2 μM using 10 kDa MWCO spin column and washed with H_2O (3 x) at 4000 rpm for 15 min to remove any impurities. The concentration of the G5-citrate was determined from its absorbance at 515 nm using the Beer Lambert law and a G5 molar extinction coefficient of 1.1×10^7 $M^{-1} \cdot cm^{-1}$. Then glycan ligands dissolved in H_2O to 5 or 10 mM were added to the G5-citrate solution in a molar ratio of G5/glycan = 1:1000, 1:500 or 1:300. The resulting solution was mixed and stirred at r.t for 2 days. The resulting mixture was passed through a 10 kDa MWCO spin column by centrifugation at 4000 rpm for 15 min and the residues were washed with H_2O (3 × 200 μL) to give the GNP-glycan stock. The concentration of the G5-glycans was determined from its absorbance at 515 nm using the Beer Lambert law and a G5 molar extinction coefficient of 1.1×10^7 $M^{-1} \cdot cm^{-1}$.

2.4.2.5 G13 and G27 cap exchange

100 mL of G13- or G27-citrate stock was concentrated to ~ 100 nM or 10 nM respectively using 30 kDa MWCO spin column and washed with H_2O (3 ×) to remove any impurities. The exact concentration of the G13- and G27-citrate was determined from its absorbance at 520 nm using the Beer Lambert law and their molar extinction coefficients of 2.32×10^8 $M^{-1}cm^{-1}$ and 2.39×10^{-9} $M^{-1}cm^{-1}$ respectively. Bis(p-sulfonatophenyl) phenylphosphine dipotassium (BSPP) dissolved in water to 5 mM was added to the G13 or G27 in a molar ratio of GNP: BSPP = 1:5000 or 1:25000 respectively. The resulting solution was sonicated for 4 minutes and then left in the dark for 24 hours. The resulting mixture was passed through a 30 kDa MWCO spin column by centrifugation at 4000 rpm for 5 min and the residues were washed with H_2O (3 × 200 μL) to give the GNP-BSPP stock. The concentration of the G13- and G27-BSPP was determined from its absorbance at 520 nm using the Beer Lambert law. Then glycan ligands dissolved in H_2O to 5 or 10 mM were added to the G13 or G27-BSPP solution in a molar ratio of GNP/glycan = 1:5000 or 1:25,000. The resulting solution was sonicated for 4 minutes and then left in the dark for 24 hours. The resulting mixture was passed through a 30 kDa MWCO spin column by centrifugation at 4000 rpm for 5 min and the residues were washed with H_2O (3 × 500 μL) to give the G13- or G27-glycans. The concentration of the G13- and G27-glycans was determined from their absorbance at 520 nm using the Beer Lambert law.

2.5 Phenol sulphuric acid colorimetry assay

The number of glycan ligands conjugated to each G5 was quantified using a phenol-sulfuric acid method of carbohydrate quantification. Calibration curves were constructed by adding sulphuric acid (175 µL) and phenol (35 µL, 5% w/w H_2O) to a known amount of LA-EG_n-glycan dissolved in 35 µL H_2O. Samples were vortexed immediately then incubated at 90 ^oC for 20 minutes and their absorbance at 490 nm read on a Varian Cary 50 bio UV-Visible Spectrophotometer in a disposable cuvette. A calibration curve of absorbance at 490 nm vs. ligand amount was constructed which was fitted with a linear fit.

After cap exchange, GNP-glycans were washed 3 x with dH_2O in a 10 kDa MWCO Amicon ultra-S2centrifugal filter. The flow through was collected, combined, lyophilised and dissolved in H_2O. 35 µL of these samples were treated as described above for the calibration samples. The calibration curve was then used to determine the quantity of unbound LA-EG_n-glycan from their absorbance at 490 nm. The number of bound ligand could then be calculated by subtracting the unbound ligand was the total used initially. By comparing this to the mols of GNP used in the initial cap exchange, the quantity of glycan per nanoparticle was calculated.

2.6 Dynamic light scattering

The hydrodynamic diameters (D_h) of GNP-glycans in pure water and in a binding buffer (20 mM HEPES, 100 mM NaCl, 10 mM $CaCl_2$, pH 7.8) were recorded on a Malvern ZETASizer-Nano using disposable polystyrene cuvettes. Three to five consecutive scans were performed for each sample and the mean volume D_h distribution histograms for each sample were obtained by fitting the averaged percentage volume hydrodynamic sizes with Gaussian distributions (Equation 2.4) using origin 2019b (where y denotes the volume percentage intensity, x denotes the hydrodynamic size, xc is the hydrodynamic size distribution centre, w is the standard deviation, A is the integrated area, and FWHM (Equation 2.5) is the full width at half of the maximum amplitude). The resulting D_h values are reported as xc ± ½ FWHM. All protein containing samples were performed by mixing GNP-glycan with wild type or atto-643 labelled DC-SIGN and incubating at r.t for 20 minutes before taking the measurement.

$$y = y_0 + \frac{A}{w\sqrt{\frac{\pi}{2}}} . e^{\frac{-2(x-xc)^2}{w^2}} \qquad \textbf{Equation 2.4}$$

$$FWHM = w\sqrt{\ln(4)}$$ **Equation 2.5**

2.7 Fluorescence quenching and thermodynamic studies

All fluorescence spectra were recorded on a Cary Eclipse Fluorescence Spectrophotometer using a 0.70 mL quartz cuvette under a fixed λ_{ex} of 630 nm over a range of 650–800 nm. All measurements were performed in HEPES binding buffer (20 mM HEPES, 100 mM NaCl, 10 mM $CaCl_2$, pH 7.8) containing 1 mg/mL of BSA. For the apparent K_d measurement, the concentrations of labelled DC-SIGN and G5-glycans were varied from 3-100 nM in a fixed protein/G5-glycan molar ratio (PGR) of 1:1. The samples were incubated at the desired temperature for 20 min before recording the fluorescence intensity. The fluorescence intensity of the protein in the absence of the G5-glycans, recorded under identical experiment conditions, were used to determine the quenching efficiency. The excitation and emission slit widths and instrument PMT voltages were adjusted to compensate the low fluorescence signals at low concentrations. The quenching efficiencies (QE) of DC-SIGN binding to each GNP-glycan was calculated via Equation 4.1 and the resulting QE-concentration relationship was fitted by Hill's Equation 4.2 to derive the apparent binding K_d values.

Thermodynamic measurements were obtained by repeating these measurements at temperatures of 22, 27 and 32 °C. The cuvette temperature was maintained by a water pump system. Buffer and sample temperatures were controlled by incubation in dry bath. The standard binding enthalpy and entropy changes were obtained using a van 't Hoff analyses of the linear fit of ln(K_d)against 1/T, were the standard binding enthalpy and entropy changes can be extracted from the slope and intercept.

2.8 Isothermal titration calorimetry

Wild-type DC-SIGN was dialysed over 48 hours against the binding buffer (20 mM HEPES, 100 mM NaCl, 2 mM $CaCl_2$, pH 7.8) at 4 °C. The post-dialysis buffer was stored at 4 °C for subsequent experiments, including preparation of all samples, control titrations, and rinsing the syringe and cell between each measurement. DC-SIGN was concentrated by centrifugal ultrafiltration (10 kDa MWCO filter) to obtain a final concentration of 30 μM. The G5-EG_n-glycans were buffer exchanged three times with the post-dialysis buffer using a 10 kDa MWCO centrifugal filter to obtain final concentrations of between 700-300 nM depending on the sample. Isothermal titration calorimetry was performed by Dr Iain Manfield in the Astbury Centre at the University of Leeds, using a MicroCal iTC200, with the G5-glycan solutions loaded into the syringe, and DC-SIGN loaded into the calorimeter cell. Titrations were conducted at 25 °C with an initial 0.5 μL injection, followed by nineteen 2 μL injections. Unless stated otherwise,

NITPIC was used to integrate the stepwise enthalpy changes for each titration using a one-site binding model and SEDPHAT was used to fit curves, globally for repeat titration.(156) A linear baseline was fitted to the data to account for heat of dilution effects. Data visualisation was performed with GUSSI.(156)

2.9 Viral inhibition

Inhibition studies were performed by Inga Nehlmeier and Amy Madeleine Kempf in Stefan Pöhlmann's group at the German Primate Centre, Göttingen, Germany. The effects of GNP-glycans on Ebola virus glyco-protein (EBOV-GP) driven entry into 293T cells were assessed using a previously established procedure.(119) Briefly, 293T cells seeded in 96-well plates were transfected with plasmids encoding DC-SIGN or DC-SIGNR or control transfected with empty plasmid (pcDNA). The cells were washed at 16h post transfection and further cultivated at 37 °C, 5% CO_2 in Dulbecco's modified eagle medium (DMEM) containing 10% fetal bovine serum (FBS). At 48h post transfection, the cells were exposed to twice the final concentration of GNP-glycan inhibitor in DMEM supplemented with 10% FBS for 30 min in a total volume of 50 µL. Thereafter, the resulting cells were inoculated with 50 µL of preparations of VSV vector particles encoding the luciferase gene and bearing either EBOV-GP (which can use DC-SIGN/R for augmentation of host cell entry) or the vesicular stomatitis virus glycoprotein (VSV-G, which cannot use DC-SIGN/R for augmentation of host cell entry). At 6h post inoculation, 100 µL of fresh DMEM culture medium was added and the cells incubated for another 72h. Thereafter, luciferase activities in cell lysates were determined using a commercially available kit (PJK), following the manufacturer's instructions and normalised by the corresponding control collected in the absence of the lectin-GNP. The normalised concentration-dependent inhibition data were fitted by a normalised variable slope four-parameter logistic (4PL) curve model using Origin.

Chapter 3 – Preparation of Gx-glycans and probing the effect of linker length, glycan density and scaffold size on DC-SIGN multivalent binding.

3.1 Introduction

Glyconanoparticles are typically characterised by a nano-sized core, polyvalently capped with glycan-containing ligands. During development in the field of glyconanotechnology, different scaffolds of various shapes, sizes and materials have been utilised as platforms from which to attach carbohydrate tendrils, including, proteins(157-159), polymers(160, 161), dendrimers(162-164), fullerenes(165, 166), vesicles(167), nucleic acids(168, 169) and inorganic nanoparticles(120, 170). Inorganic nanoparticles (NPs) in particular have been indispensable in glycoconjugate design due to their inexpensive, straightforward synthesis and easily tuneable nature in terms of size, shape and surface glycan coverage. Synthesis conditions can alter their size from a few nm to a few hundred nm, along with the shape ranging from spherical to rod-like to match the size or shape of an individual glycoprotein, or mimic a whole virus or bacterial cell. Their surfaces are also often easy to functionalise through strong covalent interactions and the extent of surface coverage or choice of functional ligands can be altered to convey specific properties such as hydrophilicity and biocompatibility and the specific glycan chosen to mimic whichever process, protein or particle is under study. Additional properties can also be introduced into the core structure of NPs, such as fluorescence, superparamagnetism, or photothermal properties.(171-173) This affords these NPs extra capabilities which can be harnessed to provide further therapeutic benefit, or information on binding behaviour via lab-based techniques. This multifunctionality is present in quantum dots (QDs) and gold nanoparticles (GNPs), which have strong fluorescence (with QDs) or fluorescence quenching (with GNPs) properties, allowing them to partake in fluorescence resonance energy transfer, a technique discussed at large in Chapter 4 to measure binding affinity.

One of the most critical considerations in the rational design of glyconanoparticles for targeting multivalent lectin glycan interactions (MLGIs) is the selection of the carbohydrate ligand and its ability to effectively engage with individual lectin binding sites. A widely adopted strategy for achieving high affinity interactions involves mimicking natural glycoproteins, which inherently present optimal glycan structures for selective and high affinity binding to their target lectins. This is often accomplished by decorating nanoparticles with monosaccharide units identified as key ligands for the target lectin. However, the binding affinity and biological performance can often be further improved by employing oligo- or polysaccharide-based ligands, which more closely resemble the native glycan presentation on glycoproteins.

For instance, in the case of DC-SIGN binding, nanoparticles functionalised with oligo mannose-based ligands have shown superior antiviral activity compared to those coated with monovalent mannose.(174) This enhancement is consistent with DC-SIGN's known preference for high mannose type glycans.(80) Despite this strategy's success, a common limitation is the overlapping carbohydrate recognition among different lectins. Several C-type lectins, including DC-SIGN, DC-SIGNR, the macrophage mannose receptor, and the mannose binding protein all bind to monovalent and polyvalent mannose, making it difficult to achieve selectivity using native carbohydrates alone. In such cases, the incorporation of glycomimetics offers a promising alternative. Glycomimetics are synthetic analogues of natural carbohydrates designed to retain biological recognition properties while introducing structural variations that enable enhanced selectivity or affinity.(59) Notably, glycomimetics have been used to discriminate between closely related lectins. For example, the substitution of a methylene guanidine triazole group at position 2 of monovalent mannose produces a ligand with 50-fold selectivity for DC-SIGNR over DC-SIGN, despite the two proteins sharing over 77% amino acid sequence identity. This ligand also represents the first known example with selective affinity for DC-SIGNR.(175)

However, the use of polysaccharide-based ligands, or glycomimetics, is not without limitations. The design and synthesis of structurally complex polysaccharides, and selective glycomimetics are often technically demanding, time-consuming, and costly. Therefore, practical compromises must be considered between the desired enhancement in binding specificity or affinity and the synthetic complexity associated with employing these strategies.

In addition to the glycan type influencing the binding affinity of glyconanoparticles, other properties of the surface ligands can significantly influence the binding affinity, particularly the flexibility of the ligand. Although linkers are primarily used as a way to tether glycans to the nanoparticle surface, they also play an active role in determining the ability of glycans to interact with their target lectins. This influence is largely thermodynamic, as linker properties affect the conformational freedom and spatial orientation of the ligands. Longer, more flexible ligands will incur greater entropic penalties upon binding and therefore increased ligand flexibility may result in disadvantageous binding.

On the other hand, the capacity of a glyconanoparticle to engage multiple CRDs simultaneously is highly dependent on linker flexibility. While rigid linkers can promote strong binding when the spatial arrangement of glycan and lectin binding sites is well matched, flexible linkers offer a distinct advantage in cases where lectin's inter-binding site distances are variable or unknown. Flexible linkers allow glycans to adopt multiple conformations, enabling better accommodation to the geometry of the lectin binding sites and thus enhancing overall binding avidity.

Understanding how aspects such as glycan type and ligand structure influence the ability of a glycoconjugate to bind a multimeric lectin is an important factor in helping to inform the rational design of more potent and specific ligands for targeting MLGIs. However, apart from the dependency on the ligand itself, binding affinity can also be tuned without resorting to more complex synthesis routes, instead manipulating the size, shape and degree of surface functionalisation of the glyconanoparticle. As discussed with ligand flexibility, the ability of a glyconanoparticle to establish effective multivalent enhancement is reliant on whether the polyvalent glycan display is able to bridge multiple binding sites simultaneously, which can instead be optimised by changing the shape, size and ligand density of glyconanoparticles.

One of the main benefits of using nanoparticles as scaffolds is their comparable size to many intracellular structures, which provides a compatible binding platform with the target lectin, allowing the surface glycans to bind efficiently with more than one binding site simultaneously. Increasing the size or shape of the core itself can enhance the spatial match, by reducing the surface curvature to better fit the target lectins binding sites, and improve the accessibility of the lectin towards the nanoparticle. Furthermore, larger particles may also provide the opportunity to bridge multiple lectins on a cell surface, more closely imitating the mechanisms of native pathogens and allowing for outcomes which may simulate that observed *in vitro* more closely. In addition to this, the size of the scaffold can also contribute to the inhibition potential of nanoparticles by enhancing steric shielding, where other binding sites may become inaccessible due to the size of the particle, despite not directly partaking in binding. Therefore, the size of the glyconanoparticle is a critical parameter to take into account when designing lectin-targeting agents.

While there is a relationship between scaffold size and its potential to bind multivalently to one lectin, or bridge multiple lectins, this will be unsuccessful if the display of glycans on the surface is ineffective. If the density is too sparse, then any increase in size will impart little enhancing effect other than that of steric shielding, as the distance between the glycans will be too large to bridge multiple binding sites of the same lectin and therefore will not benefit from multivalent enhancement. For organic scaffolds such as polymers and dendrimers, density may be controlled by increasing the distance between terminal ligands by adding repeat units to the core structure. For inorganic scaffolds, density is more easily controlled by altering the core: ligand ratio during the cap exchange process. Alternatively, if a higher density is required but the core is saturated as dictated by the ligands' anchor point, then trimer/multimer versions of the glycan be utilised, where one anchor unit will contain >1 glycan in the head group. This method has been successfully utilised to tune binding affinity previously in this group. Adding a trimer of mannose increased binding affinity to DC-SIGN 1.8-fold compared to its monomer mannose counterpart in a solution phase assay. However, discrepancies in

solution phase and surface phase data were observed, thus, further work is needed to elucidate the direct effects of introducing multimers vs monomers in solution vs surface binding.(115)

Glycan density is an important factor to consider for intra-molecular clustering of lectins on the cell surface, especially when using larger, bacterial cell sized particles which may span the length of many cell surface lectins. A study employing two bacteria strains, one with glycoconjugate ligands in high-density nanoscale clusters (MTBC mycobacteria) and one with ligands randomly and less densely displayed (non-MTBC), showed different binding profiles to DC-SIGN on host immune cells. Those with high density bound DC-SIGN with high affinity, and stimulated further recruitment and clustering of the receptor whereas the non-MTBC species precluded efficient binding to DC-SIGN.(176) Thus, controlling glycan density is an important factor in designing probes which are selective and high affinity for certain cell surface lectins.

This chapter investigated how the structural features of glycan coated gold nanoparticles (GNPs) influenced their binding interactions with DC-SIGN. To achieve this, a series of gold nanoparticles of varying core sizes, (5, 13 and 27 nm) were synthesised and functionalised with either a dimannose or fucose containing ligand, which are known to engage DC-SIGN with distinct immunological outcomes.(52) To explore the influence of the ligand presentation on DC-SIGN recognition and binding, several key aspects of the design of these GNPs were varied. Along with GNP size and glycan type, the ligand flexibility and ligand density were also modified. The resulting nanoparticles were then characterised by UV-Vis spectrometry and dynamic light scattering to confirm successful modifications to their structure, and a hydrodynamic size analysis was further used to monitor their binding mode with DC-SIGN over a concentration range.

By dissecting the individual contributions of nanoparticle size, glycan type, ligand flexibility and ligand density, this chapter provides a clearer picture on how the structural features of glyconanoparticles relates to their function. The goal is to better understand how to design glyconanoparticles with tuneable biological activity and lectin specificity, which can contribute to the development of tools for immunomodulatory applications.

3.2 Results and discussion

3.2.1 Glyconanoparticle design

The glycan-GNPs synthesised in this chapter were designed with considerations such as core material, carbohydrate type, linker length, ligand density and scaffold size in mind. As discussed, these design features are known to play critical roles in modulating the avidity and selectivity of multivalent lectin-glycan interactions. Since DC-SIGN binding and immune modulation may be sensitive to these features, fine tuning each of these variables was essential to systematically probe DC-SIGN engagement and downstream signalling outcomes, as discussed later in Chapter 4 and Chapter 7.

Firstly, gold nanoparticles were selected as the core scaffold due to several practical and functional advantages. For example, their small size offers a high surface-area to volume ratio, making them responsive to surface functionalisation with lipoic acid containing ligands, which form 2 stable gold-thiol bonds, allowing a monolayer of ligands to protrude from the GNP surface. These nanoparticles have previously been successfully employed in fluorescence quenching assays to provide quantitative information on binding, such as binding affinity and thermodynamic contributions, owing to their strong fluorescence quenching ability.(115) Importantly GNPs are well documented as biocompatible, making them suitable candidates for subsequent cell based assays to evaluate viral inhibition and biological responses such as cytokine production or T cell proliferation.(177) Their compatibility in both solution phase and cellular assays make them an ideal scaffold for these investigations.

The design of the nanoparticles for this chapter built on prior work by Budhadev *et al.*, with modifications to the linker length, density and glycan identity to better reflect biologically active bacterial and fungal motifs.(115) In Part B of this thesis, fungal and bacterial glycan biology is discussed in the context of immune modulation via DC-SIGN and the regulation of cytokines such as IL-23 and IL-10. Accordingly, glycan selection was guided by those with strong binding affinity to DC-SIGN, and relevance to fungal cell wall structures.

α-D-Mannose-(1→2)-α-D-mannose (dimannose) and α-L-fucose (fucose) were selected as the glycans of choice, based on their ability to bind DC-SIGN with high affinity when displayed multivalently on scaffolds. Notably dimannose shows a greater affinity for DC-SIGN than mono mannose, which is likely due to its ability to engage both primary and secondary glycan binding sites in the CRD of DC-SIGN. Fucose, another common fungal/bacterial sugar forming part of trisaccharide's such as the Lewis antigens which can be effectively recognised by DC-SIGN, was also included.(80) While fucose alone is a relatively weaker monovalent binder than dimannose, its multivalent presentation allows for enhancement through the multivalent effect to produce strong binders.(178)

To conjugate these glycans to the GNP surface, three oligo(ethylene glycol) linkers with varied EG repeat units (EG_n), where n = 2, 6 and 12, were chosen. The use of these linkers is two-fold, first they enable observation of the role of ligand flexibility on binding strength and second, they form a practical design feature to protrude the glycan head groups away from the gold surface. This minimises steric clashes that could hinder binding, while also enhancing solubility, GNP colloidal stability, and reducing non-specific interactions.

The ligand density on the nanoparticle was also varied to model a range of glycan displays similar to what might be observed on bacterial or fungal pathogens. To this end, three glycan densities were chosen ranging from approximately 160 to 650 glycans per 5 nm gold nanoparticle. This would later allow for an investigation into whether DC-SIGN binding is dictated by differences in spatial glycan presentation.

Finally, the size of the scaffold was considered. While it has been observed that larger glyconanoparticles (>20 nm) with a low surface curvature and can exhibit strong binding affinities with DC-SIGN, it was important to keep in mind the methods which would later be used to measure binding affinity.(130) Chapter 4 discusses methods of measuring K_d, including a fluorescence quenching assay. Due to GNP's molar absorption extinction coefficient being positively linked to its volume, larger GNPs induce a significant inner filter effect which interferes with fluorescence quenching results, and therefore a small, 5 nm gold scaffold was chosen initially as this provided a good surface for multivalent display of the carbohydrate ligands, without introducing significant inner filter effects.(115) Later in this chapter the design and decoration of larger GNP scaffolds is also discussed for use in a pull-down assay.

Putting these design features together, a schematic of the structures of the GNP-glycan conjugates and the chemical structures of the glycan ligands used in this study are shown in Figure 2.1. 5 nm Gold nanoparticles (G5) were coated in ligands containing three functional domains. A lipoic acid (LA) functionality for strong binding to the GNP surface via the formation of 2 strong Au-S bonds to impose stability, a flexible oligo-(ethylene glycol) (EG) linker of varying length to enhance water solubility and explore ligand flexibility, and a terminal dimannose or fucose for specific binding to DC-SIGN.

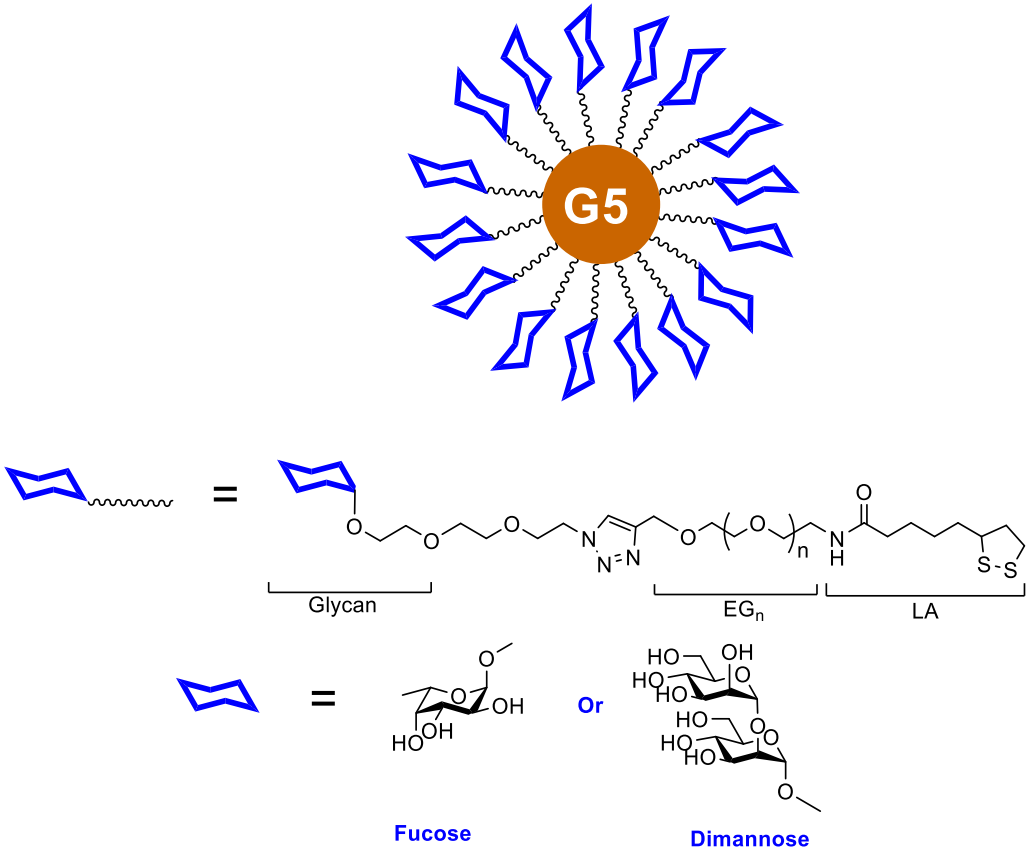

Figure 3.1 Schematic of the GNP-glycans used in this study. The GNP is coated with LA-based glycan ligand containing a terminal glycan. The chemical structures of glycan ligands are depicted underneath, where n = 2, 6, or 12.

3.2.2 G5-glycan preparation

An important factor to take into consideration during any design process is the ease of access to starting materials and the design of a common intermediate that presents opportunities for chemical and structural diversification for concomitant ligand synthesis. In this instance, the easiest way to benefit from a common intermediate was to attach different linker lengths bearing an alkyne moiety to lipoic acid from which different glycans could all be attached simultaneously via copper catalysed click chemistry. Click chemistry is consistently a useful tool in bioconjugation due to its high chemical yields, quick reaction times, stereospecificity, lack of by-products and use of simple catalytic reagents, if any at all. As the molecules described here are not strain promoted, canonical Copper(I)-catalysed azide-alkyne cycloaddition (CuAAC) between the azide and alkyne in the presence of $CuSO_4$ and sodium ascorbate, along with TBTA to stabilise the Cu^{1+} species generated by the reduction of Cu^{2+} by sodium ascorbate was employed. The H_2N-EG_n-alkyne linkers were purchased commercially.

The synthetic route to the fucose ligand and the structure of the dimannose ligand are shown in Scheme 3.1. Briefly fucoside **4** was prepared in a protecting group free Fisher glycosylation with fucose **1** and the acceptor, monochlorinated triethyleneglycol, in the presence of the Appel reagent (CBr_4, PPh_3). Acetylation followed by azidation afforded

α anomer **3** and deprotection gave desired fucose ligand **4**. The dimannose ligand **5** had previously been synthesised in house.(115)

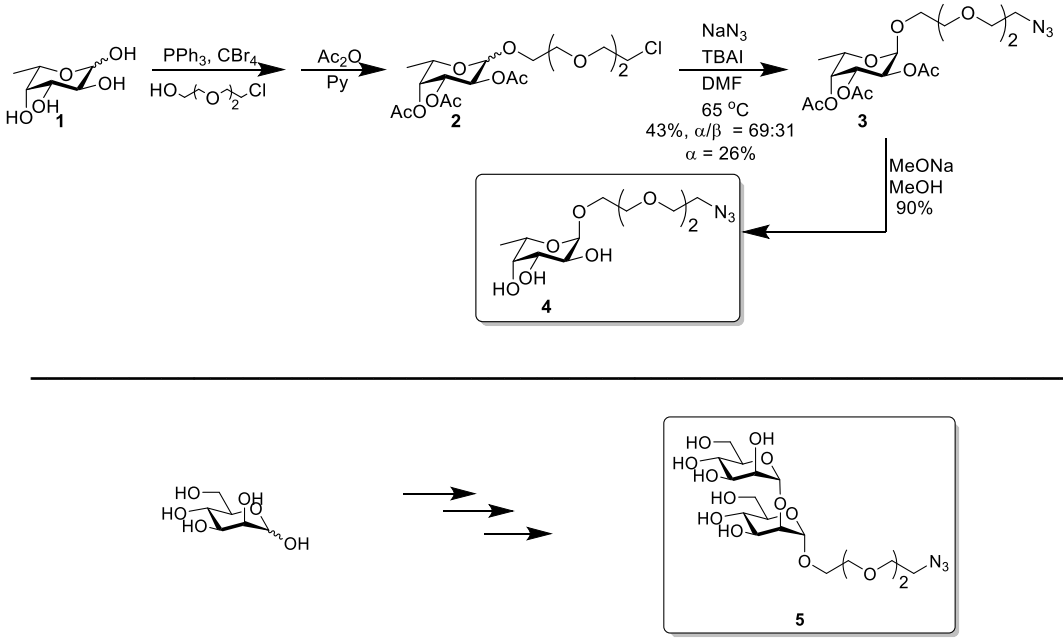

Scheme 3.1 Synthetic route to azido fucose **4**, and the structure of azido dimannose ligand **5***. *Synthesised by Dr Darshita Budhadev.

LA based linker molecules were prepared by a simple amide coupling procedure using dicyclohexylcarbodiimide (DCC) in the presence of DMAP catalyst. While other amide coupling reagents are less hazardous, the benefits they usually provide, such as water soluble by-products, are in this case detrimental as a work-up procedure involving an aqueous wash would remove the water soluble ligand too. Using DCC in DCM results in an insoluble urea by-product that can be filtered off, providing a cleaner product for easier purification. After purification, the LA linkers were coupled efficiently to the N_3-EG_2-fucose/dimannose or N_3-EG_2-OH control via Cu catalysed click chemistry to give the desired LA-EG_n-fucose/dimannose/OH ligands. These molecules were found to be unstable on silica and so purification was carried out by size exclusion on a biogel P2 column using an AKTA prime pump system. Ligands were of >95% purity as characterised by LCMS and NMR.

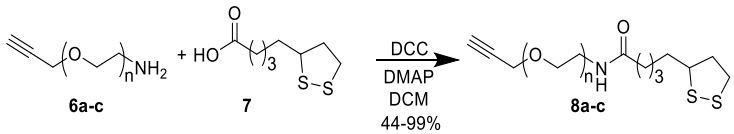

Scheme 3.2 Synthetic route to lipoic acid EG_n-linkers **8a-c**. For a) n=2 b) n=6, c) n=12

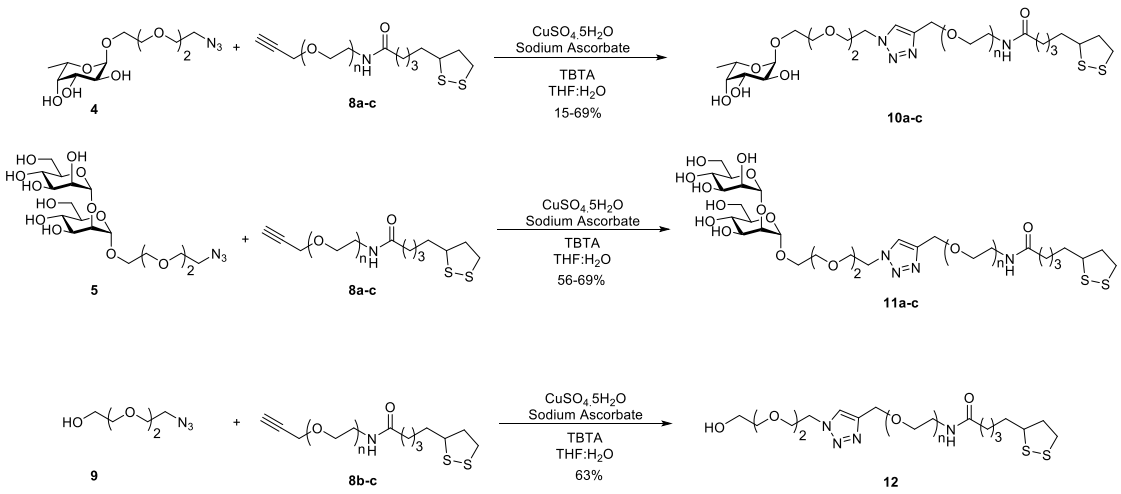

Scheme 3.3 Synthetic route to LA-EG$_n$-fucose, LA-EG$_n$-dimannose and LA-EG$_n$-OH ligands.

G5 nanoparticles were prepared via previously established protocols by refluxing gold(III) chloride trihydrate in water with trisodium citrate in the presence of potassium carbonate and tannic acid, forming citrate stabilised gold nanoparticles, roughly 5 nm in diameter.(125) By exploiting the strong interaction of gold with sulfur, the gold nanoparticles were coated with the desired ligands in a simple one-pot self-assembly procedure (Scheme 3.4). Air stable LA-ligands were stirred directly with the 5 nm nanoparticles in water for 48 hours. The disulfide rings in the LA based ligands are cleaved upon binding to gold surfaces, and displace the weakly bound citrate ions, forming identical self-assembled monolayers on the G5 surface as their reduced dihydrolipoic acid counterparts.(179) Three batches of each GNP-glycan conjugates were prepared under three different gold nanoparticle to ligand molar ratios (GLRs) of 1:1000, 1:500 and 1:300. Any free unbound ligands were removed by ultrafiltration using 10 kDa MWCO filter tubes and washing with pure water.

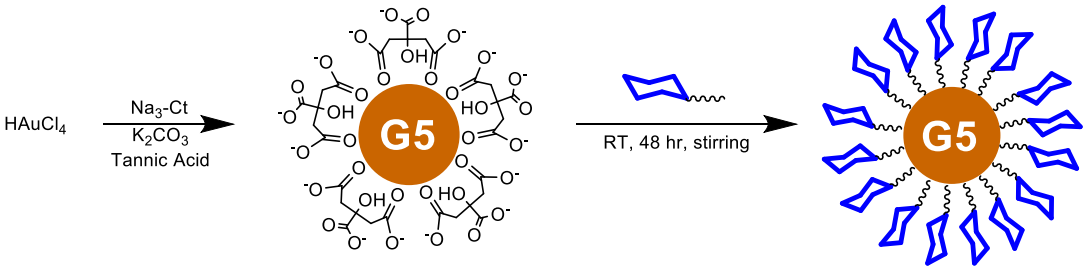

Scheme 3.4 Schematic showing the procedure used to synthesise and cap exchange citrate coated G5 particles to LA-EG$_n$-glycan coated particles.

3.2.3 G5-glycan characterisation

3.2.3.1 UV-absorbance

The successful conjugation of LA-glycan ligands on G5 surface was indicated by a small but discernible red shift in the characteristic SPR absorption peak of G5 as shown in the UV-vis absorbance traces (Figure 3.2). Using G5's absorption extinction coefficient of 1.1 x 10^7 $M^{-1}cm^{-1}$ at its SPR peak λ_{max} of ~510-520, the concentrations of G5-glycans were calculated using the Beer Lambert law (Equation 2.1)

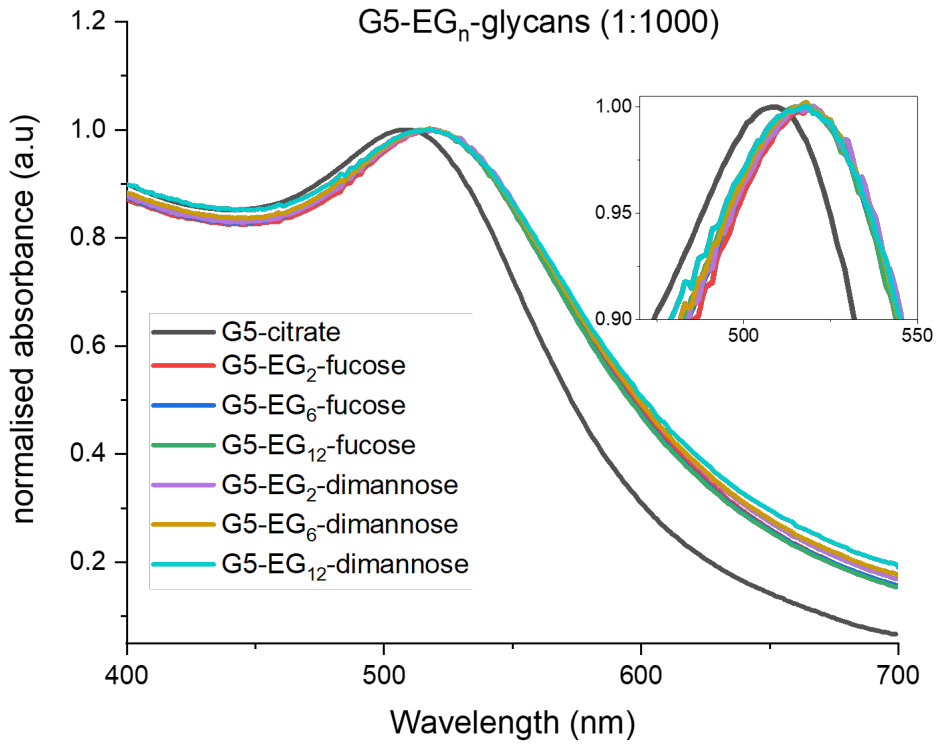

Figure 3.2 Normalised UV-Vis absorbance spectrum for G5s before and after cap exchange with LA-EG$_n$-glycans made in a GLR of 1:1000.

3.2.3.2 Hydrodynamic size

The size of the G5-EG$_n$-glycans was measured by DLS. The diameter that is measured in DLS is a value that refers to how a particle diffuses within a fluid so it is referred to as a hydrodynamic diameter (D_h). In this case, the D_h represents the core gold nanoparticle, plus the ligands and a tightly associated hydration layer. The resulting Gaussian distribution curves for G5's coated in citrate and made in a 1:1000 GLR (GNP:ligand ratio) are shown in Figure 3.3 and Figure 3.4. The Gaussian distributions for those made in a 1:500 and 1:300 GLR can be found in Figure A. 1-2 and a summary of all the hydrodynamic sizes for each GLR can be found in Table 3.1, where D_h values are

reported as the hydrodynamic size distribution centre (xc) ± ½ full width at half maximum peak height (FWHM) as calculated by Equation 2.4 and Equation 2.5.

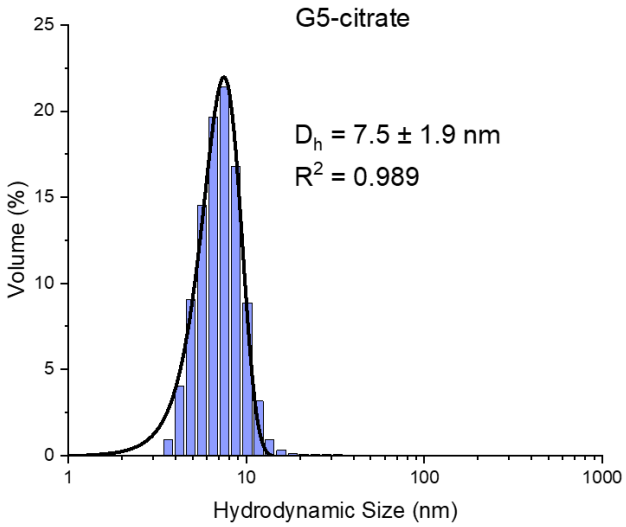

Figure 3.3 Volume population hydrodynamic size distribution histogram of G5-citrate, fitted with a Gaussian distribution curve. (D_h value given as xc ± ½ FWHM).

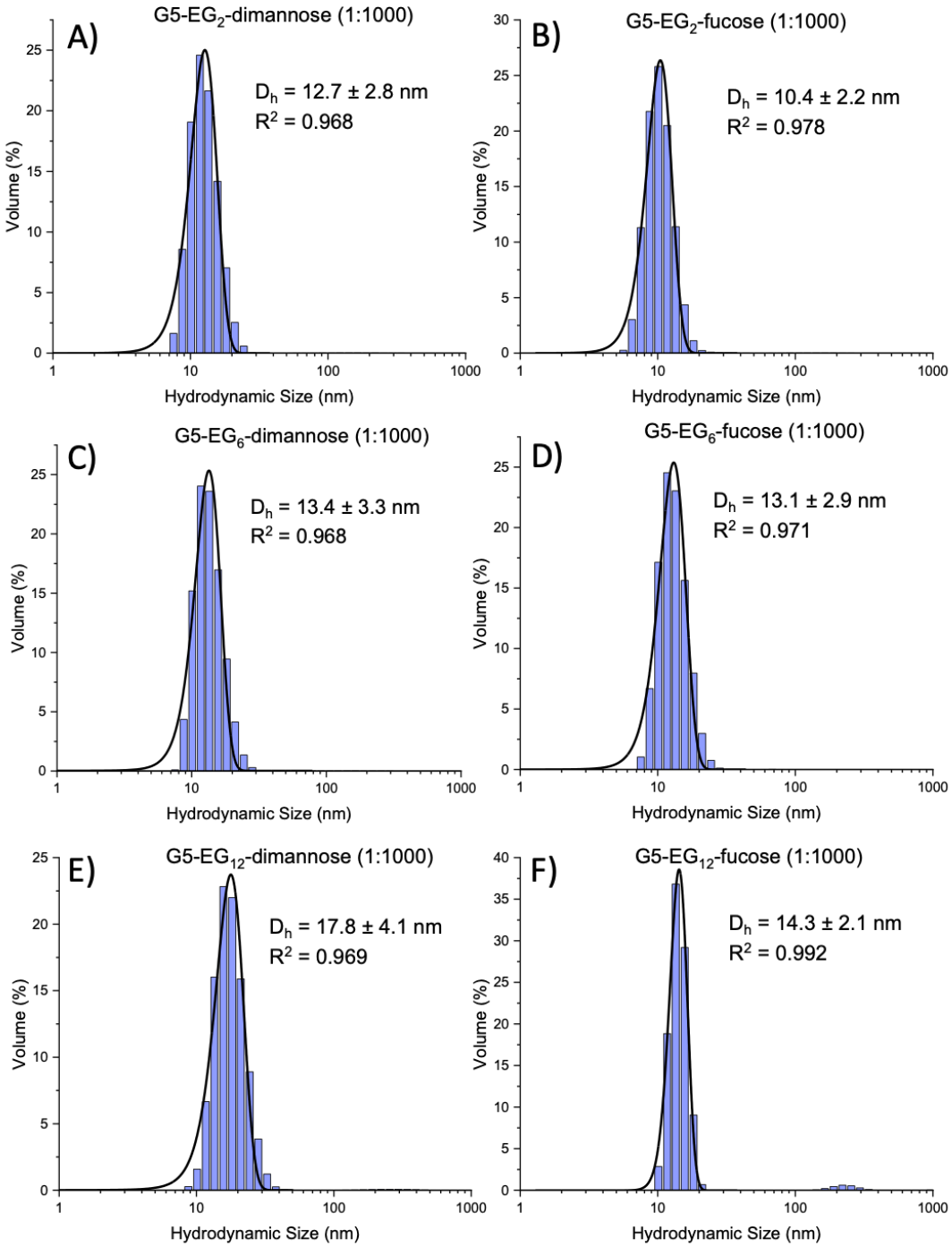

Figure 3.4 Volume population hydrodynamic size distribution histograms fitted with a Gaussian distribution curve for A) G5-EG_2-dimannose, B) G5-EG_2-fucose, C) G5-EG_6-dimannose, D) G5-EG_6-fucose, E) G5-EG_{12}-dimannose, F) G5-EG_{12}-fucose, made in a 1:1000 GLR (D_h values given as xc ± ½ FWHM).

Table 3.1 Summary of the hydrodynamic diamters (D_hs) of G5-EG$_n$-glycans made in three GNP:ligand molar ratios (1:1000, 1:500, 1:300). D_h values given as xc ± ½ FWHM.

	1:1000	**1:500**	**1:300**
G5-EG$_n$-glycan	**D_h ± ½ FWHM (nm)**	**D_h ± ½ FWHM (nm)**	**D_h ± ½ FWHM (nm)**
G5-EG$_2$-dimannose	12.7 ± 2.8	11.9 ± 3.2	10.4 ± 1.9
G5-EG$_6$-dimannose	13.4 ± 3.3	13.8 ± 4.0	12.3 ± 3.2
G5-EG$_{12}$-dimannose	17.8 ± 4.1	14.3 ± 3.5	12.9 ± 3.0
G5-EG$_2$-fucose	10.4 ± 2.2	9.8 ± 2.7	10.4 ± 2.2
G5-EG$_6$-fucose	13.1 ± 2.9	11.1 ± 2.6	12.1 ± 1.7
G5-EG$_{12}$-fucose	14.3 ± 2.5	13.2 ± 2.1	12.2 ± 2.8
G5-EG$_{12}$-OH	13.5 ± 2.5	-	-

The hydrodynamic diameter of the stock (G5-citrate) was measured to be 7.5 ± 2.2 nm (Figure 3.3). Taking into account the contribution from the citrate coating and the hydration layer, this D_h is consistent with approximately a 5 nm core size. This agrees with previous comparisons of the size of citrate GNPs, where measurements by DLS typically show a size 2-3 nm larger than when measured by TEM.(130)

The successful conjugation indicated by a λ_{max} shift was further confirmed by an increase in D_h of at least 2.9 nm after mixing G5-citrate with LA-ligands and as expected, D_h generally increased with increasing linker length. One exception was that the G5-glycans made in a 1:300 ratio showed the same D_h for the EG$_6$ and EG$_{12}$ linkers (12.3 ± 3.2 and 12.9 ± 3.0 nm respectively for terminal dimannose, and 12.1 ± 1.7 and 12.2 ± 2.8 nm respectively for terminal fucose). This indicates that when made in a 1:300 GLR, the density of LA-ligands on the gold core is sparse enough to allow the linkers sufficient space to fold up closer to the gold nanoparticle surface, reducing their effective hydrodynamic size (Figure 3.5). This is an important observation as it may impact the availability of the glycan ligands for lectin binding, as some glycans may become buried within other folded up linkers or have sub optimal orientations for tetrameric binding. To explore this further, and confirm that lowering the ligand to gold ratio reduces valency, a calculation of the number of ligands per G5 was conducted.

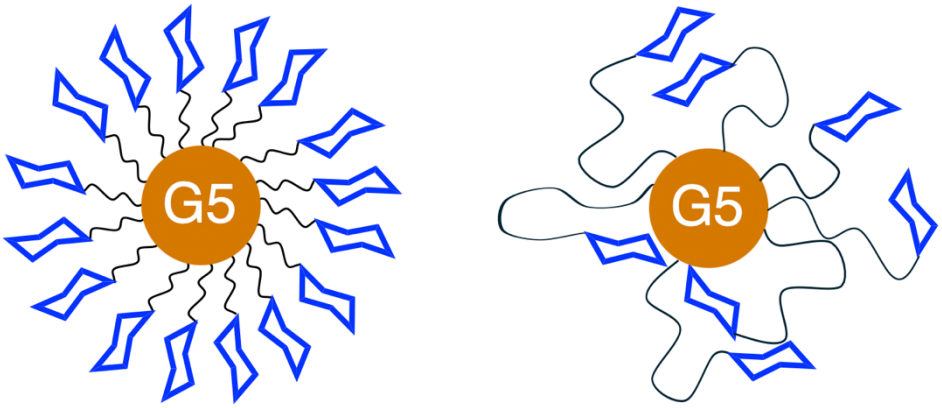

Figure 3.5 Diagram illustrating the effect of linker length and glycan valency on ligand orientation on the nanoparticle surface. As glycan valency decreases, the available surface area per glycan increases. The left structure depicts a GNP with short linkers and high ligand density, promoting uniform display of glycans. The right structure depicts a GNP with longer linkers and low ligand density, promoting folding of the ligands, resulting in non-uniform glycan presentation and variable glycan surface orientations.

3.2.3.3 Valency

During cap exchange, the G5 nanoparticles were washed through 10K MWCO filter units, and the flow-through containing unbound ligand was collected. The amount of unbound ligand present in the flow-through was quantified using a phenol sulfuric acid assay. By comparing this value to the initial amount of ligand used during cap exchange, the number of ligands bound on each G5 were estimated.(119)

For the phenol sulphuric assay, calibration curves were first calculated using known amounts of LA-EG_n-glycans, an example of which can be seen in Figure 3.6 for LA-EG_2-dimannose. The remaining calibration curves are given in Figure A. 3. The collected flow-through from cap exchange was collected, freeze dried then rediluted in a known amount of H_2O and applied in the phenol sulfuric assay. The results were analysed against the calibration curves to determine the ligand concentrations in the flow through. A summary of the valency outcomes for each G5-EG_n-glycan at the three synthesis ratios can be seen in Table 3.2.

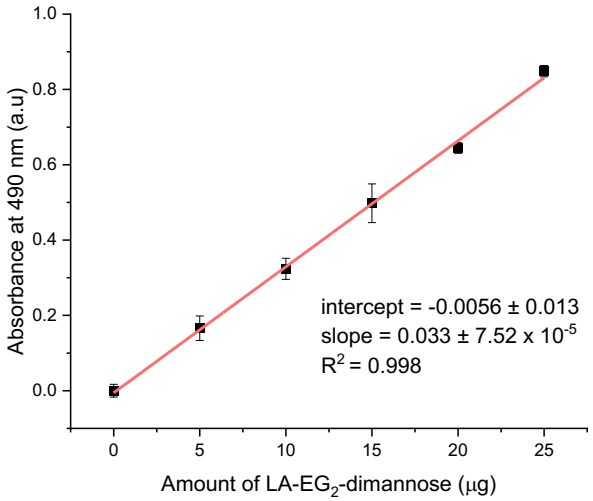

Figure 3.6 Plot of sample absorbance at 490 nm against LA-EG_2-dimannose amount, fitted by a linear relationship, giving a slope(m) = 0.033 ± 0.00008, R^2 = 0.998.

Table 3.2 Summary of the surface valency of G5-EG_n-glycans made in three GLR ratios (1:1000, 1:500 and 1:300). Valencies are given as an average of two repeat measurements with the error representing the standard deviations (SDs).

	1:1000	***1:500***	***1:300***
G5-EG_n-glycan	**Valency (N)**	**Valency (N)**	**Valency (N)**
G5-EG_2-dimannose	659 ± 145	355 ± 19	164 ± 3
G5-EG_6-dimannose	661 ± 22	360 ± 15	171 ± 16
G5-EG_{12}-dimannose	622 ± 37	379 ± 18	181 ± 13
G5-EG_2-fucose	599 ± 6	333 ± 23	157 ± 45
G5-EG_6-fucose	519 ± 96	380 ± 8	174 ± 17
G5-EG_{12}-fucose	556 ± 45	370 ± 13	184 ± 9

3.2.3.4 Deflection angle and inter-glycan distances

As expected, and consistent with the D_h analysis, reducing the ratio of ligand to gold during the cap exchange process lowered the number of ligands on a G5 particle. Varying the ratios of glycans on the surface of G5s was carried out with the intention to tune their binding affinities to the tetrameric lectin DC-SIGN, the rational being that changing the density may result in a better spatial match between the surface glycans and the four DC-SIGN CRDs. Evidence suggests that strong binding requires a close spatial match between receptor and ligand. Previous studies have shown that DC-SIGNR, a close homolog of DC-SIGN, exhibits weaker binding to spherically presented

multivalent glycans. This reduced affinity is attributed to the outward orientation of its CRDs, which results in poor spatial alignment with the glycan ligands.(115) Modulating glycan density using this approach therefore enabled the identification of the optimal inter-glycan spacing on a G5 scaffold required to simultaneously engage all four DC-SIGN CRDs, while also assessing whether linker flexibility allows for deviation from these spatial constraints. Assuming even distribution of glycans on the G5 surface the footprint (k) and the deflection angle (θ) of each glycan on the surface was measured by Equation 3.1 and 1.4 where $r = R_h = ½\ D_h$ and N is the glycan valency per G5.(180) The inter-glycan distance (X) was then calculated by Equation 3.3.

A summary of valency, deflection angle and inter-glycan distance is shown in Table 3.3, and an illustration of how the deflection angle and inter-glycan distance is affected by valency and linker length is shown in Figure 3.7.

$$k = \frac{4\pi r^2}{N} \qquad \textbf{Equation 3.1}$$

$$\theta = \frac{360\sqrt{\frac{k}{\pi}}}{r\pi} = \frac{229.3}{\sqrt{N}} \qquad \textbf{Equation 3.2}$$

$$X = 2rsin\frac{\theta}{2} \qquad \textbf{Equation 3.3}$$

Table 3.3 Summary of the deflection angle (θ) and inter-glycan distance (X) of G5-EGn-glycans made in three GNP:ligand synthesis ratios (1:1000, 1:500 and 1:300). Errors are propagated from the errors in valency and hydrodynamic size.

	1:1000		***1:500***		***1:300***	
G5-EG$_n$-glycan	***θ* (°)**	**X (nm)**	***θ* (°)**	**X (nm)**	***θ* (°)**	**X (nm)**
G5-EG$_2$-dimannose	8.9 ± 1.0	0.99 ± 0.25	12.2 ± 0.3	1.26 ± 0.34	17.9 ± 0.2	1.62 ± 0.30
G5-EG$_6$-dimannose	8.9 ± 0.2	1.04 ± 0.26	12.1 ± 0.2	1.45 ± 0.42	17.5 ± 0.8	1.87 ± 0.50
G5-EG$_{12}$-dimannose	9.2 ± 0.3	1.42 ±0.33	11.8 ± 0.3	1.46 ± 0.36	17.0 ± 0.6	1.91 ± 0.45
G5-EG$_2$-fucose	9.4 ± 0.05	0.85 ± 0.18	12.6 ± 0.4	1.07 ± 0.30	18.3 ± 2.8	1.65 ± 0.43
G5-EG$_6$-fucose	10.1 ± 1.0	1.15 ± 0.28	11.8 ± 0.1	1.13 ± 0.27	17.4 ± 0.9	1.83 ± 0.27
G5-EG$_{12}$-fucose	9.7 ± 0.4	1.21 ± 0.22	11.9 ± 0.2	1.37 ± 0.22	16.9 ± 0.4	1.79 ± 0.41

As expected, both the deflection angles and inter-glycan distances increased as the valency of the GNPs decreased, with θ ranging from 8.9° for the saturated 1:1000 GLR particles up to 18.3° for the 1:300 GLR particles. Similarly, inter-glycan distances increased from 0.85 nm up to 1.91 nm. Since the deflection angle is independent of D_h and is instead governed by the valency of the G5 particle, no correlation was observed between linker length and deflection angle within particles synthesised at the same GLR. In contrast, inter-glycan distance had a dependency on particle diameter, and since longer linkers tend to produce particles with larger D_h, the inter-glycan distance generally increased with linker length (despite one exception where the D_h of G5-EG_6-glycans and G5-EG_{12}-glycans were similar for the 1:300 synthesis ratio). This indicated that linker induced changes in size can override the effects of small changes in valency in determining glycan spacing. These observations, along with the D_h measurements, highlight how glycan density directly influences the surface presentation and spacing of carbohydrate ligands, which in turn affects their accessibility and binding potential to multivalent receptors such as DC-SIGN.

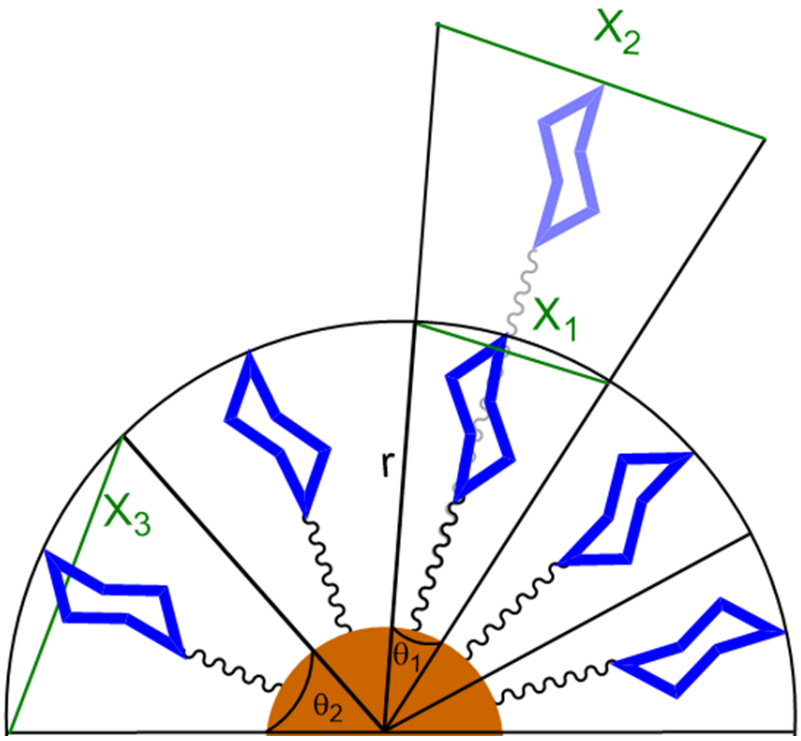

Figure 3.7 Drawing illustrating how deflection angle (θ), and inter-glycan distance (X) is affected by linker length and glycan density. Increasing linker length increases X but not θ, and reducing the density increases both θ and X.

The relevance of inter-glycan distances becomes apparent when considering the constraints on DC-SIGN binding. An *ab initio* model of the DC-SIGN extracellular domain (EDC) predicts that when bound to a pseudo dimannose ligand, the centre to centre distances of CRDs range between 3.87-4.03 nm (derived from combination of SAXS

envelope of DC-SIGN ECD, PDB: 6GHV, and STD-NMR data for the ligand).(181) Although the inter-glycan distances observed on these G5-glycans fall below this value, it is possible that certain inter-glycan distances might allow for cooperative or enthalpically enhanced binding, whereby every forth glycan is optimally spatially lined up with a CRD (e.g. 0.99 nm for G5-EG_2-dimannose). Furthermore increasing glycan density on the nanoparticle surface could also promote favourable binding by enhancing the probability that glycans will be correctly oriented for DC-SIGN engagement. Therefore both glycan valency and linker length could contribute to fine tuning multivalent interactions with DC-SIGN.

3.2.4 Probing the binding mode of G5-EG_n-glycans with DC-SIGN

To consolidate successful coverage of G5 particles in the glycans of choice, their binding mode with DC-SIGN was probed by DLS. Previously, the binding mode between DC-SIGN and G5-EG_2-dimannose was studied by monitoring the hydrodynamic size increase as varying ratios of DC-SIGN was added to a fixed concentration of G5-EG_2-dimannose. This revealed that multiple copies of DC-SIGN can bind to a single G5-EG_2-dimannose molecule, forming small lectin-G5 assemblies of approximately 40 nm in D_h when saturated.(115) This size is consistent with a single G5-EG_2-dimannose particle coated with a monolayer of DC-SIGN molecules, suggesting that all four CRDs of each DC-SIGN engage with a single G5-EG_2-dimannose. To further extend our knowledge on the binding between G5-glycans and DC-SIGN, the binding modes of G5s made in a GLR of 1:1000, 1:500 and 1:300 with DC-SIGN were studied to determine if the ethylene glycol linker length or valency is important for the binding mode and if a correspondingly lower saturation point may be reached for the lower valency particles.

The concentration of G5 was fixed at 20 nM and the ratio of DC-SIGN was increased gradually from 20 - 320 nM (i.e., protein to G5 ratio (PGR) of 1:1 – 16:1). The D_h of DC-SIGN alone displayed a single narrow Gaussian distribution of ~14.0 ± *2.0* nm (Figure 3.8). The D_h histograms (volume population) of the G5-EG_2-dimannose (1:1000)-DC-SIGN monolayer complex under variety of PGRs can be seen in Figure 3.9 and the remaining D_h histograms of all other G5-EG_n-glycans are shown in Figure A. 4-8. Their D_h-PGR relationships are shown in Figure 3.10.

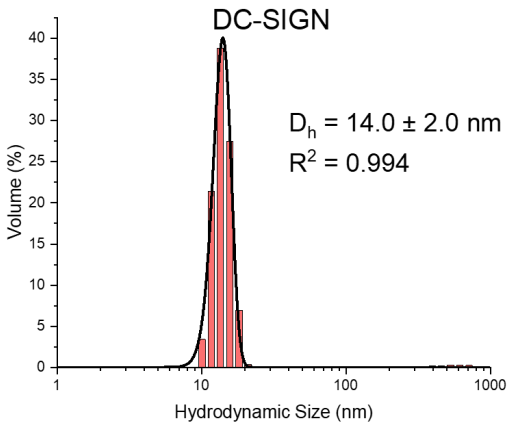

Figure 3.8 Volume population hydrodynamic size distribution histogram fitted with Gaussian fits for DC-SIGN (DC020). D_h value given as xc ± ½ FWHM.

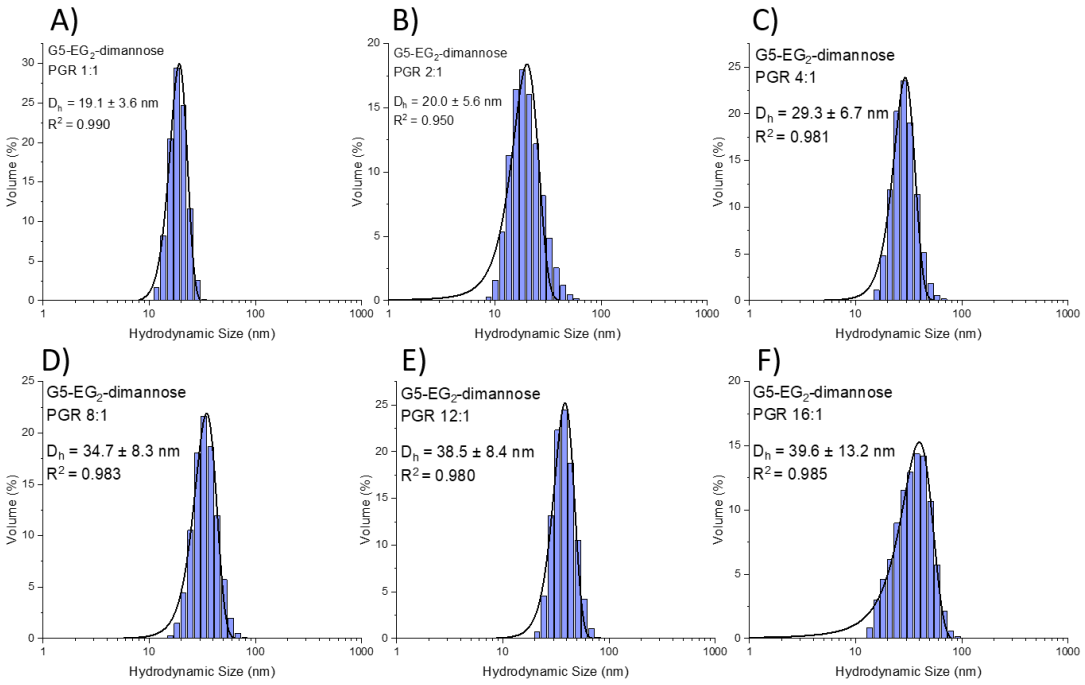

Figure 3.9 Volume population hydrodynamic size distribution histograms fitted with Gaussian fits for the binding of G5-EG2-dimannose (1:1000) (20 nM) with DC-SIGN at varying protein:G5 molar ratios (PGR) of A) 1:1, B) 2:1, C) 4:1, D) 8:1, E) 12:1, and F) 16:1 (Dh values given as xc ± ½ FWHM).

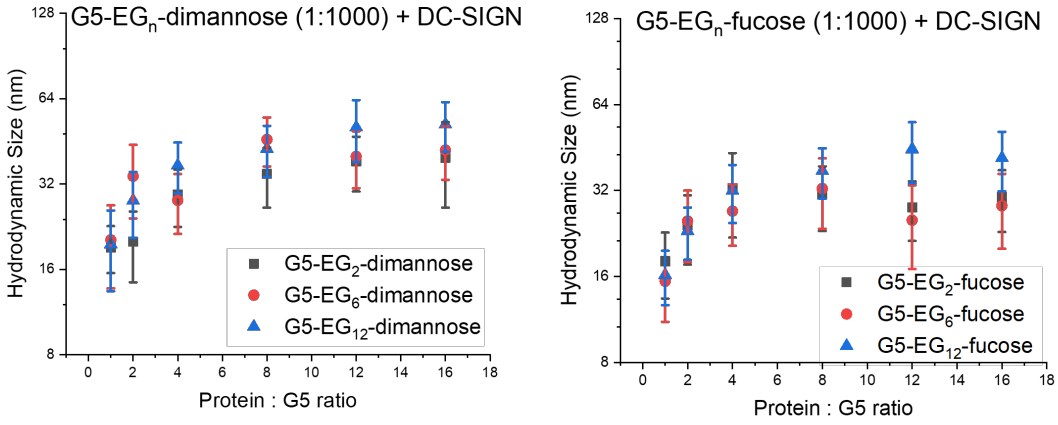

Figure 3.10 Hydrodynamic diameter (D_h, volume population) - PGR relationship for A) G5-EGn-dimannose (1:1000) with DC-SIGN and B) G5-EG_n-fucose (1:1000) with DC-SIGN.

In general the D_h of the G5-EG_n-glycan(1:1000) + DC-SIGN mixtures increased gradually with the increasing PGR, reaching a plateau at a PGR of around 8:1-12:1, after which the D_h values remained roughly constant. This behaviour was similar to that previously observed for DC-SIGN binding with G5-EG_2-dimannose. The saturated D_hs for G5 glycans with EG_{12}-linkers showed a general trend of being larger than those with EG_2 linkers (D_{hmax} 51.8 ± 10.3 nm vs 39.6 ± 13.2 for G5-EG_{12}-dimannose and G5-EG_2-dimanose, respectively). The difference between G5-EG_2-glycans and G5-EG_{12}-glycans in the absence of DC-SIGN is ~5 nm but the resulting complexes have ~12 nm difference, suggesting more DC-SIGN molecules can bind to G5-EG_{12}-glycans than G5-EG_2-glycans. This is consistent with the difference in surface areas and is reflected in the D_h plateauing at higher PGRs for G5-EG_{12}-glycans.

Although the hydrodynamic diameters plateau at low PGRs, this does not necessarily reflect the true saturation of the G5-EG_n-glycans with DC-SIGN. Using a surface binding footprint of ~35 nm^2 per DC-SIGN tetramer, and the surface areas of G5-EG_n-glycans calculated from their D_hs (~510, ~540, ~995 nm^2, for EG_2, EG_6, and EG_{12}- dimannose respectively, and ~410, ~540, and ~640 nm^2 for EG_2, EG_6, and EG_{12}- fucose, respectively) then PGRs of ~12:1 - 30:1 with DC-SIGN were estimated to be able to fully saturate the surface of G5-EG_n-glycans depending on linker lengths. At the 1:1000 GNP:ligand synthesis ratio, full saturation with 30 DC-SIGN molecules should be entirely possible for the G5-EG_{12}-glycans as this would require 120 surface glycan ligands which is considerably fewer than the G5 surface glycan valencies of 500+ described in the earlier section. The D_h plateauing at 12 DC-SIGN molecules per G5-EG_{12}-glycan may consequently be a result of an even distribution of these DC-SIGN molecules on the G5 surface, forming a roughly spherical complex, not increasing in size despite further binding occurring. The D_h plateauing at a lower PGR of 8 for the G5-EG_2-glycans may

be a combination of this same affect and steric hindrance, as crowding at near-saturation prevents further DC-SIGN molecules from binding.

Repeating this with G5-EG$_n$-glycans made in 1:500 and 1:300 GNP:ligand synthesis ratios largely followed the same trend, with the D_h plateauing at PGRs of around 6:1. The hydrodynamic diameters of the monolayer species at each PGR are shown in Figure 3.11 and Figure 3.12. Their gaussian distributions can be seen in Figure A. 9-20. Less variation was observed in the saturated D_h values for the 1:500 and 1:300 G5-glycans with the three different EG$_n$ linker lengths, consolidating the assumption that the G5-glycans made in a lower ligand to GNP ratio are less hindered and have the margin to fold up and create an observed smaller D_h even when bound to DC-SIGN.

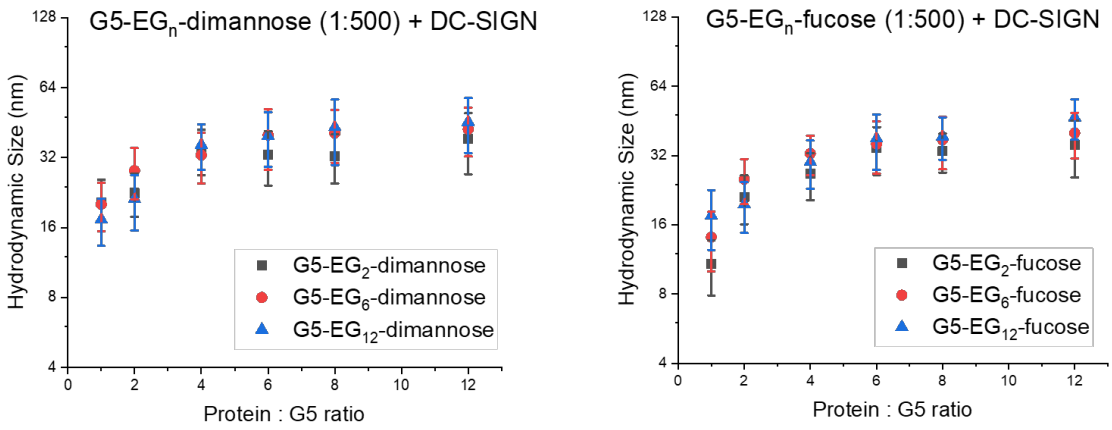

Figure 3.11 hydrodynamic diameter (D_h, volume population) - PGR relationship for A) G5-EG$_n$-dimannose (1:500) with DC-SIGN and B) G5-EG$_n$-fucose (1:500) with DC-SIGN.

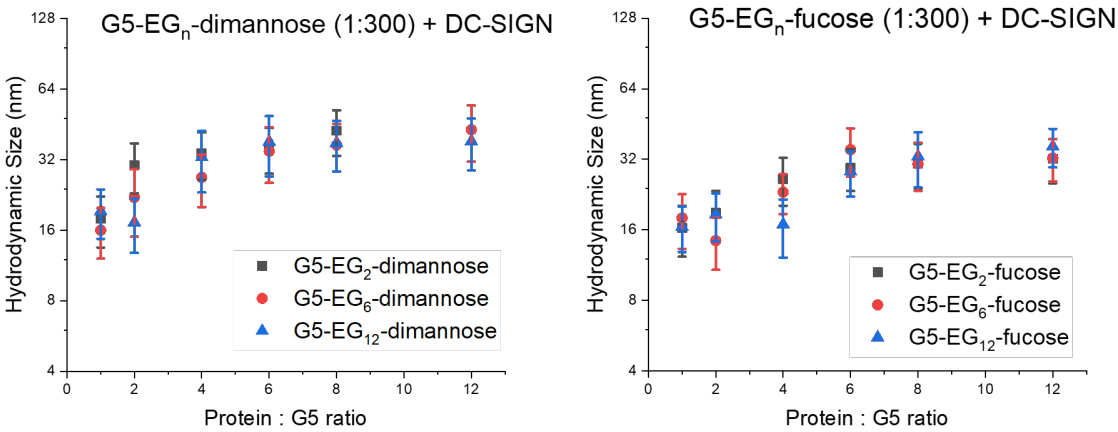

Figure 3.12 hydrodynamic diameter (D_h, volume population) - PGR relationship of monolayer species for A) G5-EG$_n$-dimannose (1:300) with DC-SIGN and B) G5-EG$_n$-fucose (1:300) with DC-SIGN.

While Figure 3.12 shows the D_h values of the monolayer DC-SIGN coated G5-glycan complex, interestingly for the higher PGRs (12:1) with 1:300 G5-$EG_{2/6}$-dimannose, some larger structures were observed, with hydrodynamic diameters of ~4000 nm (Figure 3.13) indicating that at high PGRs, a second binding mode is observed where cross-linking begins to occur. It is possible that due to the lower surface glycan valencies and bigger inter-glycan distances, there is a spatial mismatch between the binding surface of the DC-SIGN tetramers and these G5-glycans(1:300), rendering it less likely that glycans on one G5 can bridge all four CRDs of one DC-SIGN tetramer. If one or more DC-SIGN CRDs remain unbound by one G5-glycan, a second G5-glycan may fill this space, creating a cross linking network (Figure 3.14). The volume of the cross-linked species is reduced as linker length increases from EG_2 to EG_{12}, which may indicate that the increased flexibility of the longer linkers affords them the ability to bridge the CRDs of one DC-SIGN tetramer, highlighting how linker flexibility can allow for deviation from spatial constraints of the DC-SIGN CRDs. A further exploration of this, and how binding of only 2 CRDs may affect binding affinity can be found in Chapter 4.

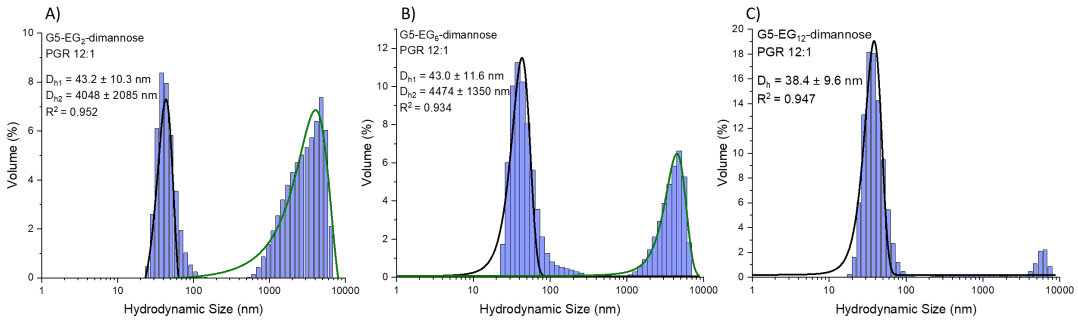

Figure 3.13 Volume population hydrodynamic size distribution histograms fitted with a Gaussian distribution curve for A) G5-EG_2-dimannose (1:300), B) G5-EG_6-dimannose (1:300) C) G5-EG_{12}-dimannose (1:300), with DC-SIGN at PGRs of 12:1 (D_h values given as xc ± ½ FWHM).

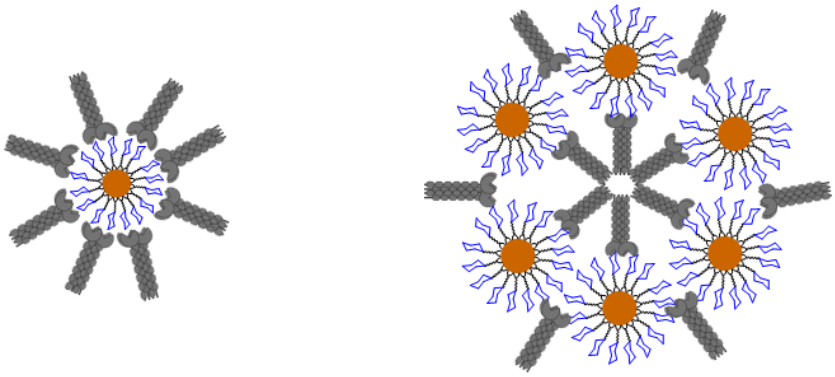

Figure 3.14 Representation of a G5-glycan coated in a monolayer of DC-SIGN molecules (left) vs a cross linked G5-glycan-DC-SIGN assembly (right) where some DC-SIGN tetramers bridge two G5-glycan particles.

3.2.5 Summary of G5-glycan preparation, characterisation, and future application

In summary, G5-glycans with different linker lengths and surface glycan densities have been successfully synthesised and characterised. These were carried out in an attempt to modify and tune their interactions with the tetrameric lectin, DC-SIGN. Using DLS to measure their hydrodynamic diameters, it was found that G5-glycans made in a 1:1000 GLR form only monolayer DC-SIGN coated G5-glycan particles upon mixing with DC-SIGN, where one G5-glycan binds simultaneously to all four CRDs in one DC-SIGN molecule. Contrastingly, G5-glycans with a lower glycan density, especially those with short EG_2 linkers, show a greater tendency to form cross-linked species, possibly due to their large inter-glycan distances resulting in an imperfect spatial match in order to bind to all four CRDs in one DC-SIGN.

To explore the G5-glycan-DC-SIGN interactions further, and to quantify parameters associated with their binding events, these particles were used in a number of other DC-SIGN binding studies. Chapter 4 explored the use of a fluorescence quenching assay based off the nano surface energy transfer (NSET), the apparent K_d of these nanoparticles with DC-SIGN were measured, along with the enthalpy and entropy contributions. This was compared to other solution based measurements obtained by isothermal titration calorimetry(ITC) using the same G5-glycans. Furthermore, their ability to inhibit cell surface DC-SIGN lectin receptor mediated viral entry into host cells was explored, and correlated to their solution binding affinity. These studies revealed key GNP-glycan design parameters such as the glycan identify, linker length, and density, that are most impactful on cell signalling processes.

Chapter 7 investigated how these G5-glycans are able to modulate cytokine production via DC-SIGN. Dendritic cells were treated concomitantly with bacterial endotoxin LPS and the G5-glycans of choice, and the production of interleukin(IL)-10 and IL-23 was measured. This chapter then further explored the implications of glycan binding on T cell proliferation. It was anticipated that these studies would reveal information on fungal mediated IL-23 production and provide insight into how this might relate to the onset of the seronegative spondyloarthropathies, a group of diseases associated with the IL-23 cytokine.

3.2.6 G27-glycan preparation and characterisation

The G5-glycan nanoparticles described above are useful tools for probing DC-SIGN based multivalent lectin-glycan binding. However, in some instances where the aim is to study the size dependency of the scaffold on DC-SIGN binding, or when the objective is to isolate protein-carbohydrate complexes, a larger particle size is often required. Therefore, 27 nm gold nanoparticles coated in the same dimannose and fucose ligands were also synthesised.

Due to their much higher extinction coefficient (2.39 x 10^9 vs 1.1. x 10^7 $M^{-1}cm^{-1}$ for G5), larger gold nanoparticles are less useful in GNP based fluorescence quenching assays due to their much larger inner filter effect, and hence G27-glycan nanoparticles were not adopted to measure binding affinity through the fluorescence quenching assay described in Chapter 4. They can however, be used in a similar fashion to measure binding affinity using a pull-down method, where the bound proteins are pelleted out of solution using centrifugation.

G27 nanoparticles were prepared via previously established protocols by NaOH treatment of gold(III) chloride trihydrate in water followed by citrate reduction at reflux, forming citrate stabilized gold nanoparticles roughly 27 nm in diameter (Scheme 3.5).(125) G27 require long water soluble EG_n chains to provide strong steric stabilisation to resist aggregation, and therefore LA-EG_6-glycan ligands were used to conjugate to the G27 surface. Directly stirring the LA-EG_6-glycans with citrate stabilised G27 resulted in aggregation. This happens due to several factors associated with surface chemistry, colloidal stability and inter-particle forces. Citrate ions stabilise gold nanoparticles through electrostatic stabilisation, but when lipoic acid based neutral ligands are added, the weakly adsorbed citrate ions are rapidly displaced, reducing this electrostatic repulsion. Since cap-exchange is not instantaneous, there is a window in which the particles are left unstable (not densely passivated by LA-EG_n-glycan ligands), in which time they may aggregate. Attempted stabilisation of G27-citrate using tween based surfactants was also found to be ineffective.

To counteract this issue, G27-citrate were exchanged with a monothiol PEG800-OMe ligand. PEG800 contains roughly 20 EG units, which provides strong steric stabilisation and therefore reduces cap exchange induced aggregation. While this alleviated the G27 aggregation issue, displacing the HS-PEG_{800}-OMe with LA-glycan ligands was unsuccessful. However, when using a two-step cap exchange process, first with bis (p-sulfonatophenyl) phenylphosphine dipotassium (BSPP), then with the LA-glycan ligands, both aqueous solutions, the G27 particles were successfully conjugated with the desired LA-glycan ligands. BSPP is a phosphine containing ligand which binds to gold surfaces with relatively high affinity. It contains two negatively charged -SO_3 groups to provide strong electrostatic stabilisation among neighbouring particles to prevent aggregation. The bulky phenyl rings also contribute the steric stabilisation, providing physical spacing between GNPs which prevents them from approaching each other closely. This is very effective in aqueous media and enhances colloidal stability. BSPP helps maintain this colloidal stability during the ligand transition, and since it binds to G27 relatively strongly, it does not desorb too quickly, which gives time for lipoic acid to anchor without leaving the gold particles bare and unstable. Successful cap exchange was confirmed by an increase in D_h (Figure 3.16) and by a small red-shift in the UV-Vis SPR absorption peak (Figure 3.15), which was also used to calculate their concentrations using Equation 2.1.

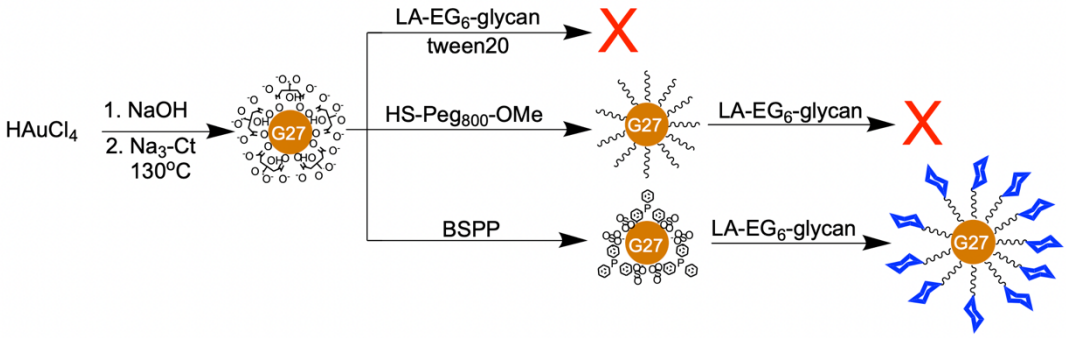

Scheme 3.5 Schematic depicting the procedure for the synthesis and cap exchange for G27 particles. Direct cap exchange of G27-Ct with LA-glycans causes aggregation, and an intermediate exchange with HS-peg$_{800}$-OMe is too stable for cap exchange with LA-glycans. G27-Ct can be cap exchanged with LA-glycans in a two-step process using BSPP as an intermediate coating.

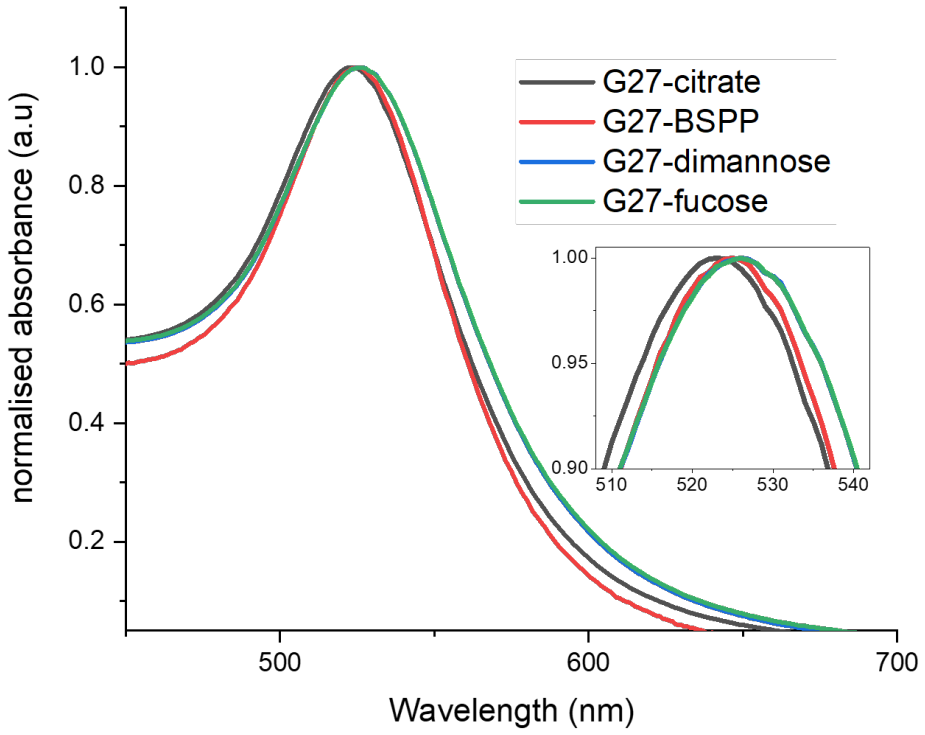

Figure 3.15 Normalised UV-Vis absorption spectrum for G27s before and after cap exchange with intermediate BSPP ligand, and then with LA-EG$_6$-glycans.

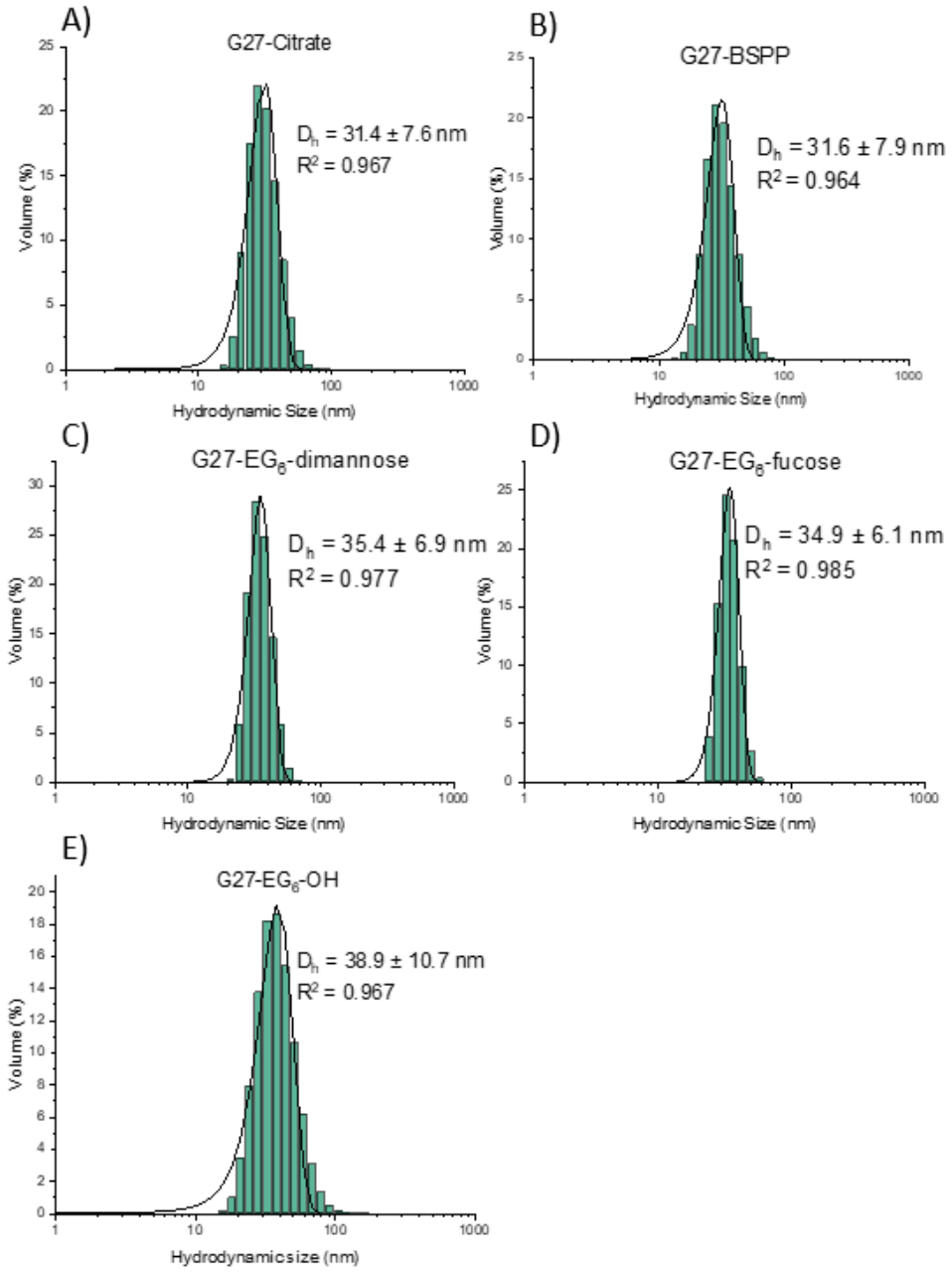

Figure 3.16 Volume population hydrodynamic size distribution histograms fitted with a Gaussian distribution curve for A) G27-citrate, B) G27-BSPP, C) G27-EG$_6$-dimannose, D) G27-EG$_6$-fucose, E) G27-EG$_{12}$-OH. D_h values given as xc ± ½ FWHM.

3.2.7 Probing the binding mode of G27-EG$_n$-glycans with DC-SIGN

As described similarly in Section 3.2.4, the binding mode of G27-glycans with DC-SIGN was explored. The concentration of G27 was fixed at 0.5 nM and the ratio of DC-SIGN was increased gradually from 1-64 nM (i.e., protein to GNP ratio (PGR) of 2:1 – 128:1). The D_h histograms (volume population) of the G27-EG$_6$-dimannose/fucose-DC-SIGN complex under variety of PGRs can be seen in Figure 3.17 and Figure 3.18 along with their D_h-PGR relationships.

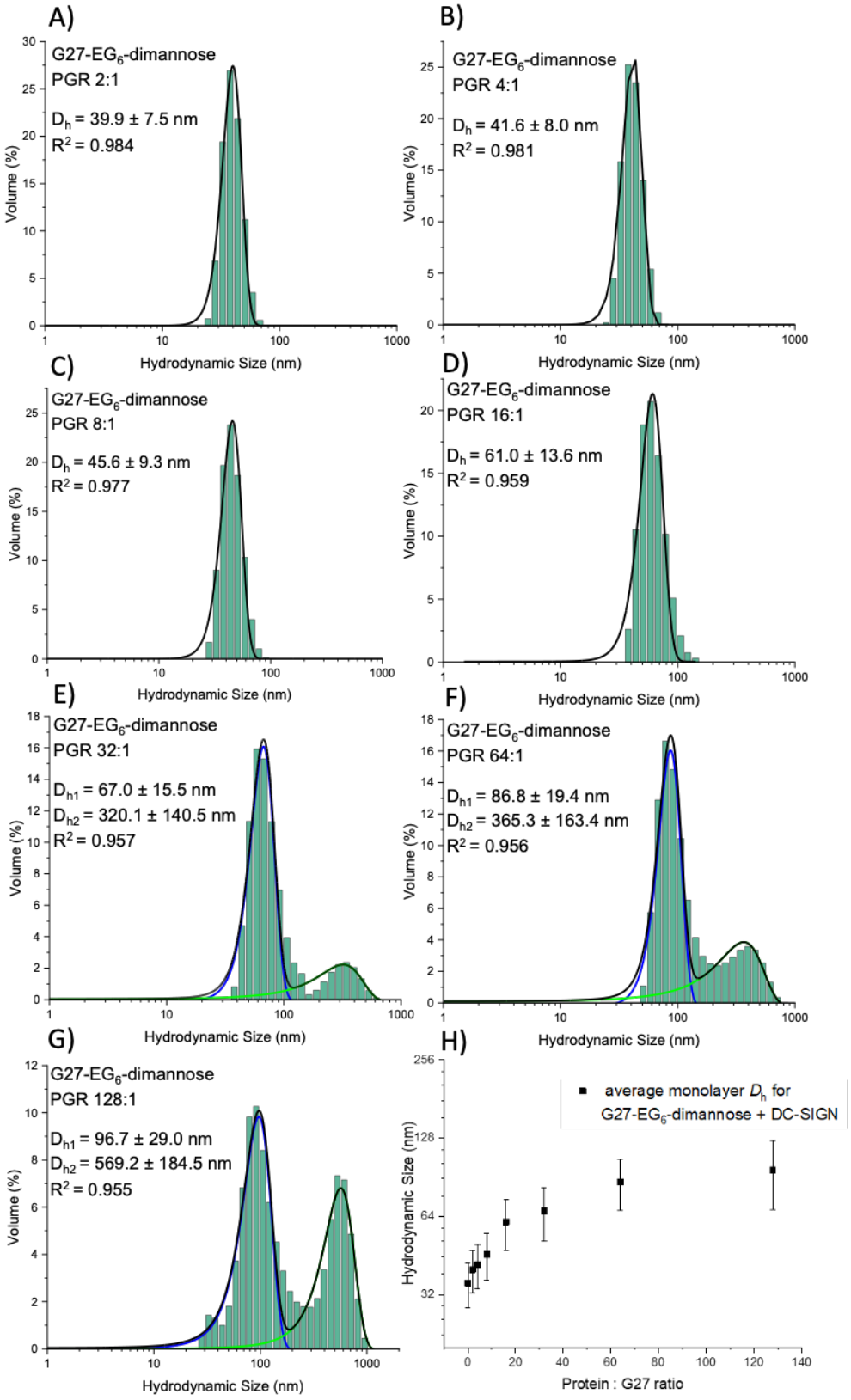

Figure 3.17 Volume population hydrodynamic size distribution histograms fitted with Gaussian fits for the binding of G27-EG_6-dimannose (0.5 nM) with DC-SIGN at varying protein:G27 molar ratios (PGR) of A) 2:1, B) 4:1, C) 8:1, D) 16:1, E) 32:1, F) 64:1 and G) 128:1. D_h values given as xc ± ½ FWHM. H) Hydrodynamic diameter (D_h, volume population) - PGR relationship for G27-EG_6-dimannose with DC-SIGN (monolayer species).

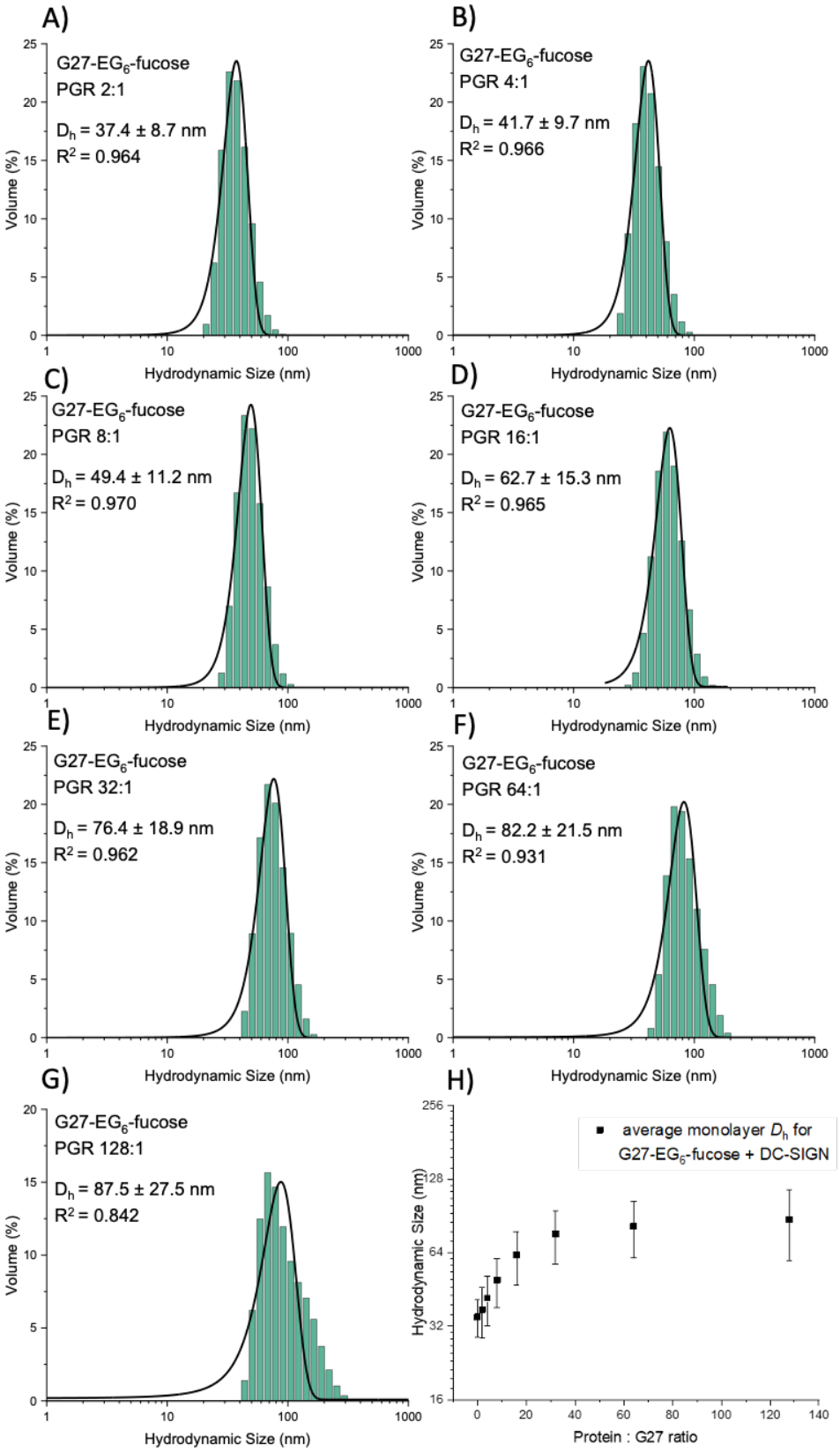

Figure 3.18 Volume population hydrodynamic size distribution histograms fitted with Gaussian fits for the binding of G27-EG$_6$-fucose (0.5 nM) with DC-SIGN at varying protein:G27 molar ratios (PGR) of A) 2:1, B) 4:1, C) 8:1, D) 16:1, E) 32:1, F) 64:1 and G) 128:1. (D_h values given as xc ± ½ FWHM). H) Hydrodynamic diameter (D_h, volume population) - PGR relationship for G27-EG$_6$-fucose with DC-SIGN.

For G27-fucose, as DC-SIGN concentration increased the D_h increased until a plateau was reached at around 32:1 ratio corresponding to a small DC-SIGN-G27 monolayer assembly. Based on their glycan surface areas calculated from their hydrodynamic diameters (~3850 nm^2) around 110 DC-SIGN molecules should be able to bind before saturation is reached, and therefore the PGR of 128 is above the saturation ratio. Despite this, even above the saturation ratio for G27-fucose (PGR 128:1), only a monolayer sized species was observed (D_h = 87.5 nm). Contrastingly, as PGR was increased for the G27-dimannose particles, a second, larger species was observed with a D_h >300 nm, increasing in volume and diameter as PGR increased. This is too large to be a monolayer of G27-dimannose coated in DC-SIGN and instead indicates some cross linked DC-SIGN-G27-dimannose must be present alongside the DC-SIGN monolayer coated G27-dimannose species.

3.2.8 G13-glycan preparation and characterisation

Along with their high absorption extinction coefficient, and resulting strong inner filter effect, rendering G27-glycans less well suited to fluorescence quenching based affinity assays, G27 also suffers from having to be used at low concentration. This is due to the large amount of $AuHCl_4$ required to make particles of this diameter, meaning only small quantities can be made in a single batch. Lower working concentrations also have to be used to avoid aggregation during experiments. Due to this, some ~13 nm gold nanoparticles (G13s) were prepared as a compromise between the high concentration range available for G5, and the low centrifugation speeds needed to pellet G27.

Similar to G27, G13 has a large absorption extinction coefficient (2.32 x 10^8 $M^{-1}cm^{-1}$) which renders it less useful in NSET based affinity assays due to the inner filter effect, and thus the need to fix the GNP concentration at low nM concentrations (~4 nM). They can, however, be used at higher concentrations than G27 in a pull-down style assay meaning a greater concentration of DC-SIGN can be pulled down from solution. As a caveat, this requires longer centrifugation times of ~60-90 minutes at 17000 x *g*.

G13 were prepared and synthesised according to previously established protocols by standard citrate reduction of $HAuCl_4$ at reflux.(125) Particles were cap exchanged with LA-EG_6-dimannose and LA-EG_6-fucose in a two-step process as described before, with a BSPP stabilised intermediate. Ligand exchange showed small red-shift in their UV-Vis absorption peak (Figure 3.19) Stock G13 citrate had a hydrodynamic diameter of 17.5 ± 4.4 nm, increasing to 19.7 ± 4.8 nm upon BSPP conjugation, and finally to ~ 20-22 nm when exchanged with LA-EG_6-dimannose and LA-EG_6-fucose. Based off their D_h, roughly 40 DC-SIGN molecules were predicted to be able to saturate the surface of a G13-glycan and therefore, their D_h in the presence of DC-SIGN in a PGR of 40:1 was measured. This showed only a monolayer of DC-SIGN coated core/shell species for both G13-dimannose and G13-fucose (Figure 3.20).

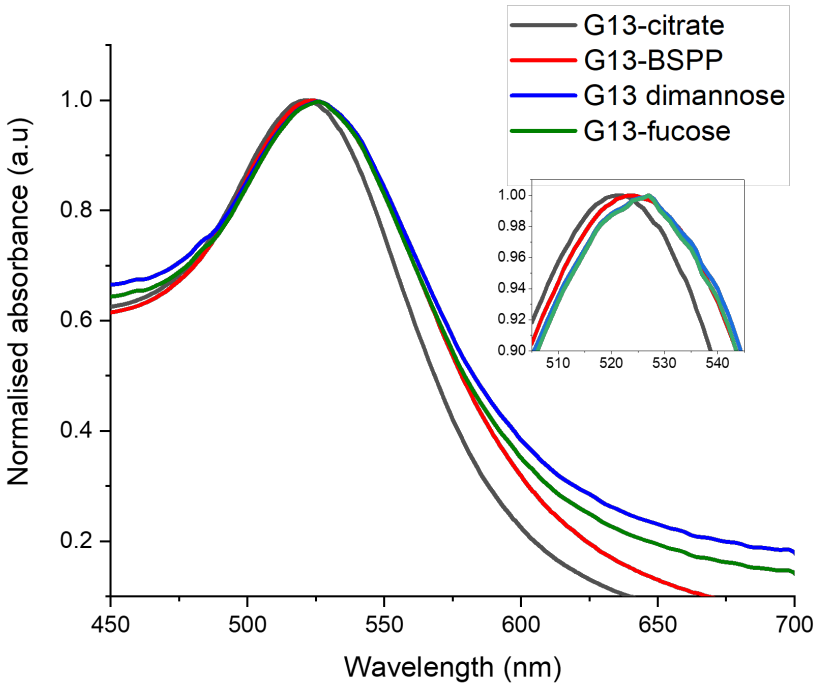

Figure 3.19 Normalised UV-VIS absorbance spectrum for G13s before and after cap exchange with intermediate BSPP ligand, and with LA-EG_6-glycans.

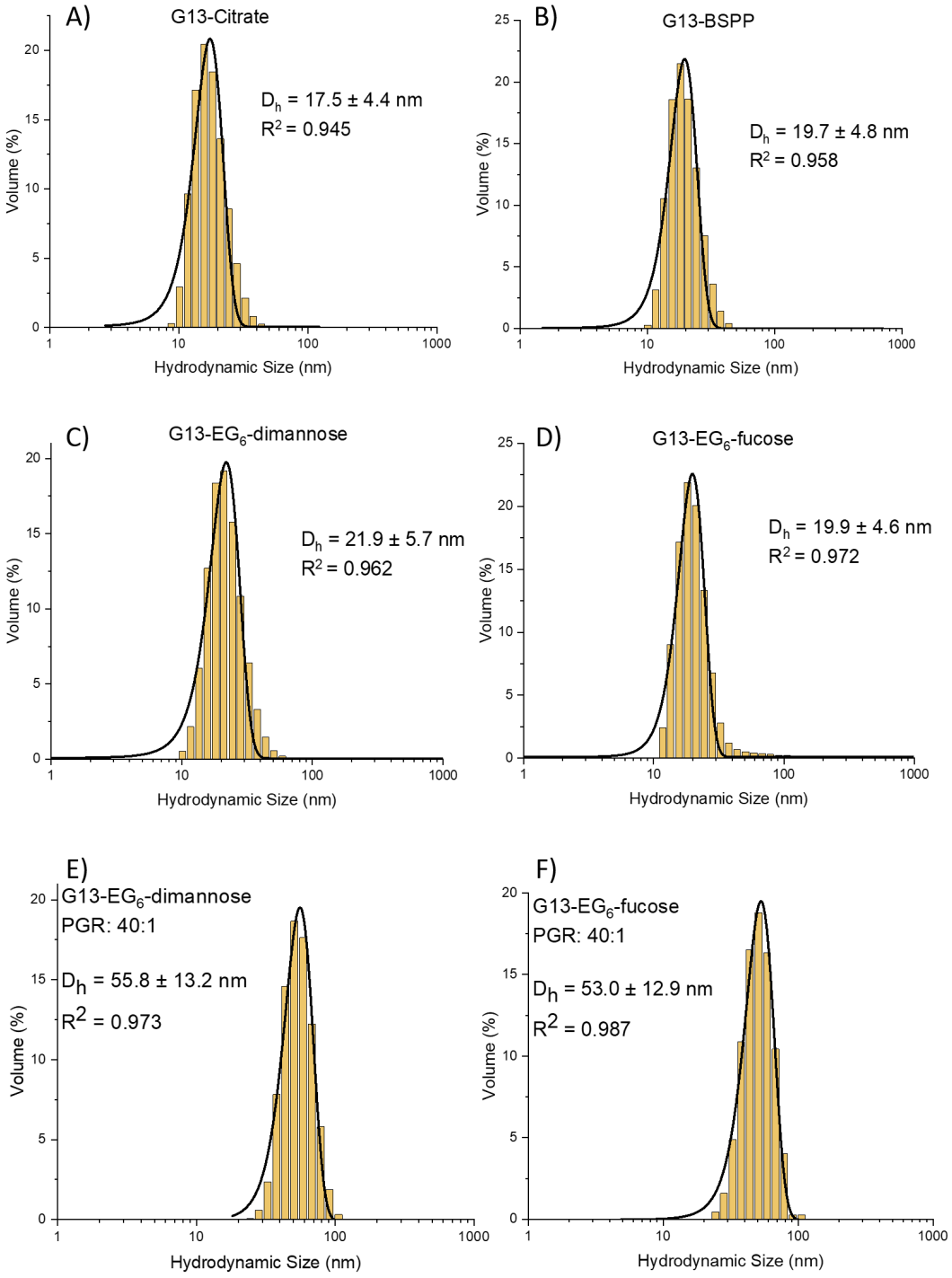

Figure 3.20 Volume population hydrodynamic size distribution histograms fitted with a Gaussian distribution curve for A) G13-citrate, B) G5-BSPP, C) G5-EG$_6$-dimannose, D) G5-EG$_6$-fucose, E) G13-EG$_6$-dimannose (1 nM) with DC-SIGN (40 nM), F) G13-EG$_6$-fucose (1 nM) with DC-SIGN. D_h values given as xc ± ½ FWHM.

3.2.9 Summary of G13- and G27-glycan preparation, characterisation, and future applications

In summary, G27 and G13-glycans were successfully synthesised and characterised. Using DLS to measure their hydrodynamic diameters, it was found that G27-fucose form only core/satellite assemblies coated with a monolayer of DC-SIGN molecules after DC-SIGN binding, where one G27 binds simultaneously to all four CRDs in one DC-SIGN molecule. Contrastingly, G27-dimannose gives DC-SIGN monolayer coated individual particles at low PGRs, but has a tendency to form cross-linked species at high PGRs. The G27-glycans synthesised here were used in a pull-down assay in Chapter 8 to measure their binding affinity with DC-SIGN. Furthermore, Chapter 8 explored the modification of these G27- and G13-glycans as affinity probes by addition of a protein reactive label (sulfonyl fluoride) onto the G27 surface, in order to isolate and identify proteins from complex cellular mixtures. The synthesis of these probes is discussed in Chapter 8, where a more detailed discussion of the design principles involved in constructing an effective affinity probe is first discussed.

Chapter 4 – Effects of linker length, glycan density and glycan type in G5-glycan-DC-SIGN/R multivalent binding affinity, thermodynamics and inhibition of viral infection

4.1 Introduction

In order to exploit multivalent glycoconjugates for applications such as therapeutics, diagnostics, imaging or other functional purposes, it is of great importance to understand the mechanisms behind MLGIs.(97) A key aspect of studying MLGIs is to link their binding mode to their binding affinity. Investigating both of these aspects is essential, as correlating the physical geometry of the interaction with the apparent binding strength can strongly aid in determining a lectins structural and spatial arrangements, and why some MLGIs are significantly stronger than others despite sharing similar structural motifs. In particular, this has been the case for the lectin pair DC-SIGN and DC-SIGNR, which despite sharing a 77% amino acid homology and the same mannose-binding motif, have significantly different binding affinities to the same mannose-based glycoconjugate (3.9 nM vs 152 nM respectively).(115) An investigation into their binding mode via DLS and TEM allowed for the proposition that the orientation of their CRDs differed, putting spatial constraints on binding for DC-SIGNR that do not exist for DC-SIGN and this therefore explains the difference in their binding affinities with the same multivalent GNP-glycan.(115, 151)

Another way to understand affinity is to measure the thermodynamic contributions to binding, as this provides scope for revealing the forces governing MLGIs. This can inform whether binding strength arises from enthalpic gains or minimal entropic penalties. The enthalpic term can infer whether binding is strongly driven by good spatial matches allowing simultaneous engagement of multiple binding sites, as this value often reflects the sum of the individual monovalent enthalpies. Comparing the change in enthalpy for a multivalent interaction to the monovalent interaction can provide quantitative data to back up the qualitative data collected by DLS binding mode in determining exactly how many LGIs are occurring in the interaction. Equally, looking at entropy change is also important. While the entropic term is often negative, the magnitude of this contribution can indicate the extent of conformational restrictions and the impact this has on binding affinity. MLGIs which have good spatial match and monolayer binding mode may still experience low binding affinities due to the entropic cost of constraining long flexible ligands.(2)

Understanding the thermodynamic aspects of binding can help guide the rational design of agents to target MLGIs. Knowing whether the interactions are driven by entropy or enthalpy can guide choices based on scaffold size, shape, density and flexibility to optimise the perfect agent for the desired application. Despite their importance,

information concerning the majority of MLGI binding modes, and how these modes influence affinity and underlying binding thermodynamics, remains largely unexplored. This knowledge gap is primarily attributed to the limitations of current biophysical techniques in probing these inherently complex and flexible interactions. For instance, isothermal titration calorimetry (ITC) and surface plasmon resonance (SPR) are two of the most commonly employed techniques for studying the thermodynamics of binding interactions, including MLGIs.(182, 183) However, ITC faces challenges in accurately determining the affinity of cross-linking interactions, which can complicate the interpretation of ITC data.(141) Similarly, SPR struggles to dissect the individual contributions of LGIs to the overall MLGI affinity and specificity, as these are heavily influenced by the density and orientation of the immobilised binding partner on the surface.(183) Therefore, these conventional biophysical techniques can only provide partial information, failing to offer a complete understanding of individual lectin binding thermodynamics, kinetics, binding modes, and binding site orientations, which are all parameters crucial for both fundamental comprehension and successful therapeutic development to target specific MLGIs.

In light of this, the development of new approaches and techniques is essential to facilitate more effective strategies to address these challenges and unlock a deeper understanding of MLGI mechanisms. GNPs have recently emerged as powerful probes for biological and biomedical research, notably possessing strong fluorescence quenching properties. Specifically, our group has utilised the strong fluorescence quenching properties of GNPs to measure the apparent K_d of dimannose coated GNPs of varying sizes (5 nm, 13 nm and 27 nm) with fluorescently labelled DC-SIGN, revealing that larger particles have stronger apparent binding affinity (with K_ds of 5.8 vs 1.0 vs 0.22 nM respectively).(130) As well as measuring the apparent K_d, these FRET and NSET assays have been used to look at the enthalpic and entropic contributions to binding affinity, to explain the inconsistency in the K_ds between different size gold nanoparticles bearing the same glycan. Findings uncovered that while all GNP sizes displayed negative ΔS of binding, their absolute values were reduced as GNP scaffold size increased (-288 vs -207 vs -138 J mol^{-1} K^{-1}), implying that the unfavourable entropy changes upon GNP-DC-SIGN binding are reduced with the increasing GNP size. This has been attributed to larger scaffolds having a higher proportion of unbound surface ligands which may have largely retained their conformational and rotational degrees of freedom. The lesser entropic penalty can explain the stronger binding (lower apparent K_d) for larger GNP sizes bearing the same glycan.

Using solution-based methods such as FRET and ITC for investigating solution-phase affinities and thermodynamic of MLGIs has several advantages. They are often simple to set up, have a high versatility and the ability to be applied to a wide range of molecular interactions for real-time affinity, equilibrium and kinetic measurements. They are able to

reveal structural details on the binding mode and importantly, they enable the studying of binding interactions without introducing significant interference from artificial constraints, surface artefacts and non-specific binding, which occur with immobilisation on a surface. However, solution-based chemistry does not accurately mimic the natural environment where most MLGIs occur, such as cell membrane proteins binding to their respective ligands *in vivo*.

It is important to look at surface-phase chemistry alongside solution-based results to gain an overall perspective of how the two relate to each other and therefore how solution based results may be used to interpret *in vivo* data. The importance of this has been demonstrated by our groups recent results in an inhibition study where glycan-coated GNPs have been explored as potential therapeutics for inhibiting viral entry to cells via the tetrameric lectin DC-SIGN.(115) Four different GNP-glycans were synthesised, coated in mannose, dimannose or their respective higher density glycan timers (Figure 4.1). The lower density glycans showed weaker binding affinities than their respective trimers in the NSET based assay, however when these glycan GNPs were applied to the inhibition of ebolavirus glycoprotein (EBOV-GP)- driven infection of DC-SIGN/R^{+} 293T cells they showed an enhanced ability to inhibit viral infection (a lower concentration was required to achieve 50% inhibition) (Table 4.1). It would be expected that higher binding affinities would lead to a greater inhibition however these results show the inverse.

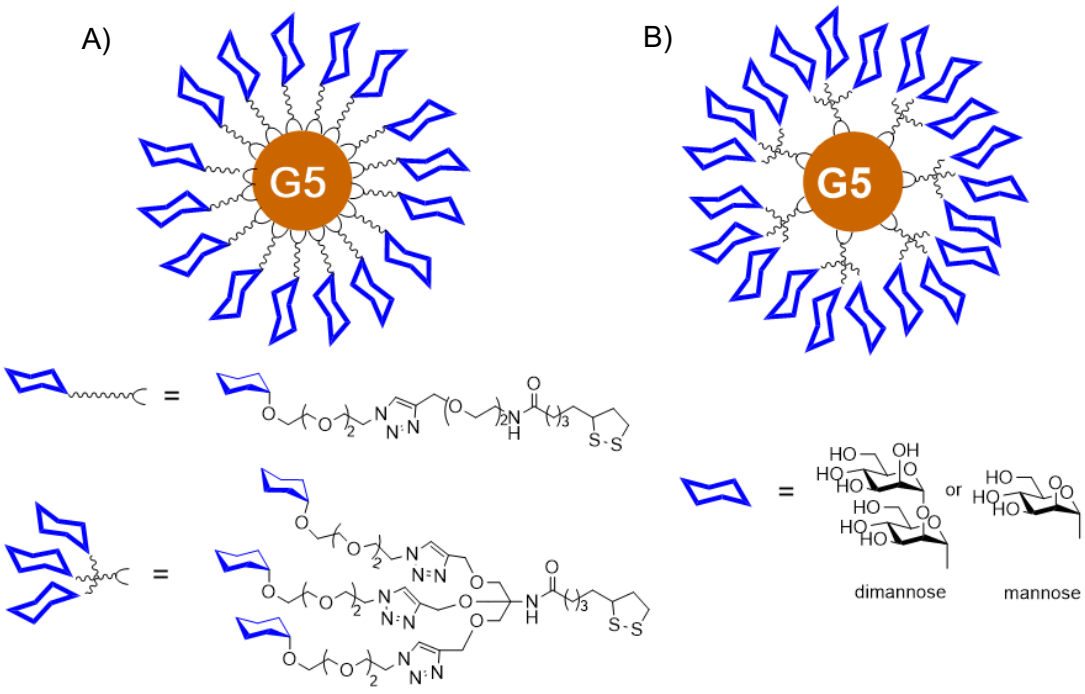

Figure 4.1 Schematic of the GNP-glycans used in the NSET quenching assay and viral inhibition studies. The GNP is coated with glycan ligand containing (A) one, or (B) three terminal α-mannose (mannose) or α-mannose-(1,2)-α-mannose (dimannose). The chemical structures of glycan ligands are depicted underneath.

Table 4.1 Summary of the binding affinities of different GNP-glycans with DC-SIGN, derived from the quenching efficiency, and the inhibition of EBOV-GP entry into DC-SIGN$^+$ 293T cells with different GNP-glycans, derived from the luciferase activity.(115)

G5-Glycan	**K_d (nM)**	**IC_{50} (nM)**
G5-mannose	33.1 ± 2.1	0.26 ± 0.08
G5-$(mannose)_3$	18.7 ± 0.3	1.57 ± 0.25
G5-dimannose	3.9 ± 0.3	0.095 ± 0.017
G5-$(dimannose)_3$	3.6 ± 0.1	0.15 ± 0.031

This study showed that solution and surface based methods may produce different results. Discrepancies such as these highlight the necessity of studying MLGIs not just in solution-phase but also in their natural states on cell surfaces. Firstly, this emphasises the importance of context in measuring the avidity. A lectin glycan pair which exhibit weak binding in solution may bind strongly when bound to a surface, due to local density and cooperative binding. Alternatively, a binding event that appears strong on surfaces may become weak in solution if it relies on fixed geometry for binding. Secondly, the enthalpy and entropy terms can change drastically between solution and surface phase experiments. Surface binding might be enthalpically less favourable due to the need bridge binding sites which are fixed in position, but entropic penalties may be less as surface bound lectins (or glycans) will have lower starting entropy and therefore suffer a lower cost upon binding compared to those in solution. Finally, surface conditions favour the true kinetic and entropic factors involved in the interaction of MLGIs on cell surfaces where proteins can move laterally, cluster together, and be endocytosed and recycled to the surface, while glycans diffuse freely, affecting how they interact. Understanding these conditions provides a clearer picture of how proteins may work together to improve glycan binding and uptake.(176, 184)

The work in this chapter extended the use of the fluorescence quenching properties of GNPs to explore the impact of changing the oligo(ethylene glycol) linker length, glycan valency and a terminal glycan on the binding affinity of G5-glycans with DC-SIGN. By studying temperature dependent binding affinities in combination with van ‘t Hoff analysis, the underlying thermodynamic contributions to binding were identified, thereby revealing how aspects of glycoconjugate design impact binding strength. Furthermore, ITC was used to verify whether the fluorescence quenching method is a quick, easy and reliable method for measuring thermodynamic binding parameters and therefore improving mechanistic understanding of multivalent lectin glycan binding interactions in solution-phase assays. Additionally, these data were compared to a surface-phase viral inhibition assay to determine if the solution-phase data can be used as a method for assessing the viral inhibition potency of G5-glycans at the cellular level. Combining all

these data, a secondary aim was to identify G5-glycans with a range of binding affinities for further study in cell-based assays to determine if binding affinity is an important factor in the modulation of G5-glycan induced cytokine expression. Further work on this can be found in Chapter 7.

4.2 Results and discussion

4.2.1 Quantifying binding affinity and thermodynamic parameters via a fluorescence quenching method

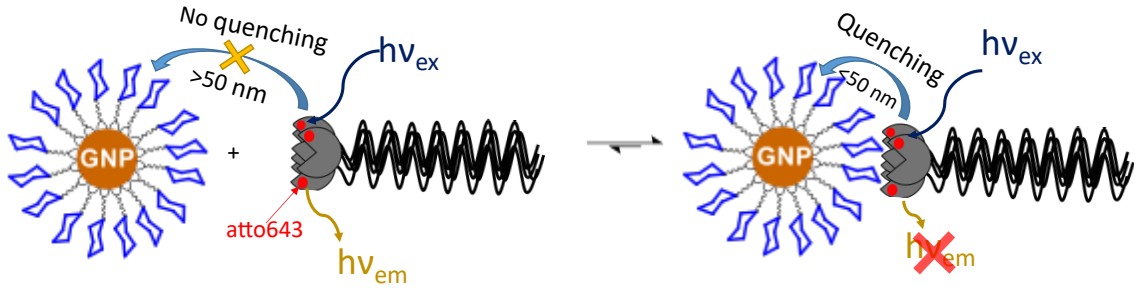

Figure 4.2 Schematic depicting the quenching process between excited DC-SIGN-atto643 upon binding to a G5-EG_n-glycan, where hv_{ex} is excitation photon energy and hv_{em} is emission photon energy. At distances greater than 50 nm between G5 and atto643 labels, no quenching is expected to occur but upon binding, their distance will be reduced to <50 nm and therefore nanosurface energy transfer (NSET) can occur, leading to quenching of the atto643 emission. This acts as a readout for binding quantification.

The principle of the G5-NSET readout for quantifying DC-SIGN (atto643 labelled) binding to G5-glycans is shown schematically in Figure 4.2. Since NSET can only happen over a short distance (e.g. < 50 nm), a distinct advantage to this method is that any unbound lectins (donor) in solution would be too far away to participate in NSET interactions with the GNP acceptor and hence will not contribute to the NSET signal (Figure 4.2). Thus, the observed NSET signal is directly linked to the equilibrium of G5-glycan-lectin binding and, more specifically, the amount of lectins bound to the GNP. Since G5s have a relatively low absorption extinction coefficient of $1.1 \times 10^7\ M^{-1}cm^{-1}$, the wide concentration range required for affinity quantification of weak binders could be measured without introducing significant inner-filter effects, which occurs when high concentrations of absorbing molecules reduce the excitation light reaching the sample, leading to an underestimation of the fluorescence intensity. Furthermore, NSET does not require spectral overlap as it depends on electromagnetic coupling to the nanoparticles conductive surface rather than resonance between emission and absorbance spectra.(185) Therefore, additionally to choosing G5 to minimise absorption of the excitation wavelength, atto643 was selected as the fluorescent dye as the spectral overlap between G5 absorption and atto643 emission is marginal. This choice reduces

any potential secondary inner-filter effect where the atto643 emission would be absorbed by G5, making the emission appear quenched beyond NSET.

The fluorescence spectra of premixed G5-EG_n-glycan + DC-SIGN samples under a fixed protein:G5 molar ratio (PGR) of 1:1 but with varying protein concentration over a range of 3-100 nM were recorded at an excitation wavelength (λ_{ex}) of 630 nm. All binding studies were carried out in a binding buffer with 1 mg/mL of bovine serum albumin (BSA). BSA is a non-target serum protein of high abundance *in vivo*, and was included in this assay in order to resemble biological binding conditions as well as reduce nonspecific interactions and adsorption of proteins and GNPs to Eppendorf and pipette surfaces (a main source of experimental errors at low concentrations, e.g. < 10 nM). Measurements were carried out at three different temperatures (22, 27 and 32 °C) for a later analysis of the thermodynamic contributions to binding.

A typical fluorescence spectrum is given in Figure 4.3A showing the binding of DC-SIGN-atto643 with G5-EG_2-dimannose over a 3-100 nM concentration range. Figure 4.3B shows that the integrated fluorescence intensity of DC-SIGN-atto643 increases linearly with concentration but in the presence of a G5-EG_n-glycan, this relationship deviates away from linear, indicating that at higher concentrations, a greater proportion of DC-SIGN is bound to and quenched by the G5-EG_n-glycan.

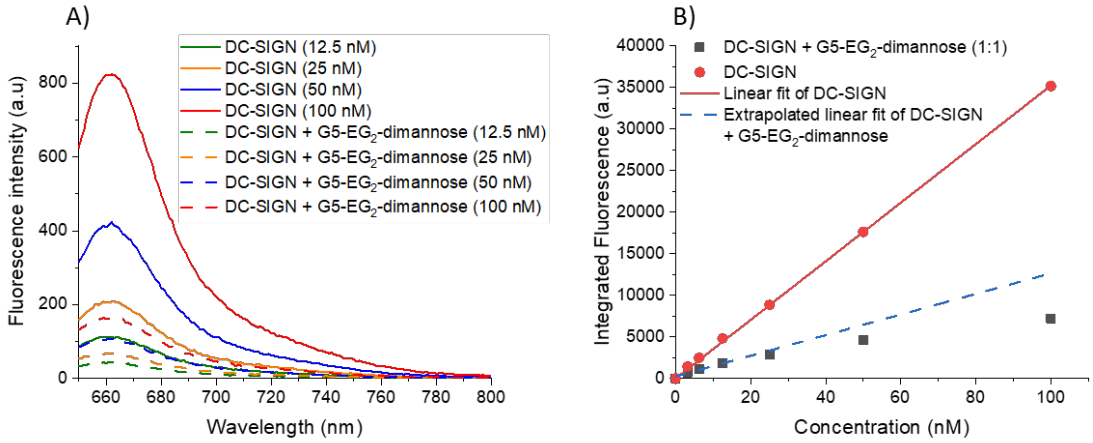

Figure 4.3 A) Typical fluorescence spectrum of varied concentrations of DC-SIGN without (solid lines) and with (broken lines) 1 molar equivalent of G5-EG_2-dimannose (λ_{ex} = 630 nm). B) Relationship between fluorescence and concentration in the absence (red dots) and presence (black squares) of one molar equivalent of G5-EG_2-dimannose. In the absence of GNP, the fluorescence is fitted well by a linear relationship, but after addition of 1 mol. equiv. of G5-EG_2-dimannose the relationship deviates more and more from linear with the increasing concentration, indicating as concentration increases a greater proportion of DC-SIGN is being bound and quenched.

In order to derive the apparent K_d, the quenching efficiency (QE) at each concentration was calculated via Equation 4.1; where IF_0 is the integrated fluorescence intensity of labelled DC-SIGN in the absence of G5-EG_n-glycan and IF is the integrated fluorescence intensity of labelled DC-SIGN in the presence of a G5-EG_n-glycan.

$$QE(\%) = \frac{IF_0 - IF}{IF_0}\ x\ 100 \qquad \textbf{Equation 4.1}$$

From this, K_d was calculated by fitting with Hill's Equation (Equation 4.2; where QE_{max} is the maximum quenching efficiency, [P] is the protein concentration, K_d is the apparent equilibrium binding dissociation constant (or effective concentration for 50% binding) and *n* is the Hill coefficient which indicates binding cooperativity (where *n*>1 indicates positive cooperativity and *n*<1 indicates negative cooperativity and *n*=1 indicates no cooperativity).

$$QE = \frac{QE_{\max}\ [P]^n}{{K_d}^n + [P]^n} \qquad \textbf{Equation 4.2}$$

Here, *n* = 1 was assumed for all fittings as no cooperativity was expected to occur since the affinity assays were performed under a PGR of 1 and therefore G5-glycans should be bound with just one lectin; thus no intermolecular lectin-lectin interactions were expected to inhibit or promote further lectin-G5-glycan binding. Omitting this fixing step resulted in non-viable fittings where QE_{max} >100%. Since quenching is distance dependent, linkers of the same length were expected to give the same QE_{max} independent of the measurement temperature and so the Hill plots for each G5-EG_n-glycan at the three measured temperatures were fitted globally, sharing a QE_{max} value (Figure 4.4). The results and remaining fitting parameters are summarised in Table 4.2 where the R^2 represents how well the fitted curve represents the observed data.

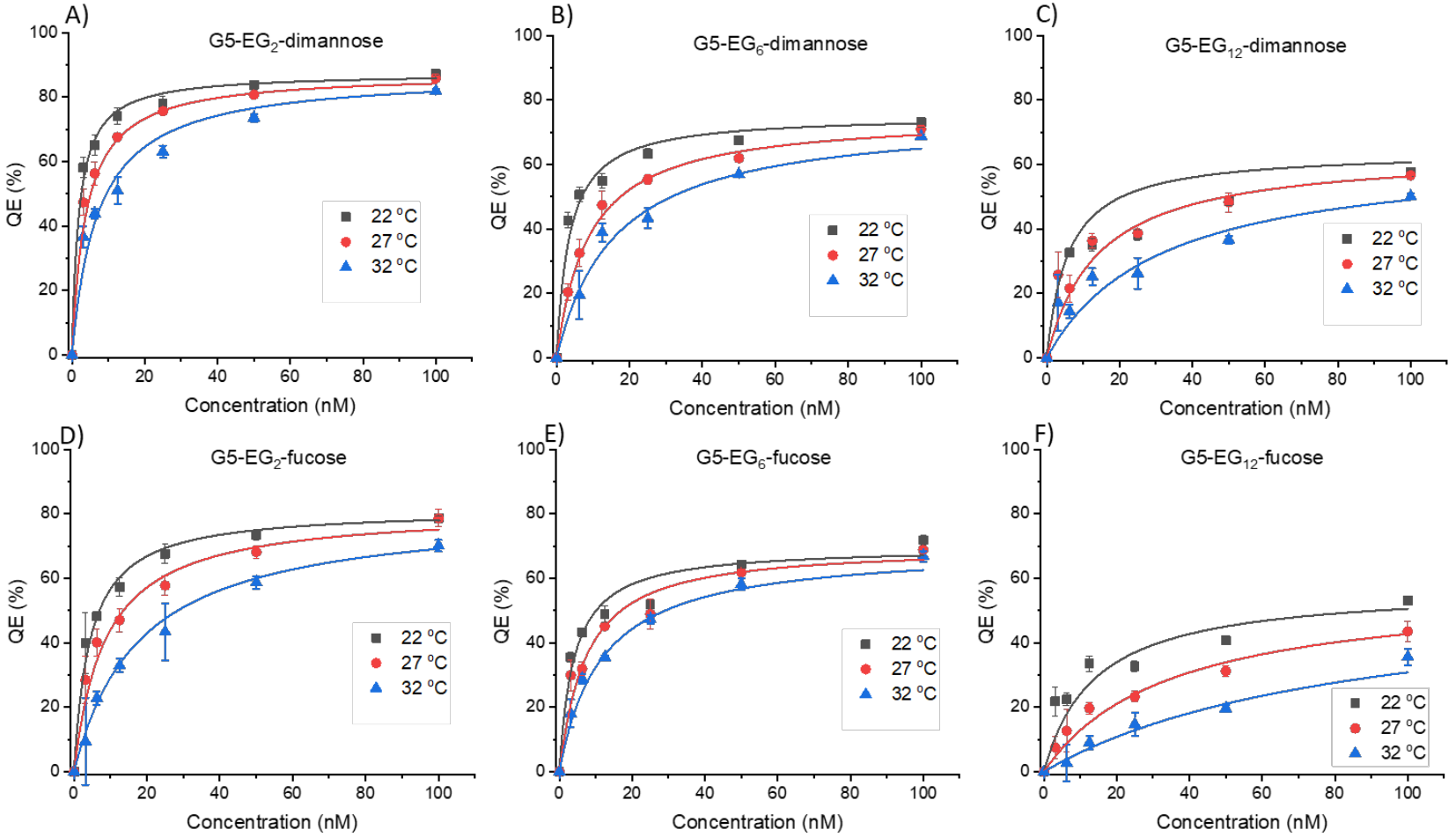

Figure 4.4 The quenching efficiency - concentration relationship for DC-SIGN binding to G5-glycans made in a 1:1000 GNP-ligand molar ratio at 22 ℃ (grey), 27 ℃ (red) and 32℃ (blue) for A) G5-EG_2-dimannose, B) G5-EG_6-dimannose, C) G5-EG_{12}-dimannose D) G5-EG_2-fucose, E) G5-EG_6-fucose, F) G5-EG_{12}-fucose. Graphs were fitted by Equation 4.2 and error bars represent the SDs of duplicate experiments at each concentration.

Table 4.2 Summary of the fitting parameters of DC-SIGN binding to G5-EG_n-glycans (1:1000). Errors represent the SDs observed by the fitting.

Ligand	Temperature (°C)	K_d (nM)	QE_{max} (%)	R^2
EG_2-dimannose	22	1.9±0.4	87.5±0.5	1
	27	3.8±03		1
	32	7.1±0.7		0.999
EG_6-dimannose	22	3.5±0.7	75.3±1.6	0.999
	27	8.9±1.5		0.998
	32	16.0±1.5		1
EG_{12}-dimannose	22	5.8±1.0	64.2±3.4	0.955
	27	14.0±6.1		1
	32	30.9±17.1		0.994
EG_2-fucose	22	4.4±0.2	81.6±0.7	0.999
	27	8.5±0.8		0.997
	32	17.9±1.1		0.999
EG_6-fucose	22	3.9±0.6	69.8±2.1	0.999
	27	7.1±0.6		0.997
	32	11.5±1.1		0.999
EG_{12}-fucose	22	13.9±3.4	57.6±3.0	0.992
	27	34.8±6.4		0.987
	32	86.6±15.1		0.987

Based on these data, four conclusions can be drawn.

(1) Binding of DC-SIGN with G5-EG_2-dimannose produced a low nM K_d (1.9 nM). This value corresponds to ~475 000-fold tighter binding than that obtained for monovalent binding between dimannose and monomeric DC-SIGN CRD (K_d = 0.9 mM), suggesting that a polyvalent display of glycans on a G5 surface is a great enhancer of the glycans' affinity for DC-SIGN.(77)

(**2**) QE_{max} decreased with the increasing EG_n linker length. Although gold nanoparticles can quench fluorescence completely in very close proximity, this quenching decays strongly with increasing distance.(129) Since the G5 particles with longer linkers have a greater hydrodynamic radii, R_h (Table 3.1), the bound DC-SIGN is placed further away from the gold core, therefore QE_{max} decreasing with increasing linker length is in line with the expected result. The maximum quenching efficiency of G5-EG_{12}-dimannose (R_h 8.9 nm) was 64.2% compared to the higher quenching efficiency max for G5-EG_2-dimannose (R_h 6.4 nm) of 87.5%. This trend was also observed for the fucose glycans.

(**3**) G5-dimannose binding with DC-SIGN was stronger than that of G5-fucose binding. While the monosaccharide fucose has previously been identified as a binder to DC-SIGN, much of the literature investigates the relationship between DC-SIGN and fucose containing glycans such as the Lewis glycans and blood group A/B antigens.(32, 48, 80, 83, 92, 186) Here it has been confirmed that a polyvalent display of fucose alone appears

to be a strong DC-SIGN binder with K_d as low as 3.9 nM. The weaker binding compared to dimannose may be explained due to the latter being able to exploit the CRD's secondary glycan binding sites, alongside forming further interactions with residues lying outside the primary binding pocket, such as with Phe313, which enhances binding interactions and results in a greater affinity enhancement.(74)

(**4**) Consistent with previous results, the binding affinity of DC-SIGN with G5-EG_n-dimannose was very strong, especially so for the short EG_2 linker (K_d = 1.9 nM) at 22 ^oC.(115) Increasing the linker length decreased binding affinity with DC-SIGN (e.g. K_d = 1.9 vs 3.5 vs 5.8 nM for EG_2, EG_6 and EG_{12}, respectively). The decrease in apparent binding affinity as linker length increases was presumably because the longer EG_n linkers result in a more flexible and disordered terminal glycan with more conformational and rotational degrees of freedom, and hence there is a greater entropic penalty upon DC-SIGN binding. It is not immediately obvious from these data why G5-EG_6-fucose had a slightly higher average apparent binding strength at all temperatures than G5-EG_2-fucose, as the entropic penalty of constraining the EG_6 linker should translate to a weaker affinity. The cause of such was therefore explored more within the following thermodynamic studies.

4.2.1.1 An investigation of thermodynamic binding parameters

The results above demonstrate that in addition to the glycan type influencing the carbohydrate binding strength, other properties such as ligand flexibility also impacts affinity. This effect is likely due to the introduction of, and balance between, additional factors such as optimal spatial matches and conformational restrictions upon binding. While the rigidity of the shorter EG_2 linkers may promote strong binding by reducing the entropy cost, the flexibility of the longer EG_{12} linkers could allow the terminal glycans to better adapt to the DC-SIGN binding sites, thereby optimising the enthalpy. Achieving a good balance between rigidity and flexibility can increase avidity by several orders of magnitude beyond what is achieved solely through statistical rebinding.(187) To better understand how ligand flexibility affects binding affinity, these influences were explored by determining the thermodynamic binding profiles of each G5-EG_n-glycan.

The binding thermodynamics were obtained by repeating the binding assay at three different temperatures (22, 27, and 32 °C). As described previously, the respective apparent K_d values were derived by fitting with the Hill equation. To extract the binding enthalpy and entropy changes, van 't Hoff plots were constructed by combining the Gibbs free energy of reaction Equation 4.3 with the Gibbs free energy isotherm Equation 4.4 to obtain Equation 4.5. Plotting the natural log of K_d ($\ln K_d$) vs the reciprocal of temperature (1/T) affords a linear plot from which to extract the binding enthalpy and entropy ($\Delta H = mR$, ΔS =-cR where m is the gradient, c is the y intercept and R is the perfect gas constant).

$$\Delta G° = \Delta H° - T\Delta S°$$ **Equation 4.3**

$$\Delta G° = -RT\,ln(K_a) = RT\,ln(K_d)$$ **Equation 4.4**

$$\ln(K_d) = \frac{\Delta H°}{R}\frac{1}{T} - \frac{\Delta S°}{R}$$ **Equation 4.5**

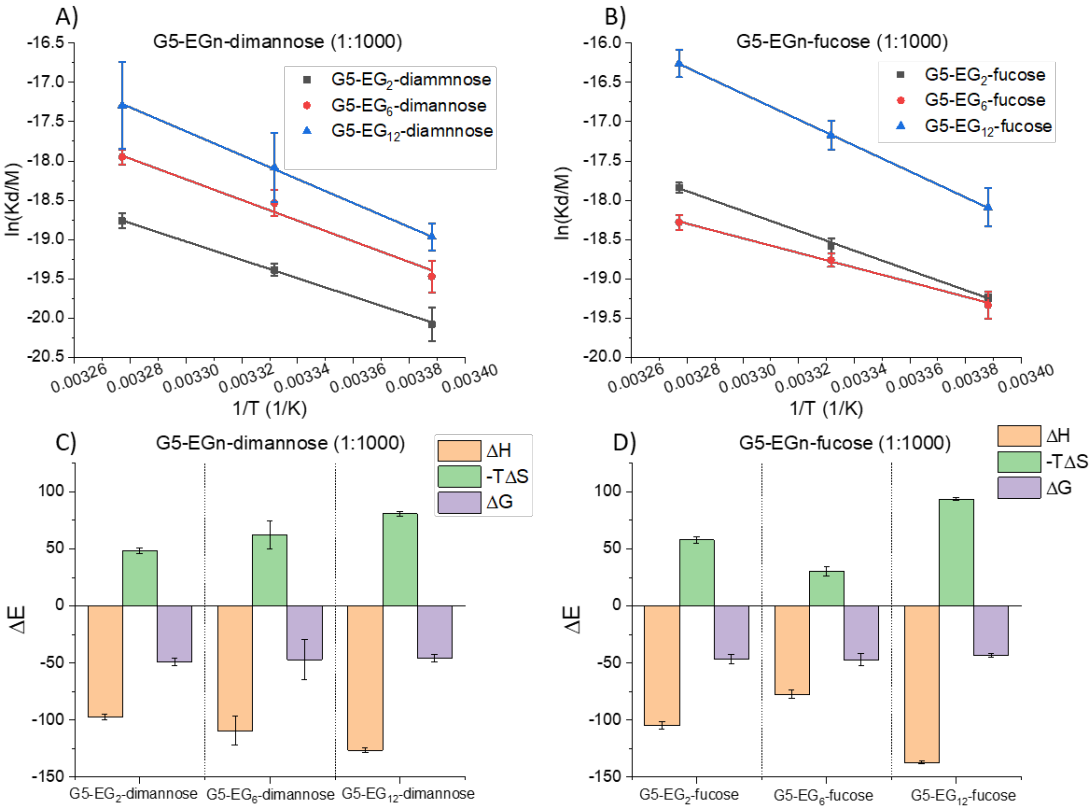

Figure 4.5 van 't Hoff analyses of the ln(K_d)–1/T relationships for DC-SIGN binding with A) G5-EG_2-dimannose (grey), G5-EG_6-dimannose (red), G5-EG_{12}-dimannose (blue) or with B) G5-EG_2-fucose (grey), G5-EG_6-fucose (red), G5-EG_{12}-fucose (blue). C) Comparison of the standard (T = 298 K) enthalpy (orange), entropy (green), and Gibbs free energy (purple) changes of G5-EGn-dimannose (1:1000) binding with DC-SIGN. D) Comparison of the standard (T = 298 K) enthalpy (orange), entropy (green), and Gibbs free energy (purple) changes of G5-EGn-Fucose (1:1000) binding with DC-SIGN. SDs represent fitting errors.

Table 4.3. Summary of the thermodynamic parameters for G5-glycan (1:1000) binding with DC-SIGN. SDs represent fitting errors, or are propagated from SDs obtained in Figure 4.5A/B.

Ligand	Δ*H*°(kJ mol^{-1})	Δ*S*°(J mol^{-1}K^{-1})	-TΔ*S*° (kJ mol-^{1})	Δ*G*°(kJ mol^{-1}) [a, b]
EG_2-dimannose	-97.2±2.5	-162.1±8.3	48.3±2.5	-48.9±3.5
EG_6-dimannose	-109.3±12.4	-208.7±40.7	62.2±12.1	-47.1±17.4
EG_{12}-dimannose	-126.4±2.3	-271.0±7.5	80.8±2.3	-45.6±3.2
EG_2-fucose	-104.7±3.1	-194.5±10.0	58.0±3.0	-46.7±4.3
EG_6-fucose	-77.4±3.9	-101.4±12.9	30.2±3.8	-47.1±5.5
EG_{12}-fucose	-137.2±1.1	-314.2±4.2	93.7±1.2	-43.5±1.7

[a] Error (δ) propagated from Δ*H*° and Δ*S*° according to $\delta\Delta G^\circ = \sqrt{(\delta\Delta H^\circ)^2 + (\delta T\Delta S^\circ)^2}$
[b] at 298 K

The thermodynamic parameters for G5-glycan binding with DC-SIGN are summarised in Table 4.3. For total binding enthalpy change (Δ*H*°), if all four CRDs in each DC-SIGN molecules are engaged in glycan binding, this value should equal ~ 100 kJ mol^{-1}, about 4-fold that of the corresponding monovalent DC-SIGN CRD: glycan binding measured by ITC (25.6 kJ mol^{-1} and 28.4 kJ mol^{-1} for dimannose and fucose respectively, Figure A. 21).(77) The total multivalent binding entropy change (Δ*S*°) of this polyvalent interaction includes contributions from translational, rotational and conformational entropies of the binding partners (G5-glycan+lectin) as well as a contribution from the changes associated in the entropy of the surrounding solvent molecules.(2) On the basis of the data presented in Table 4.3 four conclusions have been drawn.

(1) Binding is thermodynamically favourable as dictated by the negative Gibbs free energy (Δ*G*°) and is therefore spontaneous. Since the Δ*G*° values for all G5-EG_n-glycan (1:1000) samples are within error of each other, this indicates the energy release from binding is not strongly affected by linker length or glycan identity.

(2) Δ*H*° values for binding of most G5-glycans with DC-SIGN is around 4-fold that of the corresponding monovalent binding measured by ITC, indicating successful binding of all four CRDs in each DC-SIGN molecules. The G5-EG_6-fucose particle, however, has a Δ*H*° of -77.4 kJ mol^{-1} correlating to only 3-fold monovalent binding enthalpy suggesting that for this G5-glycan under these conditions, only three CRDs were engaged upon binding. Looking at the hydrodynamic size, surface valency, and deflection angles calculated in Chapter 3, it may be possible to explain why G5-EG_6-fucose behaves this way. Considering this set of G5s(1:1000) alone, G5-EG_6-fucose has the widest deflection angle (10.1 °) which could result in a sub optimal spatial match for four DC-SIGN CRDs,

however, exploration of the surface valency in Section 4.2.2 negates this by showing full tetrameric binding at wider deflection angles. This G5-EG_6-fucose-DC-SIGN interaction is therefore anomalous and the reasoning of such needs further investigation, but it is beyond the scope of this chapter.

Excluding this anomalous result, enthalpy change upon binding becomes increasingly more negative as linker length increases. While these values are similar enough to 4-fold that of equivalent monovalent CRD binding to free dimannose/fucose to suggest that tetrameric binding is occurring, it does also indicate that the length of the EG_n linker connecting the glycan to the G5 core has some impact on binding enthalpy changes. It is likely that the flexibility of the longer EG_{12} linkers allows the terminal glycans to adapt well to the DC-SIGN binding sites, thereby leading to enthalpically enhanced binding.

(3) Consistent with previous reports, generally the longer linker lengths (EG_{12}) described here are associated with a lower binding affinity than the shorter linkers.(119) As expected, the lower binding affinities correlate with an increase in entropic penalty which is due to the negative cost of constraining more flexible, disordered linkers upon binding. G5-EG_2-dimannose has a binding entropic penalty of -162 ± 8.3 J $mol^{-1}K^{-1}$ and an apparent K_d of 1.9 nM (at 22°C) compared to G5-EG_{12}-dimannose which has a larger binding entropic penalty of -271 ± 7.5 J $mol^{-1}K^{-1}$ and a correspondingly weaker apparent K_d of 5.8 nM.

Interestingly, the G5-EG_6-fucose sample which appeared to bind with only three CRDs still showed a stronger apparent binding affinity than its EG_2 counterpart, this is likely linked to the lower entropic penalty associated with constraining only three linkers per DC-SIGN rather than four. Therefore, three binding events still provides a high affinity enhancement, due to reduced binding entropic penalty.

(4) All bindings between G5-glycan and DC-SIGN are thermodynamically favourable (all with negative binding ΔG° values). All bindings have negative ΔH° values (favourable binding enthalpy) and negative ΔS° values (unfavourable entropy changes), and therefore binding is enthalpically driven.

4.2.2 Exploring the effect of G5 surface glycan valency on binding affinity and the associated thermodynamic contributions.

The ability of a glyconanoparticle to achieve effective multivalent enhancement depends not only on the crucial relationship between the type of surface glycan and their affinity for individual lectin binding sites but also on the chelate effect where two or more ligands on the same scaffold have the capacity to bind multiple sites simultaneously.(188) This capability is influenced by the spatial arrangement of the surface glycans as well as the scaffold shape/size, and the flexibility, density and valency of the ligand. Our group has previously explored the impact of factors such scaffold size, scaffold shape and the

degree of functionality on lectin binding capabilities, and so far this work has started to explore the flexibility of the glyconanoparticle by changing the linker length.(115, 120, 130). This section further explores the spatial arrangement and the effect of glycan valency on DC-SIGN binding.

It is important to investigate such matters in order to develop a greater understanding of what underpins pathogen binding *in vivo*. Pathogens carrying the same glycan on their surface are able to be identified and discriminated between despite their surface glycan similarities.(176) It is thought this is due to the affinity, pattern and valency of a pathogens surface glycans, enabling targeted detection by cells. Therefore, exploring the detailed and specific recognition *in vitro* by changing glycan presentation can aid in a better understanding of the mechanisms behind pathogen detection, and therefore enhance the development of drugs or agents to combat infections or diseases, with fewer harmful or off-target side effects.

Since strong binding in MLGIs is dependent on a good spatial match between binding partners, it is possible that tuning the surface valency of a glycoconjugate could afford the glycan ligands a more suitable spatial topology to form stronger interactions with DC-SIGN. While employing high valency scaffolds introduces large affinity enhancements based off statistical rebinding effects where the high local concentration of ligand can cause rapid rebinding after ligand dissociation, it is not necessarily a technique targeted at finding an optimal spatial match, where a complimentary ligand to the tetrameric DC-SIGN CRD platform can introduce favourable enthalpy enhancements.(189) To address this, designing smaller or lower-valency scaffolds is an excellent alternative strategy for targeting DC-SIGN with high precision. However, achieving this requires a delicate balance between the rigidity and flexibility of the linkers to optimise binding interactions, ensuring that at least two or more lectin CRDs are able to engage simultaneously to induce the desired affinity enhancement.(188, 190)

Previously in this group, valency has been controlled with the use of monomers vs. trimers and also dilution of GNP surface glycan ligands with an inert spacer ligand of the same overall EG_n- linker length. Here, the ratio of G5: ligand during the G5 cap exchange process has been modified to tune the number of glycans on the surface of each G5 particle. In addition to the saturated 1:1000 ratio, two further sets of G5-glycans were synthesised at G5:ligand ratio of 1:500 and 1:300, the resulting G5 glycan valencies can be seen in Chapter 3. Importantly, when these G5s were characterised, the hydrodynamic size analysis for the 1:300 ratio revealed sub-nm size differences between those with EG_6 and EG_{12} linked glycans, suggesting the lower valency of the G5 surface and the greater inter-glycan distance allows the linkers to fold in on themselves, reducing the effective hydrodynamic diameter of the particles. These folded PEG ligands may exhibit fewer degrees of freedom compared to their extended counterparts due to structural constraints imposed by intramolecular interactions such as hydrogen bonding,

which limits their conformational flexibility.(191) This would lower the starting entropy before binding, potentially affording these linkers a lower entropic penalty upon binding. Furthermore, the G5-EG_2-glycans made in a 1:300 ratio tended to exhibit cross-linked binding modes. Here, an investigation into the enthalpy changes of binding can confirm whether this is due to one G5-EG_2-glycan engaging fewer than 4 CRDs on one DC-SIGN molecule.

G5-EG_n-glycans (1:500, 1:300) were mixed with DC-SIGN and quenching efficiency was measured as previously described from Equation 4.1. Their Hill plots were constructed by comparing concentration vs quenching efficiency (Figure 4.6, Figure 4.8) to extract the binding affinities which are summarised in Table 4.4 and Table 4.6. van ‘t Hoff plots were then similarly plotted (Figure A. 22-23) to extract the thermodynamic binding parameters (Figure 4.7, Figure 4.9). A summary of the thermodynamic parameters can be found in Table 4.5 and Table 4.7.

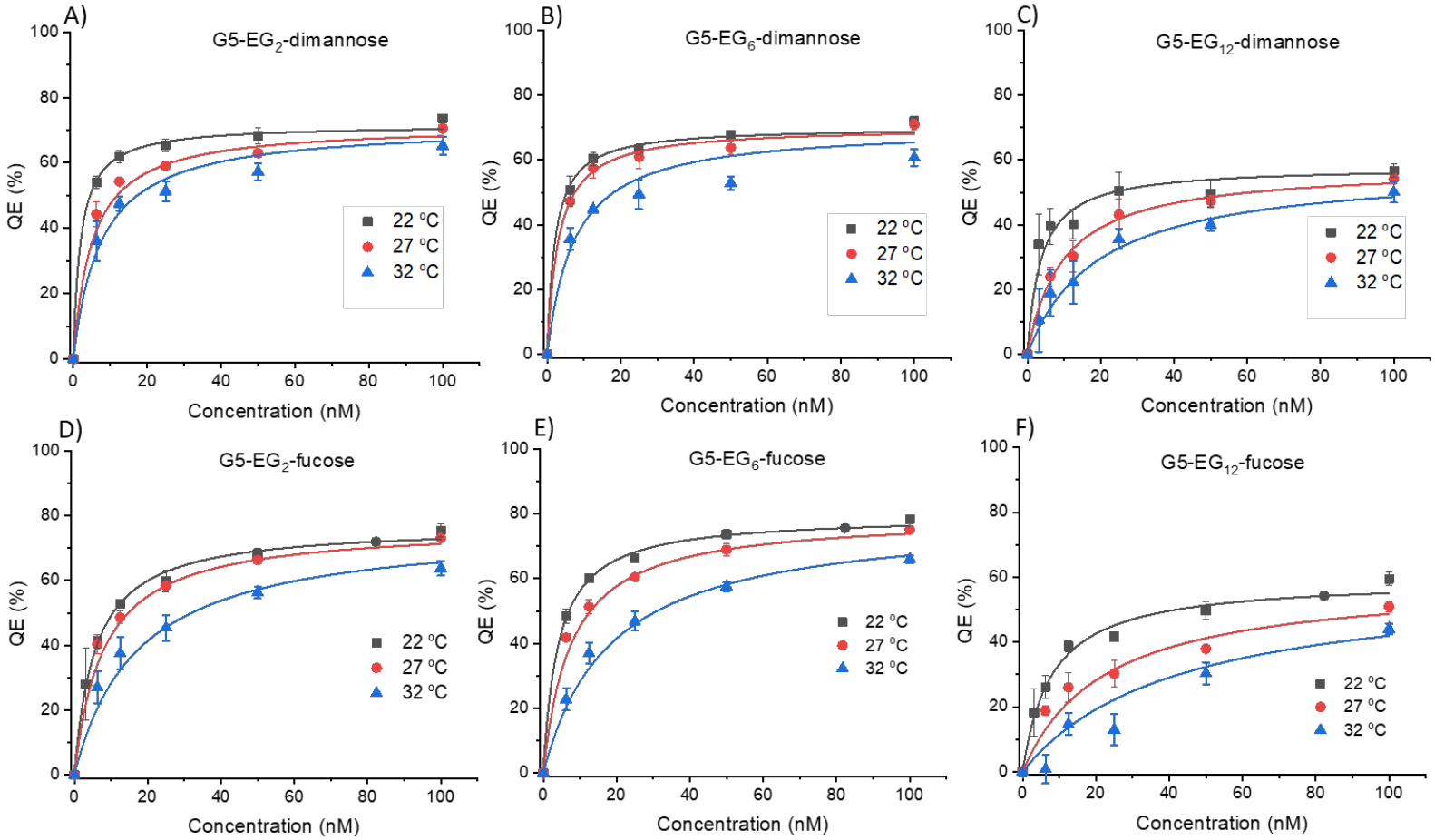

Figure 4.6 The quenching efficiency - concentration relationship for DC-SIGN binding to G5-glycans made in a 1:500 GNP-ligand molar ratio at 22 °C (grey), 27 °C (red) and 32°C (blue) for A) G5-EG_2-dimannose, B) G5-EG_6-dimannose, C) G5-EG_{12}-dimannose D) G5-EG_2-fucose, E) G5-EG_6-fucose, F) G5-EG_{12}-fucose. Graphs were fitted by Equation 4.2 and error bars represent the SDs of duplicate experiments at each concentration.

Table 4.4 Summary of the fitting parameters of DC-SIGN binding to G5-EG_n-glycans (1:500). Errors represent the SDs as observed by the fitting.

Ligand	Temperature (°C)	K_d (nM)	QE*max*	R^2
EG_2-dimannose	22	2.0±0.5	71.6±1.3	0.999
	27	5.1±0.6		0.999
	32	7.7±1.4		0.996
EG_6-dimannose	22	2.1±0.7	70.2±1.4	0.999
	27	3.0±0.5		0.999
	32	7.3±0.6		0.996
EG_{12}-dimannose	22	3.7±0.8	50.9±1.2	0.996
	27	9.6±1.3		0.999
	32	19.1±2.0		0.996
EG_2-fucose	22	5.6±0.4	77.0±1.2	1
	27	7.9±0.5		1
	32	17.2±1.9		0.998
EG_6-fucose	22	4.1±0.6	79.4±1.2	0.999
	27	7.6±0.6		0.999
	32	18.2±2.1		0.999
EG_{12}-fucose	22	7.9±1.9	59.4±3.2	0.995
	27	22.1±4.5		0.989
	32	41.8±10.1		0.987

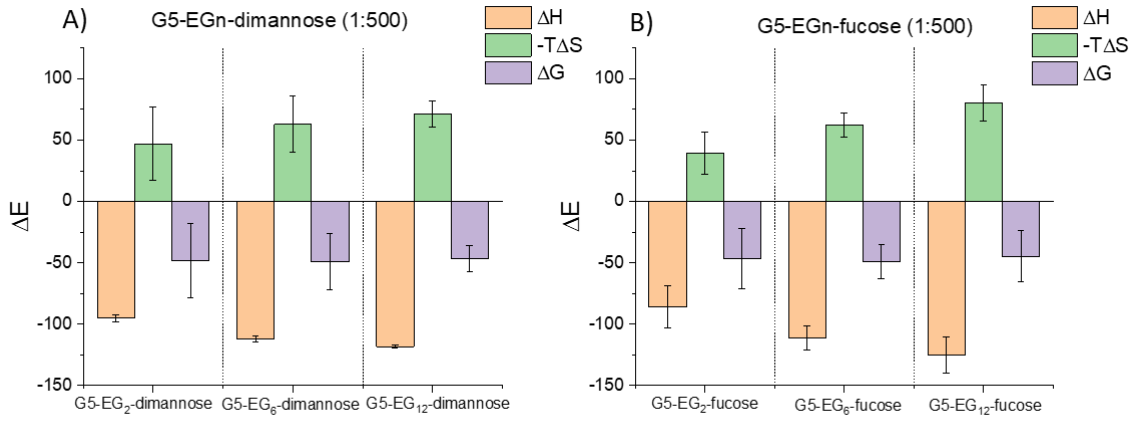

Figure 4.7 Comparison of the standard (T = 298 K) enthalpy (orange), entropy (green), and Gibbs free energy (purple) changes of A) G5-EG_n-dimannose (1:500) binding with DC-SIGN, B) G5-EG_n-fucose (1:500) binding with DC-SIGN. SDs represent fitting errors.

Table 4.5 Summary of the thermodynamic parameters for G5-EG_n-glycan (1:500) binding with DC-SIGN. SDs represent fitting errors, or are propagated from SDs obtained in Figure A. 22.

Ligand	Δ*H*°(kJ mol^{-1})	Δ*S*°(J mol^{-1}K^{-1})	-TΔ*S*° (kJ mol-^{1})	Δ*G*°(kJ mol^{-1}) [a, b]
EG_2-dimannose	-95.2±3.0	-158.0±100.1	47.1±30.0	-48.1±30.1
EG_6-dimannose	-112.1±2.3	-211.2±76.5	63.0±22.8	-49.1±22.9
EG_{12}-dimannose	-118.1±1.1	-239.4±35.8	71.4±10.7	-46.7±10.7
EG_2-fucose	-85.8±17.4	-132.2±58.2	39.4±17.4	-46.4±24.6
EG_6-fucose	-111.2±10.0	-209.5±33.3	62.5±9.9	-48.7±14.1
EG_{12}-fucose	-124.9±14.8	-268.5±40.1	80.1±14.6	-44.8±20.8

[a] Error (δ) propagated from Δ*H*° and Δ*S*° according to $\delta\Delta G° = \sqrt{(\delta\Delta H°)^2 + (\delta T\Delta S°)^2}$
[b] at 298 K

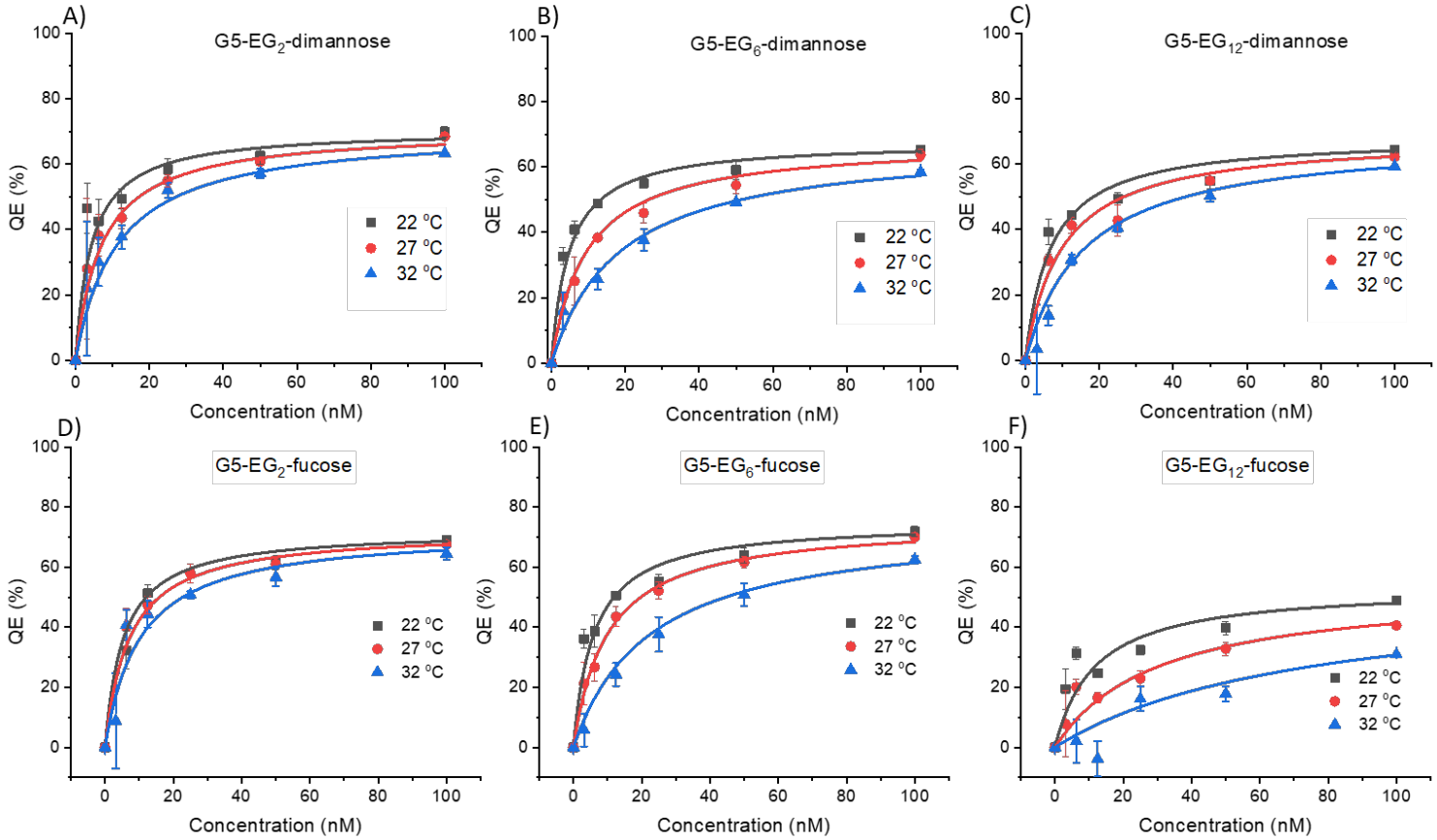

Figure 4.8 The quenching efficiency - concentration relationship for DC-SIGN binding to G5-glycans made in a 1:300 GNP-ligand molar ratio at 22 ℃ (grey), 27 ℃ (red) and 32℃ (blue) for A) G5-EG_2-dimannose, B) G5-EG_6-dimannose, C) G5-EG_{12}-dimannose D) G5-EG_2-fucose, E) G5-EG_6-fucose, F) G5-EG_{12}-fucose. Graphs were fitted by Equation 4.2 and error bars represent the SDs of duplicate experiments at each concentration.

Table 4.6 Summary of the fitting parameters of DC-SIGN binding to G5-EG_n-glycans (1:300). Errors represent the SDs as observed by the fitting.

Ligand	Temperature (°C)	K_d (nM)	QE*max*	R^2
EG_2-dimannose	22	4.3±0.8	70.1±1.0	0.997
	27	7.1±0.9		0.999
	32	11.2±1.4		1
EG_6-dimannose	22	3.8±0.5	67.8±1.1	0.999
	27	7.2±1.0		0.998
	32	16.2±1.7		1
EG_{12}-dimannose	22	4.7±0.4	68.5±0.9	0.999
	27	9.3±0.5		0.999
	32	20.0±1.4		1
EG_2-fucose	22	5.4±1.0	72.3±0.8	1
	27	7.1±1.1		1
	32	10.1±1.0		0.998
EG_6-fucose	22	6.0±0.6	67.8±1.1	0.999
	27	9.9±1.5		0.998
	32	22.4±3.3		1
EG_{12}-fucose	22	11.6±2.6	53.7±0.03	0.994
	27	30.0±5.7		0.994
	32	74.0±9.0		0.998

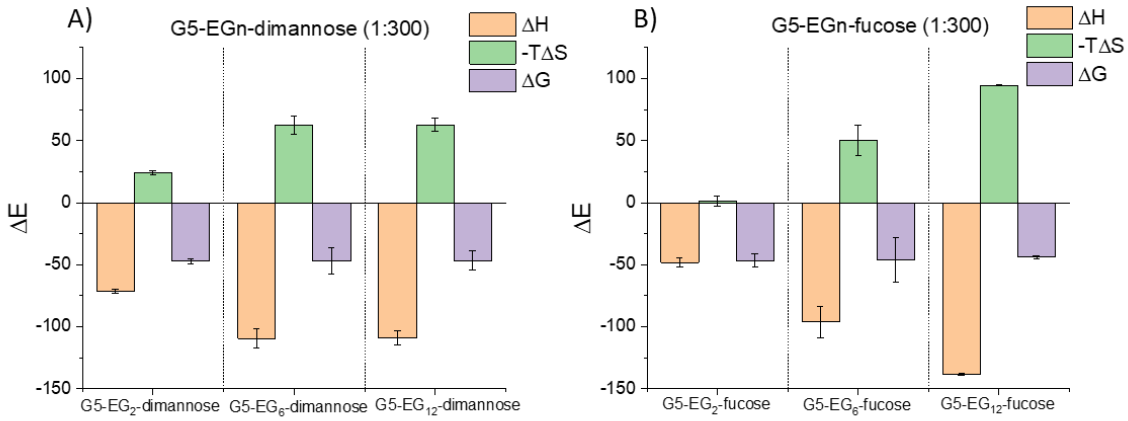

Figure 4.9 Comparison of the standard (T = 298 K) enthalpy (orange), entropy (green), and Gibbs free energy (purple) changes of A) G5-EG_n-dimannose (1:300) binding with DC-SIGN, B) G5-EG_n-fucose (1:300) binding with DC-SIGN. SDs represent fitting errors.

Table 4.7 Summary of the thermodynamic parameters for G5-EG_n-glycan (1:300) binding with DC-SIGN. SDs represent fitting errors, or are propagated from SDs obtained in Figure A. 23.

Ligand	Δ*H*°(kJ mol^{-1})	Δ*S*°(J mol^{-1}K^{-1})	-TΔ*S*° (kJ mol-^{1})	Δ*G*°(kJ mol^{-1}) [a,b]
EG_2-dimannose	-71.3±1.4	-81.5±5.0	24.3±1.5	-47.0±2.1
EG_6-dimannose	-109.4±7.6	-209.5±24.9	62.5±4.7	-46.9±10.6
EG_{12}-dimannose	-109.2±5.7	-210.3±18.3	62.7±5.5	-46.4±7.9
EG_2-fucose	-48.2±3.8	-5.0±13.3	1.5±4.0	-46.7±5.4
EG_6-fucose	-96.1±12.5	-167.9±41.6	50.1±12.4	-46.1±17.6
EG_{12}-fucose	-138.6±0.7	-317.6±2.5	94.7±0.7	-43.9±1.0

[a] Error (δ) propagated from Δ*H*° and Δ*S*° according to $\delta\Delta G° = \sqrt{(\delta\Delta H°)^2 + (\delta T\Delta S°)^2}$
[b] at 298 K

First, taking each synthesis ratio as an individual data set, similar conclusions may be drawn as those made in a 1:1000 ratio. To simplify this, the analysis has been split into sections (1) binding affinity, (2) entropy, (3) enthalpy, and (4) quenching efficiency.

(1) For both 1:300 and 1:500 ratios, G5-EG_n-dimannose remained a stronger binder with DC-SIGN than G5-EG_n-fucose when comparing those with the same linker length, synthesis ratio and temperature. For 1:300, binding affinity decreased as linker length increased, however for 1:500 the binding affinity for EG_2- and EG_6-glycans were much closer in value despite the higher associated entropic cost for EG_6. Here it is possible that the increased entropic cost of binding EG_6-glycans is balanced out by the better spatial match due to the deflection angles and ligand flexibility (see point 3).

(2) Δ*S*° generally became increasingly more negative with increasing linker length. As one exception, Δ*S*° for G5-EG_6 and EG_{12} dimannose made in the 1:300 ratio were equivalent (-209.5 ± 24.9 and -210.3 ± 18.3 J mol^{-1}K^{-1}, respectively) however, these data are consistent with the D_h measurements. These two samples also have equivalent hydrodynamic sizes (12.1 ± 1.7 and 12.2 ± 2.8 nm, respectively) despite the differences in EG chain length. The lower valency of G5-glycans made in a 1:300 ratio gives the EG_{12} linkers enough space to fold back on itself and therefore this result can be explained by the longer EG_{12} linker having a lower starting entropy due to its folded nature and intramolecular interactions between chains limiting their conformational degrees of freedom, therefore causing them to experience a similar penalty to EG_6- upon binding. The entropic penalties observed can also be closely linked to enthalpy and the number of engaged DC-SIGN CRDs, as discussed in point 3.

(3) For $EG_6/_{12}$ linked glycans, Δ*H*° remained around 4-fold that of monovalent binding. On the other hand, the G5-EG_2-glycans showed smaller changes in Δ*H*° upon binding, equalling roughly 2 or 3-fold monovalent binding, suggesting the density of the glycans on the surface were too sparse to effectively engage all four CRDs of DC-SIGN at once. This was consistent with the cross-linked binding modes observed for G5-EG_2-dimannose (1:300) in Chapter 3. EG_2 fucose/dimannose (1:300) have the greatest deflection angles of all G5-glycans made (18.3 ± 2.8° and 17.9° ± 0.2°, respectively) which combined with the shorter reach and greater rigidity, results in them being unable to bridge all four CRDs in one DC-SIGN tetramer hence the lower Δ*H*° values of -48.2 ± 3.8 and -71.3 ± 1.4 kJ mol^{-1}, respectively. G5-EG_2-dimannose (1:300) being able to engage three CRDs while G5-EG_2-fucose (1:300) seemingly only engages two, is likely related to the larger dimannose disaccharide being able to bridge the gap where monosaccharide fucose cannot. A similar trend is observed with G5-EG_2 fucose/dimannose (1:500) where G5-EG_2-fucose seems to, on average, only engage 3 CRDs (Δ*H*° = - 85.5 ± 17.4 kJ mol^{-1}) whereas G5-EG_2-dimannose can engage all four (Δ*H*° = - 95.2 ± 3.0 kJ mol^{-1}).

For the longer linkers (EG_6, EG_{12}), Δ*H*° remained ~ -100-140 kJ mol^{-1} suggesting the longer and more flexible nature of these linkers adapts well to successfully bind all four CRDs, which was also consistent with the reduced volume of cross-linked species as linker length increased in Chapter 3. The entropy data supports this with values as low at -5.0 J mol^{-1} K^{-1} for EG_2 linkers due to the lower cost of constraining only 2 linkers per tetramer. Δ*S*° is restored to more than -150 J mol^{-1} K^{-1} when tetravalent binding is occurring for $EG_6/_{12}$ linkers.

(4) In contrast to the 1:1000 ratios, QE_{max} for the 1:500 and 1:300 ratios did not necessarily decrease as linker length increased as would be expected. For example, QE_{max} for $EG_{2,6,12}$- dimannose made in a 1:300 ratio are 70.1 ± 1.0, 67.8 ± 1.1 and 68.5 ± 0.9 % respectively, which considering the errors, are roughly the same. However, this result is consistent with their comparable D_h values, allowing them to place the fluorophores at similar distances from the G5 core upon binding.

Further conclusions can be drawn when looking to compare the thermodynamics between the three synthesis ratios. Splitting into the same subcategories as before:

(1) Changing the valency did not have a large impact on binding affinity when comparing linkers of the same length and temperature, despite the sometimes large differences in thermodynamic profiles. This highlights the importance of further investigation into the mechanisms behind binding, as the binding affinity alone would suggest little impact of changing valency. This also brings to light how binding affinity is a fine balance between glycan density and linker flexibility, affecting both the binding enthalpy and entropy changes.

(2) Δ*S*° for G5-EG_{12}-dimannose became less negative as valency decreased (-271.0 ± 7.5 vs -210.3 ± 18.3 J $mol^{-1}K^{-1}$ for 1:1000 and 1:300 respectively) indicating a reduced entropic penalty upon binding. This is likely due to the lower valency providing the longer linkers sufficient space to folding inwards creating intermolecular interactions between chains, thereby reducing their initial degrees of freedom and lowering the starting entropy. Furthermore, upon DC-SIGN binding, GNPs with lower glycan density may largely retain their flexibility due to fewer steric constraints. Even with the protein bound, the linkers may still have space to move more freely whereas those with high density, may experience large steric constraints between the bound protein and close by neighbouring PEG chains, limiting their flexibility and conformational freedom.

(3) As the synthesis ratio decreased from 1:1000 to 1:500 to 1:300, Δ*H*° values became less negative for G5-EG_2-glycans (-97.2 ± 2.5, -95.2 ± 3.0, -71.3 ± 1.4 kJ mol^{-1} respectively for dimannose and 104.7 ± 3.1, 85.8 ± 17.4 , 48.2 ± 3.8 kJ mol^{-1} respectively for fucose) showing that as valency decreased (and the inter-glycan distance increased), the lack of reach/flexibility in the short EG_2-linker was not allowing for tetravalent binding to occur, and the distance between each glycan was an imperfect match for the arrangement of DC-SIGN CRDs. This effect on binding affinity was likely balanced out by a reduction in entropic penalty. Values of Δ*H*° for the EG_6/EG_{12} length linkers at each ratio remained remarkably consistent across the synthesis ratios (e.g. for G5-EG_{12}-fucose: -137.2 ± 1.1, -124.9 ± 14.8, -138.6 ± 0.7 kJ mol^{-1} for 1:1000, 1:500 and 1:300 respectively or for G5-EG_6-dimannose: -109.3 ± 12.4, -112.1 ± 2.3 and -109 ± 5.7 kJ mol^{-1}, respectively) highlighting the important role of flexible ligands in bridging CRDs at lower glycan densities.

Overall G5-glycans made in a 1:1000 and 1:500 ratio show the greatest consistency between apparent binding affinity, maximum enthalpy enhancement and minimum entropic cost, indicating that a valency of above ~350 on a G5 provides an optimal combination of spatial topology, linker entropy and local concentration for statistical rebinding to generate strong binding to four DC-SIGN CRDs. Although G5-EG_2-fucose (1:500) may not bind 4 CRDs this is more consistent than G5-EG_6-fucose (1:1000) which based off conclusions drawn from 1:500 and 1:300 ratios does not fit the profile for trivalent binding and therefore appears to be an outlier.

4.2.3 Measuring thermodynamics via isothermal titration calorimetry

Comparing binding Δ*H*° values for G5-EG_n-glycans to those measured by ITC for monovalent CRD binding generally showed a good consistency, with Δ*H*° matching 2-, 3- or 4-fold monovalent binding enthalpy change. However this does appear to be somewhat dependent on linker length with EG_{12} linkers consistently showing greater than 4-fold monovalent binding enthalpy change, suggesting G5-EG_{12}-glycans partake in

enthalpically enhanced binding (where the binding of one glycan to its lectin binding site makes the binding of subsequent glycans more favourable). To validate the NSET method and for further confirmation that the flexible linkers provided a more favourable enthalpy enhancement, the enthalpy for the same samples were measured by ITC.

ITC measurements were performed by titrating high concentration DC-SIGN (30 μM) into G5-glycans (300-700 nM) in the ITC cell to measure the binding induced heat changes. The ITC titration curves and resulting fittings are shown in Figure 4.10 and Figure 4.11 and the binding enthalpy changes and dissociation constants are given in Table 4.8 and Table 4.9.

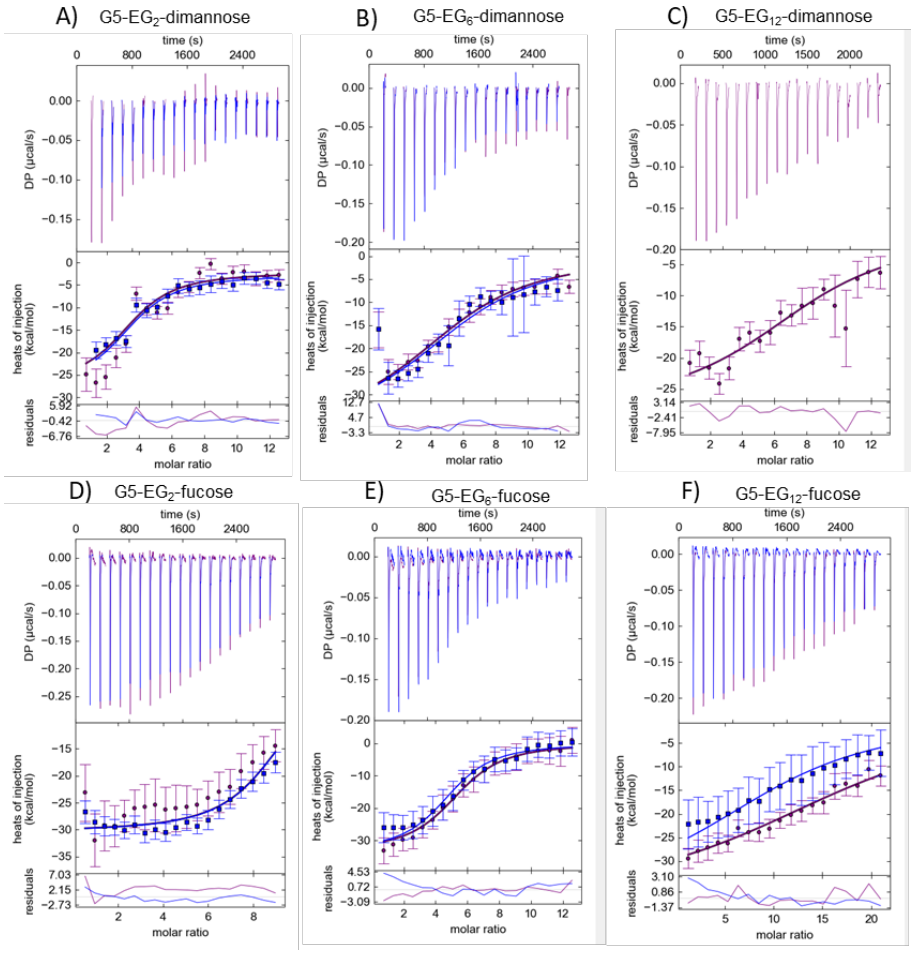

Figure 4.10 ITC thermograms and their respective fitting curves for wild type DC-SIGN with G5-glycans made in a 1:1000 G5:ligand ratio A) G5-EG_2-dimannose, B) G5-EG_6-dimannose, C) G5-EG_{12}-dimannose, D) G5-EG_2-fucose, E) G5-EG_6-fucose, F) G5-EG_{12}-fucose. Error bars represent uncertainties in the integrated heats.

Table 4.8 Summary of the standard binding enthalpy (T = 298 K) and apparent binding affinity between G5-EGn-glycans (1:1000) and DC-SIGN obtained by ITC. Errors represent the SDs as observed by the fitting. * Data represents only one sample.

Sample	$\Delta H°$(kJ mol^{-1})	K_d (μM)
G5-EG_2-dimannose	-104 ± 25	0.33 ± 0.27
G5-EG_6-dimannose	-154 ± 25	0.89 ± 0.44
G5-EG_{12}-dimannose*	-115 ± 56	0.87 ± 0.51
G5-EG_2-fucose	-127 ± 27	0.12 ± 0.12
G5-EG_6-fucose	-139 ± 25	0.22 ± 0.21
G5-EG_{12}-fucose	-154 ± 50	1.54 ± 1.16

Several of the titrations presented above are incomplete and do not exhibit full sigmoidal isotherms. As a result, the calculated enthalpy changes and apparent binding affinities are best estimates made from the available data. Despite this, generally, the enthalpy values collected by ITC were found to be consistent with those measured by fluorescence quenching, indicating that the quenching method is a reliable way to measure thermodynamic contributions in MLGIs. Discrepancies were observed between the enthalpy of binding for G5-EG_6-fucose (1:1000) where the value measured by quenching was -77.4 kJ mol^{-1} compared to -139.3 kJ mol^{-1} by ITC. Since -77.4 kJ mol^{-1} corresponds to 3-fold monovalent binding, and no other sample in this data set was observed to experience trivalent binding, the cause of this lower enthalpy value by NSET is likely to be an experimental error, or batch to batch variability. Further repeats would be needed to confirm such.

As well as showing good consistency between the number of DC-SIGN CRDs bound to each G5 glycan, the $\Delta H°$ values measured by ITC generally trend towards becoming increasingly more negative as linker length increases, matching this observation made in the NSET quenching experiment. This is further confirmation that the quenching experiment is a reliable method for measuring solution-based thermodynamic contributions to binding, and that flexible linkers induce enthalpically enhanced binding.

While the general trend in $\Delta H°$ values tends to agree with the NSET results, the quality of the ITC data and the large errors do limit the certainly with which interpretations and conclusions that can be drawn. Some of these limitations have arisen due to the curves not exhibiting sigmoidal shapes, especially those for the G5-EG_{12}-dimannose and G5-EG_2-fucose binding. When the ITC titration curve fittings are not fully sigmoidal, they cannot be used to accurately extract enthalpy values and the quoted values are instead approximations based on the available data. Since the ITC thermograms for binding between G5-EG_{12}-dimannose and DC-SIGN did not plateau within the concentration range used (Figure 4.10C) the G5-concentration was decreased from 500 nM to 300 nM,

albeit for G5-EG_{12}-fucose, to promote saturation of the G5-glycans with DC-SIGN and to facilitate a plateau in the thermogram. However under these new conditions, the curves still not exhibit strong sigmoidal shape (Figure 4.10F). To get into a high-c regime and generate sigmoidal thermograms, the ideal solution would be to increase the concentration of both the species in the cell and the syringe.(139) Unfortunately, the DC-SIGN concentration used for this experiment was already very high (30 μM tetramer) and increasing this further could cause protein aggregation, introducing unwanted or unpredictable effects in the ITC results.

On the other hand, G5-EG_2-dimannose (1:1000) binding quickly reached plateau (Figure 4.10A) therefore when measuring fucose binding, concentration of G5-EG_2-fuose (1:1000) in the cell was increased to 700 nM. This unfortunately had the opposite effect, and binding was unable to reach a plateau after many injections. Again therefore, the enthalpy value quoted by this fit may not be a true representation of the actual binding enthalpy. It is also noteworthy to mention that the errors observed in the ITC fitting are large (>1/4 of the mean value) and many of the enthalpy values are statistically indistinguishable from each other despite different average values. Large errors here mean the goodness of the fit does not change much as the parameters are varied.

A striking difference between the quenching and ITC data is the apparent binding affinities. It should be noted that while ITC can provide accurate measurements of the binding ΔH^{o} values, the binding between NSET and ITC is observed on very different time scales. When measured by NSET, the system has reached equilibrium (e.g. 20 minute incubation time) whereas in ITC the measurement occurs on the second timescale. Therefore the ITC signal reflects the initial binding events and does not consider any subsequent conformational rearrangement to achieve optimal binding which can have an impact on the measured apparent binding affinity. These rearrangements are associated with negligible additions to the enthalpy change, as most of the enthalpy comes from the initial placement of the sugar within the protein binding site, and therefore are not considered in these measurements. Therefore while ITC can offer complimentary information on binding affinity, it cannot be used to directly compare values derived from an assay where a system has reached equilibrium.

ITC was also performed on glycans prepared in a 1:500 G5:ligand ratio. While performing the titrations on G5-EGn-fucose (1:500) samples, a large drift in the thermogram baseline was observed making the measurement of the heat of injection more complex. Causes of baseline drift in ITC are usually buffer mismatches or sample aggregation, however, G5-glycans were washed thoroughly with the protein dialysis buffer and post-experiment analysis revealed a close match in buffer pH. Fida analysis, which looks at size, shape and aggregation of macromolecules, revealed the DC-SIGN sample to be 95% homologous with low levels of aggregation. Hydrodynamic size analysis of the resulting mixed G5-DC-SIGN samples by DLS showed some signs of cross-linking or aggregation

indicated by the presence of species between 100-1000 nm in size, however, the predominant species remained ~40-45 nm indicating mostly monolayer binding (Figure A. 24) and therefore the cause of baseline drift, in this instance, is still unknown. Despite the baseline drift (especially observed in Figure 4.11C), one data set for each G5-EG_n-fucose sample were fitted as described before. The ITC titration curves for G5-EG_n-fucose (1:500) and G5-EGn-dimannose (1:500) are shown in Figure 4.11 and summarised in Table 4.9.

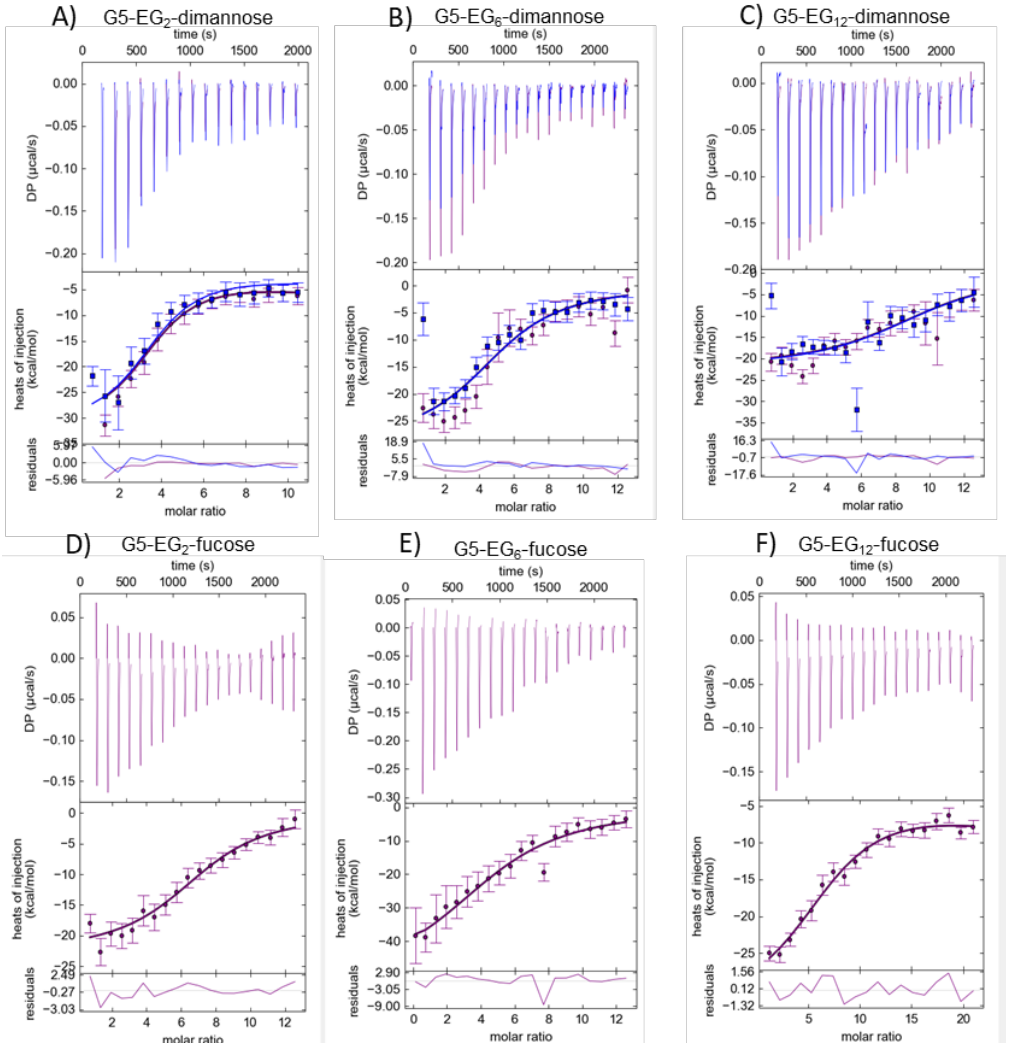

Figure 4.11 ITC thermograms and their respective fitting curves for wild type DC-SIGN with G5-glycans made in a 1:500 G5:ligand ratio A) G5-EG_2-dimannose, B) G5-EG_6-dimannose, C) G5-EG_{12}-dimannose, D) G5-EG_2-fucose, E) G5-EG_6-fucose, F) G5-EG_{12}-fucose. Error bars represent uncertainties in the integrated heat.

Table 4.9 Summary of the standard binding enthalpy (T = 298 K) and apparent binding affinity between G5-EGn-glycans (1:500) and DC-SIGN obtained by ITC. Errors represent the SDs as observed by the fitting. * Data represents only one sample.

Sample	$\Delta H°$(kJ mol^{-1})	K_d (μM)
G5-EG_2-dimannose	-117 ±13	0.18 ± 0.12
G5-EG_6-dimannose	-120 ± 20	0.47 ± 0.33
G5-EG_{12}-dimannose	-92 ± 25	0.45 ± 0.39
G5-EG_2-fucose*	-95 ± 10	0.36 ± 0.28
G5-EG_6-fucose*	-155 ± 20	0.21 ± 0.10
G5-EG_{12}-fucose*	-142 ± 21	0.63 ± 0.30

The enthalpy values measured by ITC and the quenching show a good comparability. Notably, the enthalpy change of binding for G5-EG_2-fucose (1:500) is -94.5 ± 10.0 kJ mol^{-1}, which is lower than the EG_6- and EG_{12} -linked fucose (-155 ± 19.5 kJ mol^{-1} and 142.1 ± 20.9 kJ mol^{-1} respectively). This corresponds well to the quenching experiment where it was observed that G5-EG_2-fucose (1:500) had a lower enthalpy change of binding of around -85 ± 17 kJ mol^{-1}, more likely indicating trivalent binding than tetravalent. As discussed in Section 4.2.2, this is likely due to the low valency and short rigid linkers creating a poor spatial match for tetrameric DC-SIGN binding sites. Although the fitting of the ITC thermogram for G5-EG_{12}-dimannose shows an apparent enthalpy change of ~ -92 ± 24.5 kJ mol^{-1}, the binding under these conditions does not reach saturation in the given concentration range and therefore does not give rise to a sigmoidal curve. From this shallow curve, $\Delta H°$ is likely underestimated.

Overall, despite some large uncertainties in the fitting measurements, the enthalpy measured by ITC is a good match to that measured by the fluorescence quenching experiment in Section 4.2.1.1, thus confirming that this GNP-quenching technique is a valid, sensitive method for investigating the binding thermodynamics of MLGIs. Furthermore comparing these values to those measured with monomeric DC-SIGN CRD and monovalent ligand, it can be accurately determined how many DC-SIGN CRDs in the tetramer are engaged in binding upon mixing with a G5-glycan sample. This has led to a greater understanding of what aspects of glycoconjugate design give rise to strong tetravalent binding to DC-SIGN in solution.

Although ITC is a well-established technique which has been used to validate the quenching experiment, in this instance the fluorescence quenching was more reliable in terms of producing consistent and repeatable measurements. This technique was also quicker and easier to carry out, requiring a smaller sample size and lower concentrations. It can provide accurate apparent binding affinity after equilibrium had been reached, taking into account reorganisation and if necessary (under a non 1:1 PGR) can also

provide information on binding cooperativity. It does, however, require a fluorescently labelled protein, and is an indirect measurement of Δ*H*°, which uses the van 't Hoff equation and therefore requires measurements at multiple temperatures. The strong inner filter effects of GNPs interferes with QE measurements at very high concentrations (>100 nM) and thus this technique is more suited to strong binding (sub μM K_d). On the other hand, ITC is a validated, label-free technique (e.g. does not require a fluorescently labelled protein). It also provides a direct measurement of Δ*H*° using only one measurement temperature. However, ITC it requires much higher concentrations (30 μM DC-SIGN compared to 100 nM in quenching) due to its relatively low sensitivity compared to the fluorescence quenching measurements. This pushes the DC-SIGN and GNP samples towards their concentration limits, which may be impacting the quality of the data extracted from these experiments. To maintain low heat of dilution background signal, ITC also requires perfect buffer exchange meaning sample preparation time can be increased compared to the fluorescence quenching assay. Overall, due to the higher quality fittings observed in the quenching experiment, the lower protein concentration and the inclusion of factors such as cross-linking and cooperativity, in this instance, the quenching experiment has been more valuable method for measuring the binding affinity and thermodynamics of G5-glycans interacting with DC-SIGN.

4.2.4 Measuring antiviral properties with a viral inhibition cell assay

With the intention to understand the binding of membrane proteins with their respective glycans in a natural environment, or on a cellular level, MLGIs must also be investigated via surface based methods. This enables the correlation between solution based and surfaced based methods, to be able to more accurately predict binding behaviour *in vivo*. In order to explore the binding of G5-glycans on cell surfaces, a cellular viral inhibition assay was conducted.

The strong binding affinities of these dimannose and fucose coated-G5s with the viral receptor DC-SIGN suggests that they may effectively block DC-SIGN mediated viral entry into cells. DC-SIGNR is a closely related tetrameric lectin to DC-SIGN, sharing 77% amino acid homology, with the greatest areas of sequence sharing being within the CRD domain and the neck region.(192) Despite their close homology, DC-SIGN is found mainly on dendritic cells whereas DC-SIGNR is expressed on endothelial cells, and using QD/G5-glycans it has been shown that the spatial orientation of their CRDs differ. DLS measurements accompanied by TEM imaging of binding induced lectin-nanoparticle assemblies showed that DC-SIGN binding to QD/G5-glycans afforded a monolayer of DC-SIGN molecules bound to each QD/G5-glycan surface, but contrastingly when DC-SIGNR was used, large aggregates were formed, due to many cross-linking interactions. These results have provided evidence that the CRDs in each DC-SIGN molecule are all oriented upwardly providing a good binding platform for one QD or GNP, whereas the

CRDs in DC-SIGN are oriented away from each other, facing outwards and forming a platform for cross-linking interactions. The difference in the orientation of the CRDs provides an explanation for their ability to augment different viral infections. DC-SIGN is known to be more effective in augmenting the infectivity of some HIV strains than DC-SIGNR while only DC-SIGNR, but not DC-SIGN, can effectively promote West Nile virus infection.(193-195)

The following viral inhibition assays were prepared and performed by Inga Nehlmeier, Amy Madeleine Kempf, and Professor Dr Stefan Pöhlmann (German Primate Center, Göttingen, and Faculty of Biology and Psychology, Georg-August-University Göttingen). To investigate whether G5-glycans can effectively block DC-SIGN/R mediated viral entry into cells, human embryonic kidneys 293T cells were transfected with either DC-SIGN or DC- SIGNR on their surface. Vesicular stomatitis virus (VSV) vector particles encoding the luciferase gene and bearing the Ebola virus surface glycoprotein (EBOV-GP) were then used to model Ebola virus entry into transfected cells. EBOV-GP is heavily mannosylated and can use DC-SIGN/R to attach and gain entry to the cell, therefore using the EBOV-GP here ensures vector entry into cells will be enhanced by DC-SIGN/R transfection (Figure 4.12A). If the VSV/EBOV-GP particles encoding the luciferase gain entry into the cells, then expression of the luciferase protein is induced. Cells can then be lysed and a luciferase substrate (Beetle-Juice, PJK) is added. Oxidation of Beetle-Juice by luciferase results in light emission, dependent on the quantity of luciferase present and is therefore a good method to measure viral entry (Figure 4.12B).

To test the validity of the assay, VSV/EBOV-GP particles were added to mock cells (unmodified 293T) or 293T cells transfected with either DC-SIGN or DC-SIGNR. As expected, those transfected with DC-SIGN/R showed a 10+ fold increase in luminescence activity compared to the mock cells, indicating VSV/EBOV-GP entry into cells is enhanced by DC-SIGN/R transfection. Mock cells still showed an increase in luminescence compared to when no VSV/EBOV-GP particles were present, indicating the entry of VSV/EBOV-GP is enhanced by DC-SIGN/R but is not completely specific to these receptors and can gain entry through other means. Entry of VSV/VSV-G particles (which use the VSV-glycoprotein (VSV-G) to enter the cell through the low-density lipoprotein receptor (LDL-R)) remained unaffected by transfection confirming entry of VSV/VSV-G is independent of DC-SIGN/R (Figure 4.13).

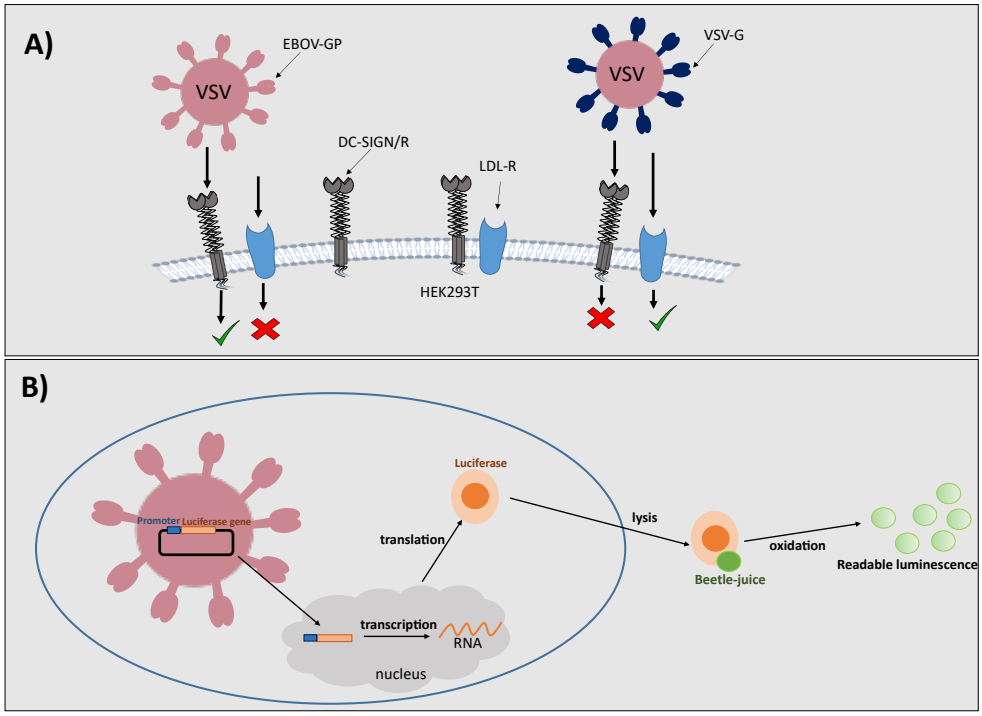

Figure 4.12 Schematic depicting the different methods of VSV/EBOV-GP or VSV/VSV-G infection in cells expressing DC-SIGN/R and the consequent luciferase activity where A) shows that VSV/EBOV-GP entry is enhanced by DC-SIGN/R transfection on the cell surface whereas VSV/VSV-G entry is independent of the presence of DC-SGN/R on the cell surface and is instead dependent on the receptor LDL-R, broadly expressed on many cell types without modification and B) shows the process of luciferase expression and consequent oxidation leading to a luminescence activity which is used for inhibition quantification.

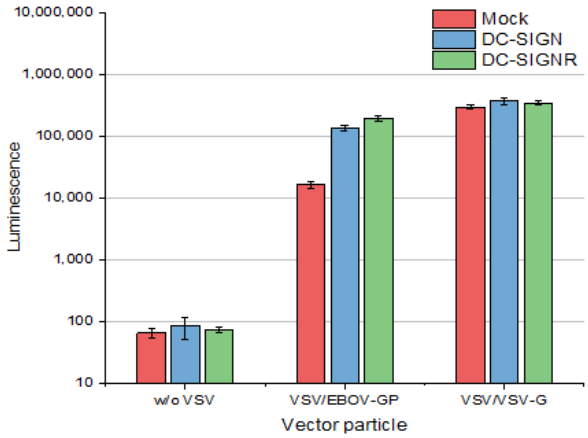

Figure 4.13 In the absence of inhibitors and after transfection with DC-SIGN (blue) or DCSIGNR (green) uptake of VSV/EBOV-GP is increased 10-fold, reflected in the luciferase activity/luminescence, compared to mock un-transfected cells (red). Entry of VSV/VSV-G remains high showing uptake is independent of transfection. When no VSV particle (containing the luciferase gene) is present, luminescence is very low, confirming luminescence is dependent on the uptake of VSV vector particles.

Since entry of VSV/EBOV-GP is enhanced by DC-SIGN/R, binding of high affinity G5-glycans should effectively block viral entry thereby reducing luciferase gene transduction and protein expression. G5-glycans prepared in a 1:500 particle to ligand ratio were used in this study as they exhibited the strongest binding affinities and most consistent binding parameters to DC-SIGN between the fluorescence quenching assay and ITC. The raw inhibition data is presented in Figure A. 25-26, and the normalised concentration-dependent inhibition data were well fitted by Equation 4.6; where NA is the luciferase activity normalised to the corresponding control collected in the absence of the G5-glycan, IC_{50} is the concentration giving 50% inhibition, C is the log of G5-glycan concentration, and p is the hill slope which indicates how sensitive the response is to the change in concentration of the inhibitor.(196, 197) A p value close to (-)1 indicates a high sensitivity to concentration changes, whereas a value of (-)0.5 indicates a lower sensitivity.

$$NA = \frac{1}{1 + 10^{(logIC50 - c)p}} \qquad \textbf{Equation 4.6}$$

While the IC_{50} value is important in determining the efficacy of viral inhibition, the Hill slope p is also of importance. For example, if two inhibitors exhibited the same IC_{50} but had p values of (-)0.5 or (-)1, using the Hill Equation 4.7 where I is the fraction of inhibition (e.g. 99%), [C] is the G5-glycan concentration and IC_{50} is the concentration for 50% inhibition and p is the hill slope, then the [C] required for 99% inhibition will be 9801- or 99- times the IC_{50} value, respectively. Therefore, an inhibitor with p = 0.5 would be much less effective than that with p = 1 requiring ~100- fold higher concentrations to achieve the same 99% inhibition despite having the same IC_{50} value.

$$I = \frac{[C]^p}{IC50^p + [C]^p} \qquad \textbf{Equation 4.7}$$

Indeed, pre-treatment of 293T cells with G5-glycans greatly reduced the luciferase gene transduction in DC-SIGN-positive cells, with IC_{50}s in the low nanomolar range, indicating high inhibition potency (Figure 4.14). Importantly, compared to VSV/EBOV-GP, luciferase activities of control virus particles bearing VSV-G, which do not use DC-SIGN/R to enhance cell entry, were not greatly affected by G5-glycan treatment, confirming a degree of selectivity of the observed inhibitory effects (Figure 4.14A/B). The small but observable reduction in luciferase activity when using VSV/VSV-G at high G5 concentration may suggest the presence of a non-specific inhibitory pathway by these G5 particles. The IC_{50} data for each G5-glycan is summarised in Table 4.10.

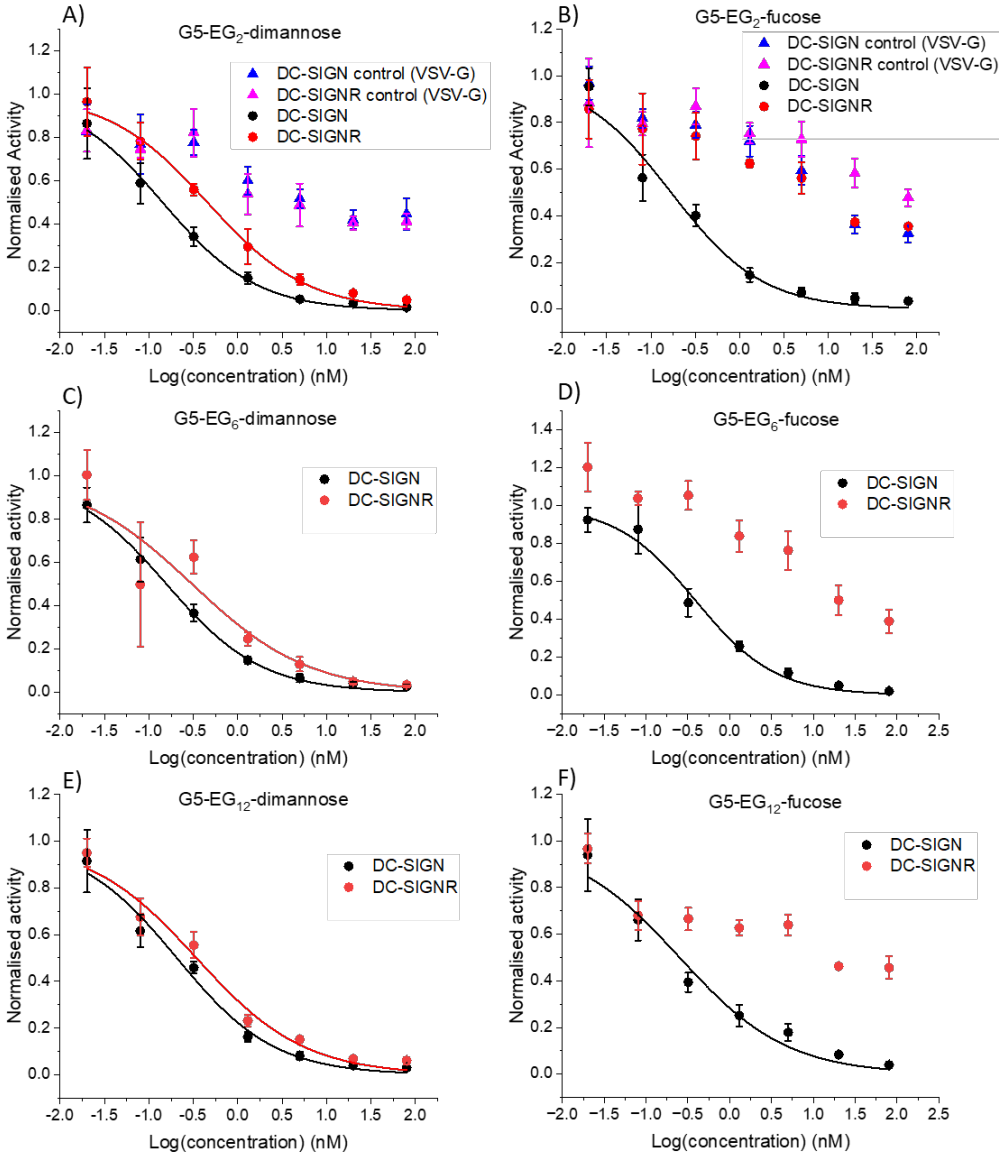

Figure 4.14 Plot of normalised luciferase activities of DC-SIGN- or DC-SIGNR-expressing 293T cells as a function of the concentration of A) G5-EG_2-dimannose B) G5-EG_2-fucose C) G5-EG_6-dimannose D) G5-EG_6-fucose E) G5-EG_{12}-dimannose F) G5-EG_{12}-fucose inhibitors. Data for virus particles bearing the EBOV-GP are shown in dots (grey for DC-SIGN, red for DC-SIGNR) while those of control virus particles bearing VSV-G are shown in triangles (blue for DC-SIGN, purple for DC-SIGNR). Graphs were fitted by Equation 4.6 and error bars represent the SDs of duplicate experiments at each concentration.

Table 4.10 Summary of the inhibition data for G5-glycans against DC-SIGN/R mediated EBOV-GP driven infection of 293T cells. Errors represent the SDs as observed by the fitting.

Glycan	IC_{50} (nM)	P	R^2	IC_{50} (nM)	P	R^2
	DC-SIGN			DC-SIGNR		
EG_2-dimannose	0.14±0.008	0.82±0.04	0.940	0.46±0.04	0.77±0.05	0.985
EG_6-dimannose	0.16±0.009	0.81±0.04	0.973	0.31±0.13	0.66±0.17	0.959
EG_{12}-dimannose	0.21±0.03	0.79±0.08	0.974	0.34±0.06	0.72±0.08	0.967
EG_2-fucose	0.17±0.03	0.84±0.13	0.957	-	-	
EG_6-fucose	0.39±0.05	0.92±0.09	0.994	-	-	
EG_{12}-fucose	0.25±0.05	0.67±0.09	0.982	-	-	

While G5-EG_n-dimannose were able to effectively block both DC-SIGN and DC-SIGNR mediated cell entry, the IC_{50}s for inhibition via DC-SIGNR were weaker. These results are consistent with previous observations in this group that G5-glycans bind more weakly to DC-SIGNR than to DC-SIGN.(115, 119) The difference in inhibition potency by G5-dimannose for DC-SIGN vs DC-SIGNR can be explained by the different positioning of their four CRDs. Each G5-dimmanose could simultaneously bind to all four of DC-SIGN's upwardly facing CRDs, completely blocking them from being able to interact with viral surface EBOV-GPs, thereby preventing cell entry. In contrast, binding between G5-dimannose and DC-SIGNRs outwardly positioned CRDs only allows each G5-dimannose to bind divalently via two outward facing binding sites (Figure 4.15A). This bridging mode of binding consequently makes it difficult to block all cell surface DC-SIGNRs, since even if all DC-SIGNR are cross-linked, those at cluster edges could still serve as a platform for VSV/EBOV-GP binding, thereby still facilitating some cell uptake and infection. Consequently, an inhibitor partaking in inter cross-linking is less effective in blocking virus infection compared to one that binds simultaneously, making complete inhibition almost impossible.

DC-SIGN mediated inhibition with G5-EG_n-dimannose showed a dependency on linker length, with IC_{50} increasing as ethylene glycol units increased. This correlates well to the NSET results where EG_2- and EG_6- dimannose exhibited similar binding affinities but EG_{12}-dimannose showed a notably weaker binding affinity. Alongside this, as linker length increased the absolute value of the Hill slope decreased, indicating poorer IC_{99} (e.g. a markedly higher concentration would be required for 99% inhibition for the longer EG_{12} linkers) (Table 4.11).

Table 4.11 Summary of the predicted IC_{99} G5-glycans against DC-SIGN/R mediated EBOV-GP driven infection of 293T cells calculated from Equation 4.7 using the values expressed in Table 4.10. Errors are propagated from the fitting errors obtained in Figure 4.14

Glycan	IC_{99} DC-SIGN (nM) [a]	IC_{99} DC-SIGNR (nM) [a]
EG_2-dimannose	38 ± 11	180 ± 71
EG_6-dimannose	47 ± 13	327 ± 603
EG_{12}-dimannose	71 ± 43	201 ± 147
EG_2-fucose	40 ± 35	-
EG_6-fucose	58 ± 29	-
EG_{12}-fucose	238 ± 224	-

[a]errors propagated from IC50, p, δIC50 and δp.

In contrast, the observed results for DC-SIGNR inhibition showed that longer EG_6 and EG_{12} linkers have stronger average potencies (lower IC_{50}) of 0.31 ± 0.13 and 0.34 ± 0.06 nM, respectively compared to the shorter EG_2 linker with an IC_{50} of 0.46 ± 0.04 nM. While it is noted that the differences here are rather small considering the errors, the difference in the average values may be explained by the longer linkers being able to simultaneously bind 4 outwardly facing DC-SIGNR CRDs, where EG_2-linkers cannot. This agrees with the data in section 4.2.2, where it was observed that, especially at low glycan valency, the longer linkers were more effective in bridging four CRDs due to their greater reach and flexibility. Alternatively G5-$EG_{6/12}$-dimannose may have a large enough diameter to be able to cross-link two DC-SIGNR cell surface receptors and block transfection more efficiently this way than shorter linkers (Figure 4.15B).

When looking at the calculated concentrations required for 99% inhibition in DC-SIGNR transfected cells, the dependency on linker length was reversed and a lower concentration of G5-EG_2-dimannose would be required than of G5-EG_6-dimannose or G5-EG_{12}-dimannose. This is likely because at low (<1 nM) concentrations, the linker length is important as the low ratio of G5:DC-SIGNR requires cross-linking to achieve efficient inhibition (e.g. three G5 bridging five DC-SIGNR), whereas at higher concentrations, there is a great enough excess of G5 that linker length becomes redundant and two G5s with shorter linkers may bind one DC-SIGNR, therefore binding affinity becomes the more important factor (Figure 4.15C).

While all G5-fucose glycans strongly inhibited viral entry through DC-SIGN, unexpectedly the IC_{50} for EG_6-fucose was somewhat weaker than EG_{12}-fucose (0.39 vs 0.25 nM respectively) caused by the lack of inhibition at the two lowest concentrations for G5-EG_6-fucose (Figure 4.14D). Despite this, taking into account the Hill slope, the

concentrations required to observe a 99% inhibition were calculated to follow a linear pattern with increasing linker length (IC_{99} = 40, 58 and 238 nM for EG_2-, EG_6-, and EG_{12}-fucose, respectively (Table 4.11)), further highlighting the importance of considering both the IC_{50} and the Hill slope p. Fucose coated glycans showed an inability to inhibit DC-SIGNR mediated transduction. This result was expected as studies have revealed DC-SIGNR is unable to bind fucose containing ligands.(80)

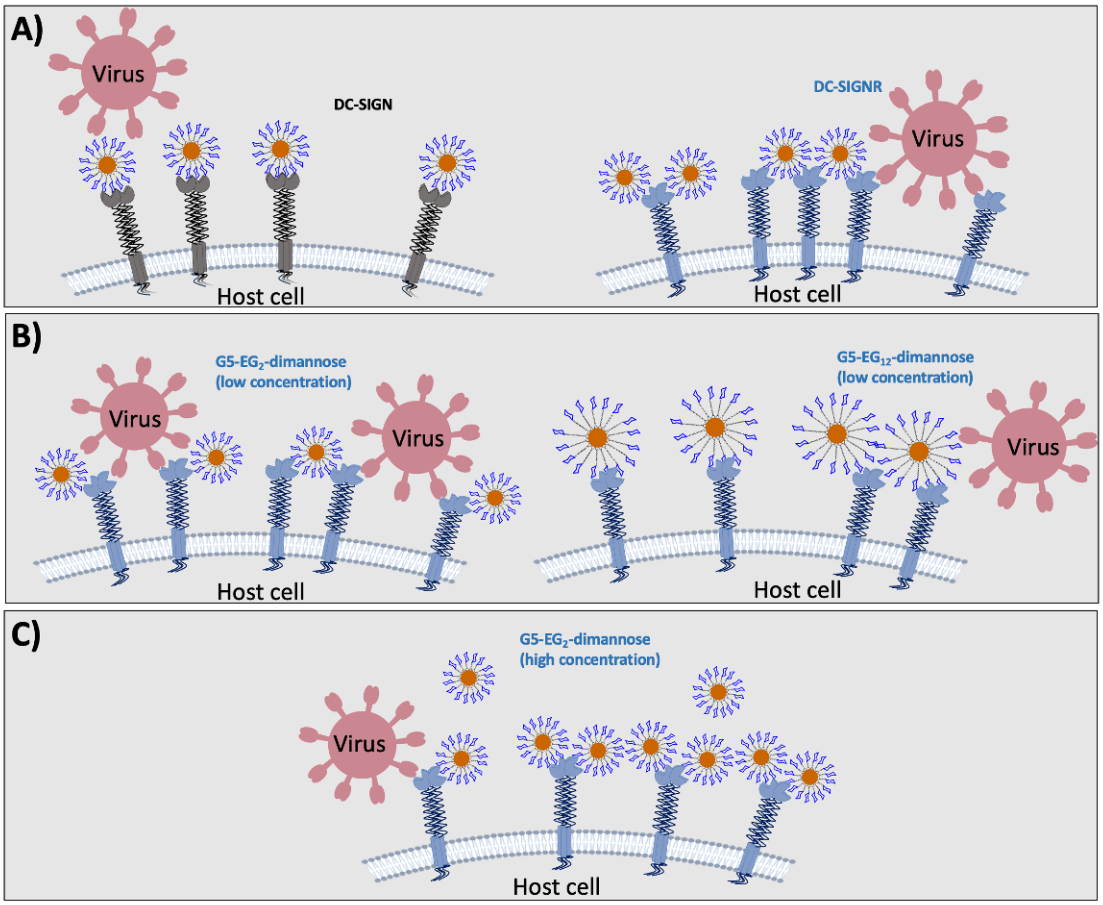

Figure 4.15 Schematic showing the different binding modes for G5-glycans with DC-SIGN/R leading to variations in inhibition ability. A) Depicts how for DC-SIGN expressing host cells, G5-glycans can bind simultaneously to all four CRDs, blocking EBOV-GP binding and therefore stopping viral infection. However for DC-SIGNR expressing cells, G5-glycans either cross-link with other surface DC-SIGNRs or only bind 2 CRDs, allowing the virus access to unblocked DC-SIGNR binding sites thereby initiating infection. B) Illustrates how at low concentrations, G5-glycans with a longer linker length of EG_{12} may be more effective at blocking DC-SIGNR mediated infection as they can either bind 4 outwardly facing CRDs simultaneously, or cross-link multiple DC-SIGNR molecules therefore blocking more sites, whereas shorter linkers do not have the reach to bind 4 outwardly facing CRDs simultaneously, or cross-link, and therefore are less effective at inhibiting viral infection. However, C) shows that at high concentrations, two G5-EG_2-glycans can bind one DC-SIGNR and therefore are more effective at blocking infection than EG_{12}-glycans since they exhibit stronger binding affinities.

Overall, the excellent ability of these G5-glycans, especially so for the G5-EG_2-linked glycans, in blocking DC-SIGN mediated augmentation of EBOV-GP-dependent entry is a highly promising result. The low nM IC_{50} values (0.14 ± 0.008 and 0.17± 0.03 nM for G5-EG_2-dimannose and fucose, respectively) are comparable/of the same order of magnitude than those measured for some of the most potent glycoconjugate inhibitors of Ebola virus infections reported previously, including our groups' previous QD-EG_3-dimannose (IC_{50}: 0.70 ± 0.2 nM).(119, 186, 198, 199) This is important since glycoconjugate viral inhibitors offer two key advantages over other antiviral approaches. Firstly they can help prevent viral mutations by blocking the virus from entering host cells, and secondly their effectiveness is less likely to be diminished by viral mutations, since viral glycans are mainly conserved. Therefore the outstanding potency of the G5-glycans in blocking DC-SIGN-mediated EBOV-GP driven infection of host cells can potentially provide a long-lasting therapeutic solution to numerous viral infections which exploit DC-SIGN for host cell entry.

4.3 Conclusions

In summary, this chapter has demonstrated the capability of these polyvalent G5-glycan's for probing multivalent lectin-glycan interactions. Firstly, by exploiting the fluorescence quenching properties of GNPs and using a ratiometric NSET method, the apparent binding affinities of G5-glycans with the dendritic cell receptor DC-SIGN were revealed to be greatly enhanced over that of monomeric mannose and fucose. Furthermore this method allowed for the dissection of the thermodynamic contributions of G5-glycans to the affinity enhancement mechanisms in MLGIs. These data revealed that increasing the EG_n linker length which connects the glycan to the gold nanoparticle surface has a negative impact on binding affinity. This negative impact on binding affinity was found to be to be driven largely by the increased entropic penalty incurred upon constraining long flexible linkers. Furthermore, while decreasing the surface glycan valency did not have a large impact on overall binding strength, the thermodynamic contributions showed variations, helping to elucidate that at lower surface valency, the two binding partners are ineffectively spatially matched making it difficult to form tetravalent 1:1 binding, especially so for the shortest, relatively rigid linkers. Despite this, binding of only two/three CRDs was counteracted by the reduced entropic penalty of only constraining two linkers and thus the binding affinity was largely unaffected. Without probing the thermodynamics, these binding modes would be concealed behind the consistently low nM binding affinities at each valency. Comparing the NSET results to those collected by conventional biophysical techniques such as ITC has verified this ratiometric GNP-NSET readout to be a reliable method for probing the thermodynamic contributions between G5-glycan-DC-SIGN based MLGIs.

Although this NSET-based approach offers an excellent platform for analysing the solution-phase MLGIs and their associated thermodynamic properties, the complexities MLGIs might experience in their native surface-phase environments are unaccounted for. Therefore in order to determine whether measuring solution K_d is a reliable method for predicting how receptors behave on the cell surface, an *in cellulo* viral inhibition assay was performed to extract their antiviral properties. During this experiment, G5-glycans were revealed to be potent inhibitors against DC-SIGN/R mediated EBOV-GP infection and uptake by human cells. Previously, discrepancies in trends between solution and surface-phase assays have been observed. For example, of two samples, the one that exhibited a stronger binding affinity (lower K_d) did not equate to being the stronger inhibitor, and had a higher IC_{50} (weaker inhibitor) than the weaker binder, which could have been due to the very high glycan density leading to rigid structures unable to adapt to the binding surface of these lectins on surfaces where there exist constraints that do not exist in solution. Thus, some obvious differences between solution phase and cell surface-phase binding are sometimes found to occur. In this example the study was comparing surface glycan density (monomer vs trimer) whereas the focus of this chapter was an investigation of the effects of the linker length, while keeping the glycan density constant across the different G5 samples, and there were notably fewer discrepancies between K_d and IC_{50} than previously observed. It is likely that the lower density used here (~350 glycans per G5) allowed the glycans to adapt well to the binding platforms of these lectins in both solution and on surfaces, allowing for the dissection of the contribution of linker length without interference from steric factors.

The IC_{50} values for DC-SIGN mediated inhibition largely follow a trend, that increasing linker length decreased inhibition potency, especially when taking into account hill slope, which describes the efficiency of the inhibitor and can be used to calculate the concentration required to achieve higher levels of inhibition. Here, the cell-based inhibition data was a close match for K_d. While IC_{50} and K_d cannot be compared directly as they do not describe the same thing, a positive correlation was observed where a lower K_d equalled a lower IC_{50}, and their relative values when comparing shorts linkers (EG_2, EG_6) with the longer linkers show the same fold differences. For example $EG_{2/6}$-dimannose have a 1.4-2-fold stronger binding affinity (lower K_d) than EG_{12}-dimannose at 22°C and the IC_{50} of $EG_{2/6}$-dimannose is again 1.5-fold lower (stronger inhibitor) than EG_{12}-dimannose. Furthermore G5-EG_n-dimannoses were observed to be both stronger binders and better inhibitors than G5-EG_n-fucoses. While cell based assays account for more complexities than solution based assays, they do not provide the high level of molecular detail involved in MLGIs, such as binding mode, binding affinity or thermodynamics therefore performing these assays in tandem and comparing the outputs provides a more comprehensive understanding of their broader mechanisms.

Overall, the close alignment between the apparent K_d and IC_{50} values confirm that the NSET-based K_d determination is a reliable and efficient method for rapidly assessing the viral inhibition potency of G5-glycans at the cellular level. These findings are important for informing the development of multivalent therapeutics targeting specific MLGIs, particularly those with uncharacterised structures. It is suggested that future directions for this chapter would focus studying lower valency G5-glycans in the viral inhibition assay. While synthesising G5-glycans in a 1:300 G5:ligand ratio did not largely impact the binding strength when compared to their higher ratio counterparts, the thermodynamic parameters such as enthalpy and entropy were indeed affected with the implication that some samples bind only two of the four DC-SIGN CRDs. With this in mind, it would be interesting to observe whether reduced CRDs binding capabilities has implications *in cellulo* on inhibition potency.

Part B

Using glyconanoparticles to investigate DC-SIGN driven IL-23 production relevant to the seronegative spondyloarthropathies, and to identify additional contributing receptors

Chapter 5 – Introduction

Several human diseases including psoriasis, psoriatic arthritis, Crohn's disease and ulcerative colitis, are associated with single nucleotide polymorphisms in the IL-23 receptor pathway. These conditions have robust experimental models confirming IL-23/IL-17 axis dependency and importantly, they respond to anti IL-23 directed therapy. On the other hand, ankylosing spondylitis, which shares the same immunogenetics, enigmatically shows little to no clinical benefit from IL-23 antagonism.(200)

Whilst lipopolysaccharide and fungal adjuvants are excellent inducers of IL-23 in various experimental systems, the *in vivo* factors that regulate IL-23 production, both overproduction and downregulation, remain poorly defined. Knowledge of the precise regulation of this pivotal IL-23 pathway is crucial, as the IL-23 pathway plays a central role in shaping immune responses. For example, the normal intestinal microbiota could be key to modulating the IL-23 pathway, offering a potential route to the development of novel strategies towards controlling inflammatory disease. This chapter gives an overview of the potential regulators of the IL-23 axis *in vivo*.

5.1 The immune system

The immune system is a complex network of molecules many of which have specialised roles, tailored for detecting and defending the body against infections whilst maintaining protection and regulation against the body's own cells. There are two branches to the immune system, the innate and the adaptive. Innate immunity is the body's first line of defence against invading microbes. Cells of innate immunity include phagocytes (neutrophils, monocytes, macrophages, dendritic cells), cells that release inflammatory proteins (basophils, mast cells, and eosinophils), and natural killer cells. Adaptive, acquired, or 'specific' immunity creates an immunological memory after an initial infection. Cells of the adaptive immune system include lymphocytes such as B cells and T cells. Adaptive immunity provides long-term protection from specific pathogens by the acquisition of pathogen-specific receptors and antibodies which remain in the system, primed to defend against a repeat infection.(201)

DCs in particular are a crucial line of defence against invading pathogens.(202) Distributed ubiquitously in tissues, immature DCs are able to sense invading pathogens and present processed antigens to T cells, thereby establishing an important link between the innate and adaptive immune response.(48, 202) This instrumental innate immune defence system first relies on the detailed recognition of conserved structures expressed on pathogenic surfaces called pathogen associated molecular patterns (PAMPs).(202, 203) These are recognised by PRRs expressed on the surface of DCs.

DCs display a vast repertoire of PRRs, including but not limited to TLRs and CLRs enabling them to detect a wide range of microbial signatures.(204) Upon binding to their respective PAMPs, these PRRs elicit distinct signalling cascades that trigger the transcription of specific cytokines and chemokines, which help to shape the downstream immune response to be appropriate to the nature of the threat. Each PRR elicits a distinct cytokine profile and the cross-talk between these signalling pathways is critical in fine tuning the magnitude and quality of the resulting adaptive immune response to different pathogens.(92, 93, 205)

The immunological plasticity exhibited by DCs is a direct result of their heterogeneity in terms of their location, phenotype and immunological functions, allowing them to shape specific immune responses to a diverse range of pathogens. However, since each PRR can have a broad or overlapping specificity, oftentimes pattern recognition is ambiguous, especially in cases where ligands share a common structural motif, thus potentially facilitating the ability of one PRR to bind to a large number of pathogens.(36, 80) To counteract this and ensure a precise response to each pathogen, presentation of antigens to T cells is a more specific process, allowing further discrimination between the pathogen recognised and the resulting immune response.

5.1.1 T cell activation

Following recognition of a specific component of an invading pathogen by a PRR, immature DCs capture and internalise the pathogen and process it into specific antigens, triggering DC maturation. During this time, receptors for antigen capture are down-regulated, whereas molecules for antigen presentation, such as major histocompatibility complexes (MHC) I and II, and co-stimulatory molecules for T cell activation are upregulated and expressed on the surface of DCs.(206) This pathogen processing and antigen presentation by DCs is the prime determinant in T helper (Th) cell activity.(207) T helper cells are prolific cytokine producers and their differentiation in response to antigen presentation is therefore crucial in helping to support the immune system in dealing with the infectious agent appropriately.

The processed antigens displayed as peptides by DC surface MHC II molecules are received by T cells via the T Cell Receptor (TCR).(208) TCR generation is achieved through random splicing of TCR gene segments, gene rearrangement and various processes of receptor diversification.(209) Expression of the resulting receptors is achieved clonally, ensuring that each naïve T cell represents a unique T cell receptor. TCR diversity is vast thus permitting the T cell system to recognise a myriad of antigens, both endogenous and exogenous. While TCRs can be highly specific, with a single change in the amino acid sequence of a peptide sometimes being able to abrogate binding, due to the immensity of receptors, cross-reactivity is also observed.(210-212) Many different TCRs can recognise the same antigenic peptide and many similar

antigenic peptides can be recognised by the same TCR.(210-212) The balance between specificity and cross-reactivity allows the immune system to recognise a wide range of pathogens, whist maintaining the ability to determine between self and non-self antigens, a key aspect of controlling autoimmunity.

Furthermore the activation of naïve T lymphocytes requires co-stimulatory signals involving the interaction of accessory molecules on APCs.(213) Co-stimulatory molecules are up-regulated upon recognition of peptide antigens and are mandatory for the induction of an effective immune response. The absence of co-stimulatory receptor engagement results in T cell anergy and abrogation of T cell proliferation.(214, 215)

CD80 and CD86 are co-stimulatory molecules for T cells and are recognised by CD28, a receptor constitutively expressed on $CD4^+$ T cells.(216) Similar to solo engagement of antigens by TCR, CD28-CD80/86 engagement alone has little effect on T cell responses, showing that signalling through CD28 is a co-stimulatory event.(217) Following activation through CD28, T cells up-regulate cytotoxic T-lymphocyte antigen 4 (CTLA-4) on their surface.(218, 219) CTLA-4 also binds to CD80/86 with a ~100 fold higher affinity than CD28, but sends antagonistic signals to down regulate T cell responses.(220, 221) This interaction is an essential part of T cell regulation and is important in maintaining immune homeostasis.(222) CTLA-4 also aids in maintaining self-antigen immunity.

Alongside both MHC II and CD80 engagement, a third signal is required for T-cell priming. Activation of PRRs trigger signalling cascades which result in the activation of transcriptional factors which control cell survival, transcription of DNA, and production of pro-inflammatory cytokines, chemokines and additional inflammatory mediators in different types of innate immune cells. The production and presence of these cytokines at the point of T cell priming becomes the third signal to determine the direction of the immune response (Figure 5.1).(223)

One of the central transcription factor families involved in this process is nuclear factor kappa-light-chain-enhancer of activated B cells (NF-κB), which consists of five structurally related members, including NF-κB1 (p50), NF-κB2 (p52), RelA (p65), RelB and c-Rel.(224) In resting cells, NF-κB proteins are typically retained in the cytoplasm in an inactive state due to association by a family of inhibitory proteins such as IκB family members.(225, 226)

Activation of NF-κB is a hallmark of most infections and is critical for initiating innate and adaptive immune responses. Although DCs, macrophages and neutrophils express distinct PRRs and signalling cascades, they all utilise NF-κB pathways to drive the expression of pro-inflammatory cytokines and other immune mediators.(226) NF-κB is activated by a broad range of stimuli including ligands which bind TLRs, CLRs, the T cell receptor and B cell receptor.(227)

In the canonical activation pathway, ligand-receptor interactions initiate a signalling cascade that activates the IκB kinase (IKK) complex, which consists of two catalytic subunits (IKKα and IKKβ) and a regulatory subunit known as IKKγ or NEMO (NF-κB essential modulator). Activated IKK phosphorylates IκB at N-terminal serine residues, marking it for ubiquitination and subsequent degradation. This degradation frees NF-κB dimers (predominantly p65/p50 or p50/p50) which translocate to the nucleus.(228) Once in the nucleus NF-κB binds specific DNA sequences known as κB response elements which recruit RNA polymerase II to initiate transcription of target genes. The resulting mRNA is translated into proteins which coordinate inflammation, immune cell recruitment, pathogen clearance and T cell differentiation.(229)

In addition to the canonical pathway a non-canonical NF-κB pathway centred around RelB and P52 exists. This is activated by a distinct set of PRRs such as tumour necrosis factor receptors (TNFR), and regulates processes such as B cell maturation, homeostasis and lymphoid organ development (Figure 5.1).(230)

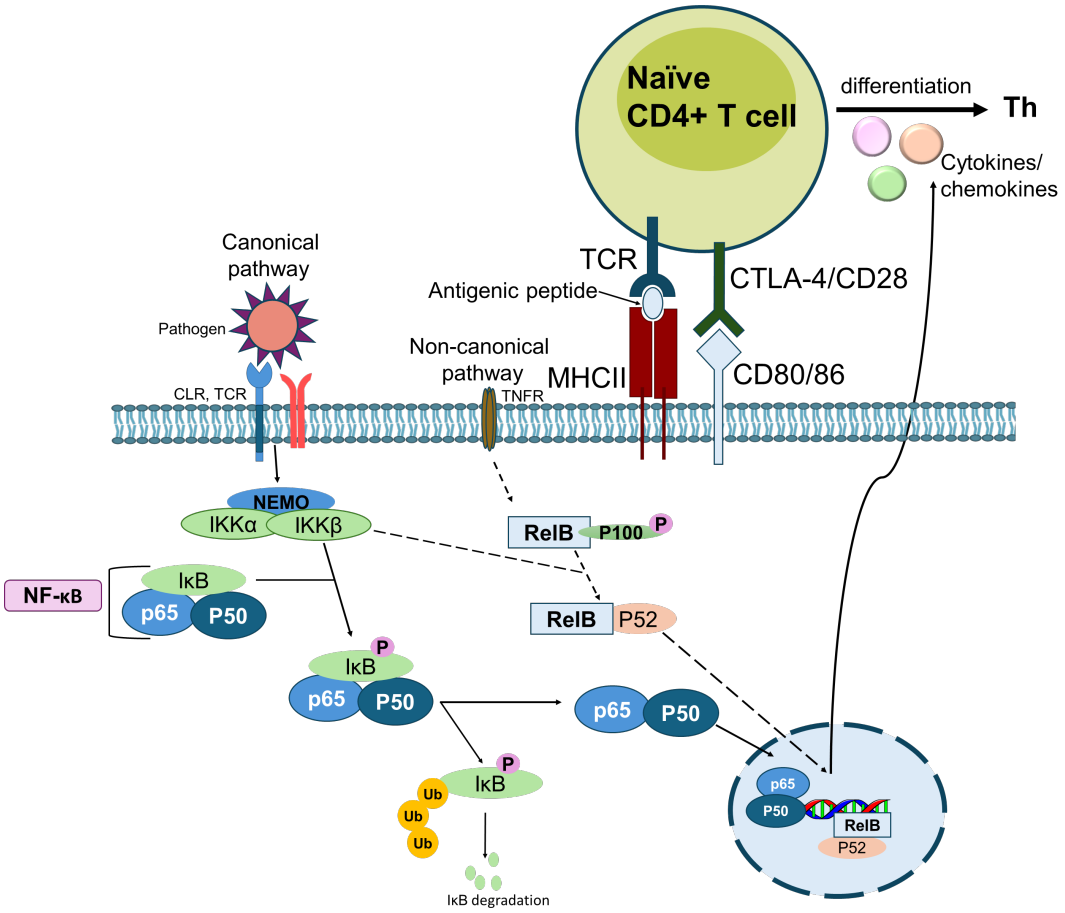

Figure 5.1 Schematic depicting three essential signals for successful T cell differentiation and the NF-κB pathways to generating cytokines. Recognition of a pathogen triggers a degradation sequences that results in peptides being presented to the TCR via MHC II molecules. CD80 and CD86 are upregulated upon pathogen recognition and DC maturation, which bind CD28/CTLA-4 on T cells. This co stimulation is essential for T cell activation. Thirdly, pathogen recognition initiates NF-κB pathways for transcription of cytokines. The canonical NF-kB pathway leads to degradation of the inhibitory protein IκB, allowing P50 and P65 subunits to translocate to the nucleus where they can initiate transcription. A non-canonical RelB-P52 heterodimer may sometimes translocate to the nucleus upon stimulation of tumour necrosis factor receptors (TNFR) leading to transcription of alternative cytokines essential for B cell development, homeostasis or lymphoid organ formation.

5.1.2 T cell differentiation

Once activated via MHC II, CD80/86 and cytokines, naïve T cells differentiate into one of several lineages of T helper (Th) cells. These include Th1, Th2 and Th17, and Tregs among others, and are defined by their pattern of cytokine production and function (Figure 5.2).(231) The commitment to each lineage is orchestrated by the lineage-defining transcription factors, T-bet, Gata3, RORγt and FOXP3 for Th1, Th2, Th17 and Tregs, respectively, which bind specific DNA sequences and ultimately control their cytokine expression profiles. Various studies conducted in the early ‘90s showed that Th2 cell differentiation occurred in the presence of both interleukin (IL)-2 and IL-4.(232-

234) Following this, Murphy *et al.* revealed that Th1 cells could be differentiated from $CD4^+$ T cells if IL-4 was neutralized and IL-12 was added to the culture.(235)

Th1 cells principally secrete the cytokine interferon-γ (IFN- γ) whereas Th2 cells produce IL-4 as their signature cytokine.(236, 237) Typically Th1 immunity creates a pro-inflammatory response which is important for defence against intracellular microbes and viral infections whereas Th2 cells, which are important for the eradication of large pathogens, parasites and helminth infection, evoke a less inflammatory antibody response which is directed more towards tissue repair.(238) There is moderation required in the development of Th1 and Th2 cells. Uncontrolled Th1 driven immunity can lead to a breakdown in self-tolerance, uncontrolled tissue damage and onset of autoimmune diseases, where Th1 cells are directed against self-antigens such as those involved in rheumatoid arthritis. Th2 responses will moderate this Th1 activity, but excessive or uncontrolled Th2 expression is instead associated with allergic diseases.(239) The need for Th1/Th2 balance to avoid the onset of disease is of vital importance and hence the pathways to the production of Th1 or Th2 are highly regulated by distinct transcriptional factors.(238) It is, however, susceptible to manipulation by pathogens. The nature of pathogens manipulating Th1 and Th2 responses is well exemplified by *Candida albicans* whereby the yeast form activates DCs to produce IL-12. IL-12 primes Th1 cells by activating signal transducer and activator of transcription 4 (STAT4) which upregulates the expression of IFN- γ and leads to Th1 production.(240) Contrastingly, the hyphal form of *C. albicans* inhibits IL-12 and induces IL-4 secretion, leading to STAT5 mediated production of Th2 cells.(82, 237)

A third category of T helper cells, Th17, drive IL-17 production that is vital for neutrophil activation and immunity against extracellular pathogens including bacteria and fungi.(241) For efficient Th17 differentiation IL-23, IL-6 and transforming growth factor-β (TGF-β) are likely to be present during T cell priming (Figure 5.2).(242) Similar to Th1 cells, Th17 cells drive inflammation, but by enabling neutrophil recruitment, they have evolved to be more sufficiently equipped for host protection against microbes that Th1 or Th2 immunity are not well suited for, including extracellular bacteria and some fungi.(243) Since their discovery the early 2000s, Th17 cells have received considerable attention due to their inextricable link to several autoimmune diseases and inflammatory disorders such as psoriasis, psoriatic arthritis and inflammatory bowel disease.(244-246)

Alongside Th1, Th2 and Th17 cells, both T regulatory (Treg) and T follicular helper (Tfh) cells have also been described. As well as being involved in the regulation of Th1, Th2 and Th17 responses, Treg cells are essential in maintaining self-tolerance to commensal microbiota.(247) Tfh cells support antigen specific B cell immunity and aid in the production of germinal centres in secondary lymphoid organs.(248)

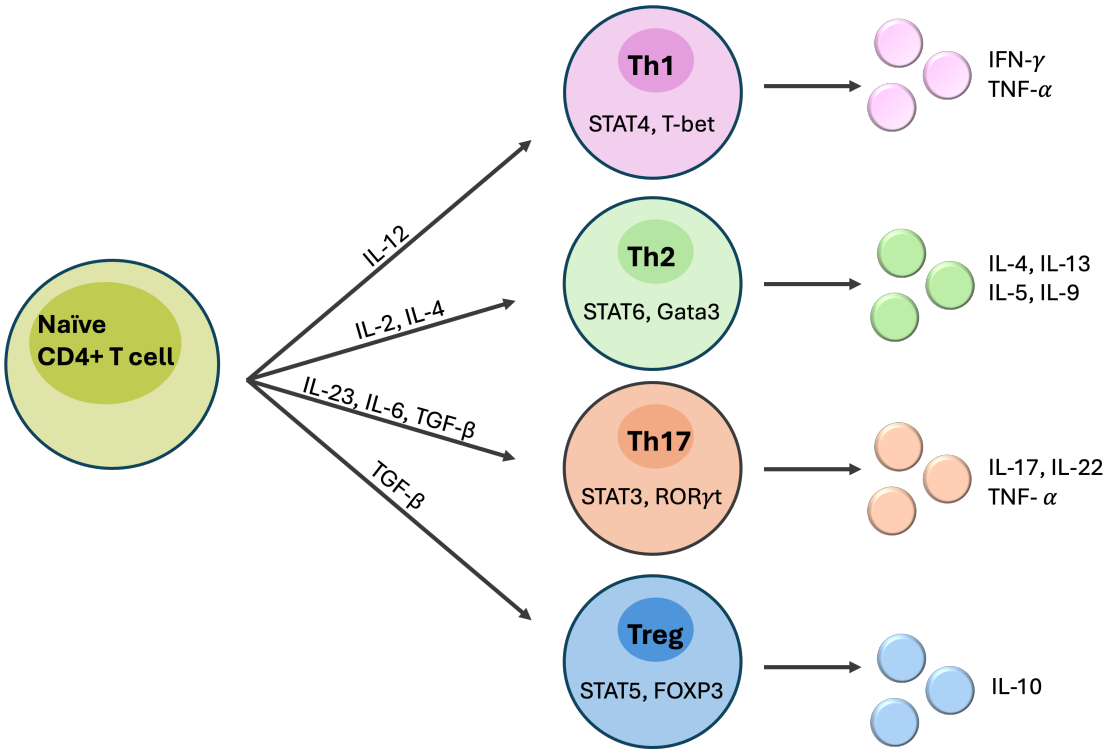

Figure 5.2 An overview of $CD4^+$ T helper (Th) cell differentiation into different T helper cell lineages including Th1, Th2, Th17 and Treg. The cytokines required for differentiation into these specific lineages are shown on the left. Differentiation in the presence of these cytokines activates different transcriptional factors (shown inside the cell) which leads to unique signalling cascades and subsequent production of additional cytokines indicated on the right, which help define the specific Th type.

5.2 IL-23 cytokine

Of special interest under the umbrella of Th17 immunity was the discovery of the interleukin-23 cytokine that was shown to be crucial for IL-17 production and also the emergence of data strongly linking this IL-23/IL-17 axis to anti-fungal immunity.(249, 250) The IL-23/IL-17 axis also plays a pivotal role in the pathogenesis of both psoriasis and psoriatic arthritis and the allied seronegative spondyloarthropathies; a family of rheumatologic disorders affecting the joints. Additionally both fungal infections and psoriasis show a propensity for the scalp, the nails and the groin areas.(251) Blockade of the IL-23/IL-17 axis has proven to be very effective for these disorders, however, signalling pathway and cytokine regulation *in vivo* for such diseases is still poorly understood.(252)

IL-23 is a heterodimeric cytokine, discovered in 2000 and classified as a member of the IL-12 cytokine family.(253) There are currently four known members of the IL-12 family in man; IL-12, IL-23, IL-27 and IL-35. While IL-12, IL-23 and IL-27 are secreted by activated antigen presenting cells such as macrophages and DCs, IL-35 is a product of regulatory T and B cells.(254, 255) Cytokines are grouped into families based of their amino acid homology and structural characteristics and the IL-12 family cytokines are categorised together as such based on the sharing of subunits and cellular receptors

with each other. IL-12 family members have unique structural properties, and each comprise of a four-helix α unit and a β unit (Figure 5.3).(254) Chain pairing promiscuity between α and β subunits results in the generation of the four family members: IL-12 (p35 + p40), IL-23 (p19 + p40), IL-27 (p28 + EBI3), and IL-35 (p35 + EBI3) (Figure 5.4).(253, 256-258)

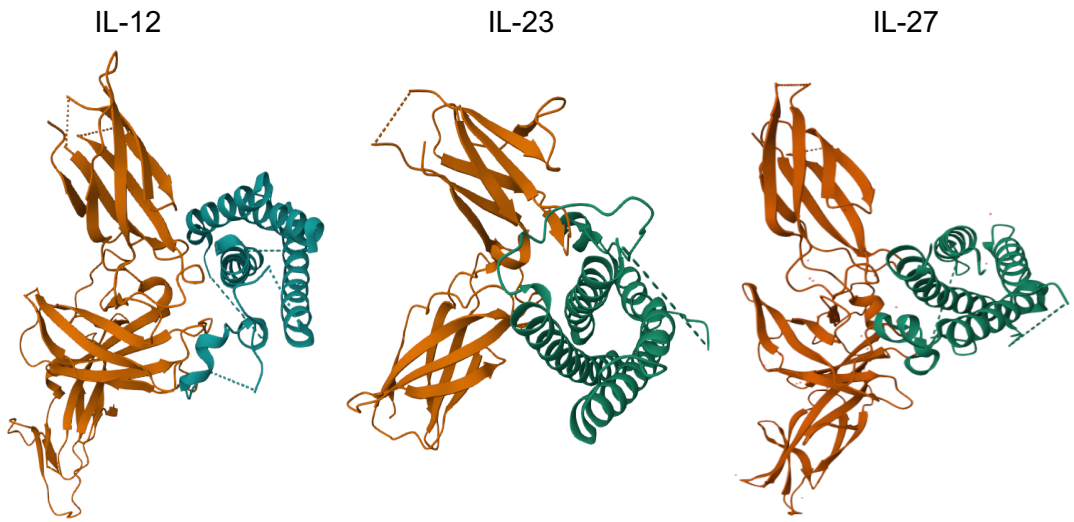

Figure 5.3 Crystal structures of IL-12 (PDB: 1F45), IL-23 (PDB: 5MXA) and IL-27 (PDB: 7ZXK) showing their four α-helix (green) and β-sheet (orange) subunits. A high-resolution crystal structure of the fully assembled IL-35 heterodimer is not readily available.

The IL-12 cytokines have a range of functions and are capable of triggering the promotion or suppression of inflammation and autoimmunity. Since IL-12 and IL-23 share the common p40 subunit, they were initially expected to have similar immune functions however it later transpired that their structural similarity does not relate to functional similarity. While it was initially thought that IL-23 would be an imitator of IL-12, these two cytokines appear to have profoundly different and unique roles in regulating host immunity.(259) IL-12 is a proinflammatory cytokine produced by dendritic cells in response to microbial pathogens, and binding of this cytokine to the receptor complex IL-12Rβ1/ IL-12Rβ2 leads to STAT4 mediated signalling which is critical in driving the typical Th1 response, characterised by INF-γ production.(260, 261) On the other hand, papers published in the early 2000 by multiple authors demonstrate that although IL-23 is a proinflammatory cytokine which also relies on STAT4, IL-23 ultimately drives IL-17 production from a subset of $CD4^+$ T cells.(262) To substantiate this claim, and explore the distinct immune responses to IL-12 and IL-23, transgenic mice were subjected to overexpression of the p19 IL-23 subunit. These mice were found to be afflicted with systemic inflammation and premature death, and furthermore these mice were found to have consistently elevated levels of neutrophils, but not INF-γ suggesting that IL-23 had

a substantially distinct biological role to that of IL-12.(263) Thus, as briefly described earlier, the concept of Th17 cells was born.(264) Consistent with the structural and biological similarities of IL-12 and IL-23, the IL-23 receptor complex shares a p40-binding subunit with that of IL-12 (IL-12Rβ1); however, the difference in immune response can be attributed to the fact that IL-23 does not use or detectably bind to IL-12Rβ2. Instead, IL-23 binds to IL-23 receptor (IL-23R).(265)

In complete contrast, IL-27 and IL-35 are inhibitory cytokines, produced by APC or Treg cell populations, respectively. IL-27 can inhibit the development of Th17 and IL-35 supresses T cell proliferation.(262, 266)

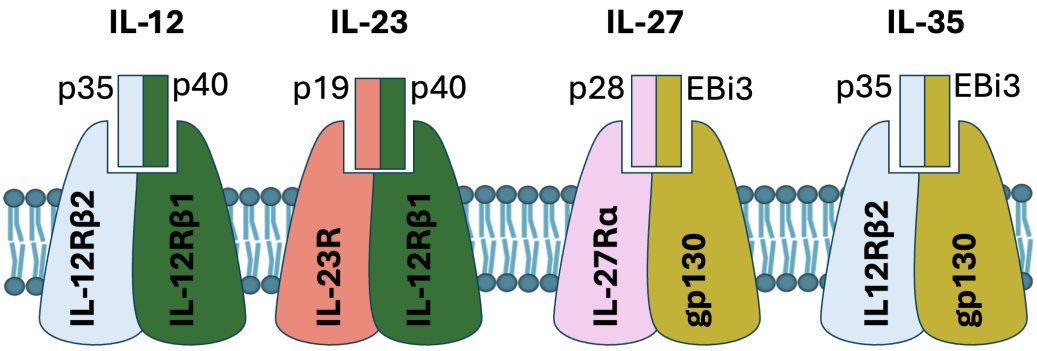

Figure 5.4 Overview and composition of the IL-12 cytokine family and its receptors. All IL-12 cytokine family members are heterodimeric proteins consisting of an α subunit (p19, p28 or p35) and a β subunit (EBi3 or P40). Receptors of the cytokines are heterodimers consisting of 2 combined subunits (IL-12Rβ1, IL-12Rβ2, IL-23R, IL27Rα and gp130)

5.2.1 IL-23 signalling

The IL-23 signalling pathway relies on the family of tyrosine kinases collectively termed Janus kinases (JAKs) which consists of JAK1, JAK2, JAK3 and TYK2, and two signalling proteins, STAT3 and STAT4.(267) Binding of IL-23 to its IL-23R and IL-12Rβ1 receptors results in the recruitment and activation of JAK kinases (Jak2 and Tyk2).(265) Activation of Jak2 and Tyk2 triggers phosphorylation of the tyrosine motifs in the IL-23R receptor complex, which results in the formation of docking sites for the STAT proteins.(268) The receptor bound STAT3 and STAT4 are subsequently phosphorylated on their thymine residues, causing dissociation from the receptor, dimerization and translocation to the nucleus where they activate target genes (Figure 5.5).(269) Phosphorylation of STAT4 is essential for increasing IFN-γ production and is a key process in IL-12 signalling, however it is STAT3 phosphorylation that is required for the augmentation of transcription factor retinoid-related orphan receptor (RORγt) during Th17 differentiation and the expression of IL-17A and IL-17F.(270)

The RORγt transcription factor is the hallmark of IL-17-producing cells and is essential for regulating Th17 differentiation, as well as supressing the expression of proteins characteristic of other T cell lineages. Its expression is predominantly observed in immune Th17 cells, and is controlled by IL-6 and IL-23 activated STAT3 pathways.(271, 272)

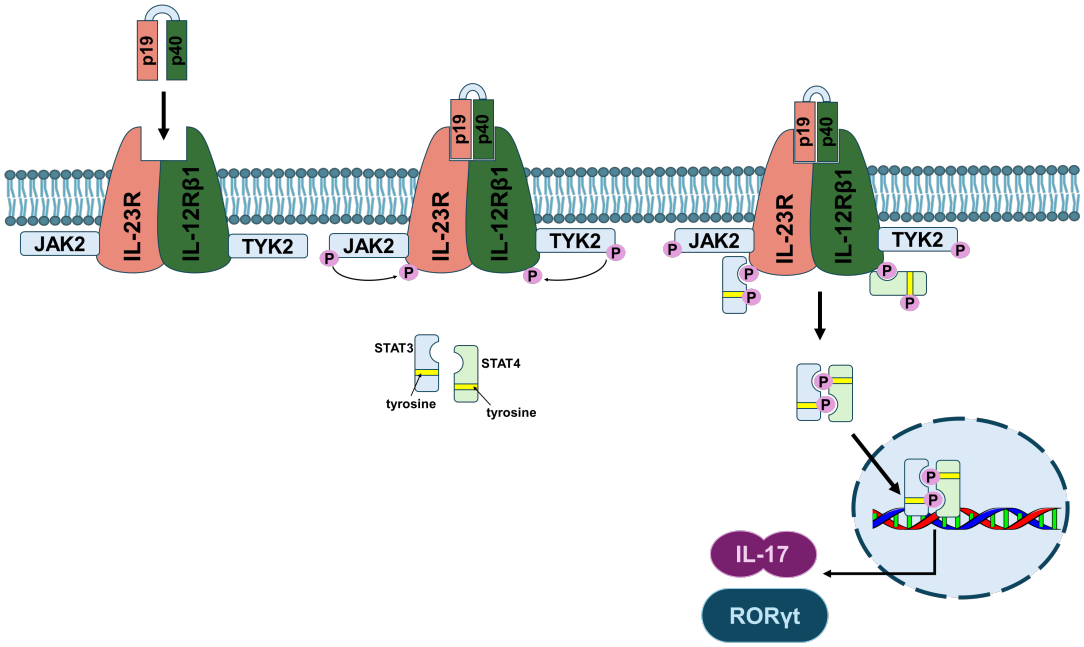

Figure 5.5 IL-23 pathway. The IL-23 cytokine binds to its receptors, initiating the downstream activation of different STATs which translocate to the nucleus to activate target genes.

Although important, it is not IL-23 alone that drives T cells to differentiate into Th17 lineage. Additional cytokines have their own role in this process and are necessary for Th17 determination. In 2006, three labs simultaneously published that the addition of both TGF-β and IL-6 must be present during T cell recognition to promote their development into Th17 cells.(242, 273, 274) Since IFN-γ inhibits Th17 production, and TGF-β has suppressive actions on IFN-γ, it was thought that TGF-β might contribute to Th17 development. When treated with TGF-β and IL-6 concurrently, 81% of T cells were induced to produce IL-17.(242) Further studies into the function of IL-6 on the differentiation of $CD4^+$ T cells cemented the roll of this cytokine in generating Th17 cells by activation of STAT3.(275) STAT3 is an essential transcriptional factor which directly drives the transcription of Th17 lineage genes such as *Il17* and *Il23r* and is also involved in the suppression of TGF-β-induced forkhead box P3 (FOXP3) expression.(242, 276) FOXP3 is the master regulator of the regulatory pathway in the development and function of regulatory T cells (Treg), and IL-6 activation of STAT3 thereby inhibits the generation of Treg cells in favour of Th17 cells.

The role of IL-1β in the induction of Th17 cells has been exemplified by Sutten *et al.* who showed that *Il1r1*$^{-/-}$ mice fail to develop Th17 cells in response to antigens and adjuvants.(277) Furthermore, these mice were resistant to Th17 inflammatory diseases such as experimental autoimmune encephalomyelitis (EAE) and collagen induced arthritis (CIA). Expression of the IL-1β receptor, IL-1R1, by Th17 cells is induced by IL-6, and signalling through this receptor promotes the transcriptional factor interferon-regulatory factor 4 (IRF4), which reinforces expression of RORγt.

5.3 IL-17 cytokine

IL-17 production is archetypal of a Th17 immune response. IL-17 (IL-17A) was the first discovered member of a family of 6 cytokines consisting of IL-17A to F. IL-17A is a homodimer cytokine produced by numerous cell types such as Th17 $CD4^+$ cells, $CD8^+$ cells, γδ-T cells, natural killer (NK) cells and innate lymphoid cells (ILC)-3 in response to cytokine stimuli such as IL-1β, IL-6, IL-21, and IL-23. All IL-17 family members have a similar protein structure, sharing four highly conserved cysteine residues which are essential to the 3-dimentional shape of the protein, however, IL-17F is the most closely related cytokine to IL-17A sharing 50% sequence homology with others sharing as little as 16%.(278-280) Like IL-17A, IL-17F is a homodimer and the two cytokines appear to have overlapping functions and are produced by the same T cells. These two cytokines can signal as their respective homodimers (IL-17AA/IL-17FF), or, since they share chain pairings, they can signal as an IL-17A/F heterodimer through the same receptor complex consisting of IL-17RA and IL-17RC.(281) IL17-AA may also signal through an IL17RA/IL17RD receptor complex (Figure 5.6). All other IL-17 cytokines signal via heterodimeric receptor complexes composed by different combination of the receptors IL-17RA through IL-17RE.(281)

Members of the IL-17R family are single transmembrane chains. The extracellular region contains two fibronectin III-like (FN) domains, which mediate protein–protein interactions and ligand binding.(281) The cytoplasmic regions of the IL-17R family are defined by a conserved sequence in the cytoplasmic tail known as the SEFIR (similar expression of fibroblast growth factor genes and IL-17Rs).(282) Upon ligand binding the cytoplasmic protein Act1, which also contains a SEFIR domain, is recruited to the IL-17R complex through homotypic SEFIR interactions in order to mediate downstream events. Once engaged, Act1 recruits TNFR-associated factor 6 (TRAF6) and TRAF3 which are essential for the activation of NF-κB pathway. This occurs through a series of molecular interactions between cytoplasmic proteins (Act1, TRAF6, mitogen-activated protein kinase (MAPK), TGF-β-activated kinase 1 (TAK1)) and consequent degradation of IκB via this cascade allows the nuclear translocation of NF-κB or activator protein 1 (AP-1) and therefore the activation of NF-κB / AP-1 targeted genes (Figure 5.6).(279) Though this molecular cascade, IL-17 is able to induce sustained production of inflammatory

cytokines, such as IL-1, GM-CSF, TNF-α and IL-6 as well as chemokines, including CXCL1 (KC), CCL2 (MCP-1), CXCL2 (MIP-2), CCL7 (MCP-3) and CCL20 (MIP-3A).(283)

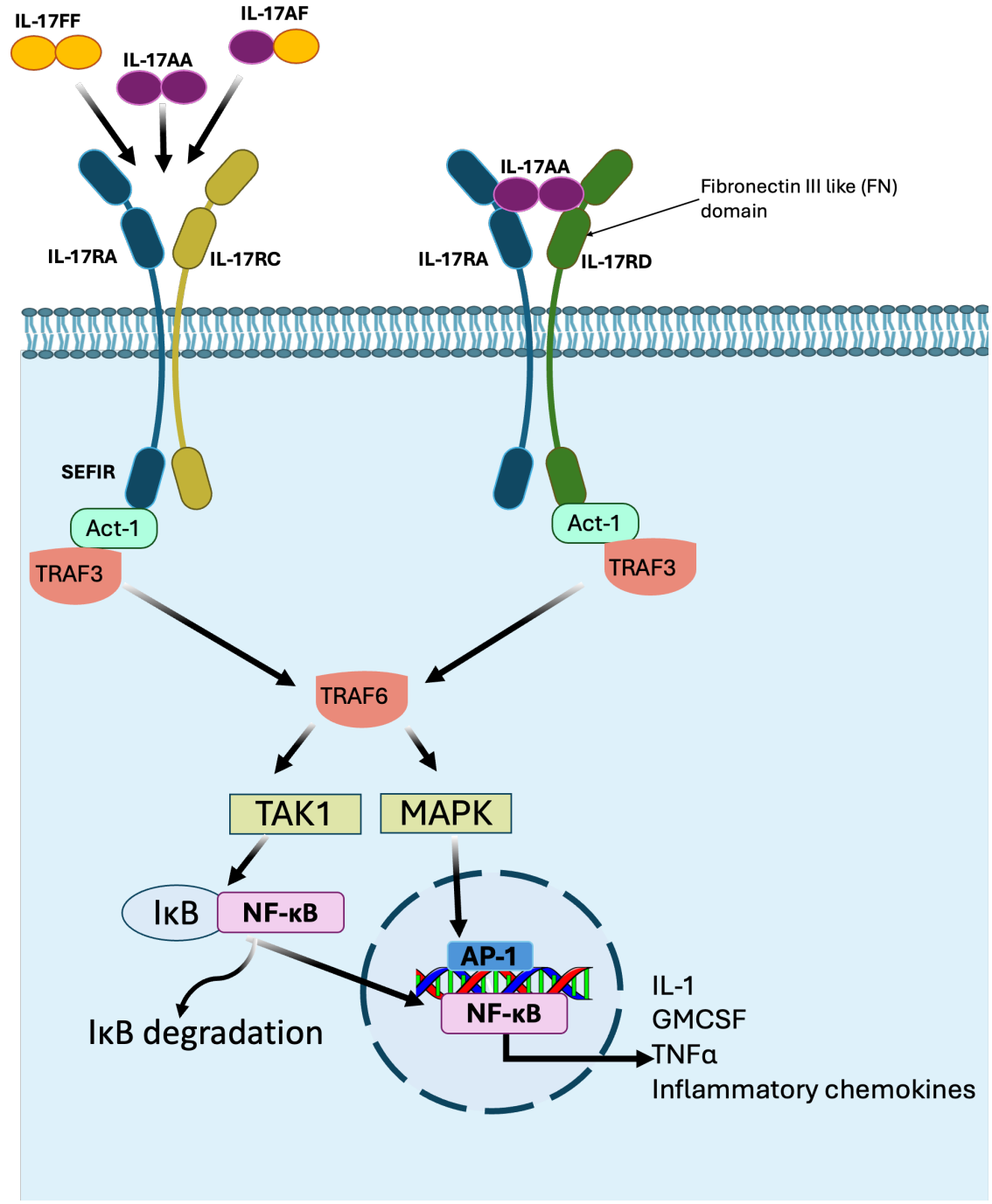

Figure 5.6 IL-17A and IL-17F cytokine signalling pathway. IL-17AA, IL-17AF, and IL-17FF heterodimers and homodimers bind to the receptor complex comprising of IL-17RA and IL-17RC. IL-17AA homodimers also are able to bind to a receptor complex of IL-17RA and IL-17RD. IL-17 cytokines activate transcription factors NF-κB and AP-1 through a series of molecular interactions between TRAF3, TRAF6, TAK1, MAPK and IκB.

5.4 IL-23/IL-17 axis in host defence

Although Th17 cells were initially studied in the context of autoimmunity, mouse experiments showed that IL-17- and IL-17R knockout mice demonstrated an increased susceptibility to infection by bacteria, parasites, fungi and viruses, hence it was uncovered that the Th17 immune response is essential to host defence against extracellular bacteria, and fungal pathogens. Th17 cells grant this protection mainly through the recruitment and activation of macrophages and neutrophils.

The first indication that IL-17 was important in host defence against bacterial pathogens was demonstrated by Kolls and co-workers in 2000.(284) The model was based on IL-17R deficient mice being compared with control mice when infected with *Klebsiella pneumonia.* Mice displaying IL-17R deficiency were shown to be highly susceptible to infection and exhibited increased numbers of recoverable bacteria in the lung, increased bacterial dissemination into the spleen, and reduced overall survival. When treated with adenovirus IL-17 gene transfer (adIL-17) to increase IL-17 levels, cytokines critical to immunity were produced, such as MIP-2, G-CSF, TNF-α and IL-1β. Neutrophil recruitment was also enhanced in mice treated with adIL-17, suggesting that augmented susceptibility of IL-17R deficient mice was associated with a reduction in cytokine production and neutrophil recruitment being reduced by up to 90%.

A follow up study by Kolls and colleagues further investigated the importance of IL-23 in host defence.(285) In mice lacking the IL-23 p19 subunit, a higher susceptibility to *K. Pneumoniae* was observed, along with abrogated upregulation of IL-17 in response to the infection compared to control mice which readily exhibited IL-17 production shortly after infection. Furthermore, bacterial burden could be significantly reduced in IL-23 $p19^{-/-}$ mice by administration of recombinant IL-17, and restoration of important chemokines for host defence such as G-CSF was observed. Following these initial studies with *K. pneumoniae*, the importance of IL-23 and IL-17 in host defence has been further established for a growing list of bacterial pathogens including *Citrobacter rodentium(274), Escherichia coli(286), Porphyromonas gingivalis(287), Streptococcus pneumonia(288) and Salmonella enterica(289).*

Regarding host defence against fungal pathogens, IL-17R is crucial for the control of, and protection against, *Candida albicans(290), Cryptococcus neoformans(291)* and *Pneumocystis carinii(292)*. As with protection against bacterial pathogens, the IL-17 pathway is also able to regulate antifungal immunity through upregulation of proinflammatory cytokines. These include neutrophil recruiting chemokines such as CXCL1 and CXCL5, proinflammatory IL-6, and antimicrobial peptides which all act synergistically to limit fungal growth.(290)

As a specific example, the protective effects of Th17 cytokines in response to *Candida albicans* has been well documented. *C. albicans* is a commensal fungus found in the

mouth, gastrointestinal tract, skin, and vagina of healthy individuals, however if host immunity is compromised then infection by *C. albicans* is common. Chronic mucocutaneous candidiasis (CMC) presents as infection of the oral cavity, mucosae, skin and nails and is often resistant to treatment. This kind of candidiasis regularly occurs in patients with genetic defects and polymorphisms in IL-17-related immunity.(293) Furthermore, mice with IL-17R deficiency, which are therefore unable to respond to IL-17, suffer increased tissue fungal burdens and decreased survival when intravenously infected with *C. albicans*.(294) This infection was shown to be associated with impaired mobilisation of neutrophils into infected organs. Additionally, IL-23 deficient mice have impaired clearance of *C. albicans* skin infection and IL-17 expression in response to candida-infected skin was found to be dependent on IL-23.(295)

From the above it is clear that co-ordinated and precisely controlled Th1, Th2, Th17 and Treg responses act to protect the host from infection via promotion of pathogen processing and eradication thereby minimising pathogen dissemination. However, in contrast to these protective effects, when dysregulated, T cell responses also have the potential to cause immunopathology. Uncontrolled Th2 driven immunity can result in allergic diseases, and excessive Th1 and Th17 driven immunity can lead to a breakdown in self-tolerance, uncontrolled tissue damage and onset of systemic autoimmune diseases.

5.5 IL-17/IL-23 axis in autoimmunity

IL-17 and IL-23 have emerged as essential factors in the pathogenesis of many autoimmune diseases. The seminal paper which incriminated IL-23 in autoimmune diseases came about shortly after the discovery of IL-23, in 2003.(296) Using EAE, an autoimmune inflammatory disease of the central nervous system as a model, mice lacking either IL-23 (*p19* $^{-/-}$), IL-12 (*p35*$^{-/-}$) or both cytokines (*p40*$^{-/-}$) were tested for their susceptibility for this disease. Initially EAE was thought to be Th1 driven based on studies revealing that mice lacking p40 were resistant to disease, however it later transpired that mice lacking IFN-γ or STAT1 (key factors in Th1 signalling) still developed EAE.(297, 298) Using this murine model it was shown that mice lacking IL-23 (*p19*$^{-/-}$), and IL-12/IL-23 (*p40*$^{-/-}$) were resistant to the development of EAE. By contrast, mice that specifically lacked IL-12p35 were still vulnerable to EAE.(296) Further experiments using IL-12 and IL-23 deficient mice have confirmed a requirement for these cytokines in EAE.(299) Additionally, experiments using IL-17, IL-22, IL-23 and IL-23R deficient mice have shown a proclivity for these mice to develop other autoimmune diseases such as CIA, inflammatory bowel disease (IBD), and in particular, seronegative spondyloarthropathy phenotypes.(296, 299-301)

5.5.1 Seronegative spondyloarthropathies

The seronegative spondyloarthropathies (SpA) are family of rheumatic diseases known to cause arthritis. They include ankylosing spondylitis (AS), psoriasis, psoriatic arthritis (PsA), reactive arthritis (RA), Crohn's disease and ulcerative colitis, uveitis, and Behcet's disease.(245, 302) These diseases differ from rheumatoid arthritis where the target of the immune response is the synovium (a specialized connective soft-tissue membrane that lines the inner surface of synovial joint capsules) which causes bone destruction and erosion. Instead, the SpA diseases are characterised by inflammation of the enthesis (the insertion point of a tendon, ligament, capsule, or fascia into bone) which is thought to be the cardinal symptom in SpA. SpA can drive both severe bone erosion, and new bone formation at peripheral (arms and legs, including the elbows, wrists, hands, and feet) and axial (spine, hip, shoulder) sites.(303) Patients with these diseases have a tendency to exhibit inflammation outside the skeleton also. External sites of inflammation include the ciliary body of the eye, the aortic root, the lung apex, and the ileum.(245) In common with the enthesis, all of these sites also represent junctional tissues that are subject to repeated motion and biomechanical stressing.(304) Importantly, all of these diseases share single nucleotide polymorphisms (SNPs) in the IL-23 receptor or the IL-23 cytokine itself and related downstream signalling pathways, leading to overexpression of IL-23 and IL-17 at the enthesis and in the gut.(245, 305, 306)

Initially, due to the efficacy of p40 blockers and thus the incrimination of IL-12, diseases such as psoriasis were widely classified as Th1. However, after the discovery of the novel p19 + p40 chain pairing, the classification of IL-23 and its distinct role to IL-12, and the discovery that p19 blockers had potentially greater efficacy in the treatment of psoriasis and PsA, these diseases were reclassified as Th17. There are currently numerous antibody treatments, tailored to target various homologues of the IL-17 family, the p40 subunit of IL-23 and IL-12, and the unique p19 subunit of IL-23. Examples of these antibodies (and their targets) include secukinumab (IL-17A)(307), ustekinumab (p40)(308) and tildrakizumab (p19)(309). These antibodies are licensed in patients with psoriasis, along with other p19 and IL-17A/A+F blockers, and show remarkable effectiveness. A >75% skin clearance has been observed in 70-80% of patients, with around half of these reaching 100% skin clearance.(310) Some p19 blockers are licenced in PsA, Crohn’s disease and ulcerative colitis too, with IL-17A/A+F blockers also licensed in PsA.(311, 312) Trials are ongoing in looking at the efficacy in other conditions, e.g. guselkumab and bimekizumab in axial SpA and axial PsA.(312, 313)

5.5.2 IL-23/IL-17 axis SNPs in SpA

Genome wide association studies (GWAS) have provided a strong genetic rational for the role of IL-23 in SpA related disease. SNPs in the genes for IL-23 production and the IL-23 receptor have been strongly associated with ankylosing spondylitis, psoriasis and

IBD suggesting IL-23 to be a shared upstream driver of pathogenic inflammation, linking these disorders through common immunopathological mechanisms, like promoting pathogenic Th17 cell responses and chronic tissue inflammation.

Initially it was discovered that polymorphisms in the IL-23R were associated with ankylosing spondylitis.(305, 306) Ankylosing spondylitis is a chronic inflammatory arthritis characterized by spinal and joint inflammation and the role of the IL-23 involvement in AS has been supported by GWAS in both human and animal models.(34) Polymorphisms identified in IL-23R or STAT3/Tyk2 have been described in AS patients, leading to an overexpression of IL-23 in joints and the gut.(314) T cell subsets expressing IL-23R in joints and entheses of mice leads to production of inflammatory cytokines and chemokines in response to IL-23.(300) Shortly after the discovery of IL-23 SNPs in AS they were also uncovered in psoriasis and PsA. PsA is a type of chronic inflammatory arthritis affecting those with skin psoriasis and is characterised by inflammation of the enthesis and dactylitis (swelling of the joints). IL-23 is found in synovial fluid of those with PsA, and it has been suggested that IL-23 expression in synovial tissue correlates with disease severity in PsA.(315) Further studies revealed the importance of IL-23 in the pathogenesis of IBD. IL-23 is active at mucosal surfaces and is produced in the gut, and it was therefore suggested that intestinal mucosa could be a key site of IL-23 production in spondyloarthropathy.(316) Up to 70% of AS patients have subclinical intestinal or bowel inflammation and indeed IL-23 association with Crohn's disease was noted.(317-319) The link between polymorphisms in the IL-23 pathway, IBD, and joint inflammation suggest that overproduction of IL-23 may be the key component to the pathogenesis of SpA.

Given the association of IL-23 with the SpA disorders, it is unsurprising that IL-17 also has a significant role within these autoimmune diseases. High levels of IL-17 are observed in AS, IBD, and psoriasis. Psoriasis is a chronic inflammatory disorder, characterised by the presence of epidermal thickening on the scalp, trunk, and extensor surfaces of affected patients due to keratinocyte (skin cell) proliferation, as well as infiltration by T lymphocytes, macrophages, dendritic cells, and polymorphonuclear cells (neutrophils, basophils, mast cells eosinophils).(320) Within psoriatic lesions a high expression of IL-17A and IL-17F is found, which are involved in neutrophil accumulation and formation of abscesses.(321) IL-23, IL-22, and IL-23R are also expressed highly in psoriatic lesions compared to healthy skin.(271) Corresponding to high IL-23 levels in the gut, increased expression of IL-17A has been reported in the intestinal mucosa for those with Crohn's disease and in AS patients, levels of Th17 cells are increased compared to healthy subjects, resulting in an increase in IL-17 in serum, synovial fluid, and spinal joints. (322, 323). It must be acknowledged that the IL-23/IL-17 axis is genetically central to the SpA diseases yet IL-17 blockers do not work in the gut and IL-23 blockers have failed in AS which is currently poorly understood.

5.5.3 Other genes associated with SpA

5.5.3.1 HLA-B27

Human leukocyte antigen B27 (HLA-B27) is a gene that codes for proteins involved in presenting antigens to the immune system. HLAs in general aid the body in being able to distinguish between human and foreign antigens, however the presence of HLA-B27 has been associated with having a higher risk of developing ankylosing spondylitis. HLA-B27 has been found in up to 90% of patients with AS compared to 5-6% in random Caucasian populations.(324) While having this gene may increase the risk factor for developing AS, it does not guarantee it. Around 8% of the population have the HLA-B27 gene, but most of those do not have AS, highlighting the need for other factors to contribute to the pathogenesis of SpA diseases.(325) HLA-B27 may simply increase susceptibility to AS when triggered by other environmental factors. Alongside this, there is not definitive evidence that peripheral symptoms in psoriatic arthritis and inflammation in the gut in IBD are linked to HLA-B27.

5.5.3.2 CARD9

Outside of HLA-B27, mutations in caspase recruitment domain-containing protein 9 (CARD9) confer a significant risk to the development of AS.(326) CARD9 is an adaptor protein with an integral role in CLR mediated host defence against fungal and mycobacterial infections. CARD9 mediates signals from the pattern recognition receptor, Dectin-1, to induce NF-kB activation and trigger the transcription of pro-inflammatory cytokines in response to infections such as *C. albicans*. Dectin-1 is known to recognise the fungal cell wall component β-glucan, which in a mouse model has been shown to trigger IL-23 dependent enthesitis, whereas card9$^{-/-}$ mice show little to no signs of clinical disease.(327, 328) In humans, CARD9 mutations have been linked to IBD and one such SNP has also been linked to AS in a separate study.(329, 330) Removal of the AS cases also known to have IBD had little effect on the strength of the association between IBD and CARD9 mutation suggesting that the AS association is independent of the IBD association.(329)

Although a direct link between DC-SIGN and CARD9 has not yet been demonstrated, both feed into overlapping NF-κB–dependent pathways.(331, 332) This makes it plausible that changes in glycan sensing through DC-SIGN could amplify CARD9-dependent inflammation. In SpA, where CARD9 variants are tied to increased disease risk and heightened neutrophil-th17 activity, abnormal DC-SIGN signalling could act as an upstream trigger, working together with CARD9 to skew the IL-23/IL-17 axis, drive enthesitis, and sustain chronic inflammation in susceptible individuals.(333)

5.6 Inducers of excessive IL-23

5.6.1 HLA-B27/unfolded protein response

Despite extensive research on IL-23 over the past 20 years and its role within host protection and disease pathogenesis, the initial triggers for excessive IL-23 production remain to be elucidated. As briefly mentioned, there is a strong relationship between HLA-B27 and AS. A central theory for the high prevalence of those with AS to have the HLA-B27 gene stems from the unfolded protein response (UPR) theory.(334) Expression of HLA-B27 in rats results in inflammatory disease resembling SpA. This is due to an accumulation of HLA misfolded heavy chains in the endoplasmic reticulum (ER) which activates the UPR. All proteins are translocated to the ER for modification before transportation to the Golgi, and it is the UPR which attempts to process the build-up of unfolded proteins. During this process secretory proteins are downregulated to reduce protein levels, and an increase in the removal of misfolded or slowly folding proteins occurs through ER-associated degradation. During this process transcriptional factors can be activated, which ultimately results in increased IL-23 secretion.(335) For example, LPS induced IL-23p19 production was augmented by HLA-B27.(335) However, most subjects with psoriatic enthesitis do not possess the HLA-B27 gene therefore this theory therefore cannot account for the majority of SpA cases.(245)

5.6.1.1 IL-36

IL-36 is a pro-inflammatory cytokine, which when bound to its receptors (IL-36R) plays a role in psoriasis and other inflammatory skin disorders, by controlling IL-23 production.(336-338) While being present in healthy skin, IL-36 is upregulated in psoriatic skin, and is mainly produced by keratinocytes but also produced by monocytes, macrophages and dendritic cells.(337) When treated with a cream containing imiquimod, the TLR7 agonist, expression of IL-23 was induced and mice developed psoriasis like skin, but when deficient in IL-36α a reduced skin pathology was observed after treatment with the same cream.(339, 340)

5.6.1.2 Fungal/Bacterial

Based on the role of the IL-23/IL-27 axis in fungal immunity, it is also possible that bacterial or fungal adjuvants are responsible for triggering excessive IL-23 production. It has been well documented for almost six decades that the initiation of psoriasis lesions begins with immune activation in susceptible individuals following exposure to environmental stimuli.(341) Strong evidence exists for the induction of psoriasis following *Streptococcus pyogenes* infection, and psoriasis flare ups/ exacerbation have also been documented after bacterial (*S. Pyogenes(342, 343), S. aureus(344)*), fungal (*C. albicans (345, 346), Malassezia(347)*) and viral (papillomaviruses(348), retroviruses(349))

infections. Both fungal infections and psoriasis show propensity for the scalp, the nails and the groin areas.

The human skin is home to millions of commensal bacteria, fungi and viruses in a symbiotic relationship.(350) Regions of the skin can provide essential components for commensal bacteria, and in turn these bacteria can serve as a regulators of skin immune functions.(351) Usually the outer most layer of the epidermis acts as a barrier to prevent invasion of foreign pathogens, however this barrier is susceptible to injuries and in circumstances when trauma to the skin is experienced it may allow the entry of opportunistic microbial agents into the skin. Regions in which psoriasis is commonly observed, such as the scalp, are also colonised by *Malassezia* due to their requirement for subcutaneous glands to provide them with fatty acids.*(352)* An association between *Malassezia* and psoriatic skin legions has been reported and furthermore, treatment of these psoriasis patients with ketoconazole, an oral antifungal drug, has resulted in a marked improvement of the legions on their scalp, correlating with a decrease in yeast cell numbers.*(353)* Moreover, the prevalence of *C. albicans* in the intestine and faeces of patients with psoriasis was elevated compared to healthy controls. *C. albicans* was found in the faeces of up to 78% of patients with psoriasis compared with 29-54% of controls.(354, 355)

Microbial dysbiosis within the gut is emerging as a common factor between other SpA diseases also. The development of IBD has been associated with an imbalance or shift from a healthy gut microbiome, and animal studies are also providing evidence of the microbiome in the development of AS.(356, 357) When raised in germ free (GF) environments, HLA-B27 transgenic rats which would normally develop SpA were found to be absent of inflammatory diseases such as arthritis and colitis, but when typical bacteria found in the gut are reintroduced, these rats go on to develop joint disease.(358, 359) In the SKG model, where mice have a single point mutation in the ZAP-70 gene which leads to reduced T cell signalling, mice housed under specific pathogen free (SPF) or completely germ free (GF) environments remain healthy whereas those raised under conventional conditions, or when treated with microbial β-1,3-glucan (curdlan), spontaneously develop SpA, psoriasis uveitis and ileitis.(360) This model has also been linked to dysbiosis within the gut microbiota whereby the severity of arthritis and ileitis in these mice was dependent on the presence and composition of the host microbiome.(361) GF mice when treated with curdlan develop less severe arthritis than SPF mice, and recolonization of GF mice with altered Schaedler flora, a limited bacterial consortium, also increased incidence of arthritis however, this response was still lessened relative to those with unrestricted microbiota.

The SKG mouse model also directly links gut microbiota to IL-23 production and development of SpA. For SKG mice which are housed in SPF conditions but treated with the microbial component curdlan (β-1,3-glucan), the development of arthritis, enthesitis,

and ileitis is shown to IL-23 dependent.(328, 362) This was demonstrated by IL-23 neutralisation and subsequent treatment with curdlan. Mice housed in SPF conditions and treated with curdlan only suffered enthesitis, wrist and ankle joint arthritis, dactylitis, vertebral inflammation, ileitis resembling Crohn's disease, and uveitis, whereas those pre-treated with anti-IL-23 showed suppressed levels of axial spondylitis, peripheral arthritis, and enthesitis.(362) IL-23 neutralisation also was shown to alter the faecal microbiota composition in response to curdlan, supressing the bacteria associated with SpA like disease.(363) Furthermore, ER stress was not detected in mice housed in GF environments after treatment with curdlan, whereas signs of ER stress was observed in mice housed with specific pathogens along with IL-23 expression in the ileum. The only difference in these conditions was the presence of pathogens, which suggests gut microbiota promotes ER stress, and gut expression of IL-23. To add to this, development of arthritis, spondylitis, enthesitis and intestinal inflammation in curdlan-treated SKG mice also seems to show a dependence on IL-17. Mice with an IL-17 deficiency demonstrated a reduced severity rating for these particular diseases after treatment with curdlan. IL-23 production in SKG mice was shown to enhance IL-17A production in lymph nodes.(362)

Changes in how microbes in the gut interact with host cells may therefore be a factor in the pathogenesis of inflammatory IL-23 related diseases. Inflammatory cytokine such as IL-1β and IL-23 are produced by the terminal ileum and excessive production in response to commensal microbes may promote rheumatic disease at distal sites if these cytokines 'spill over' into the systemic circulation (Figure 5.7).(364)

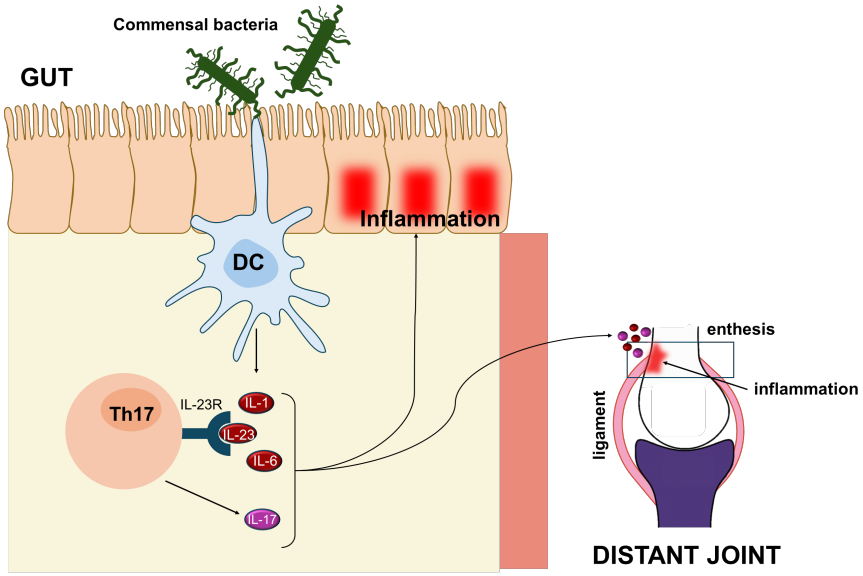

Figure 5.7 Commensal gut bacteria can stimulate production of inflammatory cytokines, including IL-1, IL6 and IL-23, within the intestinal mucosa. This triggers a Th17 response and increases IL-17 levels. While these cytokines help initiate local immune responses, excessive production has been postulated to lead to system circulation 'spillover', promoting inflammation at distant sites such as the joints. Figure adapted from reference(364).

Outside of the gut, other microbes have been linked to SpA development. *Chlamydia* species have been linked to the development of RA, spondylitis and skin lesions, with around 4-15% of individuals with *C. trachomatis* infection going on to develop RA.(365) To study this further, mice inoculated with *C. muridarum* suffered dose dependent inflammatory disease and production of IL-17 was impaired in mice with the SKG mutation when infected.(366) *Chlamydia* was able to spread from the site of infection to lymphoid organs and peripheral sites where IL-23 was produced, resulting in RA symptoms. The presence of chlamydia antigens in macrophages implicated these cells as the transporters in this process. Furthermore *C. trachomatis* triggers the ER stress response to produce IL-23.(367)

Due to the link between SpA, microbes, and the induction of IL-23 production through Dectin-1 signalling, other PRRs such as DC-SIGN have emerged as possible candidates for triggering excessive IL-23 production. Signalling through DC-SIGN via specific glycan residues present on the cell surface of commensal and pathogenic bacteria and fungi have shown a propensity to regulate IL-23 production, linking activation of DC-SIGN to the IL-23/IL-17 axis.(368) This raises the possibility that sustained signalling through DC-SIGN may contribute to the chronic induction of IL-23 in SpA. Despite a plausible connection, direct evidence for DC-SIGN as an upstream inducer of IL-23 in SpA is lacking.

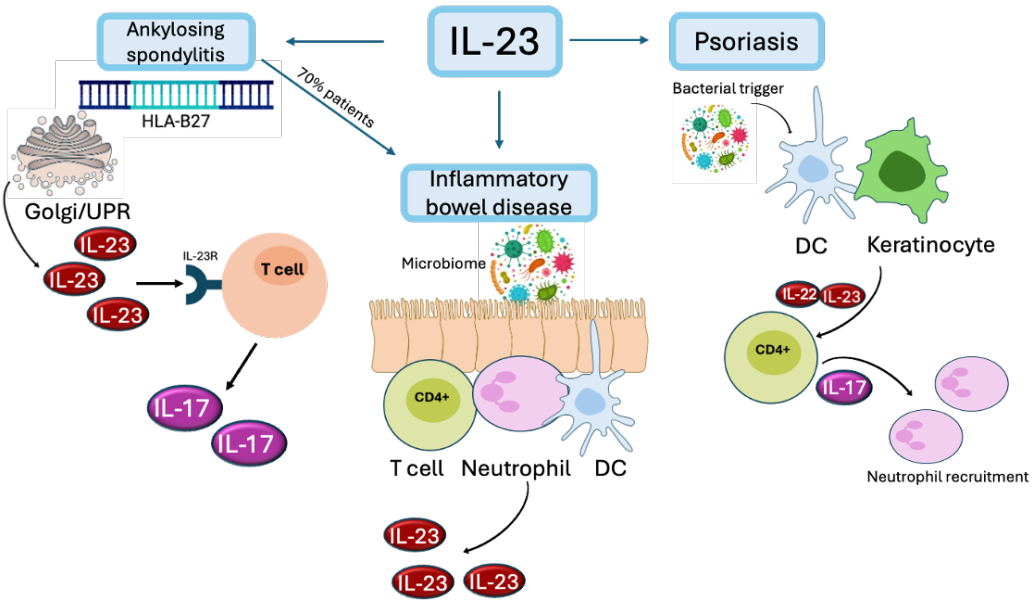

Figure 5.8 Schematic showing how IL-23 is produced in various spondyloarthropathies to cause inflammation.

5.7 Cellular producers of IL-23 in SpA

5.7.1 Dendritic cells

DCs play a central role in the immune system by capturing, processing, and presenting antigens to T cells, thereby initiating immune responses. Among their many functions, DCs are important producers of IL-23 helping to initiate immune signalling cascades that promotes inflammation and orchestrate specific immune responses, particularly through the actuation of Th17 cells. *In vivo* studies have shown that DCs stimulated by microbial ligands such as LPS(369), β-glucans(370) and peptidoglycans(371) are capable of producing IL-23. In the context of autoimmune disease, particularly psoriasis, the role of DCs in IL-23 production is well documented. Myeloid DCs are considered the primary source of IL-23 in psoriatic lesions, where overproduction of this cytokine drives IL-17A expression by Th17 cells in the dermis.(372, 373) Immunohistochemical analyses of psoriatic skin have also revealed p40 and p19 protein expression in dermal dendritic cells and increased p40 and p19 but not p35 (IL-12) mRNA in skin lesions.(372, 374).

5.7.2 Macrophages and monocytes

The role of macrophages in psoriasis has also be highlighted in mouse models where an IκB deletion results in inflamed psoriatic-like skin. When depleted of macrophages, these mice exhibit a pronounced reduction of the hyperproliferative, inflammatory skin phenotype.(375) Human studies have also described the importance of macrophages and monocytes in psoriatic skin where these cells migrate to the dermal/epidermal border in greater numbers than in healthy controls.(376) Similarly, in patients with Crohn's disease, the number of these $CD14^+$ macrophages were significantly increased compared with normal control subjects, and when isolated and stimulated with commensal bacteria, these cells produced large amounts of IL-23.(377-379)

In patients with hidradenitis suppurativa, macrophages expressing IL-23 have been detected within skin lesions.(380) Similarly in mouse models, and in histological analysis of intestinal tissue from individuals with IBD/Crohn's disease, macrophages (and DCs) have been shown to produce IL-23.(374, 375, 377) In addition, peripheral monocytes isolated from patients with enthesitis secrete higher levels of IL-23 upon stimulation compared to healthy controls.(381)

5.7.3 Neutrophils

Evidence is now growing that neutrophils may also be a source of IL-23 in SpA. A 2015 study showed that neutrophils which had infiltrated the colon of patients with IBD were the main cellular producers of IL-23 and therefore promotors of inflammation in this disease.(382) Alongside IBD, neutrophils have been associated with other IL-23 mediated diseases such as psoriasis. Neutrophils are recruited to the affected skin in

large numbers in psoriasis lesions but whether neutrophils in psoriatic lesions produce IL-23 and what triggers IL-23 production in this disease remains unknown but it may involve factors like IL-17 and TNF-α.(383, 384) The SKG mouse model of SpA shows neutrophil infiltration plays an important part in enthesitis lesions and Stavre and Bridgewood *et al.* showed that when stimulated with the fungal adjuvant zymosan, neutrophils isolated from non-inflamed human entheses are capable of producing IL-23.(385) Blood neutrophils stimulated with two different fungal adjuvants, mannan and zymosan, showed similar IL-23 induction capacity, while curdlan showed stronger induction capacity. Production of IL-23 from neutrophils *in vitro* has also been documented when the cells were stimulated with the drug imiquimod, a TLR7/8 agonist.(384)

5.7.4 Non immune cells / keratinocytes

It was previously thought that only immune cell derived IL-23 was disease relevant. However, non-immune cells such as keratinocytes and enterocytes have also been implicated in IL-23 production and disease onset. Keratinocytes constitute up to 90% of epidermal skin and therefore play a large role in psoriatic skin lesions.(386) IL-23 expression by keratinocytes was confirmed by immunostaining of skin sections and IL-23 was also found in the dermal compartment.(387) IL-23 expression was significantly higher in psoriatic lesional skin, compared with normal and psoriatic non-lesional skin. In mouse models, keratinocytes produced IL-23 in sufficient enough quantity to cause chronic skin inflammation and to confirm this result, selective loss of IL-23 in keratinocytes caused skin inflammation to be greatly reduced.(388)

5.8 Current limitations in IL-23 related research

Despite significant progress in understanding the role of IL-23 in inflammatory diseases, including SpA, there remain critical gaps in the knowledge regarding the specific stimuli that drive dendritic cells to produce IL-23 instead of IL-12. While both cytokines share the same p40 subunit, their divergent roles in immune regulation suggest distinct upstream triggers and signalling pathways. However, the precise mechanism by which DCs selectively induce IL-23 remain unclear. This ambiguity limits the ability to fully understand disease pathogenesis or design targeted interventions. In the context of SpA, no single pathogen or stimulus can account for all cases, raising the possibility that multiple diverse signals can trigger IL-23-driven inflammation.

Fungal and bacterial pathogens have emerged as a potential trigger, yet the interaction between these pathogens and the immune system, particularly in terms of their ability to induce excessive levels of IL-23, is still poorly understood. Further investigation is needed to identify other possible sources of IL-23 induction in the body and to understand how innate immune sensors and environmental signals influence the

cytokine profiles produced by DCs. A better understanding of these processes could illuminate why certain signals skew the immune response towards IL-23/IL-17 mediated inflammation rather than the classical IL-12/IFN-γ responses, offering a better comprehension of the immunopathology of these diseases and aiding in devising new avenues for therapeutic intervention.

5.9 Summary and research aims

As key producers of IL-23, DCs represent a central focus for understanding IL-23 regulation in inflammatory conditions. Since dysregulated IL-23 production is strongly implicated in the pathogenesis of SpA, investigating the molecular mechanisms that drive this process is essential. Stimulating DC with LPS, zymosan and β-glucan have all been shown to induce IL-23 production through TLR4, TLR2 and Dectin-1 respectively.(389, 390) Stimulation of the macrophage mannose receptor with *C. albicans,* a commensal organism, has also been implicated in IL-23 production in DCs.(82, 391)

In particular, DC-SIGN, a CLR on DCs which mediates glycan-dependent interactions, may also be involved in dysregulated IL-23 secretion. DC-SIGN is of particular interest to study due to its essential role in detecting and binding pathogens which have been previously linked to IL-23/IL-17 production, and its key role in shaping both innate and adaptive immune responses.(52, 392, 393) Studies have already implicated DC-SIGN in the modulation of TLR4/LPS induced IL-23 production.(52) Co-stimulation of DC-SIGN and TLR4 with mannose containing ligands and LPS led to an upregulation of inflammatory cytokines, including the IL-23 p40 subunit. However, under conditions employing fucose ligands, a downregulation of IL-23 was observed.(92) In contrast, other authors have demonstrated that engagement of DC-SIGN with the mannose containing ligand ManLAM inhibits Dectin-1 induced IL-23.(394) These divergent outcomes highlight a context-dependent role for DC-SIGN in regulating IL-23 underscoring the need for further studies to clarify how ligand-specific signalling integrates with other CLR and TLR pathways in shaping inflammatory responses.

Therefore, the study of DC-SIGN-glycan signalling pathways may begin to unravel how immune recognition contributes to chronic inflammation in SpA, offering potential insights into novel therapeutic strategies that target upstream regulatory networks of IL-23 rather than its downstream effects. Building on the glycan-GNPs explored in Part A, which provided a well-defined platform for probing DC-SIGN binding affinity and interaction modes, this section extended their use to explore how such glycan-mediated engagements might influence DC-driven IL-23 production. The multivalent display of glycans on a nanoparticle surface in this instance afforded closer physiological relevance, as they more closely resemble the multivalent nature of the glycocalyx than free ligands, and provided scope for novelty within this project.

Chapter 7 used the G5-glycans synthesised in part A as fungal/bacterial mimics to explore how DC-SIGN engagement influenced IL-23 production in dendritic cells when co-stimulated with a variety of TLR ligands and fungal adjuvants. The aim was to identify which CLR-TLR co-pathways may be involved in excessive IL-23 production in SpA and if it is related to fungal/bacterial activation. Attention was given to whether IL-23 production could be influenced by glycan type or binding affinity. This chapter also included blocking experiments to determine whether immune modulation was mediated only by DC-SIGN co-signalling or if other CLR receptors contributed to the observed effects. In addition, the impact of G5-glycan-DC-SIGN signalling on Th cell development was explored by characterising the cytokines produced upon co-stimulation with LPS and quantifying T cell proliferation.

Chapter 8 built upon the blocking experiments in Chapter 7 by developing a GNP-based pull down method, incorporating a covalent affinity tag. This method was designed to identify additional receptors on the DC cell surface which may participate in signalling pathways leading to IL-23 production.

Chapter 6 – Materials and Methods

6.1 Ethics approval

The investigation was approved by NRES Committee Yorkshire & The Humber - South Yorkshire (14/YH/0087).

6.2 Materials

Molecular biology grade porcine trypsin and molecular biology grade dithiothreitol (DTT) was purchased from Promega. 4-fluorosulfonyl benzoic acid (**16**), molecular biology grade iodoacetamide (IAA), potassium hexacyanoferrate(II) trihydrate, formic acid, ammonium bicarbonate, triton X, acetonitrile and DMF were purchased from Sigma Aldrich. Triethylamine, fluorescein isothiocyanate (FITC), ammonium chloride and potassium ferricyanide were purchased from Acros Organics. β-mercaptoethanol was purchased from Bio-Rad. LA-EG_{11}-NH_2 (**15**) was synthesised in-house using previously established protocols by Darshita Budhadev. MS: calculated m/z for $C_{32}H_{65}N_4O_{12}S_2$ (LA-EG_{11}-NH_2) $[M+H]^+$ 733.40, found 734.00.(119)

RMPI 1640 media and PBS tablets were purchased from Gibco. Foetal Bovine Serum, penicillin/streptomycin, Trypan Blue, DMSO, Normal Mouse Serum, Human IgG, bovine serum albumin and LPS from *E.Coli* were purchased from Sigma-Aldrich. Flow cytometry staining antibodies, viakrome808, fixation buffer, brilliant stain buffer and permeabilisation buffer were purchased from either BioLegend®, BD biosciences (BD horizon™, BD pharmingen™) or Beckman coulter. $CD14^+$, $CD4^+$ and $CD25^-$ antibody microbeads, T cell activation kit, magnetic LS/MS columns and MACS BSA staining buffer were purchased form Miltenyi Biotech. Pam2CSK4, Pam3CSK4 and HKST were purchased from InvivoGen. Mab161 was purchased from Bio-Techne and Clone15-2 was purchased from Bio-Rad. CFSE and C18 spin columns were purchased from Thermo Fisher. Lymphoprep was purchased from Stemcell. IL-23 and IL-10 ELISA kits were purchased from Invitrogen. LEGENDplex™ Human Th Cytokine Panel was purchased from BioLegend. GM-CSF and IL-4 were purchased from PeproTech. Tween20 was purchased from Fisher Scientific. 10X Red cell lysis buffer and endotoxin free water was purchased from VWR international. Cell culture plates were purchased from Cornings.

6.3 General instrumentation and computation

^1H NMR spectra were measured at 25° C on a 500 or 400 MHz Bruker spectrometers using D_2O, Methanol-d4 or Chloroform-d with the residual solvent as the internal standard at room temperature. Chemical shifts are given in parts per million relative to TMS and the coupling constants (*J*) are given in Hertz. High resolution mass spectra

(HR-MS) for ligands were obtained on a Bruker Impact QqTOF II mass spectrometer and m/z values are reported in Daltons to four decimal places. Liquid chromatography mass spectrometry (LC-MS) was used to analyse all other ligand samples and was performed using a Bruker AmaZon speed mass spectrometer and are quoted to two decimal places. Peptide separation was performed on a Bruker nanoElute II nanoflow or a Vanquish Neo UHPLC. Mass spectrometric analysis of peptides was performed on a timsTOF Pro 2 mass spectrometer (Bruker Daltonics) or an Orbitrap Eclipse Tribrid mass spectrometer (Thermo Fisher Scientific). UV-vis absorption spectra were recorded on a Varian Cary 50 bio UV-Visible Spectrophotometer over 200-800 nm using 1 mL quartz cuvette with an optical path length of 1 cm or on a Nanodrop 2000 spectrophotometer (Thermo scientific) over the range of 200-800nm using 1 drop of the solution with an optical path length of 1 mm. The hydrodynamic diameters were recorded on a Malvern ZETASizer-Nano using disposable polystyrene cuvettes. Centrifugation was performed using either a Hettich Universal 320/320R, a Thermo Scientific Heraeus Fresco 17, or an Eppendorf 5810R depending on the speed and volume, at room temperature (r.t) unless otherwise stated. All fluorescence spectra were recorded on a Cary Eclipse Fluorescence Spectrophotometer using a 0.70 mL quartz cuvette. Flow cytometry was conducted on a CytoFLEX LX using corning FACS tubes. OD for ELISA cytokine measurements were recorded on a BioTek citation 5 imaging plate reader. Microscopy images were taken on an Evos XL core. Cell counting was performed on a BioRad TC20 automated cell counter using BioRad dual chamber cell counting plates and trypan blue solution (Sigma Aldrich). Light microscopy was performed on an Olympus inverted light microscope and images were taken on an EVOS FL digital inverted fluorescence microscope.

All numerical data were analysed and plotted using origin 2029b or Graphpad Prism10 software.

6.4 Endotoxin removal

G5-EG_n-glycans were filtered through 0.22 um syringe filters then treated with Pierce™ High Capacity Endotoxin Removal Spin Columns (0.5 mL) according the manufacturer's instructions. Briefly, columns were regenerated 0.2N NaOH, washed with 2M NaCl, and endotoxin-free water, and equilibrated three times in 50 mM PBS pH 6-8. GNP samples were then loaded onto the equilibrated resin, capped and gently mixed end-over-end for 1 hr at 4 oC. Following incubation, the bottom closure was removed and the sample recovered by centrifugation at 500 x *g* for 1 minute. Where necessary, samples were re-applied to a freshly regenerated column for additional passes to further reduce endotoxin levels. All consumables, buffers and water were endotoxin free and non-pyrongenic. Samples were assayed for endotoxin content using the Pierce™ Rapid Gel Clot Endotoxin Assay to verify removal.

6.5 Cell culture

6.5.1 DC differentiation and stimulation

Peripheral blood was collected from healthy donors and the $CD14^+$ monocytes were isolated using CD14 microbeads (130-050-201, Miltenyi Biotec) according to the manufacturer's protocol. Monocytes (1 x 10^6/mL) were plated in RPMI 1640 media supplemented with 10% Fetal Calf Serum, streptomycin (100 units/mL) and penicillin (100 units/mL), and stimulated with 100 ng/mL granulocyte-macrophage colony stimulating factor (GM-CSF) and 50 ng/mL interleukin-4 (IL-4). After 3 days, 0.5 mL media was removed and replaced with fresh media containing IL-4 (50 ng/ml) and GM-CSF (100 ng/ml) for a further 3 days in order to obtain immature Mo-DC. On day 6, suspensions of MoDCs (1 x 10^5) in fresh RPMI 1640 (200 µL) were stimulated by addition of LPS (10 ng/mL), HKST (10^6 cells), PAM2CSK4 (100 ng/mL) or PAM3CSK4 (100 ng/mL) alone or in the presence of G5-EG_n-glycan (150 nM) or monovalent ligand (50 mM or 75 µM) for 24 hrs at 37 ^oC, 5% CO_2. Cells were harvested for flow cytometry and supernatant was collected and stored at -80 ^oC until cytokine analysis

6.5.2 DC-SIGN and Mannose receptor blocking

MoDCs (1 x 10^5) isolated and differentiated as described in Section 6.5.1 were pre-incubated with α-DC-SIGN (10 µg/ml, mab161, Bio-Techne) or α-mannose receptor (20 µg/ml, clone 15-2, BioLegend) or both in 100 µL RPMI at 37 ^oC, 5% CO_2. After 30 minutes, 100 µL RPMI containing LPS (10 ng/ml) alone or with GNP-glycan (150 nM) or monovalent ligand (50 mM or 75 µM) was added and cells were incubated for 24 hrs at 37 ^oC in the presence of 5% CO_2. After 24 hours the supernatant was collected and stored at -80 ^oC until cytokine analysis.

6.5.3 DC/T cell co-culture

$CD4^+CD25^-$ T cells were isolated from the peripheral blood of healthy donors using positive selection $CD4^+$ T cell isolation kit (130-096-533, Miltenyi Biotec) and depletion with CD25 Microbeads II (130-092-983, Miltenyi Biotec) according to the manufacturers protocols and stored in 20% DMSO in FCS at -80 ^oC for short term storage or -196 ^oC in liquid nitrogen for long term storage. When required, T cells were defrosted and stained with CellTrace™ violet (thermofisher) according to the manufacturers protocol. Mo-DCs isolated from the same donors using CD14 microbeads (130-050-201, Miltenyi Biotec) were seeded at 5 x 10^4 in 400 µL of RPMI 1640 media supplemented with 10% Fetal Calf Serum, streptomycin (100 units/mL) and penicillin (100 units/mL), and stimulated by the addition of LPS (10 ng/ml) alone or in the presence of G5-EGn-glycan (150 nM) or monovalent ligand (50 mM) and incubated at 37 ^oC, 5% CO_2. After 24 hrs, 100 µL of media was removed and 2.5x10^5 T-cells were added in 100 µL cell culture media.

Furthermore, $2.5x10^5$ $CD4^+CD25^-$ T cells were activated with Anti-Biotin MACSibead™ particles loaded with anti-CD3, anti-CD28 and anti-CD2 according the manufacturers protocol (130-092-357, Miltenyi Biotec). Cells were incubated for 5 days at 37 °C, 5% CO_2 then cells were collected for flow cytometry and the supernatant was stored at -80 °C until cytokine analysis.

6.6 Flow cytometry

Expression of cell surface markers and T cell proliferation was measured by flow cytometry. Briefly, cultured cells were collected by centrifugation at 400 x *g* for 5 minutes, washed with PBS and stained with ViaKrome 808 Fixable Viability Dye (Beckman Coulter) in the dark for 10 minutes. Cells were pelleted at 400 x *g* for 5 minutes then washed with PBS and treated with blocking buffer (hIgG and normal mouse serum) followed by BD Horizon™ brilliant stain buffer (BD biosciences) at 4 °C to prevent non-specific binding. Cells were washed and pelleted and, depending on the desired stain, were then incubated with the desired antibodies (given in Table 6.1) in the dark for 30 minutes at 4 °C. After staining, cells were washed with PBS and suspended in 200 µL of MACS BSA buffer if analysed immediately, or if analysing >24 hrs later cells were fixed with 4% PFA for 15 minutes before washing and resuspended in MACS BSA. Data acquisition was performed using a CytoFLEX LX. The data for dendritic cell markers and PBMC phenotyping was analysed using the Beckman coulter CytExpert acquisition and analysis software. T cell proliferation was analysed with FlowJO, using the T cell proliferation modelling tool.

Table 6.1 Table of antibodies used in flow cytometry for each experiment.

Experiment	Antibodies (clone, supplier)
DC surface expression	CD80-APC(2D10.4, eBioscience™), CD86-PE-Cy™7 (2231, BD pharmingen™), CD209-FITC (9E9A8, BioLegend®) and CD14-Brilliant Violet605™ (M5E2, BioLegend®)
cell proliferation	CD209-FITC (9E9A8, BioLegend®), CD4-APC (RPA-T4, BD pharmingen™)
PBMC phenotyping	CD3-BUV395 (SK7, BD Horizon™), CD19-BUV395 (SJ251, BD Horizon™), HLA-DR-BV421 (G46-6, BD Horizon™), CD14-Brilliant Violet605™ (M5E2, BioLegend®), CD1c-PE-Vio770 (AD58E7, Miltenyi Biotec), CD141-APC (1A4, BD pharmingen™), CD123-FITC (6H6, BioLegend®), CD163-PE (GHI.61, BD pharmingen™)

6.7 IL-10 and IL-23 ELISA

For the detection of IL-10 and IL-23, culture supernatants were collected after 24 hrs for MoDC stimulation and stored at -80 °C until analysis. IL-23 and IL-10 ELISAs were performed as follows. Nunc Maxisorb immunosorbent 96-well ELISA plates were coated with 2 µg/mL capture antibody (Thermo Scientific) in PBS at 4°C overnight. Plates were then washed with 0.1% Tween 20/PBS and blocked for 1 hour in 2% BSA in 0.1% Tween-20/PBS. Samples were subsequently incubated for 1 hour at room temperature before washing and incubation with 1 µg/mL biotinylated detection antibody (Thermo Scientific) for 1 hour. Plates were then washed and incubated with streptavidin–horseradish peroxidase (Thermo scentific) for 20 minutes. After washing, TMB was used as a chromogenic substrate (Thermo Scientific). The reaction was stopped with 2N H_2SO_4, and OD was measured at 450 nm. A standard curve was obtained from a 7-point serial dilution of protein standard and used to calculate IL-23 and IL-10, expressed as pg/mL.

6.8 Multiplex cytokine analysis

Multiplex cytokine analysis was performed using the LEGENDplex™ (Human T Helper Cytokine Panels Version 2) kit (BioLegend) according to the manufacturer's instructions. Briefly, the supernatant from the DC + T cell co culture samples were collected after 5 days and stored at −80 °C until analysis.

The assay was performed in a 96-well filter plate format. Standards were prepared by 1 in 4 serial dilution to generate a standard curve for each cytokine. Samples and standards (25 µL) were incubated with mixed capture beads (25 uL) and assay buffer (25 µL) for 2 hours at room temperature with shaking at 500 rpm in the dark. Wells were washed twice with 200 µL washing buffer using a vacuum manifold to remove unbound reagents. Detection antibodies (25 µL) were added and the samples incubated for 1 hour at 500 rpm in the dark. Streptavidin-PE solution (25 µL) was then added and incubated for 30 minutes at 500 rpm in the dark. Wells were washed twice with 200 µL washing buffer, using a vacuum manifold to remove unbound reagents, then beads were resuspended in 150 µL wash buffer and analysed using a CytoFLEX S cytometer (Beckman Coulter). Data were acquired using Cytexpert and analysed with LEGENDplex™ Data Analysis Software (BioLegend). Cytokine concentrations were calculated based on standard curves and expressed as pg/mL.

6.9 ICP-MS

1 x 10^5 cells were treated with 50 nM G5-glycans for 24 hours. Cells were collected, counted and frozen at -80 °C in PBS until further analysis. 2 x 10^4 cells were treated with Aqua Regia (100 µL) in glass vial, and left for 5 hours. Then, each digested sample was

diluted to 5 mL in deionised water. A series of gold standard solutions (0, 0.1, 1, 10, 50, 300 µg/L) were prepared at the same time. Samples were given to Stephen Reid in the School of Earth and Environment at the University of Leeds and analysed on a Thermos iCAP Qc ICP-MS. The quantity of Au in µg/L was converted into GNP per cell using the volume and weight of a 5 nm GNP and the number of cells in the sample.

6.10 Protein production and labelling

6.10.1 DC-SIGN, DC-SIGNQ274C, DC-SIGN-atto643

The DC-SIGN was produced and purified as described in Section 2.3.1, and its cysteine point mutation variants, DC-SIGN Q274C, was produced, purified and labelled with maleimide-Atto643as described in section 2.3.2.

6.10.2 BSA-FITC

To a solution of BSA (2 mg/mL, 4 mL, 120 nmol, 1 eq) in sodium bicarbonate (0.1 M, pH 9.0) was added FITC (1 mg/mL DMSO, 0.47 mL, 10 eq) and the reaction incubated at 4 ^{o}C in the dark for 4 hours. NH_4Cl (0.5 M, 0.5 mL) was added to a final concentration of 50 mM and incubated for 2 hours. The resulting solution was washed HEPES binding buffer (20 mM HEPES, 100 mM NaCl, 10 mM $CaCl_2$, pH 7.8) using an Amicon 30kDa MCWO filter. Concentration was calculated by Equation 8.4.

6.11 Ligand synthesis

LA-EG_n-dimannose (11a-c) and LA-EG_n-fucose (10a-c) were prepared as described in Chapter 2**.** The sulfonyl fluoride affinity tag (**17**) was prepared as follows.

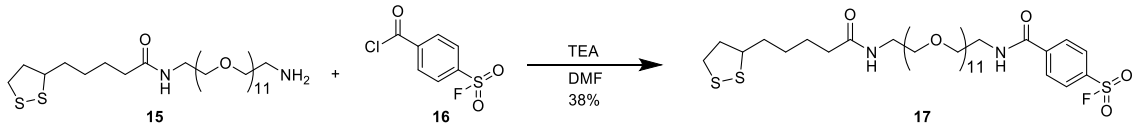

15 **16** **17**

Amine **15** (50 mg, 0.068 mmol) and TEA (10 µL, 0.068 mmol) were dissolved in dry DMF (3 mL), then 4-fluorosulfonylbenzoyl chloride **16** (15 mg, 0.068 mmol) in dry DMF (1 mL) was added dropwise. The reaction was stirred at RT for 3 days. The reaction was concentrated *in vacuo* and the residue purified by FCC (silica, 0-10% MeOH in CH_2Cl_2). The desired fractions were combined and concentrated in vacuo to afford the desired product as a yellow oil (24 mg, 0.026 mmol, 38%).

^{1}H NMR (501 MHz, $CDCl_3$) δ 8.12 (d, *J* = 8.3 Hz, 2H), 8.06 (d, *J* = 8.7 Hz, 2H), 7.69 – 7.40 (m, 1H), 6.21 (s, 1H), 3.84 – 3.48 (m, 42H), 3.43 (q, *J* = 5.2 Hz, 2H), 3.23 – 3.04 (m, 2H), 2.53 – 2.38 (m, 2H), 2.18 (td, *J* = 7.5, 1.3 Hz, 2H), 1.90 (dq, *J* = 13.9, 6.9 Hz, 1H), 1.76 – 1.57 (m, 4H), 1.56 – 1.40 (m, 2H), 1.36 – 0.73 (m, 2H).**^{13}C NMR** (126 MHz, $CDCl_3$) δ 171.79, 164.19, 140.27, 134.13, 133.93, 131.11, 131.03, 130.94, 127.70,

127.56, 127.45, 126.50, 69.55, 69.53, 69.51, 69.49, 69.46, 69.44, 69.21, 69.20, 68.90, 68.53, 55.42, 39.22, 39.20, 38.15, 37.45, 35.47, 35.32, 33.66, 32.94, 28.68, 27.92, 24.60, 24.37, 23.93. **^{19}F NMR** (376 MHz, $CDCl_3$) δ 65.96. **HRMS**: calculated m/z for $C_{39}H_{68}FN_2O_{15}S_3$ $(M+H)^+$ 919.3766; found 919.3792

6.12 Gold nanoparticle preparation

G5- G13- and G27-glycans were prepared as described in Section 2.4.2. G13- and G27-glycan:SF were prepared by premixing 5 mM solutions of glycan and affinity tag in a 5:1, 10:1 or 20:1 v/v ratios then adding to G13- or G27- BSPP as described in Section 2.4.2.5.

6.13 Dynamic light scattering

Dynamic light scattering was carried out as described in Section 2.6. The resulting Dh values are reported as xc ± ½ FWHM. All protein containing samples were performed by mixing G27-glycan:SF with DC-SIGN in a 1:25 ratio.

6.14 Affinity pull down assay

6.14.1 Binding affinity

DC-SIGN-atto643 was mixed with G27-glycans/sunfonyl fluoride at varying concentrations of DC-SIGN (1, 2, 4, 8, 16, 32, 64 nM) at a fixed protein to gold ratio of 25:1 in binding buffer with 1% triton (20 mM HEPES, 100 mM, NaCl, 10 mM CaCl2, pH 7.8). The mixture was incubated on a shaker at 4 °C for 2 hours then centrifuged at 6000 x *g* for 15 minutes. The supernatant was removed and the fluorescence intensity measured on a Cary Eclipse Fluorescence Spectrophotometer using a 0.70 mL quartz cuvette under a fixed λ_{ex} of 630 nm over a range of 650–800 nm. The excitation and emission slit widths and instrument PMT voltages were adjusted to compensate the low fluorescence signals at low concentrations. The fluorescence intensity of the protein in the absence of the G27-glycans, recorded under identical experiment conditions, were used to calculate % bound using Equation 8.1, and the resulting % bound-concentration relationship was fitted by Hill's Equation 8.2 to derive the apparent binding K_d values.

6.14.2 Covalent labelling yield

DC-SIGN-atto643 (25 nM) was mixed with G27 glycan/sunfonyl fluoride (1 nM) in 400 µL of binding buffer with 1% triton (20 mM HEPES, 100 mM, NaCl, 10 mM CaCl2, pH 7.8). The mixture was incubated on a shaker at 4 °C for 2 hours then centrifuged at 6000 x *g* for 15 minutes at 4 °C. The supernatant was carefully removed and the fluorescence intensity (F1) measured on a Cary Eclipse Fluorescence Spectrophotometer using a 0.70 mL quartz cuvette under a fixed λ_{ex} of 630 nm over a range of 650–800 nm. The pellet was washed with 400 µL HEPES containing 1% triton followed by centrifugation at 6000

x *g* for 15 minutes. The supernatant was carefully removed and 400 µL of 50 mM mannose in binding buffer with 1% triton was added to the pellet and the samples incubated at RT for 20 minutes, followed by centrifugation at 6000 x *g* for 15 minutes. The supernatant was carefully removed and measured for its fluorescence intensity (F2). The sum of F1 and F2 was then compared to the fluorescence intensity of the protein in the absence of the G27-glycans, recorded under identical experiment conditions were used to calculate the covalent labelling yield through Equation 8.3.

Alternatively BSA-FITC (25 nM) was mixed with G27 glycan/sunfonyl fluoride (1 nM) in 400 µL of binding buffer with 1% triton (20 mM HEPES, 100 mM, NaCl, 10 mM CaCl2, pH 7.8). The mixture was incubated on a shaker at 4 ^{o}C for 2 hours then centrifuged at 6000 x *g* for 15 minutes at 4 ^{o}C. The supernatant was carefully removed and the fluorescence intensity (F1) measured on a Cary Eclipse Fluorescence Spectrophotometer using a 0.70 mL quartz cuvette under a fixed λ_{ex} of 495 nm over a range of 510-630 nm. The fluorescence intensity of the protein in the absence of the G27-glycans, recorded under identical experiment conditions were used to calculate the covalent labelling yield as previously described.

6.14.3 Time course of covalent labelling

DC-SIGN-atto643 (25 nM) or BSA-FITC (25 nM) was mixed with G27 glycans/sulfonyl fluoride probes (1 nM) in 400 µL of binding buffer with 1% triton (20 mM HEPES, 100 mM, NaCl, 10 mM CaCl2, pH 7.8) and incubated on a shaker at 4 ^{o}C for 0.5, 1, 2, 6, 24 hours and 48 hours, then the same procedure as described in Section 6.14.2 was performed.

6.14.4 DC-SIGN vs BSA selectivity

DC-SIGN-atto643 (25 nM) and BSA-FITC (125 nM) were mixed with G27 glycans/sulfonyl fluoride probes (1 nM) in 400 µL of binding buffer containing 1% triton (20 mM HEPES, 100 mM, NaCl, 10 mM CaCl2, pH 7.8) and incubated on a shaker at 4 ^{o}C for 2, 24 and 48 hours, then the same procedure as described in Section 6.14.2 was performed, measuring at both a λ_{EX} of 630 nm over a range of 650–800 nm followed by λ_{EX} of 495 nm over a range of 510-630 nm.

6.14.5 Proteomics

DC-SIGN (DC020) (200 nM) was mixed with G13-dimannose:SF(5:1) or G13-fucose (5:1) (20 nM) in 1 mL HEPES buffer containing 1% triton (20 mM HEPES, 100 mM, NaCl, 10 mM CaCl2, pH 7.8) and incubated on a shaker at 4 ^{o}C for 48 hours. The mixture was centrifuged at 17000 x *g* for 60 minutes and the supernatant removed. 50 mM mannose in HEPES buffer with 1% triton X was added to the pellet and the mixture agitated on a shaker for 20 minutes at RT. The mixture was then centrifuged at 17000 x *g* for 60

minutes and the supernatant removed. This washing step was repeated. The resultant pellet was further washed with 50 mM ammonium bicarbonate buffer (50 mM ammonium bicarbonate, pH 8.0) and the mixture was centrifuged at 17000 x *g* for 60 minutes and the supernatant removed.

6.14.5.1 On-GNP trypsin digestion

The pellet was resuspended in 400 µL 50 mM ammonium bicarbonate buffer pH 8.0. Dithiothreitol (DTT) was added to a final concentration of 10 mM and the solution incubated at 37 ^{o}C for 1 hour. Iodoacetamide (IAA) was added to a final concentration of 20 mM and the mixture incubated at RT for 1 hour in the dark. A further 10 mM of DTT was added for 10 minutes at 37 ^{o}C then the mixture was centrifuged at 17000 x *g* for 60 minutes and the supernatant removed. The pellet was resuspended in 250 µL ammonium bicarbonate buffer pH 8.0.and trypsin was added in a 50:1 w/w DC-SIGN:trypsin ratio, assuming 65% covalent labelling of the original DC-SIGN concentration. The mixture was shaken at 300 rpm at 37 ^{o}C for 16 hours, then centrifuged at 17000 x *g* for 60 minutes. The supernatant was collected. The pellet was washed with 250 µL 50% ACN centrifuged at 17000 x *g* for 60 minutes and the supernatant collected. This washing step was repeated once more. The combined supernatants were then lyophilised, and desalted using a Pierce C18 spin column according to the manufacturer's instructions. After lyophilising again, the resulting desalted peptides were resuspended in 0.1% formic acid. Peptide separation was performed on a Bruker nanoElute II nanoflow UHPLC system equipped with 5mm PepMap™ Neo Trap Cartridge (product-174500) and a IonOpticks Aurora Ultimate, 15 cm, 75 µm ID, 1.6 µm particle size, 120 Å pore size. The column was maintained at 50°C. A 40 min LC was used for peptide separation, with a flow rate of 200 nL/min. The mobile phases consisted of: Solvent A: 0.1% formic acid in water, Solvent B: 0.1% formic acid in acetonitrile. The gradient profile was as follows: 10% B to 25% B over 20, min, 25% B to 35% B over 8 min, hold at 95% B for 8 min.

Mass spectrometric analysis was performed on a timsTOF Pro 2 mass spectrometer (Bruker Daltonics) operated in DDA PASEF mode (Parallel Accumulation Serial Fragmentation). The instrument was coupled online to the nanoElute II via a CaptiveSpray nano-electrospray ionization source. Instrument settings included: Capillary voltage: 1.6 kV, dry gas: 3.0 L/min, dry temperature: 200°C. TIMS settings: Mass range: m/z 100–1700, ramp rate: 9.43 Hz, ramp time: 100 ms, range: $1/K_0$ = 0.7–1.5 V·s/cm², 1 MS + 10 PASEF MS/MS scans per cycle. Total cycle time: 1.17 sec, charge state: 0 – 5.

6.14.5.2 Off-GNP trypsin digestion

The pellet was resuspended in 25 µL of Laemmli buffer (1% SDS, 10% glycerol, 61.5 mM tris-HCl (pH 6.8) 0.02% bromophenol blue) containing 2.5% mercaptoethanol and heated to 90 °C for 10 minutes. The sample was centrifuged at 17000 x *g* for 60 minutes and the supernatant collected. The resulting pellet was then retreated in this manner. The combined supernatants were then resolved by SDS page using a 5% stacking gel and 17% running gel, or submitted to the Astbury centre for analysis:

Samples were subjected to S-TRAPTM digestion, as per the instructions (PROTIFI, NY, USA). Briefly, Samples were initially reduced and alkylated using 20 mM DTT for 10 minutes and 40 mM IAA for 30 minutes respectively followed by acidification of samples using 5.5% phosphoric acid. Acidified samples were then trapped on S-TRAP columns after the addition of sample buffer (100 mM TEAB in 90% methanol) and 1 µg trypsin. Followed by washing with sample buffer, S-TRAP is covered with trypsin and incubated at 47 ˚C for 90 minutes. Eluted peptides were concentrated in the speedvac concentrator and reconstituted in 0.1% FA.

LC-MS/MS analyses of peptide mixtures were done using Vanquish Neo UHPLC system connected to Orbitrap Eclipse Tribrid mass spectrometer (Thermo Fisher Scientific). Prior to LC separation, tryptic digests were concentrated and desalted using a trapping column (300 µm × 5 mm, µPrecolumn, 5µm particles, Acclaim PepMap100 C18, Thermo Fisher Scientific) at room temperature. After washing of trapping column with 0.1 % formic acid (FA), the peptides were eluted (flow rate – 0.25 nl/min) from the trapping column onto an analytical column (EASY spray column, Acclaim Pepmap100 C18, 2µm particles, 75 µm × 500 mm, Thermo Fisher Scientific) at 45 ˚C by a 75 minute linear gradient program (2-40 % of mobile phase B; mobile phase A: 0.1 % FA in water; mobile phase B: 0.1 % FA in 80 % ACN). Equilibration of the trapping column and the analytical column was done prior to sample injection to the sample loop. The analytical column with the emitter was directly connected to the ion source.

MS data were acquired in a data-dependent strategy. The survey scan range was set to m/z 350-2000 with the resolution of 120,000 (at m/z 200) with a target value of 3×106 ions and maximum injection time of 50 ms. HCD MS/MS (30% normalized fragmentation energy) spectra were acquired for maximum injection time of 54 ms and resolution of 30 000 (at m/z 200). Dynamic exclusion was enabled for 60 s. The isolation window for MS/MS fragmentation was set to 1.2 m/z.

The mass spectrometric RAW data files were analyzed using the Proteome Discoverer software (Thermo Scientific, version 3.0.0757). Searches were done against a cRAP database containing protein contaminants like keratin, trypsin, etc., and FASTA file consisting of dedicated DC-SIGN sequence. Oxidation of methionine, deamidation (N, Q) acetylation (protein N-terminus), modifications from affinity tag, dimannose ligand and

fucose ligand as optional modification and carbamidomethyl on cysteine as static modification were used. Trypsin (full) enzyme with 2 allowed miss cleavages were set. Mass spectra were searched using precursor ion tolerance 10 ppm and fragment ion tolerance 0.02 Da. Peptides and proteins FDR threshold set to <0.01 and proteins with at least one peptide were taken for further analysis.

Acknowledgement to the Mass Spectrometry facility at Faculty of Biological Sciences, University of Leeds, Leeds, UK, for measurement of samples using The Orbitrap Eclipse Tribrid and Vanguish Neo UPLC that is funded by the Wellcome Trust (223810/Z/21/Z).

Chapter 7 – Exploring the use of G5 glycans to modulate IL-23 and IL-10 production and downstream T cell responses via DC-SIGN

7.1 Introduction

The immune system relies on carbohydrate binding proteins, such as DC-SIGN, to monitor signals from the cell's external environment. To do so, they bind pathogen associated molecular patterns (PAMPs) on microbes, interpret these binding events and relay this information to the cell and its neighbours to initiate an appropriate cellular response.(93) In DCs, these lectins not only serve as molecular anchors enabling cells to latch onto pathogens, but they facilitate internalisation and trafficking of pathogens into endolysosomal compartments where they are processed to later be presented as antigens on MHC molecules.(395) They also play a critical role in regulating DC maturation which occurs upon recognition of certain pathogenic components, and leads to the upregulation of the accessory molecules necessary for T cell co-stimulation, thereby activating T cells.(396)

Importantly, beyond pathogen uptake and T cell engagement, lectins are important molecules in the modulation of immune responses, capable of triggering specific cytokine production and therefore tailoring the immune response towards different T cell lineages (Th1, Th2, Th17, Th9 etc) depending on the pathogen recognised.(4, 397) In isolation, recognition of pathogens by lectins is often not enough to trigger these responses but in cooperation with different innate signalling molecules such as TLRs, cytokine production is activated and an immune response is generated.(398) Upon pattern recognition, some lectins such as Langerin can promote immune tolerance and suppress excessive inflammation, while others like Dectin-1 and Mincle initiate strong pro-inflammatory responses.(399-401) DC-SIGN occupies a unique position in this spectrum, capable of both regulating tolerance and driving inflammation depending on its ligand and context.(52)

A number of studies have demonstrated that DC-SIGN is capable of distinguishing between distinct glycan 'fingerprints' on pathogens, which leads to different downstream effects on cytokine production. For example, the effects of LPS recognition by TLR4 can be modulated by co-engagement of DC-SIGN, switching between pro-inflammatory and regulatory cytokine profiles depending on the specific glycan recognised.(52) Mannose containing ligands have been reported to increase production of the inflammatory cytokines IL-12 and IL-6, key cytokines involved in promoting both the Th1 and Th17 immune response associated with tissue inflammation and many auto-inflammatory

diseases.(235, 402) On the other hand, fucose containing ligands such as the Lewis antigens have demonstrated an ability to modulate the immune response towards tolerance, by decreasing the amount of IL-12, IL-6 and IL-23 observed when compared to stimulation by LPS alone.(92) Instead, fucose tends to trigger upregulation of chemokines and IL-10, which are associated with humoral immune responses and the activation of antibody producing B cells.(403)

This ligand specific signalling is believed to arise from differences in how DC-SIGN interacts with intracellular adaptor proteins following receptor engagement. Mannose ligands led to the recruitment of the raf-1 protein to the signalosome complex, which promotes NF-κB p65 subunit acetylation, leading to increased transcription of inflammatory cytokines and a Th1 immune response.(331) In contrast, fucose ligands fail to recruit raf-1 and instead trigger an alternative pathway leading to the formation and translocation of a NF-κB p50 homodimer, directing a Th2 immune response. From these studies it has been determined that the composition of the DC-SIGN signalling complex is glycan-specific with mannose and fucose ligands driving the distinct immunological outcomes.

Understanding how DCs interpret glycan signals to modulate immune responses is essential for developing new therapeutic strategies to target infection, inflammation, and cancer.(1, 402, 404) In particular, the role of DC-SIGN in regulating IL-10 and IL-23 is central to understanding how innate immune signals shape downstream T cell responses in autoimmune disease. These two cytokines represent opposing ends of the immune response spectrum: IL-10 is a potent anti-inflammatory cytokine associated with immune tolerance and the suppression of excessive immune activation, while IL-23 is a pro-inflammatory cytokine linked to Th17 cell differentiation, autoimmunity, and antifungal immunity.(405, 406) The interplay between these cytokines is significantly influenced by DC-SIGN signalling, particularly under conditions of co-stimulation with microbial components such as LPS.(52, 92)

While IL-23 has a vital role in antifungal immunity, IL-23 driven IL-17 has been implicated in the pathogenesis of numerous chronic inflammatory diseases.(245) Strong evidence supports the role of IL-23/IL-17 in conditions such as ankylosing spondylitis(304), psoriatic arthritis(407) inflammatory bowel disease(299) and skin disorders like psoriasis(315). Notably, IL-23 is required for both initial generation of Th17 cells, and sustaining their inflammatory function. (259)

Emerging evidence also suggests a compelling link between fungal infections, innate immune sensing via C-type lectins such as DC-SIGN, and the development of chronic inflammatory conditions, including the spondyloarthropathies.(358, 359, 361, 362, 408) These diseases, which include ankylosing spondylitis and psoriatic arthritis are characterised by IL-23/IL-17 driven inflammation. Several GWAS have identified

polymorphisms in the genes encoding components of the IL-23 signalling axis in SpA patients, and IL-23/IL-17 blockade has proven to be one of the best therapies for some of these diseases, far better than traditional TNF blockers which were previously considered as the gold standard for these diseases, reinforcing the role of IL-23 and IL-17 in driving pathology.(409) Fungal and bacterial cell wall glycans, such as mannose- and fucose- containing polysaccharides are potent ligands for DC-SIGN and other lectin receptors. It is hypothesised that an initial encounter with pathogens, especially in those with susceptible genetic background, could prime DCs to produce IL-23 in response to pathogen recognition, particularly when co-stimulated by microbial components like LPS. This early immune skewing may help initiate chronic inflammation, potentially contributing to the onset of SpA-like pathology. Understanding how specific glycans influence this IL-23 immune response via DC-SIGN could provide new insight into the microbial triggers of SpA.

While previous chapters have introduced the ability of DC-SIGN in recognising pathogen-associated carbohydrate structures, this chapter focused specifically on the downstream immunological effects that arise from DC-SIGN engagement by multivalent glycan nanoparticles. In particular, this chapter investigated how monocyte derived DCs interact with glycan-coated gold nanoparticles to modulate the production of IL-23 and IL-10 when co-stimulated with other pattern recognition receptor agonists including LPS, heat killed *Salmonella typhimurium* and the ligands PAM3CSK4 and PAM2CSK4. In particular, the effect of multivalent glycan type and linker length on cellular responses was investigated and discussed, as this has previously had an impact on the binding affinity of GNPs with DC-SIGN.

A key objective of this study was to determine whether these glycan mediated effects on cytokine production were driven exclusively by DC-SIGN or whether other glycan binding receptors such as the macrophage mannose receptor (MMR) also contribute to observed effects. To address this, an antibody blocking approach was employed alongside quantitative analysis of nanoparticle internalisation. Finally, the work in this chapter examined the downstream consequences of glycan-DC interactions on T cell activation and the skewing of immune responses towards or away from the LPS driven Th17 response. To explore this, T cell proliferation was quantified by flow cytometry and T cell specific cytokines were measured using a high sensitivity bead based immunoassay.

7.2 Results and discussion

7.2.1 Exploration of MoDCs for use as DC mimics

To study the modulation of IL-23 and IL-10 production relating to DC-SIGN signalling, a robust way of isolating or generating DCs needed to be obtained. DCs comprise a small population of peripheral blood mononuclear cells (PBMCs), accounting for only 1-2 % of total cells and therefore isolating DCs directly would require a high volume of sample, high reagent usage and lots of waste by products. An easier way to generate and study DCs was to differentiate them from monocytes, which were an easier population to isolate, making up 10-20 % of PMBCs. Monocyte derived DCs (MoDCs) do occur naturally in the bone marrow, but can be produced in the lab by culturing enriched monocytes in the presence of IL-4 and granulocyte macrophage colony stimulating factor (GM-CSF). Throughout this process, cells lose monocyte cell markers (CD14) and start to express DC markers, such as DC-SIGN (CD209). To follow the process and ensure successful differentiation, the cell types were characterised by flow cytometry. Cells pre- and post- culture were stained with CD14 and DC-SIGN dye conjugated antibodies and their fluorescence intensity observed via flow cytometry (Figure 7.1). The THP-1 monocyte cell line was also explored by attempting to stimulate upregulation of DC-SIGN under conditions such as phorbol myristate acetate (PMA) and conventional IL-4 + GM-CSF for different time courses as a more convenient methodology for rapid DC generation.(410)

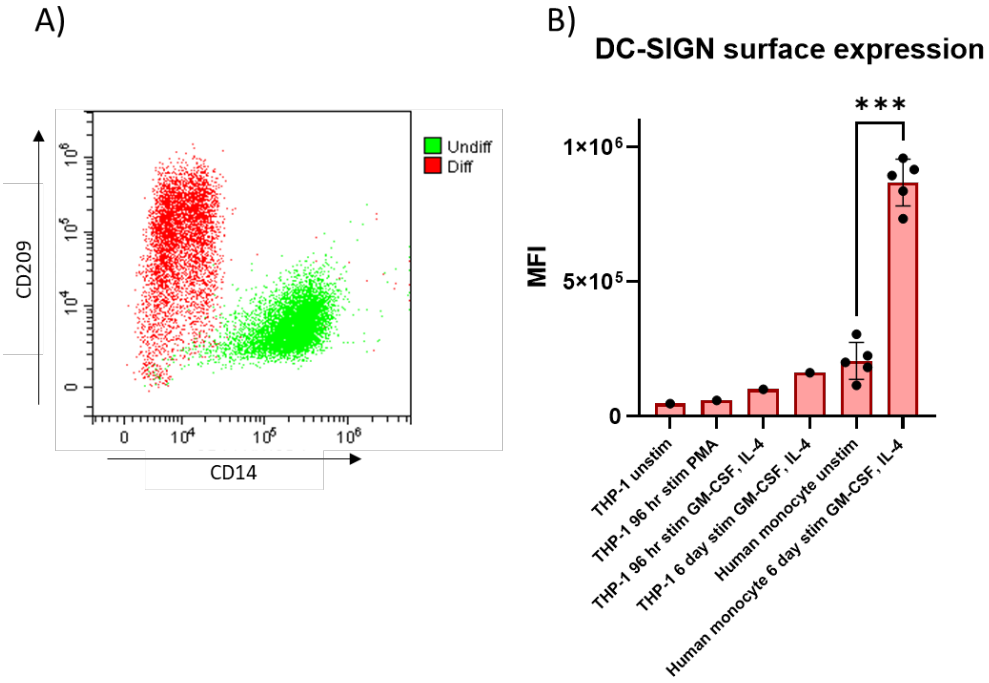

Figure 7.1 Up-regulation of DC-SIGN expression measured by flow cytometry. A) a flow cytometry dot plot showing the increase DC-SIGN (CD209) and decrease in CD14 expression upon differentiation of monocytes (green) isolated from human PBMCs into DCs(red), differentiated by culturing human monocytes with GM-CSF and IL-4 for 6 days. B) Bar graph showing DC-SIGN cell surface expression on THP-1 cells cultured in the presence of either PMA or GM-CSF and IL-4 or left untreated, or on monocytes isolated from human PBMCs or DCs differentiated from human monocytes with GM-CSF and IL-4. Median fluorescence intensity (MFI) measured by flow cytometry is used to represent DC-SIGN surface expression. ***p<0.001 (paired t-test)

As expected, monocytes left untreated for 7 days retained high levels of CD14 expression but low levels of DC-SIGN (Figure 7.1A). Treatment with IL-4 and GM-CSF caused a reduction in CD14 levels, and DC-SIGN increased significantly over four fold, confirming successful differentiation from monocytes into MoDCs (Figure 7.1A-B). The THP-1 cell line was explored in an attempt to eliminate the need for donor blood samples and increased processing times, however, stimulation under all conditions showed very minimal increases in surface DC-SIGN expression, with the highest levels still below that of undifferentiated monocytes from blood. Although it is possible that these THP-1 cells expressed other typical DC markers, and may represent DC in other forms, this thesis focuses on the modulation of immune cell responses as a direct result of DC-SIGN and therefore high DC-SIGN expression was an essential requirement in this situation and the THP-1 cell line was ruled out as a potential avenue from which to generate DCs. It is evident from Figure 7.1B that variation between donors can be large and hence, where possible, ≥5 donors were used to gain a better representation of the population.

7.2.1.1 Phenotyping DCs

In humans, DCs exist as heterogeneous population. DCs are defined as lacking T cell markers (CD3), B cell markers (CD19/20), NK markers (CD56) and monocyte markers CD14/16 but they do express HLA-DR (MHC-II). Among the DC population exists several subpopulations and subsets which can be differentiated between based on their localisation, additional surface markers and gene expression profiles, these include conventional DCs (cDCs), plasmacytoid DCs (pDCs) and common DC progenitors (pre cDCs). Each play an essential role in initiating and shaping adaptive immune responses.

Conventional DCs are typically divided into two major subsets, cDC1s and cDC2s, with the cDC2 population also subdividing into DC2 and DC3 populations.(411) cDC1s, which express the marker CD141, have a greater ability to cross-present antigens than other DC subsets and are therefore particularly efficient at initiating $CD8^+$ T cell responses, making them key players in anti-viral and anti-tumour immunity.(412) They produce type III interferons and high levels of IL-12, which is a crucial supporter of Th1 immunity.(413) On the other hand, cDC2s (which are $CD1c^+$) can drive Th1, Th2 and Th17 immunity depending on the context.(414, 415) The DC2 subset (which are $CD163^-$) secrete IL-9, IL-13 and some IL-12, but low levels of IL-10 and IL-1β and therefore produce mainly Th2 T cells.(416, 417) DC3s (which are $CD163^+$) produce IL-10, IL-1β, IL-6, TNF-α, IL-23 and IL-8, and preferentially prime Th1 and Th17 cells.(417-419) DC3s are inducers of inflammation and have particularly important roles in autoimmunity and chronic infection.(420)

pDCs are distinct from cDCs and can be identified by CD123 expression. They are best known for their ability to produce IFN-α and IFN-β in high quantity in response to viral nucleic acids.(421) They are less effective at cross presentation but can influence T cells though their cytokine expression profiles. Pre-cDCs are bone barrow-derived and can give rise to cDC1s and cDC2s upon migration to tissues. They are also CD123 positive but are not major cytokine producers before migration.(419)

To assess the percentage populations of these different DC subsets in humans and compare them to MoDCs, blood samples were taken from four donors. PBMCs were isolated using density-gradient centrifugation and were stained according to a protocol published by Heger *et al*.(Figure 7.2)(422) From the same donors, monocytes were also isolated using a magnetic antibody labelling and positive selection technique and differentiated into MoDCs using conventional IL-4 and GM-CSF conditions. They were then stained using a similar panel, minus the T cell and B cell markers (Figure 7.3). Samples were gated based off fluorescence minus one (FMO) controls (Figure B. 1) and compensations for fluorescent dyes were carried out using the CytExpert software.

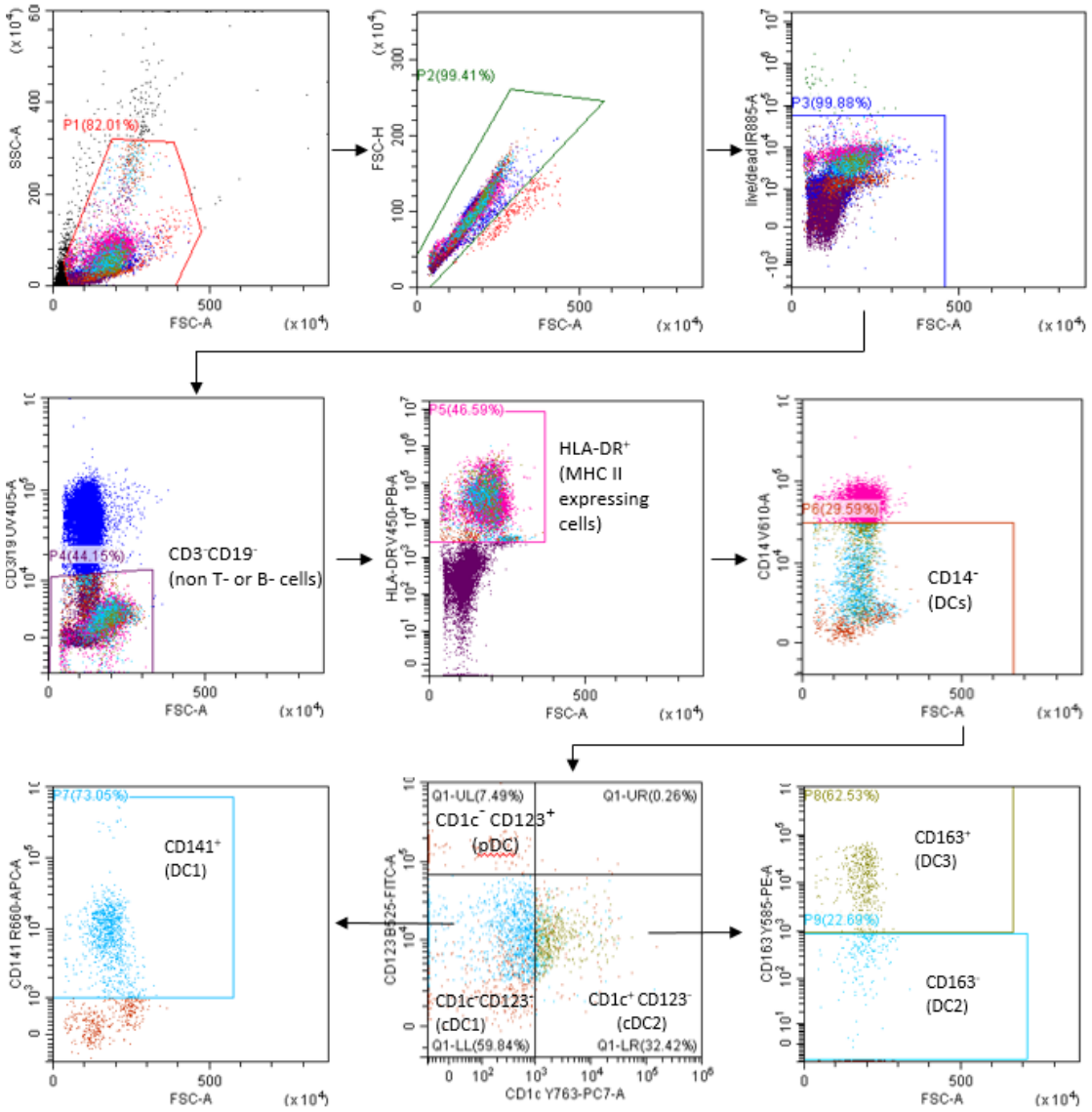

Figure 7.2 Phenotyping of peripheral blood. After a morphology gate followed by elimination of doublets, the dead cells along with T cells ($CD3^+$), B cells ($CD19^+$) were excluded. HLA-DR positive cells were selected followed by elimination of $CD14^{high}$ to distinguish between monocytes and DCs. $CD14^{mid/low}$ were included in the DC gate since CD14 can be expressed in low levels on some DC subsets. The $CD14^-$ and $CD14^{mid}$ cells were separated into CD1c-$CD123^+$ (pDCs), $CD1c^-CD123^-$(cDC1) and $CD1c^+CD123^-$ (cDC2s). Human cDC1 were identified in the $CD1c^-CD123^-$ compartment by their high expression of CD141. cDC2s were further subdivided into $CD163^+$ (DC3s) and $CD163^-$ (DC2s). Data acquisition was performed on a CytoFLEX LX and data was analysed using the CytExpert software.

Table 7.1 Table summarising the frequency of analysed DC populations in the blood (N=4)

Population	cDC1	cDC2			pDC
		cDC2 (total)	DC2	DC3	
Frequency of living cells (%)	1.80	1.38	0.42	0.96	0.27
SD (%)	0.11	0.11	0.20	0.35	0.11
Frequency of DC (%)	41.03	34.91	12.71	22.20	6.84
SD (%)	3.08	2.20	5.21	7.14	1.87

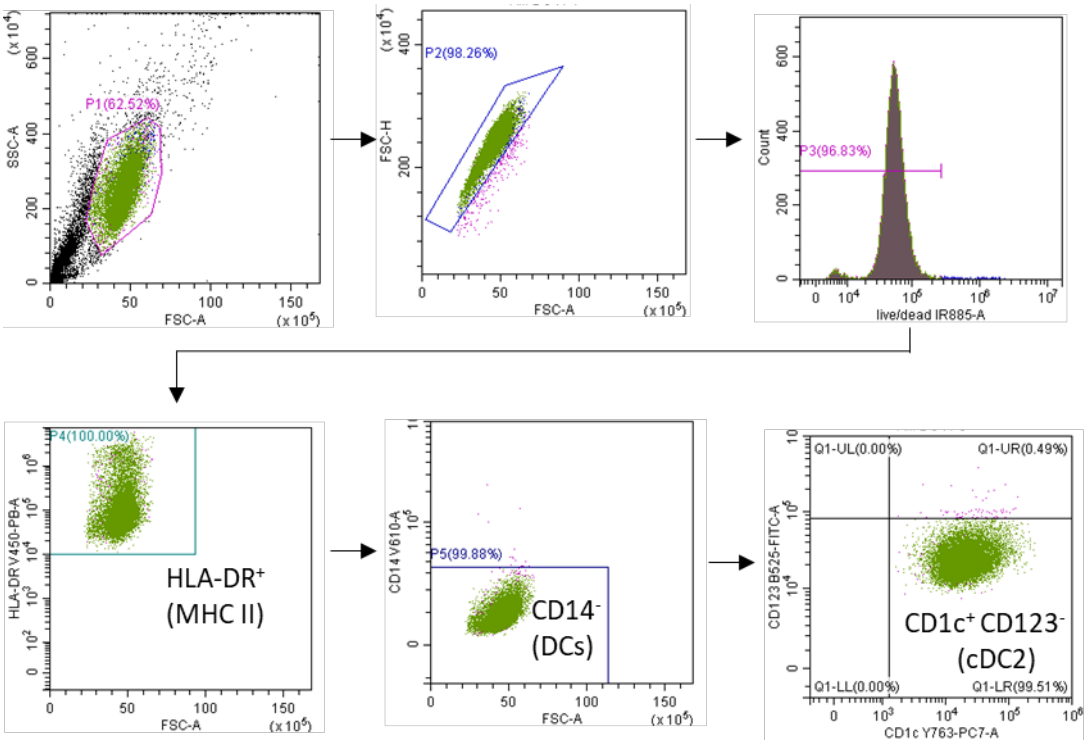

Figure 7.3 Phenotyping of MoDCs. After a morphology gate followed by elimination of doublets, the dead cells were eliminated. HLA-DR positive cells were selected followed by elimination of $CD14^{high}$ to distinguish between monocytes and DCs. $CD14^{mid/low}$ were included in the DC gate since CD14 can be expressed in low levels on some DC subsets. The $CD14^{-}$and $CD14^{mid}$ cells were separated into $CD1c^{-}CD123^{+}$ (pDCs), $CD1c^{-}CD123^{-}$ (cDC1) and $CD1c^{+}CD123^{-}$ (cDC2s). Human cDC1 were identified in the $CD1c^{-}CD123^{-}$ compartment by their high expression of CD141. cDC2s were further subdivided into $CD163^{+}$ (DC3s) and $CD163^{-}$(DC2s). Data acquisition was performed on a CytoFLEX LX and data was analysed using the CytExpert software.

As anticipated, the unenriched leukocytes contained a variety of the different DC populations, the percentages of which can be seen in Table 7.1. While it would be interesting to isolate each of these DC populations and compare their cytokine responses in the presence of DC-SIGN modulators, the percentages cDC2s which are the main producers of IL-23 and drivers of Th17 immune responses were found to be very low (1.38%) and sorting these cells would be time consuming, expensive and energy exhaustive. They were also not tested for DC-SIGN expression.

On the other hand, MoDCs were found to be mainly cDC2 type ($DC1c^{+}CD123^{-}$). While they do not encompass the full diversity of the human DC compartment, they remain a widely accepted and practical model for studying DC function, particularly when stimulated under inflammatory conditions.(423) In this thesis, MoDCs were used to investigate IL-23 production, a cytokine central to the induction of the Th17 response. Notably, this data indicating their resemblance to the cDC2 subset aligns with other transcriptional and functional observations, where they have been shown to drive Th17 polarisation.(390, 424) Therefore, given their accessibility, responsiveness to *in vitro* stimulation, relevance to inflammatory cytokine production and high DC-SIGN expression, the use of MoDCs herein provided a suitable model system for dissecting DC-SIGN driven IL-23 modulation, despite their limitations in representing the full *in vivo* heterogeneity of human DCs.

7.2.1.2 MoDC maturation

After confirming the use of MoDCs as a model for this study, the bacterial endotoxin LPS was added to induce DC maturation. During the maturation process, DCs are primed to upregulate CD80 and CD86, critical co-stimulatory molecules for T cell engagement. In addition to CD80 and CD86 expression, stimulation with LPS activates signalling pathways that lead to the transcription of cytokines through the transcriptional factor NF-κB. This is mediated by the cell surface receptor TLR4 which binds LPS and recruits a series of cytoplasmic adaptor proteins, ultimately resulting in the degradation of the inhibitory protein, IκBα. This degradation allows NF-κB to translocate to the nucleus where transcription is initiated.(425) LPS stimulation not only drives the upregulation of costimulatory surface molecules like CD80/86 but also leads to the production of inflammatory cytokine IL-23 and the anti-inflammatory cytokine IL-10. Other cytokines produced by MoDC upon LPS stimulation include IL-6, IL-8 and TNF-α, however these were not measured in this study.(426)

DC maturation was monitored by flow cytometry and as expected, stimulation with LPS resulted in significant upregulation of co-receptor expression (Figure 7.4). Initially, differences in marker expression between unstimulated DCs and LPS-stimulated DCs was assessed using the percentage of positive cells, based on a threshold determined by a gated control. However, this approach proved limited by certain donors where

baseline expression of CD80/86 was already relatively high prior to stimulation (Figure B. 2). As a result, increases in expression following LPS treatment were not reliably reflected by the percentage of positive cells, since many cells were already above the gated threshold. To address this, median fluorescence intensity (MFI) was adopted as a more accurate and quantitative measure of marker expression. Unlike using the percentage positive classification, MFI accounts for the fluorescence intensity of all events within the gated population, enabling the detection of expression changes even when cells are already expressing the marker before stimulation. This provided a more sensitive measure of shifts in co-receptor expression.

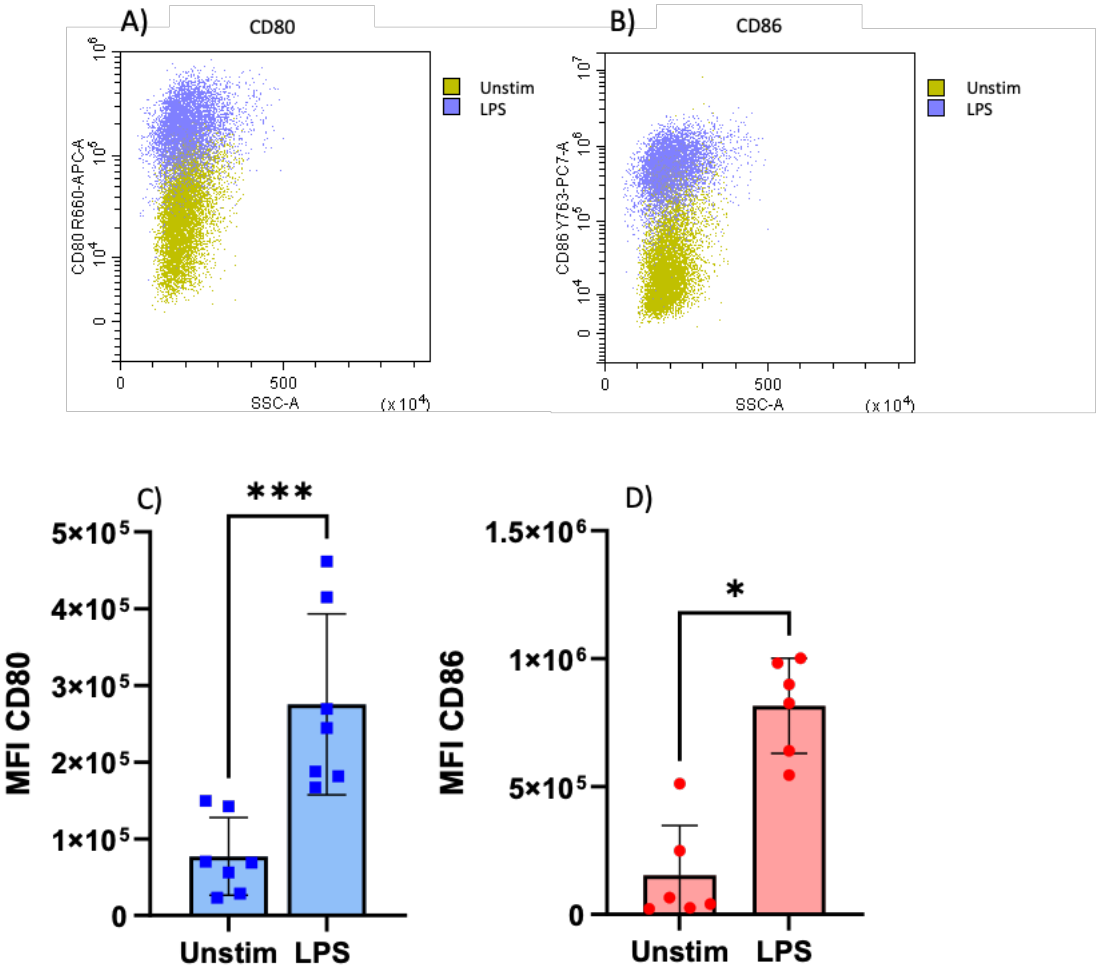

Figure 7.4 Flow cytometry dot plots representing A) CD80 expression and B) CD86 expression on unstimulated (yellow) and LPS stimulated (purple) MoDCs for one donor. Bar graphs representing C) CD80 and D) CD86 expression on unstimulated and LPS stimulated MoDCs expressed as MFI. Bar graph data are representative of at least six independent experiments.*p<0.05, ***p<0.001 (paired *t*-test)

Figure 7.4 shows that stimulation of MoDCs with LPS led to a significant increase in both CD80 and CD86 expression. This upregulation is a well-established marker of DC maturation. In addition to the observed increase in surface co-receptor expression, LPS stimulation also induced transcription of the cytokines IL-23 and IL-10. To assess

cytokine secretion, levels of IL-23 and IL-10 were quantified by an enzyme linked immunosorbent assay (ELISA) on the cell culture supernatants. A concentration of 10 ng/ml of LPS was selected to ensure detectable cytokine expression while avoiding maxing out the cellular response, thereby allowing potential modulatory effects to be detected in either direction. Under these conditions, both IL-23 and IL-10 were secreted at significantly higher levels compared to the unstimulated controls, which produced negligible amounts of both cytokines at concentrations typically falling below the ELISA detection threshold (Figure 7.5).

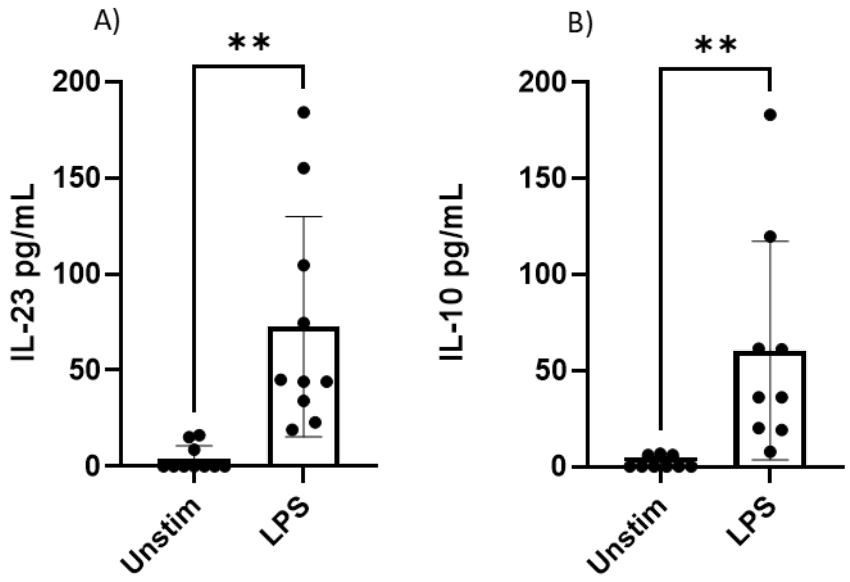

Figure 7.5 Bar graphs showing A) IL-23 and B) IL-10 production from unstimulated and LPS stimulated MoDCs. Cytokines were measured by ELISA and represented as pg/mL. Data are representative of at least nine independent experiments $^{**}p<0.01$ (Wilcoxon).

This study intended to monitor DC-SIGN mediated modulations of TLR4 induced cytokine expression, however, while DC-SIGN has been studied a modulator for LPS induced IL-23 and IL-10 production, DC-SIGN signalling alone does not lead to the translocation of NF-κB, meaning addition of G5-glycans with no co-stimulant should not trigger cytokine production. To confirm this and ensure cytokine production was not induced by G5 alone, G5-glycans were added to DCs and the supernatants were collected and measured for cytokines after 24 hrs. However, the results were not as expected and G5-glycans alone caused DCs to produce very high levels of IL-23 (Figure 7.6). In particular, the G5-OH control which should not interact with DC-SIGN at all also triggered IL-23 production. The likely cause of this result was deemed to be due to LPS or whole bacterial contamination of the gold nanoparticle samples, however endotoxin quantification tests rely heavily on a UV absorption based assay using a 405 nm wavelength. Since 5 nm gold nanoparticles absorb strongly at this wavelength, this method was unsuitable to quantify contamination. A qualitative method using a gel-clotting system which indicates the presence but not the quantity of endotoxin was

employed. This method indicated the presence of LPS in the samples, however the sensitivity of this type of test was 0.5 endotoxin units per mL equating to 0.05 ng/mL of LPS. Therefore even samples containing ~0.05 ng/mL of LPS (which would not result in substantial cytokine production) would be detected rendering this method insufficient for this purpose.

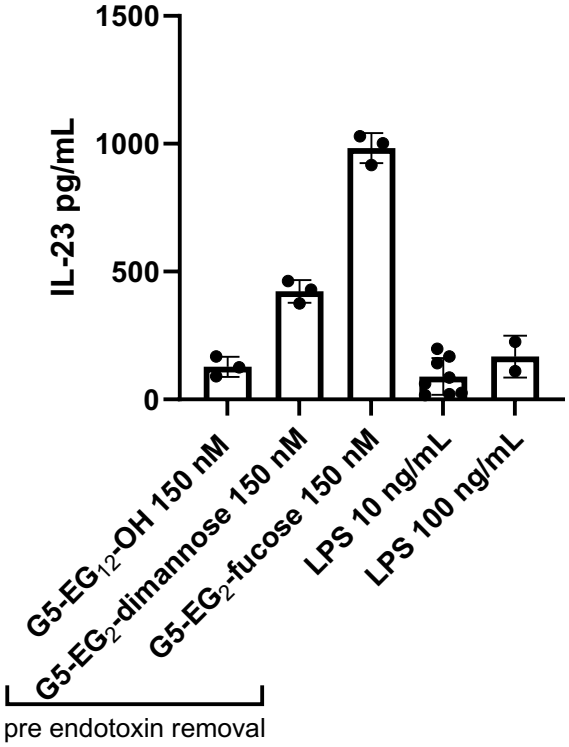

Figure 7.6 Bar graph representing IL-23 production from MoDCs when stimulated with G5-glycans. IL-23 was measured by ELISA and represented as pg/mL. Levels of LPS contamination varied between samples with G5-EG_2-fucose showing the greatest levels of contamination as seen by the large production of IL-23 compared to LPS controls. Data are representative of 3 separate experiments for G5 samples, 5 separate experiments for 10 ng/mL LPS, and 2 separate experiments for 100 ng/mL LPS.

Although it was not possible to quantify LPS contamination, it was deemed likely this was the cause of the IL-23 production when no co-stimulants were added. To remove this, samples were filtered through 0.22 µm filters and were then mixed with an endotoxin removal resin made of modified poly-L-lysine affinity ligand, capable of binding and removing 2,000,000 EU/mL (200 µg). After treating samples under this method, levels of IL-23 and IL-10 when DCs were stimulated with G5-glycans alone was reduced to background levels, suggesting successful elimination of endotoxin contamination (Figure 7.7). The G5-glycans appeared to be unaffected or modified by this process, as the G5s remained stable in aqueous solution, and endocytosis of the G5s was still observable signifying the G5s remained coated in their respective glycan or control ligands (Figure 7.9).

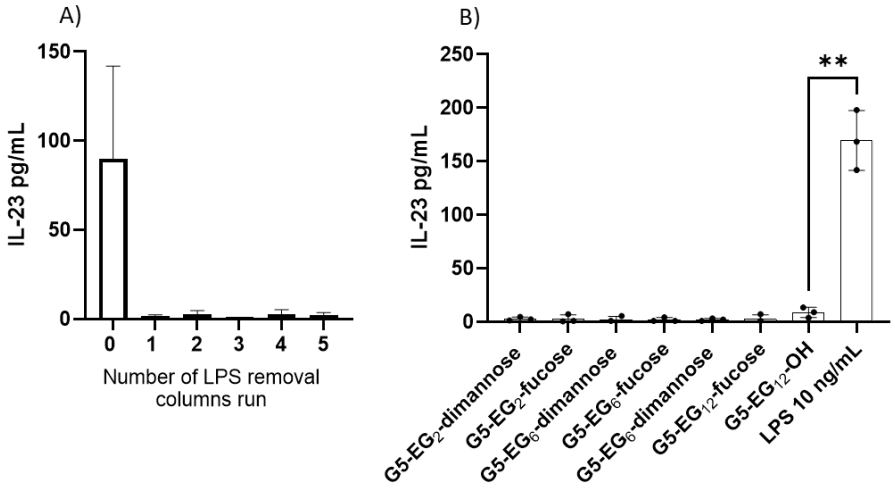

Figure 7.7 Bar graphs showing A) IL-23 production from MoDCs when stimulated with a G5-OH control ligand before and after numerous treatments with endotoxin removal resin which uses poly-L-lysine to bind LPS and other endotoxin contamination. The results showed that only one treatment is needed B) IL-23 production after all ligands were treated twice with endotoxin removal resin. Levels of IL-23 production after resin treatment when cells were stimulated with G5-glycans were restored to background levels. Data are representative of 2-3 separate experiments **p<0.01(Welch's t-test).

To test G5 toxicity on MoDCs and determine a suitable working concentration, 150 nM of purified G5s were added to cells. After 24 hours, cells were stained using a live/dead stain and analysed by flow cytometry. The stain is only able to penetrate dead cells and therefore if the cell population is alive, fluorescence intensity remains low. After treatment with G5-EG_6-dimannose, it was observed that there was no change in the live/dead population of cells, and cell viability remained high after 24 hours (Figure 7.8). Therefore 150 nM was deemed a suitable concentration to use for this assay.

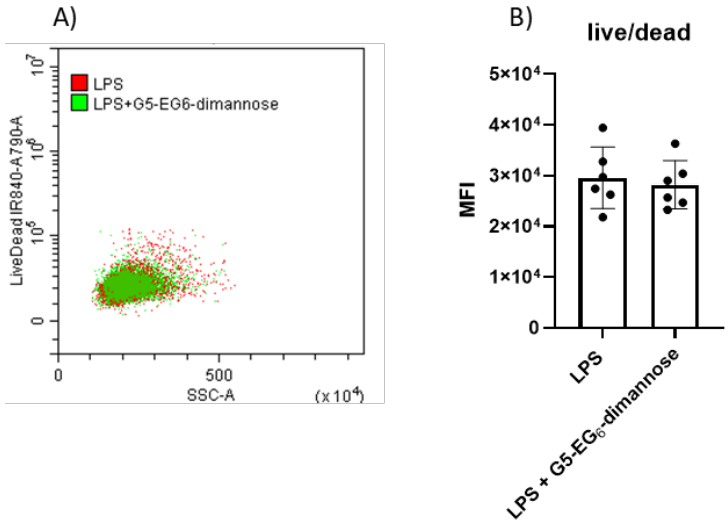

Figure 7.8. A) flow cytometry dot plot showing live/dead fluorescence after treatment with LPS (red) or LPS+G5-EG_6-dimannose (150 nM) (green) for one donor. No increase in fluorescence was observed indicating the cell population remained alive after G5 treatment. B) Bar graph showing there was no change in MFI before and after treatment with G5-glycans for 6 independent donors.

Interestingly, when imaging cells using light microscopy and visually checking the colour of the cell pellet, it appeared that endocytosis of the G5 particles was dependent on the linker length (Figure 7.9D). Cells experiencing greater levels of internalisation would be more red/purple in colour due to the colour of the nanosized G5 particles. While both the G5-EG_2 and G5-EG_6 linked glycans appeared to be largely internalised for both dimannose and fucose coated particles, the G5-EG_{12} glycans showed little internalisation, especially G5-EG_{12}-fucose which exhibited the weakest binding affinity with DC-SIGN in the florescence quenching assay (Chapter 4). As a control, G5-EG_{12}-OH was investigated and showed no visible internalisation, meaning internalisation was dependent on the presence of the glycan on the surface (Figure 3.8C,D). Quantification of this internalisation is explored in Section 7.2.4, but these data show that linker length appears visually to have an effect on internalisation, which may be as direct result of their binding affinity with DC-SIGN.

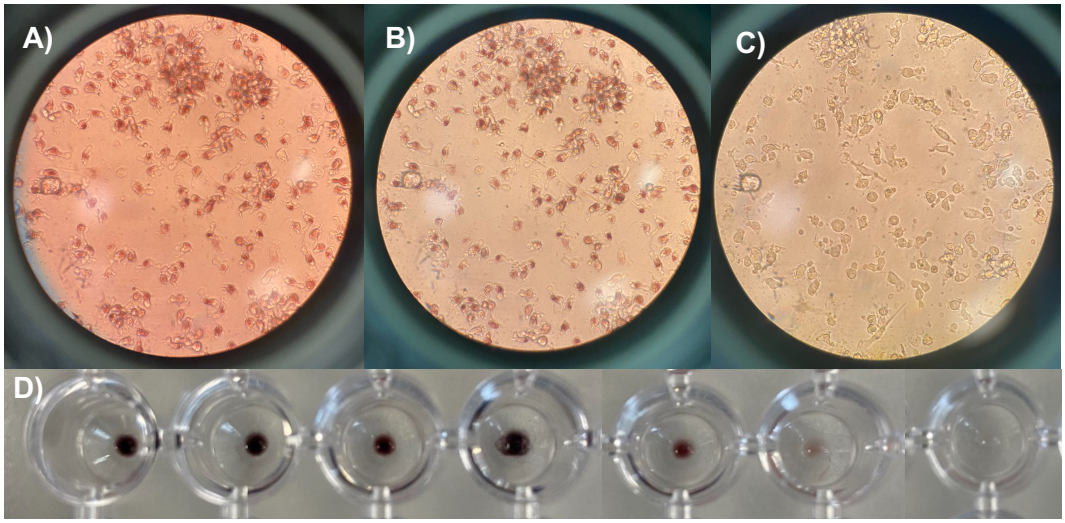

Figure 7.9 Endocytosis of G5s bearing different glycans and linker lengths. A-C) light microscopy images of DCs after 24 hrs incubation with 150 nM A) G5-EG_2-dimannose, B) G5-EG_2-fucose, C) G5-EG_{12}-OH. D) Images of cells treated with 150nM G5-glycans for 24 hours which were then centrifuged to pellet the cells and remove the supernatant. From left to right; G5-EG_2-dimannose, G5-EG_2-fucose, G5-EG_6-dimannose, G5-EG_6-fucose, G5-EG_{12}-dimannose, G5-EG_{12}-fucose, G5-EG_{12}-OH. G5-glycans were internalised, as evidenced by the purple cell pellets, which seemingly decreased as linker length increased. The G5-OH was not internalised.

7.2.2 IL-23 and IL-10 modulation

To investigate whether IL-23 and IL-10 modulation was dependent on DC-SIGN signalling pathways and if binding affinity contributed to the magnitude of modulation, gold nanoparticles bearing glycans with varying linker lengths were added to MoDCs stimulated simultaneously with LPS. Although the multivalency of gold nanoparticles allows for substantially higher local glycan concentrations at lower G5 concentrations, in addition to the G5-glycans, high concentration (50 mM) of the respective free azido-fucose (fucoseN3) (**4**) and azido-dimannose (dimannoseN3) (**5**) were included to assess

potential modulatory effects at concentrations beyond what is feasible with gold nanoparticles.

Since large variations in IL-23 and IL-10 production between donors was observed following LPS stimulation, with some showing little response to LPS (20 ng/mL IL-23) and others responding much more strongly (180 ng/mL IL-23) (Figure 7.5) trends in the raw data were difficult to see (Figure B. 3). To normalise for this donor variation and to determine whether the G5-glycans were able to influence IL-23/IL-10 production in a linker length/binding affinity or glycan dependent manner, cells treated with G5-glycans+LPS were compared to the LPS+G5-OH controls from the same donor (the free glycans were compared to the LPS only control), and were then represented as a log2 fold change. This provided equal visual weighting of modulation above and below the control (e.g. if normalised response is 1, then responses of 0.1 and 10 both represent a 10 fold change and would appear as the same size bars below or above the normal, respectively). After stimulating DCs for 24 hrs with LPS and G5-glycans, IL-23 and IL-10 production was measured by ELISA.

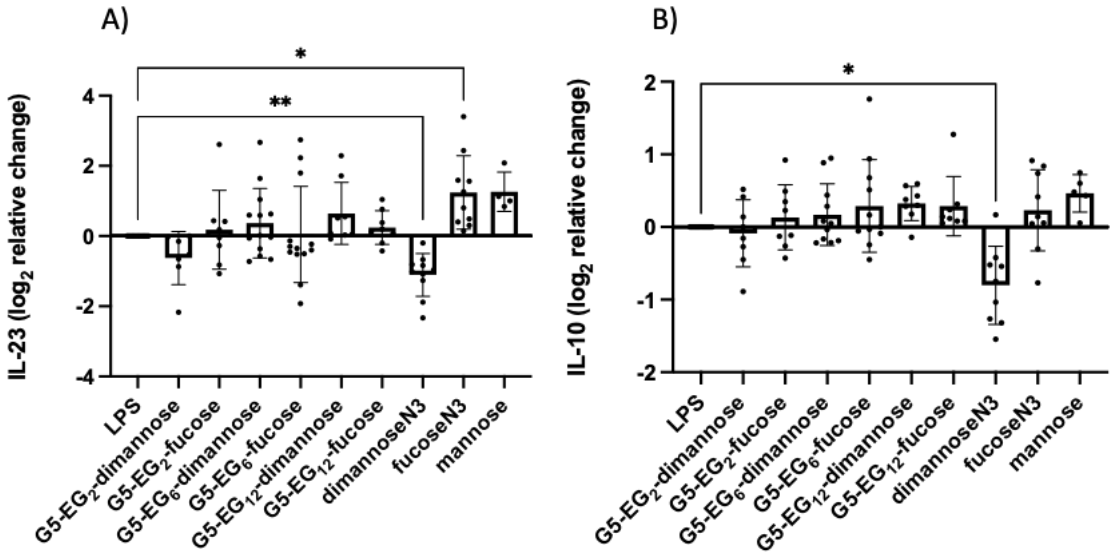

Figure 7.10 Bar graphs showing A) IL-23 and B) IL-10 production by MoDCs when stimulated with LPS or LPS plus various G5-EG_n-glycans/free ligands. Cytokines were measured by ELISA and normalised to LPS stimulated (for free azido(N3) ligands) or LPS+G5-OH cells (for G5-glycans) (set as 1) then presented as a log2 function. Data are representative of 4-10 independent experiments. *p<0.05, **p<0.01 (Dunnett's multiple comparisons test).

Firstly to note is that modulation of IL-23 using G5-glycans seemed to follow no specific pattern between donors (Figure B. 4) G5-EG_2-dimannose had the most pronounced effect on LPS induced IL-23 production for the G5-glycans, decreasing it slightly, whereas the response to fucose coated glycans was attenuated compared to this. It is noted that no G5-glycan results show any statistical significance compared to the LPS-

G5-OH control. Additionally the G5-glycans also had no significant impact on IL-10 production.

In contrast, the free ligands exhibited significant effects. Free azido-dimannose appeared to supress the ability of the cells to produce IL-23 whereas free azido-fucose upregulated LPS induced IL-23. A similar result was observed for IL-10. These results are disagreeing to some previously reported literature, where Gringhuis *et al*. state that mannose containing ligands promote proinflammatory cytokine production (IL-12p40, IL-6) through DC-SIGN signalling and fucose containing ligands dampen TLR4 induced proinflammatory signalling.(52) However, different from the literature, the free ligands used in this experiments contained an azide handle. To validate the assay, free mannose with no azide was tested, which showed upregulation of IL-23 and IL-10, more closely resembling the literature (Figure 7.10). It is interesting that the presence of an azide can reverse the modulatory effects seen without it. Addition of the azido-glycans did not affect cell viability and therefore the observed downregulation was not due to increased cell death (Figure B. 5).

Interestingly however, other authors have also demonstrated the downregulation of IL-12 and IL-23 by mannose containing DC-SIGN ligands through either TLR4 or dectin-1 co-signalling. DC-SIGN engagement with ManLAM led to decreased glucan dependent IL-23 production, but upregulation of other inflammatory cytokines such as IL-6,(394) and mannose glycopolymers were able to downregulate LPS/IFN-γ induced IL12p70 while upregulating IL-10, further highlighting how DC-SIGN occupies a unique position in immune regulation and is capable of both promoting tolerance and driving inflammation, depending on the context of its stimulation.(161)

To test if the G5-glycans failed to induce modulation due to insufficient concentration, free glycan concentrations were reduced to match the estimated glycan density on G5 particles. Assuming ~500 glycans per G5 nanoparticles (as calculated in Chapter 3) then 150 nM G5-glycan corresponds to ~75 μM of azido free ligand. At this matched concentration, the free ligands no longer induced significant cytokine modulation compared to the LPS control. This indicated that the absence of modulation observed by the G5-glycans could simply be a result of the concentration being too low.

Alternatively, it has been previously suggested that the shape of glycoconjugates play a role in their ability to induce immune responses. Small dendrons displaying mannose or fucose fail to induce cytokine production,(164) while those displaying such glycans on polyacrylamide produced glycan specific cytokines.(52) Further, a star shaped-mannose polymer, but not a linear-mannose polymer, has induced tolerance cytokines.(161) The small size of these G5-glycans may be key to their limited ability to induce cytokine modulation.

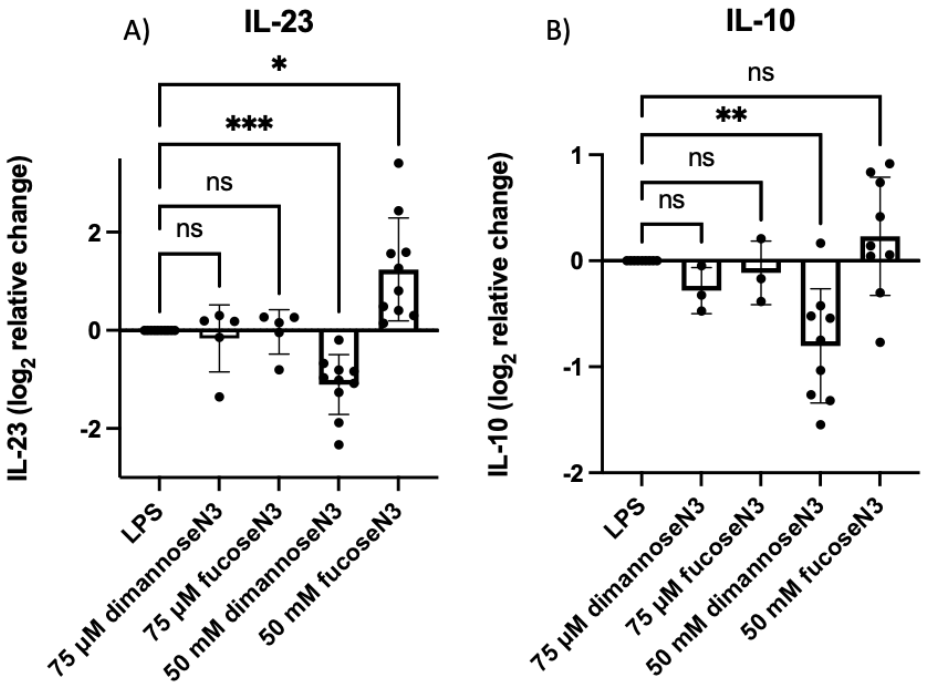

Figure 7.11 Bar graphs comparing A) IL-23 and B) IL-10 production by MoDCs when stimulated with LPS or LPS plus 75 μM dimannoseN3/ fucoseN3 or 50mM dimannoseN3/fucoseN3. Cytokines were measured by ELISA and normalised to LPS stimulated cells (set as 1) then presented as a log2 function. Data are representative of 3-10 independent experiments. *p<0.05, **p<0.01 ***p<0.001 (Dunnett's multiple comparisons test).

Alongside cytokine production, the effect of G5-glycans on the expression of co-receptors CD80 and CD86 was monitored. Addition of both G5-EG_6-dimannose and 50 mM dimannose appeared to reduce both CD80 and CD86 expression compared to when MoDCs were stimulated by LPS alone (Figure 7.12A). This is in line with the observed suppression of IL-23 and IL-10, especially for free azido-dimannose. These effects did not reach statistical significance, however, the sample size was small (4-5 donors) and biological data often requires much larger sample sizes to determine statistical significant due to large donor variations. Addition of G5-EG_6-fucose and free fucose appeared to have no effect on CD80/86 expression when compared to LPS alone despite increasing IL-23 production (Figure 7.12B). This discrepancy could be due to a ceiling effect where stimulation with LPS already leads to a maximum response and therefore further upregulation in the presence of other ligands would not be possible. Given the established role of CD80 and CD86 in promoting T cell activation, the downregulation as a result of dimannose addition could impair downstream T cell responses. This possibility is explored further in Section 7.2.5.

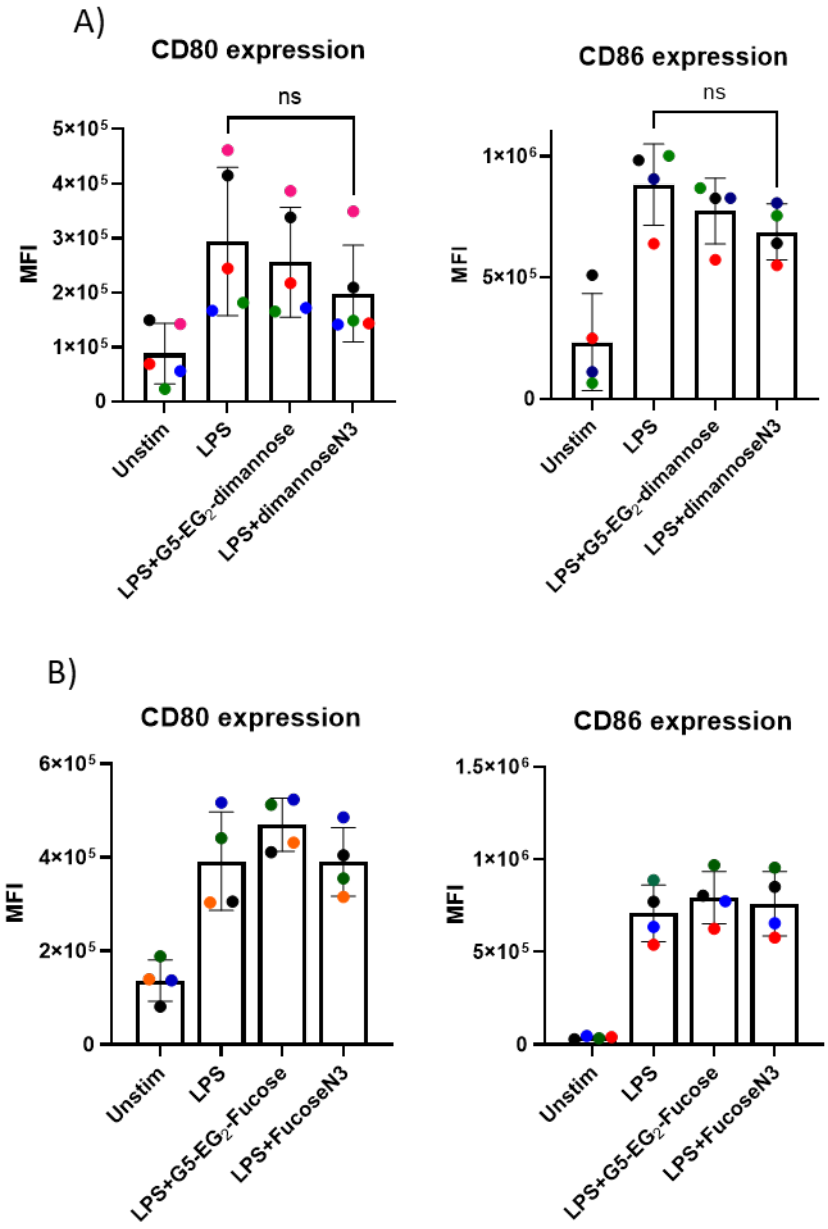

Figure 7.12 CD80(left) and CD86(right) expression by MoDCs which were either unstimulated, stimulated with LPS or stimulated with LPS in the presence of A) G5-EG_6-dimannose or free dimannoseN3, and B) G5-EG6-fucose or free fucoseN3. Data are representative of at least 4 independent experiments. Symbols of the same colour represent the same donor. ns (paired *t*-test).

7.2.3 Modulation of cytokines induced by other TLRs.

Since DC-SIGN and TLR4 co-signalling converge at the transcriptional factor NF-κB it is plausible that signalling through other TLR receptors, which also activate NF-κB, may be similarly modulated in the presence of DC-SIGN engagement. To investigate this potential modulation, three TLR ligands were chosen based on their known receptor targets and ability to activate NF-κB. These were HKST, which engages both TLR4 and TLR2, PAM2CSK4 a diacylated lipopeptide which signals through TLR2 and TLR6 and

PAM3CSK4 a triacylated peptide recognised by TLR1 and TLR2. These ligands are well characterised activators of pro-inflammatory pathways and provide a useful platform for testing whether DC-SIGN engagement differentially modulates TLR responses across distinct TLR pairs. While the ability of these TLR pairs to induce NF-κB activation is established, their roles in modulating IL-23 production remains less well defined. Flagellin, as a TLR5 ligand, was considered too however no detectable IL-23 was observed when MoDCs were stimulated with flagellin alone. This was in line with literature suggesting that although MoDCs express TLR5, stimulation induces secretion of IFN-γ, IL-1β, TNF, IL-8, IL-12p40 (but not IL-12p70) and IL-13.(427)

HSKT was studied first due to its overlapping TLR signalling pathway with LPS. It was interesting to see if the addition of TLR2 signalling could influence the cytokine outcomes. IL-23 and IL-10 were again selected as the primary cytokine of interest due to their key roles in shaping Th17 immune responses. Similarly to the LPS stimulation, addition of HKST significantly upregulated both CD80 and CD86 expression (Figure 7.13). Levels were similar to those observed with LPS, further validating the assumption that expression after LPS stimulation is maximal and cannot increase further. HKST also induced significant levels of both IL-23 and IL-10 allowing for the observation of any modulatory effects of G5-glycans and free glycans (Figure 7.14).

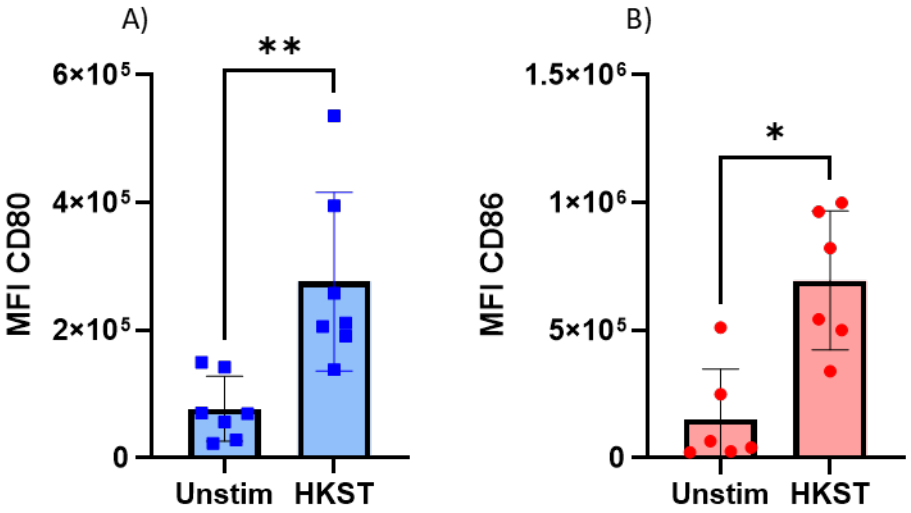

Figure 7.13 Bar graphs representing A) CD80 and B) CD86 expression on unstimulated and HKST stimulated MoDCs expressed as MFI. Data are representative of at 6-7 independent experiments (different donors) *p<0.05, **p<0.01 (paired t-test).

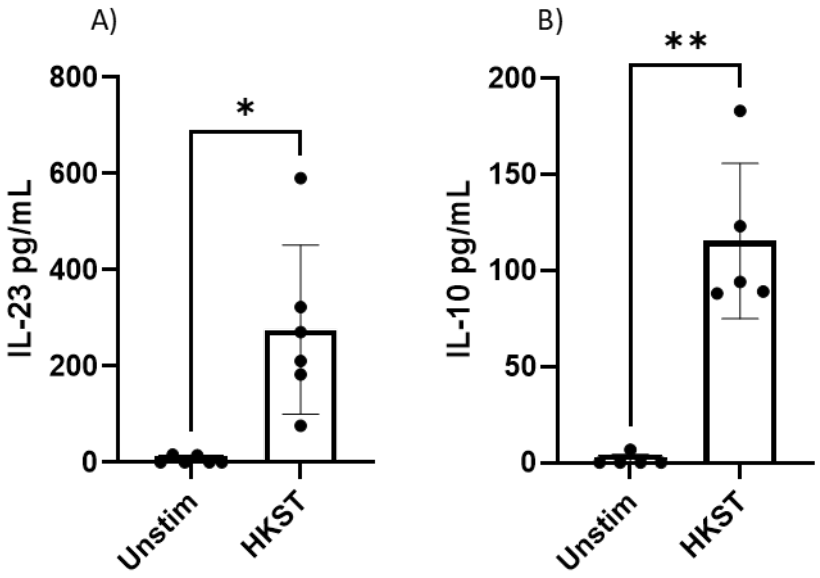

Figure 7.14 Bar graphs showing A) IL-23 and B) IL-10 production from unstimulated and HKST stimulated MoDCs. Cytokines were measured by ELISA and represented as pg/mL Data are representative of 5-6 independent experiments *p<0.05, **p<0.01 (Wilcoxon).

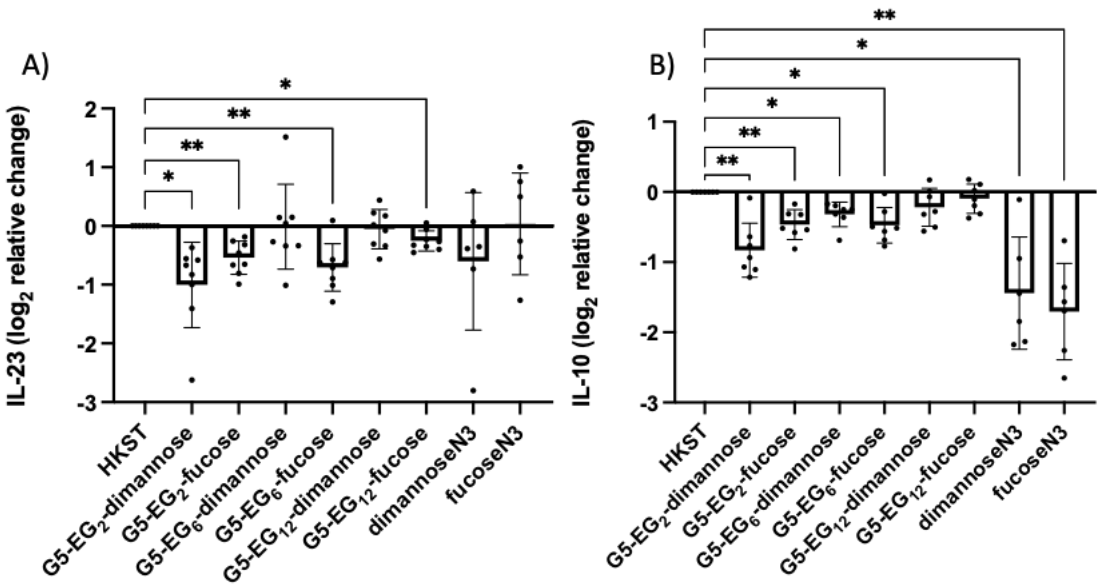

Figure 7.15 Bar graphs showing A) IL-23 and B) IL-10 production by MoDCs when stimulated with HKST or HKST plus various G5-EG$_n$-glycans/free ligands. Cytokines were measured by ELISA and normalised to HKST stimulated (for free ligands) or HKST+G5-OH cells (for G5-glycans) (set as 1) then presented as a log2 function. Data are representative of at least 6 independent experiments. *p<0.05, **p<0. (Dunnett's multiple comparison test).

For HKST conditions, G5-EG$_2$-dimannose and G5-EG$_2$-fucose induced the most significant downregulation of IL-23, suggesting that the higher affinity multivalent G5-glycans can effectively modulate signalling pathways, even at this concentration.

Notably, monovalent fucose had no effect on IL-23, indicating that multivalency may have an important role – possibly due to the induction of tetramerization or clustering of DC-SIGN on the cell surface enabling amplification signalling. The downregulation of HKST induced IL-23 in the presence of G5-fucoses is in contrast to the upregulation of LPS induced IL-23 in the presence of fucose, potentially indicating that DC-SIGN may engage differently in the TLR2 pathway than the TLR4 pathway, which may have a greater reliance on multivalency.

Similarly, all conditions downregulated HKST induced IL-10. The G5-glycans generally showed a lesser response as linker length increased, once again supporting the assumption that a stronger binding affinity leads to a greater modulatory response. The downregulation of HKST induced IL-10 under all conditions reinforces the notion that DC-SIGN may interact differently with TLR2 signalling cascades than it does for TLR4 signalling. Alternatively these data may indicate the involvement of mannose/fucose binding receptors other than DC-SIGN which actively engage in co-signalling with TLR2, but not TLR4, to regulate cytokine production. While IL-10 suppression would generally favour pro-inflammation, the simultaneous reduction in IL-23 suggests an inflammatory response that does not necessarily favour Th17 polarisation.

Next, the ligands PAM2CSK4 and PAM3CSK4 were investigated. Since HKST signals through TLR4 and TLR2, but the G5-glycan induced IL-23 and IL-10 modulations were different than when treated with LPS which signals only through TLR4, it was interesting to investigate whether signalling through other TLR2 ligands would also incur a similar responses.

First, MoDCs were treated with PAM2CSK4 or PAM3CSK4 alone which, for most donors, were poor inducers of IL-23 (Figure 7.17A). This response was largely the same when stimulating with 100 ng/ml and 1 µg/ml suggesting this is the maximum response of MoDCs to these ligands. This result was not unexpected as other studies employing these ligands on an MoDC model also showed limited IL-23 production.(390) In these same studies however, IL-23 was produced in much greater quantities in the presence of a NOD2 ligand (muramyl dipeptide) and the TLR7/8 ligand R848 - conditions used in combination with TLR2 ligands to mimic IL-12 and IL-23 production by *M. tuberculosis*. Therefore, although downregulation of IL-23 would be difficult to observe due to the low baseline levels making it difficult to compare to HKST, it was still interesting to observe if addition of these fungal ligands could mimic the upregulation induced in the presence of NOD2 or TLR7/8 ligands. IL-10 production in response to PAM2CSK4 and PAM3CSK4 was more significant (Figure 7.17B), making modulation in both directions easier to observe. PAM2CSK4 upregulated CD80 but had no significant effect on CD86 and PAM3CSK4 stimulation did not impact either CD80 or CD86 expression (Figure 7.16) indicating a lack of DC maturation which could account for the limited IL-23 production.

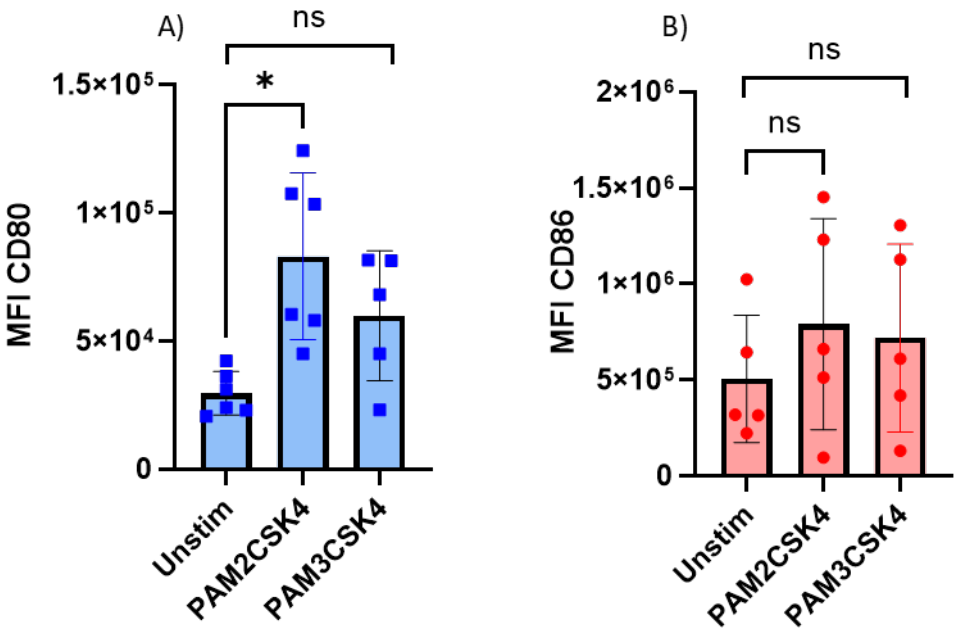

Figure 7.16 Bar graphs representing A) CD80 and B) CD86 expression on unstimulated and PAM2CSK4 or PAM3CSK4 stimulated MoDCs expressed as MFI. Data are representative of at least 5 independent experiments. *p<0.05 (paired t-test).

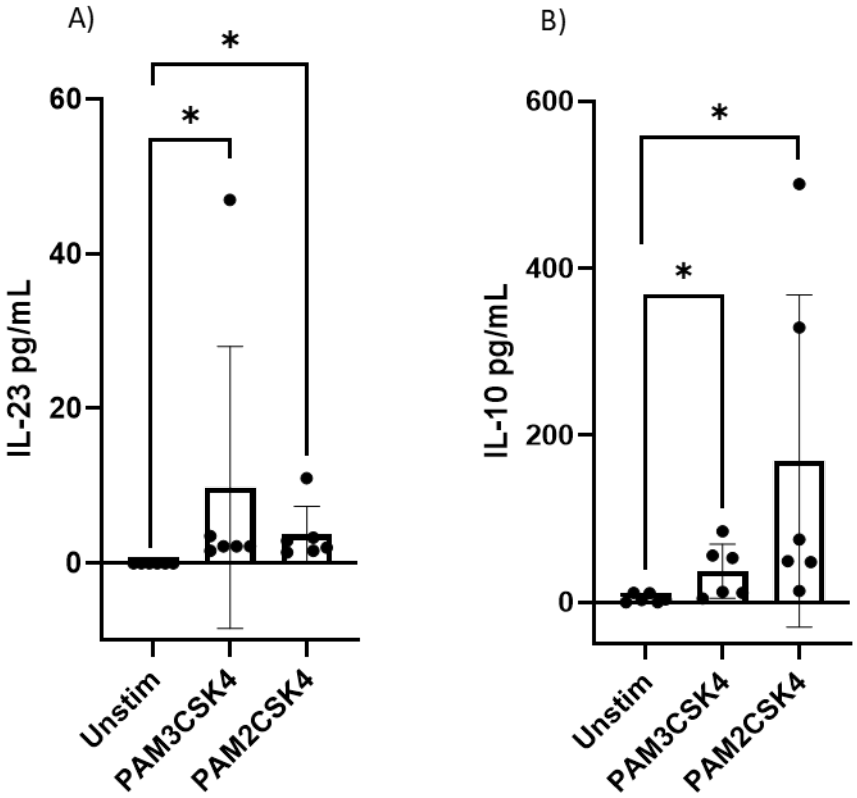

Figure 7.17 Bar graphs showing A) IL-23 and B) IL-10 production from unstimulated and PAM3CASK4 or PAM2CK4 stimulated MoDCs. Cytokines were measured by ELISA and represented as pg/mL Data are representative of 6 independent experiments (different donors) *p<0.05 (Wilcoxon).

PAM2CSK4, the TLR2/6, agonist was added to MoDCs alongside the G5-glycans and free ligands. IL-23 production was insignificantly changed for all G5-EG_n-dimannose conditions. Free dimannose, which under other conditions had, thus far, shown an ability to downregulate IL-23 production, also did not respond. However, this is likely due to the low initial baseline levels of IL-23 induced by PAM2CSK4 meaning downregulation was not observable. All G5-EG_n-fucose showed a trend of upregulating IL-23, although only G5-EG_2-fucose reached statistical significance. This would reinforce the assumption that the binding affinity is important *in vivo* and the shortest EG_2 linkers with the highest affinity for DC-SIGN have the greatest impact on cytokine production. Free fucose was also seemingly able to upregulate IL-23 although this did not reach statistical significance. While this data matches that observed for LPS it is contradictory to that observed for HKST where it was hypothesised that TLR2 involvement would lead to a reduction in IL-23 in the presence of fucose.

For IL-10, G5-glycans tended to downregulate production in a linker dependent fashion, more similar to HSKT. Although in this instance, both free dimannose and fucose showed an increase production of IL-10, which was not observed for the HKST conditions and was contradictory to the multivalent binding, again implicating a switch in signalling upon DC-SIGN clustering via multivalent binding. However, these changes were all insignificant compared to the controls. Furthermore, no conditions had any significant effect on PAM3CSK induced IL-10 and only free fucose was able to significantly modulate IL-23 under these conditions. Overall this data is largely contradictory, indicating the need for further detailed investigations into the complex and context specific nuanced signalling interactions between DC-SIGN and TLR2, TLR1 and TLR6 to determine if DC-SIGN has a significant role in modulating these TLR pathways.

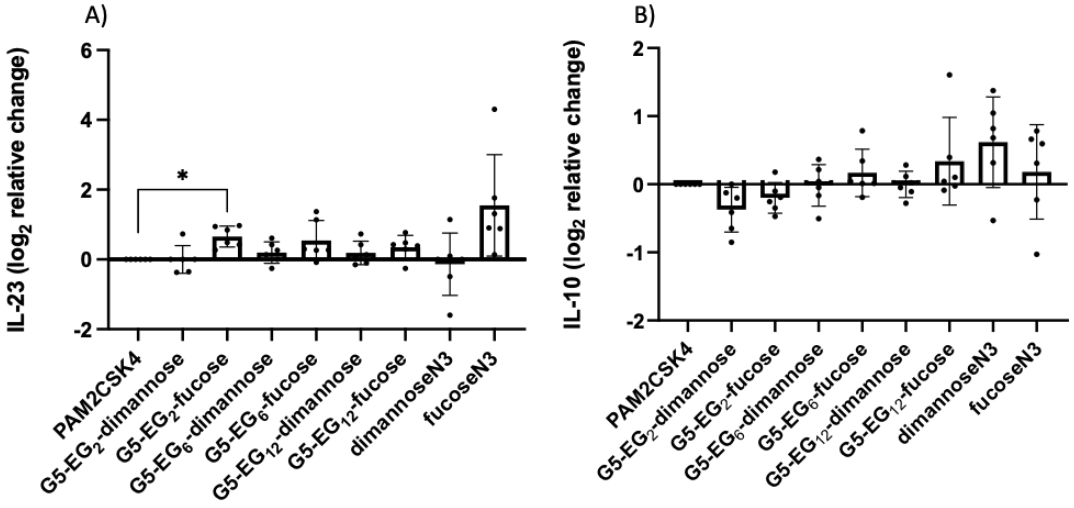

Figure 7.18 Bar graphs showing A) IL-23 and B) IL-10 production by MoDCs when stimulated with PAM2CSK4 or PAM2CSK4 plus various G5-EG_n-glycans/free ligands. Cytokines were measured by ELISA and normalised to PAM2CSK4 stimulated (for free ligands) or PAM2CSK4+G5-OH cells (for G5-glycans) (set as 1) then presented as a log2 function. Data are representative of 6 independent experiments. *p<0.05 (Dunnetts multiple comparison test).

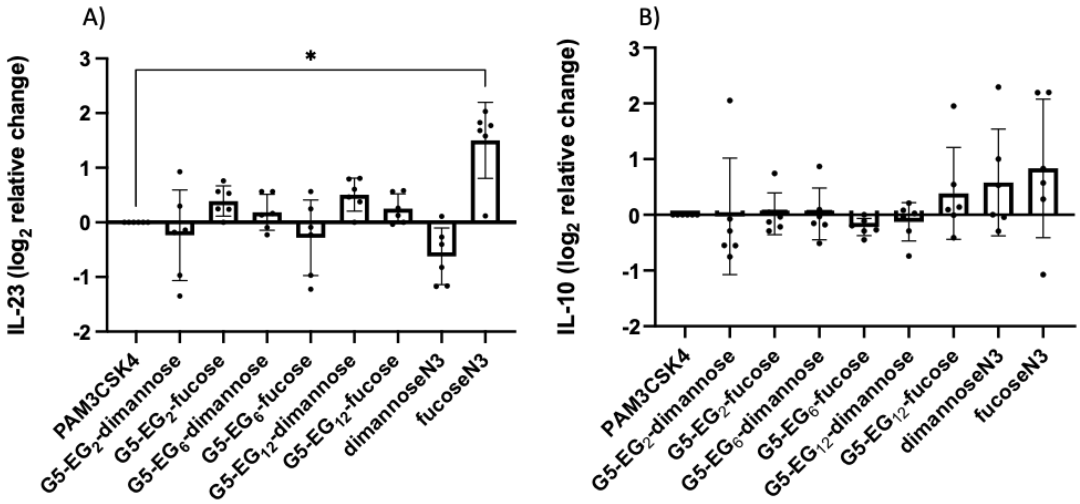

Figure 7.19 Bar graphs showing A) IL-23 and B) IL-10 production by MoDCs when stimulated with PAM3CSK4 or PAM3CSK4 plus various G5-EG_n-glycans/free ligands. Cytokines were measured by ELISA and normalised to PAM3CSK4 stimulated (for free ligands) or PAM23CSK4+G5-OH cells (for G5-glycans) (set as 1) then presented as a log2 function. Data are representative of 6 independent experiments. *p<0.05 (Dunnett's multiple comparison test).

7.2.4 DC-SIGN and macrophage mannose receptor blocking

To further study the carbohydrate mediated immune modulation of DC cytokine responses observed in Section 7.2.2, a targeted antibody inhibition strategy focussing on DC-SIGN and the macrophage mannose receptor (MMR, CD206) was employed. Specifically, the monoclonal antibody mab161 was chosen to target DC-SIGN, and clone15-2 was used to inhibit MMR. Both of these antibodies target the carbohydrate binding regions of their respective lectins, blocking the interaction between these lectins and their ligands and thereby inhibiting binding and carbohydrate mediated immune modulation capabilities.

This approach was aimed at determining whether the observed dimannose and fucose mediated modulation of LPS induced IL-23 and IL-10 production by DCs was solely dependent on DC-SIGN or whether other lectins, such as the MMR, also play a crucial role. Previous studies have shown that both DC-SIGN and the MMR bind carbohydrates such as mannose and fucose, and that blocking DC-SIGN with inhibitor AZN-1 abrogates immune modulation.(52) On the other hand, the MMR has been less intensely studied for its immune modulation capabilities, with studies largely focussing on its endocytic functions.(428) There is some evidence suggesting MMR may be involved in immune modulation of IL-17 in response to *Candida albicans*, and does strongly bind fucose despite its name.(391, 429)

To explore this, MoDCs were pre-treated with either mab161, clone15-2, or both, 1 hour prior to LPS stimulation in the presence of azido-dimannose, azido-fucose, or G5-EG_6-dimannose/fucose/ or G5-EG_{12}-OH. Cells were then incubated for a further 24 hours, after which they were imaged by light microscopy. Their supernatants were collected for cytokine analysis via ELISA and the cell pellets for those treated with G5s were collected for quantification of the amount of gold internalised via inductively coupled plasma mass spectrometry (ICP-MS).

After 2 hrs and 6 hrs, cells showed no visible signs of G5 adhesion or internalisation, however after 24 hours, cell treated with LPS and G5-glycans in the absence of any inhibitor appeared visually purple inside the cell boundaries (Figure 7.20A1, B1), indicating the G5-glycans had been successfully internalised. The G5-EG_{12}-OH showed no signs of binding (Figure 7.20C, Figure 7.21C). Adding a DC-SIGN inhibitor appeared to reduce internalisation of G5-dimannose and G5-fucose, as did the MMR inhibitor and when both were added to the same cell suspension, it appeared that internalisation was pointedly reduced based off cell pellet colour and microscopy images (Figure 7.20, Figure 7.21)

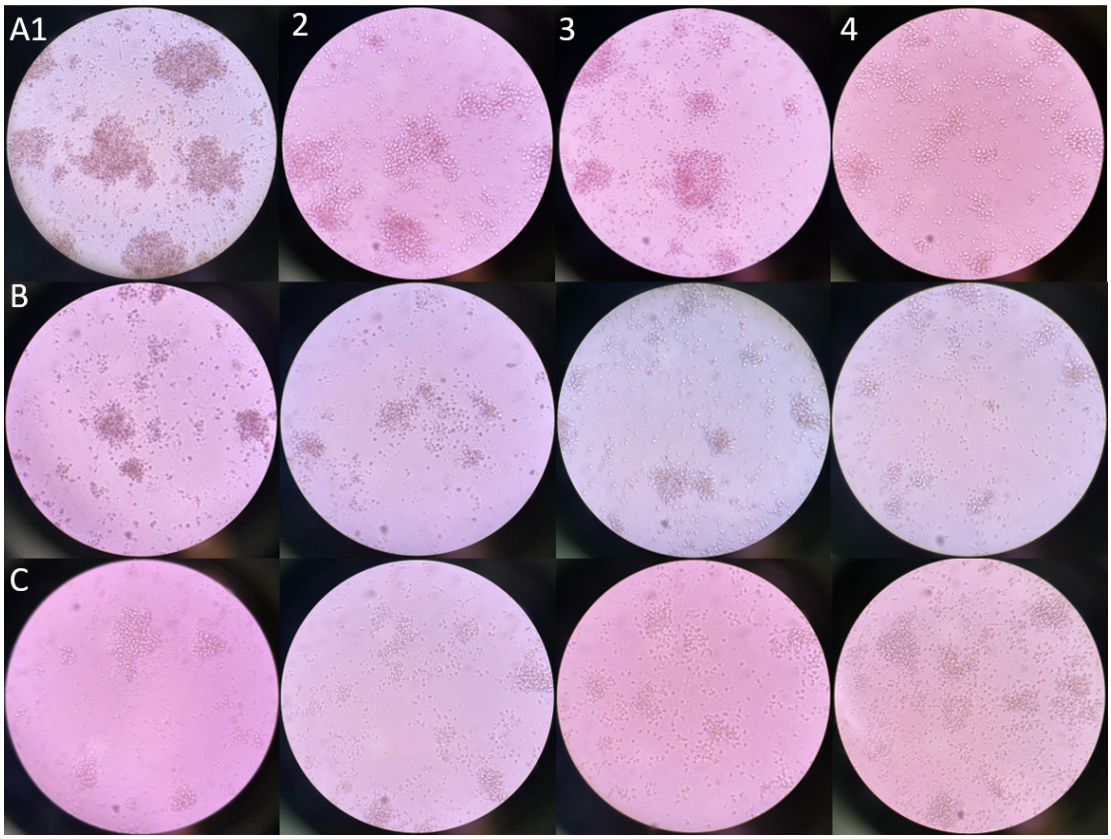

Figure 7.20 Light microscopy images of G5 endocytosis in the absence or presence of DC-SIGN and MMR inhibitors where the rows contain A) G5-EG_6-dimannose, B) G5-EG6-fucose, C) G5-EG_{12}-OH and columns contain 1) no inhibitor, 2) 10 μg/ml α-DC-SIGN inhibitor mab161 3) 20 μg/ml α-MMR inhibitor clone 15-2 4) Both 10 μg/ml α-DC-SIGN inhibitor mab161 and 20 μg/ml α-MMR inhibitor.

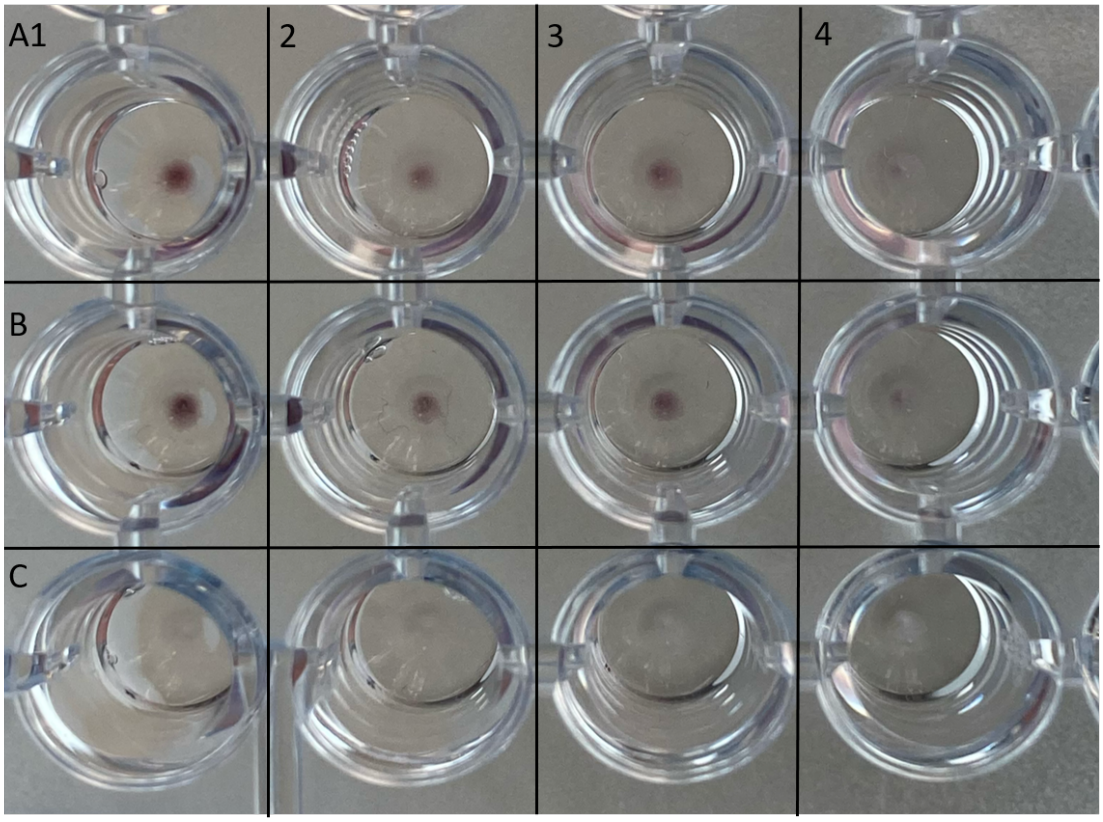

Figure 7.21 Images of pelleted cells after the supernatant was removed after being treated for 24 hours in the absence or presence of DC-SIGN and MMR inhibitors where the rows contain A) G5-EG_6-dimannose, B) G5-EG_6-fucose, C) G5-EG_{12}-OH and columns contain 1) no inhibitor, 2) 10 µg/ml α-DC-SIGN inhibitor mab161 3) 20 µg/ml α-MMR inhibitor clone 15-2 4) Both 10 µg/ml α-DC-SIGN inhibitor mab161 and 20 µg/ml α-MMR inhibitor.

To directly quantify internalisation and determine if this matched the visual colour, the pellets were stringently washed then 2 x 10^4 cells were treated with aqua regia. The solutions were then passed through an ICP-MS to determine the gold content in each sample. The quantity of gold in each sample was then converted to number of G5 per cell, based off the average volume and weight of a G5 particle. This was performed for two donors in duplicate, which were not averaged due to donor variation.

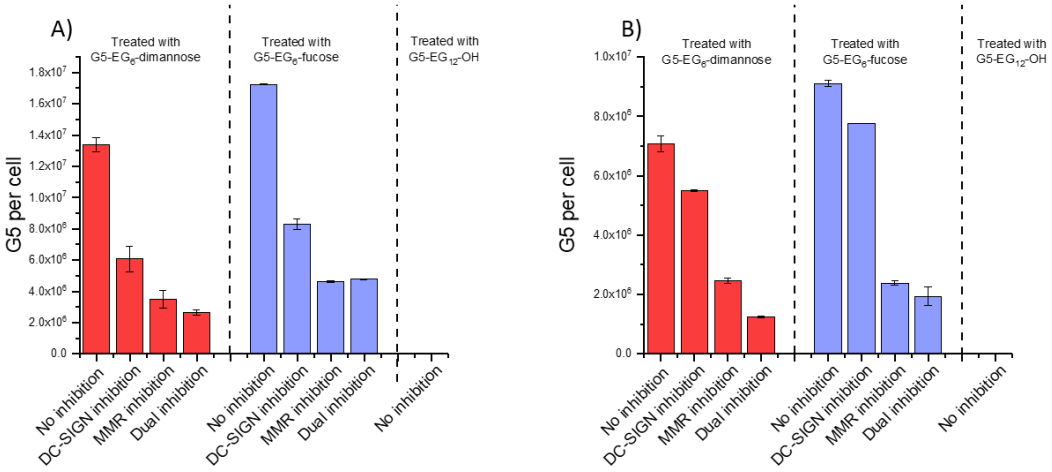

Figure 7.22 Bar chart representing number of G5-EG_6-dimannose (red bars), G5-EG_6-fucose (blue bars) or G5-EG_{12}-OH(clear bars) internalised per MoDC when treated with no inhibitor, a DC-SIGN inhibitor, a MMR inhibitor or both inhibitors, measured by ICP-MS for donors A and B. Error bars represent the SDs of duplicate measurements.

When looking at the donors separately, G5-EG_6-fucose (in the absence of any inhibitor) showed greater internalisation compared to G5-EG_6-dimannose, despite DC-SIGN having a greater affinity for dimannose as observed in Chapter 4. This signifies that there could be other endocytic receptors on MoDCs which have a greater affinity for fucose than dimannose. Furthermore, inhibiting DC-SIGN did not totally abrogate G5-uptake indicating either inefficient inhibition of DC-SIGN or the involvement of other lectins. The involvement of other lectins was validated by the MMR inhibition data. Inhibition of the MMR consistently reduced uptake more effectively than DC-SIGN inhibition for both donors and for both dimannose and fucose coated G5. These data indicate that it is not only DC-SIGN which binds and internalises G5-glycans, but MMR is also responsible. Some internalisation is still observed in the presence of both inhibitors, supporting the involvement of other lectins too. Chapter 8 focuses on developing a method to identify other cell surface proteins which bind to and internalise GNP-glycans.

On average, the number of G5-glycan internalised per cell in the absence of an inhibitor was approximately 1 x 10^7. Given that the total number of G5 particles added (150 nM, 200 uL) equates to 1.8 x 10^{16} total, or 1.8 x 10^{11} per cell, this represents only a small fraction of the overall concentration that has been bound and internalised. Notably, the control G5 showed no internalisation, even in the absence of inhibitors, indicating that

binding and uptake were dependent on the presence of a surface glycan. These findings raise the possibility that internalisation is not linearly dependent on G5-glycan concentration. Future work could explore this and determine if uptake is G5 concentration-dependent and if internalisation plateaus at higher G5 concentration, such as the concentrations used here (150 nM). Similar work looking at GNP uptake by HeLa cells reported a plateauing at higher concentrations(430). This could be used to minimise waste and any cytotoxic effects that may arise from using very high gold concentrations.

It was previously noted that the G5-glycan concentration was too low to significantly modulate LPS induced IL-23/IL-10 production. However, here it has been identified that only a fraction of the added G5-glycans bind to MoDCs. If it is indeed true that binding and internalisation reaches a plateau, it may be the case that even increasing the overall G5-glycan concentration might not guarantee sufficient binding or internalisation to trigger measurable cytokine modulation.

While blocking DC-SIGN did effectively reduce G5-glycan internalisation, due to the involvement of other lectins in this process, it was not able to completely inhibit cellular uptake. This initially appears to be in contrast to work by Gringhuis *et al*. which showed that when using the DC-SIGN inhibitor AZN-1, glycan induced modulatory effects were totally abrogated.(52) However, internalisation alone does not imply involvement in signalling cascades that lead to cytokine production and therefore the internalisation observed here via MMR or other rectors still may not be the cause of the modulation of TLR4 induced IL-23/IL-10 production observed in section 7.2.2. Since the G5-glycans did not initially show any significant modulation, the effects of inhibition on cytokine production was followed by free azido-dimannose and free azido-fucose mediated modulation.

To determine whether reduced internalisation had an impact on cytokine modulation, IL-23 and IL-10 levels in cell supernatants were measured by ELISA. Cytokine responses were normalised to LPS + inhibitor controls to account for any independent effects the inhibitors may have had on TLR4 mediated signalling. While MMR accounted for a significant proportion of G5 internalisation, this did not directly translate to the IL-23 output which largely did not change compared to when no inhibitor was added (Figure 7.23). This strongly suggests that recognition of dimannose and fucose via the MMR does not engage the pathways involved for co-signalling with TLR4 to regulate IL-23. This observation is evidenced by work completed by van de Veerdonk *et al.,* which showed that when TLR4 was blocked, there was little impact on *Candida* mannan-induced IL-17 secretion through the MMR, suggesting MMR and TLR4 do not work synergistically to regulate the IL-23/IL-17 axis.(391) On the other hand, inhibiting DC-SIGN with mab161 tended to attenuate IL-23 production to levels more similar to those observed by LPS alone, implicating DC-SIGN in this signalling pathway.

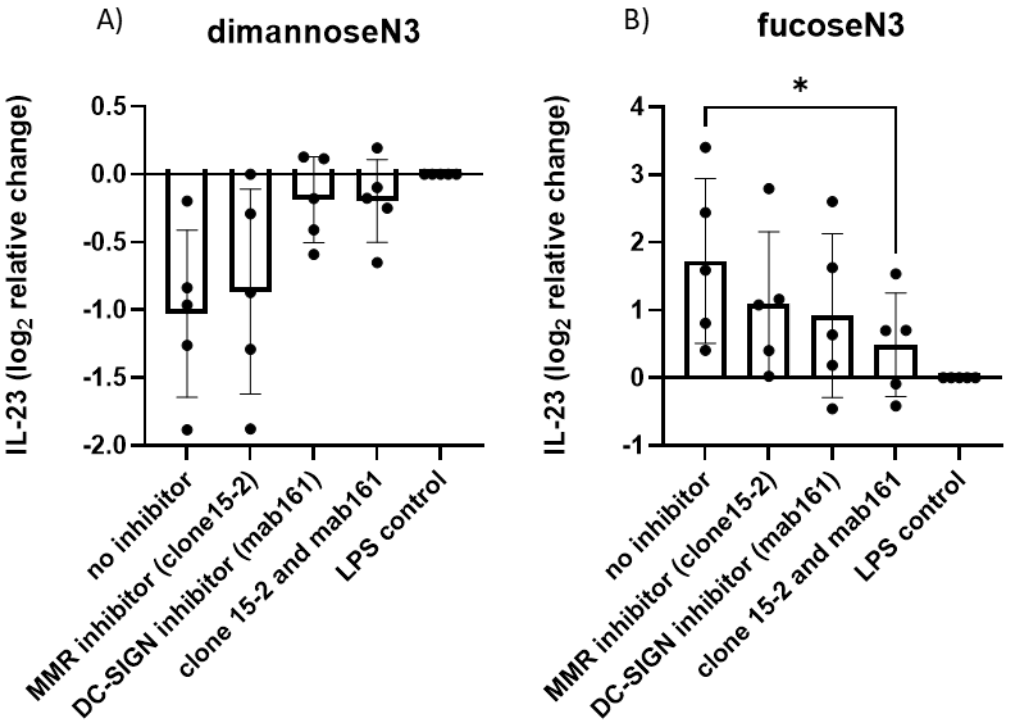

Figure 7.23 Bar graph showing IL-23 production by MoDCs when stimulated with LPS or LPS plus either A) dimannoseN3 or B) fucoseN3 alone (no inhibitor) or in the presence of MMR inhibitor (clone15-2), DC-SIGN inhibitor (mab161), or both. Cytokines were measured by ELISA and normalised to LPS stimulated cells (set as 1) then presented as a log2 function. Data are representative of 5 independent experiments * $p<0.05$ (Dunnett's multiple comparison).

Interestingly, when looking at IL-10 production, inhibiting fucose uptake through the MMR had more of an impact than inhibiting DC-SIGN. While both MMR inhibition and DC-SIGN inhibition reduce show reduced IL-10 production compared to when no inhibitor was added, none of this data reached statistical significance. Dimannose induced IL-10 modulation appeared to follow no trend when inhibitors where added. In conclusion MMR may be more involved in IL-10 production than DC-SIGN but DC-SIGN is more involved in IL-23 production. Further repeats would be required to determine if this trend becomes statistically significant with a higher donor number.

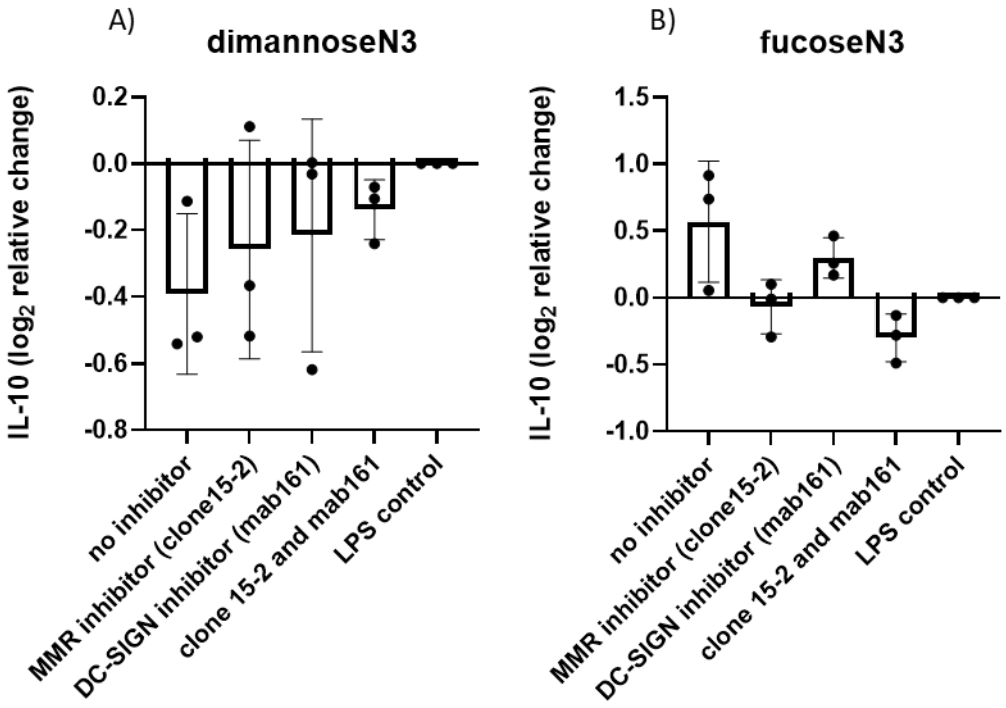

Figure 7.24 Bar graph showing IL-10 production by MoDCs when stimulated with LPS or LPS plus either A) dimannoseN3 or B) fucoseN3, alone (no inhibitor) or in the presence of MMR inhibitor (clone15-2), DC-SIGN inhibitor (mab161) or both. Cytokines were measured by ELISA and normalised to LPS stimulated (set as 1) then presented as a log2 function. Data are representative of 3 independent experiments. (No significance was observed using Dunnett's multiple comparisons test).

7.2.5 T cell proliferation

To further investigate the immunomodulatory effects of G5-glycans, a T cell proliferation assay was performed. T cell activation is a regulated process which requires three important signals; antigen recognition through engagement of the T cell receptor with peptide-MHC complexes, co-stimulation through CD80/86 interaction with CTLA-4 or CD28 and the presence of certain cytokines at the time of T cell priming. Earlier observations in this chapter showed that both free azido-dimannose and G5-EG_6-dimmannose led to a reduction in the expression of CD80 and CD86 in MoDCs when compared to an LPS control (Figure 7.12). Since these co-receptors are essential for effective T cell activation, their downregulation may impair T cell proliferation. Furthermore, LPS is known to favour Th1 and Th17 responses via induction of IL-12 and IL-23, yet changes in cytokine production upon addition of G5-glycans and free glycans were observed and hence addition of these in a co-culture may result in modulating the inflammatory or tolerogenic nature of the T cell response.

For this experiment, MoDCs were stimulated for 24 hours in the presence of LPS with either G5-glycans or free ligands. Donor matched $CD4^+$ T cells were then added and the co-culture incubated for 5 days. The added T cells were pre-stained with a cell permeable

fluorescent dye which tracks proliferation. When T cells divide the dye is equally split between two daughter cells, halving the fluorescence intensity with each division. Proliferation was therefore able to be followed by flow cytometry, as proliferating cells show a progressive loss in fluorescence with each division. Figure 7.25 shows flow cytometry dot plots and light microscopy images of unactivated T cells and T cell activated with a commercial antibody cocktail for comparative controls. In the flow cytometry plots, unactivated T cells show a single high florescence intensity population whereas the activated cells show clear bands, decreasing in fluorescence intensity, with each band representing a new daughter population (Figure 7.25A-B). Correspondingly, in the light microscopy images, the unactivated T cells remain dispersed and uniform, while the activated T cells form clusters (Figure 7.25C-D).

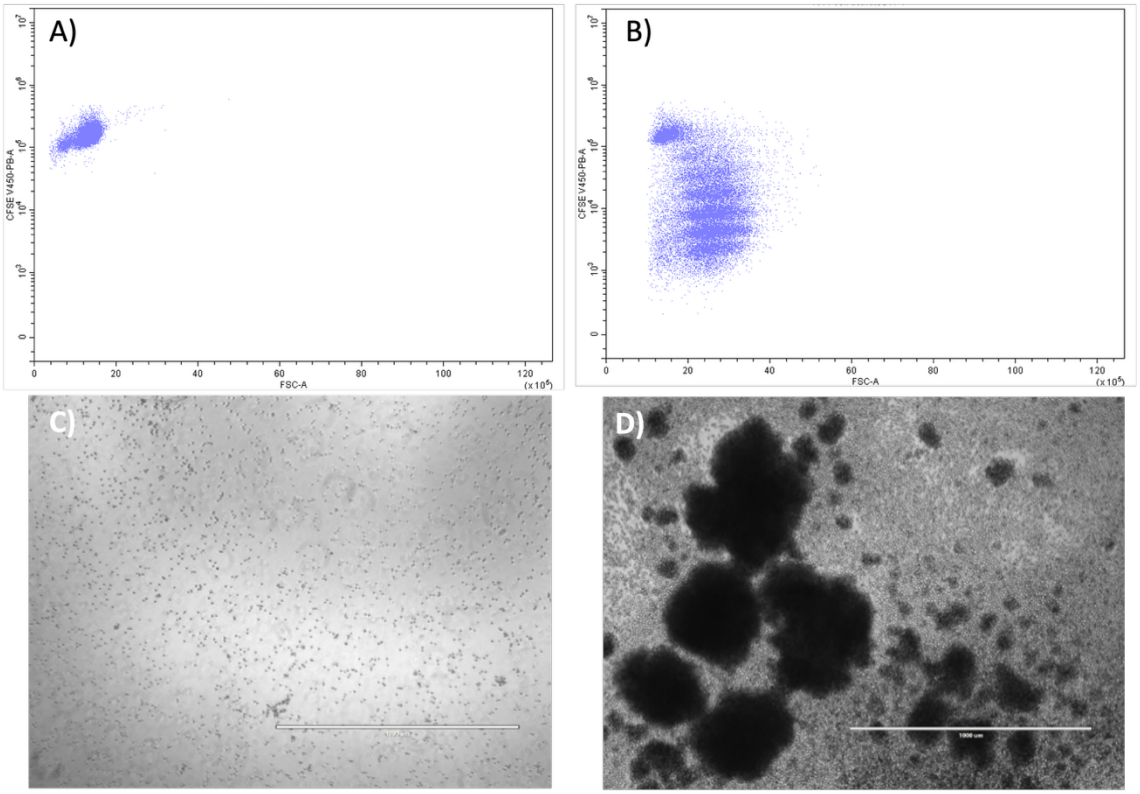

Figure 7.25 (a-b) flow cytometry dot plots showing A) Unactivated T cells characterised by a single population at high fluorescence and B) anti-CD3/anti-CD28 stimulated, proliferating T cells where each band at decreasing fluorescence intensity represents a new daughter population as the intracellular dye is diluted with each generation. (c-d) Light microscopy images of C) unactivated T cells, D) anti CD3/anti-CD28 stimulated, proliferating T cells.

On day five of the co-culture, the cells were imaged by light microscopy to visually asses T cell clustering as an indicator of activation and proliferation. The cell pellets were then collected and stained with a panel of antibodies to differentiate between MoDCs and T cells in the culture, and were subsequently analysed by flow cytometry. As expected, the MoDCs pre-stimulated with LPS induce visual T cell clustering in the light microscopy images compared to the unstimulated MoDCs (Figure 7.26A vs Figure 7.26B). However, when these LPS treated MoDCs were co-stimulated with free glycans (Figure 7.26 C-D)

or G5-glycans (Figure 7.26E-F), there were no immediate differences in clustering compared to the LPS control.

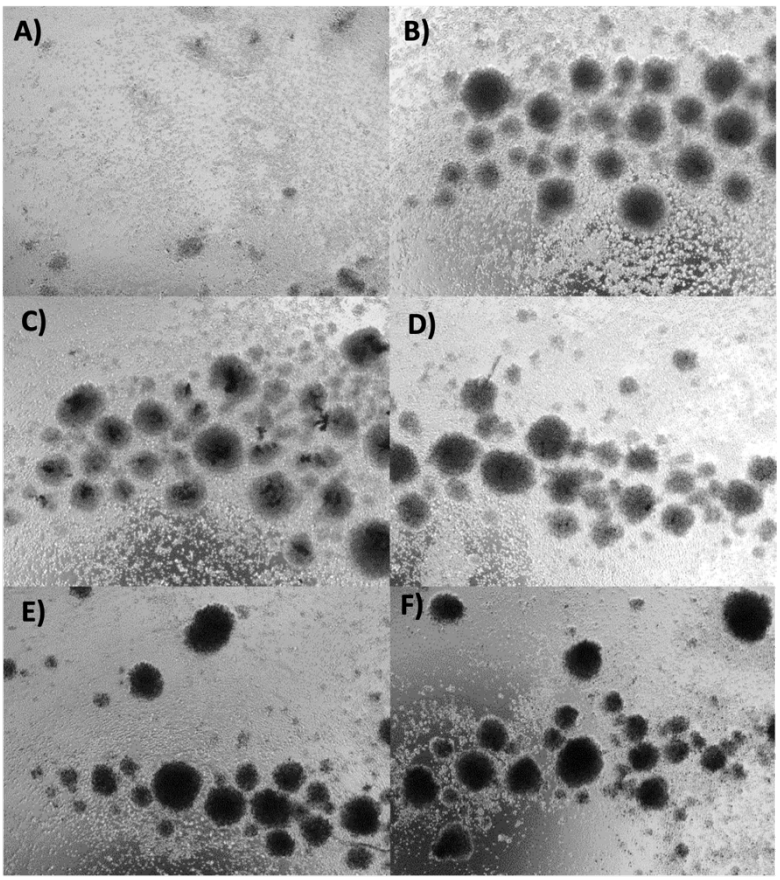

Figure 7.26 Light microscopy images of an MoDC + T-cell co-culture after 5 days of stimulation with A) nothing added, B) LPS C) LPS+dimannoseN3, D) LPS+fucoseN3, E) LPS+G5-EG_6-dimannose F) LPS+G5-EG_6-fucose.

Although limited differences were observed by light microscopy, using flow cytometry there were clear changes in T cell proliferation upon addition of free glycans and G5-glycans (Figure 7.27). T cell proliferation was quantified by comparing the proportion of the undivided population to those that had undergone at least one division, based on dilution of the intracellular dye. Results were then normalised to each donors' respective LPS control to account for donor variation, and were presented as normalised % divided. (Figure 7.29A-B) As expected, LPS stimulation led to greater proliferation than the unstimulated DC-T cell control (Figure 7.27A-B). Addition of dimannose consistently showed an increase in proliferation across all 5 donors (Figure 7.29). Although this was inconsistent with the previous observation that dimannose downregulated CD80/86 expression in MoDCs, it instead was consistent with the observation that azido-dimannose reduced IL-10 production, a cytokine known to suppress T cell activation. In contrast the effects of free fucose were more variable. In some donors, azido-fucose enhanced proliferation while in others it led to a reduction. Again, this variability matched

the IL-10 data where addition of fucose regulated IL-10 differently depending on the donors.

Interestingly, addition of both G5-EG_6-dimannose and G5-EG_6-fucose appear to suppress T cell proliferation. This trend was generally observed across 5 different donors. A G5-OH control had little impact on T cell proliferation compared to the LPS control (Figure B. 9) suggesting the reduction in proliferation was glycan dependent rather than due to the gold scaffold itself. Considering this trend was opposite to the free glycans, the G5-glycans may be involved in T cell suppression through a different mechanism, perhaps by physically blocking DC-T cell contact through steric hindrance.

The percentage divided calculated using CytExpert was compared to a division index calculation using a T cell modelling tool on FlowJo (Figure 7.28A-F). The Division Index (DI) represents the average number of cell divisions undergone by the entire original population, including undivided cells. It is calculated by averaging the number of divisions across all cells, with non-dividing cells considered to have zero divisions. Across both metrics (percentage divided and DI) the G5-glycans consistently led to reduced proliferation, reinforcing the idea that the multivalent presentation of glycans on the nanoparticle surface may influence T cell outcomes differently than free ligands.

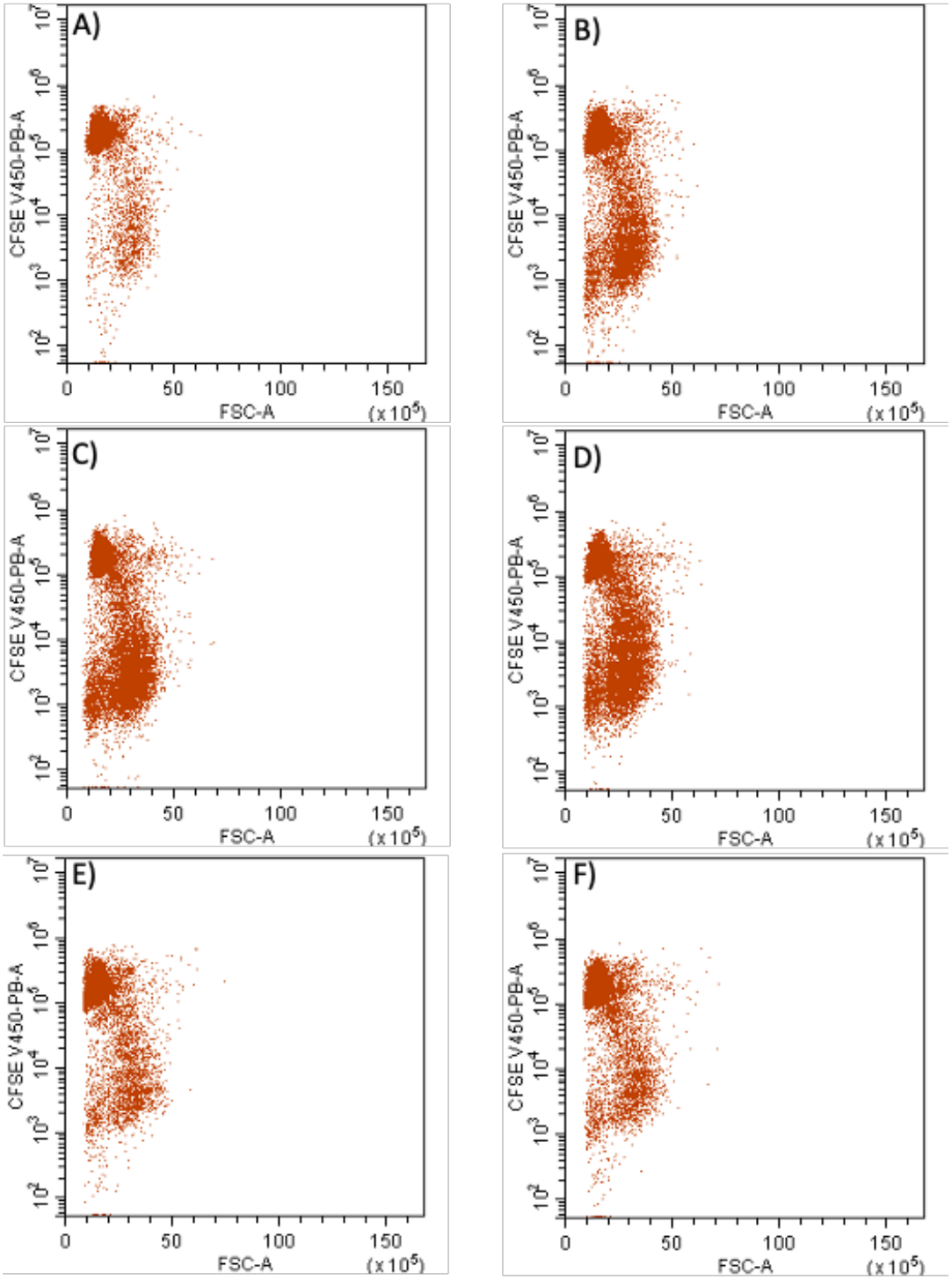

Figure 7.27 Flow cytometry plots of an MoDC + T-cell co-culture after 5 days of stimulation with A) nothing, B) LPS C) LPS+dimannoseN3, D) LPS+fucoseN3, E) LPS+G5-EG_6-dimannose F) LPS+G5-EG_6-fucose.

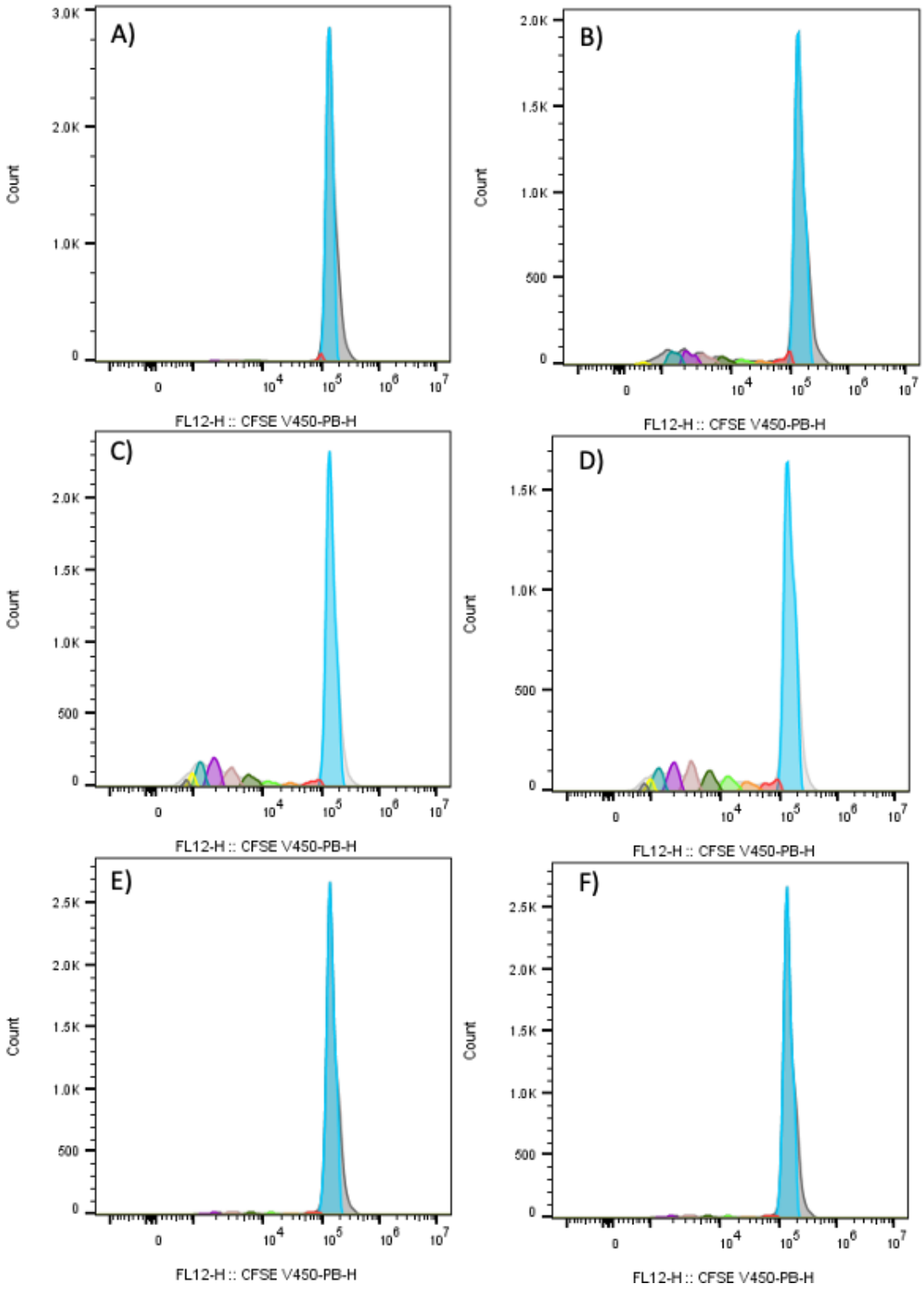

Figure 7.28 T cell proliferation modelling plots of an MoDC + T-cell co-culture after 5 days of stimulation with A) nothing, B) LPS C) LPS+dimannoseN3, D) LPS+fucoseN3, E) LPS+G5-EG_6-dimannose F) LPS+G5-EG_6-fucose. Each coloured peak in the proliferation modelling plots represents a new division, where the area of the peak is related to the number of cells in that division. The blue peak represents the undivided population

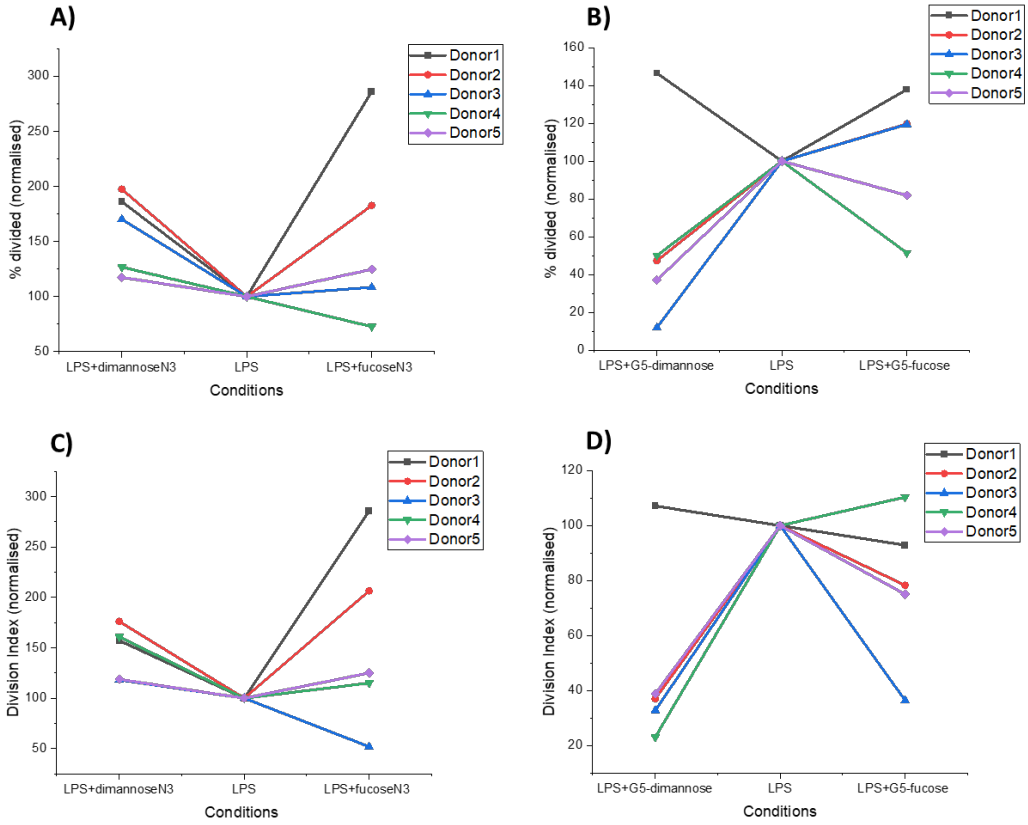

Figure 7.29 Line graphs representing (a-b) percent of T cells divided in a MoDC + T cell co-culture after 5 day stimulating with A) LPS, alone or in combination with either free dimannoseN3 or free fucoseN3 and B) LPS, alone or in combination with either G5-EG_6-dimannose or G5-EG_6-fucose. % divided calculated by gating in Cytexpert (c-d) division index of T cells in a MoDC + T cell co-culture, stimulated with C) LPS, alone or in combination with either free dimannose or free fucose and D) LPS, alone or in combination with either G5-EG_6-dimannose or G5-EG_6-fucose. DI calculated using the T cell modelling function in FlowJO. All data was normalised to a donor matched LPS stimulated cells (set to 100).

Simultaneously to collecting the cell pellets, the supernatants were collected for cytokine analysis to assess whether T cell responses were skewed towards specific helper lineages such as Th1, Th2, Th17 and Th9. The supernatants were analysed by a T helper cell specific LEGENDplex™ panel. Briefly, LEGENDplex™ is a bead based immunoassay capable of simultaneously measuring up to 13 analytes in a single small volume sample using flow cytometry. Each cytokine is captured by a distinct bead population which can be identified by its size/fluorescence signature, and the intensity of the PE signal on each bead is used to quantify each specific analyte using a standard curve.

Comparing results to those of unstimulated MoDC+T cell, LPS stimulation alone pushed the immune response towards Th17. This was reflected by the cytokine output including upregulation IL-22, IL-17A, IL-17F and IFN-γ (levels of IFN-γ after stimulation exceeded the upper limit of detection). IL-6 production was also significantly upregulated which is also primarily associated with a Th17 immune response. Th1 associated cytokines such

as IL-2 and TNF-α showed some moderate upregulation but the classical Th2 cytokines such as IL-4 and IL-5 were downregulated, and IL-13 showed little change (Figure 7.30).

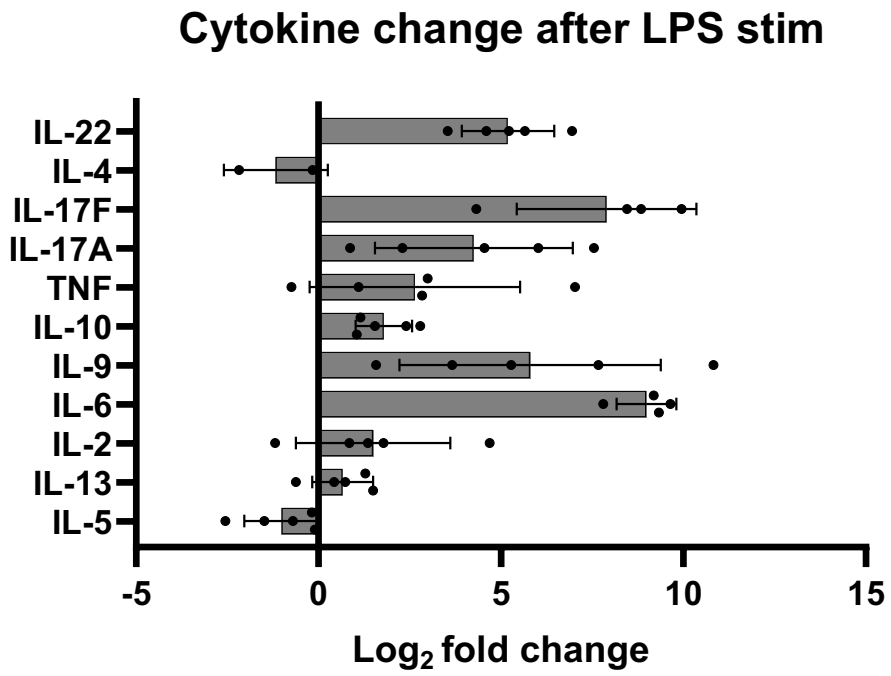

Figure 7.30 Bar graph representing changes in cytokine production after MoDC + T cell co-culture stimulation with LPS. Cytokines were measured by LEGENDplex™ and normalised to a donor matched unstimulated control (set as 1) and shown as a log2 fold change.

Following this analysis, the cytokine production from samples containing LPS plus free glycans or G5-glycans were normalised to their respective LPS controls to observe whether addition of these free glycans or G5-glycans influenced the T cell response further towards or away from this Th17 response. Addition of azido-dimannose largely skewed the response away from Th17, evidenced by the downregulation IL-6, IL-17A/F, and IL-22 (Figure 7.31A-D). Although IFN-γ was also decreased (based on reduced MFI) it remained above the quantifiable limit of detection. Azido-dimannose induced significant upregulation of the Th2 cytokines such as IL-5 and IL-13, along with 4 out of 5 donors showing elevated IL-9 levels (Figure 7.32A-C), a cytokine which supports Th2 responses. IL-4 levels also trended upwards (increased MFI) but was unquantifiable as it remained below the lower concentration limit. After averaging responses from 5 donors, the Th1 cytokine TNF-α, and IL-2 remained largely unaffected by dimannose (Figure 7.32D-E). Matching earlier observations and predictions as to why proliferation may have increased, azido-dimannose continued to downregulate IL-10 (Figure 7.31E). Azido-dimannose skewing the T cell response away from LPS induced Th17 is closely aligned with its ability to downregulate LPS induced IL-23 production in MoDCs (Figure 7.10), a cytokine essential for propagating and maintaining Th17 responses.

On the other hand, azido-fucose appeared to enhance the LPS induced Th17, despite its variable impact on T cell proliferation. IL-17A/F, IL-22 and IL-6 were all elevated in most donors (Figure 7.31A-D). This aligned with earlier observations that fucose upregulated IL-23 in MoDCs when co-stimulated with LPS. Interestingly, the G5-glycans had little impact on any cytokine production despite appearing to reduce proliferation, however they were also mostly unable to significantly induce any modulation in cytokine production by MoDCs in response to LPS (Figure 7.10) and so it is largely unsurprising that they show no impact on T cell responses either.

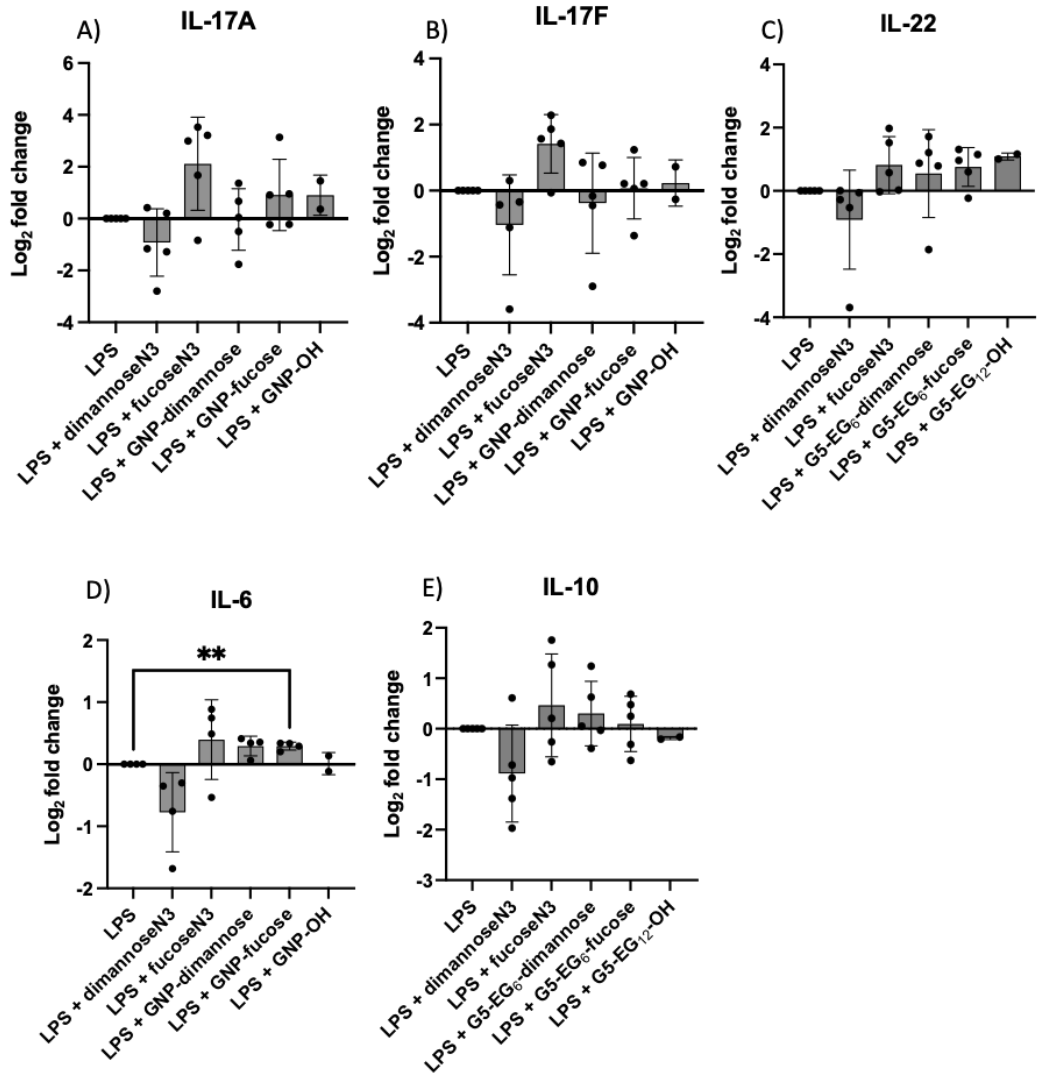

Figure 7.31 Bar graphs representing cytokine production by a MoDC + T cell co-culture after stimulation with LPS alone or with either dimannoseN3, fucoseN3, G5-EG_6-dimannose, G5-EG_6-fucose or G5-EG_{12}-OH. Production was normalised to LPS stimulated cells (set as 1) and presented as a log2 fold change for production of A) IL-17A, B) IL-17B, C) IL-22 D) IL-6, E) IL-10. Data representative of 2-5 separate experiments. ** p<0.01 (Dunnett's multiple comparisons test).

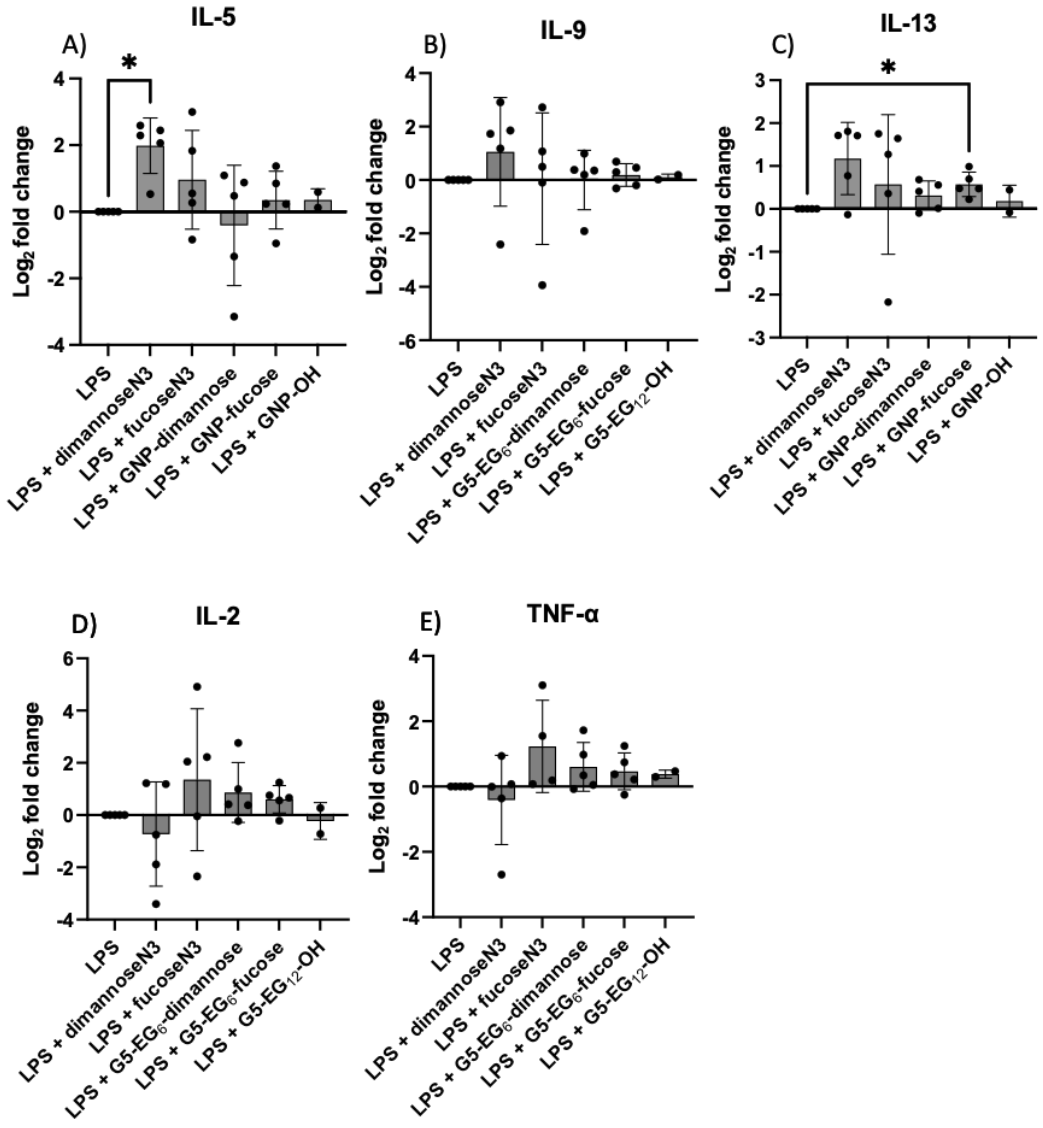

Figure 7.32 Bar graphs representing cytokine production by a MoDC + T cell co-culture after stimulation with LPS alone or with either dimannoseN3, fucoseN3, G5-EG_6-dimannose, G5-EG_6-fucose or G5-EG_{12}-OH. Production was normalised to LPS stimulated cells (set as 1) and presented as a log2 fold change for production of A) IL-5, B) IL-9, C) IL-12, D) IL-2, E) TNF-α. Data representative of 2-5 separate experiments. * p<0.05 (Dunnett's multiple comparisons test).

7.3 Conclusions and future work

7.3.1 Conclusions

In summary, this chapter has begun to explore the downstream immunological impact of G5-EG_n-glycans, specifically focussing on their role in modulating IL-23 and IL-10. A monocyte derived DCs model was established as a suitable and practical model for investigating DC-SIGN driven IL-23 modulation, overcoming the challenges of isolating and purifying primary DCs from peripheral blood. MoDCs were reliably differentiated from monocytes, evidenced by a reduction in CD14 and a substantial increase in DC-SIGN

expression. Phenotyping confirmed these MoDCs as being similar to the peripheral blood cDC2 subset, which are known to drive Th17 polarisation and produce key inflammatory cytokines like IL-23, making them highly relevant for the objectives of this chapter.

LPS was used to induce MoDC maturation, leading to an increase in both CD80 and CD86 expression, and the production of both IL-23 and IL-10. When co-stimulated with LPS and G5-EG_n-glycans, limited modulation of IL-23 and IL-10 was observed compared to an LPS and G5-OH control. This lack of significant modulation was hypothesized to be due either to the shape and size of the glycoconjugate, where small mannose/fucose dendrons have also previously failed to regulate cytokine production, or due to insufficient concentration, as free ligands at estimated matched concentrations also failed to induce significant cytokine modulation.(164) However, free ligands at much higher concentration (50 mM) did yield significant modulatory effects. While this data was agreeing to certain literature suggesting DC-SIGN engagement with either ManLAM, or mannose glycopolymers can inhibit dectin-1 induced IL-23 or LPS induced IL12p70, respectively, it is contrasting to other relevant studies employing DC-SIGN/TLR4 co-signalling pathways.(52, 92, 161, 394) This discrepancy has so far been attributed to the presence of an azide handle on the free ligands used in these experiments, as free mannose without an azide handle showed upregulation of IL-23, consistent with previous reports of mannose induced upregulation of the IL-23 subunit; IL-12p40.(52) In line with suppression IL-23 and IL-10, addition of G5-EG_6-dimannose or free dimannose showed a tendency to reduce CD80 and CD86 expression.

The modulation of other TLR signalling pathways via DC-SIGN was briefly investigated. Co-stimulation with Heat Killed *Salmonella typhimurium* (HKST) (a TLR4 and TLR2 agonist) showed some downregulation of IL-23 by G5-EG_2-dimannose and G5-EG_2-fucose, suggesting that higher binding affinity G5-glycans could exert some regulatory effect. Notably, all conditions with HKST led to downregulation of IL-10, with G5-glycans showing a linker-dependent effects, reinforcing the role of DC-SIGN and binding affinity in TLR2 signalling and potentially promoting a more inflammatory environment.

PAM2CSK4 (TLR2/6 agonist) and PAM3CSK4 (TLR1/2 agonist) poorly induced IL-23 and IL-10 on their own, and co-stimulation with G5-glycans and free ligands showed mostly insignificant modulatory effects. However, for PAM2CSK4 stimulation, G5-glycans generally downregulated IL-10 in a linker-dependent manner similar to HKST, further supporting the influence of DC-SIGN and binding affinity on TLR2 signalling. The overall data from other TLR co-stimulations were complex and at times contradictory, indicating the need for further detailed investigations into the specific signalling complexes involved.

Antibody blocking experiments with anti-DC-SIGN (mab161) and anti-MMR (clone15-2) provided further insights into internalisation and signalling. This revealed that inhibition

of the macrophage mannose receptor consistently reduced G5-glycan uptake more effectively than DC-SIGN for both dimannose and fucose coated G5s. This strongly indicated that other lectins, particularly MMR, are also significantly responsible for G5-glycan internalisation, not solely DC-SIGN, and that some internalisation persists even when both are inhibited, suggesting the involvement of additional lectins. Despite MMR accounting for a significant proportion of G5 internalisation, this did not directly translate to changes in IL-23 output, suggesting that MMR recognition does not co-signal with TLR4 for IL-23 regulation. Conversely, inhibiting DC-SIGN tended to attenuate IL-23 production, thereby implicating DC-SIGN in this specific signalling pathway for IL-23 regulation.

Finally, the effects of glycan's on downstream T cell proliferation and cytokine production was explored. LPS stimulation alone effectively increased T cell proliferation and skewed the immune response towards a Th17 profile, characterised by upregulation of IL-22, IL-17A, IL-17F, IFN-γ, and IL-6. Free azido-dimannose consistently further increased T cell proliferation compared to LPS alone, which, although seemingly inconsistent with its observed downregulation of CD80/86 on MoDCs, aligned with its concurrent reduction of the T cell suppressor cytokine IL-10. Furthermore, dimannose largely skewed the response away from Th17 and towards a Th2 phenotype, evidenced by downregulation of Th17-associated cytokines and upregulation of IL-5, IL-13, and IL-9. Free azido-fucose had more variable effects on T cell proliferation across donors, aligning with its variable impact on IL-10. It appeared to enhance the LPS-induced Th17 response, consistent with its observed upregulation of IL-23 in MoDCs.

In contrast, G5-glycans (both dimannose and fucose) appeared to suppress T cell proliferation, a trend opposite to that observed with free glycans, suggesting a potentially different mechanism of T cell modulation, possibly due to steric hindrance. However, the G5-glycans had minimal impact on T cell cytokine production, which was unsurprising given their limited modulation of MoDC cytokine production.

Overall, this chapter has provided foundational insights into the complex immunological impacts of glycans on IL-23 driven inflammation, highlighting that their effects depend significantly on the glycan type, their presentation (free vs multivalent), and the specific co-stimulation conditions.

7.3.2 Future work

Future work for this chapter should focus on resolving contradictions within the data and explore reasonings behind deviations from the literature. A key idea would be to investigate raf-1 phosphorylation upon addition of azido-dimannose and azido-fucose. The literature suggests recognition of mannose-containing glycans by DC-SIGN leads to phosphorylation of raf-1, which is linked to the production of pro-inflammatory cytokines, while fucose-containing glycans do not.(92) However, in this thesis when using azido

glycans, the opposite was observed upon co-stimulation with LPS. It would be interesting to see if this is a result of raf-1 phosphorylation or if the azido tag recruits different signalling complexes than those reported in the literature. Initial experiments using flow cytometry to observe raf-1 phosphorylation in an LPS stimulated THP-1 cell line were started. Unfortunately, due to high background fluorescence, sensitivity to dye concentration and poor separation of positive and negative controls, flow cytometry was deemed unsuitable for this purpose. An alternative method for observing raf-1 phosphorylation is a western blot, although it requires larger quantities of protein, difficult to obtain from the number of MoDCs used in this study.

Other considerations include exploration of DC-SIGN clustering, and concentration dependent gold nanoparticle uptake. When comparing the effects of multivalent glycans to their free ligand counterparts, some discrepancies in cytokine production were observed (especially in the case of PAM2CSK4 mediated IL-10), and big differences on the effects of multivalent vs free ligands on T cell proliferation were also seen. Given that clustering of DC-SIGN into microdomains is important for viral uptake, it could be true that clustering is facilitated by multivalent G5s, which in turn affects the signalling pathways. Clustering could be observed by fluorescence microscopy, or through FRET based assay where neighbouring DC-SIGNs are labelled in FRET pairs to detect clustering.(176, 184) It would also be valuable to explore whether G5 uptake is concentration dependent and if internalisation plateaus at higher concentrations. This could help minimise waste and potential cytotoxicity, while also informing whether increasing the overall G5-glycan concentration would lead to sufficient binding and internalisation to trigger measurable cytokine modulation.

Although a MoDC model provides a suitable system for dissecting DC-SIGN driven IL-23 production and Th17 responses by closely resembling the cDC2-type subset, they do not fully represent the full *in vivo* heterogeneity of human DCs. Therefore, investigating how DC-SIGN modulators affect cytokine responses in isolated conventional DCs (cDC) subsets, particularly cDC1s, cDC2s, DC2s, and DC3s, would provide a more comprehensive understanding of DC-SIGN's role across the full spectrum of human DCs. Using the methodology explained by Heger *et al.,* DC subsets can be isolated using a refined staining protocol and a high throughput cell sorter.(422)

Finally, it would be useful to identify other glycan-binding receptors on the MoDC surface. This would provide a more complete picture of glycan recognition and its impact on immune responses, especially given that some internalisation was still observed even when both DC-SIGN and MMR were inhibited. Chapter 8 explores the use of an affinity pull down assay to identify such proteins. These suggested areas aim to resolve existing contradictions and provide a deeper mechanistic understanding of how glycan type and linker length precisely modulate DC-SIGN's influence on immune responses.

Chapter 8 – Using glycan-decorated gold nanoparticles to selectively enrich DC-SIGN

8.1 Introduction

8.1.1 GNP based pull down

So far, this thesis has established that the GNP-NSET readout is a valuable approach for investigating DC-SIGN-mediated binding with multivalent glycans, providing both affinity measurements, and the thermodynamic parameters associated with these binding events. This has been especially useful in elucidating the interaction between small glycosylated gold nanoparticles (G5-glycans) and the fluorescently labelled protein of interest. Furthermore, the ability of G5-glycans to modulate cytokine production and T cell proliferation in cellular assays has been studied. However, the lectin binding profiles of the G5-glycans have been shown to extend further than just their DC-SIGN target, indicating the need to develop a method for identifying such proteins from the cell surface to further elucidate mechanisms of cytokine production. In order to do so, a larger gold nanoparticle scaffold size is required as much less time and lower centrifugation speeds are required for their agglomeration out of solution, making them well suited to an affinity 'pull down' assay to isolate cell surface bound proteins. This chapter details how 27 nm gold nanoparticles (G27-glycans) can be designed and utilised for this process, which first requires optimisation to ensure strong binding affinity and glycan specificity.

Using a setup similar to the fluorescence quenching assay described in Section 4.2.1, the binding affinity of a fluorescently labelled protein can be measured by pelleting the lectin-GNP complex via centrifugation. The reduction in fluorescence of the remaining supernatant reflects the amount of unbound proteins, so the bound protein amount can be estimated from the difference between that added and that remaining in the supernatant. A greater proportion of bound protein results in a greater reduction of fluorescence emission in the supernatant. It is also possible to measure the fluorescence recovery in the presence of an inhibitor and using the Cheng-Prusoff equation to calculate the K_d (Figure 8.1). This method has been utilized by the Yan group to quantify the binding of mannose coated gold nanoparticles of varying sizes and linker lengths with the plant lectin Concanavalin A (ConA) (fluorescently labelled).(152) Increasing concentrations of competing free mannose were added to the reaction mix and after incubation and centrifugation to remove the GNP-ConA complex, the supernatant was measured for its fluorescence intensity. By repeating this over varying lectin and mannose concentrations, a value for K_d was obtained. This study revealed that binding was less favourable at larger GNP sizes (K_d = 25 nM for 30 nm GNP but 3 nM for 7 nm GNP). It was concluded that smaller nanoparticles yielded the highest affinity

enhancement, likely due to their large surface-to-volume ratio and higher mobility in solution enabling more efficient binding. Additionally, enhanced binding affinity was observed with increasing linker length, which was attributed to the spacer elevating the terminal glycan further from the GNP surface therefore resulting in larger inter-glycan distances and reduced hindrance upon binding.

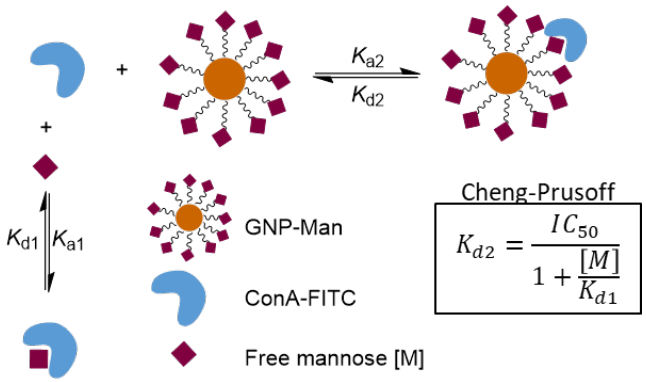

Figure 8.1 Schematic depicting how the Cheng-Prusoff equation can be used to calculate the binding affinity between GNP-Man and ConA, where IC_{50} = concentration of ligand displaying 50% of specific binding; [M] = concentration of free ligand, K_{d1} = dissociation constant of the free ligand with ConA; and K_{d2} = dissociation constant of GNPs with ConA. Figure adapted from reference(152)

The GNP-based pull down method is not restricted to fluorescently labelled proteins. The Sakurai group measured the binding affinity of 14 nm gold particles coated in lactose to various lectins by initially isolating the protein-probe complex by centrifugation, then releasing the bound protein from the pellet by denaturation in Laemmli buffer containing 10% β-mercaptoethanol, and measuring the amount of protein released by fluorescent SDS page.(431-433) By repeating this over a concentration range and comparing it to the total amount of protein used, binding curves were constructed to extract the K_d. Using this method, a value for the K_d of GNP-lactose to three lactose binding proteins were calculated to be 26 nM, 8.7 nM, and 18 nM for peanut Agglutinin (PNA), *Erythrina cristagalli* agglutinin (ECA) and RCA, respectively.(431) Thus the GNP-lactose achieved large affinity enhancements of between 2,000 and 37,000-fold when compared to monomeric lactose (K_d = 400 μM, 323 μM, and 37 μM for PNA, ECA and RCA).

These studies have demonstrated the usefulness of larger GNP scaffolds in determining the K_d for protein carbohydrate interactions, and have highlighted their potential in GNP-based affinity labelling for protein engagement and identification in more complex systems.

8.1.2 Affinity labelling

Often in modern chemical biology and drug discovery, cell- or organism-based assays are frequently employed as they benefit from preserving the cellular context of protein function. In such approaches, knowledge of the target or mechanism of a small molecule

only emerges after its medicinal or functional properties have been observed.(434, 435) It is however of great importance to determine the precise biological targets of small molecules, and any off target binding that may occur, for a comprehensive understanding of their cellular interactome and to better predict their utility, mechanisms, or reduce toxic side effects.(436) Many of the binding events occurring within the cellular interactome are protein carbohydrate interactions (PCIs) which have been a central focus of this thesis so far due to their key role in mediating cellular recognition and signalling. Studying these interactions in solution-based assays where the protein identity and concentration is known is simple, however, studying PCIs in a biological context is challenging due to their dynamic and transient nature, as well as the presence of numerous other interacting partners.(437) Isolating protein-carbohydrate complexes from a cellular environment is therefore a challenging problem, but biochemical affinity purification offers a direct method for identifying target proteins that bind small molecules of interest.(434, 438)

Small molecule protein-reactive chemical probes have emerged as an essential tool in assisting target capture and identification. Using this technique, protein-reactive groups are derivatized onto a small molecule of interest enabling them to covalently crosslink otherwise reversible protein–ligand complexes to aid in isolation, identification and further functional analysis.(436) Since many molecules other than the protein of interest exist in a cellular environment, selective labelling of the desired protein is critical in order to distinguish the protein of interest from other non-target proteins for precise analysis.(439) Since there might be no prior knowledge on the structural features of target proteins, or indeed those in the surrounding environment, introducing selectivity is a significant challenge when designing a suitable cross-linker. It must have an appropriate protein-reactive group which reacts with the target protein with high efficiency while having no or low reactivity towards non-target proteins.(440) To make the affinity probes as selective as possible, they are designed with three important functionalities in mind:

1. The affinity ligand – the small molecule or carbohydrate which reversibly binds the protein(s) of interest. This ideally binds no off-targets proteins (but in some cases may be used to identify side-effect-causing off target proteins).

2. The reactive affinity label which covalently/irreversibly binds to the target protein. It may be reactive towards other proteins or have broad substrate scope, however proximity enhanced reactivity induced by the affinity ligand is advantageous here.

3. The identification/reporter tag which allows isolation of the probe-protein adduct. This can be added later through bioconjugation methods such as click chemistry.

The main challenge is designing a suitable protein reactive affinity label. For this, two major types of functionalities exist; photoreactive groups which require UV activation to form a covalent linkage, or electrophilic groups which react spontaneously. Appropriate

photoreactive groups include arylazides, diazirines and benzophenones which non-selectively react with any proximal amino acid resides upon UV irradiation, however, these suffer from low labelling yields, making identification of labelled protein/peptides by LC-MS/MS difficult. In cases where specific amino acid selectivity is required, photo reactive probes are also unsuitable due to their non-selectivity. This non-selectivity can lead to a complex mixture of cross-linked products which make it difficult to identify specific target interactions using techniques like mass spectrometry.(441, 442)

The low labelling efficiency of photoreactive groups can be addressed by employing electrophilic groups instead. Electrophilic group functionalities include benzyl chlorides, squaramide esters, arylsulfonyl fluorides, and acrylamides which react with locally reactive surface exposed nucleophilic amino acid residues.(443) These electrophiles have been used in a variety of situations where protein labelling is required, such as affinity labelling,(444) activity-based protein profiling,(445) reactivity-based protein profiling, ligand-directed chemistries,(446) and covalent drug development.(447) Unlike photoreactive groups, they balance reactivity and chemoselectivity, allowing them to selectively target nucleophilic amino acid side chains in proteins, making them valuable tools for designing protein-reactive probes.

As evidenced by Hamachi and co-workers, it is indeed possible to label surface exposed nucleophilic residues at the periphery of the ligand binding site, facilitated through the proximity effect which relies on ligand recognition initially to then promote efficient labelling.(439) Despite these advancements, electrophile-based crosslinking of proteins has been limited to cases where a nucleophilic amino acid at the target protein's binding site is known or predictable.(448, 449) This limitation arises from the variability of the local microenvironment. In some cases, the inherent reactivity of electrophiles with free nucleophiles may lead to non-specific binding with accessible residues, or alternatively reactivity may be restricted by buried residues.(450) As a result, the broader applicability of electrophiles for covalently capturing unknown target proteins without prior structural knowledge remains unexplored.

Once both the affinity unit and the affinity label have been identified there are a number of techniques which can be utilised to isolate the protein-probe complex.

1. plant and cast

One method of chemical cross-linking is known as a 'plant and cast', where small molecule cross linkers with two functional ends are used to covalently link a pre-bound protein-carbohydrate complex.(451) One end of the small molecule contains a highly reactive succinimide ester, which reacts with protein lysine residues to 'plant' the cross linker, and the other end contains a less reactive functional group (such as a sulfonyl fluoride, SF) which is 'cast' to react with nearby functional groups on the carbohydrate, only if bound to the protein of interest. This functional group is less reactive to avoid large

scale non-specific binding, but is driven to react by proximity-enhanced reactivity when in vicinity of the protein-bound carbohydrate.(452) If the carbohydrate has been premodified with an azide, then a biotin tag can be introduced through Huisgen-Sharpless-Meldal click chemistry, and confirmation of the chemical cross-link is therefore possible by a western blot against a streptavidin-HRP antibody under denatured conditions, as this eliminates the PCI and only shows a protein if the cross link is present. The biotin tag may also be used to immobilise the PCI onto a streptavidin coated solid support to aid in isolation. Using this technique, Wang *et al.* were able to successfully cross link a sialic acid-binding immunoglobulin-like lectin 7 (siglec7) domain to an azide functionalised ganglioside sugar (Scheme 8.1).(437) Furthermore, using an SF-incorporated siglec7 mutant, they were able to crosslink a sialoglycan on a mammalian cell surface, a function which they reasoned could later be used to enhance NK cell killing of tumour cells by blocking the interaction of the tumour cell surface sialoglycan with Siglec-7 on NK cells.

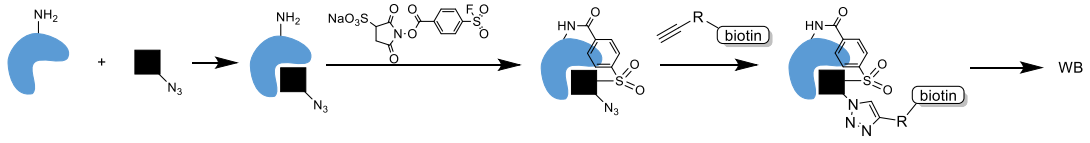

Scheme 8.1 Schematic depicting the plant and cast method of affinity labelling, where a bifunctional ligand is added to a protein-ligand complex to covalently link them together. If the ligand contains an azide tag, a biotinylated alkyne can be used to isolate these protein targets from complex proteome mixtures. Figure modified from reference (435).

2. Ligand directed chemistry.

A second technique for isolating proteins of interest involves protein reactive affinity tags that are pre-conjugated to the small molecule or ligand.(439) In ligand directed chemistry, it is important that the addition of the affinity tag does not significantly change the reactivity or rate of reaction of the small molecule, as this may interfere with identifying the target protein.(453) This method has also been used for studying protein carbohydrate interactions, and is more akin to an immunoprecipitation. While immunoprecipitation relies solely on surface immobilised-antibody to protein interactions which are extremely strong (K_d down to 10^{-12}), the transient and reversible nature of PCIs, which are generally low affinity for a single protein–carbohydrate interactions (K_d most often in the millimolar to micromolar range), means a more tangible link is required before isolation.(454) In this case it is possible to immobilise the protein reactive group onto a solid support alongside the carbohydrate, to take advantage of strong MLGIs, and to induce proximity enhanced labelling of the protein after binding to the neighbouring carbohydrate. The Sakurai group, who efficiently pulled down lectins in solution using lactose immobilised on a GNP-surface to investigate binding affinity, applied this technique to covalently cross-link PNA and RCA to the GNP surface

(Scheme 8.2).(431) Attaching the ligand and affinity tag to the gold nanoparticle scaffold promotes high local concentrations of both groups, and allows reactions to occur over a large surface area. As a consequence, these probes exert enhanced protein binding affinity and ligand-dependent reactivity.

In this manner, a number of electrophilic and photoreactive probes were immobilised onto a GNP surface in a 2:1 carbohydrate to probe ratio and their reactivity towards PNA, RCA and ECA were assessed. A sulfonyl fluoride probe was discovered to exhibit the greatest labelling yield (quantitative after 16 hrs), and showed good selectivity for PNA in a complex cell lysate mixture.(431-433, 455) Interestingly, despite being used as the carbohydrate reactive group by Wang *et al*. in the plant and cast method, here a sulfonyl fluoride affinity label did not show any cross-reactivity with the carbohydrate ligand, a polyol moiety, despite the proximity. It is noted that if the carbohydrate ligand were swapped for one containing phenols or amines then the use of photoaffinity labels over electrophiles would be more beneficial as to avoid cross reactivity and deactivation of the probes before use.

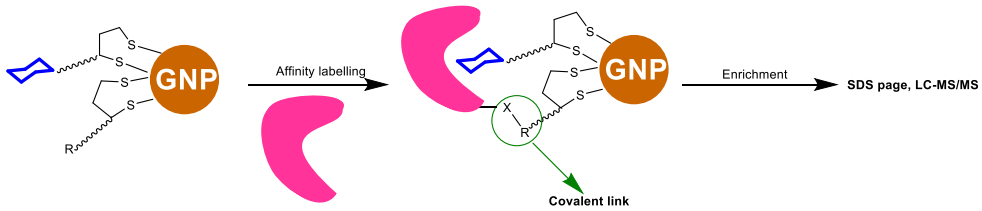

Scheme 8.2 Schematic depicting the GNP based pull down method of isolating proteins for identification by SDS-page and LC-MS/MS, where R is an electrophilic group and X is a nucleophilic amino acid residue.

Once targets have been cross-linked and isolated, mass spectrometric techniques allow for the identification of such targets immediately after release from the affinity supports, most commonly using liquid chromatography tandem mass spectrometry(LC-MS/MS).(456) If multiple targets are isolated, spectrometric analysis may be simplified by separation of the proteins by gel electrophoresis before analysis. However, recent developments in more advanced MS techniques such a modern shotgun proteomics approaches enable complex proteome profiling of thousands of proteins in a single experiment without the need for pre separation.(457)

In this chapter, the capability of a GNP-based pull-down method for identifying GNP-glycan bound proteins was assessed. Dimannose and fucose were functionalised alongside a sulfonyl fluoride (SF) affinity tag on a 27 nm gold nanoparticle (G27), and their affinity for DC-SIGN in solution was measured. Furthermore, their ability to covalently bind DC-SIGN, both alone and in competition with BSA was evaluated, which found that both G27-fucose/SF and G27-dimannose/SF were able to covalently bind DC-SIGN in high yield, but only G27-dimannose/SF were also able to selectively discriminate between DC-SIGN and BSA in protein mixture. While the binding affinities of G27-

dimannose/SF and G27-fucose/SF probes were similar, the difference in selectivity was potentially due to distinct glycan mediated SF-DC-SIGN binding sites. In order to assess this, the protein-probe complexes were digested and the labelled peptide fragments were analysed by liquid chromatography tandem mass spectrometry.

This methodology was developed to isolate and identify cell surface lectins, besides DC-SIGN, that bind to GNP-dimannose/fucose particles, with the aim of advancing our knowledge of glycan-mediated DC immune function modulation. Deeper insights into these cellular mechanisms using this methodology will enable a more comprehensive understanding of the processes involved in IL-23 regulation and fungal immunity. The successful enrichment and identification of DC-SIGN via LC-MS/MS in this chapter validated the possibility of using this approach for this application. Furthermore, this method holds potential for identifying entire signalosome complexes, enabling further investigation into the distinct signalling pathways mediated by GNP-dimannose and/or fucose binding.

8.2 Results and discussion

8.2.1 Design rational

To explore the potential of gold nanoparticle based affinity labelling for the identification of GNP-glycan binding proteins on the cell surface, the same dimannose and fucose ligands used in the DC-SIGN binding and immune modulation exploration were employed. Using these ligands ensures specific targeting of dimannose and fucose binding lectins. For the affinity label, an aryl sulfonyl fluoride (SF) was chosen. Sulfonyl fluorides are electrophilic warheads which possess a good balance between biocompatibility, including aqueous stability, and protein reactivity. They take part in sulfur fluoride exchange reactions with several nucleophilic amino acid residues, including lysine, tyrosine, cysteine, serine and threonine, to covalently bind proteins.(458)

Several other factors were considered in the design of the nanoparticle probes, such the size of the gold nanoparticle, the lengths of the linkers used to attach the SF and glycans to the gold surface, and the ratio of glycan to SF. In order to utilise a pull-down method using gold nanoparticles, a larger size was needed than the previously used G5 – one that would pellet easily upon centrifugation. Therefore, 27 nm gold nanoparticles (G27) were chosen as they possess a good balance between aqueous colloidal stability and sedimentation rate (6000 x *g* for 15 mins). The linker lengths were chosen carefully as well. Chapter 4 discussed the effect of linker length in detail and although it was revealed that the shorter ethylene glycol linkers (EG_2) afford greater affinity enhancements for G5-glycans than longer linkers (EG_6/EG_{12}) due to entropic considerations, G27 require longer EG_n chains to afford colloidal stability and resist aggregation. The glycan ligands

were therefore joined to the G27 surface with EG_6- linkers. To avoid hindering the SF functionality in between glycans which would limit its binding capabilities, a longer EG_{11} linker was selected so that the SF would protrude further out of the glycan surface to promote efficient, unhindered labelling.

Finally the ratio of glycan:SF was considered. Since the model protein binding ligands used here (dimannose and fucose) are hydrophilic, they were expected to confer colloidal stability to the G27 nanoparticles as long as the relative ratio of the electrophilic sulfonyl fluoride, which is hydrophobic, was kept relatively low. It was also desirable to change the ratios of glycan:SF on the surface to determine if labelling yield was dependent on the proportion of SF, and whether this would be at the cost of protein selectivity. Similar studies in this area have used a 2:1 ratio of ligand to SF on a G14 particle,(431) however this ratio was found to be too high to afford colloidal stability of larger G27 particles and so a reduced amount of SF was chosen. Here three glycan: SF ratios containing successively lower quantities of SF (5:1, 10:1 and 20:1 of glycan:SF) were selected. These would still provide a high local concentration of both the ligand and the sulfonyl fluoride without compromising the colloidal stability of the nanoparticles, and should promote selective binding as well as efficient labelling.

8.2.2 G27-glycan:SF synthesis

LA-EG_6-fucose (**10b**) and LA-EG_6-dimannose (**11b**) and control LA-EG_6-OH (**12**) were prepared and characterised as discussed in Chapter 2, and LA-EG_{11}-sulfonyl fluoride **17** was synthesised as following. The amine **15** was prepared previously in-house by amide coupling of lipoic acid (**7**) with PEG linker (**13**), to give **14** in 65% yield. **14** Was subjected by a Staudinger reduction to transform the terminal azide to an amine functionality.(119, 459) Amine **15** showed a distinct lack of solubility in $CHCl_3$, potentially due to the formation of intramolecular disulfide bonds creating a polymer network. Stirring in DMF in the presence of triethylamine alleviated some solubility issues, and after addition of commercial acid chloride **16** for 3 days, the desired LA-EG_{11}-aryl sulfonyl fluoride **17** was isolated. While the yield for this was low, at 38% after purification, only very small quantities (<1 mg) were needed for high volumes of G27-glycan:SF to be produced and therefore even at this yield, sufficient product was isolated. Fluorine NMR was used to confirm the presence of the sulfonyl fluoride (Figure B. 10)

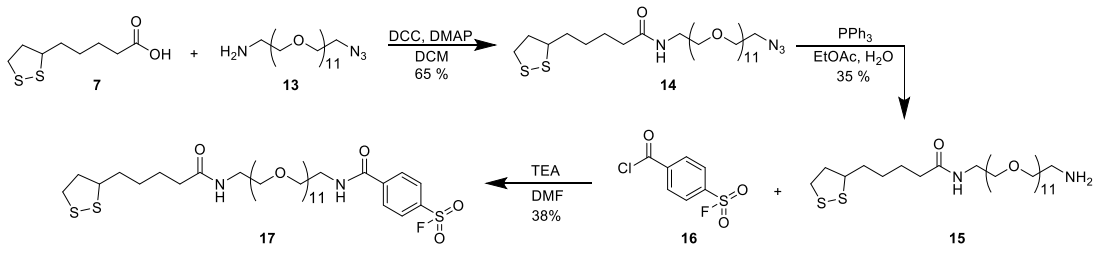

Scheme 8.3 Synthetic route to sulfonyl fluoride affinity tag **17.**

Citrate coated G27 were prepared as described in Chapter 2. Directly stirring LA-EG_6-glycan and LA-$EG1_1$-SF ligands with G27-citrate resulted in immediate aggregation, indicated by a colour change from red to purple followed by sedimentation of the GNPs (Figure 8.2). However, when using an intermediate bis (p-sulfonatophenyl) phenylphosphine dipotassium (BSPP) coating which affords electrostatic stabilisation due to the negative charge, G27-glycan:SF were successfully synthesised in all the desired ratios. A summary of all the probes made can be seen in Scheme 8.4.

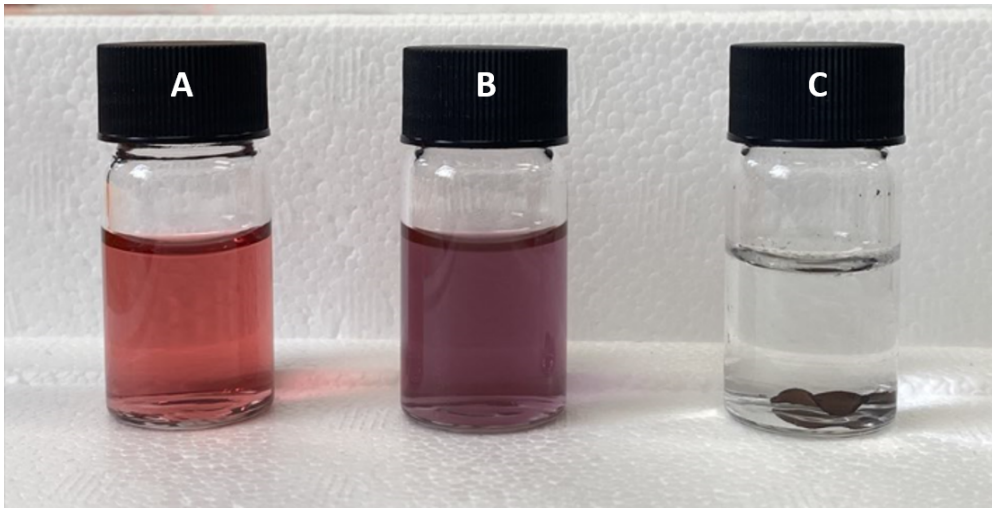

Figure 8.2 A) G27-citrate, B) G27-citrate immediately after addition of a 5:1 LA-EG_6-dimannose:LA-EG_{11}-SF mixture C) G27-citrate 48 hours after addition of a 5:1 LA-EG_6-dimannose:LA-EG_{11}-SF mixture.

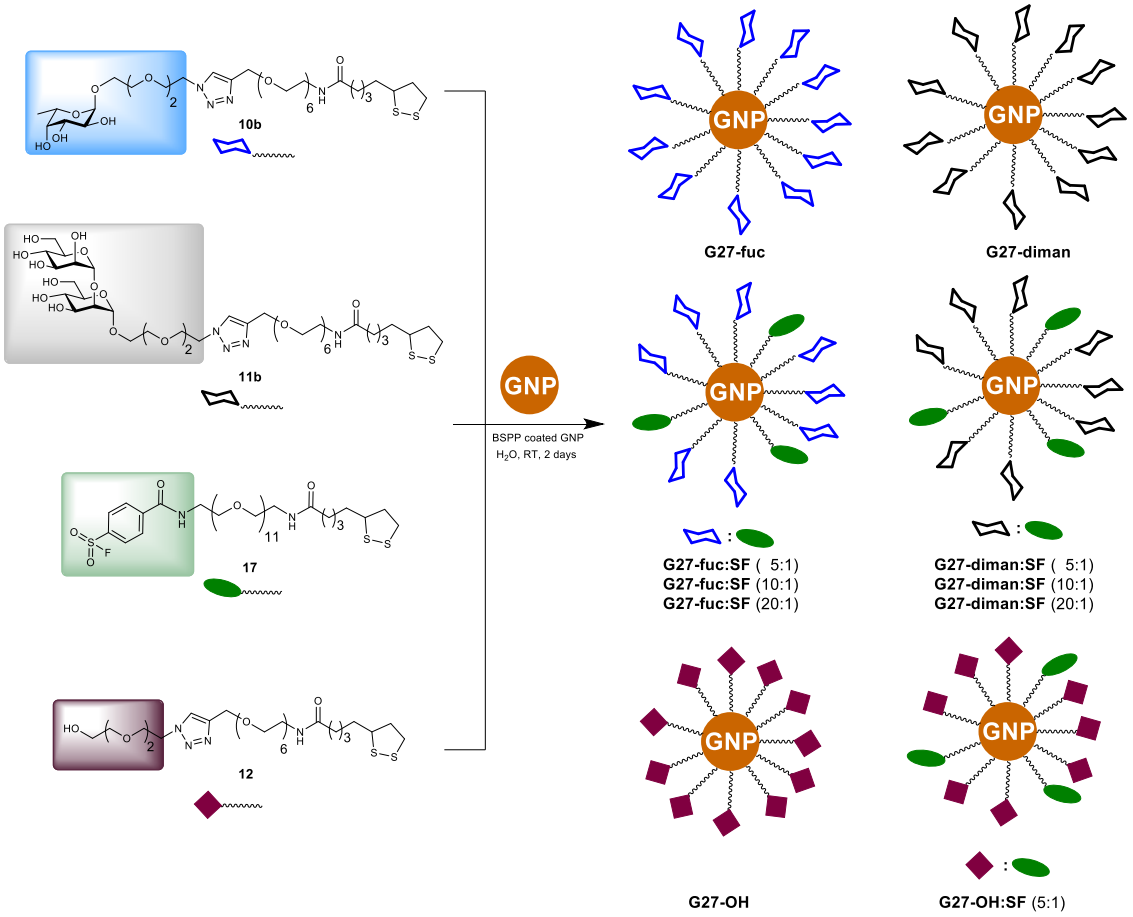

Scheme 8.4 Schematic depicting the cap exchange of G27-BSPP into into G27-glycans, G27-glycan:SF(affinity probes) or G27-OH/SF (controls). When making the affinity probes, three ratios of glycan:SF were chosen (5:1, 10:1 and 20:1) to determine if the percentage of SF on the surface would have an impact on both affinity and selectivity.

8.2.3 Probing the binding mode of G27-glycan:SF with DC-SIGN

To consolidate successful coverage of G27 in the ligands of choice, and to determine if the presence of an affinity tag impacts the binding mode (monolayer binding vs cross linking) a hydrodynamic size analysis was carried out by dynamic light scattering (DLS). The hydrodynamic diameters of G27's were measured by DLS in the absence and then presence of DC-SIGN in a 25:1 protein:gold ratio (PGR). The resulting volume population distributions were plotted as histograms and fitted with Gaussian functions to extract the average D_h. A summary of the average hydrodynamic diameters can be seen in Table 8.1 and the histograms in Appendix B (Figure B. 11-14).

Firstly to consider is that the addition of the SF tag increases the average D_h of G27s compared to those without, although it is noted that the errors overlap substantially. The increase in mean size is due to the longer EG_{11} linker of the SF ligand compared to the EG_6-EG_2 used for the dimannose/fucose ligands. In the presence of DC-SIGN the control G27-OH and G27-OH:SF(5:1) showed no increase in D_h size, indicating no binding was occurring, but the G27-dimanose:SF particles showed small assemblies with average D_h values of around 85 nm, which is consistent with a single G27 coated in a monolayer of

DC-SIGN. Interestingly, the G27-fucose:SF showed larger structures of ~ 150 nm in D_h when in the presence of DC-SIGN. This is too large to be a single G27 coated in a monolayer of DC-SIGN, and therefore represents the occurrence of cross-linked species. The G27-fucose-DC-SIGN complex in the absence of the SF affinity tag remains a monolayer sized species signifying the cross-linking observed for the G27-fucose:SF particles is dependent on the presence of the sulfonyl fluoride tags. It is possible that the bulkier dimannose structure is able to block cross-linking interactions, or that the orientation of DC-SIGN when bound to dimannose is different to that bound to fucose, which again may hinder the formation of cross-links.

Table 8.1 Summary of the hydrodynamic diamters (D_h) of G27 particles before and after binding with DC-SIGN (PGR 25). D_h values are given as xc ± ½ FWHM.

Particle	D_h	R^2	D_h **with DC-SIGN**	R^2
G27-citrate	31.4 ± 7.6	0.967	-	-
G27-BSPP	31.6 ± 7.9	0.964	-	-
G27-dimannose	35.4 ± 6.9	0.967	64.4 ± 13.6	0.963
G27-dimannose:SF (5:1)	38.5 ± 9.3	0.960	81.1 ± 20.5	0.929
G27-dimannose:SF (10:1)	38.0 ± 9.4	0.969	84.6 ± 22.5	0.924
G27-dimannose:SF (20:1)	39.1 ± 9.9	0.966	84.5 ± 21.4	0.933
G27-fucose	34.9 ± 6.1	0.985	66.3 ± 13.4	0.980
G27-fucose:SF (5:1)	35.1 ± 8.9	0.957	150.9 ± 46.5	0.982
G27-fucose:SF (10:1)	37.1 ± 9.3	0.960	153.1 ± 45.0	0.983
G27-fucose:SF (20:1)	37.6 ± 9.5	0.962	155.6 ± 54.8	0.965
G27-OH	38.9 ± 10.7	0.967	37.9 ± 9.4	0.979
G27-OH (5:1)	35.0 ± 9.2	0.951	36.5 ± 9.5	0.941

8.2.4 Measuring K_d of G27-glycan:SF with DC-SIGN-atto643 using a pull-down assay.

Previous results discussed in Chapter 4 verified that the presence of multivalent ligands on a G5 scaffold increased binding affinity with an enhancement factor, β, of up to 475,000 over monovalent binding. These results were obtained in a fluorescence quenching assay, however since G27 nanoparticles have a much greater absorption extinction coefficient (2.39 x 10^9 M^{-1} cm^{-1}) than G5 (1.1 x 10^7 M^{-1} cm^{-1}), their use in FRET or NSET assays in limited to very low concentrations (~0.5 nM) as not to introduce a

significant inner filter effect. Instead, in order to extract a binding affinity with a fixed GNP:protein ratio over a varying concentration range, a pull down assay can be employed where the GNP-protein complex is pelleted out of solution. Since centrifugation pellets all GNPs (unbound or protein-bound), the supernatant containing unbound protein can be collected for fluorescence intensity measurement without any interference from GNP's inner filter effect. Comparing the fluorescence of the supernatant to a protein control is then used calculate the % bound, which if repeated over a concentration range can be used to calculate the binding affinity. This also removes any further complication based on Förster radius dependent quenching and can be used to directly calculate the % of protein bound the gold scaffold. The 27 nm GNPs used here are dense enough that they can be pelleted out of solution at achievable centrifugation speeds in relatively short periods of time (~6000 × *g*, 15 minutes). Since these probes contain the sulfonyl fluoride tag which is potentially capable of reacting with non-target proteins, this assay is carried out in 1% triton, rather than the 1 mg/mL BSA which was previously used to avoid non-specific adsorption of proteins and GNPs to surfaces – a cause of experimental error, especially at very low concentrations.

While it is ideal to measure binding in a 1:1 PGR to avoid the complexities associated with multiple binding sites or cooperative binding, the amount of G27 required in this instance to match the protein concentration would be difficult and expensive to make. Fortunately, it was previously found that the quenching efficiency remained almost constant for a fixed Gx-dimannose concentration after mixing with DC-SIGN over a certain PGR range.(130) Therefore, as long as the concentration of DC-SIGN does not exceed the saturation of G27-glycans, a lower concentration of G27 can be used while still accurately measuring apparent K_d. Based on a DC-SIGN binding footprint of 35 nm^2,(119) and the surface area of a G27-glycan/SF probe calculated using their hydrodynamic sizes, roughly 110 DC-SIGN molecules were calculated to be able to bind one G27-glycan before saturation is reached, well above the chosen 25:1 PGR ratio for this assay.

Samples of DC-SIGN-atto643 and G27s mixed in protein:G27 molar ratio of 25:1 over a protein concentration range 1-64 nM were incubated for 2 hours and then centrifuged to pellet the G27-DC-SIGN-atto643 complexes out of solution. The fluorescence intensity of the supernatants containing unbound DC-SIGN-atto643 were then recorded at an excitation wavelength (λ_{ex}) of 630 nm. When carried out using a control particle bearing no glycan on its surface (G27-OH), negligible reduction in the fluorescence intensity of each sample was observed (Figure 8.3). This result matched those obtained in the hydrodynamic size analysis which indicated no DC-SIGN binding and verified that any reduction in fluorescence observed for glycan coated probes would be due to specific MLGIs between G27-glycans and DC-SIGN-atto643.

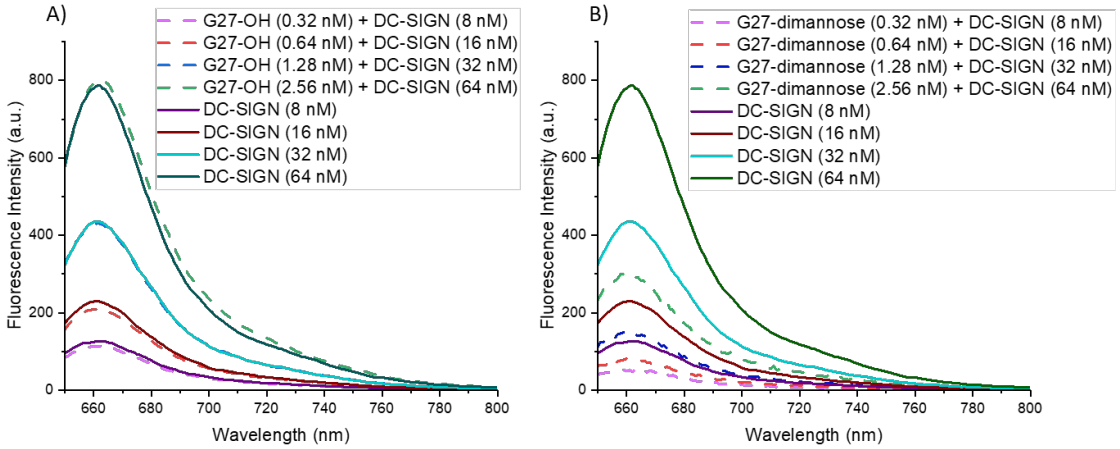

Figure 8.3 Fluorescence intensity spectrum of DC-SIGN-atto643 over a concentration range of 8-64 nM and the corresponding fluorescence intensities of the supernatant of DC-SIGN-atto643 mixed in a 25:1 ratio with A) G27-OH or B) G27-dimannose, after centrifugation.

To calculate the enhancement factor, β, of multivalent G27 particles, G27s bearing only dimannose or fucose were used. G27-dimannose and G27-fucose were mixed with DC-SIGN-atto643 as described above. The % of DC-SIGN bound was calculated via Equation 8.1 where IF_1 is the integrated fluorescence intensity of the sample supernatant and IF_0 the integrated fluorescence intensity of the DC-SIGN-atto643 control. Since G27-OH showed no DC-SIGN binding and no reduction in fluorescence intensity when mixed with DC-SIGN-atto643 in two separate experiments, for further experiments the fluorescence intensity of the DC-SIGN-atto643 only was used as the control (F_0/IF_0). The % bound was then plotted vs protein concentration and fitted to the Hill Equation 8.2, where V is the % of DC-SIGN-atto643 bound to GNPs, Vmax is the maximum % bound, [P] is the protein concentration, K_d is the apparent binding dissociation constant (or effective concentration for 50% binding) and n is the Hill coefficient which indicates binding cooperativity (where n>1 indicates positive cooperativity and n<1 indicates negative cooperativity and n=1 indicates no cooperativity). Previously in the quenching experiment, n was fixed at 1 due to the binding occurring in a 1:1 PGR where no intermolecular lectin-lectin interactions were expected to inhibit or promote the lectin-GNP binding. Here, n was not fixed since the assay was performed in a 25:1 ratio and therefore it is reasonable that binding of one lectin may inhibit binding of further lectins to the same GNP as a result of steric hindrance, especially as higher concentrations are reached and the number of lectins per GNP increases.

$$\%bound = \frac{IF_0 - IF_1}{IF_0} \times 100$$

Equation 8.1

$$V = \frac{Vmax\,[P]^n}{{K_d}^n + [P]^n}$$ **Equation 8.2**

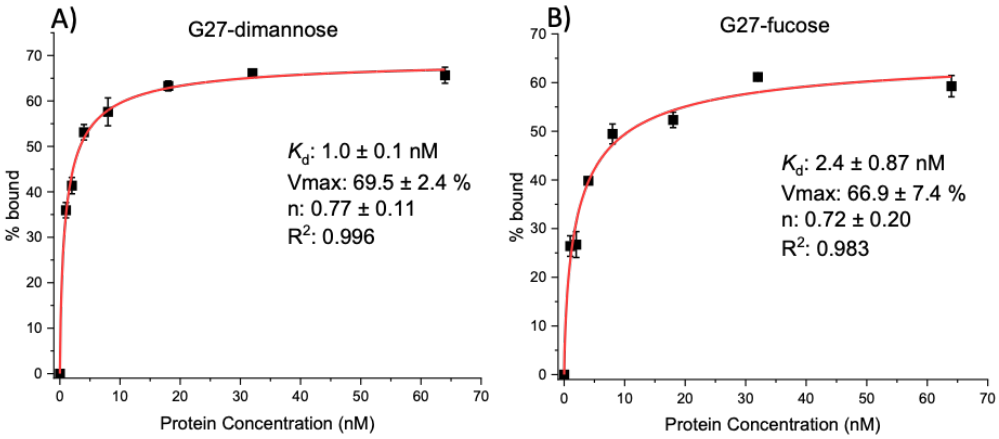

Figure 8.4 Percentage DC-SIGN-atto643 bound – DC-SIGN-atto643 concentration relationship for binding to A) G27-dimannose and B) G27-fucose. Graphs were fitted by the Hill Equation 8.1 and error bars represent the SDs of duplicate experiments at each concentration.

Binding of DC-SIGN-atto643 to G27-dimannose and G27-fucose produced low nM K_ds (1.0 nM and 2.4 nM, respectively) correlating to high affinity enhancement factor, β, of up to ~9 x 10^5 over the respective monovalent binding (0.9 mM for dimannose) (Figure 8.4).(77) These binding affinities were similar to those obtained by G5-glycan-DC-SIGN-atto643 binding through the quenching assay discussed in Chapter 4 (3.5 nM and 3.9 nM for G5-EG_6-dimannose and G5-EG_6-fucose respectively). Although on the same order of magnitude, the slightly stronger binding for G27-glycans compared to G5-glycans can be attributed to both a higher local concentration of ligand on the larger G27 surface, and a lower surface curvature which improves the accessibility of glycans on the surface to DC-SIGN CRDs for multivalent binding. Despite the PGR being lower than the DC-SIGN saturation of one G27, quantitative binding was not reached even at high concentrations, with the maximum DC-SIGN-atto643 bound to G27-dimannose reaching only 70% and G27-fucose reaching 67%. As expected *n* had a value of <1, indicating that binding of DC-SIGN-atto643 to G27-glycans inhibits subsequent binding events, likely due to increased hindrance as the number of DC-SIGN per G27 increases.

To determine the effects the affinity tag has on DC-SIGN binding, the pull-down assay was repeated with the glycan and sulfonyl fluoride loaded G27 particles. Similar to the G27-glycan only experiments, DC-SIGN-atto643 was incubated with the G27-glycans:SF probes for two hours with shaking to ensure sufficient time for some covalent binding to occur between the sulfonyl fluoride and any surface exposed nucleophilic amino acid residues within reach. The results were processed as before and the Hill plots are shown in Figure 8.5. Since there is a covalent element to this interaction, this gives

an apparent K_d which describes only the non-covalent binding interaction. However, as the covalent portion reduces the concentration of the non-covalent complex, the equilibrium for the reversible binding step shifts toward complex formation, leading to a lower K_d value (stronger apparent binding) even though the core non-covalent K_d may remain unchanged. Therefore, while this value is not a true equilibrium K_d, it can provide information on the formation of covalent interactions for the different ratio affinity tags, as it is expected that the 5:1 ratio will induce the highest covalent interactions in this timeframe and will therefore shift the equilibrium the most.

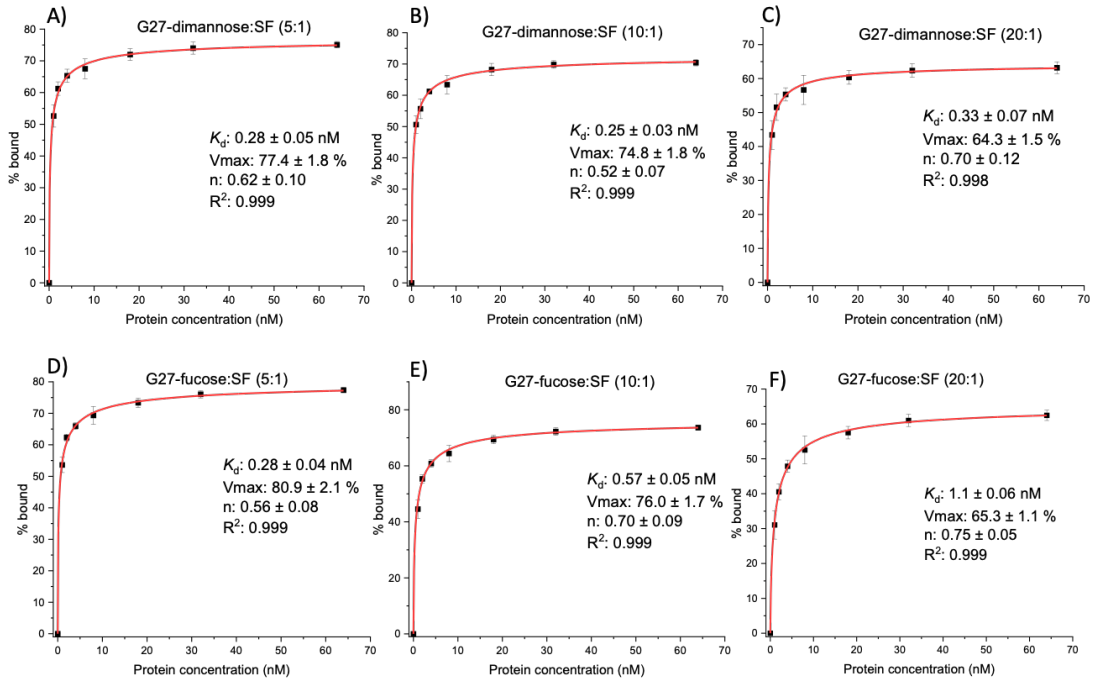

Figure 8.5 Percentage bound vs concentration relationship for DC-SIGN binding to A) G27-dimannose:SF(5:1), B) G27-dimannose:SF(10:1), C) G27-dimannose:SF (20:1), D) G27-fucose:SF(5:1), E) G27-fucose:SF(10:1), F) G27-fucose:SF (20:1). Graphs were fitted by the Hill Equation 8.1 and error bars represent the SDs of duplicate experiments at each concentration.

Firstly of note is that the presence of the SF tag, especially for G27-fucose:SF(5:1), reduced the apparent K_d compared to G27-fucose by an order of magnitude (0.2 nM vs 2.0 nM). For the G27-dimannose:SF probes, the apparent K_d remained almost the same over the varying SF surface loading (0.28 ± 0.05, 0.25 ± 0.03, 0.33 ± 0.07 nM for 5:1, 10:1 and 20:1 dimannose: SF, respectively) whereas the apparent K_d for the fucose probes became weaker as the amount of SF decreased (0.28 ± 0.04, 0.57 ± 0.05, 1.1 ± 0.06 nM for 5:1, 10:1 20:1 fucose: SF, respectively). This would indicate that the presence of the sulfonyl fluoride has more of an enhancement on fucose binding than dimannose binding. At the 5:1 ratio, the high local concentration of SF plays a large role in the overall binding which explains why the apparent K_d for G27-dimannose:SF(5:1) and G27-fucose:SF(5:1) are similar, but as the % of SF decreases the dimannose and fucose ligands play a greater role in the binding. Since dimannose is a stronger binder

than fucose, the apparent K_d for the G27-dimannose:SF remains low when there is less influence from the SF covalent linkage at the 10:1 and 20:1 ratios, whereas the apparent K_d for fucose gets weaker as the ratio of SF decreases. Nonetheless, even at lowest proportion of SF (20:1), the SF still afford an affinity enhancement, albeit small, over the G27-glycan only probes.

In addition, agglutination of the G27-glycan:SF nanoparticles by DC-SIGN may contribute to the overall affinity enhancement by forming large complexes composed of three-dimensional networks of lectins and probes. Larger complexes were observed for G27-fucose:SF-DC-SIGN by DLS, and could also contribute to G27-fucose:SF (5:1) and G27-dimannose:SF(5:1) having the same apparent K_d despite fucose being a weaker DC-SIGN binder.

It is promising that the presence of the sulfonyl fluoride affinity tag improved the apparent binding affinity of these probes with DC-SIGN. While the 5:1 ratio appears to enhance binding the most, especially so when neighbouring to fucose, it must be kept in mind that the SF itself is not a selective molecule and a high ratio of SF on the gold surface may lead to non-specific binding when in a more complex mixture of proteins. A more detailed analysis of this is explored later in this chapter.

8.2.5 Covalent labelling yield

The increase in apparent binding strength upon addition of the sulfonyl fluoride tag would indicate the presence of a covalent link. To confirm the sulfonyl fluoride was truly able to covalently bind to DC-SIGN and that the affinity enhancement was not owing to a different mechanism, an experiment was carried out to measure the covalent labelling yield. DC-SIGN-atto643 and G27-glycan:SF were mixed and incubated in a 25:1 PGR, and the integrated fluorescence (IF_1) of the supernatant was measured as described in the section above for measuring apparent K_d (Figure 8.7A). To remove any residual supernatant containing unbound DC-SIGN, the pellet was washed with HEPES buffer. After removing the supernatant from the HEPES buffer wash, the pellet was then incubated with 50 mM mannose in buffer, which would outcompete the G27-dimannose/fucose ligands binding with DC-SIGN and release any non-covalently bound DC-SIGN-atto643 from the G27 particles, leaving only those covalently bound by the SF. After pelleting again, the supernatant was then measured for its integrated fluorescence intensity (IF_2) to determine the proportion of DC-SIGN-atto643 released/non-covalently bound (Figure 8.7B). IF_1 and IF_2 were combined (Figure 8.7C) to give the total DC-SIGN-atto643 recovery, and provide the proportion covalently bound using Equation 8.3, where IF_0 is the integrated fluorescence of the 25 nM protein control sample. An overview of the method is given in Figure 8.6.

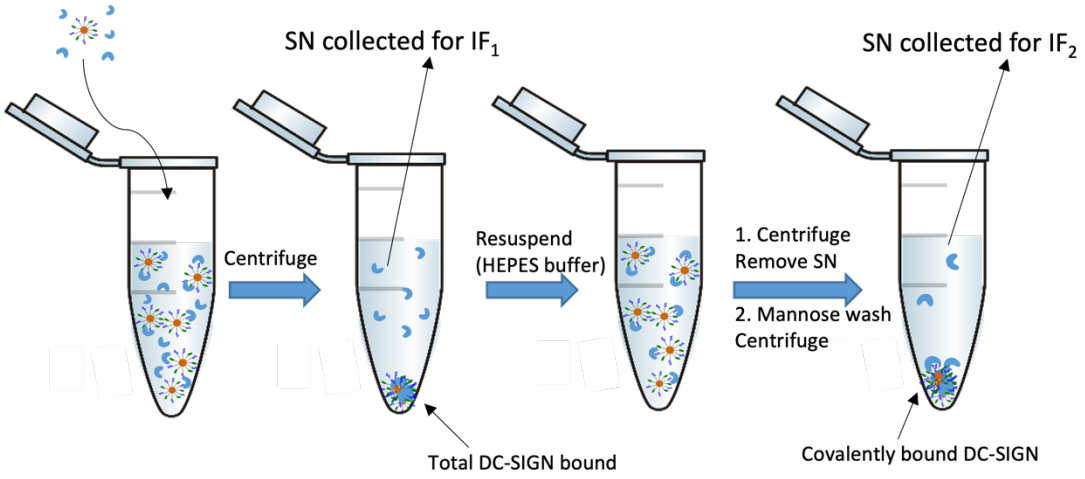

Figure 8.6 Schematic of the method for the fluorescence based pull-down assay. Combining the fluorescence intensities of the initial supernatant with the supernatant after a mannose wash allows for the calculation of the % of DC-SIGN that is covalently bound to the nanoparticles.

$$\% \text{ covalently bound} = \frac{IF_0 - (IF_1 + IF_2)}{IF_0} \times 100$$

Equation 8.3

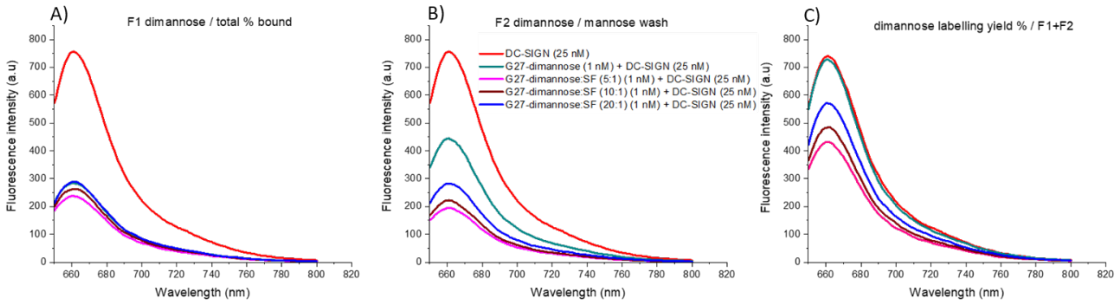

Figure 8.7 Fluorescence intensity spectra of the supernatant of G27 dimannose + DC-SIGN-atto643 samples after A) incubation for two hours followed by centrifugation, where the area under the curve represents unbound DC-SIGN-atto643, B) incubation of the remaining pellet with 50 mM mannose followed by centrifugation where the the area under the curve represents the amount of DC-SIGN-atto643 non-covalently bound C) combined fluorescence intensity of A and B, where the difference in the area under the curve between the samples and the protein control represents the amount of DC-SIGN-atto643 covalently bound.

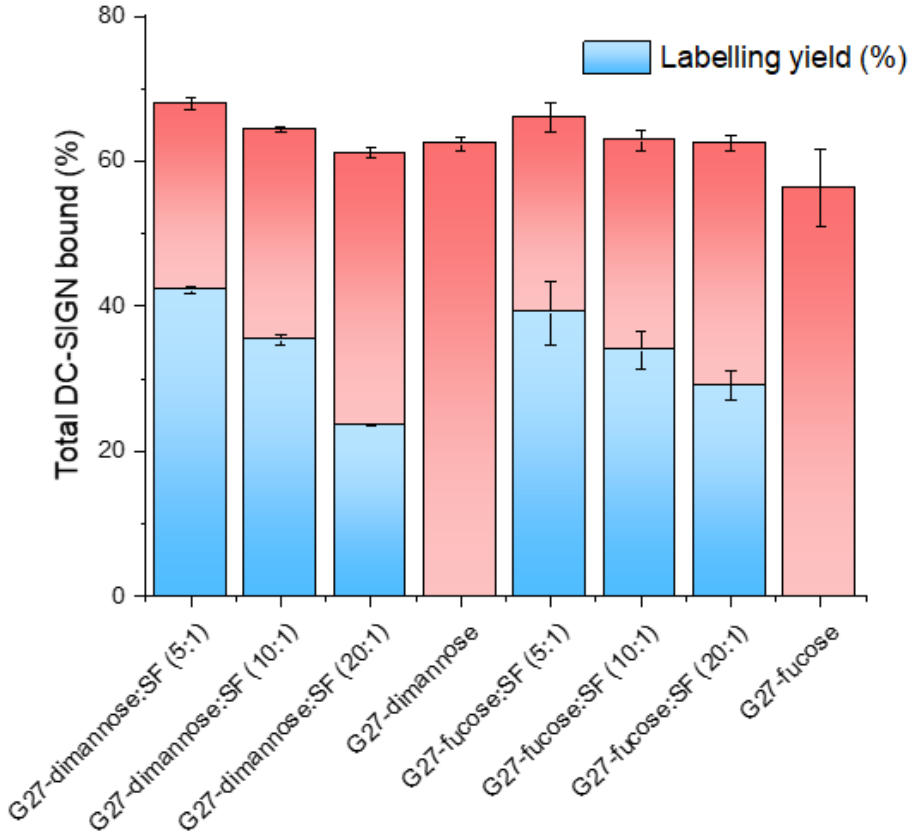

Figure 8.8 Bar graph representing the total amount of DC-SIGN-atto643 bound to each G27 particle and the proportion of this total which represents covalently bound DC-SIGN-atto643 (blue) and non-covalently bound (red) after a 2 hour incubation. G27 with the highest proportion of SF covalently binds the highest proportion of DC-SIGN-atto643, decreasing as the proportion of SF decreases, and particles containing no SF do not covalently label any DC-SIGN-atto643. The % yields were calculated based on the amount of DC-SIGN-atto643 used for a given reaction.

Using Equation 8.1 and IF_1, the total % of DC-SIGN-atto643 bound (covalent + non-covalent) to G27-dimannose:SF was found to be 68%, 64%, 61%, 62% for 5:1, 10:1, 20:1, 1:0 dimannose:SF. Equation 8.3 was then used to calculate what proportion of DC-SIGN-atto643 was covalently bound to the G27-dimannose:SF. The data showed that 42%, 35% and 24% of the original DC-SIGN was covalently bound for 5:1, 10:1 and 20:1 dimannose:SF ratios, respectively, while the G27-dimannose showed full fluorescence recovery after the mannose wash since no covalent linkages were able to form and all DC-SIGN-atto643 molecules were released from the pellet. As expected, the G27 particles with a lower proportion of SF showed the lowest % of DC-SIGN-atto643 covalently bound since DC-SIGN-atto643 would be less likely to come into contact with the sparsely positioned SF tags, instead binding non-covalently to the glycans on the gold surface. The higher the proportion of SF ligands, the more likely they would be in close enough proximity to be able to covalently tag a DC-SIGN-atto643, resulting in a higher proportion being covalently bound after 2 hrs (Figure 8.9).

A similar pattern was observed with fucose:SF samples, with total % of DC-SIGN-atto643 bound to G27 particles found to be 63%, 63%, 66% and 56% for 5:1, 10:1, 20:1, 1:0 fucose:SF particles and the % covalently bound were found to be 39%, 34% and 29% for 5:1, 10:1 and 20:1 fucose:SF ratios with G27-fucose showing complete DC-SIGN-atto643 release after a mannose wash. These data match the K_d measurements, with both K_d and covalent labelling efficiency becoming weaker/ decreasing with lower proportions of SF.

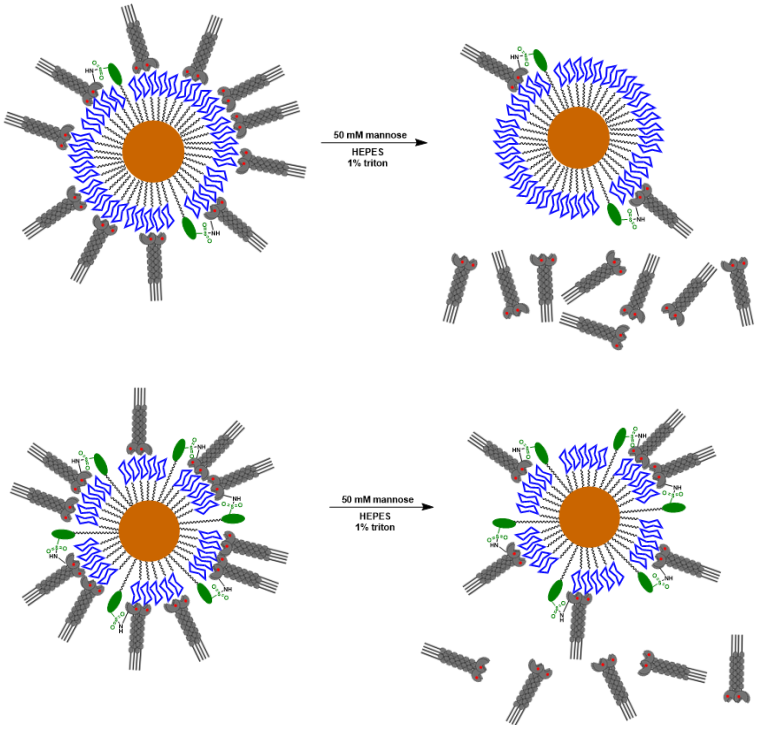

Figure 8.9 Schematic depicting how G27-glycans:SF (5:1) (bottom) are able to covalently label more DC-SIGN over a two hour incubation period than G27-glycan:SF(20:1) (top). The local concentration of SF on the G27-glycans:SF (5:1) is higher and therefore DC-SIGN is more likely to bind in close proximity to an SF ligand, enhancing the covalent binding ability over this time period. Washing the particles with excess mannose releases any non-covalently bound DC-SIGN from the G27 surface, leaving only those bound to SF.

8.2.5.1 Glycan dependency

Two control experiments were conducted to determine if SF labelling was dependent on an initial contact between the glycans and DC-SIGN which draws the SF in close enough proximity to covalently interact, or whether covalent binding is independent of the presence of glycans. Firstly, a G27-OH:SF (5:1) control particle which produces no MLGI interactions was employed to determine if formation of the covalent bond was dependent on glycan binding. Indeed, no binding was observed between DC-SIGN-atto643 and the control particle after 2 hours, determined by the preserved fluorescence intensity of the supernatant after pelleting (Figure 8.10A). Secondly, when the initial incubation between DC-SIGN-atto643 and G27-glycan:SF was repeated in the presence of 50 mM mannose, no binding of DC-SIGN was observed for the G27-dimannose:SF (5:1) or G27-fucose:SF

(5:1) particles either (Figure 8.10B). It is possible that the nucleophilic amino acid residues available for covalent binding are close to the DC-SIGN CRDs, and can therefore only bind to SF after the rapid and selective binding of fucose and dimannose with DC-SIGN. This catalyses the formation of the covalent bond by bringing the neighbouring SF ligands in close enough proximity to the residues for a reaction to occur (Figure 8.10B). The control OH is unable to induce proximity enhanced labelling and therefore covalent binding is more difficult to achieve from short, random collisions.

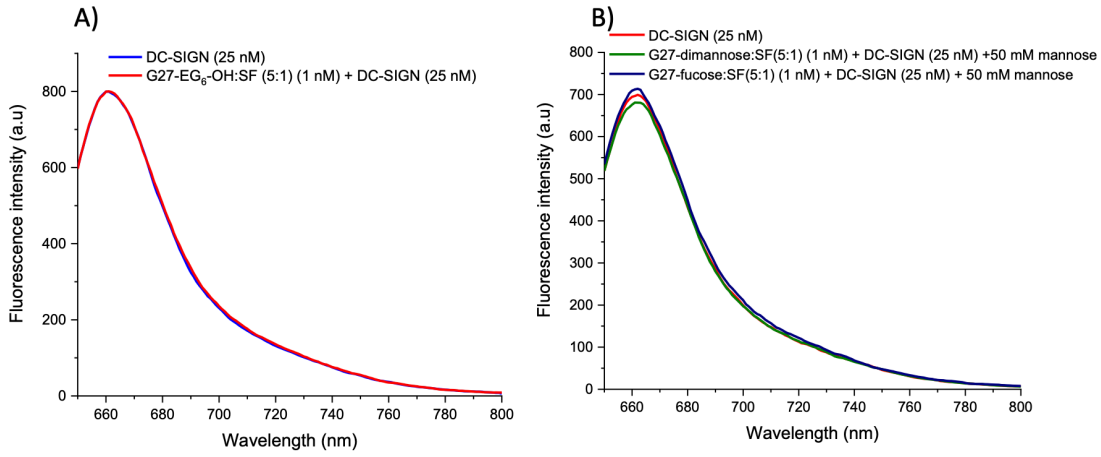

Figure 8.10 The fluoresence intensity sprecra of the supernatant of DC-SIGN-atto643 (25 nM) before and after a 2 hour incubation with 1 nM of A) G27-OH:SF(OH) and B) G27-dimannose:SF(5:1) and G27-fucose:SF(5:1) in the presence of 50 mM mannose. No reduction in the intensity was observed in either case validating that binding of SF probes to DC-SIGN is glycan dependent.

8.2.5.2 Time course analysis

After determining the labelling yields with a 2 hour incubation, a time course analysis was carried out to investigate whether a longer reaction time would lead to higher, or even quantitative labelling yields. Samples were measured at 5 time intervals over a 24 hour period and treated as described above for labelling yield. Although total binding % remained roughly constant, the covalent labelling yield increased over the 24 hour period. After 24 hours, the labelling yield for the G27-glycan:SF (5:1) was within error of the total binding (Figure 8.11A). This highlights that formation of covalent bonds was time dependent, and that even if a DC-SIGN molecule is not bound close enough initially, the process of statistical binding over the 24 hour period allows a greater proportion of DC-SIGN molecules to eventually land and bind non-covalently to a glycan ligand in close enough vicinity to an SF ligand for a covalent bond to then occur. Previous valency calculations for a G27-EG_4-dimannose indicated the presence of up to 6700 ligands on a G27 the surface, meaning that a 5:1 dimannose:SF would contain over 1000 SF groups.(130) Despite this far outweighing the number of DC-SIGN per G27 in this experiment, quantitative binding is not achieved even after 24 hours.

The 10:1 and 20:1 glycan:SF samples followed a similar pattern with labelling yield increasing with time although at a slower rate, and despite continuing to increase over a further 24 hours, some non-covalently bound DC-SIGN-atto643 was still observed at 48 hours (Figure 8.11B/C). The control G27-OH:SF which showed no initial binding after 2 hrs (Figure 8.10A), continued to show no covalent binding to DC-SIGN-atto643 over a 24 hour period, further confirming that labelling is initiated by the glycan-DC-SIGN binding induced proximity effect (Figure B. 15).

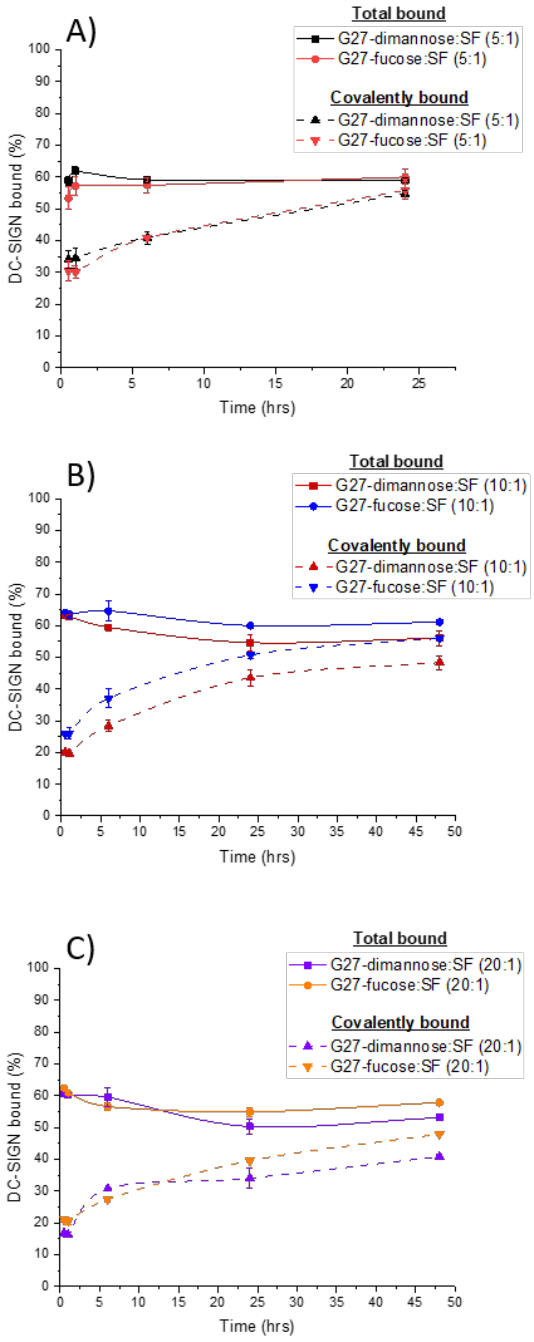

Figure 8.11 Time course of the total labelling and covalent labelling efficiency of DC-SIGN by G27-glycan:SF probes containing glycan:SF ratios of A) 5:1, B) 10:1 and C) 20:1. The % yields were calculated based on the amount of DC-SIGN used for a given reaction.

8.2.6 Selectivity of G27-glycan:SF towards DC-SIGN over non-glycan binding proteins

While the G27s with the highest proportion of SF generally exhibited the greatest binding affinity and covalent labelling yields, it was desirable to find out if the ratio of glycan:SF had an effect on the selectivity of these particles for DC-SIGN over non-target proteins to assess whether they might be useful for covalent labelling or selective isolation in a complex proteome. The glycan dependency of SF binding to DC-SIGN was a promising start, but could not rule out their binding in a glycan independent manner to other proteins.

8.2.6.1 BSA binding

To determine if G27-glycan:SF probes could bind other proteins and if this was dependent on the proportion of SF on the gold surface, the non CLR protein, BSA, a highly abundant serum protein in blood, was chosen as a model non-target protein. Firstly BSA was labelled with FITC. FITC was chosen as an appropriate dye since its excitation and emission spectra has no overlap with that of atto643. They can therefore be used in conjunction with each other -something later required for a competition study without FRET occurring between the two dyes and interfering with the results. After mixing BSA with FITC, the solution was filtered and washed with HEPES binding buffer through a 30 kDa MWCO to remove unbound dye. Using the ratio of the absorbance of FITC at pH 7.8 at 280 nm (where proteins absorb) and 495 nm (FITC A_{max}), the correction factor to account for the contribution of the dye to the absorbance at 280 nm was determined to be 0.32. BSA-FITC concentration was then calculated via Equation 8.4 where C is BSA concentration, 43824 M^{-1} cm^{-1} is the extinction coefficient of BSA and p is the path length.

$$C_{BSA-FITC} = \frac{A_{280} - (A_{495} \,.\, 0.32)}{43{,}824 \,.\, p} \qquad \textbf{Equation 8.4}$$

BSA-FITC was mixed with G27-probes in a 25:1 molar ratio and the % bound was measured as previously described, using Equation 8.1. For FITC, a lower excitation wavelength of 495 nm was used and emission was measured between 510-630 nm, correlating to the excitation and emission spectrum of FITC respectively. BSA is not a C-type lectin or other glycan binding protein and therefore, as expected, did not bind the G27-glycans (no reduction in FITC emission was observed). However, G27-fucose:SF of all three SF ratios, as well as the G27-OH:SF control were able to efficiently label BSA-FITC, with up to a 69% labelling yield, even at a 2 hour time period. No further increase in the labelling yield was observed over a further 22 hrs (Figure 8.12). Unlike

the binding to DC-SIGN the labelling of BSA was not correlated to the % of SF on the gold surface, with 5:1, 10:1 and 20:1 fucose:SF all showing 60-70% yield. It is interesting that binding of DC-SIGN is glycan dependent but BSA is not - perhaps BSA has a greater presence of accessible nucleophilic amino acid residues on its surface.

In contrast, the G27-dimannose:SF affinity probes were unable to label BSA-FITC, even over a 24 hour period (Figure 8.12B). This is a strange results considering the extent of BSA labelling for the G27-OH:SF or G27-fucose:SF particles, but might be explained by the bulkier size of a dimannose ligand vs a fucose/OH ligand being able to hinder the entry of BSA towards a surface SF for binding. If this is the case, it may be possible to optimise the G27-fucose:SF particles to be specific to fucose binding proteins by using a longer linker to attach the fucose to the GNP as to hinder the SF to only be accessible once a protein is bound to fucose.

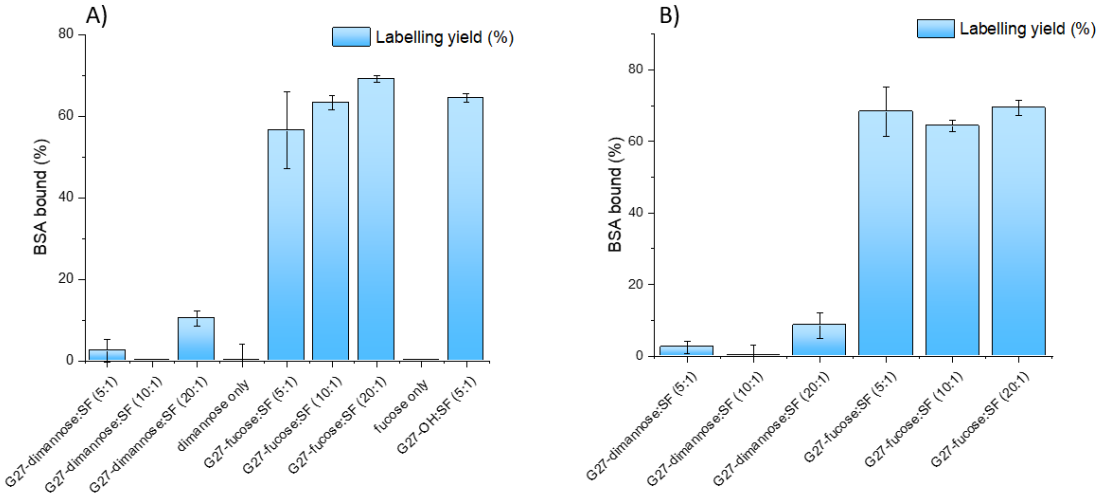

Figure 8.12 labelling efficiency of BSA-FITC by G27-glycan:SF probes after a) 2 hrs and b) 24 hrs. The % yields were calculated based on the amounts of BSA-FITC used for a given reaction.

8.2.6.2 DC-SIGN vs BSA selectivity

While G27-fucose:SF bound BSA-FITC with high efficiency, it was of interest to evaluate their selectivity when mixed simultaneously with DC-SIGN and BSA. Since MLG binding typically occurs on a shorter time scale than the formation of covalent bonds, it was hypothesised that when in competition, DC-SIGN would outcompete BSA. G27-gylcan:SF were mixed with a solution of DC-SIGN-atto643 and 5 fold excess BSA-FITC and the selectivity measured over a 48 hour period by the reduction in the fluorescence signals. Figure 8.13 shows the time course covalent labelling efficiency for DC-SIGN-atto643 by G27-glycan:SF probes in the presence of excess BSA-FITC. As expected, G27-dimannose:SF maintained labelling selectivity to DC-SIGN-atto643 over the duration of 48 hours, with the 5:1 ratio labelling only 4 % of BSA-FITC. Despite low BSA-

FITC labelling, the labelling yields for DC-SIGN-atto643 after 48 hrs were slightly lower than when in the absence of BSA-FITC for all SF ratios. This is likely due to sequestration by BSA reducing the availability of the DC-SIGN molecules. In the absence of BSA, each G27-dimannose:SF (5:1) covalently binds ~15 DC-SIGN-atto643 which was reduced to ~10 when in the presence of 5-fold excess BSA.

Interestingly, the fucose:SF G27 particles were not selective for DC-SIGN over BSA at any glycan:SF ratio, and instead bound both simultaneously. As observed before, the quantity of BSA bound is independent of glycan:SF ratio and remained roughly 38 BSA (~30% of the total based on a 125:1 PGR) per G27-fucose:SF. Binding of DC-SIGN however, remained dependent on SF proportion with the 5:1 binding 13 DC-SIGN tetramers (51% of a 25:1 PGR), 10:1 binding 11 (46%) and 20:1 binding 10 (41%).

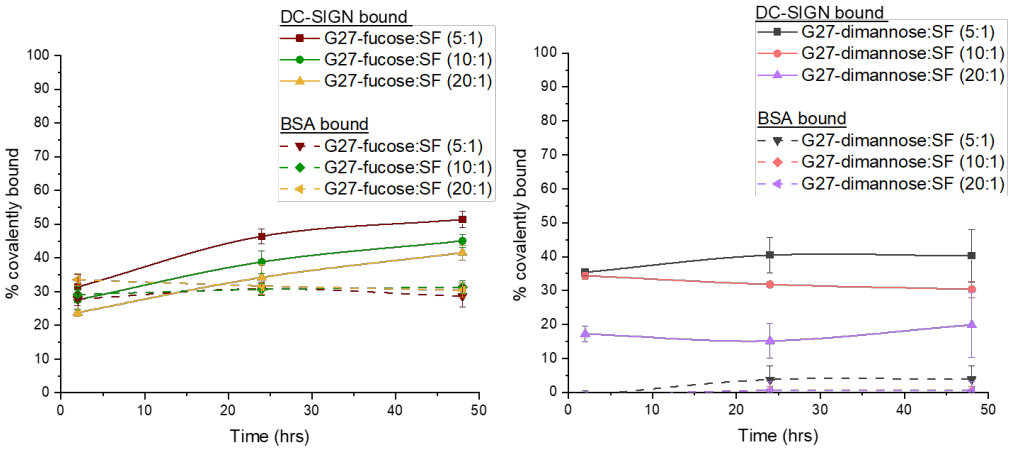

Figure 8.13 Time course of the covalent labelling of DC-SIGN-atto643 (25 nM) by A) G27-fucose:SF or B) G27-dimannose:SF probes (1 nM) in the presence of excess BSA-FITC (125 nM). The % yields were calculated based on the amounts of protein used for a given reaction.

8.2.7 Developing a method to label, isolate and identify proteins from the cell surface.

Results from Section 7.2.4 revealed that binding of G5-EG_n-glycans to dendritic cell surfaces was not solely dependent on DC-SIGN. Endocytosis quantification experiments using both a DC-SIGN inhibitor and a macrophage mannose receptor (MMR) inhibitor showed that while some endocytosis is dependent on DC-SIGN, the MMR is also responsible for a large proportion of binding and internalisation of G5-EG_6-dimannose and G5-EG_6-fucose on dendritic cells. Inhibiting both receptors simultaneously did not completely abrogate G5-glycan internalisation, and this is a strong indicator that other mannose or fucose binding cell surface lectins could be responsible for the immune modulation responses seen in Chapter 7.

The affinity probes in this chapter were developed as a way to isolate and identify such proteins. They should be able to covalently label proteins in a glycan dependent way in a complex cellular environment to ensure only those which would bind G5-dimannose and G5-fucose in the absence of SF are isolated. So far, the G27-dimannose:SF probes have shown a promising ability to do such, and are able to discriminate and selectively label DC-SIGN when in competition with BSA.

In order to use these affinity probes in a cellular environment, first a method of identifying proteins off the GNP must be developed. The most common method to do such is through liquid chromatography tandem mass spectrometry based proteomics, where proteins are first digested into their peptide fragments, which can then be used to confirm the identity of the whole protein through MS/MS based methods.(456) In order for this to work with the gold-nanoparticle pull down system, a way to remove and isolate the protein from the surface of the gold nanoparticle must first be developed. Two methods for this have been recognised.

The first method would be to take the GNP-protein pellet after stringent washes to remove non-covalently bound proteins, and add a protease directly to the solution while the protein is still covalently bound to the GNP. This would leave the labelled peptide attached to the GNP, but the remaining peptides could be easily isolated through pelleting the GNP and collecting the supernatant containing the peptide fragments (Figure 8.14A). The protein should still be able to be identified from the digested fragments despite the labelled one being attached to the GNP pellet.

The second method involves removing the intact labelled protein by displacing the LA-ligands from the surface of the gold nanoparticle and isolating the labelled protein. The protein can then be digested (Figure 8.14B). This would allow for the identification of the protein, the labelled peptide, and the exact labelled amino acids, but is a more complex process.

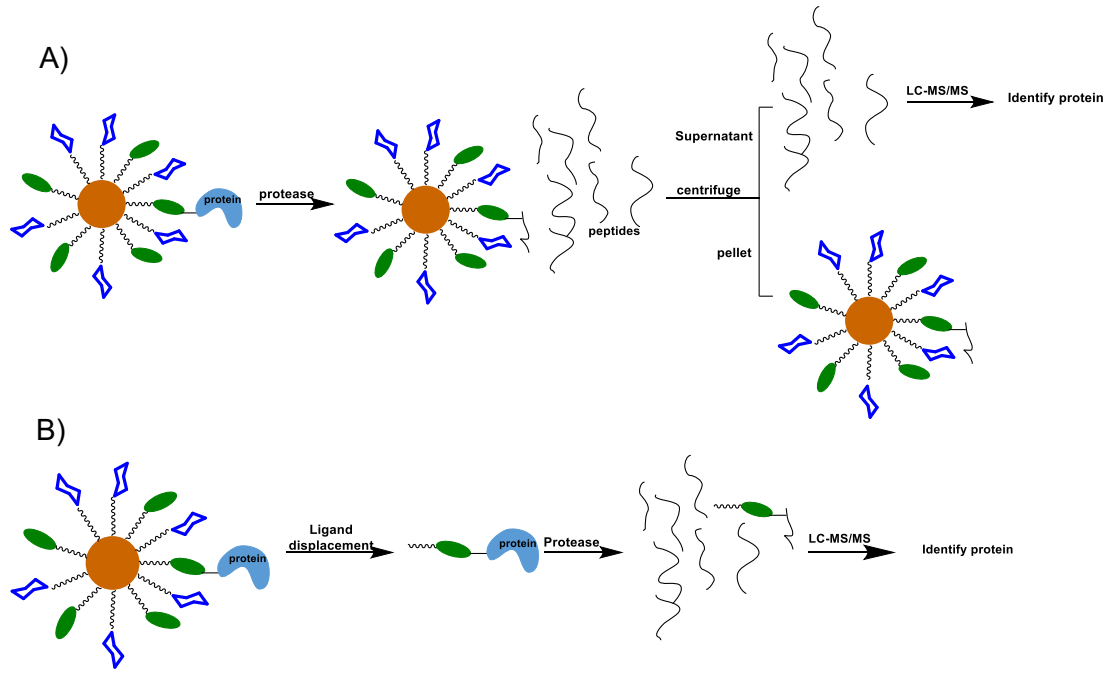

Figure 8.14 Shematic depicting A) and on-GNP protein digestion which would leave the lablled peptide attached the the gold pellet after centrigugation but would still allow for protein identification using the remaining peptides in the supernatant and B) an off-GNP protein digestion where the protein is first released from the GNP along with the covalent affinity ligand before digestion, which allows for both identifcation of the protein identity, and the amino acid location of the covalent tag.

8.2.7.1 On-GNP digestion

This experiment was performed using smaller G13 particles as the concentration range available for G27 particles was insufficient to isolate enough protein for further analysis. G13, which can be easily prepared in larger amount and in higher concentrations, enabled the isolation of higher concentrations of DC-SIGN while still amenable to pelleting at centrifugation speeds of 17,000 x *g* on a standard lab bench. They were prepared as described in Section 2.4.2.2 with the 5:1 glycan:affinity tag modification.

Using the optimal labelling conditions found in Figure 8.11A, DC-SIGN (unlabelled) was reacted with G13-dimannose:SF(5:1) and G27:13-fucose:SF(5:1) for 48 hours at 4 ^{o}C with shaking. The GNP-DC-SIGN pellet was purified by a few cycles of stringent washes containing excess mannose, then the pellet was resuspended in ammonium bicarbonate buffer. The solution was treated with dithiothreitol (DTT) and iodoacetamide (IAA) to reduce and alkylate any disulfide bonds, and then trypsin was added to digest the DC-SIGN. After centrifugation, the supernatant containing the peptides was collected, desalted and subjected to LC-MS/MS analysis. Figure 8.15 shows a representative MS/MS spectra for a digested peptide fragment from a control sample where DC-SIGN was digested in the absence of G13, and the same sequence was identified from the G13-fucose:SF(5:1) and G13-dimannose:SF(5:1) + DC-SIGN samples, indicating the

presence and successful identification of DC-SIGN via this method. A list of the other DC-SIGN related peptides identified by MS/MS is given in Appendix B for the DC-SIGN control (Figure B. 16) which showed 64 % amino acid sequence coverage, and the G13-fucose:SF(5:1) and G13-dimannose:SF samples (Figure B. 17-18) which showed 52 % and 53 % amino acid sequence coverage respectively. Missing peptides/amino acid sequences may be due to very long or very short peptides after digestion, which are difficult to detect by MS.

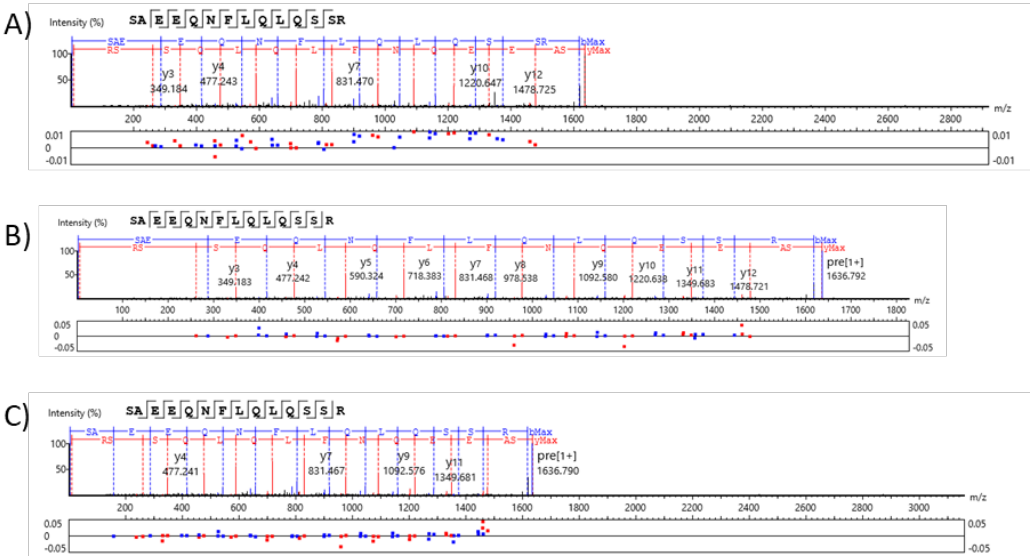

Figure 8.15 LC–MS/MS spectrum of a peptide fragment observed for both A) control sample of DC-SIGN digested with trypsin and B) DC-SIGN treated first with G13-fucose:SF(5:1), then pulled down and digested with trypsin. B) DC-SIGN treated first with G13-dimannose:SF(5:1), then pulled down and digested with trypsin.

Coverage of the DC-SIGN amino acid sequence was not full using this on-GNP LC-MS/MS method and analysis, however, typically a 30-50% coverage is enough to identify a protein.(460) The benefit of a higher protein sequence coverage (>50%) is a greater identity confidence and higher probability of detecting post-translationally modified peptides however, since the main aim was to identify the protein and not the modified peptide, this technique of on-GNP digestion could be viable way of identifying other unknown proteins present in the sample when carried out in a more complex mixture of proteins/on a whole cell.

While identifying the labelled peptide was not necessary for protein identification, it is noted here that samples for both G13-glycan:SF treated DC-SIGN show almost identical sequence coverage, but the control sample contained the presence of an extra peptide from 253-280 in the extracellular DC-SIGN amino acid sequence (Figure 8.16, highlighted in blue). This peptide ends just 5 amino acids away from the start of the mannose binding motif and contains nucleophilic amino acid residues (serine, lysine) capable of being labelled by the sulfonyl fluoride. It is therefore possible that the lack of this peptide in the affinity tag samples means this is a labelled peptide which remained

covalently attached to the G13 pellet after trypsin digestion. Further repeats would help in confirming this.

Other amino acids present in the control but not in the G13-glycan:SF-samples include nucleophilic serine and lysine residues, although these residues are located in the neck region of DC-SIGN and are likely too far away from the CRD to have been labelled. Furthermore, it is impossible to tell whether some of the sequences which are missing due to being too long or short to detect by MS have been labelled in the G13-glycan:SF treated samples as they would not be present either way.

1 AKVPSSISQE QSRQDAIYQN LTQLKAAVGE LSEK**SK**LQEI YQELTQLKAA VGELPEKSKL QEIYQELTRL
71 KAAVGELPEK **SK**LQEIYQEL TWLKAAVGEL PEKSKMQEIY QELTRLKAAV GELPEKSKQQ EIYQELTRLK
140 AAVGELPEKS KQQEIYQELT RLKAAVGELP EK**SK**QQEIYQ ELTQLK**AAVE** **R**LCHPCPWEW TFFQGNCYFM
210 SNSQRNWHDS ITACKEVGAQ LVVIKSAEEQ NFLQLQSSRS NR**FTWMGLSD** **LNQEGTWQWV** **DGSPLLPSFK**
280 QYWNRG**EPNN** **VGEEDCAEFS** **GNGWND**DKCN LAKFWICKKS AASCSRDEEQ FLSPAPATPN PPPA

Figure 8.16 The extracellular DC-SIGN sequence where the blue bold letters are the amino acids identified in the control DC-SIGN sample but not in either of the G13-glycan:SF treated samples and the bold red letters are the mannose binding motif. The results were obtained by combining the LC-MS/MS analysis for each sample, found in Figure B. 16-18.

8.2.7.2 Off-GNP digestion

Since the gold-thiol bond is strong, a number of methods were trialled for displacing the LA-SF-DC-SIGN off the gold surface. One method involved the use of a gold etching solution containing 0.01M $K_3[Fe(CN)_6]$, 0.001M $K_4Fe(CN)_6$, 0.1M sodium thiosulfate and 0.1M ammonia.(461) Using the optimal labelling conditions found in Figure 8.11A, DC-SIGN-atto643 was mixed with G13-dimannose:SF(5:1) and G13-dimannose:SF(5:1) for 48 hours at 4 ^{o}C with shaking. To determine if the etching solution could displace the ligand from the surface, the mixture was first centrifuged and the fluorescence intensity of the supernatant was measured (F1). The pellet was resuspended in buffer containing excess mannose and after centrifugation, the supernatant was again collected and measured for fluorescence intensity (F2). Finally, the pellet was incubated in the etching solution for 2 hours, and after a third round of centrifugation, the supernatant was measured for fluorescence intensity (F3). The supernatant after etching showed high fluorescence intensity, indicating that the LA-SF-DC-SIGN-atto643 had been successfully displaced from the GNP surface. Furthermore, combining F1, F2 and F3 showed fluorescence comparable to the DC-SIGN control (Figure B. 19).

A difficulty with this method was the effect the etching solution had on DC-SIGN. DC-SIGN (unlabelled) was treated with this etching solution. The mixture was then purified using a MWCO filter and analysed by high resolution mass spectrometry. After a 2 hour incubation with the etching solution, a reduction in the DC-SIGN peak intensity was observed and a new peak at a retention time of 2.4 minutes was detected. After 24 hours, the DC-SIGN peak was no longer present, indicating degradation of DC-SIGN. To avoid

interference from degraded DC-SIGN fragments during MS acquisition, a second method was trialled.

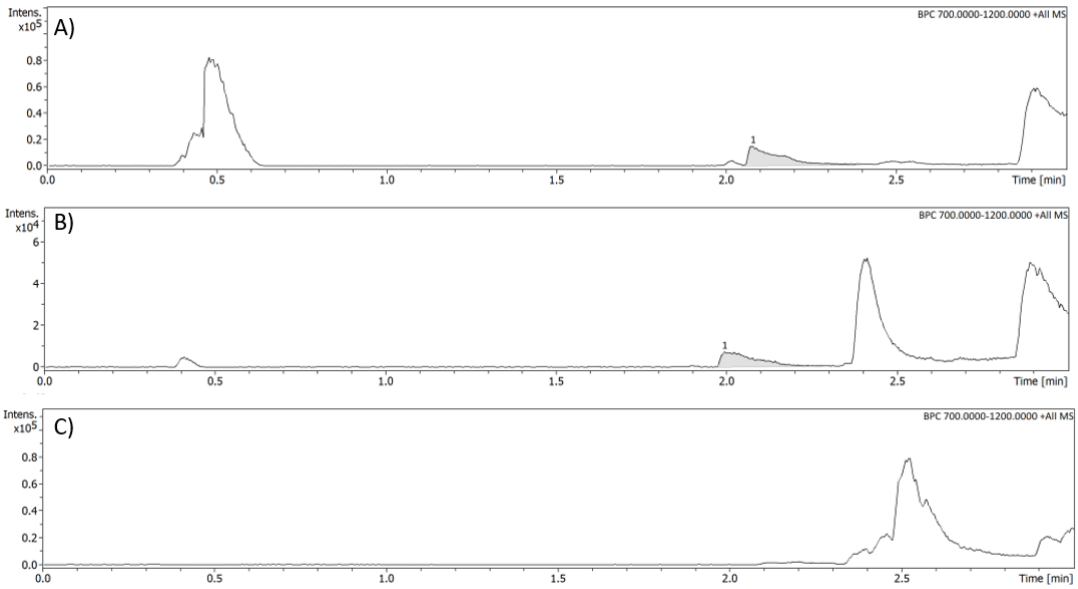

Figure 8.17 LCMS elution profiles of DC-SIGN (unlabelled, 10 μM, monomer) after treatment with the gold etching solution for A) 0 minutes B) 2 hours C) 24 hours.

For method 2, β-mercaptoethanol was used as a way to etch the GNP and displace the LA-SF-DC-SIGN. Once again, using the optimal labelling conditions found in Figure 8.11A, DC-SIGN was mixed with G13-dimannose:SF(5:1) and G13-fucose:SF(5:1) for 48 hours at 4 ^{o}C with shaking. The labelled proteins were then purified by a few cycles of stringent washes containing excess mannose. The pellet was then suspended in Laemmli buffer containing 2.5% β-mercaptoethanol and heated to 90 ^{o}C for 10 minutes. During this time the solution became grey, indicating the aggregation or etching of the G13 particles. The sample was centrifuged and the supernatant collected. SDS-page analysis of the supernatant verified that DC-SIGN had been released from the surface of the GNP (Figure 8.18). These are common conditions used to denature proteins before SDS page and do not interfere with the primary structure of DC-SIGN.

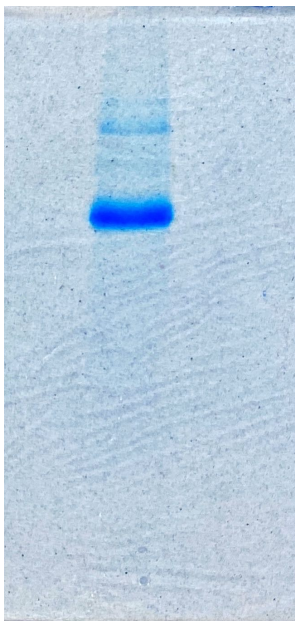

Figure 8.18 SDS page of the affinity labelling of DC-SIGN (200 nM) with G13-dimannose:SF(5:1) (20 nM). The G13-dimmannose:SF-DC-SIGN pellet was washed with 50 mM mannose in HEPES buffer, then the pellet treated with 2.5% mercaptoethanol in Laemmli buffer and heated to 90 ^{o}C for 10 minutes. The supernatant was collected and analysed using a 5% stacking gel and 17% running gel. The presence of the blue protein band on the gel confirm that covalently labelled DC-SIGN had been released from the GNP pellet.

The Laemmli buffer supernatant containing the protein was processed for LC-MS/MS analysis by the Astbury Centre at the University of Leeds. Briefly, an s-trap was used to remove the SDS, mercaptoethanol and other salts, then trypsin was used to digest the protein. The sample was then subjected to LC-MS/MS analysis. A control sample of DC-SIGN, not pre incubated with G13-glycan:SF, was included for comparison. The identified peptide fragments for each sample are shown in Figure 8.19. For both G13-dimannose:SF(5:1) and G13-fucose:SF(5:1) samples, >98% of the amino acid sequence for DC-SIGN was identified by LC-MS/MS, highlighting this as a viable method for confidently identifying the proteins pulled down by the G13 particles.

Figure 8.19 Amino acid sequences found by LC-MS/MS for A) control DC-SIGN B) DC-SIGN pulled down by G13-fucose:SF(5:1) and C) pulled down by G13-dimannose:SF(5:1) where green highlighted letters indicate the identified amino acids.

With the help of Dr Hannah Britt in the School of Chemistry at the University of Leeds, the data files were analysed using PEAKS studio X software, however, the labelled peptides eluded detection. The lack of observed modification can most likely be attributed to the relatively low abundance of these modified species below the limit of instrument detection. Since the G13-glycan:SF probes were designed to display both glycans and the protein reactive sulfonyl fluoride in a multivalent fashion, it was anticipated that multiple sites in the proximity of the ligand binding site could be labelled. This provided an added complexity to the analysis. If not all peptides in the sample had incorporated the label equally, e.g. some had multiple labels or were labelled at different sites, some were partially labelled and some were unlabelled, then the species would be spread across multiple masses, diluting the overall signal to below the limit of instrument detection. Despite searching for all mass increases associated with expected fragmentation of the sulfonyl fluoride tag, the labelled peptides have not been identified from these samples so far.

Alternatively, while lysine- and tyrosine-sulfonyl labels may be stable, if labelled at a serine or cysteine, then the sulfonyl group becomes a good leaving group when in the presence of the reducing agent DTT, which is required before protein digestion (Scheme 8.5). This would result in the label not being present at all at the time of data acquisition.

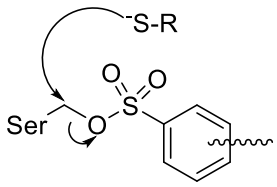

Scheme 8.5 Schematic showing how the sulfonyl ligand becomes a good leaving group in the presence of DTT, when covalently bound to a serine residue.

8.3 Conclusion and future work

8.3.1 Conclusions

In summary, this chapter has begun to develop an approach for targeting and selectively labelling GNP-glycan binding proteins on the cell surface, with the intention of isolating and identifying them to elucidate the pathways involved in glycan mediate cytokine signalling processes. Gold nanoparticles 27 nm in diameter (G27) supporting both a glycan ligand and a protein reactive aryl sulfonyl fluoride tag were synthesised and their ability to bind DC-SIGN was assessed in a pull-down assay, where the protein-G27 complex was pelleted out of solution to facilitate measuring the fluorescence of the unbound protein in the supernatant. Using the Hill equation to fit the data and extract apparent binding affinities, it was found that the introduction of a SF affinity tag increased the ability of the G27-glycans binding to DC-SIGN, improving the binding affinity by up to an order of magnitude in a sulfonyl fluoride proportion dependent manner. This was especially the case for G27-fucose:SF particles where a higher proportion of SF resulted in stronger binding. To support this finding, the percentage of DC-SIGN covalently bound to the G27 was measured and was found to be greater for particles containing the highest proportion of sulfonyl fluoride on their surface as expected. The covalent labelling yield was also found to increase over a 48 hour period till all DC-SIGN bound were turned into covalently bound. Covalent labelling of these particles to DC-SIGN appeared to be glycan dependent, and the G27-dimannose:SF particles were found to be specific for DC-SIGN when in the presence of BSA, a non-target protein. The confirmed presence of the glycan dependent covalent bond is important for isolating the desired proteins in a more complex mixture, where covalent tag is required to provide a more tangible link, but must remain specific to proteins which bind dimannose and fucose to avoid isolation of non-target species.

Using the method developed for specific labelling, G13-glycan:SF-DC-SIGN complexes were isolated, processed and analysed by liquid chromatography tandem mass spectrometry, which identified a greater than 98% extracellular DC-SIGN amino acid sequence coverage. These data are important as it validates the use of this method for identifying unknown proteins that may bind to GNP-dimannose or GNP-fucose on the cell surface.

8.3.2 Future work

While this approach has so far allowed for the identification of the whole protein bound to the G13-glycan:SF, it is yet to identify which amino acids have been labelled by the affinity tag, and if the identity of the glycan directs covalent labelling to different residues, which may account for the differences in the binding affinities and binding motifs. Analysis of the LC-MS/MS data is ongoing to identify these sites. Although this work is on-going, the overarching aim of this chapter was to develop a method that could be used to identify which cell surface proteins, in addition to DC-SIGN, bind the G5-glycans discussed in Chapter 7. Future work will therefore focus on optimising these conditions and carry out on whole-cell based assays. Being able to identify which receptors are responsible for fucose and dimannose mediated cytokine modulation will provide us with a more comprehensive picture of the cellular processes involved in not just IL-23 regulation, but also the whole DC immune regulation process, and the implications this may have on fungal immunity and how it might relate to the onset of the seronegative spondyloarthropathies.

Chapter 9 – General discussion and concluding remarks

The seronegative spondyloarthropathies encompass a spectrum of inflammatory diseases including ankylosing spondylitis, psoriatic arthritis, inflammatory bowel disease, reactive arthritis, and the arthritis related to anterior uveitis. These conditions share overlapping clinical features such as axial skeletal inflammation (hip, spine shoulder), enthesitis, and external sites of inflammation (ciliary body, aortic root, lung apex and ilium), and their immunopathology is increasing recognised as being strongly associated with dysregulation of the IL-23/IL-17 axis.(245) Genetic studies including polymorphisms in the IL-23R gene, functional data from animal models, and blockade of the IL-23/IL-17 proving a successful therapy in SpA patients, have underscored the central role of IL-23 in promoting joint and entheseal inflammation.(305, 361, 462) Elevated IL-23 has been reported in patient samples and experimental systems, implicating this cytokine as a pivotal upstream driver of SpA pathology.(463)

Despite these insights, the underlying mechanisms for IL-23 induction in SpA remain incompletely understood. Attention has been directed towards the role of gut dysbiosis, barrier disruption and microbial triggers in shaping systemic immune responses.(303, 362, 398) However, the precise receptors and signalling pathways that connect microbial or endogenous ligands to IL-23 production are less well defined. Mouse models have implicated the role of the C-type lectin Dectin-1 in triggering IL-23 dependent enthesitis in the presence of fungal cell wall component β-glucan, but one other potential candidate is DC-SIGN, a C-type lectin receptor expressed on dendritic cells which recognises high-mannose and fucosylated glycans.(362, 390) Beyond its role in pathogen recognition, DC-SIGN is known to modulate downstream immune responses though signalling pathways than can promote both pro-inflammatory and tolerogenic outcomes depending on the ligand context.(52, 394) Importantly, studies have demonstrated that DC-SIGN engagement can drive IL-23 production, linking the activation of DC-SIGN to the IL-23/IL-17 axis.(368) This raises the possibility that sustained signalling through DC-SIGN may contribute to the chronic induction of IL-23 in SpA. Despite a plausible connection, direct evidence for DC-SIGN as an upstream inducer of IL-23 in SpA is lacking, and the structural or biophysical principles that govern DC-SIGN mediated cytokine modulation remain under characterised.

Identifying whether DC-SIGN serves as a critical trigger for IL-23 in SpA therefore represents an important knowledge gap. Elucidating this pathway could not only clarify the molecular link between innate recognition and the adaptive inflammatory repones, but also reveal new opportunities for therapeutic intervention. Specifically understanding how multivalent glycan structures and their presentation influence DC-SIGN signalling may provide a basis for rationally designing strategies to selectively modulate IL-23 production.

9.1 Key findings

9.1.1 DC-SIGN - GNP-glycan interactions

Multimeric lectins are widely distributed across biological systems and serve essential roles in the immune response as pattern recognition receptors. They participate in diverse processes, including cell-cell adhesion, internalisation of pathogens, and modulation of cytokine and chemokine activity in response to infection. The strength and specificity of LGIs are strongly influenced by factors such as glycoconjugate size, three dimensional shape, ligand flexibility and glycan density. Despite their importance, relatively little research has addressed the structural and biophysical principles that determine how these design elements govern lectin selectivity. A deeper understanding of the mechanisms underlying MLGIs and the ways in which glycan presentation shapes these interactions is critical. Such insights will not only advance fundamental knowledge but also provide a foundation for the rational design of novel and therapeutic strategies which exploit or modulate lectin recognition.

The first part of this thesis set out to investigate what aspects of glycoconjugate design have an impact on DC-SIGN binding strength. Particular attention was given to glycan type (dimannose vs fucose), glycan density, and glycan flexibility on the nanoparticle surface. The objective was to identify a series of GNP-glycans displaying a range of binding affinities with DC-SIGN and to use thermodynamic studies to identify the enthalpic and entropic contributions to binding. This, combined with methods to measure their binding mode, could help elucidate structural information on DC-SIGN e.g. binding site orientation, and inter-binding site spacing. These structural insights, in turn, could be linked to how the organisation and composition of the glycocalyx influences downstream responses such as IL-23 production.

By exploiting the fluorescence quenching properties of GNPs and using a ratiometric NSET method, the apparent binding affinities of G5-glycans with DC-SIGN were measured. Furthermore a study employing dynamic light scattering shed light on their binding modes. The findings, presented across Chapters 3-4, indicated that glycan type, glycan density and glycan flexibility all impact DC-SIGN binding strength and binding mode. In particular, it was observed that G5s with a high surface density of glycans form only monolayer DC-SIGN coated G5-glycan particles upon mixing with DC-SIGN, where one G5-glycan binds simultaneously to all four CRDs in one DC-SIGN molecule. Contrastingly, G5-glycans with a lower glycan density, especially those with shorter, more rigid linkers, showed a greater tendency to form cross-linked species. This was likely due to their large inter-glycan distances resulting in a lack of complementarity with the binding sites, and therefore engaging fewer than four CRDs on one lectin. The volume of the cross-linked species was reduced as linker length increased, indicating that the increased flexibility of the longer linkers afforded them the ability to bridge the

CRDs of one DC-SIGN tetramer, highlighting how linker flexibility can allow for deviation from spatial constraints of the DC-SIGN CRDs.

This observation was substantiated by a GNP-fluorescence quenching study to determine the thermodynamic contributions of G5-glycans to the affinity enhancement mechanisms in MLGIs, in which the enthalpy change of binding is directly linked to the number of CRDs engaged in an MLGI. These data revealed that high density G5-glycans binding with DC-SIGN resulted in binding enthalpy changes of ~4-fold the monovalent binding, which was thus attributed to binding of all four binding sites. However, when displaying low glycan density and short linkers, the enthalpy change of binding for these G5-glycans translated to 2-3 CRD binding events. This confirmed that the cross-linked binding mode was due to each low density, short linker G5-glycan engaging fewer than four CRDs on one DC-SIGN, allowing a second GNP-glycan to bind the remaining unoccupied CRDs and so on, creating a cross-linked network.

Furthermore, it was observed that GNPs with longer flexible dodeca(ethylene glycol) (EG_{12}) linkers which tether the glycans to the GNP surface experienced weaker binding than those tethered by shorter and thus more rigid di(ethylene glycol) (EG_2) linkers. It was hypothesised that this was due to the increased entropic penalty of constraining longer more flexible linkers, which have greater conformational degrees of freedom. Indeed, when measuring the thermodynamic contributions, entropy change of binding became increasingly more negative with increasing linker length, confirming this hypothesis. The design of potent multivalent binders is therefore a balance between controlling the spatial arrangement of glycans and providing sufficient flexibility to allow the glycoconjugate to adapt to the binding sites to maximise enthalpy enhancements, while simultaneously minimising the entropic cost associated with that flexibility.

Comparing the NSET results to those collected by conventional biophysical techniques such as ITC verified this ratiometric GNP-NSET readout to be a reliable method for probing the thermodynamic contributions between G5-glycan-DC-SIGN based MLGIs. These approaches employed solution-based systems to investigate the biophysical and structural features of multivalent lectin-glycan-GNP interactions, in isolation from the additional aspects present on surfaces. However, these systems do not represent the complexities MLGIs might experience in their native surface-phase environments. Therefore in order to determine whether calculating solution based K_d measurements was a reliable method for predicting how receptors behave on the cell surface, an *in cellulo* viral inhibition assay was performed to extract antiviral properties of G5-glycans. During this experiment, G5-glycans were revealed to be potent inhibitors DC-SIGN/R mediated EBOV-GP infection and uptake by human cells. The IC_{50} values for DC-SIGN mediated inhibition largely followed a trend, that increasing linker length decreased inhibition potency. While cell-based assays account for more complexities than solution based assays, they do not provide the high level of detail such as binding mode, binding

affinity or thermodynamics therefore performing these assays in tandem and comparing the outputs helps provide a more comprehensive understanding of the broader mechanisms of MLGIs.

Together, these data demonstrate the importance of being able to identify structural information on the binding site of the target lectin, which can be used to inform the design of high affinity glycoconjugates to optimise multivalency and target lectins with high specificity.

9.1.2 DC-SIGN induced modulation of IL-23

The second half of this thesis set out to investigate IL-23 modulation with particular emphasis on the potential for DC-SIGN to cross-talk with TLRs to shape cytokine and T cell responses. The objective was to determine if the GNP-glycans synthesised and characterised in part A could induce DC-SIGN signalling pathways which would co-signal with TLR receptors to drive enhanced or suppressed IL-23 production.

The findings presented in Chapter 7 indicated that glycan identity is important in DC-SIGN modulated IL-23 production. In particular it was observed that addition of high concentration azido-modified dimannose significantly downregulated IL-23 and IL-10 production in a monocyte derived dendritic cell model, when co-stimulated with the TLR4 ligand LPS. In contrast, it was found that azido-modified fucose upregulated both IL-23 and IL-10.

The modulation of other TLR signalling pathways via DC-SIGN was briefly investigated. Co-stimulation with Heat Killed *Salmonella typhimurium* (HKST) (a TLR4 and TLR2 agonist) showed some downregulation of IL-23 by high affinity G5-glyans suggesting that higher binding affinity G5-glycans could exert some regulatory effect. Notably, all conditions with HKST led to downregulation of IL-10, with G5-glycans showing linker-dependent effects, reinforcing the role of DC-SIGN and binding affinity in TLR2 signalling and potentially promoting a more inflammatory environment.

Outside of TLR2/4 signalling, GNP-glycans often failed to induce significant modulation of both IL-10 and IL-23 despite exhibiting strong nM binding affinities to DC-SIGN in part A. When the free ligand concentration was reduced to match the effective glycan concentration on the gold nanoparticles, the free ligands no longer induced significant cytokine modulation compared to the LPS control. This indicated that the absence of modulation observed by the G5-glycans could likely be due to insufficient concentrations.

What was particularly interesting about the high concentration free ligand data was its discrepancy from the literature. Gringhuis *et al*. reported that mannose containing ligands promoted proinflammatory cytokine production (IL-12p40, IL-6) through DC-SIGN and TLR4 co-signalling. While IL-23 was not directly measured in this study, it shares its p40 subunit with IL-12, which was found to be upregulated in the presence of mannose

containing ligands.(52) Fucose containing ligands such as Lewis^x were observed to dampen TLR4 induced proinflammatory signalling, with a direct reduction in IL-23 compared to LPS stimulation alone.(92) In this thesis the opposite was observed, where dimannose downregulated IL-23 and fucose was found to upregulate IL-23. This discrepancy has so far been attributed to the presence of an azide handle on the free ligands used in these experiments, as free mannose without an azide handle showed upregulation consistent with previous reports. This highlights how small structural modifications to glycan ligands can have a large impact on their cellular activity. However, in agreement with the data in this thesis, other authors have shown that engagement of DC-SIGN with the mannose containing ligand ManLAM or mannose glycopolymers inhibit Dectin-1 induced IL-23 and TLR4 induced IL-12p70, respectively, but promote Dectin-1 induced IL-6 and LPS induced IL-10.(161, 394) Combined, these data indicate the need for further detailed investigations into the complex and context specific nuanced signalling interactions between DC-SIGN and other CLRs and TLRs to determine the specific role of DC-SIGN in modulating these individual pathways.

Inhibiting DC-SIGN and the macrophage mannose receptor during these experiments provided further insights into internalisation and signalling mechanisms in DCs. Inhibition of MMR consistently reduced G5-glycan uptake more effectively than DC-SIGN for both dimannose and fucose coated G5s. This strongly indicated that other lectins, particularly MMR, were also significantly responsible for G5-glycan internalisation. Despite MMR accounting for a significant proportion of G5 internalisation, this did not directly translate to changes in IL-23 output, suggesting that under these conditions, MMR does not co-signal with TLR4 to regulate IL-23 production. Conversely, inhibiting DC-SIGN tended to attenuate IL-23 modulation, thereby implicating DC-SIGN in this specific signalling pathway for IL-23 regulation.

Consistent with the observed suppression of IL-23 by dimannose, this ligand also largely skewed the response away from the LPS induced Th17, towards a Th2 phenotype, evidenced by downregulation of Th17-associated cytokines and upregulation of Th2 cytokines. Free azido-fucose had variable effects on T cell proliferation across donors, aligning with its variable impact on IL-10, and appeared to enhance the LPS-induced Th17 response, consistent with its ability to upregulate IL-23 in MoDCs. In contrast, G5-glycans (both dimannose and fucose) appeared to suppress T cell proliferation, a trend opposite to that observed with free glycans, suggesting a potentially different mechanism of T cell modulation, possibly due to steric hindrance. However, the G5-glycans had minimal impact on T cell cytokine production, which was unsurprising given their limited modulation of MoDC cytokine production.

Overall, the work provided in Chapter 7 provided some foundational insights into the complex immunological impacts of glycans on IL-23 driven inflammation, highlighting

that their effects depend significantly on the glycan type, their presentation (free vs multivalent), and the specific co-stimulation conditions.

9.2 Drawbacks and study limitations

This study has several important limitations that should be acknowledged. Namely, all blood samples came from healthy donors with no underlying inflammatory diseases. While this provided a controlled baseline for examining the effects of GNP-glycan-DC-SIGN signalling, it limited the ability to directly understand DC-SIGN driven IL-23 production in a disease setting. Ideally, it would have been beneficial to compare the results from healthy donors to patients with SpA. This would have offered insight into whether individuals with SpA exhibit altered or predisposed responses to DC-SIGN engagement.

Second, the experimental work relied on a monocyte derived dendritic cell model, which display similarity to just one dendritic cell subset. While MoDCs are widely used, they do not encompass the full diversity of the primary dendritic cell compartment, many of which may differ in their expression of DC-SIGN and TLRs to modify downstream signalling pathways differently.

Third, the GNP-glycans used in this study, while highly defined and structurally controlled, represent only a small fraction of the glycan complexity of the glycocalyx displayed by fungi, bacteria, and host cells. In a natural infection or tissue microenvironment, glycan structures are far more heterogeneous, and their spatial organisation, density, and presentation likely play key roles in shaping lectin signalling. It would be valuable in the future to study to effects of scaffold size and shape on immune modulation, to more accurately mimic the size of bacterial and fungal pathogens.

In addition, while this thesis centred on DC-SIGN-mediated signalling it is important to note that GNP-dimannose and fucose can also be recognised by other mannose or fucose binding cell surface receptors. These receptors, either independently or in combination with DC-SIGN, may have contributed to the observed cytokine responses, making it difficult to attribute the effects solely to DC-SIGN signalling. To address this, Chapter 8 detailed the development of an experimental protocol to isolate and identify all lectin receptors which may be involved in glycan-GNP stimulated IL-23 and other cytokine signalling.

Finally, while IL-23 modulation was a central readout of this study, the upregulation of IL-23 alone cannot be taken as definitive evidence of a trigger for SpA. Establishing a causal role would require *in vivo* models that capture the complexity of disease pathogenesis, including the relationship between genetic risk factors, microbial exposure, and location specific immune responses. Mouse models or patient-derived

systems will therefore be necessary to validate and extend these findings in a physiologically relevant context.

Taken together, these limitations highlight the need for further studies using patient samples, diverse dendritic cell subsets, more complex glycan repertoires, and disease-relevant models to fully elucidate the role of DC-SIGN in IL-23 regulation and its potential contribution to SpA pathogenesis.

9.3 Theoretical and practical implications

The studies presented here provide some important insight for understanding how the multimeric structure of lectins and the design of glycoconjugates influence the specificity and potency of multivalent lectin glycan interactions. A productive use to these findings is to inform the design of glyco therapeutics for medical applications. Several key design principles have emerged from this work. First minimising glycan ligand flexibility can reduce the entropic penalty of binding, thereby enhancing affinity. However, in order for this to still retain optimal enthalpy, the rigid linkers must closely match the spatial organisation of the lectin binding sites as deviations from these spatial constraints cannot be made up for by flexibility. In the same vein, reducing glycan density reduces the ability of glycans to simultaneously bind four CRDs, but tetrameric binding can be reintroduced in low density systems by introducing long flexible linkers which can meld to CRD binding sites. Therefore finding a balance between enthalpic and entropic factors is vital.

Beyond contributing to revealing details on the design of glycol-therapeutics, this thesis has demonstrated the practical therapeutic potential of GNP-based glycoconjugates. Functionalised GNP-glycans were shown to act as potent inhibitors of EBOV-GP-driven viral infection by binding to DC-SIGN and DC-SIGNR on the cell surface, thereby blocking viral entry. Importantly this inhibitor mechanism is unlikely to be compromised by viral mutation, as it targets highly conserved glycosylation patterns on the EBOV glycoprotein. These findings highlight the promise of GNP-glycans as a potential durable antiviral strategy.

Although this work did not conclusively establish a direct link between GNP-induced DC-SIGN signalling and IL-23 regulation in the context of SpA, the observed downregulation of IL-23 following azido dimannose-DC-SIGN engagement suggests that specific glycan designs can modulate inflammatory cytokine expression. Furthermore these studies have begun to investigate whether glycoconjugate design elements such as linker length and glycan type influence lectin-associated cytokine expression. This opens up avenues for exploring whether other glycoconjugate properties such as glycan density or scaffold size can be tuned to selectively influence DC-SIGN mediated immune pathways. Such strategies could have far-reaching implications, enabling the design of ligands that either

activate protective immune responses (e.g. against viruses, bacteria or cancer) or promote tolerance in contexts such as autoimmunity, allergy or transplantation.

9.4 Concluding remarks and future work

Taken all together, this work established polyvalent GNP based glycoconjugates as a versatile platform with both investigative function and therapeutic potential. Their structural tunability, low-toxicity and biocompatibility make them valuable for not only probing the mechanisms of lectin-glycan recognition but also for directing immune responses in clinically relevant ways. Beyond acting as proof of principle viral inhibitors, GNP-glycans offer a flexible foundation for developing new strategies to combat infection and immune mediated disease.

Although this project identified GNP-glycans with low nM binding affinity to DC-SIGN, the driving force behind excessive IL-23 production in SpA remains unknown, and is unlikely driven by DC-SIGN alone. Further work should focus on identifying other lectin receptors which may co-signal with DC-SIGN to modulate immune outcomes. This could be done using the GNP-based pull down assay developed in Chapter 8. It is also recommended to compare patient and healthy controls, employ more complex glycan repertories and scaffold sizes which more closely mimic natural fungi, and use a wider range of relevant DCs subtypes.

Appendix A

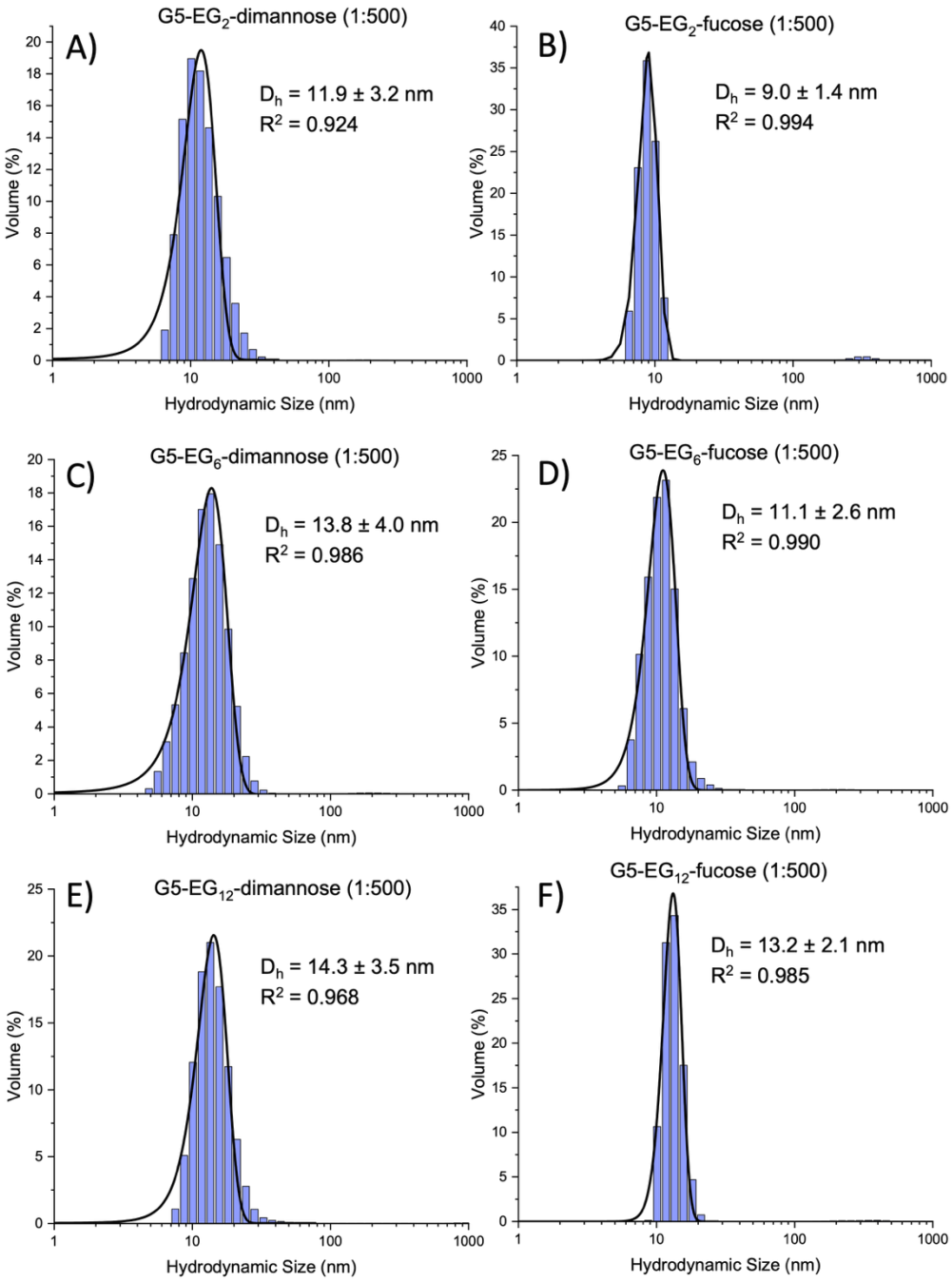

Figure A. 1 Volume population hydrodynamic size distribution histograms fitted with a Gaussian distribution curve for A) G5-EG_2-dimannose, B) G5-EG_2-fucose, C) G5-EG_6-dimannose, D) G5-EG_6-fucose, E) G5-EG_{12}-dimannose, F) G5-EG_{12}-fucose, made in a 1:500 GLR (D_h values given as xc ± ½ FWHM).

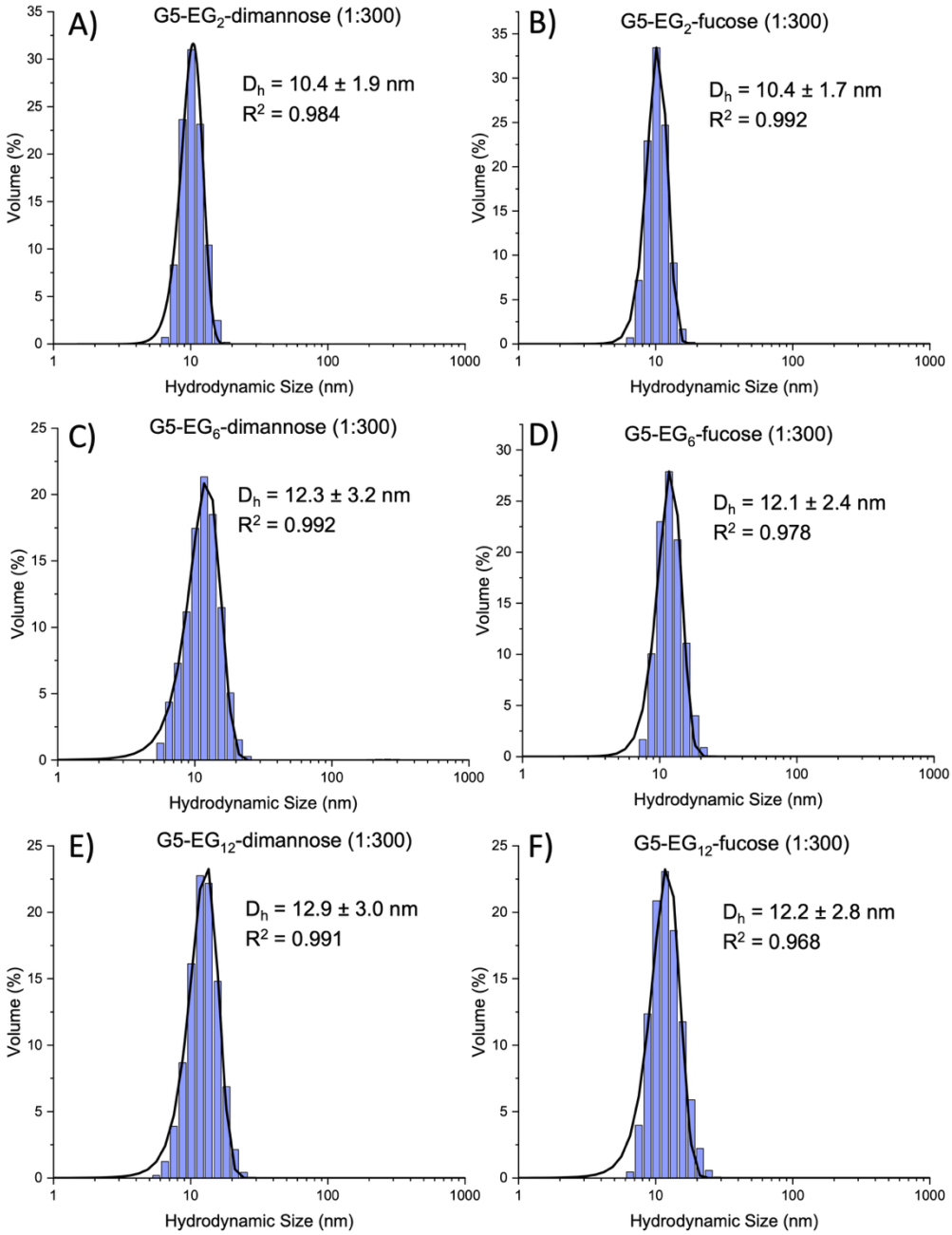

Figure A. 2 Volume population hydrodynamic size distribution histograms fitted with a Gaussian distribution curve for A) G5-EG_2-dimannose, B) G5-EG_2-fucose, C) G5-EG_6-dimannose, D) G5-EG_6-fucose, E) G5-EG_{12}-dimannose, F) G5-EG_{12}-fucose, made in a 1:300 GLR (D_h values given as xc ± ½ FWHM).

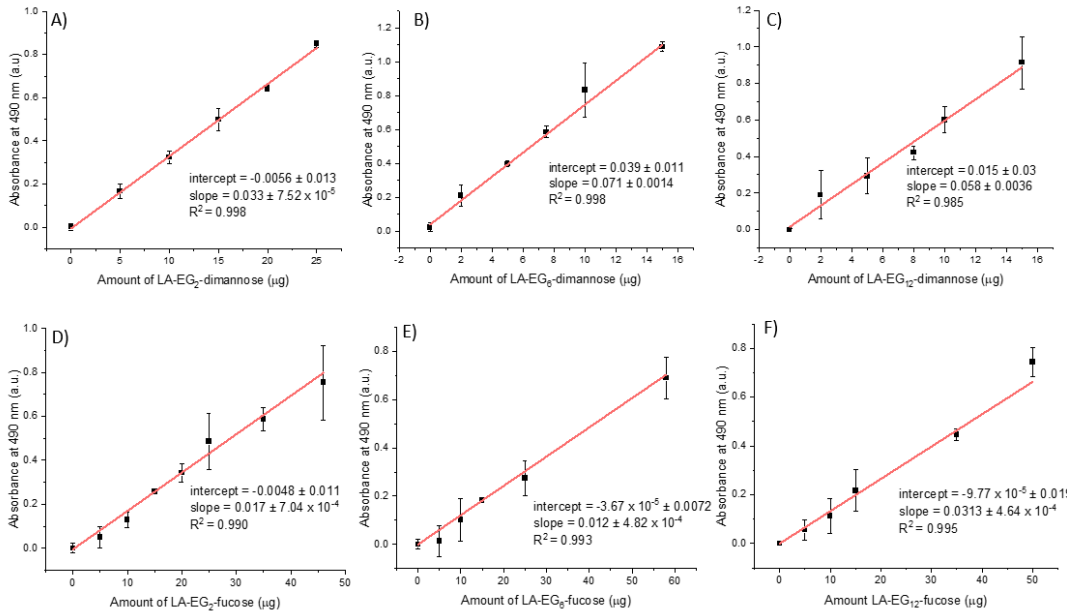

Figure A. 3 Plot of absorbance at 490 nm against amount of A) LA-EG_2-dimannose, B) LA-EG_6-dimannose, C) LA-EG_{12}-dimannose, D) LA-EG_2-fucose, E) LA-EG_6-fucose, F) LA-EG_{12}-fucose fitted by the linear relationship; y=mx+c.

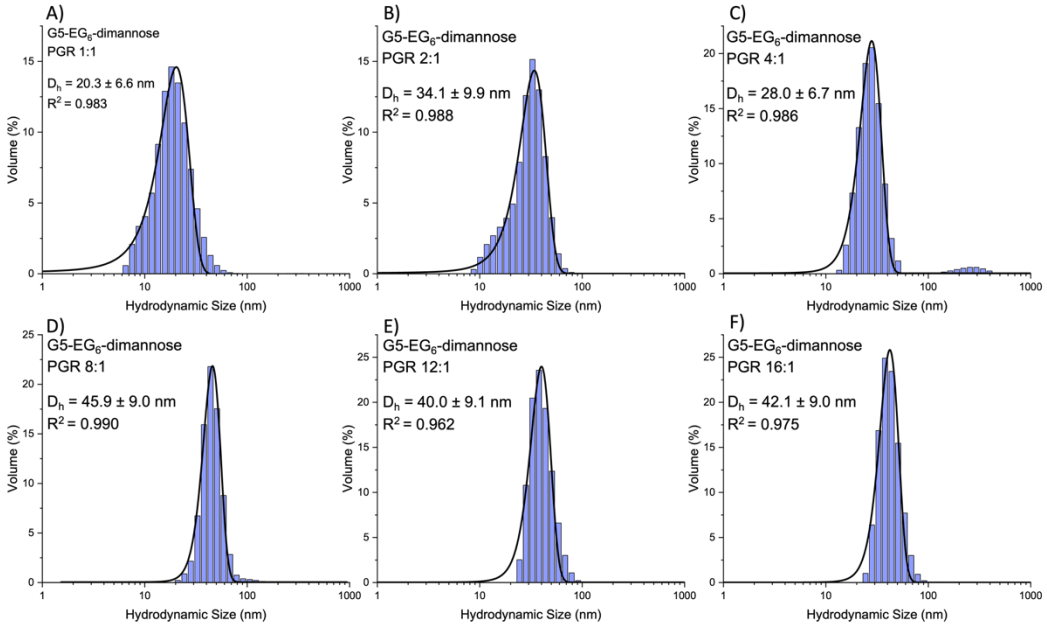

Figure A. 4 Volume population hydrodynamic size distribution histograms fitted with Gaussian fits for the binding of G5-EG_6-dimannose (1:1000) (20 nM) with DC-SIGN at varying protein:G5 molar ratios (PGR) of (A) 1:1, (B) 2:1, (C) 4:1, (D) 8:1, (E) 12:1, and (F) 16:1 (D_h values given as xc ± ½ FWHM).

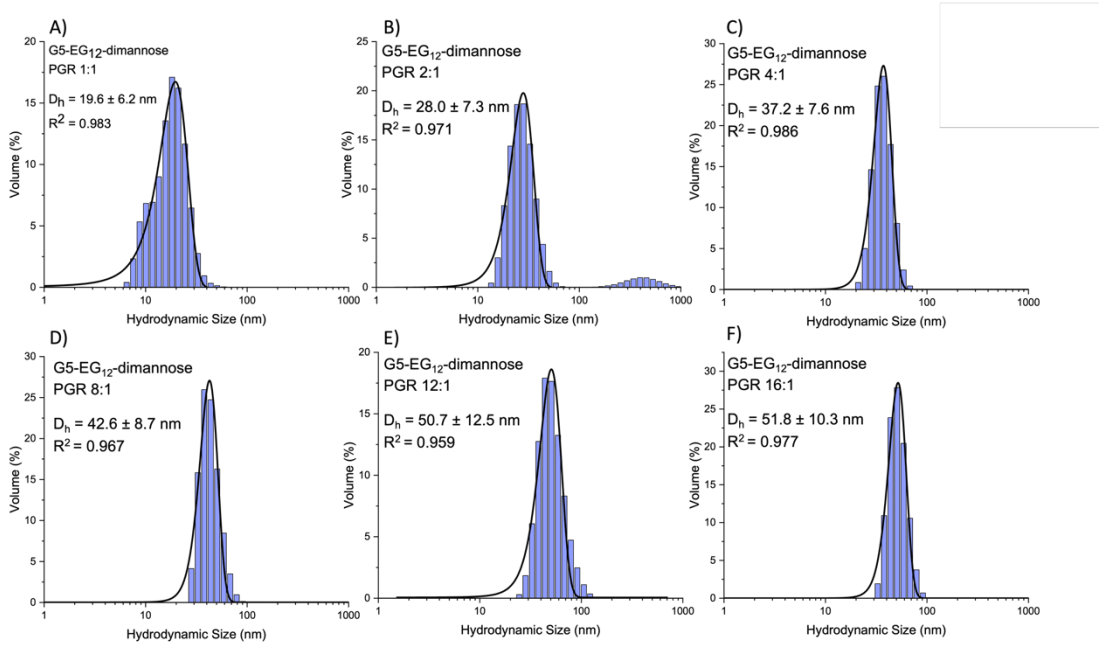

Figure A. 5 Volume population hydrodynamic size distribution histograms fitted with Gaussian fits for the binding of G5-EG_{12}-dimannose (1:1000) (20 nM) with DC-SIGN at varying protein:G5 molar ratios (PGR) of (A) 1:1, (B) 2:1, (C) 4:1, (D) 8:1, (E) 12:1, and (F) 16:1 (D_h values given as xc ± ½ FWHM).

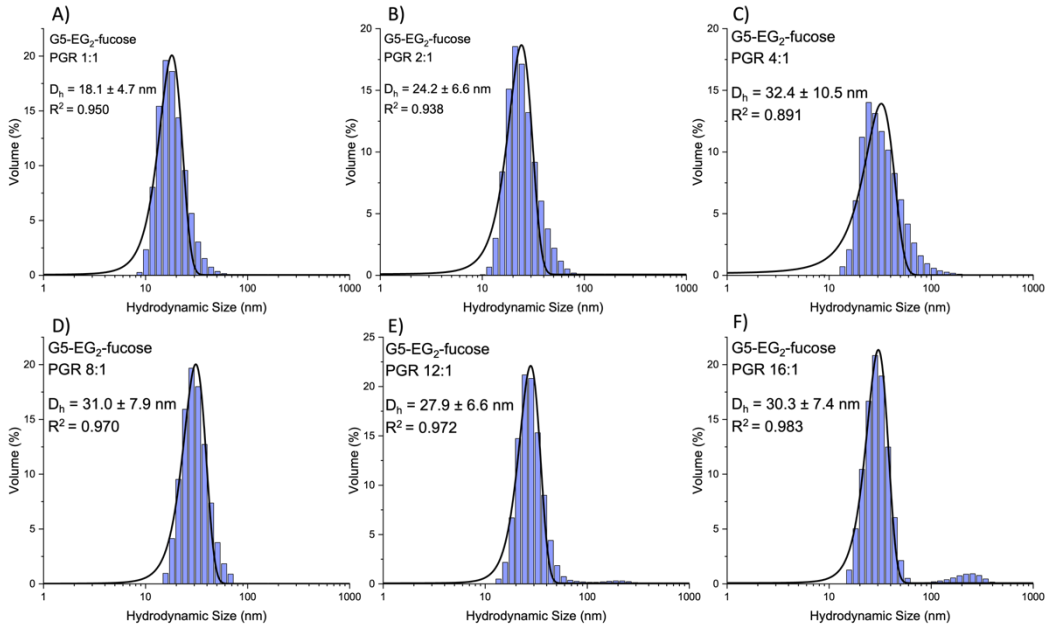

Figure A. 6 Volume population hydrodynamic size distribution histograms fitted with Gaussian fits for the binding of G5-EG_2-fucose (1:1000) (20 nM) with DC-SIGN at varying protein:G5 molar ratios (PGR) of (A) 1:1, (B) 2:1, (C) 4:1, (D) 8:1, (E) 12:1, and (F) 16:1 (D_h values given as xc ± ½ FWHM).

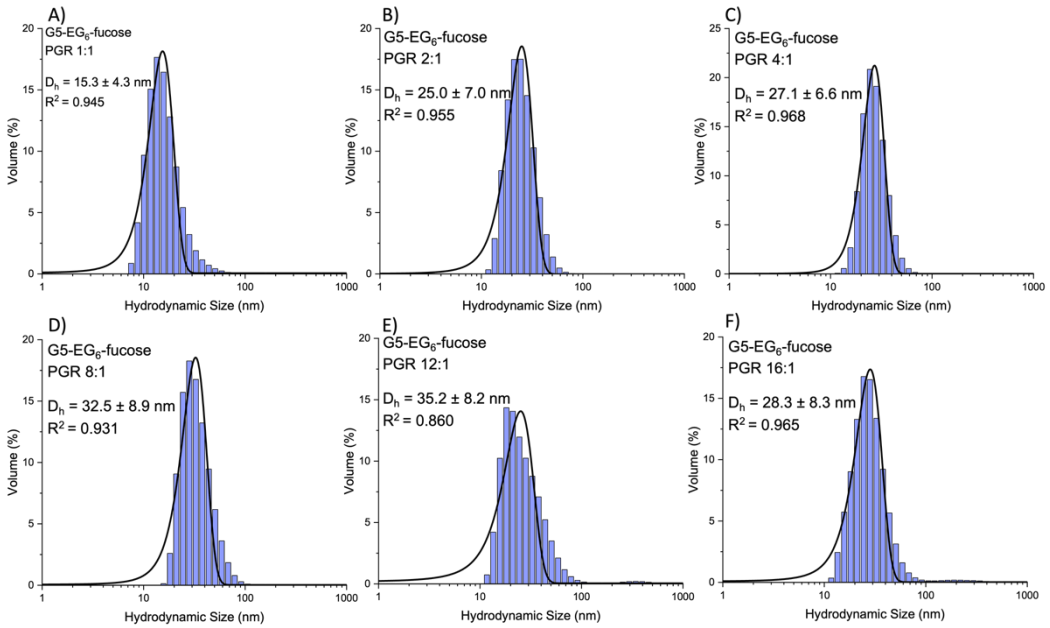

Figure A. 7 Volume population hydrodynamic size distribution histograms fitted with Gaussian fits for the binding of G5-EG_6-fucose (1:1000) (20 nM) with DC-SIGN at varying protein:G5 molar ratios (PGR) of (A) 1:1, (B) 2:1, (C) 4:1, (D) 8:1, (E) 12:1, and (F) 16:1 (D_h values given as xc ± ½ FWHM).

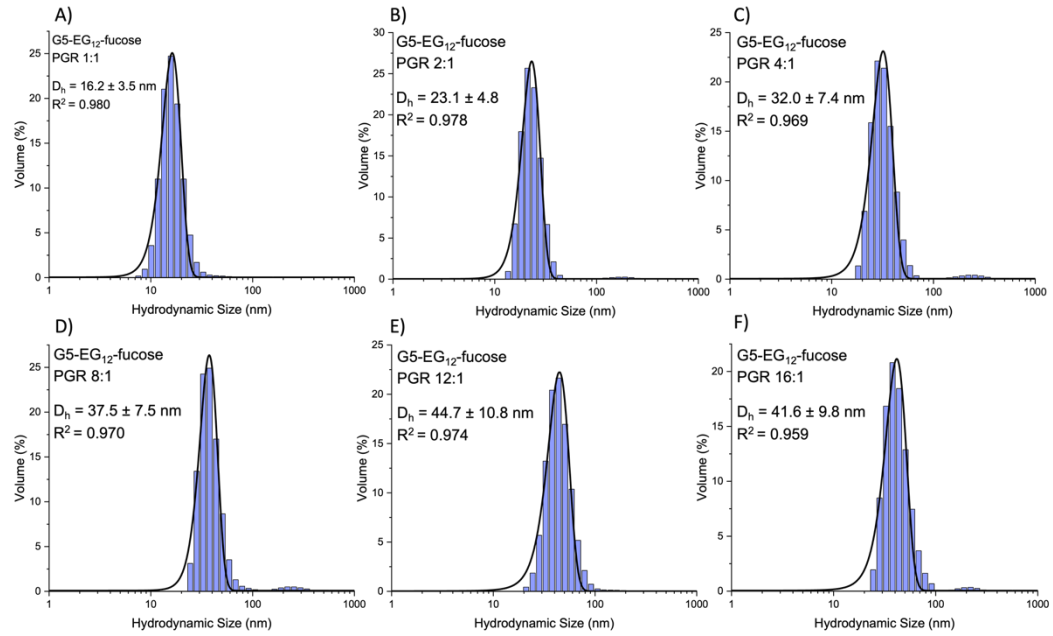

Figure A. 8 Volume population hydrodynamic size distribution histograms fitted with Gaussian fits for the binding of G5-EG_{12}-fucose (1:1000) (20 nM) with DC-SIGN at varying protein:G5 molar ratios (PGR) of (A) 1:1, (B) 2:1, (C) 4:1, (D) 8:1, (E) 12:1, and (F) 16:1 (D_h values given as xc ± ½ FWHM).

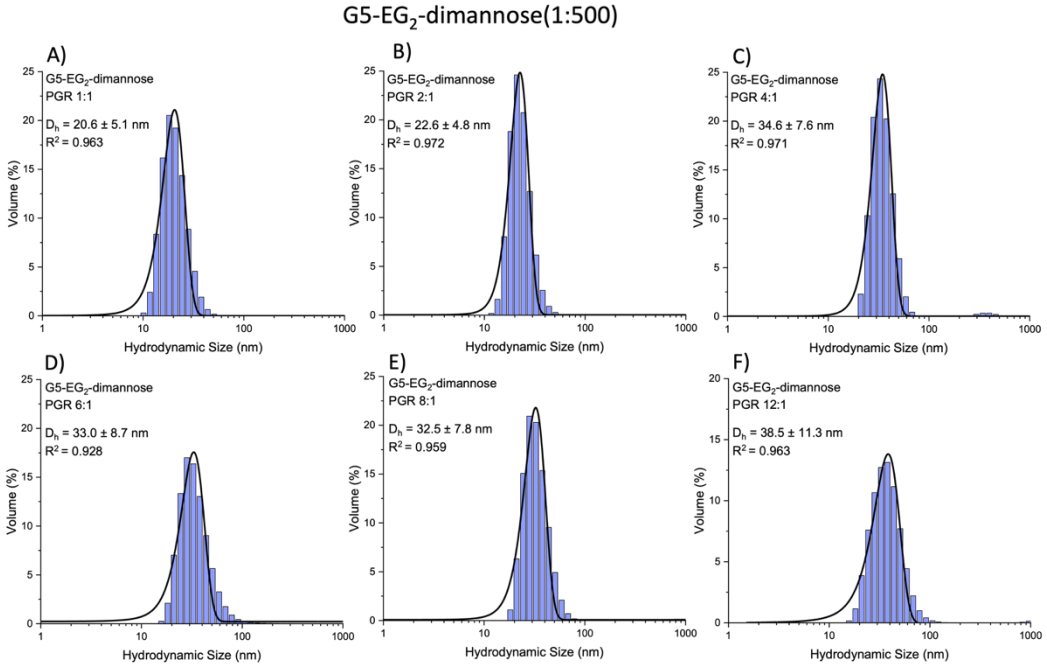

Figure A. 9 Volume population hydrodynamic size distribution histograms fitted with Gaussian fits for the binding of G5-EG_2-dimannose (1:500) (20 nM) with DC-SIGN at varying protein:G5 molar ratios (PGR) of (A) 1:1, (B) 2:1, (C) 4:1, (D) 8:1, (E) 12:1, and (F) 16:1 (D_h values given as xc ± ½ FWHM).

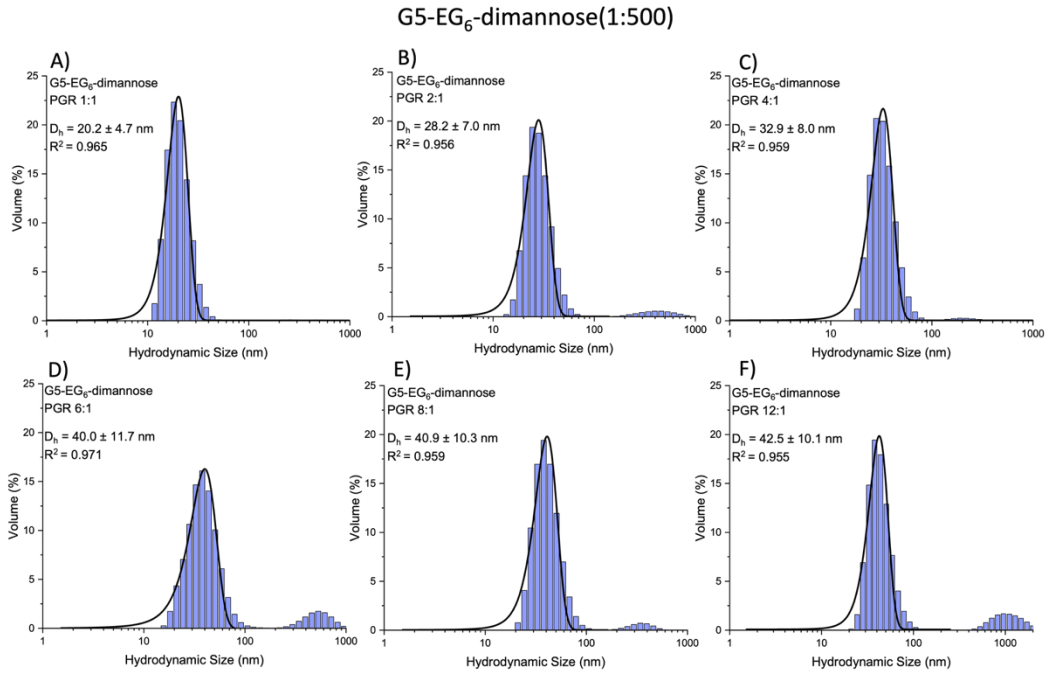

Figure A. 10 Volume population hydrodynamic size distribution histograms fitted with Gaussian fits for the binding of G5-EG_6-dimannose (1:500) (20 nM) with DC-SIGN at varying protein:G5 molar ratios (PGR) of (A) 1:1, (B) 2:1, (C) 4:1, (D) 8:1, (E) 12:1, and (F) 16:1 (D_h values given as xc ± ½ FWHM).

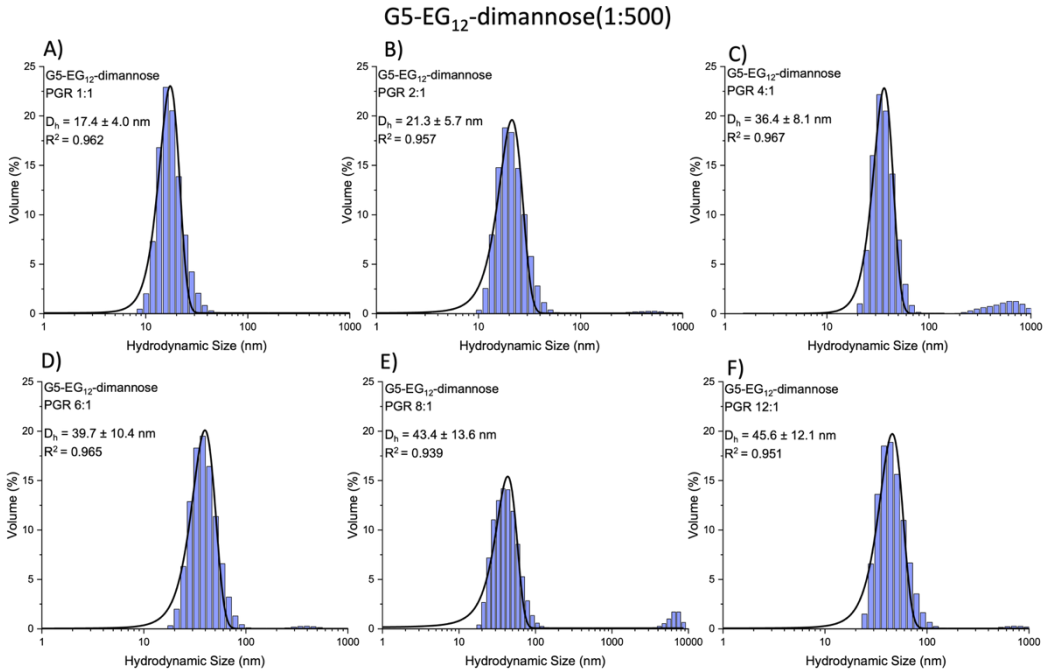

Figure A. 11 Volume population hydrodynamic size distribution histograms fitted with Gaussian fits for the binding of G5-EG_{12}-dimannose (1:500) (20 nM) with DC-SIGN at varying protein:G5 molar ratios (PGR) of (A) 1:1, (B) 2:1, (C) 4:1, (D) 8:1, (E) 12:1, and (F) 16:1 (D_h values given as xc ± ½ FWHM).

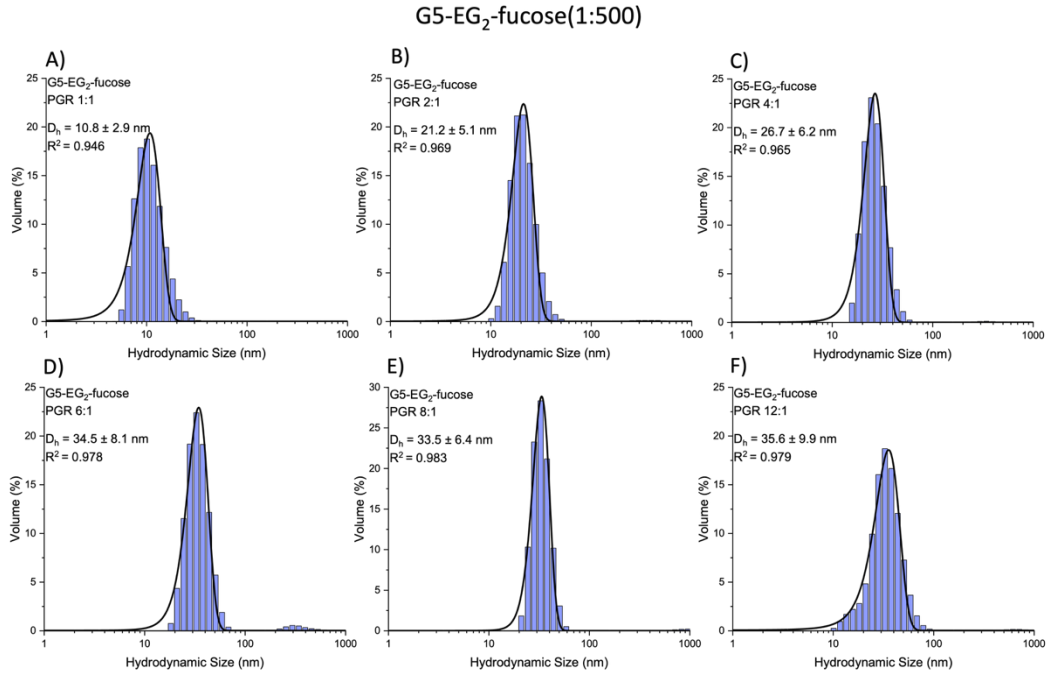

Figure A. 12 Volume population hydrodynamic size distribution histograms fitted with Gaussian fits for the binding of G5-EG_2-fucose (1:500) (20 nM) with DC-SIGN at varying protein:G5 molar ratios (PGR) of (A) 1:1, (B) 2:1, (C) 4:1, (D) 8:1, (E) 12:1, and (F) 16:1 (D_h values given as xc ± ½ FWHM).

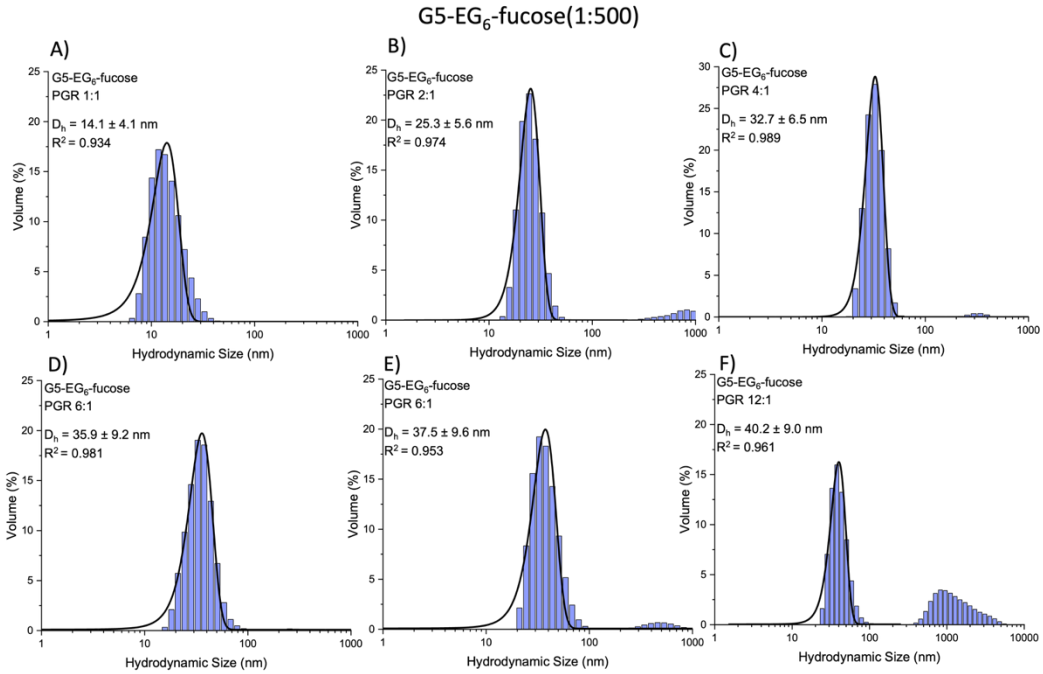

Figure A. 13 Volume population hydrodynamic size distribution histograms fitted with Gaussian fits for the binding of G5-EG$_6$-fucose (1:500) (20 nM) with DC-SIGN at varying protein:G5 molar ratios (PGR) of (A) 1:1, (B) 2:1, (C) 4:1, (D) 8:1, (E) 12:1, and (F) 16:1 (D_h values given as xc ± ½ FWHM).

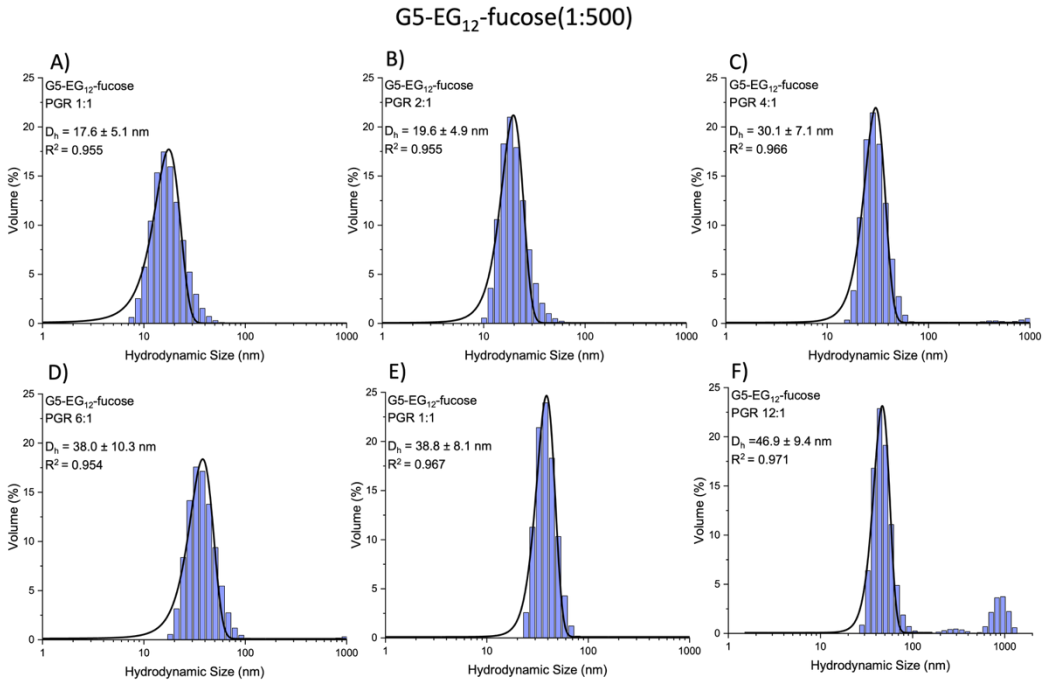

Figure A. 14 Volume population hydrodynamic size distribution histograms fitted with Gaussian fits for the binding of G5-EG$_{12}$-fucose (1:500) (20 nM) with DC-SIGN at varying protein:G5 molar ratios (PGR) of (A) 1:1, (B) 2:1, (C) 4:1, (D) 8:1, (E) 12:1, and (F) 16:1 (D_h values given as xc ± ½ FWHM).

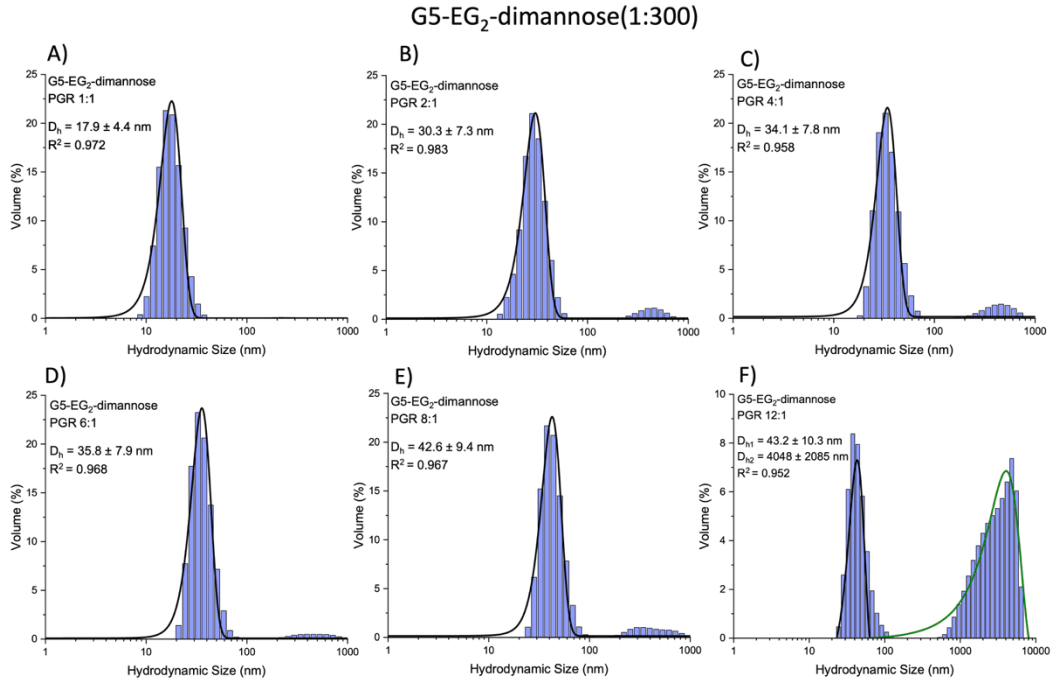

Figure A. 15 Volume population hydrodynamic size distribution histograms fitted with Gaussian fits for the binding of G5-EG$_2$-dimannose (1:300) (20 nM) with DC-SIGN at varying protein:G5 molar ratios (PGR) of (A) 1:1, (B) 2:1, (C) 4:1, (D) 8:1, (E) 12:1, and (F) 16:1 (D_h values given as xc ± ½ FWHM).

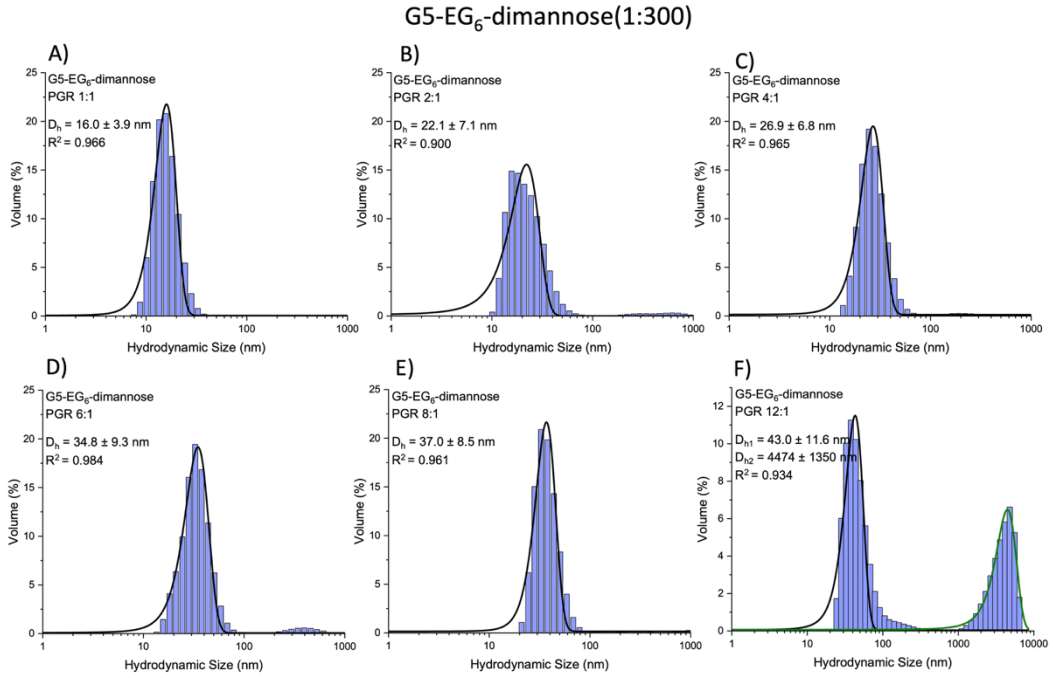

Figure A. 16 Volume population hydrodynamic size distribution histograms fitted with Gaussian fits for the binding of G5-EG$_6$-dimannose (1:300) (20 nM) with DC-SIGN at varying protein:G5 molar ratios (PGR) of (A) 1:1, (B) 2:1, (C) 4:1, (D) 8:1, (E) 12:1, and (F) 16:1 (D_h values given as xc ± ½ FWHM).

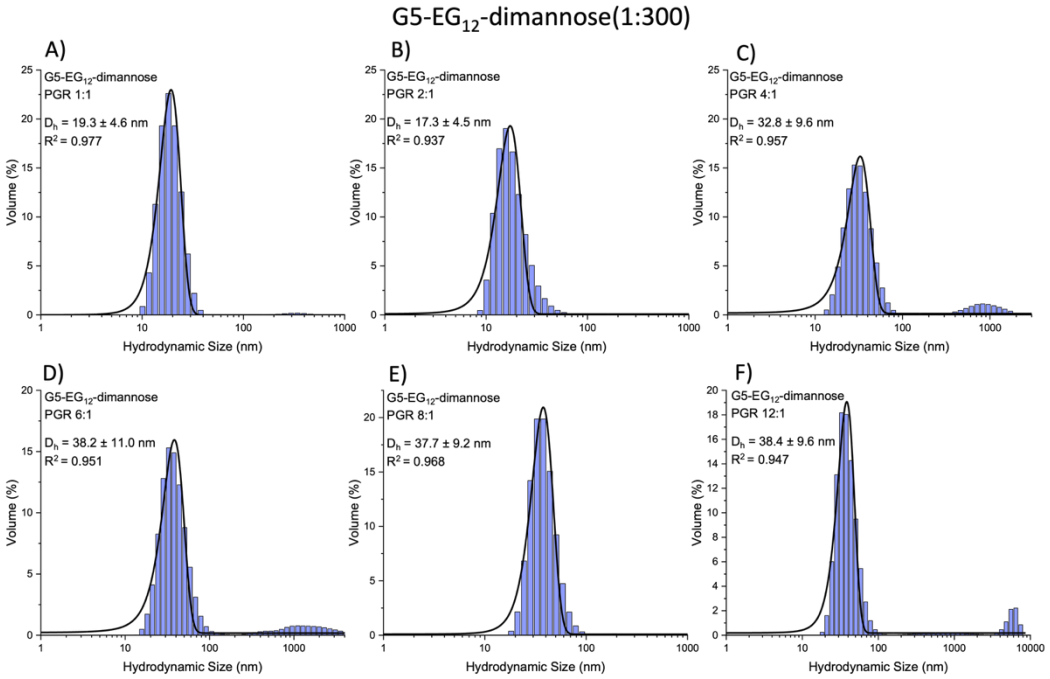

Figure A. 17 Volume population hydrodynamic size distribution histograms fitted with Gaussian fits for the binding of G5-EG_{12}-dimannose (1:300) (20 nM) with DC-SIGN at varying protein:G5 molar ratios (PGR) of (A) 1:1, (B) 2:1, (C) 4:1, (D) 8:1, (E) 12:1, and (F) 16:1 (D_h values given as xc ± ½ FWHM).

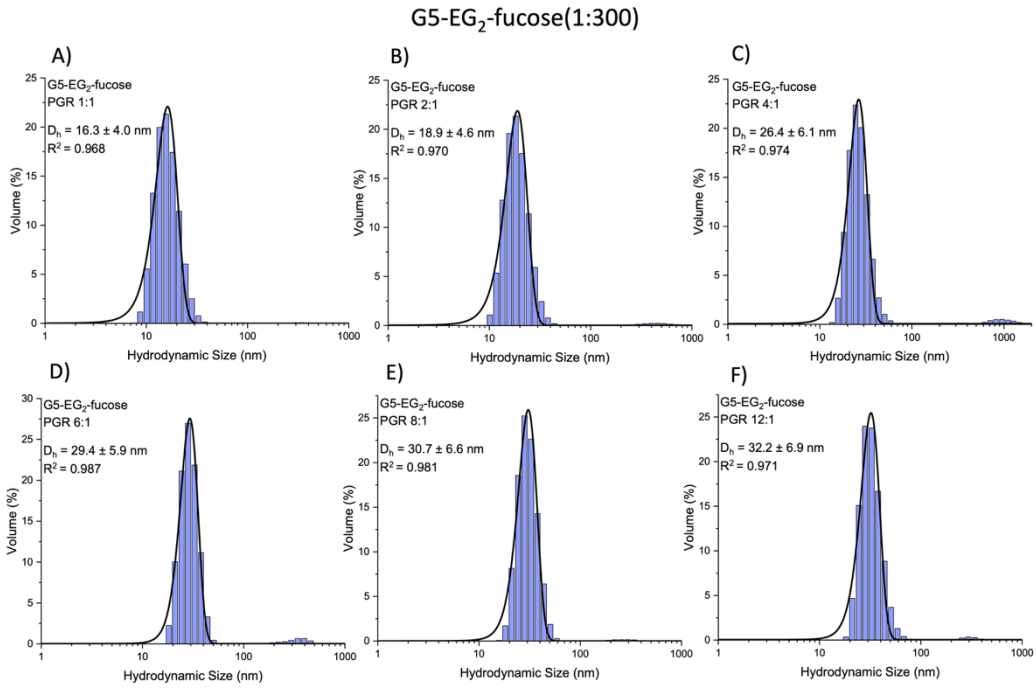

Figure A. 18 Volume population hydrodynamic size distribution histograms fitted with Gaussian fits for the binding of G5-EG_2-fucose (1:300) (20 nM) with DC-SIGN at varying protein:G5 molar ratios (PGR) of (A) 1:1, (B) 2:1, (C) 4:1, (D) 8:1, (E) 12:1, and (F) 16:1 (D_h values given as xc ± ½ FWHM).

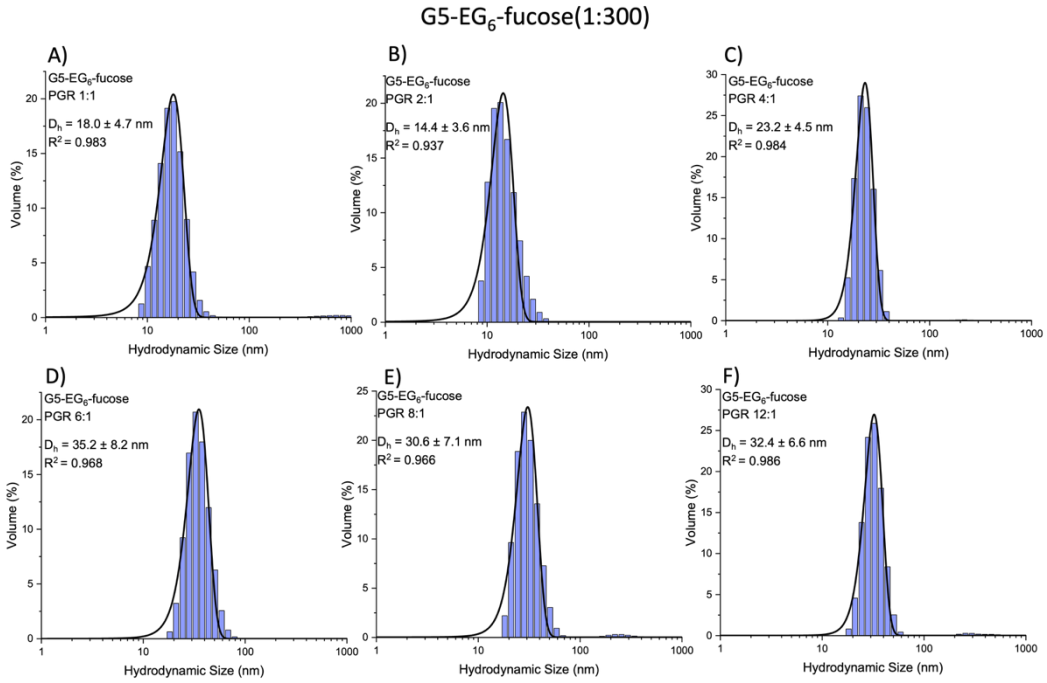

Figure A. 19 Volume population hydrodynamic size distribution histograms fitted with Gaussian fits for the binding of G5-EG_6-fucose (1:300) (20 nM) with DC-SIGN at varying protein:G5 molar ratios (PGR) of (A) 1:1, (B) 2:1, (C) 4:1, (D) 8:1, (E) 12:1, and (F) 16:1 (D_h values given as xc ± ½ FWHM).

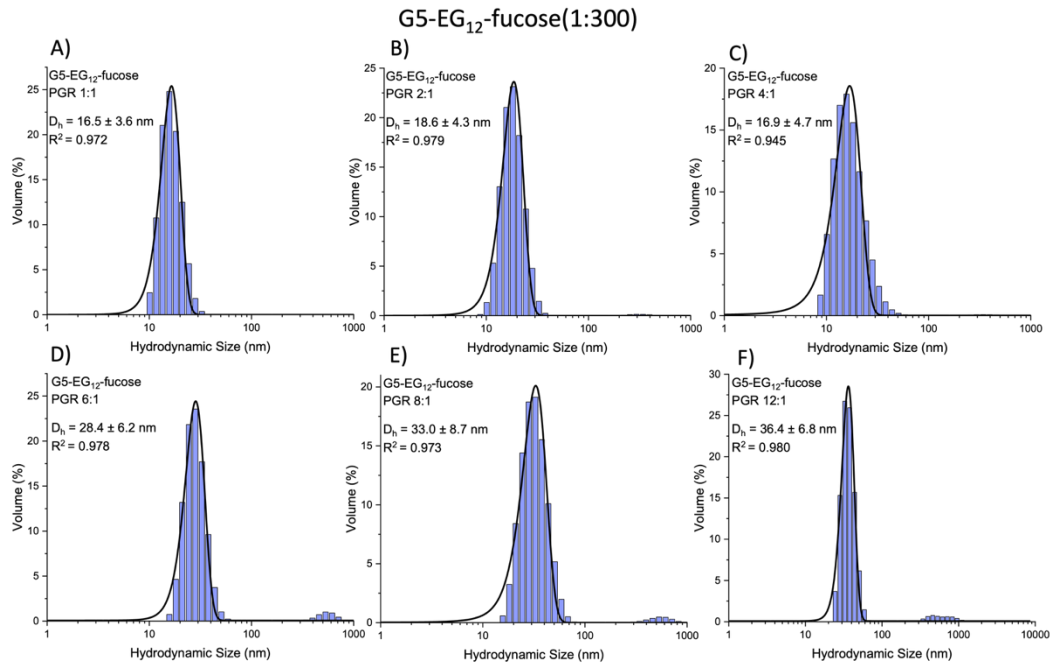

Figure A. 20 Volume population hydrodynamic size distribution histograms fitted with Gaussian fits for the binding of G5-EG_{12}-fucose (1:300) (20 nM) with DC-SIGN at varying protein:G5 molar ratios (PGR) of (A) 1:1, (B) 2:1, (C) 4:1, (D) 8:1, (E) 12:1, and (F) 16:1 (D_h values given as xc ± ½ FWHM).

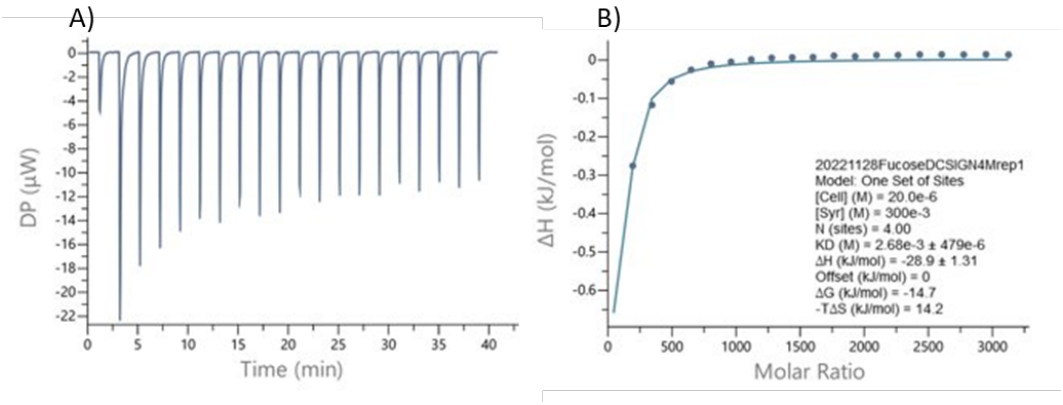

Figure A. 21 A) ITC thermogram and B) titration curve, for monovalent fucose with DC-SIGN.

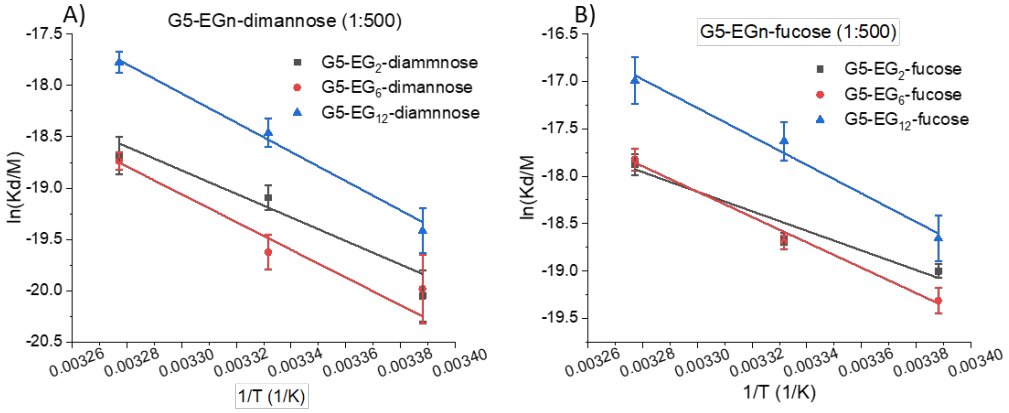

Figure A. 22 van 't Hoff analyses of the ln(K_d)–1/T relationships for DC-SIGN binding with G5-glycans(1:500) A) G5-EG_2-dimannose (grey), G5-EG_6-dimannose (red), G5-EG_{12}-dimannose (blue) or with B) G5-EG_2-fucose (grey), G5-EG_6-fucose (red), G5-EG_{12}-fucose (blue).

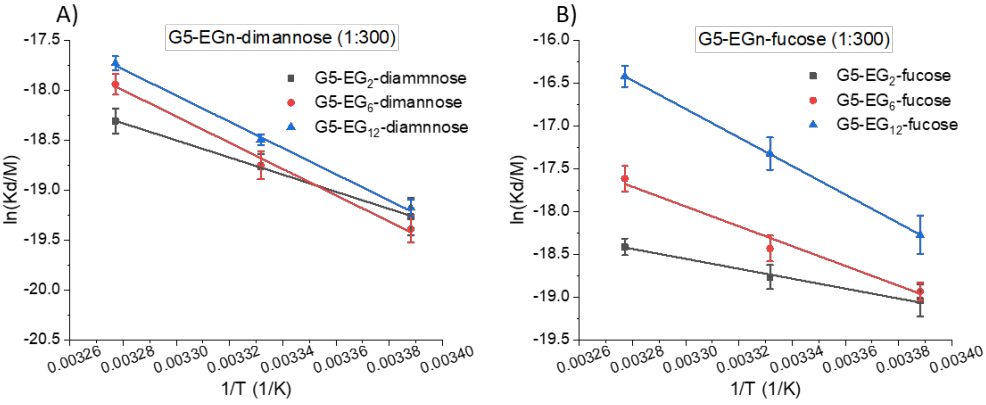

Figure A. 23 van 't Hoff analyses of the ln(K_d)–1/T relationships for DC-SIGN binding with G5-glycans(1:300) A) G5-EG_2-dimannose (grey), G5-EG_6-dimannose (red), G5-EG_{12}-dimannose (blue) or with B) G5-EG_2-fucose (grey), G5-EG_6-fucose (red), G5-EG_{12}-fucose (blue).

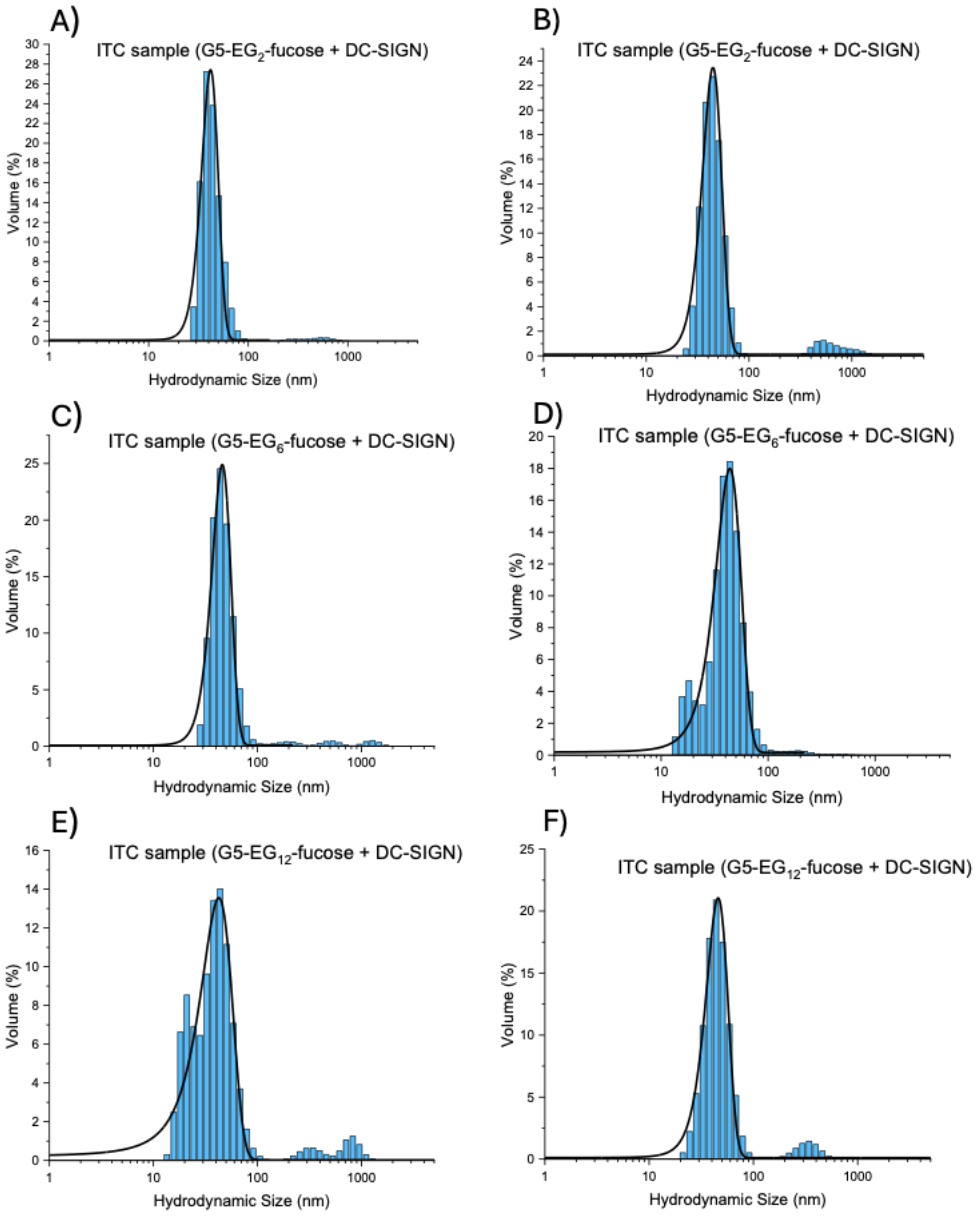

Figure A. 24 Volume population hydrodynamic size distribution histograms fitted with a Gaussian distribution curve for G5-glycan + DC-SIGN samples after mixing in the ITC cell for A) G5-EG_2-fucose sample a, B) G5-EG_2-fucose sample b, C) G5-EG_6-fucose sample a, D) G5-EG_6-fucose sample b, E) G5-EG_{12}-fucose sample a, F) G5-EG_{12}-fucose sample b, made in a 1:500.

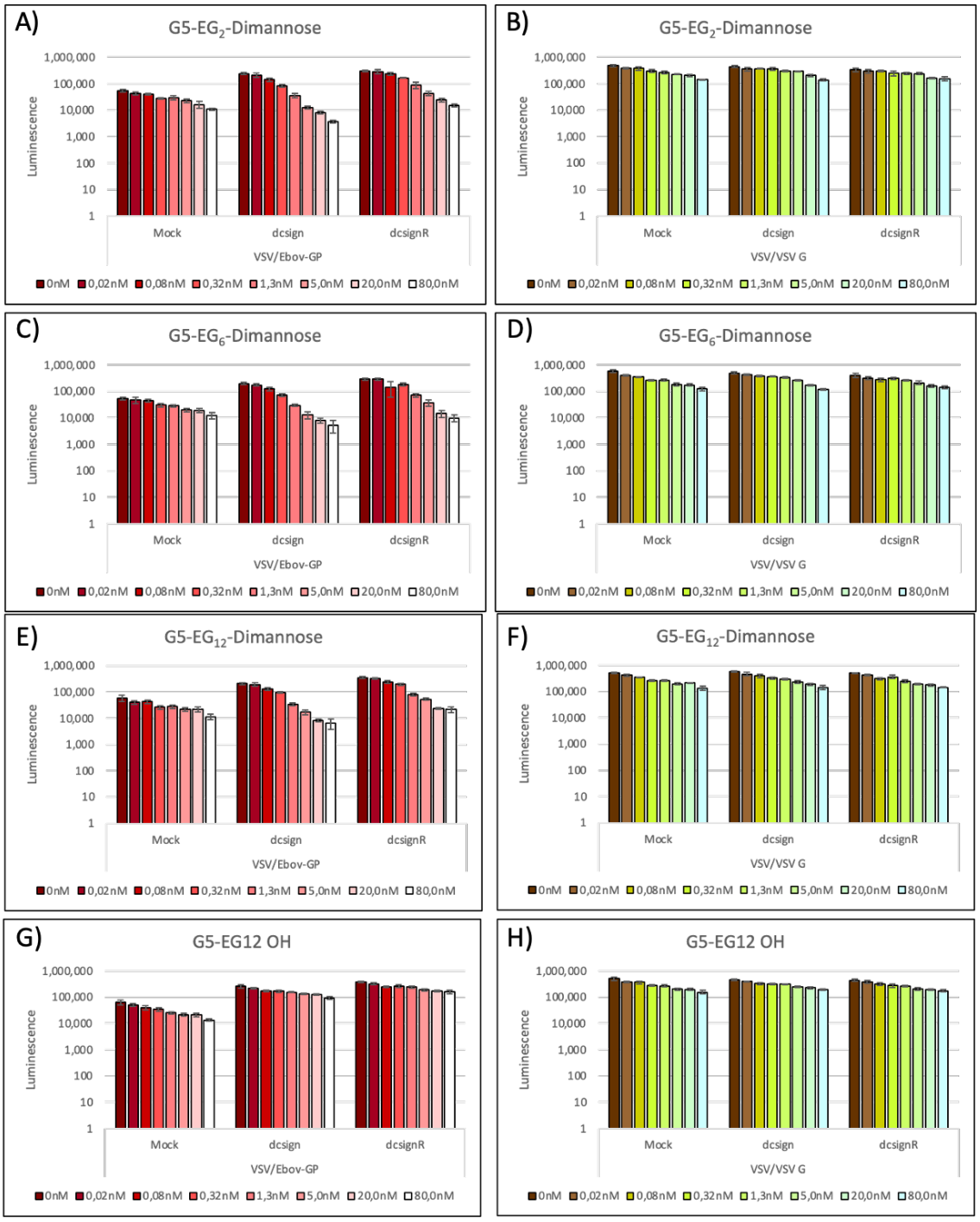

Figure A. 25 Comparison of cellular luciferase activities of 293T cells after being trans-infected with DC-SIGN or DC-SIGNR, pre-incubated with varying concentrations of G5-EG_n-dimannose (A-F) or G5-EG_{12}-OH (G-H) and inoculated with VSV reporter particles bearing the EBOV-GP (A,C,E,G) or VSV-G (B, D, F, H). Luciferase activities in cell lysates were measured after 72 hours post-transduction. Error bars indicate the SDs of experiments performed in quadruplicate.

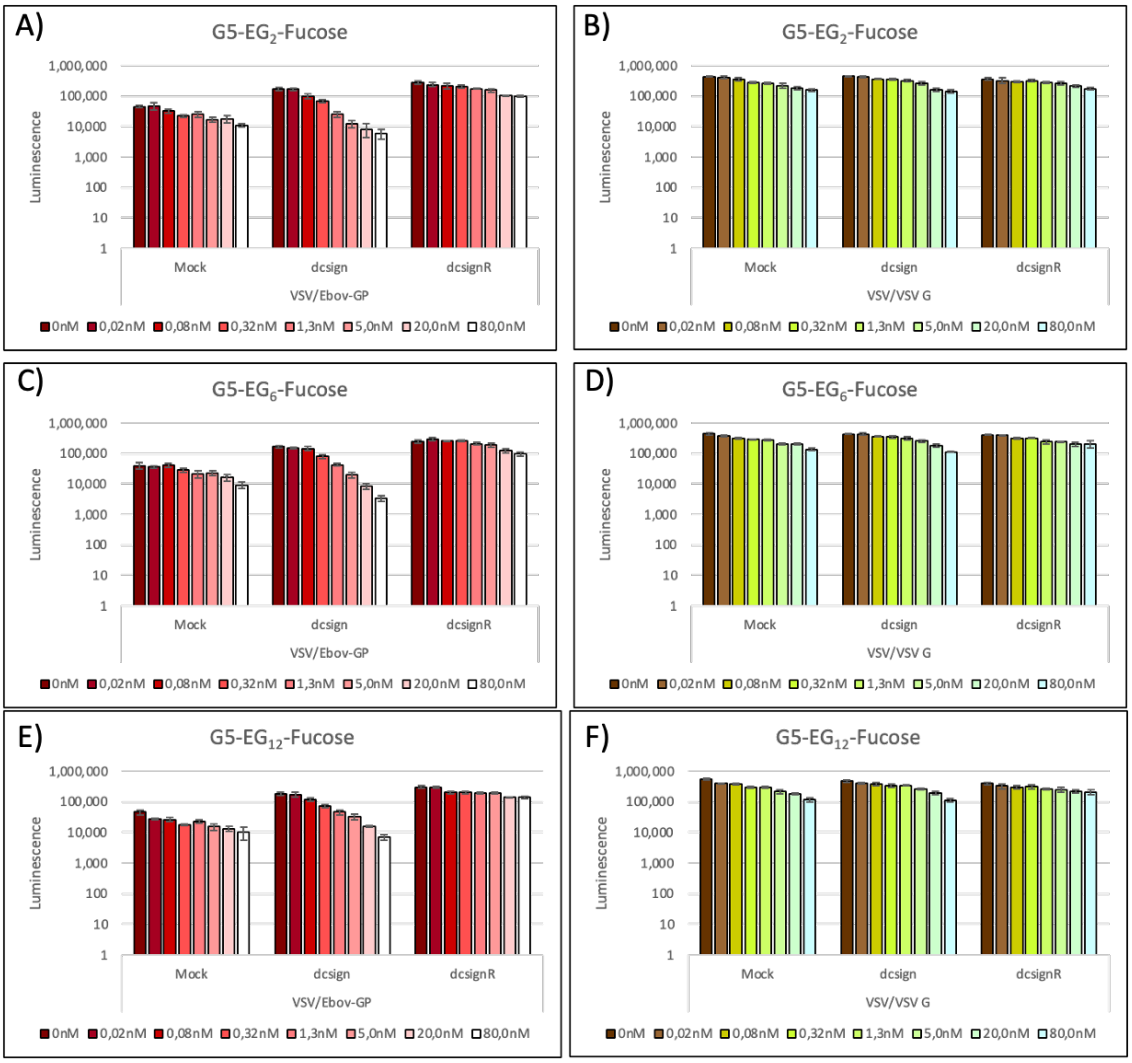

Figure A. 26 Comparison of cellular luciferase activities of 293T cells after being trans-infected with DC-SIGN or DC-SIGNR, pre-incubated with varying concentrations of G5-EG_n-fucose and inoculated with VSV reporter particles bearing the EBOV-GP (A,C,E) or VSV-G (B, D, F). Luciferase activities in cell lysates were measured after 72 hours post-transduction. Error bars indicate the SDs of experiments performed in quadruplicate.

Appendix B

NHS
Health Research Authority
NRES Committee Yorkshire & The Humber - South Yorkshire
North East REC Centre
Unit 002, TEDCO Business Centre
Rolling Mill Road
Jarrow
Tyne and Wear
NE32 3DT

Telephone: 0191 428 3561

14 April 2014

Professor Dennis McGonagle
Professor of Investigative Rheumatology
Division of Musculoskeletal Disease
Leeds Institute of Molecular Medicine
Chapel Allerton Hospital
Chapeltown Road
Leeds
LS7 4SA

Dear Professor McGonagle

Study title:	**Collection of joint Mesenchymal Stem Cells by aspiration, biopsy, joint retrieval at arthroplasty or by synovium agitation during arthroscopy.**
REC reference:	**14/YH/0087**
IRAS project ID:	**100077**

Thank you for your letter of 11 April 2014, responding to the Committee's request for further information on the above research and submitting revised documentation.

The further information has been considered on behalf of the Committee by the Chair.

We plan to publish your research summary wording for the above study on the HRA website, together with your contact details, unless you expressly withhold permission to do so. Publication will be no earlier than three months from the date of this favourable opinion letter. Should you wish to provide a substitute contact point, require further information, or wish to withhold permission to publish, please contact the REC Manager Joan Brown, nrescommittee.yorkandhumber-southyorks@nhs.net

Confirmation of ethical opinion

On behalf of the Committee, I am pleased to confirm a favourable ethical opinion for the above research on the basis described in the application form, protocol and supporting documentation as revised, subject to the conditions specified below.

Ethical review of research sites

NHS sites

The favourable opinion applies to all NHS sites taking part in the study, subject to management permission being obtained from the NHS/HSC R&D office prior to the start of the study (see "Conditions of the favourable opinion" below).

Conditions of the favourable opinion

The favourable opinion is subject to the following conditions being met prior to the start of the study.

- Amend the "gifting" statement in point 4 in the Consent Form to: "I confirm I am providing my joint tissues and joint fluid as a gift for this research and agree for them to be stored and used in future ethically approved musculoskeletal research".

- Amend the version number and date of the consent form.

You should notify the REC in writing once all conditions have been met (except for site approvals from host organisations) and provide copies of any revised documentation with updated version numbers. The REC will acknowledge receipt and provide a final list of the approved documentation for the study, which can be made available to host organisations to facilitate their permission for the study. Failure to provide the final versions to the REC may cause delay in obtaining permissions.

Management permission or approval must be obtained from each host organisation prior to the start of the study at the site concerned.

Management permission ("R&D approval") should be sought from all NHS organisations involved in the study in accordance with NHS research governance arrangements.

Guidance on applying for NHS permission for research is available in the Integrated Research Application System or at http://www.rdforum.nhs.uk.

Where a NHS organisation's role in the study is limited to identifying and referring potential participants to research sites ("participant identification centre"), guidance should be sought from the R&D office on the information it requires to give permission for this activity.

For non-NHS sites, site management permission should be obtained in accordance with the procedures of the relevant host organisation.

Sponsors are not required to notify the Committee of approvals from host organisations

Registration of Clinical Trials

All clinical trials (defined as the first four categories on the IRAS filter page) must be registered on a publically accessible database within 6 weeks of recruitment of the first participant (for medical device studies, within the timeline determined by the current registration and publication trees).

There is no requirement to separately notify the REC but you should do so at the earliest opportunity e.g when submitting an amendment. We will audit the registration details as part of the annual progress reporting process.

To ensure transparency in research, we strongly recommend that all research is registered but for non clinical trials this is not currently mandatory.

If a sponsor wishes to contest the need for registration they should contact Catherine Blewett (catherineblewett@nhs.net), the HRA does not, however, expect exceptions to be made. Guidance on where to register is provided within IRAS.

It is the responsibility of the sponsor to ensure that all the conditions are complied with before the start of the study or its initiation at a particular site (as applicable).

Approved documents

The final list of documents reviewed and approved by the Committee is as follows:

Document	*Version*	*Date*
Covering Letter	Email from Thomas Baboolal	11 April 2014
Evidence of insurance or indemnity	Henderson Insurance Brokers	19 September 2013
Investigator CV	CV for Dennis McGonagle	
Other: Letter of Support from Dr Nicholas London		06 November 2013
Other: Correspondence with MHRA		04 April 2014
Other: Amendments to REC IRAS Form		
Participant Consent Form	Version 1.1	08 April 2014
Participant Information Sheet: Arthroscopy	Version 1.1	08 April 2014
Participant Information Sheet: Open Knee Surgery	Version 1.1	08 April 2014
Protocol	Version 1.0	03 March 2014
REC application	IRAS 3.5	11 March 2014
Response to Request for Further Information		11 April 2014

Statement of compliance

The Committee is constituted in accordance with the Governance Arrangements for Research Ethics Committees and complies fully with the Standard Operating Procedures for Research Ethics Committees in the UK.

After ethical review

Reporting requirements

The attached document *"After ethical review – guidance for researchers"* gives detailed guidance on reporting requirements for studies with a favourable opinion, including:

- Notifying substantial amendments
- Adding new sites and investigators
- Notification of serious breaches of the protocol
- Progress and safety reports
- Notifying the end of the study

The NRES website also provides guidance on these topics, which is updated in the light of changes in reporting requirements or procedures.

Feedback

You are invited to give your view of the service that you have received from the National Research Ethics Service and the application procedure. If you wish to make your views known please use the feedback form available on the website.

Further information is available at National Research Ethics Service website > After Review

14/YH/0087	**Please quote this number on all correspondence**

We are pleased to welcome researchers and R & D staff at our NRES committee members' training days – see details at http://www.hra.nhs.uk/hra-training/

With the Committee's best wishes for the success of this project.

Yours sincerely

pp

Dr Ian Woollands
Chair

Email: nrescommittee.yorkandhumber-southyorks@nhs.net

Enclosures: "After ethical review – guidance for researchers"

Copy to: *Clare E Skinner, Faculty of Medicine and Health Research*
Ms Anne Gowing, The Leeds Teaching Hospitals NHS Trust

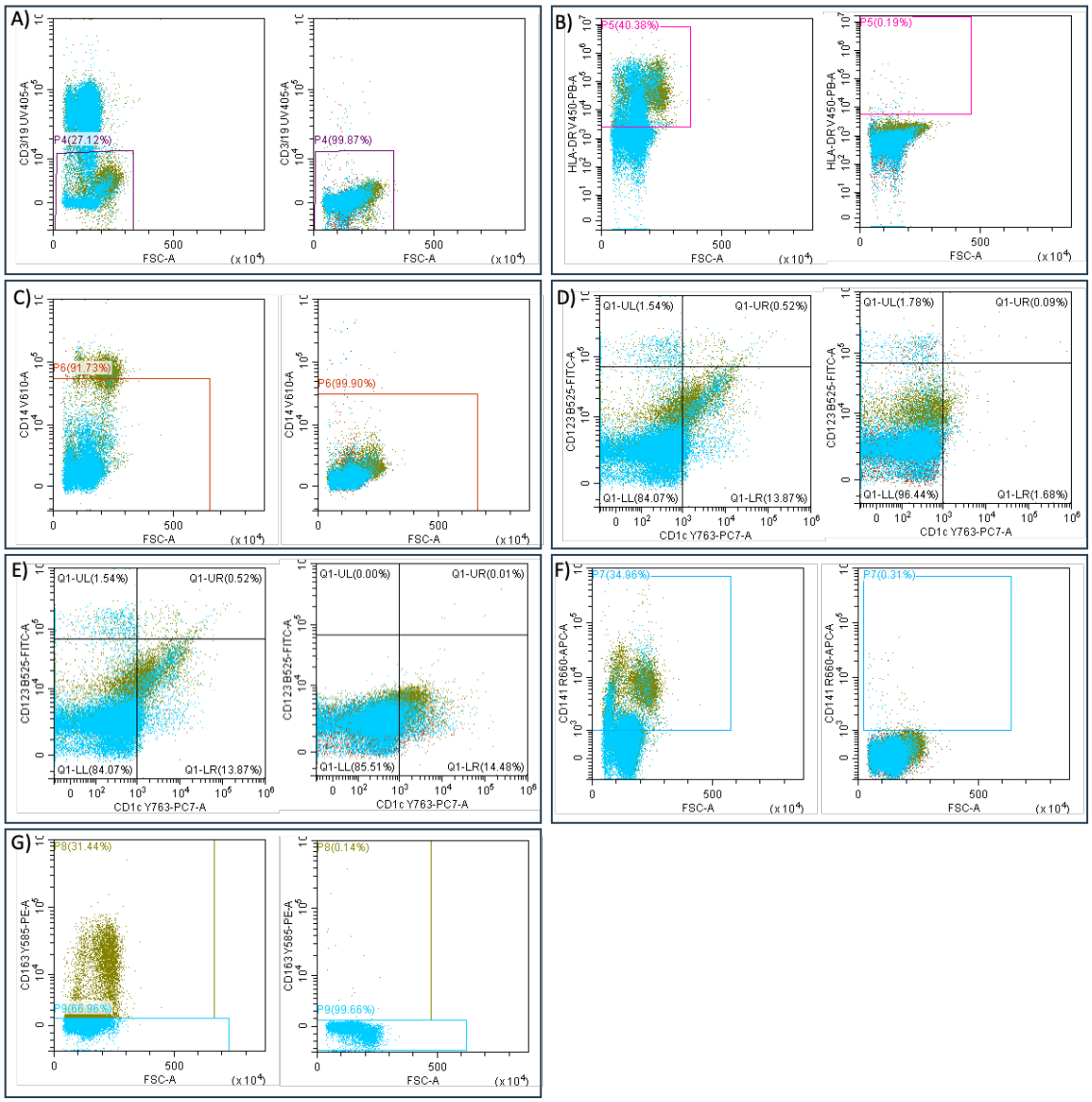

Figure B. 1 Flow cytometry dot plots showing fluorescence minus one (FMO) controls. The left panel displays fully stained PBMCs, while the right panel shows the FMO control for each antibody-dye conjugate: A) CD3/19 B) HLA-DR C) CD14 D) CD1c E) CD123 F) CD 141 E) CD163.

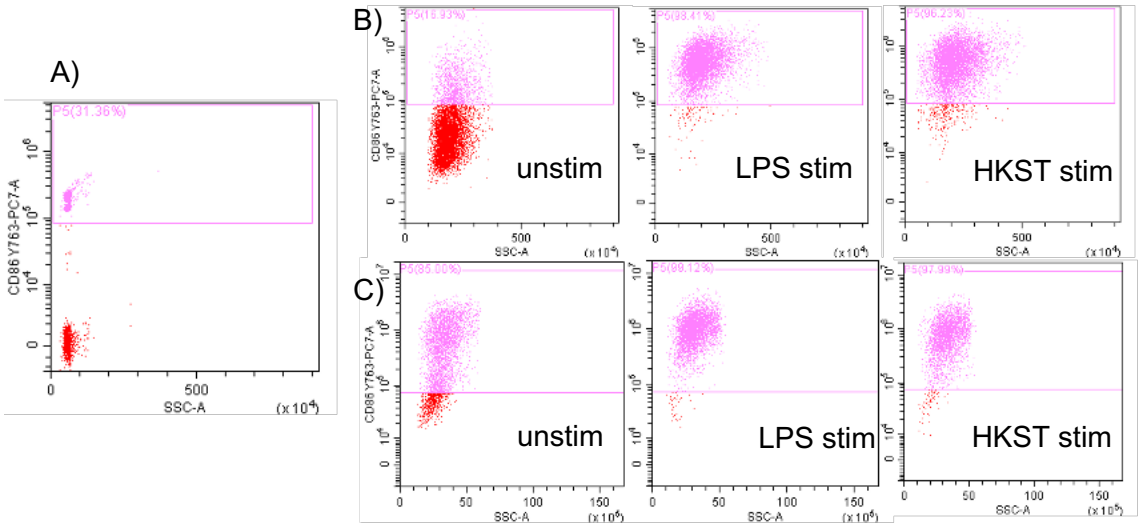

Figure B. 2 Flow cytometry dot plots for CD86 expression where A) is the bead control where the purple and red indicate the positive and negative controls respectively. B) shows CD86 expression on MoDCs for Donor 1 pre LPS, after LPS and after HKST stimulations and C) shows CD86 expression on MoDCs for Donor 2 pre LPS, after LPS and after HKST stimulations. While donor 1 shows an obvious increase in % of cells positive for CD86 after stimulation, the increase in expression for donor 2 is less obvious by % positive, as they already had high expression pre stimulation.

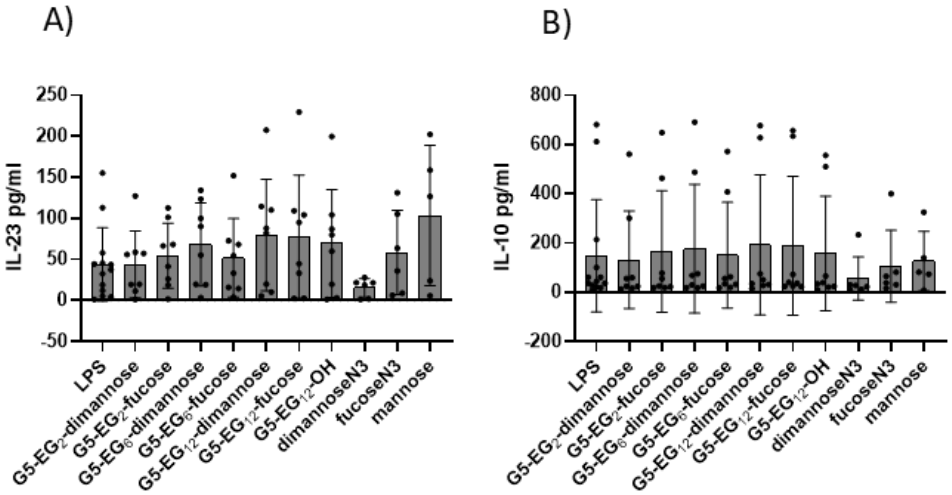

Figure B. 3 Bar graphs showing raw A) IL-23 and B) IL-10 production by MoDCs when stimulated with LPS or LPS plus various G5-EGx-Glycans/free ligands. Cytokines were measured by ELISA.

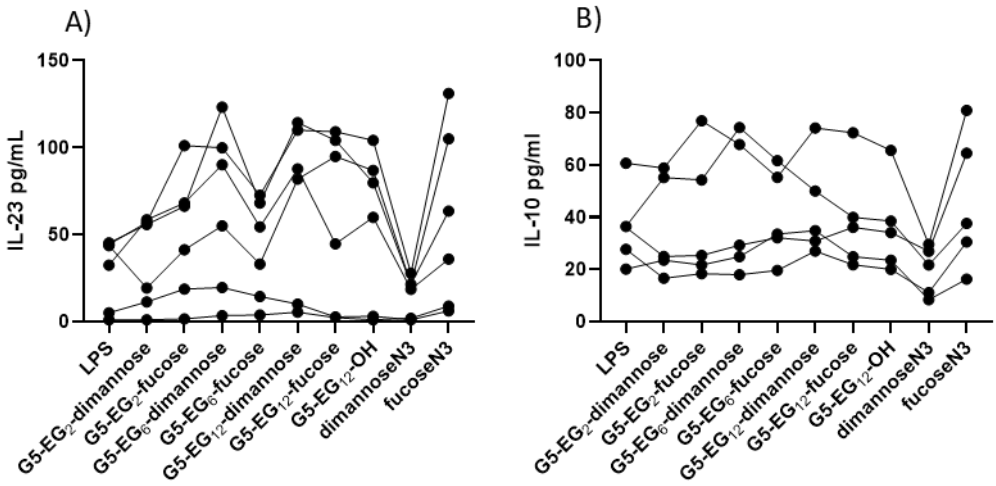

Figure B. 4 Line graph showing raw A) IL-23 and B) IL-10 production by MoDCs when stimulated with LPS or LPS plus various G5-EGx-Glycans/free ligands. Cytokines were measured by ELISA. The lines connect donor matched samples to highlight there is no particular pattern to cytokine production.

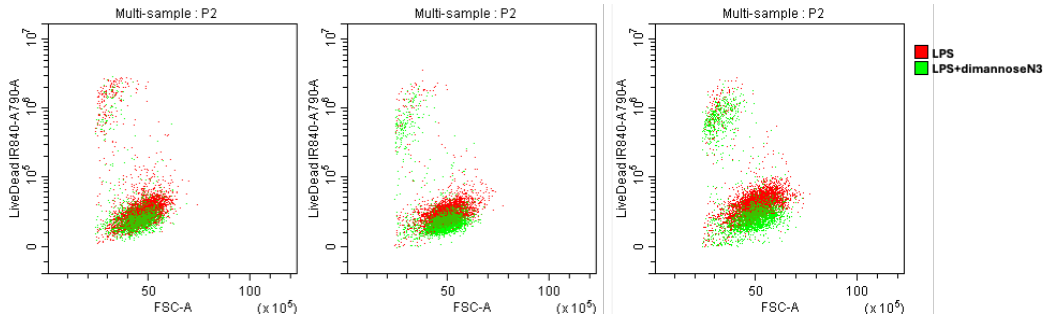

Figure B. 5 Flow cytometry dot plots for three different donors showing live/dead cells after LPS stimulation(red) or LPS+50 mM dimannoseN3(green). Azido dimannose did not impact cell viability(no increase in fluoresce).

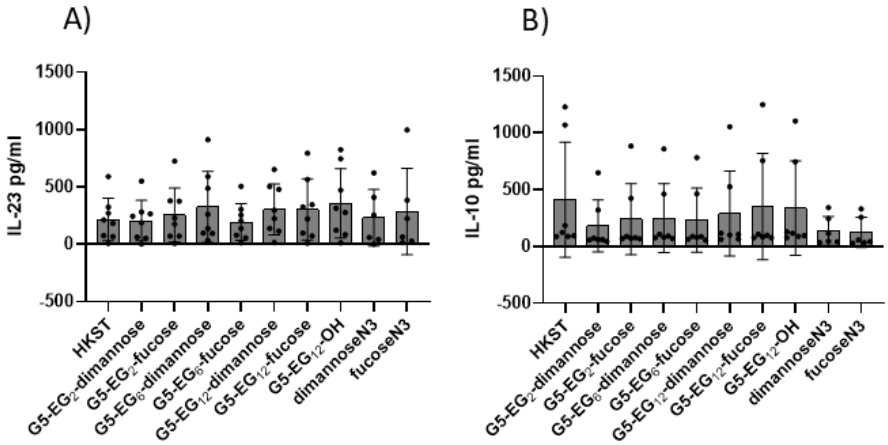

Figure B. 6 Bar graphs showing raw A) IL-23 and B) IL-10 production by MoDCs when stimulated with HKST or HKST plus various G5-EGx-Glycans/free ligands. Cytokines were measured by ELISA.

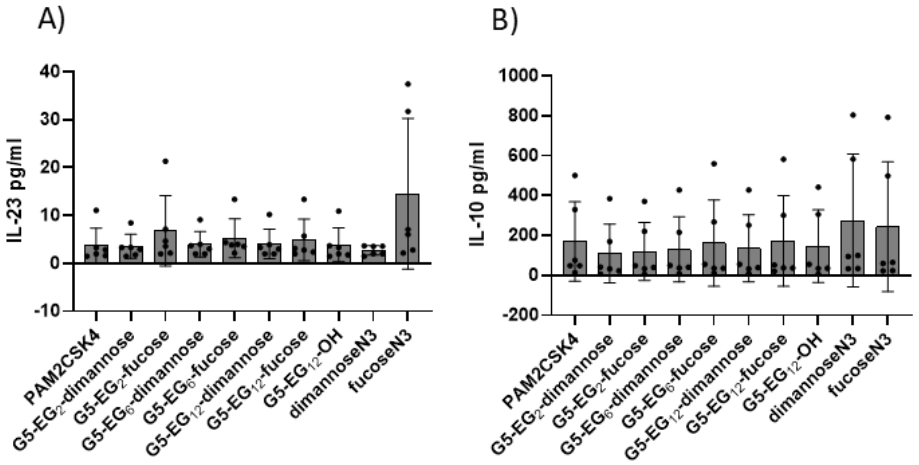

Figure B. 7 Bar graphs showing raw A) IL-23 and B) IL-10 production by MoDCs when stimulated with PAM2CSK4 or PAM2CSK4 plus various G5-EGx-Glycans/free ligands. Cytokines were measured by ELISA.

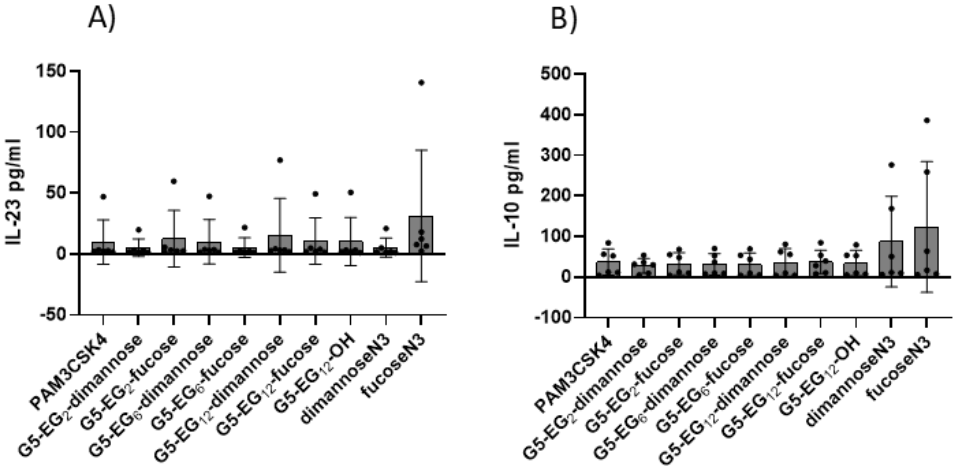

Figure B. 8 Bar graphs showing raw A) IL-23 and B) IL-10 production by MoDCs when stimulated with PAM3CSK4 or PAM3CSK4 plus various G5-EGx-Glycans/free ligands. Cytokines were measured by ELISA.

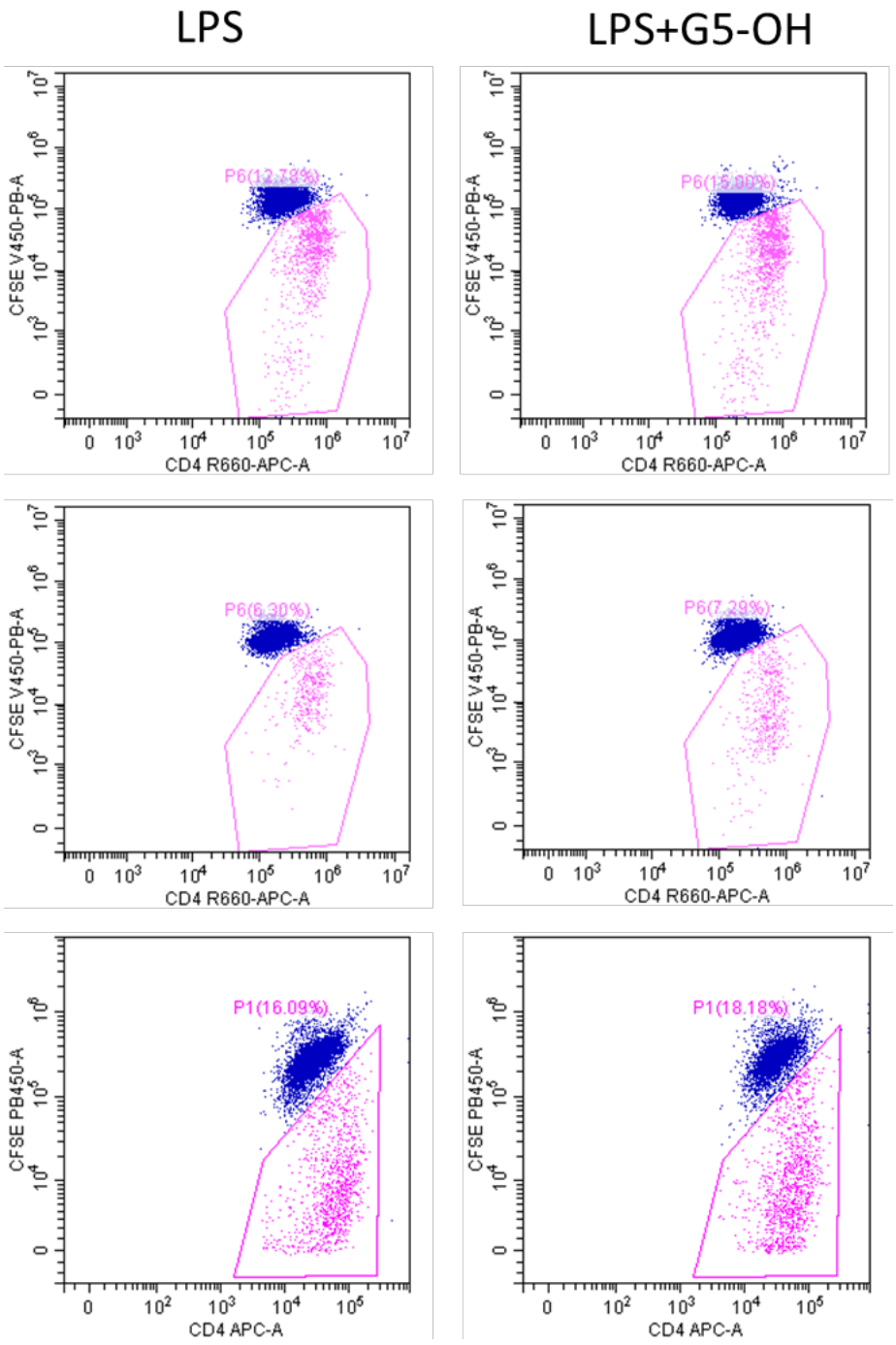

Figure B. 9 Flow cytometry dot plots showing T cell proliferation (pink gate indicating the % proliferated) with either LPS or LPS+G5-OH for three different donors. No decrease in proliferation was observed in any case.

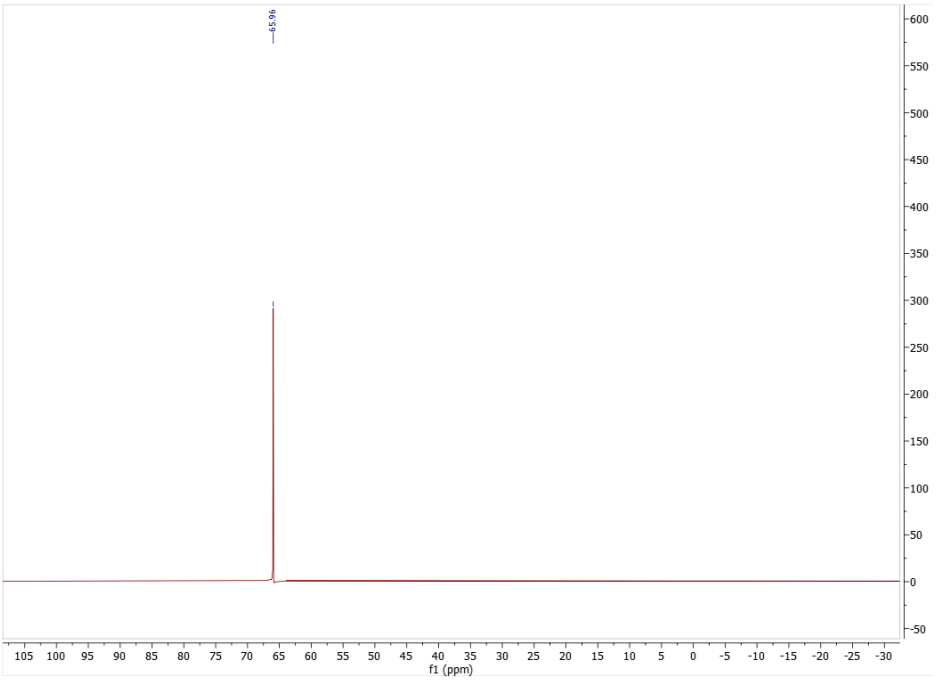

Figure B. 10 Fluorine^{19} NMR spectrum of sulfonyl fluoride 17 in $CDCl_3$

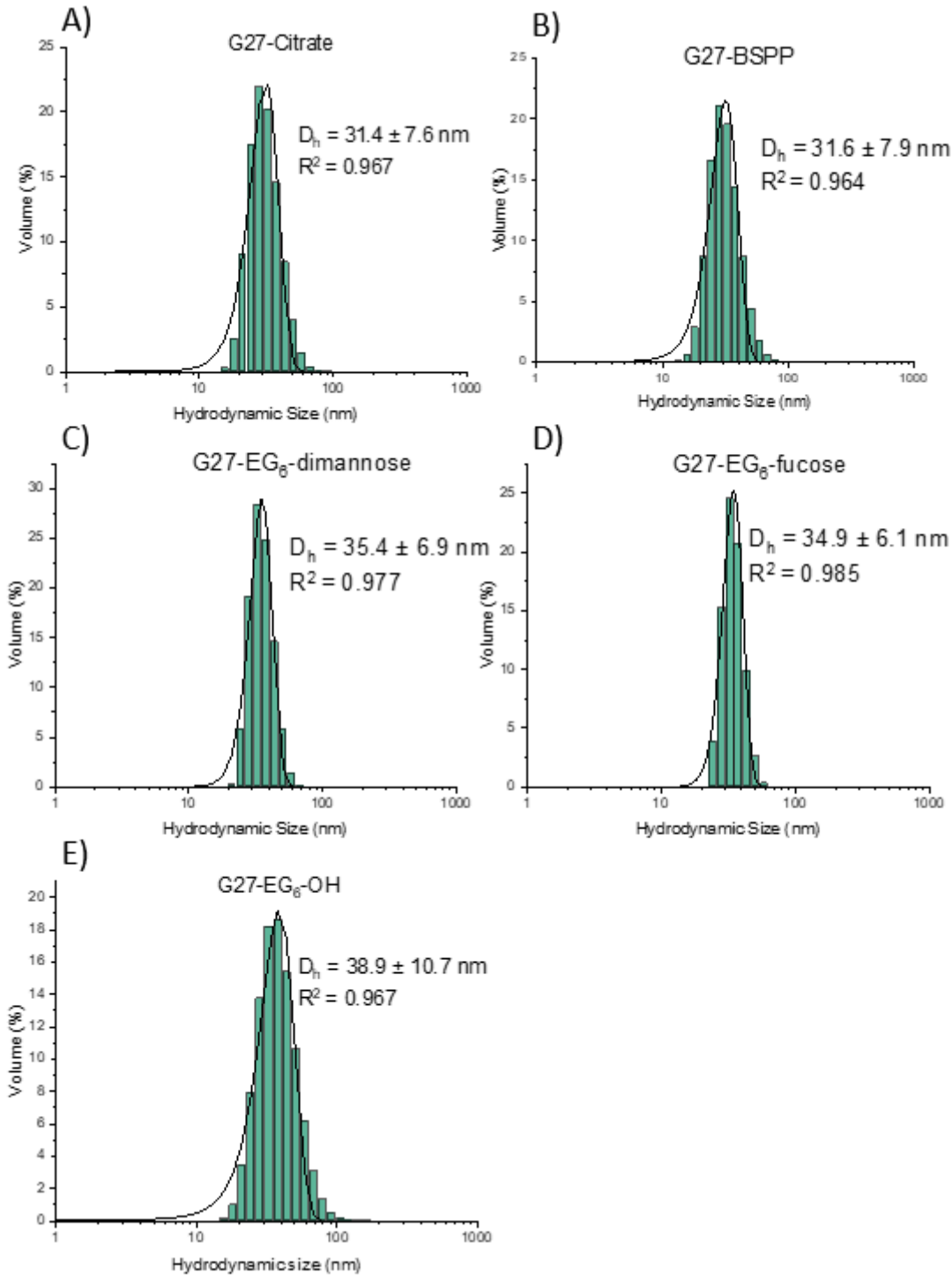

Figure B. 11 Volume population hydrodynamic size distribution histograms fitted with a Gaussian distribution curve for A) G27-cirate, B) G27-BSPP, C) G27-EG$_6$-dimannose, D) G27-EG$_6$-fucose, E) G5-EG$_6$-OH. (D_h values given as xc ± ½FWHM).

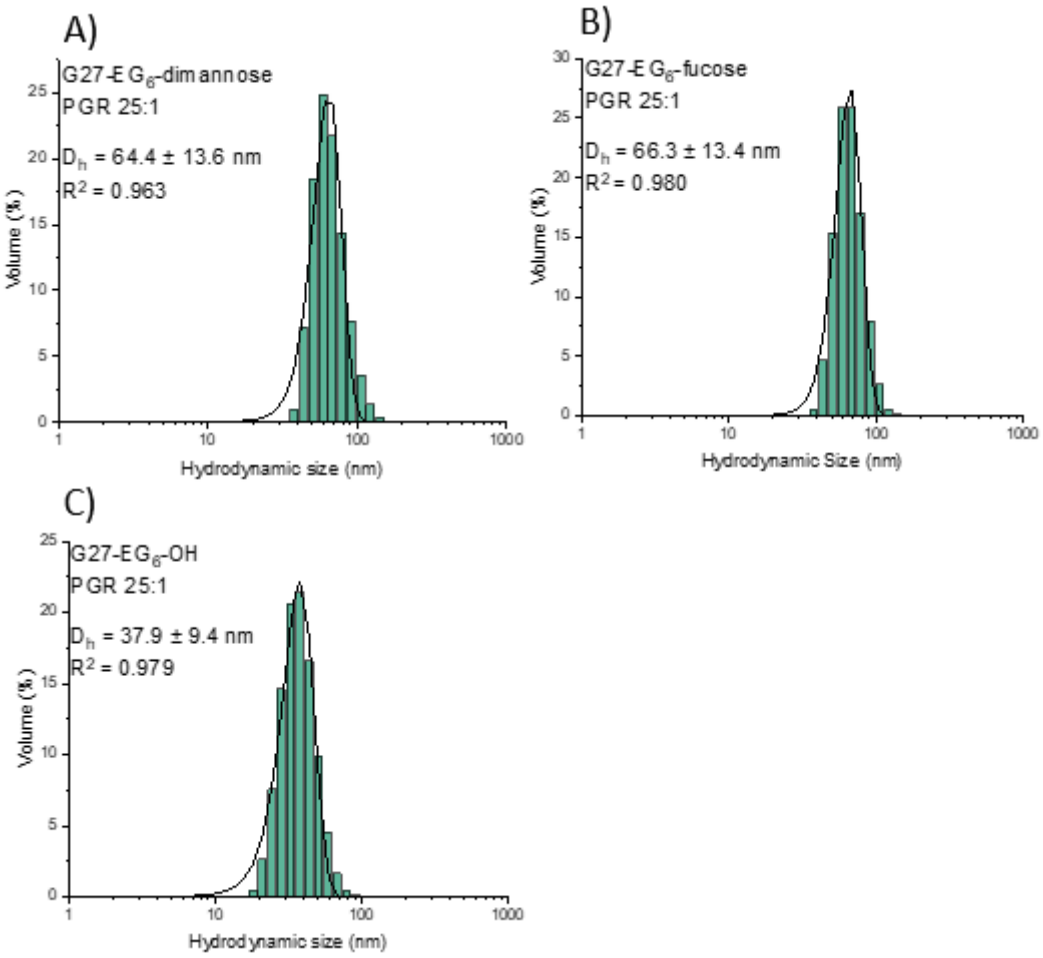

Figure B. 12 Volume population hydrodynamic size distribution histograms fitted with a Gaussian distribution curve for the binding of 25 nM DC-SIGN with 1 nM of A) G27-EG_6-dimannose, B) G27-EG_6-fucose, C) G5-EG_6-OH with DC-SIGN (D_h values given as xc ± ½ FWHM).

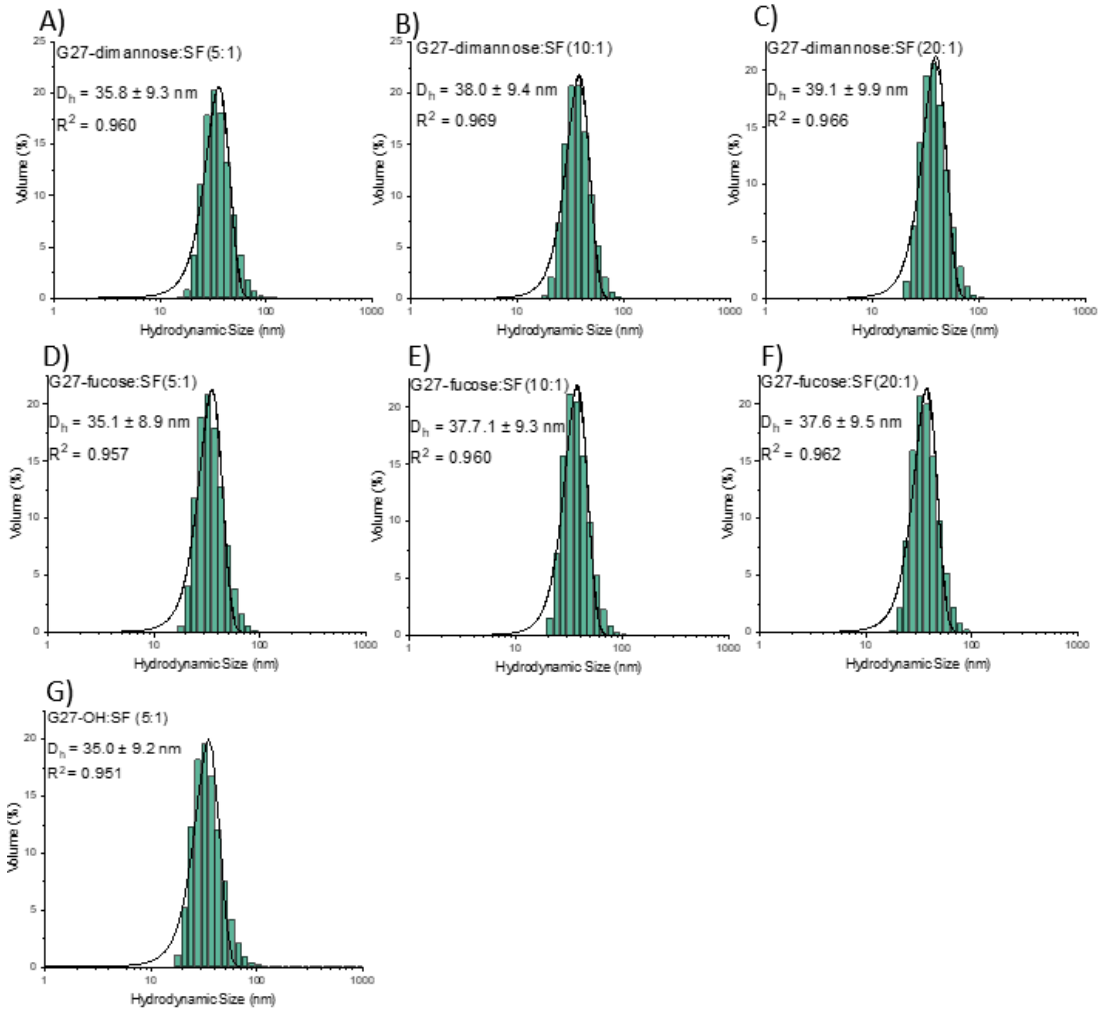

Figure B. 13 Volume population hydrodynamic size distribution histograms fitted with a Gaussian distribution curve for A) G27-dimannose:SF(5:1), B) G27-dimannose:SF(10:1), C) G27-dimannose:SF(20:1), D) G27-fucose:SF(5:1), E) G27-fucose:SF(10:1), F) G27-fucose:SF(20:1), G) G27-OH:SF(5:1). D_h values given as xc ± ½ FWHM.

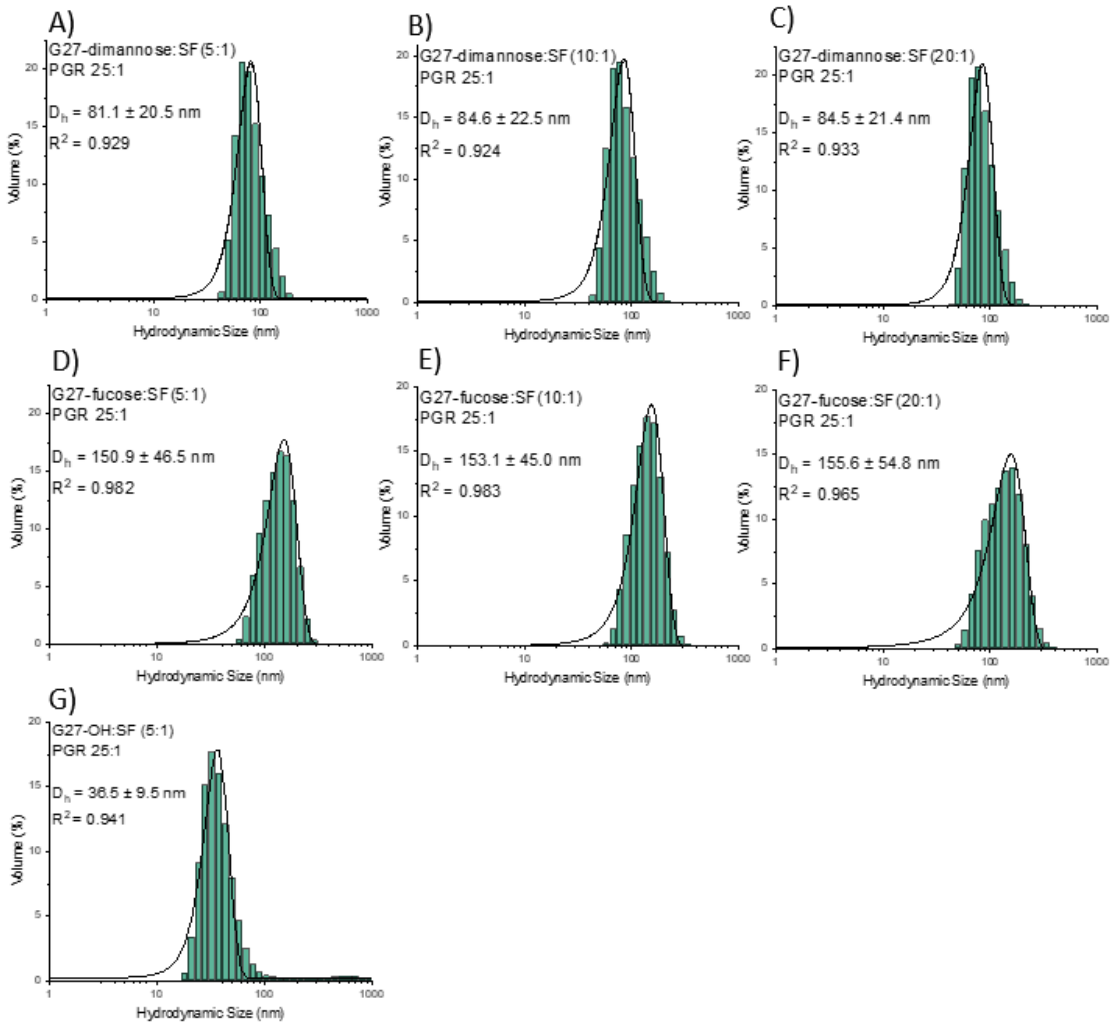

Figure B. 14 Volume population hydrodynamic size distribution histograms fitted with a Gaussian distribution curve for 25 nM DC-SIGN binding with 1nM of A) G27-dimannose:SF(5:1), B) G27-dimannose:SF(10:1), C) G27-dimannose:SF(20:1), D) G27-fucose:SF(5:1), E) G27-fucose:SF(10:1), F) G27-fucose:SF(20:1), G) G27-OH:SF(5:1). D_h values given as xc ± ½ FWHM.

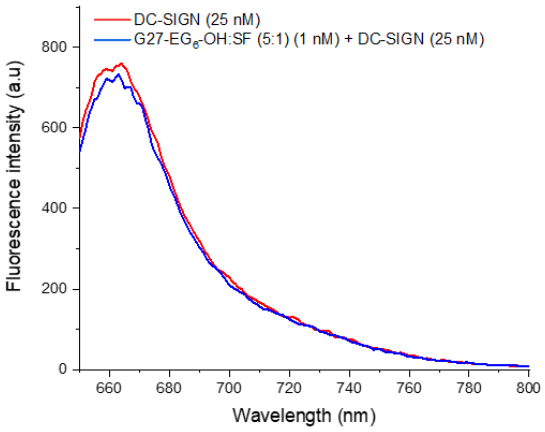

Figure B. 15 The fluoresence intensity spretcrum of the supernatant of DC-SIGN-atto643(25 nM) before and after a 24 hour incubation with G27-OH:SF(5:1) (1nM).

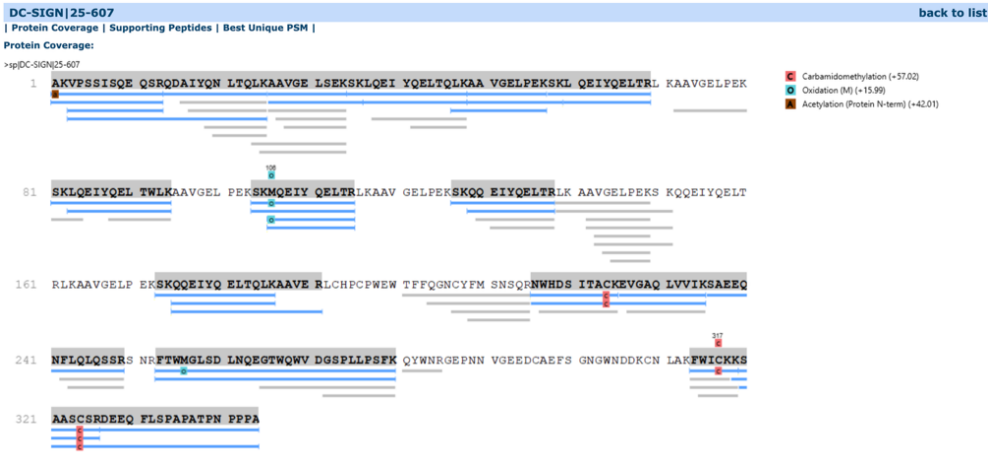

Peptide	Uniq	-10lgP	Mass	Length	ppm	m/z	z	RT	1/k0 Start	1/k0 End	Precursor ID	Area Sample 1	#Feature	#Feature Sample 1	Start	End
K.SAEEQNFLQLQSSR.S	Y	122.74	1635.7852	14	2.99	818.9023	2	25.89	1.0203	1.043	7443	4.5e5	7	7	236	249
AKVPSSISQEQSR.Q	Y	119.8	1415.7368	13	3.23	472.9211	3	11.64	0.739	0.7622	1369	2.21e5	9	9	1	13
R.DEEQFLSPAPATPNPPPA	Y	112.58	1876.8843	18	3.38	939.4526	2	24.52	1.1218	1.1444	6648	2.3e5	20	20	327	344
R.NWHDSITAC(+57.02)KEVGAQLVVIK.S	Y	106.97	2267.1732	20	0.83	756.7323	3	30.16	0.9088	0.9317	9365	1.19e4	2	2	216	235
K.SKLQEIYQELTWLK.A	Y	95.67	1777.9614	14	2.19	889.9899	2	34.93	1.111	1.1336	11295	2.89e4	3	3	81	94
K.SKLQEIYQELTQLK.A	Y	93.56	1719.9407	14	4.74	860.9817	2	34.40	1.102	1.1246	11224	2.04e5	2	2	35	48
K.SKQQEIYQELTQLK.A	Y	93.42	1734.9152	14	4.47	868.4688	2	27.48	1.0992	1.1218	7903	9.73e4	4	4	173	186
K.SKQQEIYQELTR.L	Y	92.21	1521.7787	12	2.86	761.8988	2	21.15	1.0084	1.0312	4637	2.53e5	19	19	127	138
K.AAVGELPEKSK.L	Y	88.05	1127.6186	11	-0.08	564.8165	2	12.44	0.9097	0.9326	1539	6.93e5	20	20	49	59
R.QDAIYQNLTQLK.A	Y	87.52	1433.7514	12	0.52	717.8834	2	24.02	1.0002	1.023	6371	1.2e5	1	1	14	25
K.SKMQEIYQELTR.L	Y	86.65	1524.7606	12	1.27	763.3885	2	30.07	0.9875	1.0103	9291	2.95e4	3	3	104	115
K.SKLQEIYQELTR.L	Y	86.03	1506.8042	12	4.61	754.4128	2	32.00	1.0166	1.0394	10135	1.29e5	6	6	58	69
R.NWHDSITAC(+57.02)K.E	Y	85.14	1230.5451	10	0.59	616.2802	2	16.21	0.8886	0.9115	2743	9.39e4	3	3	216	225
K.QQEIYQELTQLK.A	Y	83.25	1519.7882	12	1.11	760.9022	2	26.29	1.043	1.0657	7507	3.77e5	7	7	175	186
K.VPSSISQEQSR.Q	Y	81.94	1216.6048	11	-0.35	609.3094	2	10.73	0.9015	0.9244	1208	6.03e4	2	2	3	13
A(+42.01)KVPSSISQEQSR.Q	Y	81.38	1457.7474	13	1.93	729.8824	2	14.21	0.9884	1.0112	2406	2.61e2	1	1	1	13
K.SAASC(+57.02)SRDEEQFLSPAPATPNPPPA	Y	81.25	2596.1863	25	3.87	866.4061	3	22.03	0.9491	0.9719	5292	9.81e4	8	8	320	344
K.AAVGELSEKSK.L	Y	80.7	1117.5979	11	1.1	559.8068	2	11.13	0.8886	0.9115	1302	4.68e3	1	1	26	36
K.EVGAQLVVIK.S	Y	79.44	1054.6386	10	-0.77	528.3262	2	22.89	0.8362	0.8592	5817	2.21e5	6	6	226	235
K.LQEIYQELTWLK.A	Y	79.32	1562.8344	12	1.42	782.4256	2	32.20	1.0466	1.0693	10152	6.63e5	4	4	83	94
Q.LKAAVGELPEK.S	Y	78.51	1153.6706	11	-0.74	577.8422	2	16.66	0.907	0.9299	3008	1.37e6	7	7	47	57
K.LQEIYQELTQLK.A	Y	76.24	1504.8137	12	1.38	753.4152	2	29.06	1.0475	1.0702	8583	4.94e5	4	4	37	48
K.SKM(+15.99)QEIYQELTR.L	Y	74.14	1540.7555	12	3.76	771.3879	2	27.36	1.0084	1.0312	8056	2.39e3	4	4	104	115
R.FTWMGLSDLNQEGTWQWVDGSPLLPSFK.Q	Y	69.27	3238.5433	28	1.26	1080.5231	3	35.84	1.0575	1.0802	11755	2.79e2	1	1	253	280
K.MQEIYQELTR.L	Y	66.69	1309.6336	10	0.66	655.8245	2	22.19	0.9646	0.9875	5335	4.88e5	4	4	106	115
K.AAVGELPEK.S	Y	58.64	912.4916	9	2.75	457.2543	2	14.71	0.7863	0.8094	2320	6.36e5	17	17	49	57
K.QQEIYQELTR.L	Y	54.72	1306.6517	10	-0.2	654.333	2	19.92	0.9646	0.9875	3965	7.79e5	3	3	129	138
K.AAVGELSEK.S	Y	54.03	902.4709	9	4.71	452.2448	2	12.69	0.7455	0.7687	1861	3.79e5	2	2	26	34
K.QQEIYQELTQLKAAVER.L	Y	53.93	2046.0745	17	-7.27	683.0272	3	30.68	0.9216	0.9445	9691	0	0	0	175	191
R.FTWM(+15.99)GLSDLNQEGTWQWVDGSPLLPSFK.Q	Y	53.57	3254.5382	28	14.78	1085.8694	3	35.31	1.0603	1.0829	11432	0	0	0	253	280
K.LQEIYQELTR.L	Y	52.42	1291.6772	10	-0.17	646.8458	2	23.06	0.9692	0.992	5755	6.57e5	3	3	60	69
K.M(+15.99)QEIYQELTR.L	Y	51.22	1325.6285	10	3.75	663.824	2	21.02	0.9656	0.9884	4593	7.45e5	8	8	106	115
K.FWIC(+57.02)KK.S	Y	29.01	880.4629	6	-1.72	441.238	2	20.64	0.7752	0.7983	4597	1.03e5	3	3	314	319
K.VPSSISQEQSRQDAIYQNLTQLK.A	Y	24.85	2632.3456	23	3.33	878.4587	3	26.39	0.9646	0.9875	7604	3.02e2	1	1	3	25
K.SAASC(+57.02)SR.D	Y	19.01	737.3126	7	7.4	369.6663	2	8.40	0.7102	0.7335	900	0	0	0	320	326
K.KSAASC(+57.02)SR.D	Y	18.98	865.4076	8	4.55	433.713	2	8.50	0.7669	0.79	926	0	0	0	319	326
total 36 peptides																

Figure B. 16 Peptide ID list and amino acid sequence coverage observed for a sample of DC-SIGN digested with trypsin, analysed by LC-MS/MS. Grey highlight indicates identified peptides.

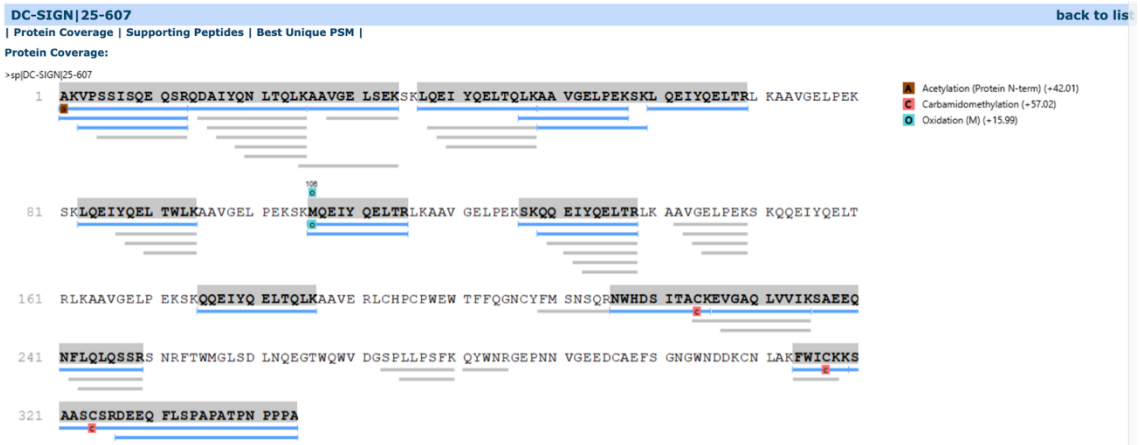

Peptide	Uniq	-10lgP	Mass	Length	ppm	m/z	z	RT	1/k0 Start	1/k0 End	Precursor ID	Area Sample 2	#Feature	#Feature Sample 2	Start	End	PTM
K.SAEEQNFLQLQSSR.S	Y	119.02	1635.7852	14	1.21	818.899	2	10.27	1.0334	1.0562	3923	1.7e5	4	4	236	249	
R.DEEQFLSPAPATPNPPPA	Y	106.67	1876.8843	18	1.94	939.449	2	12.23	1.1205	1.1431	5257	1.09e5	20	20	327	344	
R.QDAIYQNLTQLK.A	Y	97.18	1433.7514	12	-1.32	717.8804	2	10.64	0.9551	0.9779	4596	1.95e5	2	2	14	25	
K.QQEIYQELTQLK.A	Y	96.27	1519.7882	12	1.35	760.9006	2	11.30	1.0334	1.0562	5010	5.1e4	3	3	175	186	
AKVPSSISQEQSR.Q	Y	94.17	1415.7368	13	2.46	472.9196	3	6.42	0.7343	0.7575	977	1.24e5	6	6	1	13	
K.VPSSISQEQSR.Q	Y	89.62	1216.6048	11	-0.42	609.308	2	6.09	0.8818	0.9048	917	1.06e5	7	7	3	13	
K.LQEIYQELTQLK.A	Y	89.41	1504.8137	12	1.93	753.4138	2	12.19	1.0216	1.0444	5667	3.84e4	1	1	37	48	
R.NWHDSITAC(+57.02)K.E	Y	85.63	1230.5451	10	0.54	616.2787	2	8.10	0.8828	0.9057	1940	4.03e4	3	3	216	225	Carbamidomethylation
Q.LKAAVGELPEK.S	Y	80.38	1153.6706	11	0.32	577.8414	2	8.70	0.8956	0.9185	2597	1.12e5	4	4	47	57	
K.SAASC(+57.02)SRDEEQFLSPAPATPNPPPA	Y	78.83	2596.1863	25	1.75	866.4022	3	10.24	0.9222	0.945	4350	6.36e3	1	1	320	344	Carbamidomethylation
K.MQEIYQELTR.L	Y	75.55	1309.6336	10	1.97	655.8239	2	10.49	0.956	0.9788	3924	2e5	1	1	106	115	
K.LQEIYQELTWLK.A	Y	73.09	1562.8344	12	1.8	782.4241	2	13.65	1.038	1.0607	6472	1.09e3	1	1	83	94	
K.EVGAQLVVIK.S	Y	72.92	1054.6386	10	-0.99	528.3248	2	10.29	0.8405	0.8635	4186	2.25e5	3	3	226	235	
K.LQEIYQELTR.L	Y	72.24	1291.6772	10	0.46	646.8447	2	10.30	0.9478	0.9706	4154	2.55e5	2	2	60	69	
K.AAVGELPEKSK.L	Y	72.15	1127.6186	11	2.36	564.8166	2	6.39	0.9048	0.9277	1014	9.05e2	1	1	49	59	
K.QQEIYQELTR.L	Y	70.92	1306.6517	10	4.57	654.3346	2	9.18	0.9542	0.977	3192	1.72e3	4	4	129	138	
K.AAVGELPEK.S	Y	64.51	912.4916	9	-2.41	457.2509	2	7.50	0.7916	0.8147	2026	1.54e6	4	4	49	57	
K.AAVGELSEK.S	Y	63.7	902.4709	9	-1.14	452.2411	2	6.92	0.7676	0.7907	1344	1.79e3	3	3	26	34	
K.M(+15.99)QEIYQELTR.L	Y	61.41	1325.6285	10	1.48	663.821	2	9.71	0.9752	0.998	3303	1.6e5	4	4	106	115	Oxidation (M)
K.SKQQEIYQELTR.L	Y	57.6	1521.7787	12	-5.88	761.8904	2	9.36	1.0034	1.0262	3418	0	0	0	127	138	
A(+42.01)KVPSSISQEQSR.Q	Y	49.87	1457.7474	13	2.17	729.8809	2	7.33	0.9688	0.9916	1745	0	0	0	1	13	Acetylation (Protein N-term)
K.FWIC(+57.02)KK.S	Y	32.18	880.4629	6	5.54	441.2401	2	8.78	0.7695	0.7926	2847	0	0	0	314	319	Carbamidomethylation
total 22 peptides																	

Figure B. 17 peptide ID list and amino acid sequence coverage for DC-SIGN treated with G27-fucose:SF(5:1) then trypsin digested using the on-GNP technique, analysed by LC-MS/MS. Grey highlight indicates identified peptides.

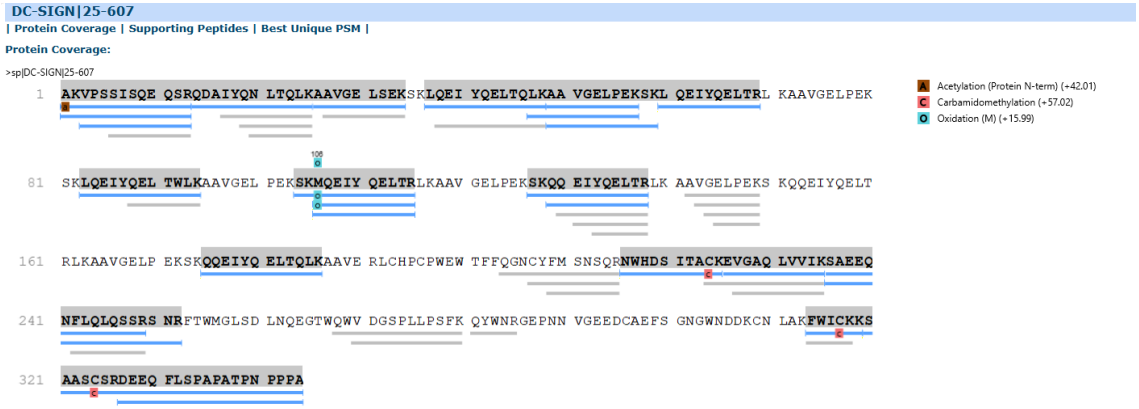

Supporting Peptides:

Peptide	Uniq	-10lgP	Mass	Length	ppm	m/z	z	RT	1/k0 Start	1/k0 End	Precursor ID	Area Sample 1	#Feature	#Feature Sample 1	Start	End
K.SAEEQNFLQLQSSR.S	Y	131.98	1635.7852	14	2.32	818.8984	2	10.25	1.0271	1.0498	4562	1.55e5	3	3	236	249
R.DEEQFLSPAPATPNPPPA	Y	116.62	1876.8843	18	1.06	939.4465	2	11.32	1.1051	1.1277	6114	1.1e5	28	28	327	344
R.QDAIYQNLTQLK.A	Y	113.6	1433.7514	12	-2.11	717.8785	2	10.68	1.0007	1.0234	5360	1.58e5	4	4	14	25
AKVPSSISQEQSR.Q	Y	108.73	1415.7368	13	4.25	472.9196	3	6.49	0.7371	0.7602	1249	1.11e5	6	6	1	13
K.QQEIYQELTQLK.A	Y	104.26	1519.7882	12	3.76	760.9011	2	11.30	1.0353	1.058	5937	6.66e4	2	2	175	186
K.VPSSISQEQSR.Q	Y	102.24	1216.6048	11	-1.28	609.3063	2	6.18	0.8855	0.9084	1132	9.12e4	5	5	3	13
K.LQEIYQELTQLK.A	Y	97.63	1504.8137	12	4.02	753.414	2	12.24	1.0225	1.0453	6723	3.51e4	3	3	37	48
R.NWHDSITAC(+57.02)K.E	Y	94.14	1230.5451	10	0.01	616.2773	2	8.20	0.8846	0.9075	2320	5.72e4	5	5	216	225
K.SAASC(+57.02)SRDEEQFLSPAPATPNPPPA	Y	92.83	2596.1863	25	1.63	866.4005	3	10.13	0.9533	0.9761	4808	7.16e3	3	3	320	344
Q.LKAAVGELPEK.S	Y	87.26	1153.6706	11	0.69	577.8406	2	9.89	0.902	0.9249	6479	9.37e4	4	4	47	57
K.MQEIYQELTR.L	Y	83.16	1309.6336	10	2.05	655.8227	2	10.40	0.956	0.9788	4592	1.62e5	3	3	106	115
K.LQEIYQELTWLK.A	Y	80.74	1562.8344	12	2.79	782.4234	2	13.63	1.0025	1.0253	7684	1.88e3	2	2	83	94
K.EVGAQLVVIK.S	Y	80.54	1054.6386	10	-0.41	528.3242	2	10.34	0.8534	0.8763	4905	2.26e5	4	4	226	235
K.LQEIYQELTR.L	Y	78.15	1291.6772	10	0.89	646.8438	2	10.34	0.9478	0.9706	4842	2.07e5	4	4	60	69
K.AAVGELPEKSK.L	Y	75.92	1127.6186	11	-0.66	564.8138	2	6.46	0.9048	0.9277	1281	5.79e2	1	1	49	59
K.QQEIYQELTR.L	Y	75.38	1306.6517	10	0.06	654.3304	2	9.59	0.9313	0.9542	3793	3.73e5	4	4	129	138
K.M(+15.99)QEIYQELTR.L	Y	75.12	1325.6285	10	2.13	663.8202	2	9.74	0.9597	0.9825	4152	1.36e5	1	1	106	115
K.AAVGELSEK.S	Y	72.15	902.4709	9	1.19	452.2414	2	7.21	0.7695	0.7926	1401	3.5e5	6	6	26	34
K.AAVGELPEK.S	Y	70.79	912.4916	9	-4.1	457.2493	2	7.79	0.7796	0.8027	2404	5.46e4	1	1	49	57
A(+42.01)KVPSSISQEQSR.Q	Y	69.41	1457.7474	13	-2.01	729.8765	2	7.49	0.9706	0.9934	2144	0	0	0	1	13
K.SKQQEIYQELTR.L	Y	64.12	1521.7787	12	7.28	761.899	2	9.20	0.9952	1.018	3784	0	0	0	127	138
K.SAEEQNFLQLQSSRSNR.F	Y	37.27	1992.9613	17	11.57	997.4953	2	10.00	1.1376	1.1602	4658	0	0	0	236	252
K.SKM(+15.99)QEIYQELTR.L	Y	37.26	1540.7555	12	-11.79	771.3727	2	9.67	1.0153	1.038	4286	0	0	0	104	115
K.FWIC(+57.02)KK.S	Y	26.76	880.4629	6	-12.78	441.2313	2	9.44	0.7778	0.8009	4092	0	0	0	314	319
total 24 peptides																

Figure B. 18 peptide ID list and amino acid sequence coverage for DC-SIGN treated with G27-dimannose:SF(5:1) then trypsin digested using the on-GNP technique, analysed by LC-MS/MS. Grey highlight indicates identified peptides.

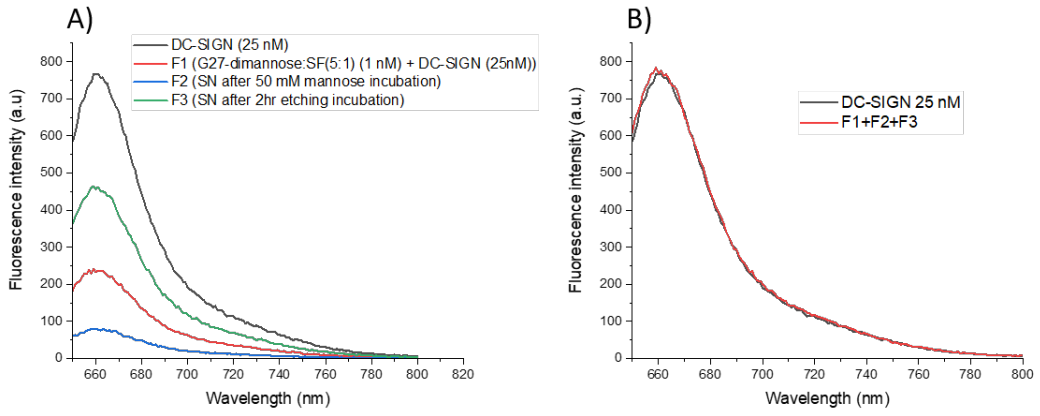

Figure B. 19 The fluoresence intensity spretcrum of A) The supernatants of DC-SIGN (25 nM)+G27-dimannose:SF(5:1) after an initial incubation(F1), after incubating the pellet with 50mM mannose (F2) and after incubating the pellet with etching solution(F3), and B) the combined fluorescence intensity of F1, F2 and F3 showing complete fluorescence recvoery when compared to the DC-SIGN control indicating complete DC-SIGN displacement form the GNP surface.

Chapter 10 References

1. van Kooyk, Y. and Rabinovich, G.A. Protein-glycan interactions in the control of innate and adaptive immune responses. *Nature Immunology.* 2008, **9**(6), pp.593-601.
2. Mammen, M., Choi, S.K. and Whitesides, G.M. Polyvalent interactions in biological systems: Implications for design and use of multivalent ligands and inhibitors. *Angewandte Chemie-International Edition.* 1998, **37**(20), pp.2755-2794.
3. Sharon, N. Lectins: Carbohydrate-specific Reagents and Biological Recognition Molecules. *Journal of Biological Chemistry.* 2007, **282**(5), pp.2753-2764.
4. Brown, G.D., Willment, J.A. and Whitehead, L. C-type lectins in immunity and homeostasis. *Nature Reviews Immunology.* 2018, **18**(6), pp.374-389.
5. Dambuza, I.M. and Brown, G.D. C-type lectins in immunity: recent developments. *Current Opinion in Immunology.* 2015, **32**, pp.21-27.
6. Lafouresse, F., Bellard, E., Laurent, C., Moussion, C., Fournié, J.-J., Ysebaert, L. and Girard, J.-P. L-selectin controls trafficking of chronic lymphocytic leukemia cells in lymph node high endothelial venules in vivo. *Blood.* 2015, **126**(11), pp.1336-1345.
7. Choteau, L., Parny, M., François, N., Bertin, B., Fumery, M., Dubuquoy, L., Takahashi, K., Colombel, J.F., Jouault, T., Poulain, D., Sendid, B. and Jawhara, S. Role of mannose-binding lectin in intestinal homeostasis and fungal elimination. *Mucosal Immunology.* 2016, **9**(3), pp.767-776.
8. Cibrián, D. and Sánchez-Madrid, F. CD69: from activation marker to metabolic gatekeeper. *European Journal of Immunology.* 2017, **47**(6), pp.946-953.
9. Ivetic, A., Hoskins Green, H.L. and Hart, S.J. L-selectin: A Major Regulator of Leukocyte Adhesion, Migration and Signaling. *Front Immunol.* 2019, **10**, p.1068.
10. Crocker, P.R., Mucklow, S., Bouckson, V., McWilliam, A., Willis, A.C., Gordon, S., Milon, G., Kelm, S. and Bradfield, P. Sialoadhesin, a macrophage sialic acid binding receptor for haemopoietic cells with 17 immunoglobulin-like domains. *The EMBO Journal.* 1994, **13**(19), pp.4490-4503-4503.
11. Acton, S.E., Farrugia, A.J., Astarita, J.L., Mourão-Sá, D., Jenkins, R.P., Nye, E., Hooper, S., van Blijswijk, J., Rogers, N.C., Snelgrove, K.J., Rosewell, I., Moita, L.F., Stamp, G., Turley, S.J., Sahai, E. and Reis e Sousa, C. Dendritic cells control fibroblastic reticular network tension and lymph node expansion. *Nature.* 2014, **514**(7523), pp.498-502.
12. Jarvis, C.M., Zwick, D.B., Grim, J.C., Alam, M.M., Prost, L.R., Gardiner, J.C., Park, S., Zimdars, L.L., Sherer, N.M. and Kiessling, L.L. Antigen structure affects cellular routing through DC-SIGN. *Proceedings of the National Academy of Sciences of the United States of America.* 2019, **116**(30), pp.14862-14867.
13. Trumpfheller, C., Park, C.G., Finke, J., Steinman, R.M. and Granelli-Piperno, A. Cell type-dependent retention and transmission of HIV-1 by DC-SIGN. *International Immunology.* 2003, **15**(2), pp.289-298.
14. Geijtenbeek, T.B.H., Kwon, D.S., Torensma, R., van Vliet, S.J., van Duijnhoven, G.C.F., Middel, J., Cornelissen, I., Nottet, H., KewalRamani, V.N., Littman, D.R., Figdor, C.G. and van Kooyk, Y. DC-SIGN, a dendritic cell-specific HIV-1-binding protein that enhances trans-infection of T cells. *Cell.* 2000, **100**(5), pp.587-597.
15. Zhou, T., Chen, Y.X., Hao, L. and Zhang, Y.Y. DC-SIGN and Immunoregulation. *Cellular & Molecular Immunology.* 2006, **3**(4), pp.279-283.
16. Bouckaert, J., Mackenzie, J., De Paz, J.L., Chipwaza, B., Choudhury, D., Zavialov, A., Mannerstedt, K., Anderson, J., Piérard, D., Wyns, L., Seeberger,

P.H., Oscarson, S., De Greve, H. and Knight, S.D. The affinity of the FimH fimbrial adhesin is receptor-driven and quasi-independent of Escherichia coli pathotypes. *Molecular Microbiology.* 2006, **61**(6), pp.1556-1568.
17. Vajaria, B.N. and Patel, P.S. Glycosylation: a hallmark of cancer? *Glycoconjugate Journal.* 2017, **34**(2), pp.147-156.
18. Hudak, J.E., Canham, S.M. and Bertozzi, C.R. Glycocalyx engineering reveals a Siglec-based mechanism for NK cell immunoevasion. *Nature Chemical Biology.* 2014, **10**(1), pp.69-75.
19. Ding, D., Yao, Y., Zhang, S., Su, C. and Zhang, Y. C-type lectins facilitate tumor metastasis (Review). *Oncol Lett.* 2017, **13**(1), pp.13-21.
20. Guo, J., Wu, X., Too, C.L., Yin, F., Lu, X., He, J., Li, R., Liu, X., Murad, S. and Padyukov, L. A replication study confirms the association of dendritic cell immunoreceptor (DCIR) polymorphisms with ACPA-negative RA in a large Asian cohort. *Plos one.* 2012, **7**(7), p.e41228.
21. Soleimanpour, Scott A., Gupta, A., Bakay, M., Ferrari, Alana M., Groff, David N., Fadista, J., Spruce, Lynn A., Kushner, Jake A., Groop, L., Seeholzer, Steven H., Kaufman, Brett A., Hakonarson, H. and Stoffers, Doris A. The Diabetes Susceptibility Gene Clec16a Regulates Mitophagy. *Cell.* 2014, **157**(7), pp.1577-1590.
22. Rojas, M., Restrepo-Jiménez, P., Monsalve, D.M., Pacheco, Y., Acosta-Ampudia, Y., Ramírez-Santana, C., Leung, P.S.C., Ansari, A.A., Gershwin, M.E. and Anaya, J.-M. Molecular mimicry and autoimmunity. *Journal of Autoimmunity.* 2018, **95**, pp.100-123.
23. Pinho, S.S., Alves, I., Gaifem, J. and Rabinovich, G.A. Immune regulatory networks coordinated by glycans and glycan-binding proteins in autoimmunity and infection. *Cellular & Molecular Immunology.* 2023, **20**(10), pp.1101-1113.
24. Cheng, S., Li, M., Feng, Y., Liu, T., He, L., Xu, M., Ma, L. and Li, X. Glycan-Modified Peptides for Dual Inhibition of Human Immunodeficiency Virus Entry into Dendritic Cells and T Cells. *Journal of Medicinal Chemistry.* 2024, **67**(5), pp.4225-4233.
25. Yu, T., Li, Y., Gu, X. and Li, Q. Development of a Hyaluronic Acid-Based Nanocarrier Incorporating Doxorubicin and Cisplatin as a pH-Sensitive and CD44-Targeted Anti-Breast Cancer Drug Delivery System. *Frontiers in Pharmacology.* 2020, **11**.
26. Conde, P., Rodriguez, M., van der Touw, W., Jimenez, A., Burns, M., Miller, J., Brahmachary, M., Chen, H.M., Boros, P., Rausell-Palamos, F., Yun, T.J., Riquelme, P., Rastrojo, A., Aguado, B., Stein-Streilein, J., Tanaka, M., Zhou, L., Zhang, J., Lowary, T.L., Ginhoux, F., Park, C.G., Cheong, C., Brody, J., Turley, S.J., Lira, S.A., Bronte, V., Gordon, S., Heeger, P.S., Merad, M., Hutchinson, J., Chen, S.H. and Ochando, J. DC-SIGN(+) Macrophages Control the Induction of Transplantation Tolerance. *Immunity.* 2015, **42**(6), pp.1143-1158.
27. Robinson, M.J., Sancho, D., Slack, E.C., LeibundGut-Landmann, S. and Sousa, C.R.E. Myeloid C-type lectins in innate immunity. *Nature Immunology.* 2006, **7**(12), pp.1258-1265.
28. Mayer, S., Raulf, M.K. and Lepenies, B. C-type lectins: their network and roles in pathogen recognition and immunity. *Histochemistry and Cell Biology.* 2017, **147**(2), pp.223-237.
29. Figdor, C.G., van Kooyk, Y. and Adema, G.J. C-type lectin receptors on dendritic cells and Langerhans cells. *Nature Reviews Immunology.* 2002, **2**(2), pp.77-84.
30. Monteiro, J.T. and Lepenies, B. Myeloid C-Type Lectin Receptors in Viral Recognition and Antiviral Immunity. *Viruses-Basel.* 2017, **9**(3).
31. Sancho, D. and Reis e Sousa, C. Signaling by Myeloid C-Type Lectin Receptors in Immunity and Homeostasis. *Annual Review of Immunology.* 2012, **30**(Volume 30, 2012), pp.491-529.
32. Valverde, P., Delgado, S., Martinez, J.D., Vendeville, J.B., Malassis, J., Linclau, B., Reichardt, N.C., Canada, F.J., Jimenez-Barbero, J. and Arda, A. Molecular

Insights into DC-SIGN Binding to Self-Antigens: The Interaction with the Blood Group A/B Antigens. *Acs Chemical Biology.* 2019, **14**(7), pp.1660-1671.

33. Geijtenbeek, T.B.H., van Vliet, S.J., Engering, A., t Hart, B.A. and van Kooyk, Y. Self- and nonself-recognition by C-type lectins on dendritic cells. *Annual Review of Immunology.* 2004, **22**, pp.33-54.
34. Newport, M., Sirugo, G., Lyons, E., Vannberg, F., Hill, A.V.S., Bradbury, L.A., Farrar, C., Pointon, J.J., Wordsworth, P., Brown, M.A., Franklyn, J.A., Heward, J.M., Simmonds, M.J., Gough, S.C., Seal, S., Stratton, M.R., Rahman, N., Ban, M., Goris, A., Sawcer, S.J., Compston, A., Conway, D., Jallow, M., Rockett, K.A., Kwiatkowski, D.P., Bumpstead, S.J., Chaney, A., Downes, K., Ghori, M.J., Gwilliam, R., Hunt, S.E., Inouye, M., Keniry, A., King, E., McGinnis, R., Potter, S., Ravindrarajah, R., Whittaker, P., Widden, C., Withers, D., Deloukas, P., Leung, H.T., Nutland, S., Stevens, H.E., Walker, N.M., Todd, J.A., Easton, D., Clayton, D.G., Burton, P.R., Tobin, M.D., Barrett, J.C., Evans, D.M., Morris, A.P., Cardon, L.R., Cardin, N.J., Davison, D., Ferreira, T., Pereira-Gale, J., Hallgrimsdottir, I.B., Howie, B.N., Marchini, J.L., Spencer, C.C., Su, Z., Teo, Y.Y., Vukcevic, D., Donnelly, P., Bentley, D., Caulfield, M., Craddock, N., Farrall, M., Barton, A., Bruce, I.N., Donovan, H., Eyre, S., Gilbert, P.D., Hilder, S.L., Hinks, A.M., John, S.L., Potter, C., Silman, A.J., Symmons, D.P.M., Thomson, W., Worthington, J., Hall, A.S., Hattersley, A.T., Matthew, C.G., McCarthy, M.I., Ouwehand, W.H., Parkes, M., Pembrey, M., Samani, N.J., Mitchell, S.L., Newby, P.R., Brand, O.J., Carr-Smith, J., Pearce, S.H.S., Gough, S.C.L., Reveille, J.D., Zhou, X., Sims, A.M., Dowling, A., Taylor, J., Doan, T., Davis, J.C., Savage, L., Ward, M.M., Learch, T.L. and Weisman, M.H. Association scan of 14,500 nonsynonymous SNPs in four diseases identifies autoimmunity variants. *Nature Genetics.* 2007, **39**(11), pp.1329-1337.
35. Zelensky, A.N. and Gready, J.E. The C-type lectin-like domain superfamily. *Febs Journal.* 2005, **272**(24), pp.6179-6217.
36. Cramer, J. Medicinal chemistry of the myeloid C-type lectin receptors Mincle, Langerin, and DC-SIGN. *Rsc Medicinal Chemistry.* 2021, **12**(12), pp.1985-2000.
37. Weis, W.I., Taylor, M.E. and Drickamer, K. The C-type lectin superfamily in the immune system. *Immunological Reviews.* 1998, **163**, pp.19-34.
38. Willment, J.A., Gordon, S. and Brown, G.D. Characterization of the human beta-glucan receptor and its alternatively spliced isoforms. *Journal of Biological Chemistry.* 2001, **276**(47), pp.43818-43823.
39. Bates, E.E.M., Fournier, N., Garcia, E., Valladeau, J., Durand, I., Pin, J.J., Zurawski, S.M., Patel, S., Abrams, J.S., Lebecque, S., Garrone, P. and Saeland, S. APCs express DCIR, a novel C-type lectin surface receptor containing an immunoreceptor tyrosine-based inhibitory motif. *Journal of Immunology.* 1999, **163**(4), pp.1973-1983.
40. Valladeau, J., Ravel, O., Dezutter-Dambuyant, C., Moore, K., Kleijmeer, M., Liu, Y., Duvert-Frances, V., Vincent, C., Schmitt, D., Davoust, J., Caux, C., Lebecque, S. and Saeland, S. Langerin, a novel C-type lectin specific to Langerhans cells, is an endocytic receptor that induces the formation of Birbeck granules. *Immunity.* 2000, **12**(1), pp.71-81.
41. Colonna, M., Samaridis, J. and Angman, L. Molecular characterization of two novel C-type lectin-like receptors, one of which is selectively expressed in human dendritic cells. *European Journal of Immunology.* 2000, **30**(2), pp.697-704.
42. Taylor, M.E., Conary, J.T., Lennartz, M.R., Stahl, P.D. and Drickamer, K. Primary structure of the mannose receptor contains multiple motifs resembling carbohydrate-recognition domains. *Journal of Biological Chemistry.* 1990, **265**(21), pp.12156-12162.
43. Kato, M., Neil, T.K., Clark, G.J., Morris, C.M., Sorg, R.V. and Hart, D.N.J. cDNA cloning of human DEC-205, a putative antigen-uptake receptor on dendritic cells. *Immunogenetics.* 1998, **47**(6), pp.442-450.

44. Stahl, P.D. and Ezekowitz, R.A.B. The mannose receptor is a pattern recognition receptor involved in host defense. *Current Opinion in Immunology.* 1998, **10**(1), pp.50-55.
45. Sallusto, F., Cella, M., Danieli, C. and Lanzavecchia, A. Dendritic cells use macropinocytosis and the mannose receptor to concentrate macromolecules in the major histocompatibility complex class-II compartment - down-regulation by cytokines and bacterial products. *Journal of Experimental Medicine.* 1995, **182**(2), pp.389-400.
46. Fehres, C.M., Duinkerken, S., Bruijns, S.C.M., Kalay, H., van Vliet, S.J., Ambrosini, M., de Gruijl, T.D., Unger, W.W.J., Garcia-Vallejo, J.J. and van Kooyk, Y. Langerin-mediated internalization of a modified peptide routes antigens to early endosomes and enhances cross-presentation by human Langerhans cells. *Cellular & Molecular Immunology.* 2017, **14**(4), pp.360-370.
47. Pandey, K.N. Functional roles of short sequence motifs in the endocytosis of membrane receptors. *Frontiers in Bioscience-Landmark.* 2009, **14**, pp.5339-5360.
48. Appelmelk, B.J., van Die, I., van Vliet, S.J., Vandenbroucke-Grauls, C., Geijtenbeek, T.B.H. and van Kooyk, Y. Cutting edge: Carbohydrate profiling identifies new pathogens that interact with dendritic cell-specific ICAM-3-grabbing nonintegrin on dendritic cells. *Journal of Immunology.* 2003, **170**(4), pp.1635-1639.
49. Engering, A., Geijtenbeek, T.B.H. and van Kooyk, Y. Immune escape through C-type lectins on dendritic cells. *Trends in Immunology.* 2002, **23**(10), pp.480-485.
50. Stahl, P., Schlesinger, P.H., Sigardson, E., Rodman, J.S. and Lee, Y.C. Receptor-mediated pinocytosis of mannose glycoconjugates by macrophages – characterisation and evidence for receptor recycling. *Cell.* 1980, **19**(1), pp.207-215.
51. Osorio, F. and Sousa, G.R.E. Myeloid C-type Lectin Receptors in Pathogen Recognition and Host Defense. *Immunity.* 2011, **34**(5), pp.651-664.
52. Gringhuis, S.I., den Dunnen, J., Litjens, M., van der Vlist, M. and Geijtenbeek, T.B.H. Carbohydrate-specific signaling through the DC-SIGN signalosome tailors immunity to Mycobacterium tuberculosis, HIV-1 and Helicobacter pylori. *Nature Immunology.* 2009, **10**(10), pp.1081-U1058.
53. Nigou, J., Zelle-Rieser, C., Gilleron, M., Thurnher, M. and Puzo, G. Mannosylated lipoarabinomannans inhibit IL-12 production by human dendritic cells: Evidence for a negative signal delivered through the mannose receptor. *Journal of Immunology.* 2001, **166**(12), pp.7477-7485.
54. Iobst, S.T., Wormald, M.R., Weis, W.I., Dwek, R.A. and Drickamer, K. Binding of sugar ligands to Ca2+ dependent animal lectins. 1. Analysis of mannose-binding by site-directed mutagenesis and NMR. *Journal of Biological Chemistry.* 1994, **269**(22), pp.15505-15511.
55. Drickamer, K. C-type lectin-like domains. *Current Opinion in Structural Biology.* 1999, **9**(5), pp.585-590.
56. Geijtenbeek, T.B.H., van Duijnhoven, G.C.F., van Vliet, S.J., Krieger, E., Vriend, G., Figdor, C.G. and van Kooyk, Y. Identification of different binding sites in the dendritic cell-specific receptor DC-SIGN for intercellular adhesion molecule 3 and HIV-1. *Journal of Biological Chemistry.* 2002, **277**(13), pp.11314-11320.
57. Keller, B.G. and Rademacher, C. Allostery in C-type lectins. *Current Opinion in Structural Biology.* 2020, **62**, pp.31-38.
58. Aretz, J., Wamhoff, E.C., Hanske, J., Heymann, D. and Rademacher, C. Computational and experimental prediction of human C-type lectin receptor druggability. *Frontiers in Immunology.* 2014, **5**, pp.1-12.
59. Ernst, B. and Magnani, J.L. From carbohydrate leads to glycomimetic drugs. *Nature Reviews Drug Discovery.* 2009, **8**(8), pp.661-677.
60. Alam, M.M., Jarvis, C.M., Hincapie, R., McKay, C.S., Schimer, J., Sanhueza, C.A., Xu, K., Diehl, R.C., Finn, M.G. and Kiessling, L.L. Glycan-Modified Virus-

like Particles Evoke T Helper Type 1-like Immune Responses. *Acs Nano.* 2021, **15**(1), pp.309-321.

61. Dam, T.K. and Brewer, C.F. Multivalent lectin-carbohydrate interactions energetics and mechanisms of binding. *Advances in Carbohydrate Chemistry and Biochemistry.* 2010, **63**, pp.139-164.
62. Bernardi, A., Jimenez-Barbero, J., Casnati, A., De Castro, C., Darbre, T., Fieschi, F., Finne, J., Funken, H., Jaeger, K.E., Lahmann, M., Lindhorst, T.K., Marradi, M., Messner, P., Molinaro, A., Murphy, P.V., Nativi, C., Oscarson, S., Penades, S., Peri, F., Pieters, R.J., Renaudet, O., Reymond, J.L., Richichi, B., Rojo, J., Sansone, F., Schaffer, C., Turnbull, W.B., Velasco-Torrijos, T., Vidal, S., Vincent, S., Wennekes, T., Zuilhof, H. and Imberty, A. Multivalent glycoconjugates as anti-pathogenic agents. *Chemical Society Reviews.* 2013, **42**(11), pp.4709-4727.
63. den Dunnen, J., Gringhuis, S.I. and Geijtenbeek, T.B.H. Dusting the sugar fingerprint: C-type lectin signaling in adaptive immunity. *Immunology Letters.* 2010, **128**(1), pp.12-16.
64. Balzarini, J. Targeting the glycans of glycoproteins: a novel paradigm for antiviral therapy. *Nature Reviews Microbiology.* 2007, **5**(8), pp.583-597.
65. Kato, M., Neil, T.K., Fearnley, D.B., McLellan, A.D., Vuckovic, S. and Hart, D.N.J. Expression of multilectin receptors and comparative FITC-dextran uptake by human dendritic cells. *International Immunology.* 2000, **12**(11), pp.1511-1519.
66. Mitchell, D.A., Fadden, A.J. and Drickamer, K. A novel mechanism of carbohydrate recognition by the C-type lectins DC-SIGN and DC-SIGNR - Subunit organization and binding to multivalent ligands. *Journal of Biological Chemistry.* 2001, **276**(31), pp.28939-28945.
67. Curtis, B.M., Scharnowske, S. and Watson, A.J. Sequence and expression of a membrane-associated C-type lectin that exhibits CD4-independent binding of human immunodeficiency virus envelope glycoprotein gp120. *Proc Natl Acad Sci U S A.* 1992, **89**(17), pp.8356-8360.
68. Geijtenbeek, T.B.H., Torensma, R., van Vliet, S.J., van Duijnhoven, G.C.F., Adema, G.J., van Kooyk, Y. and Figdor, C.G. Identification of DC-SIGN, a novel dendritic cell-specific ICAM-3 receptor that supports primary immune responses. *Cell.* 2000, **100**(5), pp.575-585.
69. Tabarani, G., Thepaut, M., Stroebel, D., Ebel, C., Vives, C., Vachette, P., Durand, D. and Fieschi, F. DC-SIGN neck domain is a pH-sensor controlling oligomerization: SAXS and hydrodynamic studies of extracellular domain. *Journal of Biological Chemistry.* 2009, **284**(32), pp.21229-21240.
70. Yu, Q.D., Oldring, A.P., Powlesland, A.S., Tso, C.K.W., Yang, C., Drickamer, K. and Taylor, M.E. Autonomous Tetramerization Domains in the Glycan-binding Receptors DC-SIGN and DC-SIGNR. *Journal of Molecular Biology.* 2009, **387**(5), pp.1075-1080.
71. Feinberg, H., Guo, Y., Mitchell, D.A., Drickamer, K. and Weis, W.I. Extended neck regions stabilize tetramers of the receptors DC-SIGN and DC-SIGNR. *Journal of Biological Chemistry.* 2005, **280**(2), pp.1327-1335.
72. Frison, N., Taylor, M.E., Soilleux, E., Bousser, M.T., Mayer, R., Monsigny, M., Drickamer, K. and Roche, A.C. Oligolysine-based oligosaccharide clusters - Selective recognition and endocytosis by the mannose receptor and dendritic cell-specific intercellular adhesion molecule 3 (ICAM-3)-grabbing nonintegrin. *Journal of Biological Chemistry.* 2003, **278**(26), pp.23922-23929.
73. Svajger, U., Anderluh, M., Jeras, M. and Obermajer, N. C-type lectin DC-SIGN: An adhesion, signalling and antigen-uptake molecule that guides dendritic cells in immunity. *Cellular Signalling.* 2010, **22**(10), pp.1397-1405.
74. Feinberg, H., Castelli, R., Drickamer, K., Seeberger, P.H. and Weis, W.I. Multiple modes of binding enhance the affinity of DC-SIGN for high mannose N-linked glycans found on viral glycoproteins. *Journal of Biological Chemistry.* 2007, **282**(6), pp.4202-4209.

75. Feinberg, H., Mitchell, D.A., Drickamer, K. and Weis, W.I. Structural basis for selective recognition of oligosaccharides by DC-SIGN and DC-SIGNR. *Science.* 2001, **294**(5549), pp.2163-2166.
76. Brzezicka, K., Echeverria, B., Serna, S., van Diepen, A., Hokke, C.H. and Reichardt, N.C. Synthesis and Microarray-Assisted Binding Studies of Core Xylose and Fucose Containing N-Glycans. *Acs Chemical Biology.* 2015, **10**(5), pp.1290-1302.
77. Holla, A. and Skerra, A. Comparative analysis reveals selective recognition of glycans by the dendritic cell receptors DC-SIGN and Langerin. *Protein Engineering Design & Selection.* 2011, **24**(9), pp.659-669.
78. Funatsu, O., Sato, T., Kotovuori, P., Gahmberg, C.G., Ikekita, M. and Furukawa, K. Structural study of N-linked oligosaccharides of human intercellular adhesion molecule-3 (CD50). *European Journal of Biochemistry.* 2001, **268**(4), pp.1020-1029.
79. van Kooyk, Y. and Geijtenbeek, T.B.H. A novel adhesion pathway that regulates dendritic cell trafficking and T cell interactions. *Immunological Reviews.* 2002, **186**, pp.47-56.
80. Guo, Y., Feinberg, H., Conroy, E., Mitchell, D.A., Alvarez, R., Blixt, O., Taylor, M.E., Weis, W.I. and Drickamer, K. Structural basis for distinct ligand-binding and targeting properties of the receptors DC-SIGN and DC-SIGNR. *Nature Structural & Molecular Biology.* 2004, **11**(7), pp.591-598.
81. Simmons, G., Reeves, J.D., Grogan, C.C., Vandenberghe, L.H., Baribaud, F., Whitbeck, J.C., Burke, E., Buchmeier, M.J., Soilleux, E.J., Riley, J.L., Doms, R.W., Bates, P. and Pohlmann, S. DC-SIGN and DC-SIGNR bind Ebola glycoproteins and enhance infection of macrophages and endothelial cells. *Virology.* 2003, **305**(1), pp.115-123.
82. Cambi, A., Gijzen, K., de Vries, J.M., Torensma, R., Joosten, B., Adema, G.J., Netea, M.G., Kullberg, B.J., Romani, L. and Figdor, C.G. The C-type lectin DC-SIGN (CD209) is an antigen-uptake receptor for Candida albicans on dendritic cells. *European Journal of Immunology.* 2003, **33**(2), pp.532-538.
83. van Liempt, E., Bank, C.M.C., Mehta, P., Garcia-Vallejo, J.J., Kawar, Z.S., Geyer, R., Alvarez, R.A., Cummings, R.D., van Kooyk, Y. and van Die, I. Specificity of DC-SIGN for mannose- and fucose-containing glycans. *Febs Letters.* 2006, **580**(26), pp.6123-6131.
84. Azad, A.K., Torrelles, J.B. and Schlesinger, L.S. Mutation in the DC-SIGN cytoplasmic triacidic cluster motif markedly attenuates receptor activity for phagocytosis and endocytosis of mannose-containing ligands by human myeloid cells. *Journal of Leukocyte Biology.* 2008, **84**(6), pp.1594-1603.
85. Garcia-Vallejo, J.J. and van Kooyk, Y. The physiological role of DC-SIGN: A tale of mice and men. *Trends in Immunology.* 2013, **34**(10), pp.482-486.
86. Unger, W.W.J., van Beelen, A.J., Bruijns, S.C., Joshi, M., Fehres, C.M., van Bloois, L., Verstege, M.I., Ambrosini, M., Kalay, H., Nazmi, K., Bolscher, J.G., Hooijberg, E., de Gruijl, T.D., Storm, G. and van Kooyk, Y. Glycan-modified liposomes boost CD4(+) and CD8(+) T-cell responses by targeting DC-SIGN on dendritic cells. *Journal of Controlled Release.* 2012, **160**(1), pp.88-95.
87. Garcia-Vallejo, J.J., van Liempt, E., Martins, P.D., Beckers, C., van het Hof, B., Gringhuis, S.I., Zwaginga, J.J., van Dijk, W., Geijtenbeek, T.B.H., van Kooyk, Y. and van Die, I. DC-SIGN mediates adhesion and rolling of dendritic cells on primary human umbilical vein endothelial cells through Lewis(Y) antigen expressed on ICAM-2. *Molecular Immunology.* 2008, **45**(8), pp.2359-2369.
88. van Gisbergen, K., Sanchez-Hernandez, M., Geijtenbeek, T.B.H. and van Kooyk, Y. Neutrophils mediate immune modulation of dendritic cells through glycosylation-dependent interactions between Mac-1 and DC-SIGN. *Journal of Experimental Medicine.* 2005, **201**(8), pp.1281-1292.
89. Bergman, M.P., Engering, A., Smits, H.H., van Vliet, S.J., van Bodegraven, A.A., Wirth, H.P., Kapsenberg, M.L., Vandenbroucke-Grauls, C., van Kooyk, Y. and Appelmelk, B.J. Helicobacter pylori modulates the T helper cell 1/T helper

cell 2 balance through phase-variable interaction between lipopolysaccharide and DC-SIGN. *Journal of Experimental Medicine.* 2004, **200**(8), pp.979-990.
90. Smits, H.H., Engering, A., van der Kleij, D., de Jong, E.C., Schipper, K., van Capel, T.M.M., Zaat, B.A.J., Yazdanbakhsh, M., Wierenga, E.A., van Kooyk, Y. and Kapsenberg, M.L. Selective probiotic bacteria induce IL-10-producing regulatory T cells in vitro by modulating dendritic cell function through dendritic cell-specific intercellular adhesion molecule 3-grabbing nonintegrin. *Journal of Allergy and Clinical Immunology.* 2005, **115**(6), pp.1260-1267.
91. Steeghs, L., van Vliet, S.J., Uronen-Hansson, H., van Mourik, A., Engering, A., Sanchez-Hernandez, M., Klein, N., Callard, R., van Putten, J.P.M., van der Ley, P., van Kooyk, Y. and van de Winkel, J.G.J. Neisseria meningitidis expressing lgtB lipopolysaccharide targets DC-SIGN and modulates dendritic cell function. *Cellular Microbiology.* 2006, **8**(2), pp.316-325.
92. Gringhuis, S.I., Kaptein, T.M., Wevers, B.A., Mesman, A.W. and Geijtenbeek, T.B.H. Fucose-specific DC-SIGN signalling directs T helper cell type-2 responses via IKK epsilon- and CYLD-dependent Bcl3 activation. *Nature Communications.* 2014, **5**.
93. Geijtenbeek, T.B.H. and Gringhuis, S.I. Signalling through C-type lectin receptors: shaping immune responses. *Nature Reviews Immunology.* 2009, **9**(7), pp.465-479.
94. Geijtenbeek, T.B.H., van Vliet, S.J., Koppel, E.A., Sanchez-Hernandez, M., Vandenbroucke-Grauls, C., Appelmelk, B. and van Kooyk, Y. Mycobacteria target DC-SIGN to suppress dendritic cell function. *Journal of Experimental Medicine.* 2003, **197**(1), pp.7-17.
95. Turner, J. and Torrelles, J.B. Mannose-capped lipoarabinomannan in Mycobacterium tuberculosis pathogenesis. *Pathogens and Disease.* 2018, **76**(4).
96. Schoen, A. and Freire, E. Thermodynamics of intersubunit interactions in cholera toxin upon binding to the oligosaccharide portion of its cell surface receptor, ganglioside GM1. *Biochemistry.* 1989, **28**(12), pp.5019-5024.
97. Dam, T.K. and Brewer, C.F. Chapter 5 - Multivalent Lectin—Carbohydrate Interactions: Energetics and Mechanisms of Binding. In: Horton, D. ed. *Advances in Carbohydrate Chemistry and Biochemistry*. Academic Press, 2010, pp.139-164.
98. Mansoori, G.A. and Soelaiman, T.A.F. *Nanotechnology--An introduction for the standards community.* ASTM International Chicago, IL, USA, 2005.
99. Bayda, S., Adeel, M., Tuccinardi, T., Cordani, M. and Rizzolio, F. The History of Nanoscience and Nanotechnology: From Chemical–Physical Applications to Nanomedicine. *Molecules.* [Online]. 2020. **25**(1).
100. Feynman, R. There's plenty of room at the bottom. In: *Feynman and computation*. CRC Press, 2018, pp.63-76.
101. Seeman, N.C. Nucleic acid junctions and lattices. *Journal of Theoretical Biology.* 1982, **99**(2), pp.237-247.
102. Rothemund, P.W.K. Folding DNA to create nanoscale shapes and patterns. *Nature.* 2006, **440**(7082), pp.297-302.
103. Singh, A. and Amiji, M.M. Application of nanotechnology in medical diagnosis and imaging. *Current Opinion in Biotechnology.* 2022, **74**, pp.241-246.
104. Reichardt, N.C., Martín-Lomas, M. and Penadés, S. Glyconanotechnology. *Chemical Society Reviews.* 2013, **42**(10), pp.4358-4376.
105. Katz, E. and Willner, I. Integrated Nanoparticle–Biomolecule Hybrid Systems: Synthesis, Properties, and Applications. *Angewandte Chemie International Edition.* 2004, **43**(45), pp.6042-6108.
106. Niikura, K., Matsunaga, T., Suzuki, T., Kobayashi, S., Yamaguchi, H., Orba, Y., Kawaguchi, A., Hasegawa, H., Kajino, K., Ninomiya, T., Ijiro, K. and Sawa, H. Gold Nanoparticles as a Vaccine Platform: Influence of Size and Shape on Immunological Responses in Vitro and in Vivo. *ACS Nano.* 2013, **7**(5), pp.3926-3938.

107. Ojeda, R., de Paz, J.L., Barrientos, A.G., Martín-Lomas, M. and Penadés, S. Preparation of multifunctional glyconanoparticles as a platform for potential carbohydrate-based anticancer vaccines. *Carbohydrate Research.* 2007, **342**(3), pp.448-459.
108. Khan, H., Mirzaei, H.R., Amiri, A., Kupeli Akkol, E., Ashhad Halimi, S.M. and Mirzaei, H. Glyco-nanoparticles: New drug delivery systems in cancer therapy. *Seminars in Cancer Biology.* 2021, **69**, pp.24-42.
109. Losada-Garcia, N., Garcia-Sanz, C., Andreu, A., Velasco-Torrijos, T. and Palomo, J.M. Glyconanomaterials for Human Virus Detection and Inhibition. *Nanomaterials.* [Online]. 2021. **11**(7).
110. Durka, M., Buffet, K., Iehl, J., Holler, M., Nierengarten, J.-F., Taganna, J., Bouckaert, J. and Vincent, S.P. The functional valency of dodecamannosylated fullerenes with Escherichia coli FimH—towards novel bacterial antiadhesives. *Chemical Communications.* 2011, **47**(4), pp.1321-1323.
111. Vaidya, S.P. and Patra, M. Platinum glycoconjugates: “Sweet bullets” for targeted cancer therapy? *Current Opinion in Chemical Biology.* 2023, **72**, p.102236.
112. Brinãs, R.P., Sundgren, A., Sahoo, P., Morey, S., Rittenhouse-Olson, K., Wilding, G.E., Deng, W. and Barchi, J.J., Jr. Design and Synthesis of Multifunctional Gold Nanoparticles Bearing Tumor-Associated Glycopeptide Antigens as Potential Cancer Vaccines. *Bioconjugate Chemistry.* 2012, **23**(8), pp.1513-1523.
113. Ohyanagi, T., Nagahori, N., Shimawaki, K., Hinou, H., Yamashita, T., Sasaki, A., Jin, T., Iwanaga, T., Kinjo, M. and Nishimura, S.-I. Importance of Sialic Acid Residues Illuminated by Live Animal Imaging Using Phosphorylcholine Self-Assembled Monolayer-Coated Quantum Dots. *Journal of the American Chemical Society.* 2011, **133**(32), pp.12507-12517.
114. Perrier, M., Gary-Bobo, M., Lartigue, L., Brevet, D., Morère, A., Garcia, M., Maillard, P., Raehm, L., Guari, Y., Larionova, J., Durand, J.-O., Mongin, O. and Blanchard-Desce, M. Mannose-functionalized porous silica-coated magnetic nanoparticles for two-photon imaging or PDT of cancer cells. *Journal of Nanoparticle Research.* 2013, **15**(5), p.1602.
115. Budhadev, D., Poole, E., Nehlmeier, I., Liu, Y.Y., Hooper, J., Kalverda, E., Akshath, U.S., Hondow, N., Turnbull, W.B., Pohlmann, S., Guo, Y. and Zhou, D.J. Glycan-Gold Nanoparticles as Multifunctional Probes for Multivalent Lectin-Carbohydrate Binding: Implications for Blocking Virus Infection and Nanoparticle Assembly. *Journal of the American Chemical Society.* 2020, **142**(42), pp.18022-18034.
116. Martinez-Avila, O., Hijazi, K., Marradi, M., Clavel, C., Campion, C., Kelly, C. and Penades, S. Gold Manno-Glyconanoparticies: Multivalent Systems to Block HIV-1 gp120 Binding to the Lectin DC-SIGN. *Chemistry-a European Journal.* 2009, **15**(38), pp.9874-9888.
117. Turnbull, W.B., Precious, B.L. and Homans, S.W. Dissecting the cholera toxin-ganglioside GM1 interaction by isothermal titration calorimetry. *Journal of the American Chemical Society.* 2004, **126**(4), pp.1047-1054.
118. Zihlmann, P., Silbermann, M., Sharpe, T., Jiang, X., Mühlethaler, T., Jakob, R., Rabbani, S., Sager, C., Frei, P., Pang, L., Maier, T. and Ernst, B. KinITC-One Method Supports both Thermodynamic and Kinetic SARs as Exemplified on FimH Antagonists. *Chemistry-A European Journal.* 2018, **24**, pp.13049-13057.
119. Guo, Y., Nehlmeier, I., Poole, E., Sakonsinsiri, C., Hondow, N., Brown, A., Li, Q., Li, S., Whitworth, J., Li, Z.J., Yu, A.C., Brydson, R., Turnbull, W.B., Pohlmann, S. and Zhou, D.J. Dissecting Multivalent Lectin-Carbohydrate Recognition Using Polyvalent Multifunctional Glycan-Quantum Dots. *Journal of the American Chemical Society.* 2017, **139**(34), pp.11833-11844.
120. Hooper, J., Liu, Y.Y., Budhadev, D., Ainaga, D.F., Hondow, N., Zhou, D.J. and Guo, Y. Polyvalent Glycan Quantum Dots as a Multifunctional Tool for Revealing Thermodynamic, Kinetic, and Structural Details of Multivalent Lectin-

Glycan Interactions. *Acs Applied Materials & Interfaces.* 2022, **14**(42), pp.47385-47396.
121. Jares-Erijman, E. and Jovin, T. FRET imaging. *Nature Biotechnology.* 2003, **21**, pp.1387-1395.
122. Zhang, H., Feng, G., Guo, Y. and Zhou, D. Robust and specific ratiometric biosensing using a copper-free clicked quantum dot-DNA aptamer sensor. *NANOSCALE.* 2013, **5**, pp.10307-10315.
123. Chen, C. and Hildebrandt, N. Resonance energy transfer to gold nanoparticles: NSET defeats FRET. *Trac-Trends in Analytical Chemistry.* 2020, **123**.
124. Kus-Liśkiewicz, M., Fickers, P. and Ben Tahar, I. Biocompatibility and Cytotoxicity of Gold Nanoparticles: Recent Advances in Methodologies and Regulations. *Int J Mol Sci.* 2021, **22**(20).
125. Ji, X., Song, X., Li, J., Bai, Y., Yang, W. and Peng, X. Size Control of Gold Nanocrystals in Citrate Reduction: The Third Role of Citrate. *Journal of the American Chemical Society.* 2007, **129**(45), pp.13939-13948.
126. Dubertret, B., Calame, M. and Libchaber, A.J. Single-mismatch detection using gold-quenched fluorescent oligonucleotides (vol 19, pg 365, 2001). *Nature Biotechnology.* 2001, **19**(7), pp.680-681.
127. Jennings, T.L., Singh, M.P. and Strouse, G.F. Fluorescent lifetime quenching near d=1.5 nm gold nanoparticles: Probing NSET validity. *Journal of the American Chemical Society.* 2006, **128**(16), pp.5462-5467.
128. Chowdhury, S., Wu, Z., Jaquins-Gerstl, A., Liu, S., Dembska, A., Armitage, B.A., Jin, R. and Peteanu, L.A. Wavelength Dependence of the Fluorescence Quenching Efficiency of Nearby Dyes by Gold Nanoclusters and Nanoparticles: The Roles of Spectral Overlap and Particle Size. *The Journal of Physical Chemistry C.* 2011, **115**(41), pp.20105-20112.
129. Dubertret, B., Calame, M. and Libchaber, A.J. Single-mismatch detection using gold-quenched fluorescent oligonucleotides. *Nature Biotechnology.* 2001, **19**(4), pp.365-370.
130. Basaran, R., Budhadev, D., Kempf, A., Nehlmeier, I., Hondow, N., Pöhlmann, S., Guo, Y. and Zhou, D. Probing scaffold size effects on multivalent lectin–glycan binding affinity, thermodynamics and antiviral properties using polyvalent glycan-gold nanoparticles. *Nanoscale.* 2024.
131. Ning, X., Budhadev, D., Pollastri, S., Nehlmeier, I., Kempf, A., Manfield, I., Turnbull, W.B., Pöhlmann, S., Bernardi, A., Li, X., Guo, Y. and Zhou, D. Polyvalent Glycomimetic-Gold Nanoparticles Revealing Critical Roles of Glycan Display on Multivalent Lectin-Glycan Interaction Biophysics and Antiviral Properties. *JACS Au.* 2024, **4**(8), pp.3295-3309.
132. Ghai, R., Falconer, R. and Collins, B. Applications of isothermal titration calorimetry in pure and applied researchusurvey of the literature from 2010. *Journal of Molecular Recognition.* 2012, **25**, pp.32-52.
133. Cooper, A. Thermodynamic analysis of biomolecular interactions. *Current Opinion in Chemical Biology.* 1999, **3**(5), pp.557-563.
134. Archer, W.R. and Schulz, M.D. Isothermal titration calorimetry: practical approaches and current applications in soft matter. *Soft Matter.* 2020, **16**(38), pp.8760-8774.
135. Wiseman, T., Williston, S., Brandts, J.F. and Lin, L.-N. Rapid measurement of binding constants and heats of binding using a new titration calorimeter. *Analytical Biochemistry.* 1989, **179**(1), pp.131-137.
136. Zhang, Y.-L. and Zhang, Z.-Y. Low-Affinity Binding Determined by Titration Calorimetry Using a High-Affinity Coupling Ligand: A Thermodynamic Study of Ligand Binding to Protein Tyrosine Phosphatase 1B. *Analytical Biochemistry.* 1998, **261**(2), pp.139-148.
137. Tellinghuisen, J. Volume errors in isothermal titration calorimetry. *Analytical biochemistry.* 2004, **333**(2), pp.405-406.

138. Bundle, D.R. and Sigurskjold, B.W. [20] Determination of accurate thermodynamics of binding by titration microcalorimetry. In: *Methods in Enzymology*. Academic Press, 1994, pp.288-305.
139. Turnbull, W. and Daranas, A. On the value of c:: Can low affinity systems be studied by isothermal titration calorimetry? *Journal of the American Chemical Society.* 2003, **125**(48), pp.14859-14866.
140. Huang, Y. and Lapitsky, Y. Determining the Colloidal Behavior of Ionically Cross-Linked Polyelectrolytes with Isothermal Titration Calorimetry. *The Journal of Physical Chemistry B.* 2013, **117**(32), pp.9548-9557.
141. Liyanage, S.H. and Yan, M. Quantification of binding affinity of glyconanomaterials with lectins. *Chemical Communications.* 2020, **56**(88), pp.13491-13505.
142. Wang, X., Matei, E., Gronenborn, A.M., Ramström, O. and Yan, M. Direct Measurement of Glyconanoparticles and Lectin Interactions by Isothermal Titration Calorimetry. *Analytical Chemistry.* 2012, **84**(10), pp.4248-4252.
143. Wang, Z., Chen, G., Lu, J., Hong, L. and Ngai, T. Investigation of the factors affecting the carbohydrate–lectin interaction by ITC and QCM-D. *Colloid and Polymer Science.* 2014, **292**(2), pp.391-398.
144. Reynolds, M., Marradi, M., Imberty, A., Penadés, S. and Pérez, S. Multivalent Gold Glycoclusters: High Affinity Molecular Recognition by Bacterial Lectin PA-IL. *Chemistry – A European Journal.* 2012, **18**(14), pp.4264-4273.
145. Sharma, S., Pradhan, S.S., Gupta, N., Mondal, S., Ghosal, D., Kumar, S., Swamy, M.J. and Saha, S. Synthesis of mannose conjugated biodegradable polyester-based nanocarriers and their binding study with Concanavalin A. *Polymer.* 2024, **308**, p.127324.
146. Schwab, J.H., Bailey, J.B., Gembicky, M. and Stauber, J.M. Programmable synthesis of well-defined, glycosylated iron(ii) supramolecular assemblies with multivalent protein-binding capabilities. *Chemical Science.* 2023, **14**(4), pp.1018-1026.
147. Sha, Q., Fei, J., Tu, C., Liu, B.-F., Hu, Z. and Liu, X. A universal strategy of glyconanoparticle preparation using a bifunctional linker for lectin sensing and cell imaging. *Microchimica Acta.* 2022, **189**(4), p.154.
148. Hone, D.C., Haines, A.H. and Russell, D.A. Rapid, Quantitative Colorimetric Detection of a Lectin Using Mannose-Stabilized Gold Nanoparticles. *Langmuir.* 2003, **19**(17), pp.7141-7144.
149. Sánchez-Pomales, G., Morris, T.A., Falabella, J.B., Tarlov, M.J. and Zangmeister, R.A. A lectin-based gold nanoparticle assay for probing glycosylation of glycoproteins. *Biotechnology and Bioengineering.* 2012, **109**(9), pp.2240-2249.
150. Liu, X., Dai, Q., Austin, L., Coutts, J., Knowles, G., Zou, J., Chen, H. and Huo, Q. A One-Step Homogeneous Immunoassay for Cancer Biomarker Detection Using Gold Nanoparticle Probes Coupled with Dynamic Light Scattering. *Journal of the American Chemical Society.* 2008, **130**(9), pp.2780-2782.
151. Hooper, J., Budhadev, D., Fernandez Ainaga, D.L., Hondow, N., Zhou, D. and Guo, Y. Polyvalent Glycan Functionalized Quantum Nanorods as Mechanistic Probes for Shape-Selective Multivalent Lectin-Glycan Recognition. *ACS Applied Nano Materials.* 2023, **6**(6), pp.4201-4213.
152. Wang, X., Ramström, O. and Yan, M. Quantitative Analysis of Multivalent Ligand Presentation on Gold Glyconanoparticles and the Impact on Lectin Binding. *Analytical Chemistry.* 2010, **82**(21), pp.9082-9089.
153. Pecora, R. Dynamic light scattering measurement of nanometer particles in liquids. *Journal of Nanoparticle Research.* 2000, **2**(2), pp.123-131.
154. Wang, X., Ramström, O. and Yan, M. Dynamic light scattering as an efficient tool to study glyconanoparticle–lectin interactions. *Analyst.* 2011, **136**(20), pp.4174-4178.
155. Guo, Y., Bruce Turnbull, W. and Zhou, D. Chapter Three - Probing Multivalent Protein–Carbohydrate Interactions by Quantum Dot-Förster Resonance Energy

Transfer. In: Imperiali, B. ed. *Methods in Enzymology*. Academic Press, 2018, pp.71-100.
156. Schuck, P. Size-distribution analysis of macromolecules by sedimentation velocity ultracentrifugation and Lamm equation modeling. *Biophysical Journal.* 2000, **78**(3), pp.1606-1619.
157. Rendle, P.M., Seger, A., Rodrigues, J., Oldham, N.J., Bott, R.R., Jones, J.B., Cowan, M.M. and Davis, B.G. Glycodendriproteins: A synthetic glycoprotein mimic enzyme with branched sugar-display potently inhibits bacterial aggregation. *Journal of the American Chemical Society.* 2004, **126**(15), pp.4750-4751.
158. Davis, B.G. Synthesis of glycoproteins. *Chemical Reviews.* 2002, **102**(2), pp.579-601.
159. Li, C. and Wang, L.X. Chemoenzymatic Methods for the Synthesis of Glycoproteins. *Chemical Reviews.* 2018, **118**(17), pp.8359-8413.
160. Otsuka, I., Blanchard, B., Borsali, R., Imberty, A. and Kakuchi, T. Enhancement of Plant and Bacterial Lectin Binding Affinities by Three-Dimensional Organized Cluster Glycosides Constructed on Helical Poly(phenylacetylene) Backbones. *Chembiochem.* 2010, **11**(17), pp.2399-2408.
161. Mitchell, D.A., Zhang, Q., Voorhaar, L., Haddleton, David M., Herath, S., Gleinich, A.S., Randeva, H.S., Crispin, M., Lehnert, H., Wallis, R., Patterson, S. and Becer, C.R. Manipulation of cytokine secretion in human dendritic cells using glycopolymers with picomolar affinity for DC-SIGN. *Chemical Science.* 2017, **8**(10), pp.6974-6980.
162. Turnbull, W.B. and Stoddart, J.F. Design and synthesis of glycodendrimers. *J Biotechnol.* 2002, **90**(3-4), pp.231-255.
163. Imberty, A., Chabre, Y.M. and Roy, R. Glycomimetics and glycodendrimers as high affinity microbial anti-adhesins. *Chemistry-a European Journal.* 2008, **14**(25), pp.7490-7499.
164. Ribeiro-Viana, R., García-Vallejo, J.J., Collado, D., Pérez-Inestrosa, E., Bloem, K., van Kooyk, Y. and Rojo, J. BODIPY-Labeled DC-SIGN-Targeting Glycodendrons Efficiently Internalize and Route to Lysosomes in Human Dendritic Cells. *Biomacromolecules.* 2012, **13**(10), pp.3209-3219.
165. Cecioni, S., Oerthel, V., Iehl, J., Holler, M., Goyard, D., Praly, J.P., Imberty, A., Nierengarten, J.F. and Vidal, S. Synthesis of Dodecavalent Fullerene-Based Glycoclusters and Evaluation of Their Binding Properties towards a Bacterial Lectin. *Chemistry-a European Journal.* 2011, **17**(11), pp.3252-3261.
166. Nierengarten, J.F., Iehl, J., Oerthel, V., Holler, M., Illescas, B.M., Munoz, A., Martin, N., Rojo, J., Sanchez-Navarro, M., Cecioni, S., Vidal, S., Buffet, K., Durka, M. and Vincent, S.P. Fullerene sugar balls. *Chemical Communications.* 2010, **46**(22), pp.3860-3862.
167. Mouline, Z., Mahon, E., Gomez, E., Barragan-Montero, V., Montero, J.L. and Barboiu, M. Entropy-driven lectin-recognition of multivalent glycovesicles. *Chemical Communications.* 2014, **50**(6), pp.731-733.
168. Spinelli, N., Defrancq, E. and Morvan, F. Glycoclusters on oligonucleotide and PNA scaffolds: synthesis and applications. *Chemical Society Reviews.* 2013, **42**(11), pp.4557-4573.
169. Muller, C., Despras, G. and Lindhorst, T.K. Organizing multivalency in carbohydrate recognition. *Chemical Society Reviews.* 2016, **45**(11), pp.3275-3302.
170. Marradi, M., Martin-Lomas, M. and Penades, S. Glyconanoparticles: Polyvalent tools to study carbohydrate based interactions. *Advances in Carbohydrate Chemistry and Biochemistry, Vol 64.* 2010, **64**, pp.211-290.
171. Kim, M., Lee, J.-H. and Nam, J.-M. Plasmonic Photothermal Nanoparticles for Biomedical Applications. *Advanced Science.* 2019, **6**(17), p.1900471.
172. Farr, T.D., Lai, C.-H., Grünstein, D., Orts-Gil, G., Wang, C.-C., Boehm-Sturm, P., Seeberger, P.H. and Harms, C. Imaging Early Endothelial Inflammation

Following Stroke by Core Shell Silica Superparamagnetic Glyconanoparticles That Target Selectin. *Nano Letters.* 2014, **14**(4), pp.2130-2134.

173. Smith, A.M., Duan, H., Mohs, A.M. and Nie, S. Bioconjugated quantum dots for in vivo molecular and cellular imaging. *Advanced Drug Delivery Reviews.* 2008, **60**(11), pp.1226-1240.
174. Martínez-Ávila, O., Bedoya, L.M., Marradi, M., Clavel, C., Alcamí, J. and Penadés, S. Multivalent Manno-Glyconanoparticles Inhibit DC-SIGN-Mediated HIV-1 Trans-Infection of Human T Cells. *ChemBioChem.* 2009, **10**(11), pp.1806-1809.
175. Delaunay, C., Pollastri, S., Thépaut, M., Cavazzoli, G., Belvisi, L., Bouchikri, C., Labiod, N., Lasala, F., Gimeno, A., Franconetti, A., Jiménez-Barbero, J., Ardá, A., Delgado, R., Bernardi, A. and Fieschi, F. Unprecedented selectivity for homologous lectin targets: differential targeting of the viral receptors L-SIGN and DC-SIGN. *Chemical Science.* 2024, **15**(37), pp.15352-15366.
176. Viljoen, A., Vercellone, A., Chimen, M., Gaibelet, G., Mazères, S., Nigou, J. and Dufrêne, Y.F. Nanoscale clustering of mycobacterial ligands and DC-SIGN host receptors are key determinants for pathogen recognition. *Science Advances.* 2023, **9**(20), p.eadf9498.
177. Bansal, S.A., Kumar, V., Karimi, J., Singh, A.P. and Kumar, S. Role of gold nanoparticles in advanced biomedical applications. *Nanoscale Advances.* 2020, **2**(9), pp.3764-3787.
178. Arosio, D., Chiodo, F., Reina, J.J., Marelli, M., Penades, S., van Kooyk, Y., Garcia-Vallejo, J.J. and Bernardi, A. Effective Targeting of DC-SIGN by alpha-Fucosylamide Functionalized Gold Nanoparticles. *Bioconjugate Chemistry.* 2014, **25**(12), pp.2244-2251.
179. Love, J.C., Estroff, L.A., Kriebel, J.K., Nuzzo, R.G. and Whitesides, G.M. Self-assembled monolayers of thiolates on metals as a form of nanotechnology. *Chemical Reviews.* 2005, **105**(4), pp.1103-1169.
180. Hill, H.D., Millstone, J.E., Banholzer, M.J. and Mirkin, C.A. The Role Radius of Curvature Plays in Thiolated Oligonucleotide Loading on Gold Nanoparticles. *ACS Nano.* 2009, **3**(2), pp.418-424.
181. Porkolab, V., Lepšík, M., Ordanini, S., St John, A., Le Roy, A., Thépaut, M., Paci, E., Ebel, C., Bernardi, A. and Fieschi, F. Powerful Avidity with a Limited Valency for Virus-Attachment Blockers on DC-SIGN: Combining Chelation and Statistical Rebinding with Structural Plasticity of the Receptor. *ACS Central Science.* 2023, **9**(4), pp.709-718.
182. Velazquez-Campoy, A. and Freire, E. Isothermal titration calorimetry to determine association constants for high-affinity ligands. *Nature Protocols.* 2006, **1**(1), pp.186-191.
183. Porkolab, V., Pifferi, C., Sutkeviciute, I., Ordanini, S., Taouai, M., Thépaut, M., Vivès, C., Benazza, M., Bernardi, A., Renaudet, O. and Fieschi, F. Development of C-type lectin-oriented surfaces for high avidity glycoconjugates: towards mimicking multivalent interactions on the cell surface. *Organic & Biomolecular Chemistry.* 2020, **18**(25), pp.4763-4772.
184. Cambi , A., de Lange , F., van Maarseveen , N.M., Nijhuis , M., Joosten , B., van Dijk , E.M.H.P., de Bakker , B.r.l., Fransen , J.A.M., Bovee-Geurts , P.H.M., van Leeuwen , F.N., Van Hulst , N.F. and Figdor , C.G. Microdomains of the C-type lectin DC-SIGN are portals for virus entry into dendritic cells. *Journal of Cell Biology.* 2004, **164**(1), pp.145-155.
185. Yun, C.S., Javier, A., Jennings, T., Fisher, M., Hira, S., Peterson, S., Hopkins, B., Reich, N.O. and Strouse, G.F. Nanometal Surface Energy Transfer in Optical Rulers, Breaking the FRET Barrier. *Journal of the American Chemical Society.* 2005, **127**(9), pp.3115-3119.
186. Chakroun, K., Taouai, M., Porkolab, V., Luczkowiak, J., Sommer, R., Cheneau, C., Mathiron, D., Ben Maaouia, M.A., Pilard, S., Abidi, R., Mullié, C., Fieschi, F., Cragg, P.J., Halary, F., Delgado, R. and Benazza, M. Low-Valent Calix[4]arene Glycoconjugates Based on Hydroxamic Acid Bearing Linkers as Potent

Inhibitors in a Model of Ebola Virus Cis-Infection and HCMV-gB-Recombinant Glycoprotein Interaction with MDDC Cells by Blocking DC-SIGN. *Journal of Medicinal Chemistry.* 2021, **64**(19), pp.14332-14343.

187. Martínez-Bailén, M., Rojo, J. and Ramos-Soriano, J. Multivalent glycosystems for human lectins. *Chemical Society Reviews.* 2023, **52**(2), pp.536-572.
188. Bachem, G., Wamhoff, E.-C., Silberreis, K., Kim, D., Baukmann, H., Fuchsberger, F., Dernedde, J., Rademacher, C. and Seitz, O. Rational Design of a DNA-Scaffolded High-Affinity Binder for Langerin. *Angewandte Chemie International Edition.* 2020, **59**(47), pp.21016-21022.
189. van Heteren, J. and Pieters, R.J. Chapter Nine - Carbohydrate-protein interactions: Enhancing multivalency effects through statistical rebinding. In: Tiwari, V.K. ed. *Carbohydrates in Drug Discovery and Development*. Elsevier, 2020, pp.383-402.
190. Ordanini, S., Varga, N., Porkolab, V., Thépaut, M., Belvisi, L., Bertaglia, A., Palmioli, A., Berzi, A., Trabattoni, D., Clerici, M., Fieschi, F. and Bernardi, A. Designing nanomolar antagonists of DC-SIGN-mediated HIV infection: ligand presentation using molecular rods. *Chemical Communications.* 2015, **51**(18), pp.3816-3819.
191. Liebau, J., Laatsch, B.F., Rusnak, J., Gunderson, K., Finke, B., Bargender, K., Narkiewicz-Jodko, A., Weeks, K., Williams, M.T., Shulgina, I., Musier-Forsyth, K., Bhattacharyya, S. and Hati, S. Polyethylene Glycol Impacts Conformation and Dynamics of Escherichia coli Prolyl-tRNA Synthetase Via Crowding and Confinement Effects. *Biochemistry.* 2024, **63**(13), pp.1621-1635.
192. Soilleux, E.J., Barten, R. and Trowsdale, J. Cutting edge: DC-SIGN; a related gene, DC-SIGNR; and CD23 form a cluster on 19p13. *Journal of Immunology.* 2000, **165**(6), pp.2937-2942.
193. Pöhlmann, S., Baribaud, F., Lee, B., Leslie, G.J., Sanchez, M.D., Hiebenthal-Millow, K., Münch, J., Kirchhoff, F. and Doms, R.W. DC-SIGN interactions with human immunodeficiency virus type 1 and 2 and simian immunodeficiency virus. *Journal of Virology.* 2001, **75**(10), pp.4664-4672.
194. Chung, N.P.Y., Breun, S.K.J., Bashirova, A., Baumann, J.G., Martin, T.D., Karamchandani, J.M., Rausch, J.W., Le Grice, S.F.J., Wu, L., Carrington, M. and KewalRamani, V.N. HIV-1 Transmission by Dendritic Cell-specific ICAM-3-grabbing Nonintegrin (DC-SIGN) Is Regulated by Determinants in the Carbohydrate Recognition Domain That Are Absent in Liver/Lymph Node-SIGN (L-SIGN). *Journal of Biological Chemistry.* 2010, **285**(3), pp.2100-2112.
195. Davis, C.W., Nguyen, H.Y., Hanna, S.L., Sánchez, M.D., Doms, R.W. and Pierson, T.C. West Nile virus discriminates between DC-SIGN and DC-SIGNR for cellular attachment and infection. *Journal of Virology.* 2006, **80**(3), pp.1290-1301.
196. Howell, K.A., Brannan, J.M., Bryan, C., McNeal, A., Davidson, E., Turner, H.L., Vu, H., Shulenin, S., He, S., Kuehne, A., Herbert, A.S., Qiu, X., Doranz, B.J., Holtsberg, F.W., Ward, A.B., Dye, J.M. and Aman, M.J. Cooperativity Enables Non-neutralizing Antibodies to Neutralize Ebolavirus. *Cell Reports.* 2017, **19**(2), pp.413-424.
197. Sampah, M.E.S., Shen, L., Jilek, B.L. and Siliciano, R.F. Dose–response curve slope is a missing dimension in the analysis of HIV-1 drug resistance. *Proceedings of the National Academy of Sciences.* 2011, **108**(18), pp.7613-7618.
198. Muñoz, A., Sigwalt, D., Illescas, B.M., Luczkowiak, J., Rodríguez-Pérez, L., Nierengarten, I., Holler, M., Remy, J.-S., Buffet, K., Vincent, S.P., Rojo, J., Delgado, R., Nierengarten, J.-F. and Martín, N. Synthesis of giant globular multivalent glycofullerenes as potent inhibitors in a model of Ebola virus infection. *Nature Chemistry.* 2016, **8**(1), pp.50-57.
199. Ribeiro-Viana, R., Sánchez-Navarro, M., Luczkowiak, J., Koeppe, J.R., Delgado, R., Rojo, J. and Davis, B.G. Virus-like glycodendrinanoparticles

displaying quasi-equivalent nested polyvalency upon glycoprotein platforms potently block viral infection. *Nature Communications.* 2012, **3**(1), p.1303.
200. McGonagle, D., Watad, A., Sharif, K. and Bridgewood, C. Why Inhibition of IL-23 Lacked Efficacy in Ankylosing Spondylitis. *Front Immunol.* 2021, **12**, p.614255.
201. Delves, P.J. and Roitt, I.M. The immune system - First of two parts. *New England Journal of Medicine.* 2000, **343**(1), pp.37-49.
202. Ueno, H., Klechevsky, E., Morita, R., Aspord, C., Cao, T., Matsui, T., Di Pucchio, T., Connolly, J., Fay, J.W., Pascual, V., Palucka, A.K. and Banchereau, J. Dendritic cell subsets in health and disease. *Immunological Reviews.* 2007, **219**, pp.118-142.
203. Medzhitov, R. Recognition of microorganisms and activation of the immune response. *Nature.* 2007, **449**(7164), pp.819-826.
204. Nish, S. and Medzhitov, R. Host Defense Pathways: Role of Redundancy and Compensation in Infectious Disease Phenotypes. *Immunity.* 2011, **34**(5), pp.629-636.
205. Kawai, T. and Akira, S. Toll-like Receptors and Their Crosstalk with Other Innate Receptors in Infection and Immunity. *Immunity.* 2011, **34**(5), pp.637-650.
206. Banchereau, J. and Steinman, R.M. Dendritic cells and the control of immunity. *Nature.* 1998, **392**(6673), pp.245-252.
207. Geijtenbeek, T.B.H. and Gringhuis, S.I. C-type lectin receptors in the control of T helper cell differentiation. *Nature Reviews Immunology.* 2016, **16**(7), pp.433-448.
208. Janeway, C.A. and Bottomly, K. Signals and signs for lymphocyte-responses. *Cell.* 1994, **76**(2), pp.275-285.
209. van der Merwe, P.A. and Dushek, O. Mechanisms for T cell receptor triggering. *Nature Reviews Immunology.* 2011, **11**(1), pp.47-55.
210. Turner, S.J., La Gruta, N.L., Kedzierska, K., Thomas, P.G. and Doherty, P.C. Functional implications of T cell receptor diversity. *Current Opinion in Immunology.* 2009, **21**(3), pp.286-290.
211. Arstila, T.P., Casrouge, A., Baron, V., Even, J., Kanellopoulos, J. and Kourilsky, P. A direct estimate of the human alpha beta T cell receptor diversity. *Science.* 1999, **286**(5441), pp.958-961.
212. Sewell, A.K. Why must T cells be cross-reactive? *Nature Reviews Immunology.* 2012, **12**(9), pp.668-677.
213. Chen, L.P. and Flies, D.B. Molecular mechanisms of T cell co-stimulation and co-inhibition. *Nature Reviews Immunology.* 2013, **13**(4), pp.227-242.
214. Jenkins, M.K., Chen, C., Jung, G., Mueller, D.L. and Schwartz, R.H. Inhibition of antigen-specific proliferation of type-1 murine T-cell clones after stimulation with immobilized anti-CD3 monoclonal-antibody. *Journal of Immunology.* 1990, **144**(1), pp.16-22.
215. Leitner, J., Grabmeier-Pfistershammer, K. and Steinberger, P. Receptors and ligands implicated in human T cell costimulatory processes. *Immunology Letters.* 2010, **128**(2), pp.89-97.
216. Keir, M.E. and Sharpe, A.H. The B7/CD28 costimulatory family in autoimmunity. *Immunological Reviews.* 2005, **204**, pp.128-143.
217. Shahinian, A., Pfeffer, K., Lee, K.P., Kundig, T.M., Kishihara, K., Wakeham, A., Kawai, K., Ohashi, P.S., Thompson, C.B. and Mak, T.W. Differential T-cell costimulatory requirements in CD28-deficient mice. *Science.* 1993, **261**(5121), pp.609-612.
218. Lindsten, T., Lee, K.P., Harris, E.S., Petryniak, B., Craighead, N., Reynolds, P.J., Lombard, D.B., Freeman, G.J., Nadler, L.M., Gray, G.S., Thompson, C.B. and June, C.H. Characterisation of CTLA-4 structure and expression on human T-cells. *Journal of Immunology.* 1993, **151**(7), pp.3489-3499.
219. Teft, W.A., Kirchhof, M.G. and Madrenas, J. A molecular perspective of CTLA-4 function. *Annual Review of Immunology.* 2006, **24**, pp.65-97.

220. Linsley, P.S., Greene, J.L., Brady, W., Bajorath, J., Ledbetter, J.A. and Peach, R. Human B7-1 (CD80) and B7-2 (CD86) bind with similar avidities but distinct kinetics to CD28 and CTLA-4 receptors. *Immunity.* 1994, **1**(9), pp.793-801.
221. vanderMerwe, P.A., Bodian, D.L., Daenke, S., Linsley, P. and Davis, S.J. CD80 (B7-1) binds both CD28 and CTLA-4 with a low affinity and very fast kinetics. *Journal of Experimental Medicine.* 1997, **185**(3), pp.393-403.
222. Rudd, C.E. and Schneider, H. Unifying concepts in CD28, ICOS and CTLA4 co-receptor signalling. *Nature Reviews Immunology.* 2003, **3**(7), pp.544-556.
223. Curtsinger, J.M. and Mescher, M.F. Inflammatory cytokines as a third signal for T cell activation. *Current Opinion in Immunology.* 2010, **22**(3), pp.333-340.
224. Perkins, N.D. The diverse and complex roles of NF-κB subunits in cancer. *Nature Reviews Cancer.* 2012, **12**(2), pp.121-132.
225. Smale, S.T. Dimer-specific regulatory mechanisms within the NF-κB family of transcription factors. *Immunological Reviews.* 2012, **246**(1), pp.193-204.
226. Hayden, M.S. and Ghosh, S. Shared Principles in NF-κB Signaling. *Cell.* 2008, **132**(3), pp.344-362.
227. Staudt, L.M. Oncogenic activation of NF-kappaB. *Cold Spring Harb Perspect Biol.* 2010, **2**(6), p.a000109.
228. Zhang, Q., Lenardo, M.J. and Baltimore, D. 30 Years of NF-κB: A Blossoming of Relevance to Human Pathobiology. *Cell.* 2017, **168**(1), pp.37-57.
229. Medzhitov, R. and Horng, T. Transcriptional control of the inflammatory response. *Nature Reviews Immunology.* 2009, **9**(10), pp.692-703.
230. Sun, S.-C. The non-canonical NF-κB pathway in immunity and inflammation. *Nature Reviews Immunology.* 2017, **17**(9), pp.545-558.
231. Zhu, J.F., Yamane, H. and Paul, W.E. Differentiation of Effector CD4 T Cell Populations. *Annual Review of Immunology, Vol 28.* 2010, **28**, pp.445-489.
232. Legros, G., Bensasson, S.Z., Seder, R., Finkelman, F.D. and Paul, W.E. Generation of interleukin-4 (IL-4)-producing cells in vivo and invitro - IL-2 and IL-4 are required for invitro generation of IL-4-producing cells. *Journal of Experimental Medicine.* 1990, **172**(3), pp.921-929.
233. Swain, S.L., Weinberg, A.D., English, M. and Huston, G. IL-4 directs the development of TH2-like helper effectors. *Journal of Immunology.* 1990, **145**(11), pp.3796-3806.
234. Seder, R.A., Paul, W.E., Davis, M.M. and Fazekas De St Groth, B. The presence of interleukin-4 during invitro priming determines the lymphokine-producing potential of CD4+ T-cells from T-cell receptor transgenic mice. *Journal of Experimental Medicine.* 1992, **176**(4), pp.1091-1098.
235. Hsieh, C.-S., Macatonia, S.E., Tripp, C.S., Wolf, S.F., O'Garra, A. and Murphy, K.M. Development of TH1 CD4+ T Cells Through IL-12 Produced by Listeria-Induced Macrophages. *Science.* 1993, **260**(5107), pp.547-549.
236. de Jong, E.C., Vieira, P.L., Kalinski, P., Schuitemaker, J.H.N., Tanaka, Y., Wierenga, E.A., Yazdanbakhsh, M. and Kapsenberg, M.L. Microbial compounds selectively induce Th1 cell-promoting or Th2 cell-promoting dendritic cells in vitro with diverse Th cell-polarizing signals. *Journal of Immunology.* 2002, **168**(4), pp.1704-1709.
237. d'Ostiani, C.F., Del Sero, G., Bacci, A., Montagnoli, C., Spreca, A., Mencacci, A., Ricciardi-Castagnoli, P. and Romani, L. Dendritic cells discriminate between yeasts and hyphae of the fungus Candida albicans: Implications for initiation of T helper cell immunity in vitro and in vivo. *Journal of Experimental Medicine.* 2000, **191**(10), pp.1661-1673.
238. Pulendran, B., Tang, H. and Manicassamy, S. Programming dendritic cells to induce T(H)2 and tolerogenic responses. *Nature Immunology.* 2010, **11**(8), pp.647-655.
239. Wilson, C.B., Rowell, E. and Sekimata, M. Epigenetic control of T-helper-cell differentiation. *Nature Reviews Immunology.* 2009, **9**(2), pp.91-105.

240. Kaplan, M.H., Sun, Y.L., Hoey, T. and Grusby, M.J. Impaired IL-12 responses and enhanced development of Th2 cells in Stat4-deficient mice. *Nature.* 1996, **382**(6587), pp.174-177.
241. Ouyang, W.J., Kolls, J.K. and Zheng, Y. The biological functions of T helper 17 cell effector cytokines in inflammation. *Immunity.* 2008, **28**(4), pp.454-467.
242. Bettelli, E., Carrier, Y.J., Gao, W.D., Korn, T., Strom, T.B., Oukka, M., Weiner, H.L. and Kuchroo, V.K. Reciprocal developmental pathways for the generation of pathogenic effector T(H)17 and regulatory T cells. *Nature.* 2006, **441**(7090), pp.235-238.
243. Hilligan, K.L. and Ronchese, F. Antigen presentation by dendritic cells and their instruction of CD4+T helper cell responses. *Cellular & Molecular Immunology.* 2020, **17**(6), pp.587-599.
244. Lubberts, E. The IL-23-IL-17 axis in inflammatory arthritis. *Nature Reviews Rheumatology.* 2015, **11**(7), pp.415-429.
245. Bridgewood, C., Sharif, K., Sherlock, J., Watad, A. and McGonagle, D. Interleukin-23 pathway at the enthesis: The emerging story of enthesitis in spondyloarthropathy. *Immunological Reviews.* 2020, **294**(1), pp.27-47.
246. Langrish, C.L., Chen, Y., Blumenschein, W.M., Mattson, J., Basham, B., Sedgwick, J.D., McClanahan, T., Kastelein, R.A. and Cua, D.J. IL-23 drives a pathogenic T cell population that induces autoimmune inflammation. *Journal of Experimental Medicine.* 2005, **201**(2), pp.233-240.
247. Magee, C.N., Boenisch, O. and Najafian, N. The Role of Costimulatory Molecules in Directing the Functional Differentiation of Alloreactive T Helper Cells. *American Journal of Transplantation.* 2012, **12**(10), pp.2588-2600.
248. Fazilleau, N., Mark, L., McHeyzer-Williams, L.J. and McHeyzer-Williams, M.G. Follicular Helper T Cells: Lineage and Location. *Immunity.* 2009, **30**(3), pp.324-335.
249. Nur, S., Sparber, F., Lemberg, C., Guiducci, E., Schweizer, T.A., Zwicky, P., Becher, B. and LeibundGut-Landmann, S. IL-23 supports host defense against systemic Candida albicans infection by ensuring myeloid cell survival. *Plos Pathogens.* 2019, **15**(12).
250. Fahlquist-Hagert, C., Sareila, O., Rosendahl, S. and Holmdahl, R. Variants of beta-glucan polysaccharides downregulate autoimmune inflammation. *Communications Biology.* 2022, **5**(1).
251. Kumar, R., Sharma, A. and Dogra, S. Prevalence and clinical patterns of psoriatic arthritis in Indian patients with psoriasis. *Indian Journal of Dermatology Venereology & Leprology.* 2014, **80**(1), pp.15-23.
252. Gandhi, M., Alwawi, E. and Gordon, K.B. Anti-p40 Antibodies Ustekinumab and Briakinumab: Blockade of Interleukin-12 and Interleukin-23 in the Treatment of Psoriasis. *Seminars in Cutaneous Medicine and Surgery.* 2010, **29**(1), pp.48-52.
253. Oppmann, B., Lesley, R., Blom, B., Timans, J.C., Xu, Y.M., Hunte, B., Vega, F., Yu, N., Wang, J., Singh, K., Zonin, F., Vaisberg, E., Churakova, T., Liu, M.R., Gorman, D., Wagner, J., Zurawski, S., Liu, Y.J., Abrams, J.S., Moore, K.W., Rennick, D., de Waal-Malefyt, R., Hannum, C., Bazan, J.F. and Kastelein, R.A. Novel p19 protein engages IL-12p40 to form a cytokine, IL-23, with biological activities similar as well as distinct from IL-12. *Immunity.* 2000, **13**(5), pp.715-725.
254. Hasegawa, H., Mizoguchi, I., Chiba, Y., Ohashi, M., Xu, M.L. and Yoshimoto, T. Expanding Diversity in Molecular Structures and Functions of the IL-6/IL-12 Heterodimeric Cytokine Family. *Frontiers in Immunology.* 2016, **7**.
255. Vignali, D.A.A. and Kuchroo, V.K. IL-12 family cytokines: immunological playmakers. *Nature Immunology.* 2012, **13**(8), pp.722-728.
256. Gately, M.K., Renzetti, L.M., Magram, J., Stern, A.S., Adorini, L., Gubler, U. and Presky, D.H. The interleukin-12/interleukin-12-receptor system: Role in normal and pathologic immune responses. *Annual Review of Immunology.* 1998, **16**, pp.495-521.

257. Pflanz, S., Timans, J.C., Cheung, J., Rosales, R., Kanzler, H., Gilbert, J., Hibbert, L., Churakova, T., Travis, M., Vaisberg, E., Blumenschein, W.M., Mattson, J.D., Wagner, J.L., To, W., Zurawski, S., McClanahan, T.K., Gorman, D.M., Bazan, J.F., Malefyt, R.D., Rennick, D. and Kastelein, R.A. IL-27, a heterodimeric cytokine composed of EB13 and p28 protein, induces proliferation of naive CD4(+) T cells. *Immunity.* 2002, **16**(6), pp.779-790.
258. Collison, L.W., Workman, C.J., Kuo, T.T., Boyd, K., Wang, Y., Vignali, K.M., Cross, R., Sehy, D., Blumberg, R.S. and Vignali, D.A.A. The inhibitory cytokine IL-35 contributes to regulatory T-cell function. *Nature.* 2007, **450**(7169), pp.566-U519.
259. McKenzie, B.S., Kastelein, R.A. and Cua, D.J. Understanding the IL-23-IL-17 immune pathway. *Trends in Immunology.* 2006, **27**(1), pp.17-23.
260. Athie-Morales, V., Smits, H.H., Cantrell, D.A. and Hilkens, C.M.U. Sustained IL-12 signaling is required for Th1 development. *Journal of Immunology.* 2004, **172**(1), pp.61-69.
261. Chua, A.O., Chizzonite, R., Desai, B.B., Truitt, T.P., Nunes, P., Minetti, L.J., Warrier, R.R., Presky, D.H., Levine, J.F., Gately, M.K. and Gubler, U. Expression cloning of a human IL-12 receptor component a new member of the cytokine receptor superfamily with strong homology to gp130. *Journal of Immunology.* 1994, **153**(1), pp.128-136.
262. Collison, L.W. and Vignali, D.A.A. Interleukin-35: odd one out or part of the family? *Immunological Reviews.* 2008, **226**, pp.248-262.
263. Wiekowski, M.T., Leach, M.W., Evans, E.W., Sullivan, L., Chen, S.C., Vassileva, G., Bazan, J.F., Gorman, D.M., Kastelein, R.A., Narula, S. and Lira, S.A. Ubiquitous transgenic expression of the IL-23 subunit p19 induces multiorgan inflammation, runting, infertility, and premature death. *Journal of Immunology.* 2001, **166**(12), pp.7563-7570.
264. Romagnani, S., Maggi, E., Liotta, F., Cosmi, L. and Annunziato, F. Properties and origin of human Th17 cells. *Molecular Immunology.* 2009, **47**(1), pp.3-7.
265. Parham, C., Chirica, M., Timans, J., Vaisberg, E., Travis, M., Cheung, J., Pflanz, S., Zhang, R., Singh, K.P., Vega, F., To, W., Wagner, J., O'Farrell, A.M., McClanahan, T., Zurawski, S., Hannum, C., Gorman, D., Rennick, D.M., Kastelein, R.A., Malefyt, R.D. and Moore, K.W. A receptor for the heterodimeric cytokine IL-23 is composed of IL-12R beta 1 and a novel cytokine receptor subunit, IL-23R. *Journal of Immunology.* 2002, **168**(11), pp.5699-5708.
266. Stumhofer, J.S., Silver, J.S., Laurence, A., Porrett, P.M., Harris, T.H., Turka, L.A., Ernst, M., Saris, C.J.M., O'Shea, J.J. and Hunter, C.A. Interleukins 27 and 6 induce STAT3-mediated T cell production of interleukin 10. *Nature Immunology.* 2007, **8**(12), pp.1363-U1365.
267. Xue, C., Yao, Q.F., Gu, X.Y., Shi, Q.M., Yuan, X., Chu, Q.F., Bao, Z.Y., Lu, J. and Li, L.J. Evolving cognition of the JAK-STAT signaling pathway: autoimmune disorders and cancer. *Signal Transduction and Targeted Therapy.* 2023, **8**(1).
268. Raychaudhuri, S.K., Abria, C. and Raychaudhuri, S.P. Regulatory role of the JAK STAT kinase signalling system on the IL-23/IL-17 cytokine axis in psoriatic arthritis. *Annals of the Rheumatic Diseases.* 2017, **76**(10).
269. Hubbard, S.R. and Miller, W.T. Receptor tyrosine kinases: mechanisms of activation and signaling. *Current Opinion in Cell Biology.* 2007, **19**(2), pp.117-123.
270. Mathur, A.N., Chang, H.C., Zisoulis, D.G., Stritesky, G.L., Yu, Q., O'Malley, J.T., Kapur, R., Levy, D.E., Kansas, G.S. and Kaplan, M.H. Stat3 and Stat4 direct development of IL-17-secreting Th cells. *Journal of Immunology.* 2007, **178**(8), pp.4901-4907.
271. Fragoulis, G.E., Siebert, S. and McInnes, I.B. Therapeutic Targeting of IL-17 and IL-23 Cytokines in Immune-Mediated Diseases. *Annual Review of Medicine, Vol 67.* 2016, **67**, pp.337-353.
272. Ciofani, M., Madar, A., Galan, C., Sellars, M., Mace, K., Pauli, F., Agarwal, A., Huang, W.D., Parkurst, C.N., Muratet, M., Newberry, K.M., Meadows, S.,

Greenfield, A., Yang, Y., Jain, P., Kirigin, F.K., Birchmeier, C., Wagner, E.F., Murphy, K.M., Myers, R.M., Bonneau, R. and Littman, D.R. A Validated Regulatory Network for Th17 Cell Specification. *Cell.* 2012, **151**(2), pp.289-303.

273. Veldhoen, M., Hocking, R.J., Atkins, C.J., Locksley, R.M. and Stockinger, B. TGF beta in the context of an inflammatory cytokine milieu supports de novo differentiation of IL-17-producing T cells. *Immunity.* 2006, **24**(2), pp.179-189.
274. Mangan, P.R., Harrington, L.E., O'Quinn, D.B., Helms, W.S., Bullard, D.C., Elson, C.O., Hatton, R.D., Wahl, S.M., Schoeb, T.R. and Weaver, C.T. Transforming growth factor-beta induces development of the T(H)17 lineage. *Nature.* 2006, **441**(7090), pp.231-234.
275. Yang, X.X.O., Panopoulos, A.D., Nurieva, R., Chang, S.H., Wang, D.M., Watowich, S.S. and Dong, C. STAT3 regulates cytokine-mediated generation of inflammatory helper T cells. *Journal of Biological Chemistry.* 2007, **282**(13), pp.9358-9363.
276. Durant, L., Watford, W.T., Ramos, H.L., Laurence, A., Vahedi, G., Wei, L., Takahashi, H., Sun, H.W., Kanno, Y., Powrie, F. and O'Shea, J.J. Diverse Targets of the Transcription Factor STAT3 Contribute to T Cell Pathogenicity and Homeostasis. *Immunity.* 2010, **32**(5), pp.605-615.
277. Sutton, C., Brereton, C., Keogh, B., Mills, K.H.G. and Lavelle, E.C. A crucial role for interleukin (IL)-1 in the induction of IL-17-producing T cells that mediate autoimmune encephalomyelitis. *Journal of Experimental Medicine.* 2006, **203**(7), pp.1685-1691.
278. Pappu, R., Ramirez-Carrozzi, V. and Sambandam, A. The interleukin-17 cytokine family: critical players in host defence and inflammatory diseases. *Immunology.* 2011, **134**(1), pp.8-16.
279. Brembilla, N.C., Senra, L. and Boehncke, W.H. The IL-17 Family of Cytokines in Psoriasis: IL-17A and Beyond. *Frontiers in Immunology.* 2018, **9**.
280. Hymowitz, S.G., Filvaroff, E.H., Yin, J.P., Lee, J., Cai, L.P., Risser, P., Maruoka, M., Mao, W.G., Foster, J., Kelley, R.F., Pan, G.H., Gurney, A.L., de Vos, A.M. and Starovasnik, M.A. IL-17s adopt a cystine knot fold: structure and activity of a novel cytokine, IL-17F, and implications for receptor binding. *Embo Journal.* 2001, **20**(19), pp.5332-5341.
281. Gaffen, S.L. Structure and signalling in the IL-17 receptor family. *Nature Reviews Immunology.* 2009, **9**(8), pp.556-567.
282. Novatchkova, M., Leibbrandt, A., Werzowa, J., Neubuser, A. and Eisenhaber, F. The STIR-domain superfamily in signal transduction, development and immunity. *Trends in Biochemical Sciences.* 2003, **28**(5), pp.226-229.
283. Qian, Y.C., Kang, Z.Z., Liu, C.N. and Li, X.X. IL-17 signaling in host defense and inflammatory diseases. *Cellular & Molecular Immunology.* 2010, **7**(5), pp.328-333.
284. Ye, P., Garvey, P.B., Zhang, P., Nelson, S., Bagby, G., Summer, W.R., Schwarzenberger, P., Shellito, J.E. and Kolls, J.K. Interleukin-17 and lung host defense against Klebsiella pneumoniae infection. *American Journal of Respiratory Cell and Molecular Biology.* 2001, **25**(3), pp.335-340.
285. Happel, K.I., Dubin, P.J., Zheng, M.Q., Ghilardi, N., Lockhart, C., Quinton, L.J., Odden, A.R., Shellito, J.E., Bagby, G.J., Nelson, S. and Kolls, J.K. Divergent roles of IL-23 and IL-12 in host defense against Klebsiella pneumoniae. *Journal of Experimental Medicine.* 2005, **202**(6), pp.761-769.
286. Shibata, K., Yamada, H., Hara, H., Kishihara, K. and Yoshikai, Y. Resident V delta 1(+) gamma delta T cells control early infiltration of neutrophils after Escherichia coli infection via IL-17 production. *Journal of Immunology.* 2007, **178**(7), pp.4466-4472.
287. Yu, J.J., Ruddy, M.J., Wong, G.C., Sfintescu, C., Baker, P.J., Smith, J.B., Evans, R.T. and Gaffen, S.L. An essential role for IL-17 in preventing pathogen-initiated bone destruction: Recruitment of neutrophils to inflamed bone requires IL-17 receptor-dependent signals. *Blood.* 2007, **109**(9), pp.3794-3802.

288. Lu, Y.J., Gross, J., Bogaert, D., Finn, A., Bagrade, L., Zhang, Q., Kolls, J.K., Srivastava, A., Lundgren, A., Forte, S., Thompson, C.M., Harney, K.F., Anderson, P.W., Lipsitch, M. and Malley, R. Interleukin-17A mediates acquired immunity to pneumococcal colonization. *Plos Pathogens.* 2008, **4**(9).
289. Schulz, S.M., Kohler, G., Holscher, C., Iwakura, Y. and Alber, G. IL-17A is produced by T(h)17, gamma delta T cells and other CD4(-) lymphocytes during infection with Salmonella enterica serovar Enteritidis and has a mild effect in bacterial clearance. *International Immunology.* 2008, **20**(9), pp.1129-1138.
290. Conti, H.R. and Gaffen, S.L. IL-17-Mediated Immunity to the Opportunistic Fungal Pathogen Candida albicans. *Journal of Immunology.* 2015, **195**(3), pp.780-788.
291. Kleinschek, M.A., Muller, U., Brodie, S.J., Stenzel, W., Kohler, G., Blumenschein, W.M., Straubinger, R.K., McClanahan, T., Kastelein, R.A. and Alber, G. IL-23 enhances the inflammatory cell response in Cryptococcus neoformans infection and induces a cytokine pattern distinct from IL-12. *Journal of Immunology.* 2006, **176**(2), pp.1098-1106.
292. Rudner, X.L., Happel, K.I., Young, E.A. and Shellito, J.E. Interleukin-23 (IL-23)-IL-17 cytokine axis in murine Pneumocystis carinii infection. *Infection and Immunity.* 2007, **75**(6), pp.3055-3061.
293. Puel, A., Cypowyj, S., Bustamante, J., Wright, J.F., Liu, L.Y., Lim, H.K., Migaud, M., Israel, L., Chrabieh, M., Audry, M., Gumbleton, M., Toulon, A., Bodemer, C., El-Baghdadi, J., Whitters, M., Paradis, T., Brooks, J., Collins, M., Wolfman, N.M., Al-Muhsen, S., Galicchio, M., Abel, L., Picard, C. and Casanova, J.L. Chronic Mucocutaneous Candidiasis in Humans with Inborn Errors of Interleukin-17 Immunity. *Science.* 2011, **332**(6025), pp.65-68.
294. Huang, W.T., Na, L., Fidel, P.L. and Schwarzenberger, P. Requirement of interleukin-17A for systemic anti-Candida albicans host defense in mice. *Journal of Infectious Diseases.* 2004, **190**(3), pp.624-631.
295. Kagami, S., Rizzo, H.L., Kurtz, S.E., Miller, L.S. and Blauvelt, A. IL-23 and IL-17A, but Not IL-12 and IL-22, Are Required for Optimal Skin Host Defense against Candida albicans. *Journal of Immunology.* 2010, **185**(9), pp.5453-5462.
296. Cua, D.J., Sherlock, J., Chen, Y., Murphy, C.A., Joyce, B., Seymour, B., Lucian, L., To, W., Kwan, S., Churakova, T., Zurawski, S., Wiekowski, M., Lira, S.A., Gorman, D., Kastelein, R.A. and Sedgwick, J.D. Interleukin-23 rather than interleukin-12 is the critical cytokine for autoimmune inflammation of the brain. *Nature.* 2003, **421**(6924), pp.744-748.
297. Constantinescu, C.S., Hilliard, B., Ventura, E., Wysocka, M., Showe, L., Lavi, E., Fujioka, T., Scott, P., Trinchieri, G. and Rostami, A. Modulation of susceptibility and resistance to an autoimmune model of multiple sclerosis in prototypically susceptible and resistant strains by neutralization of interleukin-12 and interleukin-4, respectively. *Clinical Immunology.* 2001, **98**(1), pp.23-30.
298. Bettelli, E., Sullivan, B., Szabo, S.J., Sobel, R.A., Glimcher, H. and Kuchroo, V.K. Loss of T-bet, but not STAT1, prevents the development of experimental autoimmune encephalomyelitis. *Journal of Experimental Medicine.* 2004, **200**(1), pp.79-87.
299. Yen, D., Cheung, J., Scheerens, H., Poulet, F., McClanahan, T., McKenzie, B., Kleinschek, M.A., Owyang, A., Mattson, J., Blumenschein, W., Murphy, E., Sathe, M., Cua, D.J., Kastelein, R.A. and Rennick, D. IL-23 is essential for T cell-mediated colitis and promotes inflammation via IL-17 and IL-6. *Journal of Clinical Investigation.* 2006, **116**(5), pp.1310-1316.
300. Sherlock, J.P., Joyce-Shaikh, B., Turner, S.P., Chao, C.C., Sathe, M., Grein, J., Gorman, D.M., Bowman, E.P., McClanahan, T.K., Yearley, J.H., Eberl, G., Buckley, C.D., Kastelein, R.A., Pierce, R.H., LaFace, D.M. and Cua, D.J. IL-23 induces spondyloarthropathy by acting on ROR-gamma t(+) CD3(+)CD4(-)CD8(-) entheseal resident T cells. *Nature Medicine.* 2012, **18**(7), pp.1069-+.
301. Chen, Y., Langrish, C.L., McKenzie, B., Joyce-Shaikh, B., Stumhofer, J.S., McClanahan, T., Blumenschein, W., Churakovsa, T., Low, J., Presta, L.,

Hunter, C.A., Kastelein, R.A. and Cua, D.J. Anti-IL-23 therapy inhibits multiple inflammatory pathways and ameliorates autoimmune encephalomyelitis. *Journal of Clinical Investigation.* 2006, **116**(5), pp.1317-1326.

302. Nash, P., Mease, P.J., Braun, J. and van der Heijde, D. Seronegative spondyloarthropathies: to lump or split? *Annals of the Rheumatic Diseases.* 2005, **64**, pp.9-13.
303. Bridgewood, C., Watad, A., Cuthbert, R.J. and McGonagle, D. Spondyloarthritis: new insights into clinical aspects, translational immunology and therapeutics. *Current Opinion in Rheumatology.* 2018, **30**(5), pp.526-532.
304. Watad, A., Bridgewood, C., Russell, T., Marzo-Ortega, H., Cuthbert, R. and McGonagle, D. The Early Phases of Ankylosing Spondylitis: Emerging Insights From Clinical and Basic Science. *Frontiers in Immunology.* 2018, **9**.
305. Zhu, K.J., Zhu, C.Y., Shi, G. and Fan, Y.M. Association of IL23R polymorphisms with psoriasis and psoriatic arthritis: a meta-analysis. *Inflammation Research.* 2012, **61**(10), pp.1149-1154.
306. Lee, Y.H., Choi, S.J., Ji, J.D. and Song, G.G. Associations between interleukin-23R polymorphisms and ankylosing spondylitis susceptibility: a meta-analysis. *Inflammation Research.* 2012, **61**(2), pp.143-149.
307. Rich, P., Sigurgeirsson, B., Thaci, D., Ortonne, J.P., Paul, C., Schopf, R.E., Morita, A., Roseau, K., Harfst, E., Guettner, A., Machacek, M. and Papavassilis, C. Secukinumab induction and maintenance therapy in moderate-to-severe plaque psoriasis: a randomized, double-blind, placebo-controlled, phase II regimen-finding study. *British Journal of Dermatology.* 2013, **168**(2), pp.402-411.
308. Sands, B.E., Sandborn, W.J., Panaccione, R., O'Brien, C.D., Zhang, H., Johanns, J., Adedokun, O.J., Li, K., Peyrin-Biroulet, L., Van Assche, G., Danese, S., Targan, S., Abreu, M.T., Hisamatsu, T., Szapary, P., Marano, C. and Grp, U.S. Ustekinumab as Induction and Maintenance Therapy for Ulcerative Colitis. *New England Journal of Medicine.* 2019, **381**(13), pp.1201-1214.
309. Kolli, S.S., Gabros, S.D., Pona, A., Cline, A. and Feldman, S.R. Tildrakizumab: A Review of Phase II and III Clinical Trials. *Annals of Pharmacotherapy.* 2019, **53**(4), pp.413-418.
310. Galluzzo, M., D'Adamio, S., Silvaggio, D., Lombardo, P., Massaro, A., Egan, C.G., Bianchi, L. and Talamonti, M. Ustekinumab treatment for moderate-to-severe plaque psoriasis: eight-year real-life experience. *Expert Opin Biol Ther.* 2020, **20**(1), pp.95-104.
311. D'Amico, F., Bencardino, S., Magro, F., Dignass, A., Gutiérrez Casbas, A., Verstockt, B., Hart, A., Armuzzi, A., Peyrin-Biroulet, L. and Danese, S. Positioning Guselkumab in The Treatment Algorithm of Patients with Crohn's Disease. *Biologics.* 2025, **19**, pp.351-363.
312. Sarrand, J., Baglione, L., Bouvy, C. and Soyfoo, M. Bimekizumab in the Treatment of Axial Spondyloarthritis and Psoriatic Arthritis: A New Kid on the Block. *International Journal of Molecular Sciences.* [Online]. 2025. **26**(5).
313. Gladman, D.D., Mease, P.J., Bird, P., Soriano, E.R., Chakravarty, S.D., Shawi, M., Xu, S., Quinn, S.T., Gong, C., Leibowitz, E., Poddubnyy, D., Tam, L.-S., Helliwell, P.S., Kavanaugh, A., Deodhar, A., Østergaard, M. and Baraliakos, X. Efficacy and safety of guselkumab in biologic-naïve patients with active axial psoriatic arthritis: study protocol for STAR, a phase 4, randomized, double-blinded, placebo-controlled trial. *Trials.* 2022, **23**(1), p.743.
314. Danoy, P., Pryce, K., Hadler, J., Bradbury, L.A., Farrar, C., Pointon, J., Ward, M., Weisman, M., Reveille, J.D., Wordsworth, B.P., Stone, M.A., Maksymowych, W.P., Rahman, P., Gladman, D., Inman, R.D., Brown, M.A., Australo Anglo, A. and Spondyloarthrit Res, C. Association of Variants at 1q32 and STAT3 with Ankylosing Spondylitis Suggests Genetic Overlap with Crohn's Disease. *Plos Genetics.* 2010, **6**(12).

315. Celis, R., Planell, N., Fernandez-Sueiro, J.L., Sanmarti, R., Ramirez, J., Gonzalez-Alvaro, I., Pablos, J.L. and Canete, J.D. Synovial cytokine expression in psoriatic arthritis and associations with lymphoid neogenesis and clinical features. *Arthritis Research & Therapy.* 2012, **14**(2).
316. Becker, C., Wirtz, S., Blessing, M., Pirhonen, J., Strand, D., Bechthold, O., Frick, J., Galle, P.R., Autenrieth, I. and Neurath, M.F. Constitutive p40 promoter activation and IL-23 production in the terminal ileum mediated by dendritic cells. *Journal of Clinical Investigation.* 2003, **112**(5), pp.693-706.
317. Mielants, H., Veys, E.M., Cuvelier, C., Devos, M., Goemaere, S., Declercq, L., Schatteman, L. and Elewaut, D. The evolution of spondyloarthropathies in relation to gut histology .2. Histological aspects. *Journal of Rheumatology.* 1995, **22**(12), pp.2273-2278.
318. Duerr, R.H., Taylor, K.D., Brant, S.R., Rioux, J.D., Silverberg, M.S., Daly, M.J., Steinhart, A.H., Abraham, C., Regueiro, M., Griffiths, A., Dassopoulos, T., Bitton, A., Yang, H.Y., Targan, S., Datta, L.W., Kistner, E.O., Schumm, L.P., Lee, A.T., Gregersen, P.K., Barmada, M.M., Rotter, J.I., Nicolae, D.L. and Cho, J.H. A genome-wide association study identifies IL23R as an inflammatory bowel disease gene. *Science.* 2006, **314**(5804), pp.1461-1463.
319. Cotterill, L., Payne, D., Levison, S., McLaughlin, J., Wesley, E., Feeney, M., Durbin, H., Lal, S., Makin, A., Campbell, S., Roberts, S.A., O'Neill, C., Edwards, C. and Newman, W.G. Replication and meta-analysis of 13,000 cases defines the risk for interleukin-23 receptor and autophagy-related 16-like 1 variants in Crohn's disease. *Canadian Journal of Gastroenterology and Hepatology.* 2010, **24**(5), pp.297-302.
320. Suzuki, E., Mellins, E.D., Gershwin, M.E., Nestle, F.O. and Adamopoulos, I.E. The IL-23/IL-17 axis in psoriatic arthritis. *Autoimmunity Reviews.* 2014, **13**(4-5), pp.496-502.
321. Johansen, C., Usher, P.A., Kjellerup, R.B., Lundsgaard, D., Iversen, L. and Kragballe, K. Characterization of the interleukin-17 isoforms and receptors in lesional psoriatic skin. *British Journal of Dermatology.* 2009, **160**(2), pp.319-324.
322. Fujino, S., Andoh, A., Bamba, S., Ogawa, A., Hata, K., Araki, Y., Bamba, T. and Fujiyama, Y. Increased expression of interleukin 17 in inflammatory bowel disease. *Gut.* 2003, **52**(1), pp.65-70.
323. Shen, H., Goodall, J.C. and Gaston, J.S.H. Frequency and Phenotype of Peripheral Blood Th17 Cells in Ankylosing Spondylitis and Rheumatoid Arthritis. *Arthritis and Rheumatism.* 2009, **60**(6), pp.1647-1656.
324. Colbert, R.A., DeLay, M.L., Klenk, E.I. and Layh-Schmitt, G. From HLA-B27 to spondyloarthritis: a journey through the ER. *Immunological Reviews.* 2010, **233**, pp.181-202.
325. Sheehan, N.J. The ramifications of HLA-B27. *Journal of the Royal Society of Medicine.* 2004, **97**(1), pp.10-14.
326. Cortes, A., Hadler, J., Pointon, J.P., Robinson, P.C., Karaderi, T., Leo, P., Cremin, K., Pryce, K., Harris, J., Lee, S., Joo, K.B., Shim, S.C., Weisman, M., Ward, M., Zhou, X.D., Garchon, H.J., Chiocchia, G., Nossent, J., Lie, B.A., Forre, O., Tuomilehto, J., Laiho, K., Jiang, L., Liu, Y., Wu, X., Bradbury, L.A., Elewaut, D., Burgos-Vargas, R., Stebbings, S., Appleton, L., Farrah, C., Lau, J., Kenna, T.J., Haroon, N., Ferreira, M.A., Yang, J., Mulero, J., Fernandez-Sueiro, J.L., Gonzalez-Gay, M.A., Lopez-Larrea, C., Deloukas, P., Donnelly, P., Bowness, P., Gafney, K., Gaston, H., Gladman, D.D., Rahman, P., Maksymowych, W.P., Xu, H.J., Crusius, J.B.A., van der Horst-Bruinsma, I.E., Chou, C.T., Valle-Onate, R., Romero-Sanchez, C., Hansen, I.M., Pimentel-Santos, F.M., Inman, R.D., Videm, V., Martin, J., Breban, M., Reveille, J.D., Evans, D.M., Kim, T.H., Wordsworth, B.P., Brown, M.A., Int Genetics, A., Australo Anglo, A., Gfegs, Nord-Trondelag Hlth Study, H., Spondyloarthrit Res, C. and Wtccc. Identification of multiple risk variants for ankylosing spondylitis

through high-density genotyping of immune-related loci. *Nature Genetics.* 2013, **45**(7), pp.730-+.

327. Rosenzweig, H.L., Vance, E.E., Asare-Konadu, K., Koney, K., Lee, E.J., Deodhar, A.A., Sen, R., Caplan, L. and Napier, R.J. Card9/neutrophil signalling axis promotes IL-17A-mediated ankylosing spondylitis. *Annals of the Rheumatic Diseases.* 2023.
328. Ruutu, M., Thomas, G., Steck, R., Degli-Esposti, M.A., Zinkernagel, M.S., Alexander, K., Velasco, J., Strutton, G., Ai, T., Benham, H., Rehaume, L., Wilson, R.J., Kikly, K., Davies, J., Pettit, A.R., Brown, M.A., McGuckin, M.A. and Thomas, R. beta-glucan triggers spondylarthritis and Crohn's disease-like ileitis in SKG mice. *Arthritis and Rheumatism.* 2012, **64**(7), pp.2211-2222.
329. Pointon, J.J., Harvey, D., Karaderi, T., Appleton, L.H., Farrar, C., Stone, M.A., Sturrock, R.D., Brown, M.A. and Wordsworth, B.P. Elucidating the chromosome 9 association with AS; CARD9 is a candidate gene. *Genes and Immunity.* 2010, **11**(6), pp.490-496.
330. Zhernakova, A., Festen, E.M., Franke, L., Trynka, G., van Diemen, C.C., Monsuur, A.J., Bevova, M., Nijmeijer, R.M., van't Slot, R., Heijmans, R., Boezen, H.M., van Heel, D.A., van Bodegraven, A.A., Stokkers, P.C.F., Wijmenga, C., Crusius, J.B.A. and Weersma, R.K. Genetic analysis of innate immunity in Crohn's disease and ulcerative colitis identifies two susceptibility loci harboring CARD9 and IL18RAP. *American Journal of Human Genetics.* 2008, **82**(5), pp.1202-1210.
331. Gringhuis, S.I., den Dunnen, J., Litjens, M., van het Hof, B., van Kooyk, Y. and Geijtenbeek, Teunis B.H. C-Type Lectin DC-SIGN Modulates Toll-like Receptor Signaling via Raf-1 Kinase-Dependent Acetylation of Transcription Factor NF-κB. *Immunity.* 2007, **26**(5), pp.605-616.
332. Gross, O., Gewies A Fau - Finger, K., Finger K Fau - Schäfer, M., Schäfer M Fau - Sparwasser, T., Sparwasser T Fau - Peschel, C., Peschel C Fau - Förster, I., Förster I Fau - Ruland, J. and Ruland, J. Card9 controls a non-TLR signalling pathway for innate anti-fungal immunity. (1476-4687 (Electronic)).
333. Rosenzweig, H.L., Vance, E.A.-O., Asare-Konadu, K., Koney, K.V., Lee, E.J., Deodhar, A.A.-O., Sen, R., Caplan, L. and Napier, R.A.-O. Card9/neutrophil signalling axis promotes IL-17A-mediated ankylosing spondylitis. (1468-2060 (Electronic)).
334. Colbert, R.A., Tran, T.M. and Layh-Schmitt, G. HLA-B27 misfolding and ankylosing spondylitis. *Molecular Immunology.* 2014, **57**(1), pp.44-51.
335. Delay, M.L., Turner, M.J., Klenk, E.I., Smith, J.A., Sowders, D.P. and Colbert, R.A. HLA-B27 Misfolding and the Unfolded Protein Response Augment Interleukin-23 Production and Are Associated With Th17 Activation in Transgenic Rats. *Arthritis and Rheumatism.* 2009, **60**(9), pp.2633-2643.
336. Buhl, A.-L. and Wenzel, J. Interleukin-36 in Infectious and Inflammatory Skin Diseases. *Frontiers in Immunology.* 2019, **Volume 10 - 2019**.
337. Bridgewood, C., Fearnley, G.W., Berekmeri, A., Laws, P., Macleod, T., Ponnambalam, S., Stacey, M., Graham, A. and Wittmann, M. IL-36γ Is a Strong Inducer of IL-23 in Psoriatic Cells and Activates Angiogenesis. *Frontiers in Immunology.* 2018, **Volume 9 - 2018**.
338. Goldstein, J.D., Bassoy, E.Y., Caruso, A., Palomo, J., Rodriguez, E., Lemeille, S. and Gabay, C. IL-36 signaling in keratinocytes controls early IL-23 production in psoriasis-like dermatitis. *Life Sci Alliance.* 2020, **3**(6).
339. van der Fits, L., Mourits, S., Voerman, J.S.A., Kant, M., Boon, L., Laman, J.D., Cornelissen, F., Mus, A.-M., Florencia, E., Prens, E.P. and Lubberts, E. Imiquimod-Induced Psoriasis-Like Skin Inflammation in Mice Is Mediated via the IL-23/IL-17 Axis1. *The Journal of Immunology.* 2009, **182**(9), pp.5836-5845.
340. Alvarez, P. and Jensen, L.E. Imiquimod Treatment Causes Systemic Disease in Mice Resembling Generalized Pustular Psoriasis in an IL-1 and IL-36 Dependent Manner. *Mediators of Inflammation.* 2016, **2016**(1), p.6756138.

341. Hawkes, J.E., Yan, B.Y., Chan, T.C. and Krueger, J.G. Discovery of the IL-23/IL-17 Signaling Pathway and the Treatment of Psoriasis. *Journal of Immunology.* 2018, **201**(6), pp.1605-1613.
342. Telfer, N.R., Chalmers, R.J.G., Whale, K. and Colman, G. The role of streptococcal infection in the initiation of guttate psoriasis. *Archives of Dermatology.* 1992, **128**(1), pp.39-42.
343. Wardrop, P., Weller, R., Marais, J. and Kavanagh, G. Tonsillitis and chronic psoriasis. *Clinical Otolaryngology.* 1998, **23**(1), pp.67-68.
344. Tomi, N.S., Kranke, B. and Aberer, E. Staphylococcal toxins in patients with psoriasis, atopic dermatitis, and erythroderma, and in healthy control subjects. *Journal of the American Academy of Dermatology.* 2005, **53**(1), pp.67-72.
345. Leung, D.Y.M., Walsh, P., Giorno, R. and Norris, D.A. A potential role for superantigens in the pathogenesis of psoriasis. *Journal of Investigative Dermatology.* 1993, **100**(3), pp.225-228.
346. Pietrzak, A., Grywalska, E., Socha, M., Rolinski, J., Franciszkiewicz-Pietrzak, K., Rudnicka, L., Rudzki, M. and Krasowska, D. Prevalence and Possible Role of Candida Species in Patients with Psoriasis: A Systematic Review and Meta-Analysis. *Mediators of Inflammation.* 2018, **2018**.
347. Baroni, A., Paoletti, I., Ruocco, E., Agozzino, M., Tufano, M.A. and Donnarumma, G. Possible role of Malassezia furfur in psoriasis: modulation of TGF-beta 1, integrin, and HSP70 expression in human keratinocytes and in the skin of psoriasis-affected patients. *Journal of Cutaneous Pathology.* 2004, **31**(1), pp.35-42.
348. Favre, M., Orth, G., Majewski, S., Baloul, S., Pura, A. and Jablonska, S. Psoriasis: A possible reservoir for human papillomavirus type 5, the virus associated with skin carcinomas of epidermodysplasia verruciformis. *Journal of Investigative Dermatology.* 1998, **110**(4), pp.311-317.
349. Duvic, M., Johnson, T.M., Rapini, R.P., Freese, T., Brewton, G. and Rios, A. Acquired Immunodeficiency Syndrome— Associated Psoriasis and Reiter's Syndrome. *Archives of Dermatology.* 1987, **123**(12), pp.1622-1632.
350. Byrd, A.L., Belkaid, Y. and Segre, J.A. The human skin microbiome. *Nature Reviews Microbiology.* 2018, **16**(3), pp.143-155.
351. Naik, S., Bouladoux, N., Wilhelm, C., Molloy, M.J., Salcedo, R., Kastenmuller, W., Deming, C., Quinones, M., Koo, L., Conlan, S., Spencer, S., Hall, J.A., Dzutsev, A., Kong, H., Campbell, D.J., Trinchieri, G., Segre, J.A. and Belkaid, Y. Compartmentalized Control of Skin Immunity by Resident Commensals. *Science.* 2012, **337**(6098), pp.1115-1119.
352. Fry, L. and Baker, B.S. Triggering psoriasis: the role of infections and medications. *Clinics in Dermatology.* 2007, **25**(6), pp.606-615.
353. Farr, P.M., Marks, J.M., Krause, L.B. and Shuster, S. Response of scalp psoriasis to oral ketoconazole. *Lancet.* 1985, **2**(8461), pp.921-922.
354. Buslau, M., Menzel, I. and Holzmann, H. Fungal flora of human feces in psoriasis and atopic-dermatitis. *Mycoses.* 1990, **33**(2), pp.90-94.
355. Waldman, A., Gilhar, A., Duek, L. and Berdicevsky, I. Incidence of Candida in psoriasis - a study on the fungal flora of psoriatic patients. *Mycoses.* 2001, **44**(3-4), pp.77-81.
356. Cebra, J.J. Influences of microbiota on intestinal immune system development. *American Journal of Clinical Nutrition.* 1999, **69**(5), pp.1046S-1051S.
357. Rehakova, Z., Capkova, J., Stepankova, R., Sinkora, J., Louzecka, A., Ivanyi, P. and Weinreich, S. Germ-free mice do not develop ankylosing enthesopathy, a spontaneous joint disease. *Human Immunology.* 2000, **61**(6), pp.555-558.
358. Taurog, J.D., Maika, S.D., Satumtira, N., Dorris, M.L., McLean, I.L., Yanagisawa, H., Sayad, A., Stagg, A.J., Fox, G.M., O'Brien, A.L., Rehman, M., Zhou, M., Weiner, A.L., Splawski, J.B., Richardson, J.A. and Hammer, R.E. Inflammatory disease in HLA-B27 transgenic rats. *Immunological Reviews.* 1999, **169**, pp.209-223.

359. Rath, H.C., Herfarth, H.H., Ikeda, J.S., Grenther, W.B., Hamm, T.E., Balish, E., Taurog, J.D., Hammer, R.E., Wilson, K.H. and Sartor, R.B. Normal luminal bacteria, especially bacteroides species, mediate chronic colitis, gastritis, and arthritis in HLA-B27/human beta(2) microglobulin transgenic rats. *Journal of Clinical Investigation.* 1996, **98**(4), pp.945-953.
360. Sakaguchi, N., Takahashi, T., Hata, H., Nomura, T., Tagami, T., Yamazaki, S., Sakihama, T., Matsurtani, T., Negishi, I., Nakatsuru, S. and Sakaguchi, S. Altered thymic T-cell selection due to a mutation of the ZAP-70 gene causes autoimmune arthritis in mice. *Nature.* 2003, **426**(6965), pp.454-460.
361. Rehaume, L.M., Mondot, S., de Carcer, D.A., Velasco, J., Benham, H., Hasnain, S.Z., Bowman, J., Ruutu, M., Hansbro, P.M., McGuckin, M.A., Morrison, M. and Thomas, R. ZAP-70 Genotype Disrupts the Relationship Between Microbiota and Host, Leading to Spondyloarthritis and Ileitis in SKG Mice. *Arthritis & Rheumatology.* 2014, **66**(10), pp.2780-2792.
362. Benham, H., Rehaume, L.M., Hasnain, S.Z., Velasco, J., Baillet, A.C., Ruutu, M., Kikly, K., Wang, R., Tseng, H.W., Thomas, G.P., Brown, M.A., Strutton, G., McGuckin, M.A. and Thomas, R. Interleukin-23 Mediates the Intestinal Response to Microbial beta-1,3-Glucan and the Development of Spondyloarthritis Pathology in SKG Mice. *Arthritis & Rheumatology.* 2014, **66**(7), pp.1755-1767.
363. Rehaume, L.M., Matigian, N., Mehdi, A.M., Lachner, N., Bowerman, K.L., Daly, J., Le Cao, K.A., Hugenholtz, P. and Thomas, R. IL-23 favours outgrowth of spondyloarthritis-associated pathobionts and suppresses host support for homeostatic microbiota. *Annals of the Rheumatic Diseases.* 2019, **78**(4), pp.494-503.
364. Cua, D.J. and Sherlock, J.P. Autoimmunity's collateral damage: Gut microbiota strikes 'back'. *Nature Medicine.* 2011, **17**(9), pp.1055-1056.
365. Rich, E., Hook, E.W., Alarcon, G.S. and Moreland, L.W. Reactive arthritis in patients attending an urban sexually transmitted diseases clinic. *Arthritis and Rheumatism.* 1996, **39**(7), pp.1172-1177.
366. Baillet, A.C., Rehaume, L.M., Benham, H., O'Meara, C.P., Armitage, C.W., Ruscher, R., Brizard, G., Harvie, M.C.G., Velasco, J., Hansbro, P.M., Forrester, J.V., Degli-Esposti, M.A., Beagley, K.W. and Thomas, R. High Chlamydia Burden Promotes Tumor Necrosis Factor-Dependent Reactive Arthritis in SKG Mice. *Arthritis & Rheumatology.* 2015, **67**(6), pp.1535-1547.
367. Goodall, J.C., Wu, C.X., Zhang, Y.S., McNeill, L., Ellis, L., Saudek, V. and Gaston, J.S.H. Endoplasmic reticulum stress-induced transcription factor, CHOP, is crucial for dendritic cell IL-23 expression. *Proceedings of the National Academy of Sciences of the United States of America.* 2010, **107**(41), pp.17698-17703.
368. Švajger, U., Obermajer, N., Anderluh, M., Kos, J. and Jeras, M. DC-SIGN ligation greatly affects dendritic cell differentiation from monocytes compromising their normal function. *Journal of Leukocyte Biology.* 2011, **89**(6), pp.893-905.
369. Higgins, S.C., Jarnicki, A.G., Lavelle, E.C. and Mills, K.H.G. TLR4 Mediates Vaccine-Induced Protective Cellular Immunity to Bordetella pertussis: Role of IL-17-Producing T Cells1. *The Journal of Immunology.* 2006, **177**(11), pp.7980-7989.
370. Chamilos, G., Ganguly, D., Lande, R., Gregorio, J., Meller, S., Goldman, W.E., Gilliet, M. and Kontoyiannis, D.P. Generation of IL-23 Producing Dendritic Cells (DCs) by Airborne Fungi Regulates Fungal Pathogenicity via the Induction of TH-17 Responses. *PLOS ONE.* 2010, **5**(9), p.e12955.
371. Re, F. and Strominger, J.L. Toll-like Receptor 2 (TLR2) and TLR4 Differentially Activate Human Dendritic Cells *. *Journal of Biological Chemistry.* 2001, **276**(40), pp.37692-37699.
372. Lee , E., Trepicchio , W.L., Oestreicher , J.L., Pittman , D., Wang , F., Chamian , F., Dhodapkar , M. and Krueger , J.G. Increased Expression of Interleukin 23

p19 and p40 in Lesional Skin of Patients with Psoriasis Vulgaris. *Journal of Experimental Medicine.* 2004, **199**(1), pp.125-130.
373. Fitch, E., Harper E Fau - Skorcheva, I., Skorcheva I Fau - Kurtz, S.E., Kurtz Se Fau - Blauvelt, A. and Blauvelt, A. Pathophysiology of psoriasis: recent advances on IL-23 and Th17 cytokines. (1523-3774 (Print)).
374. Yawalkar, N., Tscharner, G.G., Hunger, R.E. and Hassan, A.S. Increased expression of IL-12p70 and IL-23 by multiple dendritic cell and macrophage subsets in plaque psoriasis. *Journal of Dermatological Science.* 2009, **54**(2), pp.99-105.
375. Stratis, A., Pasparakis, M., Rupec, R.A., Markur, D., Hartmann, K., Scharffetter-Kochanek, K., Peters, T., van Rooijen, N., Krieg, T. and Haase, I. Pathogenic role for skin macrophages in a mouse model of keratinocyte-induced psoriasis-like skin inflammation. *Journal of Clinical Investigation.* 2006, **116**(8), pp.2094-2104.
376. Vandenoord, J.J. and Dewolfpeeters, C. Epithelium-lining macrophages in psoriasis. *British Journal of Dermatology.* 1994, **130**(5), pp.589-594.
377. McGovern, D. and Powrie, F. The IL23 axis plays a key role in the pathogenesis of IBD. *Gut.* 2007, **56**(10), pp.1333-1336.
378. Kamada, N., Hisamatsu, T., Okamoto, S., Chinen, H., Kobayashi, T., Sato, T., Sakuraba, A., Kitazume, M.T., Sugita, A., Koganei, K., Akagawa, K.S. and Hibi, T. Unique CD14⁺ intestinal macrophages contribute to the pathogenesis of Crohn disease via IL-23/IFN-γ axis. *Journal of Clinical Investigation.* 2008, **118**(6), pp.2269-2280.
379. Kamada, N., Hisamatsu, T., Okamoto, S., Sato, T., Matsuoka, K., Arai, K., Nakai, T., Hasegawa, A., Inoue, N., Watanabe, N., Akagawa, K.S. and Hibi, T. Abnormally differentiated subsets of intestinal macrophage play a key role in Th1-dominant chronic colitis through excess production of IL-12 and IL-23 in response to bacteria. *Journal of Immunology.* 2005, **175**(10), pp.6900-6908.
380. Schlapbach, C., Hänni, T., Yawalkar, N. and Hunger, R.E. Expression of the IL-23/Th17 pathway in lesions of hidradenitis suppurativa. *Journal of the American Academy of Dermatology.* 2011, **65**(4), pp.790-798.
381. Bridgewood, C., Watad, A., Russell, T., Palmer, T.M., Marzo-Ortega, H., Khan, A., Millner, P.A., Dunsmuir, R., Rao, A., Loughenbury, P., Wittmann, M., Cuthbert, R.J. and McGonagle, D.G. Identification of myeloid cells in the human enthesis as the main source of local IL-23 production. *Annals of the Rheumatic Diseases.* 2019, **78**(7), p.929.
382. Kvedaraite, E., Lourda, M., Ideström, M., Chen, P.R., Olsson-Akefeldt, S., Forkel, M., Gavhed, D., Lindforss, U., Mjösberg, J., Henter, J.I. and Svensson, M. Tissue-infiltrating neutrophils represent the main source of IL-23 in the colon of patients with IBD. *Gut.* 2016, **65**(10), pp.1632-1641.
383. Katayama, H. Development of psoriasis by continuous neutrophil infiltration into the epidermis. *Experimental Dermatology.* 2018, **27**(10), pp.1084-1091.
384. Tamassia, N., Arruda-Silva, F., Wright, H.L., Moots, R.J., Gardiman, E., Bianchetto-Aguilera, F., Gasperini, S., Capone, M., Maggi, L., Annunziato, F., Edwards, S.W. and Cassatella, M.A. Human neutrophils activated via TLR8 promote Th17 polarization through IL-23. *Journal of Leukocyte Biology.* 2019, **105**(6), pp.1155-1165.
385. Stavre, Z., Bridgewood, C., Zhou, Q., Maeda, Y., Huang, T.T., Karman, J., Khan, A., Giryes, S., Sharif, K., McGonagle, D. and Gravallese, E.M. A role for neutrophils in early enthesitis in spondyloarthritis. *Arthritis Research & Therapy.* 2022, **24**(1).
386. Ortiz-Lopez, L.I., Choudhary, V. and Bollag, W.B. Updated Perspectives on Keratinocytes and Psoriasis: Keratinocytes are More Than Innocent Bystanders. *Psoriasis: Targets and Therapy.* 2022, **12**(null), pp.73-87.
387. Li, H., Yao, Q., Mariscal, A.G., Wu, X., Hülse, J., Pedersen, E., Helin, K., Waisman, A., Vinkel, C., Thomsen, S.F., Avgustinova, A., Benitah, S.A., Lovato, P., Norsgaard, H., Mortensen, M.S., Veng, L., Rozell, B. and Brakebusch, C.

Epigenetic control of IL-23 expression in keratinocytes is important for chronic skin inflammation. *Nature Communications.* 2018, **9**(1), p.1420.

388. Piskin, G., Sylva-Steenland, R.M., Bos, J.D. and Teunissen, M.B. In vitro and in situ expression of IL-23 by keratinocytes in healthy skin and psoriasis lesions: enhanced expression in psoriatic skin. *J Immunol.* 2006, **176**(3), pp.1908-1915.
389. Liu, W., Ouyang, X., Yang, J., Liu, J., Li, Q., Gu, Y., Fukata, M., Lin, T., He, J.C., Abreu, M., Unkeless, J.C., Mayer, L. and Xiong, H. AP-1 activated by toll-like receptors regulates expression of IL-23 p19. *J Biol Chem.* 2009, **284**(36), pp.24006-24016.
390. Gerosa, F., Baldani-Guerra B Fau - Lyakh, L.A., Lyakh La Fau - Batoni, G., Batoni G Fau - Esin, S., Esin S Fau - Winkler-Pickett, R.T., Winkler-Pickett Rt Fau - Consolaro, M.R., Consolaro Mr Fau - De Marchi, M., De Marchi M Fau - Giachino, D., Giachino D Fau - Robbiano, A., Robbiano A Fau - Astegiano, M., Astegiano M Fau - Sambataro, A., Sambataro A Fau - Kastelein, R.A., Kastelein Ra Fau - Carra, G., Carra G Fau - Trinchieri, G. and Trinchieri, G. Differential regulation of interleukin 12 and interleukin 23 production in human dendritic cells. (1540-9538 (Electronic)).
391. van de Veerdonk, F.L., Marijnissen, R.J., Kullberg, B.J., Koenen, H.J.P.M., Cheng, S.-C., Joosten, I., van den Berg, W.B., Williams, D.L., van der Meer, J.W.M., Joosten, L.A.B. and Netea, M.G. The Macrophage Mannose Receptor Induces IL-17 in Response to Candida albicans. *Cell Host & Microbe.* 2009, **5**(4), pp.329-340.
392. Krylov, V.B., Gómez-Redondo, M., Solovev, A.S., Yashunsky, D.V., Brown, A.J.P., Stappers, M.H.T., Gow, N.A.R., Ardá, A., Jiménez-Barbero, J. and Nifantiev, N.E. Identification of a new DC-SIGN binding pentamannoside epitope within the complex structure of Candida albicans mannan. *The Cell Surface.* 2023, **10**, p.100109.
393. Serrano-Gómez, D., Antonio Leal, J. and Corbí, A.L. DC-SIGN mediates the binding of Aspergillus fumigatus and keratinophylic fungi by human dendritic cells. *Immunobiology.* 2005, **210**(2), pp.175-183.
394. Zenaro, E., Donini, M. and Dusi, S. Induction of Th1/Th17 immune response by Mycobacterium tuberculosis: role of dectin-1, mannose receptor, and DC-SIGN. *Journal of Leukocyte Biology.* 2009, **86**(6), pp.1393-1401.
395. Geijtenbeek, T.B.H., Krooshoop, D.J.E.B., Bleijs, D.A., van Vliet, S.J., van Duijnhoven, G.C.F., Grabovsky, V., Alon, R., Figdor, C.G. and van Kooyk, Y. DC-SIGN–ICAM-2 interaction mediates dendritic cell trafficking. *Nature Immunology.* 2000, **1**(4), pp.353-357.
396. Speakman, E.A., Dambuza, I.M., Salazar, F. and Brown, G.D. T Cell Antifungal Immunity and the Role of C-Type Lectin Receptors. *Trends in Immunology.* 2020, **41**(1), pp.61-76.
397. Vautier, S., MacCallum, D.M. and Brown, G.D. C-type lectin receptors and cytokines in fungal immunity. *Cytokine.* 2012, **58**(1), pp.89-99.
398. Gantner, B.N., Simmons Rm Fau - Canavera, S.J., Canavera Sj Fau - Akira, S., Akira S Fau - Underhill, D.M. and Underhill, D.M. Collaborative induction of inflammatory responses by dectin-1 and Toll-like receptor 2. (0022-1007 (Print)).
399. Kankkunen, P., Teirilä, L., Rintahaka, J., Alenius, H., Wolff, H. and Matikainen, S. (1,3)-β-Glucans Activate Both Dectin-1 and NLRP3 Inflammasome in Human Macrophages. *The Journal of Immunology.* 2010, **184**(11), pp.6335-6342.
400. Yamasaki, S., Ishikawa, E., Sakuma, M., Hara, H., Ogata, K. and Saito, T. Mincle is an ITAM-coupled activating receptor that senses damaged cells. *Nature Immunology.* 2008, **9**(10), pp.1179-1188.
401. Ohkawa, Y., Kanto, N., Nakano, M., Fujinawa, R., Kizuka, Y., Johnson, E.L., Harada, Y., Tamura, J.-i. and Taniguchi, N. *Journal of Biological Chemistry.* 2023, **299**(8).
402. Shuttleworth, S., Townsend, P., Silva, F., Cecil, A., Hill, T., Tomassi, C., Rogers, H. and Harrison, R. Progress in the Development of Small Molecule

Therapeutics Targeting Th17 Cell Function for the Treatment of Immune-Inflammatory Diseases. In: Lawton, G. and Witty, D.R. eds. *Progress in Medicinal Chemistry*. Elsevier, 2011, pp.109-133.

403. Wilhelm, I., Levit-Zerdoun, E., Jakob, J., Villringer, S., Frensch, M., Übelhart, R., Landi, A., Müller, P., Imberty, A., Thuenauer, R., Claudinon, J., Jumaa, H., Reth, M., Eibel, H., Hobeika, E. and Römer, W. Carbohydrate-dependent B cell activation by fucose-binding bacterial lectins. *Science Signaling.* 2019, **12**(571), p.eaao7194.
404. Pinho, S.S. and Reis, C.A. Glycosylation in cancer: mechanisms and clinical implications. *Nature Reviews Cancer.* 2015, **15**(9), pp.540-555.
405. Saraiva, M. and O'Garra, A. The regulation of IL-10 production by immune cells. *Nature Reviews Immunology.* 2010, **10**(3), pp.170-181.
406. McGeachy, M.J. and Cua, D.J. Th17 Cell Differentiation: The Long and Winding Road. *Immunity.* 2008, **28**(4), pp.445-453.
407. Boutet, M.-A., Nerviani, A., Gallo Afflitto, G. and Pitzalis, C. Role of the IL-23/IL-17 Axis in Psoriasis and Psoriatic Arthritis: The Clinical Importance of Its Divergence in Skin and Joints. *International Journal of Molecular Sciences.* [Online]. 2018. **19**(2).
408. Yoshitomi, H., Sakaguchi, N., Kobayashi, K., Brown, G.D., Tagami, T., Sakihama, T., Hirota, K., Tanaka, S., Nomura, T., Miki, I., Gordon, S., Akira, S., Nakamura, T. and Sakaguchi, S. A role for fungal beta-glucans and their receptor Dectin-1 in the induction of autoimmune arthritis in genetically susceptible mice. *Journal of Experimental Medicine.* 2005, **201**(6), pp.949-960.
409. Boswell, N.D., Ries, A., Gordon, K.B. and Singla, S.A.-O. Biologic Sequence for the Treatment of Psoriatic Arthritis Following Nonresponse: A Narrative Review. (2193-8210 (Print)).
410. Puig-Kröger, A., Serrano-Gómez, D., Caparrós, E., Domínguez-Soto, A., Relloso, M., Colmenares, M., Martínez-Muñoz, L., Longo, N., Sánchez-Sánchez, N., Rincon, M., Rivas, L., Sánchez-Mateos, P., Fernández-Ruiz, E. and Corbí, A.L. Regulated Expression of the Pathogen Receptor Dendritic Cell-specific Intercellular Adhesion Molecule 3 (ICAM-3)-grabbing Nonintegrin in THP-1 Human Leukemic Cells, Monocytes, and Macrophages *. *Journal of Biological Chemistry.* 2004, **279**(24), pp.25680-25688.
411. Villani, A.-C., Satija, R., Reynolds, G., Sarkizova, S., Shekhar, K., Fletcher, J., Griesbeck, M., Butler, A., Zheng, S., Lazo, S., Jardine, L., Dixon, D., Stephenson, E., Nilsson, E., Grundberg, I., McDonald, D., Filby, A., Li, W., De Jager, P.L., Rozenblatt-Rosen, O., Lane, A.A., Haniffa, M., Regev, A. and Hacohen, N. Single-cell RNA-seq reveals new types of human blood dendritic cells, monocytes, and progenitors. *Science.* 2017, **356**(6335), p.eaah4573.
412. Böttcher, J.P. and Reis e Sousa, C. The Role of Type 1 Conventional Dendritic Cells in Cancer Immunity. *Trends in Cancer.* 2018, **4**(11), pp.784-792.
413. Jongbloed, S.L., Kassianos, A.J., McDonald, K.J., Clark, G.J., Ju, X., Angel, C.E., Chen, C.-J.J., Dunbar, P.R., Wadley, R.B., Jeet, V., Vulink, A.J.E., Hart, D.N.J. and Radford, K.J. Human CD141+ (BDCA-3)+ dendritic cells (DCs) represent a unique myeloid DC subset that cross-presents necrotic cell antigens. *Journal of Experimental Medicine.* 2010, **207**(6), pp.1247-1260.
414. Leal Rojas, I.M., Mok, W.H., Pearson, F.E., Minoda, Y., Kenna, T.J., Barnard, R.T. and Radford, K.J. Human Blood CD1c(+) Dendritic Cells Promote Th1 and Th17 Effector Function in Memory CD4(+) T Cells. (1664-3224 (Print)).
415. Yin, X., Yu, H., Jin, X., Li, J., Guo, H., Shi, Q., Yin, Z., Xu, Y., Wang, X., Liu, R., Wang, S. and Zhang, L. Human Blood CD1c+ Dendritic Cells Encompass CD5high and CD5low Subsets That Differ Significantly in Phenotype, Gene Expression, and Functions. *The Journal of Immunology.* 2017, **198**(4), pp.1553-1564.
416. Santegoets, S.A.-O., Duurland, C.L., Jordanova, E.J., van Ham, V.J., Ehsan, I., Loof, N.M., Narang, V., Dutertre, C.A., Ginhoux, F., van Egmond, S.L., M, J.P.W. and van der Burg, S.A.-O. CD163(+) cytokine-producing cDC2 stimulate

intratumoral type 1 T cell responses in HPV16-induced oropharyngeal cancer. LID - 10.1136/jitc-2020-001053 [doi] LID - e001053. (2051-1426 (Electronic)).
417. Cytlak, U., Resteu, A., Pagan, S., Green, K., Milne, P., Maisuria, S., McDonald, D., Hulme, G., Filby, A., Carpenter, B., Queen, R., Hambleton, S., Hague, R., Lango Allen, H., Thaventhiran, J.E.D., Doody, G., Collin, M. and Bigley, V. Differential IRF8 Transcription Factor Requirement Defines Two Pathways of Dendritic Cell Development in Humans. *Immunity.* 2020, **53**(2), pp.353-370.e358.
418. Bourdely, P., Anselmi, G., Vaivode, K., Ramos, R.N., Missolo-Koussou, Y., Hidalgo, S., Tosselo, J., Nuñez, N., Richer, W., Vincent-Salomon, A., Saxena, A., Wood, K., Lladser, A., Piaggio, E., Helft, J. and Guermonprez, P. Transcriptional and Functional Analysis of CD1c⁺ Human Dendritic Cells Identifies a CD163⁺ Subset Priming CD8⁺CD103⁺ T Cells. *Immunity.* 2020, **53**(2), pp.335-352.e338.
419. Collin, M.A.-O. and Bigley, V.A.-O. Human dendritic cell subsets: an update. (1365-2567 (Electronic)).
420. Decker, A.H., van den Hoogen, L.L., van Oorschot, T., Sanchez-Rocha, L., Boks, M.A., Bakdash, G., Thomas, R., Popa, C.D., Verdoes, M., Thurlings, R.M., Becker, A.M.D. and de Vries, I.J.M. Interleukin-6 in synovial fluid drives the conversion of DC2s to DC3s in inflammatory arthritis. (2589-0042 (Electronic)).
421. Krug, A., Rothenfusser, S., Hornung, V., Jahrsdörfer, B., Blackwell, S., Ballas, Z.K., Endres, S., Krieg, A.M. and Hartmann, G. Identification of CpG oligonucleotide sequences with high induction of IFN-α/β in plasmacytoid dendritic cells. *European Journal of Immunology.* 2001, **31**(7), pp.2154-2163.
422. Heger, L.A.-O., Dudziak, D., Amon, L., Hatscher, L., Kaszubowski, T. and Lehmann, C.H.K. Guidelines for DC preparation and flow cytometric analysis of human lymphohematopoietic tissues. (1521-4141 (Electronic)).
423. Tang-Huau, T.L., Gueguen, P.A.-O., Goudot, C., Durand, M., Bohec, M., Baulande, S.A.-O., Pasquier, B., Amigorena, S. and Segura, E.A.-O. Human in vivo-generated monocyte-derived dendritic cells and macrophages cross-present antigens through a vacuolar pathway. (2041-1723 (Electronic)).
424. van Beelen, A.J., Zelinkova, Z., Taanman-Kueter, E.W., Muller, F.J., Hommes, D.W., Zaat, S.A.J., Kapsenberg, M.L. and de Jong, E.C. Stimulation of the Intracellular Bacterial Sensor NOD2 Programs Dendritic Cells to Promote Interleukin-17 Production in Human Memory T Cells. *Immunity.* 2007, **27**(4), pp.660-669.
425. Sun, S.C. Non-canonical NF-κB signaling pathway. *Cell Research.* 2011, **21**(1), pp.71-85.
426. Verhasselt, V., Buelens, C., Willems, F., DeGroote, D., HaeffnerCavaillon, N. and Goldman, M. Bacterial lipopolysaccharide stimulates the production of cytokines and the expression of costimulatory molecules by human peripheral blood dendritic cells - Evidence for a soluble CD14-dependent pathway. *Journal of Immunology.* 1997, **158**(6), pp.2919-2925.
427. Schreibelt, G., Tel, J., Sliepen, K.H., Benitez-Ribas, D., Figdor, C.G., Adema, G.J. and de Vries, I.J. Toll-like receptor expression and function in human dendritic cell subsets: implications for dendritic cell-based anti-cancer immunotherapy. *Cancer Immunol Immunother.* 2010, **59**(10), pp.1573-1582.
428. Schweizer, A., Stahl, P.D. and Rohrer, J. A Di-aromatic Motif in the Cytosolic Tail of the Mannose Receptor Mediates Endosomal Sorting *. *Journal of Biological Chemistry.* 2000, **275**(38), pp.29694-29700.
429. Feinberg, H., Jégouzo, S.A.F., Lasanajak, Y., Smith, D.F., Drickamer, K., Weis, W.I. and Taylor, M.E. Structural analysis of carbohydrate binding by the macrophage mannose receptor CD206. *Journal of Biological Chemistry.* 2021, **296**.

430. Zhang, Q. and Reinhard, B.M. Ligand Density and Nanoparticle Clustering Cooperate in the Multivalent Amplification of Epidermal Growth Factor Receptor Activation. *ACS Nano.* 2018, **12**(10), pp.10473-10485.
431. Suto, N., Kamoshita, S., Hosoya, S. and Sakurai, K. Exploration of the Reactivity of Multivalent Electrophiles for Affinity Labeling: Sulfonyl Fluoride as a Highly Efficient and Selective Label. *Angewandte Chemie-International Edition.* 2021, **60**(31), pp.17080-17087.
432. Sakurai, K., Kato, A. and Adachi, K. Design and synthesis of small molecule-conjugated photoaffinity nanoprobes for a streamlined analysis of binding proteins. *Bioorganic & Medicinal Chemistry Letters.* 2018, **28**(19), pp.3227-3230.
433. Sakurai, K., Hatai, Y. and Okada, A. Gold nanoparticle-based multivalent carbohydrate probes: selective photoaffinity labeling of carbohydrate-binding proteins. *Chemical Science.* 2016, **7**(1), pp.702-706.
434. Schenone, M., Dančík, V., Wagner, B.K. and Clemons, P.A. Target identification and mechanism of action in chemical biology and drug discovery. *Nature Chemical Biology.* 2013, **9**(4), pp.232-240.
435. Swinney, D.C. and Anthony, J. How were new medicines discovered? *Nature Reviews Drug Discovery.* 2011, **10**(7), pp.507-519.
436. Ziegler, S., Pries, V., Hedberg, C. and Waldmann, H. Target Identification for Small Bioactive Molecules: Finding the Needle in the Haystack. *Angewandte Chemie International Edition.* 2013, **52**(10), pp.2744-2792.
437. Li, S., Wang, N., Yu, B., Sun, W. and Wang, L. Genetically encoded chemical crosslinking of carbohydrate. *Nature Chemistry.* 2023, **15**(1), pp.33-42.
438. Burdine, L. and Kodadek, T. Target Identification in Chemical Genetics: The (Often) Missing Link. *Chemistry & Biology.* 2004, **11**(5), pp.593-597.
439. Shiraiwa, K., Cheng, R., Nonaka, H., Tamura, T. and Hamachi, I. Chemical Tools for Endogenous Protein Labeling and Profiling. *Cell Chemical Biology.* 2020, **27**(8), pp.970-985.
440. Zheng, W., Li, G. and Li, X. Affinity purification in target identification: the specificity challenge. *Archives of Pharmacal Research.* 2015, **38**(9), pp.1661-1685.
441. Hashimoto, M. and Hatanaka, Y. Recent Progress in Diazirine-Based Photoaffinity Labeling. *European Journal of Organic Chemistry.* 2008, **2008**(15), pp.2513-2523.
442. Ge, S.-S., Chen, B., Wu, Y.-Y., Long, Q.-S., Zhao, Y.-L., Wang, P.-Y. and Yang, S. Current advances of carbene-mediated photoaffinity labeling in medicinal chemistry. *RSC Advances.* 2018, **8**(51), pp.29428-29454.
443. Shannon, D.A. and Weerapana, E. Covalent protein modification: the current landscape of residue-specific electrophiles. *Current Opinion in Chemical Biology.* 2015, **24**, pp.18-26.
444. Hayashi, T. and Hamachi, I. Traceless Affinity Labeling of Endogenous Proteins for Functional Analysis in Living Cells. *Accounts of Chemical Research.* 2012, **45**(9), pp.1460-1469.
445. Uttamchandani, M., Li, J., Sun, H. and Yao, S.Q. Activity-Based Protein Profiling: New Developments and Directions in Functional Proteomics. *ChemBioChem.* 2008, **9**(5), pp.667-675.
446. Benns, H.J., Wincott, C.J., Tate, E.W. and Child, M.A. Activity- and reactivity-based proteomics: Recent technological advances and applications in drug discovery. *Current Opinion in Chemical Biology.* 2021, **60**, pp.20-29.
447. Singh, J., Petter, R.C., Baillie, T.A. and Whitty, A. The resurgence of covalent drugs. *Nature Reviews Drug Discovery.* 2011, **10**(4), pp.307-317.
448. Yang, P.-Y., Liu, K., Ngai, M.H., Lear, M.J., Wenk, M.R. and Yao, S.Q. Activity-Based Proteome Profiling of Potential Cellular Targets of Orlistat − An FDA-Approved Drug with Anti-Tumor Activities. *Journal of the American Chemical Society.* 2010, **132**(2), pp.656-666.

449. Clulow, J.A., Storck, E.M., Lanyon-Hogg, T., Kalesh, K.A., Jones, L.H. and Tate, E.W. Competition-based, quantitative chemical proteomics in breast cancer cells identifies new target profiles for sulforaphane. *Chemical Communications.* 2017, **53**(37), pp.5182-5185.
450. Haedke, U., Küttler, E.V., Vosyka, O., Yang, Y. and Verhelst, S.H.L. Tuning probe selectivity for chemical proteomics applications. *Current Opinion in Chemical Biology.* 2013, **17**(1), pp.102-109.
451. Yang, B., Wu, H., Schnier, P.D., Liu, Y., Liu, J., Wang, N., DeGrado, W.F. and Wang, L. Proximity-enhanced SuFEx chemical cross-linker for specific and multitargeting cross-linking mass spectrometry. *Proceedings of the National Academy of Sciences.* 2018, **115**(44), pp.11162-11167.
452. Cao, L. and Wang, L. New covalent bonding ability for proteins. *Protein Science.* 2022, **31**(2), pp.312-322.
453. Keppler, A., Gendreizig, S., Gronemeyer, T., Pick, H., Vogel, H. and Johnsson, K. A general method for the covalent labeling of fusion proteins with small molecules in vivo. *Nature Biotechnology.* 2003, **21**(1), pp.86-89.
454. Sears, P. and Wong, C.-H. Carbohydrate Mimetics: A New Strategy for Tackling the Problem of Carbohydrate-Mediated Biological Recognition. *Angewandte Chemie International Edition.* 1999, **38**(16), pp.2300-2324.
455. Mori, K. and Sakurai, K. Clickable gold-nanoparticles as generic probe precursors for facile photoaffinity labeling application. *Organic & Biomolecular Chemistry.* 2021, **19**(6), pp.1268-1273.
456. Mendoza, V.L. and Vachet, R.W. Probing protein structure by amino acid-specific covalent labeling and mass spectrometry. *Mass Spectrometry Reviews.* 2009, **28**(5), pp.785-815.
457. Zhang, Z., Wu, S., Stenoien, D.L. and Paša-Tolić, L. High-Throughput Proteomics. *Annual Review of Analytical Chemistry.* 2014, **7**(Volume 7, 2014), pp.427-454.
458. Wang, N., Yang, B., Fu, C., Zhu, H., Zheng, F., Kobayashi, T., Liu, J., Li, S., Ma, C., Wang, P.G., Wang, Q. and Wang, L. Genetically Encoding Fluorosulfate-l-tyrosine To React with Lysine, Histidine, and Tyrosine via SuFEx in Proteins in Vivo. *Journal of the American Chemical Society.* 2018, **140**(15), pp.4995-4999.
459. Guo, Y., Sakonsinsiri, C., Nehlmeier, I., Fascione, M.A., Zhang, H.Y., Wang, W.L., Pohlmann, S., Turnbull, W.B. and Zhou, D.J. Compact, Polyvalent Mannose Quantum Dots as Sensitive, Ratiometric FRET Probes for Multivalent Protein-Ligand Interactions. *Angewandte Chemie-International Edition.* 2016, **55**(15), pp.4738-4742.
460. Sinitcyn, P., Richards, A.L., Weatheritt, R.J., Brademan, D.R., Marx, H., Shishkova, E., Meyer, J.A.-O., Hebert, A.S., Westphall, M.S., Blencowe, B.A.-O., Cox, J.A.-O.X. and Coon, J.A.-O. Global detection of human variants and isoforms by deep proteome sequencing. (1546-1696 (Electronic)).
461. Sun, S., Chong, K.S.L. and Leggett, G.J. Photopatterning of self-assembled monolayers at 244 nm and applications to the fabrication of functional microstructures and nanostructures. *Nanotechnology.* 2005, **16**(9), p.1798.
462. Patel, D.D., Lee, D.M., Kolbinger, F. and Antoni, C. Effect of IL-17A blockade with secukinumab in autoimmune diseases. *Annals of the Rheumatic Diseases.* 2013, **72**, pp.116-123.
463. Mei, Y., Pan F Fau - Gao, J., Gao J Fau - Ge, R., Ge R Fau - Duan, Z., Duan Z Fau - Zeng, Z., Zeng Z Fau - Liao, F., Liao F Fau - Xia, G., Xia G Fau - Wang, S., Wang S Fau - Xu, S., Xu S Fau - Xu, J., Xu J Fau - Zhang, L., Zhang L Fau - Ye, D. and Ye, D. Increased serum IL-17 and IL-23 in the patient with ankylosing spondylitis. (1434-9949 (Electronic)).